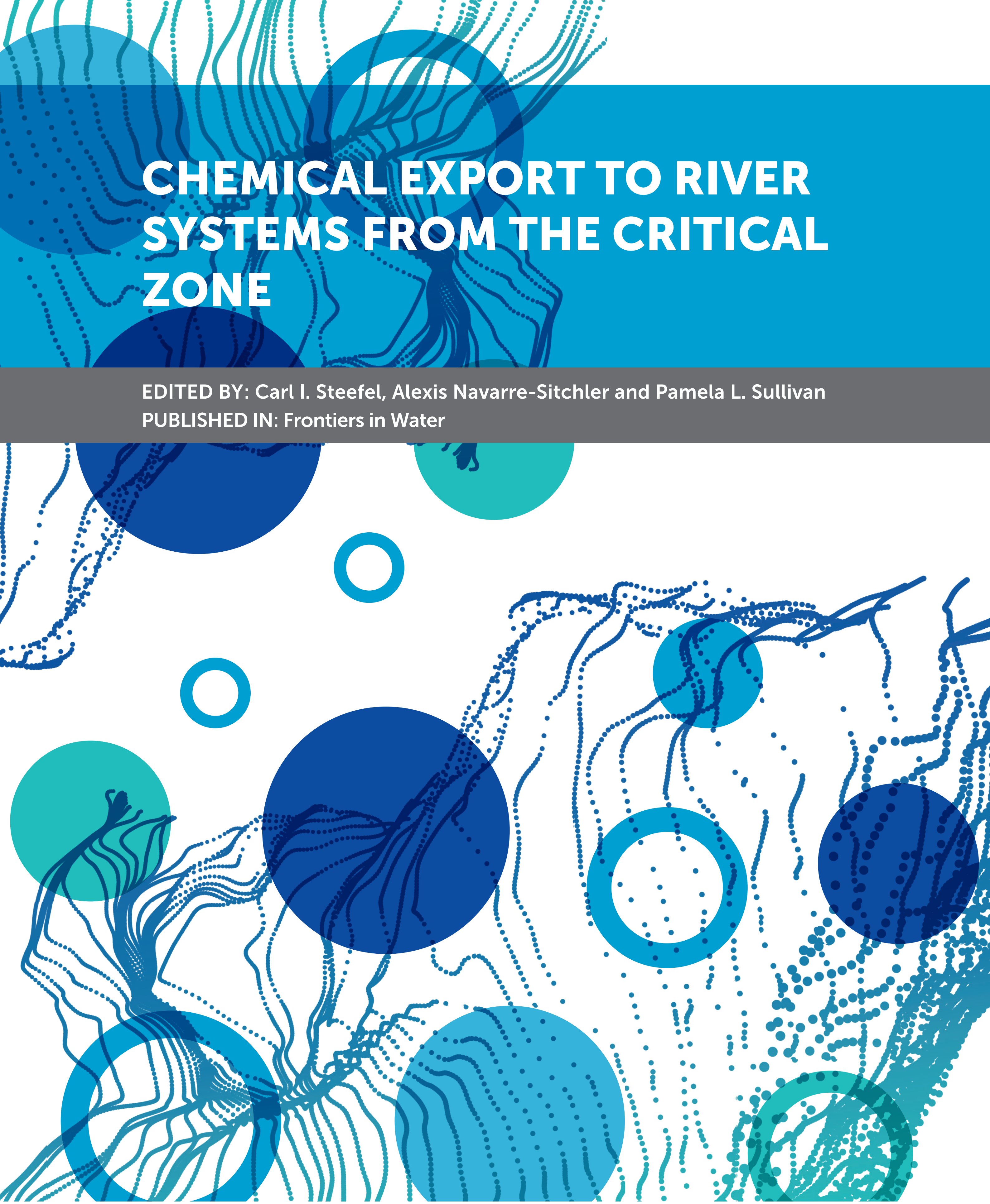

CHEMICAL EXPORT TO RIVER SYSTEMS FROM THE CRITICAL ZONE

EDITED BY: Carl I. Steefel, Alexis Navarre-Sitchler and Pamela L. Sullivan
PUBLISHED IN: Frontiers in Water

frontiers Research Topics

ISSN 1664-8714
ISBN 978-2-88971-734-7
DOI 10.3389/978-2-88971-734-7

About Frontiers

Frontiers is more than just an open-access publisher of scholarly articles: it is a pioneering approach to the world of academia, radically improving the way scholarly research is managed. The grand vision of Frontiers is a world where all people have an equal opportunity to seek, share and generate knowledge. Frontiers provides immediate and permanent online open access to all its publications, but this alone is not enough to realize our grand goals.

Frontiers Journal Series

The Frontiers Journal Series is a multi-tier and interdisciplinary set of open-access, online journals, promising a paradigm shift from the current review, selection and dissemination processes in academic publishing. All Frontiers journals are driven by researchers for researchers; therefore, they constitute a service to the scholarly community. At the same time, the Frontiers Journal Series operates on a revolutionary invention, the tiered publishing system, initially addressing specific communities of scholars, and gradually climbing up to broader public understanding, thus serving the interests of the lay society, too.

Dedication to Quality

Each Frontiers article is a landmark of the highest quality, thanks to genuinely collaborative interactions between authors and review editors, who include some of the world's best academicians. Research must be certified by peers before entering a stream of knowledge that may eventually reach the public - and shape society; therefore, Frontiers only applies the most rigorous and unbiased reviews.
Frontiers revolutionizes research publishing by freely delivering the most outstanding research, evaluated with no bias from both the academic and social point of view. By applying the most advanced information technologies, Frontiers is catapulting scholarly publishing into a new generation.

What are Frontiers Research Topics?

Frontiers Research Topics are very popular trademarks of the Frontiers Journals Series: they are collections of at least ten articles, all centered on a particular subject. With their unique mix of varied contributions from Original Research to Review Articles, Frontiers Research Topics unify the most influential researchers, the latest key findings and historical advances in a hot research area! Find out more on how to host your own Frontiers Research Topic or contribute to one as an author by contacting the Frontiers Editorial Office: frontiersin.org/about/contact

CHEMICAL EXPORT TO RIVER SYSTEMS FROM THE CRITICAL ZONE

Topic Editors:
Carl I. Steefel, Lawrence Berkeley National Laboratory, United States
Alexis Navarre-Sitchler, Colorado School of Mines, United States
Pamela L. Sullivan, Oregon State University, United States

Citation: Steefel, C. I., Navarre-Sitchler, A., Sullivan, P. L., eds. (2021). Chemical Export to River Systems from the Critical Zone. Lausanne: Frontiers Media SA. doi: 10.3389/978-2-88971-734-7

Table of Contents

frontiers in Water

EDITORIAL
published: 06 January 2022
doi: 10.3389/frwa.2021.826731

Editorial: Chemical Export to River Systems From the Critical Zone

Carl I. Steefel[1]*, *Alexis Navarre-Sitchler*[2] *and Pamela L. Sullivan*[3]

[1] *Energy Geosciences Division, Lawrence Berkeley National Laboratory, Berkeley, CA, United States,* [2] *Department of Geology and Geological Engineering, Colorado School of Mines, Golden, CO, United States,* [3] *College of Earth, Ocean, and Atmospheric Sciences, Oregon State University, Corvallis, OR, United States*

Keywords: chemical export, Critical Zone, weathering, rivers, watersheds

Editorial on the Research Topic

Chemical Export to River Systems From the Critical Zone

There is a growing recognition that the Critical Zone (CZ), extending from the vegetation canopy into soils and deeper permeable bedrock, is an important source of chemical constituents that make their way into river systems. In this regard, the Critical Zone exercises a primary control on water quality. Chemical fluxes to river systems may originate in soils, where various plant and carbon-mediated physical and biogeochemical processes are expected to dominate, or from weathering of bedrock (saprolite) in the shallow Critical Zone where rock forming minerals dissolve, to the deeper Critical Zone where flow paths with long travel times may produce more concentrated solutions high in metals, anions, and cations. All of these compartments within the Critical Zone export solutes to rivers within watersheds, and their relative contribution is expected to change due to seasonal and longer-term transients.

The export of chemical constituents to a river system requires hydrological gradients, which typically follow muted contours of the land surface. Relatively flat-lying terrain bordering a river system is expected to export water and solutes from shallow flow paths, while steeper terrain may result in export from both shallow and deeper flow paths. The topic of chemical export to river systems has created renewed interest into hillslope models, which historically have been primarily hydrological, but are now beginning to include chemical processes as well. Characterization of the hillslope environment in terms of geochemistry, plant distribution, and hydrological flow is now considered an important part of the study of chemical weathering, which previously focused primarily on purely vertical profiles (1D downward flow). Studies by Lebedeva and Brantley (2020) and Wan et al. (2021) provided the basis for a new conceptual model that places the chemical weathering front in the hillslope at the position of the water table, which moves up and down by about 2 m over the course of the year. In this case, the primary mineralogy of the shale undergoing weathering includes pyrite, which reacts with oxygen in the soil porewater to form sulfate and acidity that contribute further to the weathering process. Because oxygen diffuses 3–4 orders of magnitude faster in the unsaturated zone where a gas phase is present than it does in fully saturated media, the position of the water table becomes an important constraint on the location of any redox fronts that develop, if such exist. The rise and fall of the water table over the course of a year provides an additional transport mechanism for oxygen beyond pure diffusion (Yabusaki et al., 2017; Dwivedi et al., 2018; Lebedeva and Brantley, 2020; Wan et al., 2021).

OPEN ACCESS

Edited and reviewed by:
Jon Chorover,
University of Arizona, United States

****Correspondence:***
Carl I. Steefel
cisteefel@lbl.gov

Specialty section:
This article was submitted to
Water and Critical Zone,
a section of the journal
Frontiers in Water

Received: *01 December 2021*
Accepted: *06 December 2021*
Published: *06 January 2022*

Citation:
Steefel CI, Navarre-Sitchler A and Sullivan PL (2022) Editorial: Chemical Export to River Systems From the Critical Zone. Front. Water 3:826731.
doi: 10.3389/frwa.2021.826731

MODELING CHEMICAL EXPORT FROM CRITICAL ZONE

Most of the interest in modeling of chemical weathering has come from the role that it can play in the long-term regulation of atmospheric CO_2. This important effect has been known to geochemists for many years of course, but more recently has been "rediscovered" by those interested in engineering CO_2 uptake by weathering processes (so-called "negative emissions"). The earliest models for chemical weathering were one-dimensional (Lichtner and Waber, 1992; Soler and Lasaga, 1998), and perhaps because they appeared before the community was able to assimilate such modeling approaches, they quickly fell into the dustbins of Google Scholar. A more complete modeling study was built on a comprehensive weathering dataset from White and co-workers, and demonstrated that both present-day aqueous geochemical porewater and mineralogical profiles could be captured with a single model that required little adjustment of laboratory rate constants (Maher et al., 2009). At even smaller scales, Navarre-Sitchler et al. (2011) considered diffusion-controlled reactions in weathering basaltic andesite and showed that rates of weathering rind propagation could be captured with a single model that included porosity-permeability feedbacks between weathering reactions and diffusivity. For recent 2D hillslope modeling studies (see Dontsova et al., 2009; Gu et al., 2020; Lebedeva and Brantley, 2020; Xiao et al., 2021).

Flow and reactive transport processes not only govern the formation and evolution of reaction zones (or weathering fronts) in the Critical Zone, they also control the chemical export to the river system. One can speak of concentration-discharge or C-Q relationships within the hillslope environment itself, but these represent exports to the larger riverine system where C-Q relationships record the aggregated response of the watershed. In the study by Ackerer et al. (this volume), geomorphologic analysis, C-Q relations and reactive-transport modeling are used together with a rich dataset from an elevation gradient of eight watersheds in the Southern Sierra Nevada, California. The authors found that the CZ structure exerts a strong control on the C-Q relations, and on the hydrogeochemical behavior of headwater watersheds. Watersheds with thin regolith, a large stream network, and limited water storage have fast mean transit times along subsurface flow lines, and show limited seasonal variability in ionic concentrations in streamflow as a result (i.e., they demonstrate chemostatic behavior). In contrast, watersheds with thicker regolith, a smaller stream network, and more water storage have longer transit times along subsurface flow lines, and exhibit greater chemical variability (i.e., they show chemodynamic behavior). Note that in this pioneering study, the stream chemistry and its variability were controlled by lateral flow within the regolith, and no mixing with deep groundwater was needed to explain the observed chemical variability.

SOIL MOISTURE AND HYDROLOGIC CONNECTIVITY

In a contribution from Hermes et al. (this volume), the authors determine how the interacting drivers of precipitation and physical controls of the critical zone (CZ) dictate the spatial pattern and time evolution of soil water storage. The authors developed an analytical framework that combines intensive hydrologic measurements and extensive remotely-sensed observations with statistical modeling to identify areas with similar temporal trends in soil water storage focusing on 0.26 km^2 alpine catchment in the Colorado Rocky Mountains, U.S.A. Repeat measurements of soil moisture were used to drive an unsupervised clustering algorithm, which identified six unique groups of locations ranging from predominantly dry to persistently very wet, within the catchment. Following this unsupervised learning exercise, the authors used a supervised machine learning random forest algorithm to map each of the six hydrologic groups across the catchment based on distributed CZ properties and evaluated their aggregate relationships at the catchment scale. Their analysis indicated that ∼40–50% of the catchment is hydrologically connected to the stream channel. Their approach identifies a useful approach to categorizing patches within the landscape with similar hydrologic function, as well as the connectivity of these zones to the stream network.

EXPORT OF CARBON

Streams and rivers integrate and transport particulate organic carbon from a variety of aquatic and terrestrial sources. In the study by Blair et al. (this volume), a 3rd-4th order agricultural stream network was sampled at a nested series of stations through storm events to determine how suspended particulate organic carbon (POC) changes over time and with distance along the stream network. Carbon and nitrogen stable isotope ratios were used to identify changes in POC. A temporal sequence of inputs was identified: in-channel algal production prior to heavy precipitation, row crop surface soils mobilized during peak precipitation, and material associated with the peak hydrograph that is hypothesized to be an integrated product from upstream. Tile drains delivered relatively 13C- and 15N-depleted particulate organic carbon that represent a small contribution to the total POC inventory in the return to baseflow. The storm POC signal evolved with passage downstream, the principal transformation being the diminution of the early flush surface soil peak in response to a loss of connectivity between the hillslope and channel. Bank erosion is hypothesized to become increasingly important as the signal propagates downstream. The evolution of the POC signal along the length of the river system has implications for C-budgets associated with soil erosion, and ultimately for the interpretation of the organic geochemical sedimentary record.

A second study by Adler et al. (this volume) aims to understand and predict catchment responses of carbon to regional disturbances, an objective that is difficult because catchments represent spatially heterogeneous systems. The authors used a novel dataset that integrates regional and catchment-scale atmospheric deposition data, catchment characteristics, and co-located stream Q and stream chemistry data through a pattern-to-process approach. This approach is used to explore regional patterns of reduced acid deposition, catchment characteristics, and stream DOC response and specific soil processes at select locations. For pattern investigation, they quantified long-term trends of flow-adjusted DOC concentrations in stream water, along with wet deposition trends in sulfate and then compare trend results to catchment attributes. Their investigation of climatic, topographic and hydrologic catchment attributes vs. directionality of DOC trends suggests soil depth and catchment connectivity as possible modulating factors for DOC concentrations. Results from this work illustrate the value of an iterative process and pattern approach to understand catchment-scale response to regional disturbance.

TRACE ELEMENT AND ISOTOPE EXPORT

The Critical Zone is an important source of trace elements to headwater streams during the snowmelt runoff period, yet the mechanisms of trace element export are poorly known. To evaluate changes in water chemistry in response to snowmelt, Checketts et al. (this volume) measured trace element and major ion concentrations at three sites in the upper Provo River in northern Utah, USA over a 5–year period spanning years with below– and above–average discharge. Concentrations of specific trace metals (Be, Al, Cu, and Pb) and rare earth elements (represented by La and Y) increased during snowmelt runoff each year at all three sites, with decreasing concentrations from upstream to downstream. In contrast, major ion concentrations, including Ca^{2+} and SO_4^{2-}, remained relatively constant at the upper site and were diluted during snowmelt at the lower sites. The snowmelt runoff period accounted for >84% of the annual trace element loading, with most trace element inputs occurring above the upper sampling site. Trace element concentrations were relatively low in snowpack but elevated in ephemeral streams and soil water, suggesting that flushing of shallow soils by snowmelt causes increased trace element concentrations with positive C–Q relationships in the upper part of the river. Their results demonstrate that soil water flushing in the Critical Zone at the headwaters of mountain streams is an important control on downstream water chemistry.

In another study, Garcia et al. (this volume) found that in semi-arid to arid regions, both anthropogenic sources (urban and agriculture) and deeper Critical Zone (groundwater) may play an important role in controlling chemical exports to rivers. The authors combined two anthropogenic isotope tracers: uranium isotope ratios ($^{234}U/^{238}U$) and boron isotope ratios ($\delta^{11}B$), with the $^{87}Sr/^{86}Sr$ ratios to identify and quantify multiple solute (salinity) sources in the Rio Grande river in southern New Mexico and western Texas.

In another study, Moquet et al. (this volume) investigated cratonic environments that are characterized by strongly variable weathering rates. They studied the weathering rates in two inter-tropical river basins from the Atlantic Central Africa: the Ogooué and Mbei River basins, Gabon. Based on the determination of the major element sources they estimated that the Ogooué and Mbei rivers total dissolved solids (TDS) derive primarily from silicate chemical weathering. Chemical weathering rates span the entire range of chemical weathering intensities hitherto recorded in worldwide cratonic environments. In the Ogooué-Mbei systems, three regions can be distinguished: (i) the Eastern sub-basins underlain by quartz-rich sandstones exhibit the lowest weathering rates, (ii) the Northern sub-basins and the Mbei sub-basins, which drain the southern edge of the tectonically quiescent South Cameroon Plateau, show intermediate rates, and (iii) the Southern sub-basins characterized by steeper slopes record the highest weathering rates. In region (ii), higher DOC concentrations are associated with enrichment of elements, suggesting enhanced transport of these elements in the colloidal phase. The study points out that erosion of lateritic covers in cratonic areas can significantly enhance chemical weathering rates by bringing fresh minerals in contact with meteoric water.

METALS EXPORT

High concentrations of trace metal(loid)s exported from abandoned mine wastes and acid- rock drainage may pose a risk to the health of aquatic ecosystems. In a study by Hoagland et al. (this volume), the authors aim to determine if and when the hyporheic zone mediates metal(loid) export by investigating the relationship between streamflow, groundwater-stream connectivity, and subsurface metal(loid) concentrations in two ∼1 km stream reaches within the Bonita Peak Mining District near Silverton, Colorado, USA. The hyporheic zones of reaches in two streams—Mineral Creek and Cement Creek—were characterized using a combination of salt-tracer injection tests, transient-storage modeling, and geochemical sampling of the shallow streambed. Based on these data, the authors present two conceptual models for subsurface metal(loid) behavior in the hyporheic zones, including (1) well-connected systems characterized by strong hyporheic mixing of infiltrating stream water and upwelling groundwater and (2) poorly connected systems delineated by physical barriers that limit hyporheic mixing. Comparison of the conceptual models to stream concentration-discharge relationships indicated a clear link between geochemical processes occurring within the hyporheic zone of the well-connected system and export of particulate Al, Cu, Fe, and Mn, while the poorly connected system did not have a significant influence on metal concentration-discharge trends. Mineral Creek was an example of a hyporheic system that serves as a natural dissolved metal(loid) sink, while a poorly connected system such as Cement Creek may benefit more from subsurface remediation than surface-water treatment to mitigate metal export.

Dong et al. (this volume) further investigate the role of hyporheic zones as critical ecological links between terrestrial and aquatic systems where redox-sensitive metals (notably Fe and Mn) significantly impact nutrient cycling and water quality. The authors conducted batch incubation experiments and analyzed Fe K-edge extended X-ray absorption fine structure (EXAFS) spectroscopy data using sediment samples from a hyporheic zone of the East River floodplain in Colorado to understand the production, release and speciation of Fe(II) and Mn(II) in groundwater. The sediments with higher Fe(II) production rates did not necessarily result in higher export of dissolved Fe(II), since $\geq$ 97% Fe(II) is accumulated in solid phase. They found that most of the Fe(II) exists as siderite (FeCO3), Fe(II)-natural organic matter (NOM) complexes, and ferro-smectite.

In contrast, dissolved Mn(II) increases slowly and linearly in batch experiments, and an equilibrium concentration was not reached during the incubation period. This work reveals that siderite and dissolved NOM are the controlling phases in release and speciation of dissolved Fe(II), and the finding is expected to be applicable in many hyporheic zones and subsurface environments with similar geochemical conditions.

EXPORT IN KARST ENVIRONMENTS

In a study by Qin et al. (this volume) designed to explore hydrogeochemical sources, dynamics and their responses to rainstorms, rainwater, throughfall, hillslope runoff, surface water and groundwater were sampled during rainstorms at a karst Critical Zone Observatory (CZO) in southwest China. Results showed that the total dissolved solids (TDS) concentration in throughfall increased by about 30% relative to rainwater, but both throughfall and rainwater contributed little to TDS in surface water and groundwater compared with terrestrial sources. Hydrochemistry in surface water and groundwater were diluted by rainstorms, but typically displayed chemostatic responses. Ca^{2+} and Mg^{2+} dynamics were regulated primarily by carbonate and gypsum weathering along with sulfate-induced dedolomitization. The chemostatic behaviors of NO_3^-, Cl^-, and K^+ were related to agricultural activities. The heterogeneous permeability of epikarst (the skin of the karst) can affect the mixture of groundwater from different sources and flowing pathways, enabling hydrochemistry under different hydrogeological conditions to display quite different responses to rainstorms.

CONCLUDING REMARKS

The contributions in this special issue point to the emergence of a new field in coupled chemical and hydrological processes of importance to the Critical Zone and to the chemistry of river systems. Chemical weathering results in release of elements that can then be transported via flow to nearby river systems. The hillslope environment is critical here, since the topography provides the basis for the hydrological gradients driving flow to the riverine system. Ultimately, the chemistry of river systems can only be understood by tracing chemical and flow processes back to their origin in the watershed.

AUTHOR CONTRIBUTIONS

All authors listed have made a substantial, direct, and intellectual contribution to the work and approved it for publication.

FUNDING

CS was supported by the Watershed Function Science Focus Area and ExaSheds projects at Lawrence Berkeley National Laboratory funded by the U.S. Department of Energy, Office of Science, and Biological and Environmental Research under Contract No. DE-AC02-05CH11231. AN-S was supported in part by the National Science Foundation under Award 436 No. EAR-15540.

REFERENCES

Dontsova, K., Steefel, C. I., Desilets, S., Thompson, A., and Chorover, J. (2009). Solid phase evolution in the Biosphere 2 hillslope experiment as predicted by modeling of hydrologic and geochemical fluxes. *Hydrol. Earth Syst. Sci.* 13, 2273–2286. doi: 10.5194/hess-13-2273-2009

Dwivedi, D., Steefel, C. I., Arora, B., Newcomer, M., Moulton, J. D., Dafflon, B., et al. (2018). Geochemical exports to river from the intrameander hyporheic zone under transient hydrologic conditions: East River Mountainous Watershed, Colorado. *Water Res. Res.* 54, 8456–8477. doi: 10.1029/2018WR023377

Gu, X., Rempe, D. M., Dietrich, W. E., West, A. J., Lin, T.-C., Jin, L., et al. (2020). Chemical reactions, porosity, and microfracturing in shale during weathering: The effect of erosion rate. *Geochim. Cosmochim. Acta* 269, 63–100. doi: 10.1016/j.gca.2019.09.044

Lebedeva, M. I., and Brantley, S. L. (2020). Relating the depth of the water table to the depth of weathering. *Earth Surface Process. Landforms* 45, 2167–2178. doi: 10.1002/esp.4873

Lichtner, P. C., and Waber, N. (1992). Redox front geochemistry and weathering: theory with application to the Osamu Utsumi uranium mine, Pocos de Caldas, Brazil. *J. Geochem. Explorat.* 45, 521–564. doi: 10.1016/0375-6742(92)90138-X

Maher, K., Steefel, C. I., White, A. F., and Stonestrom, D. A. (2009). The role of reaction affinity and secondary minerals in regulating chemical weathering rates at the Santa Cruz Soil Chronosequence, California. *Geochim. Cosmochim. Acta* 73, 2804–2831. doi: 10.1016/j.gca.2009.01.030

Navarre-Sitchler, A., Steefel, C. I., Sak, P. B., and Brantley, S. L. (2011). A reactive transport model for weathering rind formation on basalt. *Geochim. Cosmochim. Acta* 75, 7644–7667. doi: 10.1016/j.gca.2011.09.033

Soler, J. M., and Lasaga, A. C. (1998). An advection-dispersion-reaction model of bauxite formation. *J. Hydrol.* 209, 311–330. doi: 10.1016/S0022-1694(98)00090-0

Wan, J., Tokunaga, T. K., Brown, W., Newman, A. W., Dong, W., Bill, M., et al. (2021). Bedrock weathering contributes to subsurface reactive nitrogen and nitrous oxide emissions. *Nat. Geosci.* 14, 217–224. doi: 10.1038/s41561-021-00717-0

Xiao, D., Brantley, S. L., and Li, L. (2021). Vertical connectivity regulates water transit time and chemical weathering at the hillslope scale. *Water Res. Res.* 57:e2020WR029207. doi: 10.1029/2020WR029207

Yabusaki, S. B., Wilkins, M. J., Fang, Y., Williams, K. H., Arora, B., Bargar, J., et al. (2017). Water table dynamics and biogeochemical cycling in a shallow, variably-saturated floodplain. *Environ. Sci. Technol.* 51, 3307–3317. doi: 10.1021/acs.est.6b04873

Conflict of Interest: The authors declare that the research was conducted in the absence of any commercial or financial relationships that could be construed as a potential conflict of interest.

frontiers in Water

ORIGINAL RESEARCH
published: 21 August 2020
doi: 10.3389/frwa.2020.00023

Determining How Critical Zone Structure Constrains Hydrogeochemical Behavior of Watersheds: Learning From an Elevation Gradient in California's Sierra Nevada

Julien Ackerer[1,2]*, *Carl Steefel*[2], *Fengjing Liu*[3], *Ryan Bart*[1], *Mohammad Safeeq*[1,4], *Anthony O'Geen*[5], *Carolyn Hunsaker*[6] and *Roger Bales*[1]

[1] Sierra Nevada Research Institute, University of California, Merced, Merced, CA, United States, [2] Lawrence Berkeley National Laboratory, Berkeley, CA, United States, [3] College of Forest Resources and Environmental Science, Michigan Technological University, Houghton, MI, United States, [4] Division of Agriculture and Natural Resources, University of California, Davis, Davis, CA, United States, [5] Department of Land, Air and Water Resources, University of California, Davis, Davis, CA, United States, [6] Pacific Southwest Research Station, United States Forest Service, Fresno, CA, United States

Edited by:
Kamini Singha,
Colorado School of Mines,
United States

Reviewed by:
Matthys Alois Dippenaar,
University of Pretoria, South Africa
Adam Wymore,
University of New Hampshire,
United States
Beth Hoagland,
Colorado School of Mines,
United States

***Correspondence:**
Julien Ackerer
julien.ackerer@orange.fr

Specialty section:
This article was submitted to
Water and Critical Zone,
a section of the journal
Frontiers in Water

Received: *23 March 2020*
Accepted: *14 July 2020*
Published: *21 August 2020*

Citation:
Ackerer J, Steefel C, Liu F, Bart R, Safeeq M, O'Geen A, Hunsaker C and Bales R (2020) Determining How Critical Zone Structure Constrains Hydrogeochemical Behavior of Watersheds: Learning From an Elevation Gradient in California's Sierra Nevada. Front. Water 2:23. doi: 10.3389/frwa.2020.00023

Concentration-discharge (C-Q) relations can provide insight into the dynamic behavior of the Critical Zone (CZ), as C-Q relations integrate the spatial distribution and timing of watershed hydrogeochemical processes. This study blends geomorphologic analysis, C-Q relations and reactive-transport modeling using a rich dataset from an elevation gradient of eight watersheds in the Southern Sierra Nevada, California. We found that the CZ structure exerts a strong control on the C-Q relations, and on the hydrogeochemical behavior of headwater watersheds. Watersheds with thin regolith, a large stream network, and limited water storage have fast mean transit times along subsurface flow lines, and show limited seasonal variability in ionic concentrations in streamflow (i.e., chemostatic behavior). In contrast, watersheds with thicker regolith, a small stream network and more water storage have longer transit times along subsurface flow lines, and exhibit greater chemical variability (i.e., chemodynamic behavior). Independent estimates of mean transit times and water storage from other isotopic, hydrologic and geophysical studies were consistent with results from modeling C-Q relations. The stream chemistry and its variability were controlled by lateral flow within the regolith, and no mixing with deep groundwater was needed to explain the observed chemical variability. This study opens the possibility to estimate water-storage capacity and mean transit times, and thus drought resistance in watersheds, by using quantitative modeling of C-Q relations.

Keywords: critical zone, hydrogeochemical modeling, elevation gradient, watershed, C-Q relation

INTRODUCTION

Improving our understanding of the critical zone (CZ), which is defined as the uppermost layer of Earth and is a key interface between the lithosphere, atmosphere, hydrosphere and biosphere, is important for predicting future soil and water societal issues. One of the most important questions in CZ science is what are the links and feedbacks between long-term CZ evolution (i.e., soil and regolith mineralogy, CZ structure and thickness) and the short-term hydrogeochemical behavior of watersheds (i.e., water availability, stream chemistry and water storage). This question is raised by the growing need for accurate estimates for water storage capacity and water transit times in watersheds, which are central to understanding water availability, water quality and drought responses (Hubbert et al., 2001; Bart and Hope, 2014; Safeeq and Hunsaker, 2016; Bales et al., 2018; Klos et al., 2018; O'Geen et al., 2018; Visser et al., 2019). How regolith structure and landscape evolution influence the hydrochemical behavior of watersheds depends on multiple physical, chemical and biological processes (Chorover et al., 2011; Ackerer et al., 2016; Reis and Brantley, 2019). Depicting how these processes are linked will depend on our ability to cross long-term monitoring efforts and the development of integrative modeling approaches (Steefel et al., 2015; Brantley et al., 2017; Li et al., 2017; Ackerer et al., 2018).

One promising approach to link CZ structure with the spatial distribution and timing of hydrogeochemical processes in watersheds is the quantitative interpretation of Concentration-Discharge (C-Q) relations (e.g., Godsey et al., 2009; Chorover et al., 2017; Moatar et al., 2017; Diamond and Cohen, 2018; Zhi et al., 2019). C-Q relations from stream water are acknowledged to aggregate a large number of processes, from climate, geochemical and ionic exchange reactions to hydrologic, biological and transport processes (Chorover et al., 2017). Recent reports show that C-Q relations can provide constraints on water flow paths along hillslopes (Ameli et al., 2017), mixing of different water end members in rivers (Liu et al., 2017; Torres et al., 2017) or seasonal variability of water transit times in headwater watersheds (Ackerer et al., 2018). There are ongoing debates around the extent to which C-Q relations are controlled by mixing between deep and shallow waters (Kim et al., 2017), synchronous dissolution of clay minerals (Li et al., 2017) and/or seasonally variable flow paths (Herndon et al., 2018).

Although C-Q relations have been intensively studied, few studies have coupled reactive-transport modeling, geomorphological investigations and regolith sciences to clearly assess what are the main CZ attributes that control the shapes of C-Q relations. Recent reports indicate that landscape heterogeneities are an important determinant of C-Q relations (e.g., Herndon et al., 2015; Musolff et al., 2015; Wymore et al., 2017; Sullivan et al., 2019). Understanding the specific roles of regolith thickness, bedrock geochemistry and watershed structures is an important new step to use C-Q relations to gain insight into water storage and water availability across landscapes. A detailed knowledge on how CZ structure controls the hydrogeochemical behavior of watersheds is also needed to anticipate the response of watersheds to perturbations from global warming, because this response will rely on regolith properties acquired through its long-term evolution (Bales et al., 2011; Safeeq et al., 2013; O'Geen et al., 2018).

The major objectives of the research reported here were to determine: (a) how the CZ structure constrains the hydrogeochemical behavior of watersheds, and (b) how the variability of bedrock geochemistry and regolith thickness can impact stream water chemistry, mean transit times and water storage in headwater watersheds. Our hypotheses were that the features of subsurface flow lines and stream networks, together with the regolith thickness, have a strong control on the stream water chemistry and hydrological behavior of watersheds. To evaluate these points, our work combines a detailed analysis of geomorphologic features, C-Q relations, and reactive-transport modeling in eight headwater watersheds along a unique elevation gradient in California's Sierra Nevada.

METHODS

Watershed Study Areas

This study focused on the Kings River Experimental Watersheds (KREW), an elevation gradient of watersheds characterized by different climates and geomorphologic features in the southern Sierra Nevada in California (37,068°N, 119,191°W; Goulden et al., 2012; Liu et al., 2013; Holbrook et al., 2014; Safeeq and Hunsaker, 2016; Hunsaker and Johnson, 2017; Bales et al., 2018; O'Geen et al., 2018). KREW is a long-term and integrated project for CZ research and is operated by the U.S. Forest Service, Pacific Southwest Research Station.

KREW includes eight watersheds, four in Providence site (P301, P303, P304, and D102) and four in Bull site (B201, B203, B204, and T003; **Figure 1**). The study area is underlain by the Sierra Nevada Batholith with bedrock dominated by Mesozoic granitoids and metamorphic rocks from granitic roof pendants (Lackey et al., 2012; Callahan et al., 2019). The Landscape is characterized by a sequence of range-parallel ridges and valleys, with alternating steep and gentle terrain (Holbrook et al., 2014). Providence is located east of a tread edge in an area with generally intermediate slopes (Jessup et al., 2011). Bull is located southeast of Providence, with erosion and soil formation rates that are generally slower than Providence (Callahan et al., 2019). More geological description of the region and additional chemical and mineralogical data are available from the US Geological Survey (Bateman and Lockwood, 1976; Bateman and Busacca, 1983).

The climate is mountainous and Mediterranean with long dry summers and the majority of precipitation falling in winter. Providence watersheds have mean elevations between 1782 and 1979 m (**Figure 1**), a mean annual temperature around 8°C and a mean annual precipitation of approximately 1015 mm.yr^{-1} (Safeeq and Hunsaker, 2016). The Providence group is located near the rain-snow transition zone (30–60% snow). Bull watersheds have mean elevations ranging from 2122 to 2373 m, a mean annual temperature around 7°C and a mean annual precipitation of approximately 1386 mm.yr^{-1}. Most of the winter precipitation falls as snow in the Bull watersheds (70–90%; Hunsaker and Johnson, 2017). Soils are relatively shallow (<1 m) Shaver and Cagwin soils and are all derived from granite

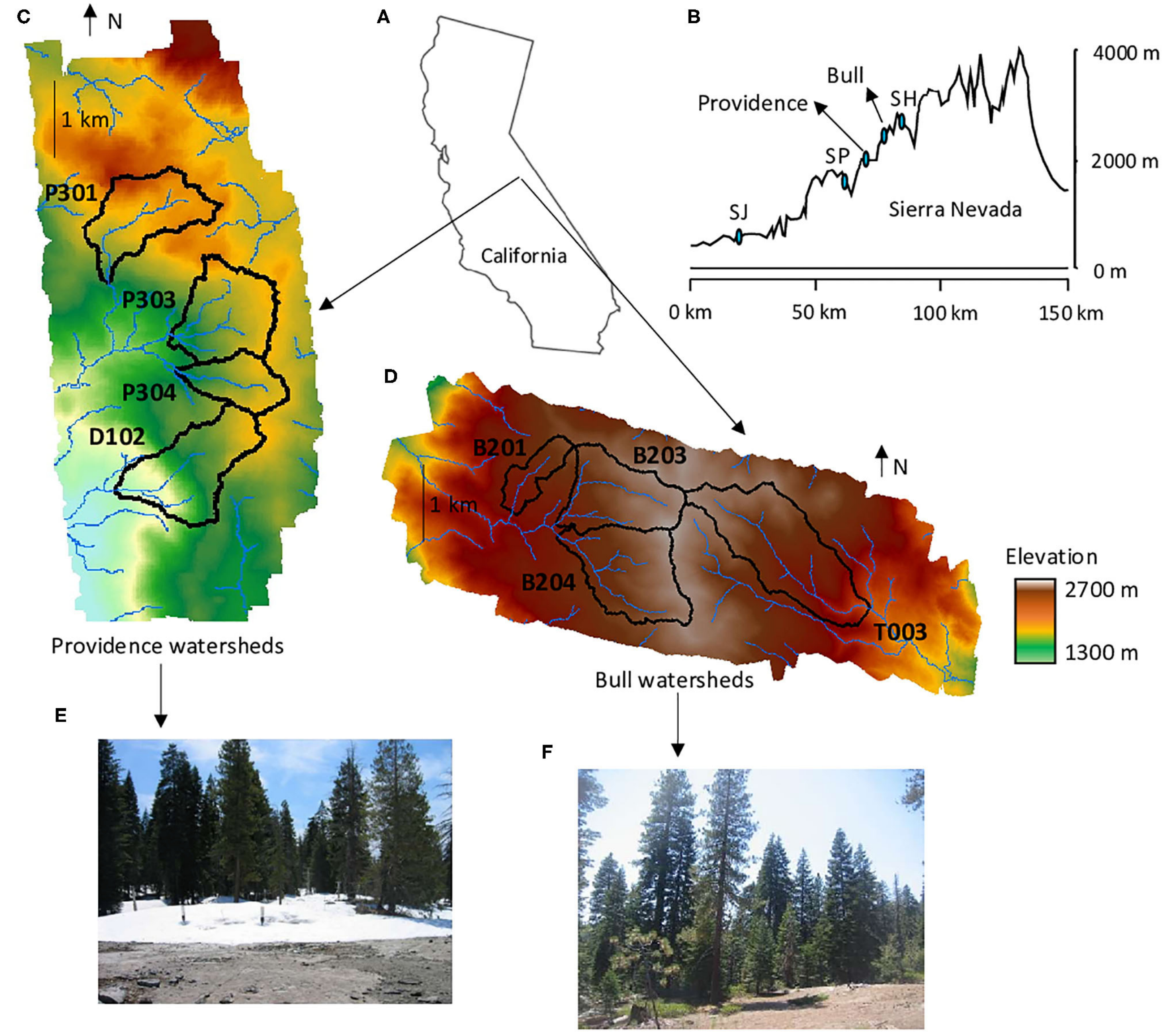

FIGURE 1 | (A) Providence and Bull watershed locations in California, USA. **(B)** West to East elevation transect from the San Joaquin valley over the Sierra Nevada, and showing SSCZO sites at the San Joaquin Experimental Range (SJ), Soaproot Saddle (SP) and Short Hair (SH). **(C)** Topographic map of the area including Providence watersheds: P301, P303, P304, and D102, **(D)** and of the area including Bull watersheds: B201, B203, B204, and T003. Topographic maps are derived from a 1m-resolution DEM. **(E)** Photo from Providence. **(F)** Photo from Bull.

(Johnson et al., 2011). Vegetation in Providence is dominated by Sierran mixed-conifer forest with some mixed chaparral and barren land cover (Bales et al., 2011; Safeeq and Hunsaker, 2016). Vegetation in Bull is predominately red fir forest with some mixed-conifer forest at lower elevations.

Data

This study is based on the long-term monitoring of the KREW and on the database from the Southern Sierra Critical Zone Observatory (SSCZO, Liu et al., 2013; Holbrook et al., 2014; Safeeq and Hunsaker, 2016; Hunsaker and Johnson, 2017; Bales et al., 2018). Recent efforts have been undertaken to characterize the CZ structure and regolith properties along the SSCZO elevation gradient (O'Geen et al., 2018; Tian et al., 2019).

A drilling campaign involving Geoprobe sampling was organized to better estimate the regolith thickness and its variability across the SSCZO (O'Geen et al., 2018). Measured regolith thicknesses indicated thin regolith (1–2 m) at low elevation (400 m, SJ site, **Figure 1B**) and at high elevation (2,700 m, SH site, **Figure 1B**). From 1,100 to 2,000 m, measured thicknesses were higher but tended to decrease with elevation, with mean values around 5–6 m at 1,100 m and around 2–3 m at 2,000 m (O'Geen et al., 2018). For the Providence and Bull watersheds (**Figure 1B**), regolith thickness was investigated in P301, P303, and D102 (1,700–2,000 m, 49 sampled sites), with mean thicknesses around 4–6 m.

Regolith density and porosity were estimated at several sites on samples collected during the Geoprobe campaigns (O'Geen et al., 2018). Mean regolith density was approximately 1.5–1.7 $g.cm^{-3}$ and mean regolith porosity was approximately 0.35–0.40 between 0 and 6 m of depth. Hydraulic conductivities at saturation (K_{sat}) were also measured on Geoprobe samples collected by O'Geen et al. (2018), and ranged from 0 to 7×10^{-5} $m.s^{-1}$. K_{sat} values were high for a few points near the surface

TABLE 1 | Geochemical and mineralogical data for the regolith of the KREW.

Oxide concentration[a]	**CaO**	**Na_2O**	**MgO**	**K_2O**	**SiO_2**	**Al_2O_3**	**Fe_2O_3**
Providence	4.35	2.52	2.56	2.42	62.45	17.75	6.37
Bull	0.56	0.91	0.59	2.66	81.25	10.58	2.66
Mass fraction[b]	**Quartz**	**Albite**	**K-feldspar**	**Biotite**	**Muscovite**	**Anorthite**	**Apatite**
Providence	30	32	6	15	6	10.5	0.5
Bull	52	19	9	10	4.5	5.3	0.2
Reactive surface[c]	**Quartz**	**Albite**	**K-feldspar**	**Biotite**	**Muscovite**	**Anorthite**	**Apatite**
Providence	15.5	3.2	0.7	3	0.6	3.2	0.005
Bull	23.3	1.9	0.9	2	0.5	1.6	0.002

[a] *Data presented are mean values from all the regolith samples collected in Providence and Bull watersheds. Regolith samples were collected from top soil to the bottom of regolith by soil pit, hand auger or geoprobe sampling campaigns. Concentrations have been determined by ICP-AES and are expressed in % of mass of oxides. Analytical uncertainties are 5% for concentrations.*

[b] *Mineral mass fractions have been determined by XRD analysis and are expressed in %. Analytical uncertainties are 10 % for mineral mass fractions.*

[c] *Geometric surfaces are used as reactive surfaces for reactive-transport modeling. Reactive surfaces are expressed in* $m^2.kg\ H_2O^{-1}$.

TABLE 2 | Main geomorphologic features and stream water chemistry data.

	Providence watersheds				**Bull watersheds**			
	P301	**P303**	**P304**	**D102**	**B201**	**B203**	**B204**	**T003**
GEOMORPHOLOGIC FEATURES[a]								
Area, km^2	0.97	1.04	0.55	1.17	0.46	1.40	1.65	2.29
Mean elevation, m	1979	1905	1899	1782	2257	2373	2365	2289
Mean slope, %	19	20	22	27	18	18	17	24
Relief, m	318	292	213	491	225	303	289	414
% of channel in meadows	16.4	0	8.9	2.5	92	28.6	61.7	22.9
Number of subsurface flow line	42	46	30	49	17	62	59	56
Cumulative subsurface flow line length, km	7.16	8.75	3.72	12.18	3.02	10.59	10.57	11.48
Mean subsurface flow line length, m	200	244	121	346	130	148	211	225
Standard deviation of flow line length, m	140	233	90	225	90	83	185	213
Cumulative stream network length, km	2.40	3.12	1.34	2.15	1.10	4.07	4.31	4.23
STREAM WATER[b]								
Base flow index, BFI, %	71.6	74.3	88.1	76.0	73.3	68.2	68.1	76.1
Mean annual water discharge, $L.s^{-1}$	34.1	45.5	13.7	32.6	23.3	83.1	74.2	82.6
Standard deviation of water discharge, $L.s^{-1}$	56.5	77.5	15.6	47.1	34.5	117.9	114.1	107.4
Mean Ca^{2+} concentration, $\mu mol.L^{-1}$	214	268	327	261	109	73	106	165
Mean Na^{+} concentration, $\mu mol.L^{-1}$	114	132	161	171	56	45	55	70
a_{Ca2+}	277	384	489	340	161	92	141	263
b_{Ca2+}	−0.117	−0.154	−0.196	−0.110	−0.195	−0.080	−0.095	−0.135

[a] *Geomorphologic features were determined using a 1-m resolution DEM and ArcGIS. Cumulative subsurface-flow-line and river-network lengths are given for average hydrologic conditions. BFI are from Safeeq and Hunsaker (2016).*

[b] *Stream chemistry data are from the 2003–2007 monitoring campaigns presented in Liu et al. (2013). The complete hydrogeochemical data are provided in Supplementary Material (**Table SM1**). The coefficients* a_{Ca2+} *and* b_{Ca2+} *were obtained by fitting a power law* $C = aQ^b$ *along the C-Q relations from the KREW stream waters (**Figure 3**).*

(7×10^{-5} m.s^{-1}), but much lower over the rest of the regolith column (0–8 $\times 10^{-6}$ m.s^{-1}). The mean value of K_{sat} was 6×10^{-6} m.s^{-1} for the entire regolith column.

Soil and regolith samples were also collected in the KREW for geochemical and mineralogical analysis from soil-pit, hand-auger and/or Geoprobe campaigns (Johnson et al., 2011; O'Geen et al., 2018; Tian et al., 2019). Sampling depth was between 0 and 2 m, with a few samples from Geoprobe campaigns reaching 10 m in Providence. Mineralogical composition of regolith samples was determined by the quantitative interpretation of X-ray analysis reported by Tian et al. (2019), following Ackerer et al. (2016). Elemental concentrations in bulk regolith samples were also determined by ICP-AES following Tian et al. (2019). Regolith geochemistry and mineralogy were significantly different between Providence and Bull. The granite from Providence showed higher contents of Biotite, Anorthite, Albite and higher concentrations of Ca and Mg compared to Bull (**Table 1**). Bull bedrock is a quartz-rich granite with higher concentrations of SiO_2 but lower concentrations of Ca and Mg than Providence. Abundances of K-feldspar (6–9%) and concentrations of K (2.42–2.66 %) were much more similar in the regolith of Providence and Bull watersheds (**Table 1**).

The SSCZO database on regolith geochemistry and mineralogy is supplemented by the hydrologic and geochemical monitoring of stream waters in the KREW (Liu et al., 2013; Safeeq and Hunsaker, 2016; Hunsaker and Johnson, 2017). Water discharge, pH, specific conductivity and solute concentrations of Na^+, Ca^{2+}, K^+, and Mg^{2+} were reported for the stream water at the KREW outlets for 2003–2007 (Liu et al., 2013). Mean annual water discharge, standard deviation of water discharge, and mean annual concentrations of Ca^{2+} and Na^+ are given in **Table 2**. The complete database for stream chemistry over the 2003–2007 period is available in Supplementary Materials (**Table SM1**). The hydroclimatic characteristics and other hydrologic signatures (e.g., base flow index) of the KREW have been reported by Safeeq and Hunsaker (2016).

Geomorphologic Features

A 1-m resolution digital elevation model (DEM) derived from a recent airborne Lidar survey was analyzed to better constrain the geomorphologic features of all watersheds (**Figure 1**). Watershed areas, elevations, slopes and reliefs were calculated (**Table 2**). Accumulated flow from up-slope contributing areas to each cell of the DEM was determined (ArcGIS) to map the hydrologic drainage networks (Storck et al., 1998; Liu et al., 2003). A flow-accumulation threshold of 2,000 m^2 was selected to capture the main hydrologic drainage network along slopes, and the same threshold was used to highlight the inter-watershed differences. Comparison with the topographic maps from the U.S. Geological Survey and with field observations was performed to evaluate the hydrologic drainage networks and to distinguish streams and subsurface drainage networks. The stream networks represent observed channelized streams that are directly connected with the watershed outlets. The subsurface drainage networks represent the hydrologic drainage along the slopes, following the main topographic depressions, but where streams are not observed. Subsurface drainage networks connect with stream networks on the valley floors.

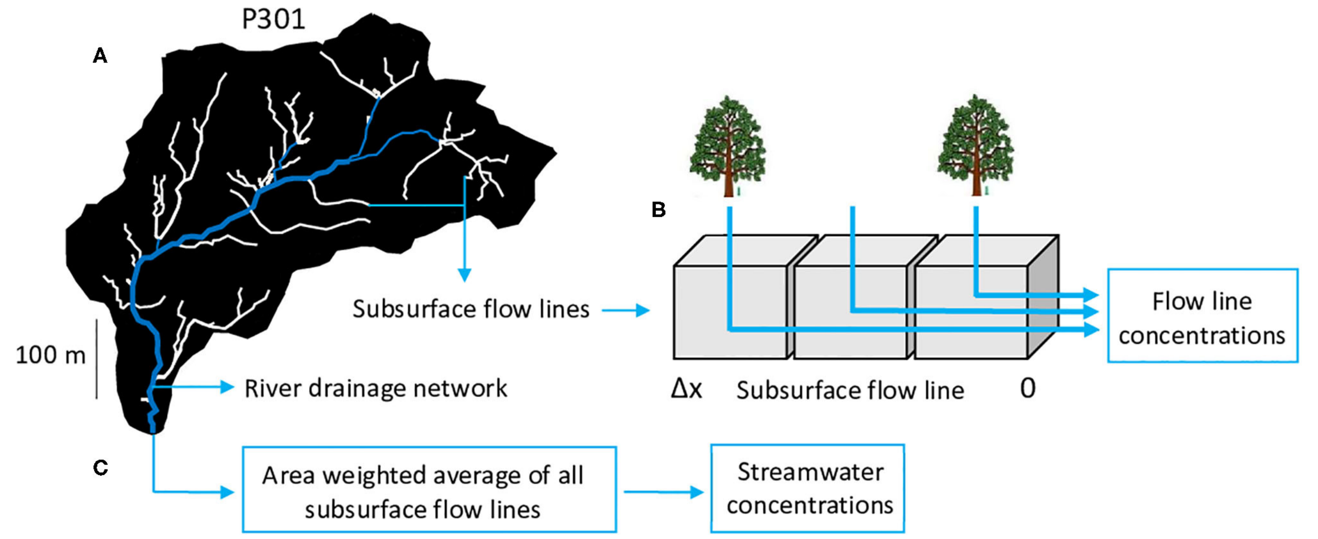

FIGURE 2 | Conceptual scheme used in modeling ionic concentrations in streamwater for all watersheds. **(A)** River network (in blue) and subsurface flow lines (in white) are determined by geomorphologic analysis using a 1-m DEM. The river network collects water coming from the subsurface flow lines, and the water chemical composition is assumed unchanged during the fast transfer in the streams. **(B)** Reactive-transport modeling along the 1D subsurface flow lines in the watersheds. The regolith is horizontally discretized into a 1D succession of cells along the subsurface flow lines. Within each cell, the geochemical and transport equations are numerically solved using the KIRMAT hydrogeochemical code. Subsurface flow lines are assumed to deliver subsurface water to the stream once reaching the river network. Δx to 0 is the distance from stream along the subsurface flow lines. A single layer with depth-averaged regolith properties is used along the vertical direction. **(C)** Final streamwater concentrations are calculated by taking the average chemical compositions across all subsurface flow lines. This average is weighed by the drainage area of each subsurface flow line to consider that long flow lines carry more water than shorter ones.

C-Q Relations

C-Q relations were studied at the outlet of the KREW on the basis of the hydrologic and geochemical database of stream waters. Concentration-discharge relations were interpreted by fitting power laws of type $C = aQ^b$ (e.g., Godsey et al., 2009; Chorover et al., 2017; Kim et al., 2017; Liu et al., 2017), with C the solute concentrations in stream waters (μmol.L^{-1}) and Q the stream discharges at watershed outlets (L.s^{-1}). Linear scales were preferred to better visualize the contrasting behavior of watersheds during dry periods. The *a* coefficient of the power law $C = aQ^b$ controls the height of the C-Q relation (y-intercept, the constant in the power law equation), and has a strong correlation with the mean annual concentrations of stream waters. The *b* coefficient controls the curvature of the C-Q relation (the exponent in the power law equation), and is an indicator of the degree of chemodynamic behavior of stream waters. We used the threshold $b = -0.1$ to distinguish chemostatic $(0 > b > -0.1)$ and chemodynamic watersheds $(-0.1 > b)$ as in Herndon et al. (2015) and Hunsaker and Johnson (2017).

To highlight the control of CZ structure on C-Q relations, we recommend working with a lithogenic solute sensitive to transit time variations along the subsurface flow lines: a solute with a strong Concentration-Mean Transit Time slope (C-MTT slope, Ackerer et al., 2020). The C-MTT slope considers the competition between primary mineral dissolution and incorporation into clay minerals, and indicates how fast a solute concentration rises with an increase of water transit time. A strong C-MTT slope facilitates the expression of CZ structure (e.g., length of subsurface flow paths, topography, watershed structure) on water chemical composition because stream water concentrations will be sensitive to physical attributes controlling water circulations in the watershed. In contrast, a solute with a low C-MTT slope may have stream water concentrations that are weakly responsive to the seasonal variability of transit times. In granitic watersheds, Ca^{2+} and H_4SiO_4 typically have strong C-MTT slopes, while K^+ and Mg^{2+} frequently show lower C-MTT slopes (Ackerer et al., 2020). We focused in this study on the detailed understanding of C-Q relations for Ca^{2+} as this ion has an extensive database, a strong C-MTT slope, and shows the most contrast in C-Q relations across the KREW. The *a* and *b* coefficients for Ca^{2+} are written a_{Ca2+} and b_{Ca2+} in the following sections.

The KIRMAT Reactive-Transport Code

Hydrogeochemical simulations were performed with the 1D thermo-kinetic code KIRMAT (KInectic of Reaction and MAss Transport; Gérard et al., 1998; Ngo et al., 2014; Lucas et al., 2017; Ackerer et al., 2018). KIRMAT is based on the Transition State Theory (TST) and solves the equations describing geochemical reactions and transport mass balance in a porous medium. Transport processes include the effects of convection, diffusion and kinematic dispersion. Chemical reactions account for the dissolution of primary minerals, oxido-reduction reactions, and the formation of secondary minerals and clay minerals. The clay fraction is defined in KIRMAT as a solid solution made up of a combination of pure clay end-members (Tardy and Fritz, 1981). The clay solid solution is precipitated at thermodynamic equilibrium and its composition varies over time depending on the water chemistry and the evolution of regolith mineralogy (Ackerer et al., 2018). The KIRMAT code also considers feedback effects between mineral mass budgets, reactive surfaces, and changes in bedrock porosity (Ngo et al., 2014). The framework of geochemical modeling with KIRMAT in granitic watersheds is available in Ackerer et al. (2018, 2020). More specific data on the geochemical modeling, kinetic and thermodynamic constants are available in **Tables SM2–SM5**.

Hydrogeochemical Modeling Strategy

The modeling strategy to consider the variability of the CZ structure over the KREW is adapted from Ackerer et al. (2018, 2020). Reactive-transport modeling was first performed on P301, as this reference watershed has the most extensive database and a high density of regolith-thickness measurements. Regolith mineralogy and geochemistry were constrained in P301 by the mineralogical and geochemical analysis (**Table 1**). Simple geometric surfaces are used as reactive surfaces for the dissolution reactions of primary minerals (**Table 1**). Estimates from Geoprobe campaigns of mean porosity (0.35) and mean hydraulic conductivity (6×10^{-6} m.s^{-1}) along the regolith column were used for all simulations. Slopes are known from the DEM, and the C-Q relations at the P301 outlet were constrained by the hydrochemical database (**Table 2**, **Table SM1**). Average saturated zone thickness is unknown over P301 but measurements of regolith thickness provide a maximum value.

TABLE 3 | Modeling results for the eight watersheds.

	Providence				Bull			
	P301	**P303**	**P304**	**D102**	**B201**	**B203**	**B204**	**T003**
MODELING RESULTS[a]								
Saturated thickness, m	4	4.5	7	4.5	6	3	3	4
RMSE (%)	6.5	8.0	4.9	7.2	5.4	12.8	11.2	9.1
Mean subsurface flow velocity, m.yr^{-1}	53	53	19	76	27	70	63	39
Mean stream water transit time, yr	4.1	5.7	7.6	5.1	4.9	2.8	3.5	6.5

[a] *Estimated saturated thicknesses are determined through hydrogeochemical modeling by fitting C-Q data. Root mean square errors are given for the fit of C-Q relations. Mean subsurface flow velocities are given for average hydrologic conditions and for simulations matching C-Q data. Mean subsurface water transit times are given for average hydrologic conditions and by combining subsurface flow line lengths and flow velocities.*

A schematic view of the modeling strategy is presented for P301 in **Figure 2**. Modeling was performed for a selection of dates covering the entire range of hydrologic conditions, from summer and fall dry periods to winter and spring floods. Dates were selected on the basis of stream discharges at the outlets by selecting days corresponding to 1, 10, 35, 50, and 100% of the maximum observed stream discharge. The selection is biased toward lower discharges because chemical concentrations vary dramatically at lower discharges, which dictates the C-Q power-law curvature. A set of simulations was done for each date. Reactive-transport simulations were performed along the subsurface drainage network identified by the geomorphologic analysis. For a given date and along each subsurface flow line, a 1D simulation with KIRMAT was performed to constrain the evolution of the subsurface water chemistry (**Figure 2**). Soil solutions were used as input solutions percolating into the regolith (**Figure 2B**, chemical data from Liu et al., 2013). Flow velocities along the subsurface flow lines were estimated using the ArcGIS groundwater toolset. Flow velocities were controlled by slopes, porosity, hydraulic conductivity and saturated thickness. These parameters were generated from the KREW database, except the saturated zone thicknesses, which was adjusted by a Monte-Carlo approach to obtain the best fit between modeled and measured C-Q relations at the P301 outlet. The fits were quantified using the root mean square error (RMSE, **Table 3**) and the mean value of regolith thickness on P301 was used as a maximum boundary.

The modeled C-Q relations were determined as follows. The simulated concentrations in the stream at a watershed's outlet were calculated by taking the landscape surface-area-weighted average of concentrations from all the subsurface flow lines (**Figure 2**). The simulated stream discharge was calculated by

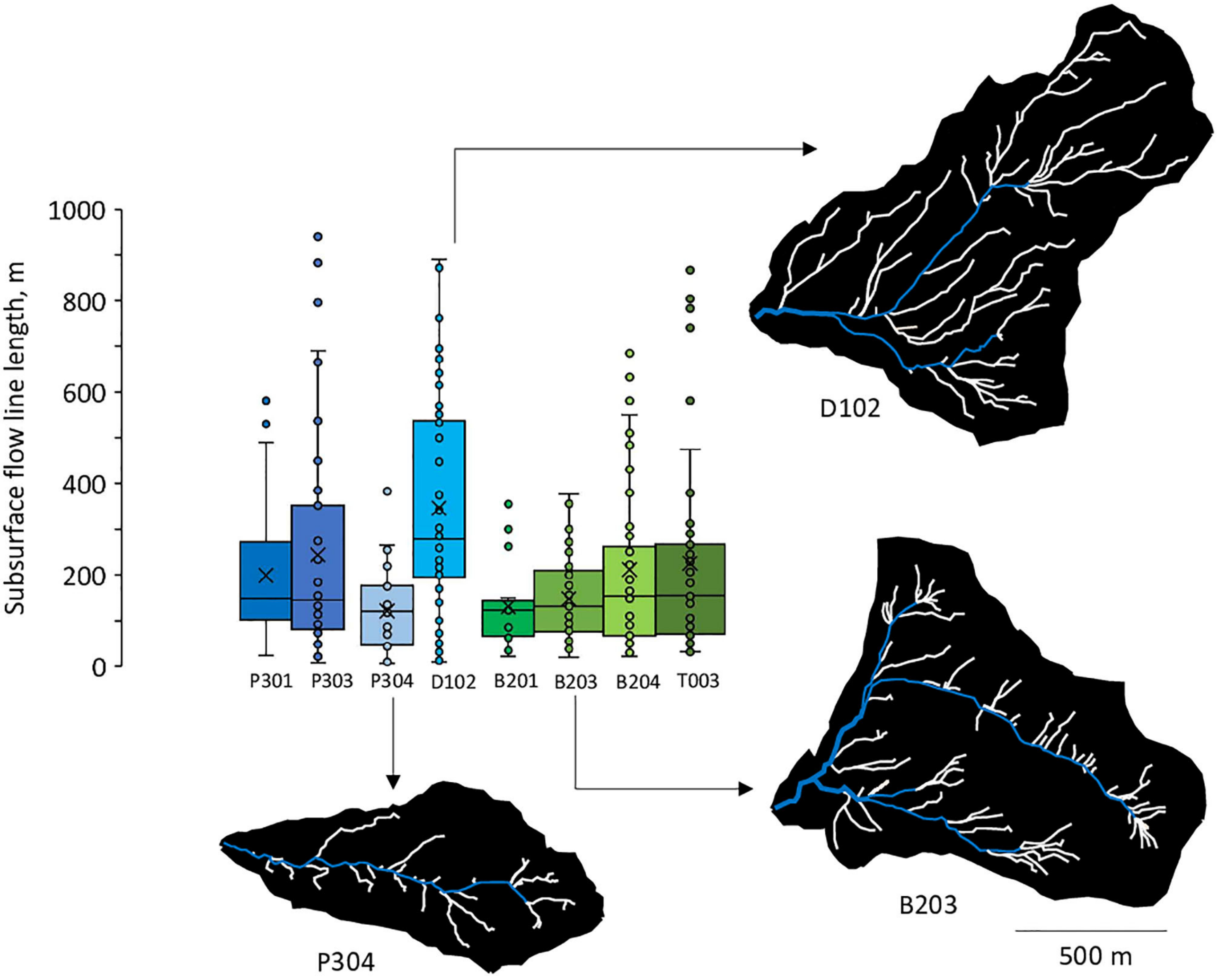

FIGURE 3 | Distribution of the subsurface flow line lengths. Boxes, crosses, vertical lines and points represent interquartile ranges, mean values, variability outside the interquartile ranges and outliers, respectively. The distribution is shown for average hydrologic conditions. River network (in blue) and subsurface flow lines (in white) were determined by the geomorphological study and the delineation of a 1-m DEM. Illustrations are provided for three watersheds: P304, D102, and B203.

summing the water discharges over all the subsurface flow lines. This sum was also landscape surface-area weighted to consider that longer subsurface flow lines draining large areas carry more water than shorter flow lines. Water transit times were calculated along each subsurface flow line by combining lengths of subsurface flow lines and subsurface flow velocities. The mean transit time for stream water was determined by taking the surface-area-weighted average of transit times from all subsurface flow lines.

Our depth-integrated, reactive-transport modeling was performed within a single regolith layer with averaged mineralogical, geochemical and physical properties. It is assumed that the subsurface waters are delivered to stream once the subsurface flow lines reach the stream network. Chemical composition of stream water is also assumed to remain unchanged during the fast transfer within the stream network. This assumption is supported by the short length of the stream network in this type of headwater watersheds (<1 km).

After the P301 watershed, this modeling strategy was extended to other seven watersheds. Differences in regolith mineralogy and chemical composition were considered for the Providence and the Bull groups (**Table 1**). Modeling also considers the variability of the geomorphologic features between the watersheds (**Table 2**). Regolith porosity and hydraulic conductivity measured in P301 were used for all the other watersheds. Modeled stream water concentrations and stream discharges were compared to measured values. The modeling of C-Q relations was used to estimate the saturated thicknesses over the watersheds where data on stream water and regolith are available but where regolith thicknesses are unknown (**Table 3**).

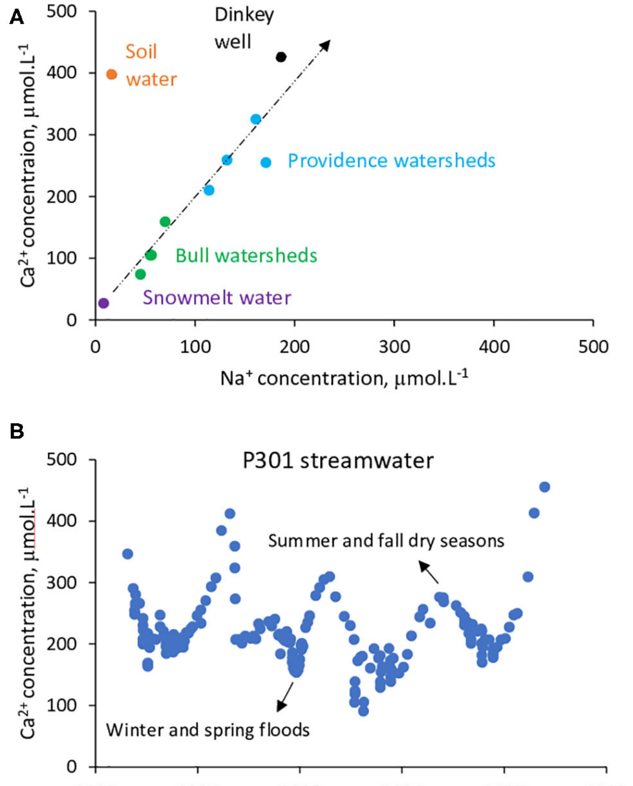

FIGURE 4 | Overview of the chemical variability for Providence and Bull stream waters. **(A)** Elemental Na^{+} – Ca^{2+} diagram with mean annual solute concentrations for Providence and Bull stream waters, snowmelt, soil water and Dinkey well groundwater (4 km from Providence). Data from Liu et al. (2013). **(B)** Seasonal variability of Ca^{2+} concentrations for P301 streamwaters. Data are shown for period studied (2003–2007).

RESULTS

Variability of CZ Structure

The watersheds show contrasting CZ structures and subsurface-flow line distributions along the elevation gradient (**Figure 3** and **Table 2**, **Figure SM1** in Supplementary Materials). P304 and B201 are the smallest watersheds (0.5 km^2), with limited stream networks (1.2 km), and a limited number of subsurface flow lines (20) characterized by compact length distributions around low values. T003 and B204 are the largest watersheds (2 km^2), with the longest stream networks (4.2 km), and a high number of subsurface flow lines (60) characterized by relatively scattered length distributions around intermediate values. P301, P303, and D102 are intermediate size watersheds (1 km^2), with intermediate stream networks (2.5 km), and a moderate number of subsurface flow lines (40). The standard deviation of the subsurface-flow-line lengths increases from P301 to P303 and D102. B203 is a relatively large watershed (1.7 km^2), with a large stream network (4 km), but a high number of subsurface flow lines (60) characterized by a compact length distribution around short value. These contrasting CZ structures imply different degrees of connectivity between the subsurface drainage networks and streams.

Hydrology and C-Q Relations

The watersheds are characterized by distinctive hydrogeochemical behaviors. Mean annual stream discharges are generally higher at Bull (B203, B204, T003), but stream discharges in these watersheds also show a higher annual variability with higher standard deviations (**Table 2**). B201 is an exception in the Bull group, with lower mean discharge and standard deviation. Providence watersheds have relatively low mean annual stream discharges, with P304 having the lowest discharge and standard deviation (**Table 2**). These trends in stream discharge are consistent with the base flow index (BFI) calculated over the KREW watersheds by Safeeq and Hunsaker (2016). The BFI is low for watersheds with a greater variability of discharge (B203, B204) and high for the watersheds with low and less variable discharges (B201, P304; **Table 2**).

Mean annual Ca^{2+} concentrations in stream water are lower in Bull compared to Providence watersheds (**Table 2** and **Figure 4A**). The mean ionic concentrations in stream waters in Providence and Bull span the range between those of snowmelt and deep groundwater (**Figure 4A**). The mean concentrations in soil water are outside of this trend. Concentrations in stream water also vary seasonally, as illustrated by Ca^{2+} concentrations on **Figure 4B**. Periods of higher discharge during winter and spring are typically characterized by lower concentrations, while values during summer and fall being frequently higher. The interannual variability of stream concentrations mainly follows climatic patterns, with higher concentrations in dry years and lower ones in wet years.

The diversity of CZ structures produces contrasting C-Q relations along the elevation gradient (**Figure 5** and **Figure SM4**). B203 and B204 show low *a* coefficient and chemostatic behavior (a_{Ca2+}= 92 to 141, $0>b_{Ca2+}>-0.1$ with b_{Ca2+}= −0.080 to −0.095) (**Figures 5F,G**). P301, P303, D102, and T003 show

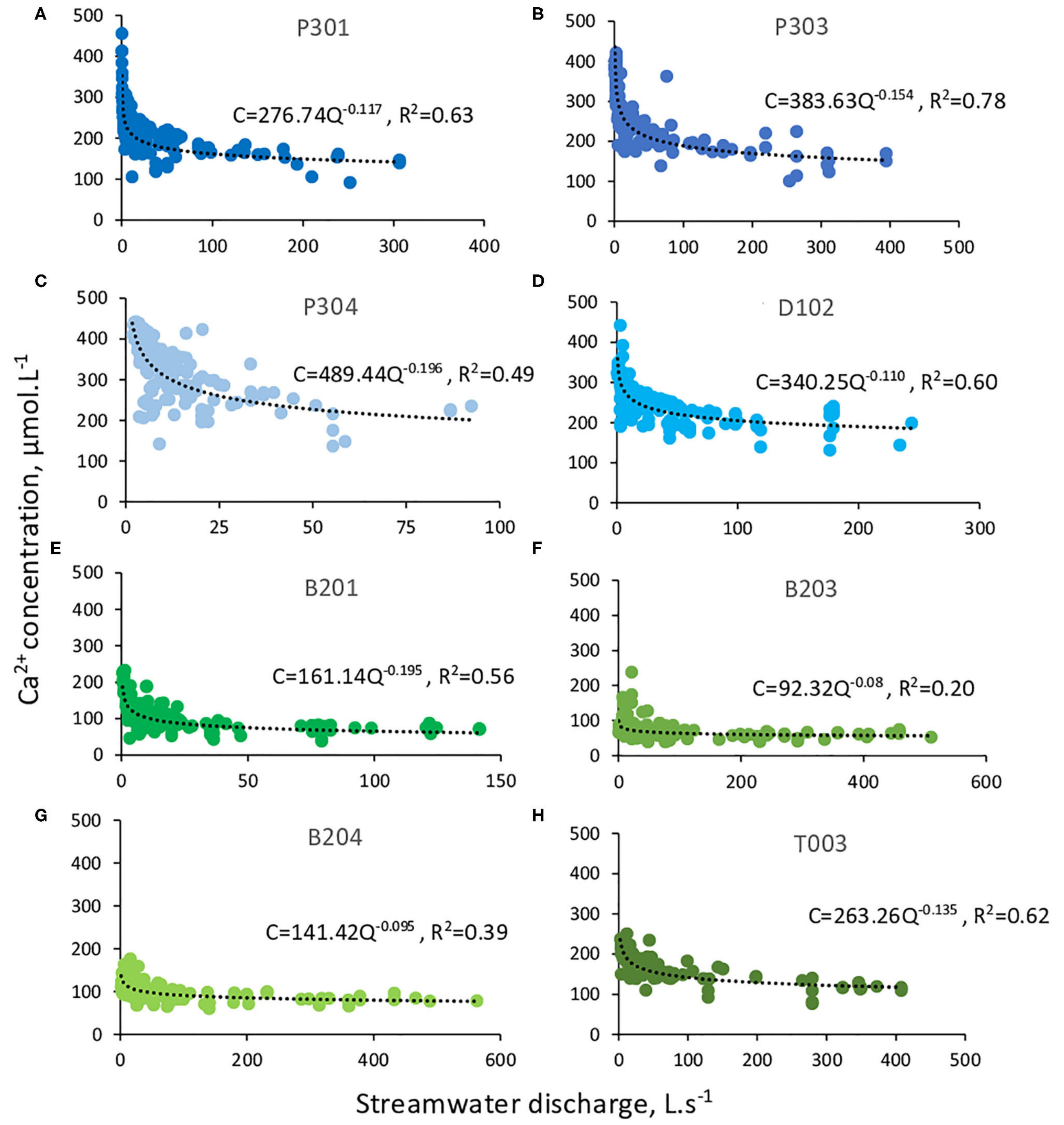

FIGURE 5 | (A–H) Ca^{2+} concentration-discharge relations for the eight watersheds. Each point represents a stream water sample. Power laws were fitted by using the expression $C = aQ^b$, with C the solute concentration in µmol.L^{-1}, Q the streamwater discharge in L.s^{-1}, a the coefficient determining the height of the law and b the coefficient setting the curvature of the law.

intermediate *a* coefficient and slightly chemodynamic behavior (a_{Ca2+} =277 to 384, $-0.1 > b_{Ca2+} > -0.16$ with $b_{Ca2+} = -0.110$ to -0.154) (**Figures 5A,B,D,H**). B201 and P304 are the most chemodynamic watersheds ($-0.1 > b_{Ca2+}$with $b_{Ca2+} = -0.195$ to -0.196) (**Figures 5C,E**), but B201 displays low *a* coefficient ($a_{Ca2+} = 161$), while P304 is characterized by high *a* coefficient ($a_{Ca2+} = 489$). Two extreme end members can be identified. P304 is the most chemodynamic, with also the highest *a* coefficient ($b_{Ca2+} = -0.196$, $a_{Ca2+} = 489$, **Table 2** and **Figure 5C**). In contrast, B203 is the most chemostatic, with also the lowest *a* coefficient ($b_{Ca2+} = -0.080$, $a_{Ca2+} = 92$, **Table 2** and **Figure 5F**). The combination of chemostatic behavior with high mean concentration is not observed in any of the watersheds. Although a different threshold for distinguishing chemostatic and chemodynamic behavior ($b_{Ca2+} = -0.1$) would slightly change the above classification, we highlight that we did not necessarily seek an absolute separation between watersheds classified as chemostatic or chemodynamic. Instead, our objective was to interpret the general trend of $b_{Ca2+}$and to propose a physical interpretation of this trend.

The a_{Ca2+} coefficient tends to decrease with increasing watershed elevation (**Figure 6A**), following the first-order difference of regolith geochemistry between the Providence and Bull groups (**Table 1**). The a_{Ca2+} coefficient is also strongly correlated with the base flow index (BFI) calculated over the watersheds (**Figure 6B**). In **Figure 6B**, Providence and Bull groups are shifted, with higher a_{Ca2+} values for Providence, but within each group the a_{Ca2+} coefficient clearly increases with BFI. The b_{Ca2+} coefficient shows correlations with cumulative subsurface-flow-line length and to a lesser extent with mean annual stream discharge (**Figures 6C,D**). Watersheds with lower values of cumulative subsurface flow line length and with both lower annual mean discharge and discharge variability are the most chemodynamic (P304 and B201, $b_{Ca2+} = -0.195$ to -0.196). Watersheds with higher values of cumulative subsurface flow line length and with both higher annual mean discharge and discharge variability are more chemostatic (B203 and B204, b_{Ca2+}=-0.080 to -0.095). No correlations were found between stream discharge, a_{Ca2+}, b_{Ca2+} and the meadow area (**Table 2**).

Modeling Results for the Reference Watershed P301

The best agreement between measured and modeled C-Q relations for the reference watershed P301 was obtained with a mean saturated thickness of 4 m (**Figure 7**). With a 4-m thickness both discharge and Ca^{2+} concentrations were correctly

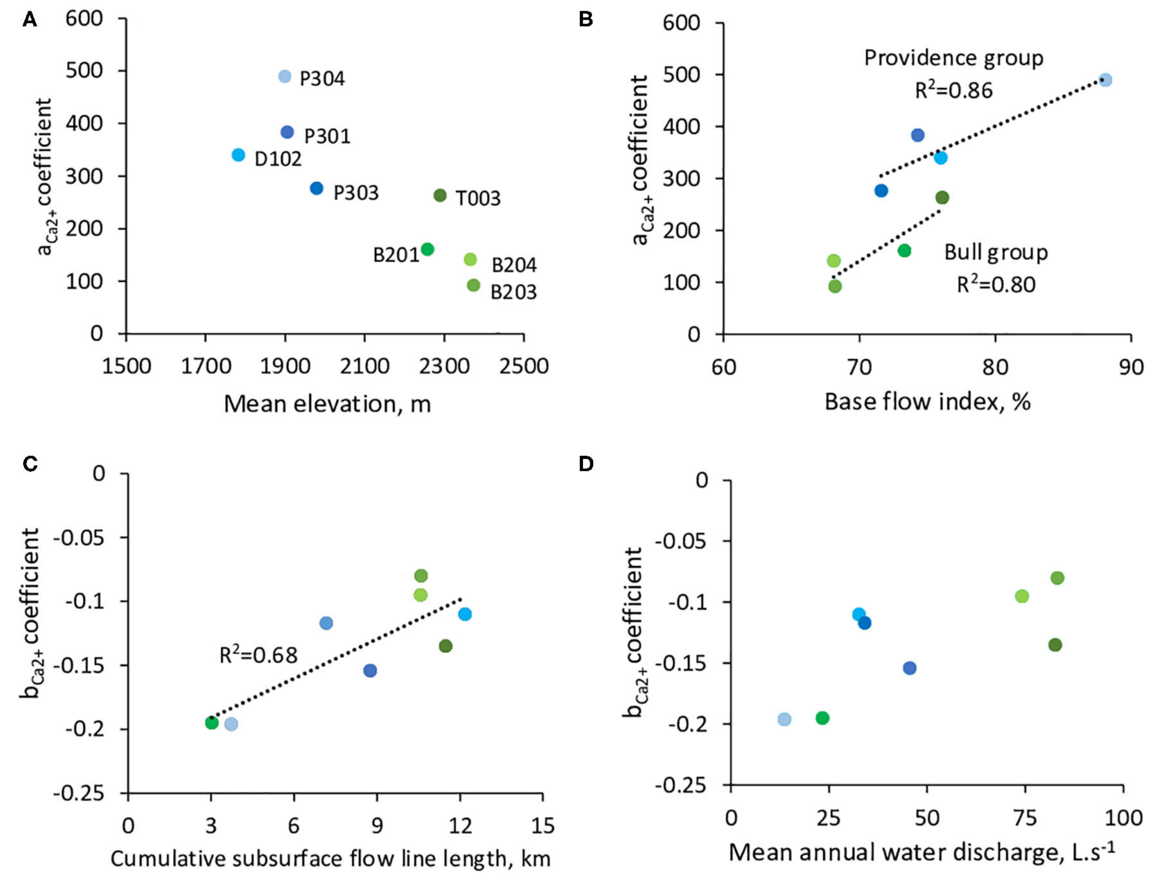

FIGURE 6 | Relations between C-Q shapes (a_{ca2+} and b_{ca2+} coefficients) and a selection of geomorphologic and hydrologic features for the KREW watersheds. **(A)** a_{ca2+} vs. mean watershed elevations (m). **(B)** Relationship between a_{ca2+} and the base flow index for the KREW watersheds. The values of base flow index are from Safeeq and Hunsaker (2016). **(C)** b_{ca2+} vs. cumulative length of the subsurface flow lines. **(D)** b_{ca2+} vs. mean annual water discharge from the streams at the outlets.

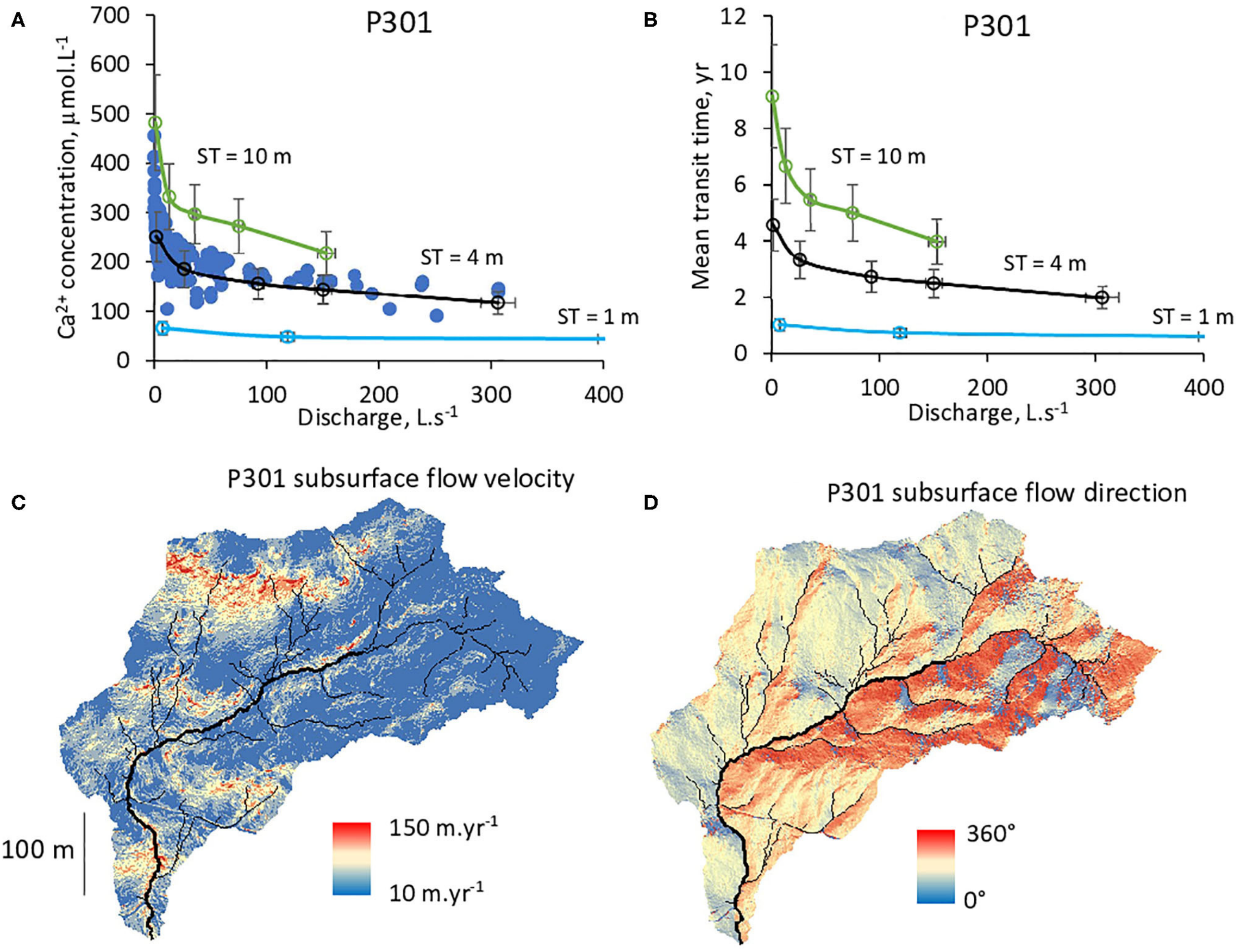

FIGURE 7 | Hydrogeochemical modeling of the P301 watershed. **(A)** C-Q diagram for Ca^{2+} and stream water. Dark blue points represent measured values. Green, black and light blue lines represent modeling results with saturated thicknesses (ST) of 10, 4, and 1 m, respectively. **(B)** Modeled mean transit times. **(C)** Map of subsurface flow velocity generated with a saturated thickness of 4 m. **(D)** Map of subsurface flow direct ion generated with a saturated thickness of 4 m.

captured at the P301 outlet (**Figure 7A**). Simulations with a thinner or thicker mean saturated thicknesses underestimate or overpredict Ca^{2+} concentrations, respectively. For illustration, simulations with a mean saturated thickness of 1 m produced faster subsurface flows, shorter transit times and underestimated the Ca^{2+} concentrations at the outlet (**Figures 7A,B**). In contrast, simulations with a mean saturated thickness of 10 m generated slower flows and longer transit times, but overpredict stream water Ca^{2+} concentrations (**Figures 7A,B**).

For the best fit with a saturated thickness of 4 m, the simulated subsurface flow velocities vary between 10 and 150 $m.yr^{-1}$ along the watershed's slopes (**Figure 7C**). Gentle parts (slope < 20 %) of the watershed have slower velocities while faster subsurface flows take place in the steep (slope >20 %) northern parts (**Figure 7C**). The calculated mean transit times for the stream waters range between 2 year for the wettest conditions and 5 year for the driest periods observed between 2003 and 2007 (**Figure 7B**). The average mean transit time over the 2003–2007 period for the P301 stream water is 4.1 year (**Table 3**).

Modeling Results for All Watersheds

The estimated values of mean saturated thicknesses that best match the C-Q relations vary between 3 and 7 m (**Table 3**). The thinnest mean saturated thicknesses (ST) are located in the higher-elevation B203 and B204 watersheds (3 m). T003, D102, P301, and P303 have intermediate values (4–5 m). The largest estimates of mean saturated thickness are in B201 and P304 (6–7 m). Mean subsurface flow velocities are between 27 and 76 $m.yr^{-1}$ (**Table 3**). Steep slopes (D102) and/or thin saturated thicknesses (B203) generate higher velocities (**Figure 8**), while watersheds with gentler slopes and thicker saturated thicknesses (B201, P304) have lower velocities (**Figure 8**, **Figure SM2** in Supplementary Materials).

The contrasting CZ structures and subsurface-drainage networks imply different distributions of mean transit times

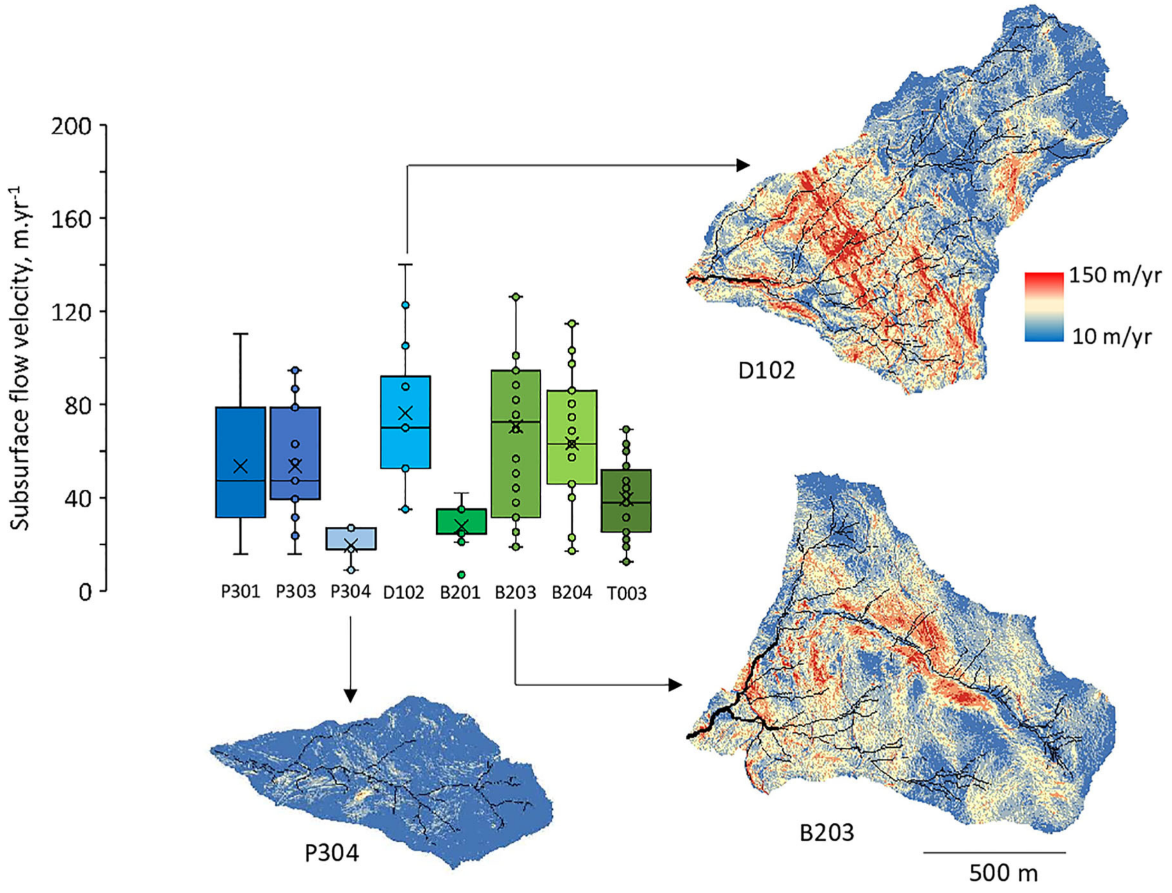

FIGURE 8 | Distribution of the simulated subsurface flow velocities along the flow lines. The distribution is shown for average hydrologic conditions. Illustrations are provided for three watersheds: P304, D102, and B203. The color scale is identical for all the watersheds to highlight the contrast between sites.

along the subsurface flow lines. Both velocities and flow line lengths control mean transit times. Shorter flow lines and faster velocities generate shorter transit times (**Figures 9**, **10**, i.e. B203 and B204). Watersheds with longer subsurface flow lines and/or slower velocities tend to have longer transit times (**Figures 9**, **10**, i.e., B201, T003 and P304, **Figure SM3** in Supplementary Materials). Estimated average mean transit times range from 2.8 year (B203) to 7.6 year (P304, **Table 3**). The simulated C-Q relations and mean transit times for all the KREW are given in **Figure 10**. Simulations capture the observed C-Q relations for the watersheds.

A strong negative correlation is observed between b_{Ca2+} and the estimated saturated thicknesses ($R^2 = 0.86$, **Figure 11A**). Watersheds with thin saturated thicknesses are the most chemostatic (B203 and B204, ST = 3 m, $b_{Ca2+} = -0.080$ to -0.095), while watersheds with thicker saturated thicknesses are more chemodynamic (B201 and P304, ST=6 to 7 m, $b_{Ca2+}= -0.195$ to -0.196). A good correlation is also found between the calculated mean transit times of stream water and BFI (**Figure 11B**). The watersheds with a higher proportion of base flows are consistently characterized by longer mean transit times.

DISCUSSION

Sensitivity Tests and Model Uncertainties

Multiple tests and simulations were performed to evaluate the sensitivity of the model to data uncertainties. This exercise allows to estimate how the uncertainties from regolith properties could impact model results and simulated C-Q relations. The first set of simulations was performed to estimate the impact of analytical uncertainties in regolith mineralogy on ionic concentrations in stream water. Increasing the mass fraction of Ca-bearing minerals by 10% while keeping other parameters constant increases the Ca^{2+} concentrations in P301 stream water by approximately 6%. The a_{Ca2+} coefficient of the simulated C-Q relation increases by 6%, while the b_{Ca2+} coefficient increases only by 1%. Thus, the simulated C-Q relation is affected by the mineralogical variations primarily though changes in the height of the C-Q relation (a_{Ca2+}). Simulated mean transit times are not impacted by mineralogical variations.

We also tested the impact of uncertainties in soil-solution composition on simulated stream water concentrations. An increase of 1% of Ca^{2+} concentration in soil solutions has a negligible impact on mean Ca^{2+} concentrations in stream

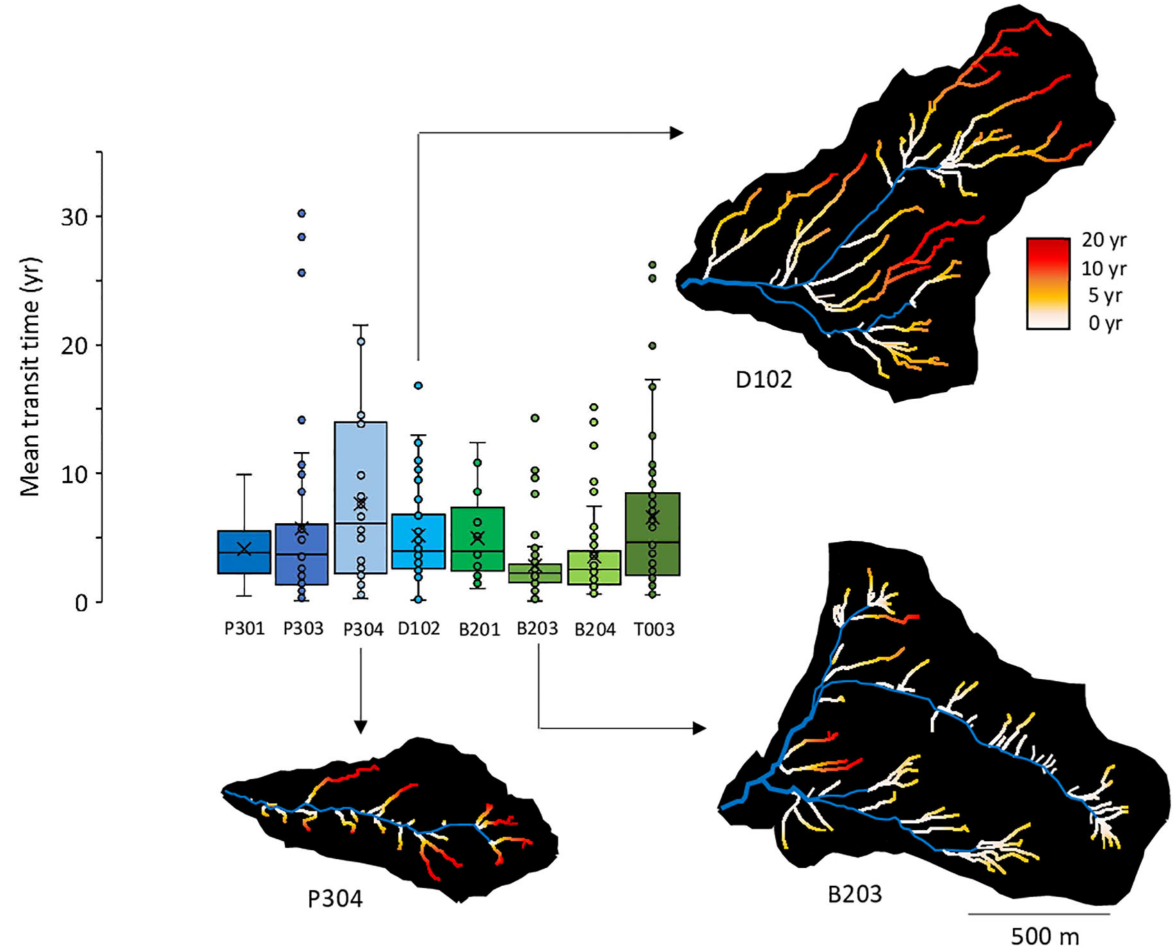

FIGURE 9 | Distribution of the simulated mean transit times along the subsurface flow lines. The distribution is shown for average hydrologic conditions. Mean transit times were calculated by combining subsurface flow line lengths and flow velocities. Illustrations are provided for three watersheds: P304, D102, and B203. The color scale is identical for all the watersheds to highlight the contrast between sites.

waters and a_{Ca2+} (variations of 0.5%). The coefficient b_{Ca2+} is insensitive to variations of soil solution concentrations. Variations of the soil solution pH from 6 to 6.5 modify a_{Ca2+} by 1–8 % but have no effects on b_{Ca2+}. The modeled chemodynamic behavior is therefore not very sensitive to chemical compositions of soil solutions used as input solutions into the regolith. Simulated mean transit times are not impacted by soil-solution variations.

The model sensitivity to variations of regolith porosity and hydraulic conductivity at saturation (K_{sat}) has been also explored. a_{Ca2+} is affected by variations of porosity, with a 5–20% increase associated with 5–30% increase in porosity. b_{Ca2+} only weakly responds by 1–2%, and the mean transit times are not impacted by porosity variation alone. Our sensitivity analysis reveals that hydraulic conductivity is a key parameter for the modeling of C-Q relations. Both a_{Ca2+} and b_{Ca2+} are sensitive to modifications of K_{sat}. Increasing K_{sat} by 5–30% decreases a_{Ca2+} by 6–20% and decreases b_{Ca2+} by 3–6%. Mean transit times inferred from the modeling are also sensitive to K_{sat}, with transit times decreasing by 5–30% when K_{sat} increases by 5–30%. Relying on field measurements of K_{sat} as well as porosity and regolith mineralogical characterization is therefore important for accurate modeling of C-Q relations.

Comparison With Independent Estimates

Modeling results can be compared with independent estimates from field campaigns, geophysical sampling and results from isotopic studies. In a recent study, cosmogenic isotopes in stream water (tritium, sodium-22 and sulfur-35) were combined with the modeling of age-ranked storage selection to estimate water ages for the P301 stream (Visser et al., 2019). They found the mean age of stream water for 2004–2016 was 4.4 year. The value for 2003–2007 was 4.5 year, which was similar to the 4.1 year estimate of mean transit time our study computed from hydrogeochemical modeling over the same period (**Table 3**).

On the basis of age-ranked storage-selection modeling, Visser et al. (2019) also found that the regolith of P301 averaged 3 m of water in storage, varying between 2.7 m for dry years and

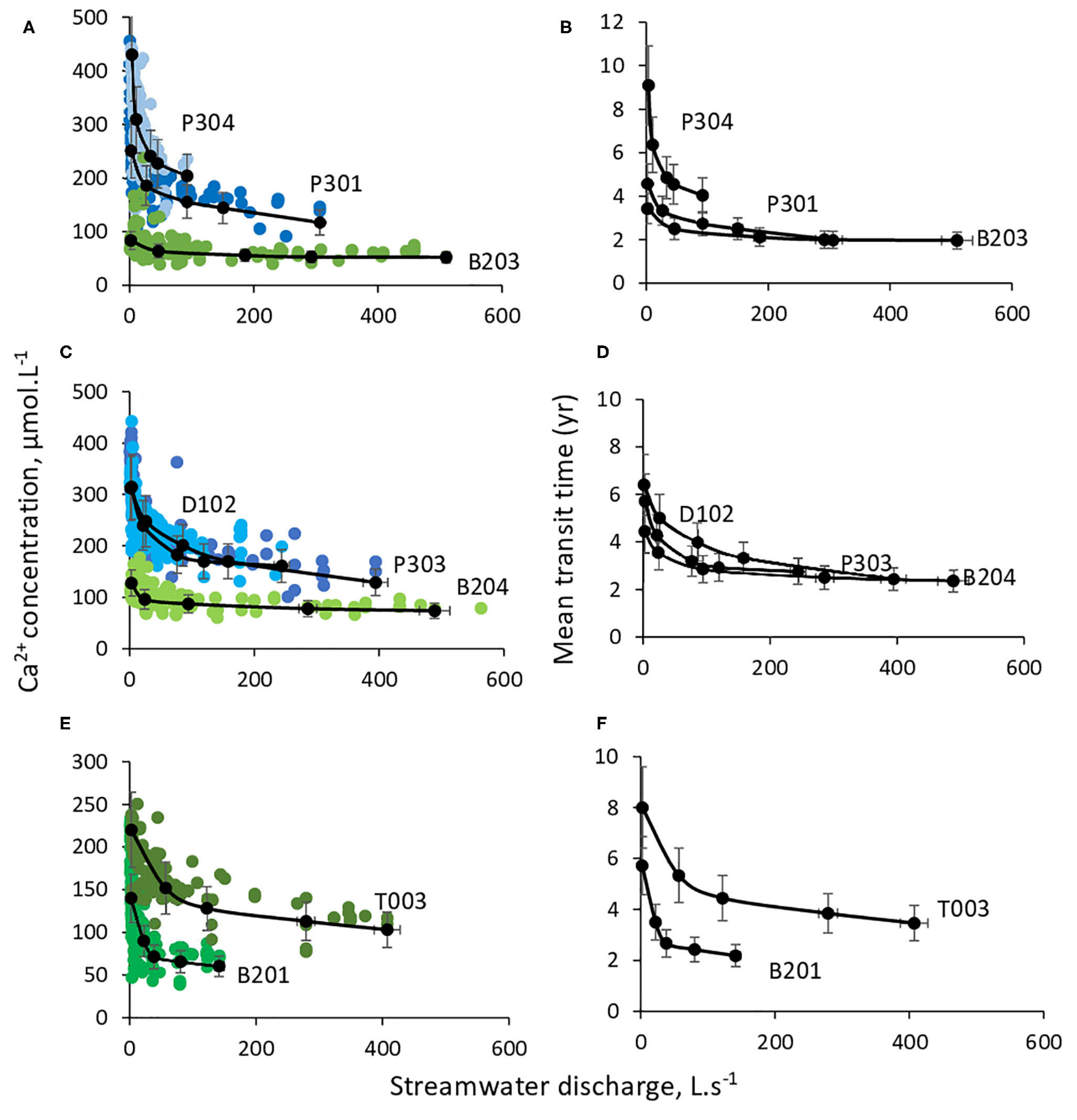

FIGURE 10 | Modeling results of C-Q relations **(A,C,E)** and mean transit times **(B,D,F)** for all the KREW stream waters. Black lines show modeling results and color points represent measured values.

4 m for wet years. Other geophysical investigations involving seismic refraction and tomographic inversion have estimated a water-storage potential between 1 and 5 m along P301 slopes, averaging 3 m for P301 (Holbrook et al., 2014). All of these mean values are similar to the average saturated thickness of 4 m inferred in P301 from our hydrogeochemical modeling of C-Q relations.

The estimates of mean saturated thicknesses obtained from hydrogeochemical modeling can be compared with the regolith thicknesses that have been measured from Geoprobe sampling in Providence (O'Geen et al., 2018). The mean saturated thicknesses must be equal or less than the average regolith thicknesses measured in the watersheds. In all cases our mean saturated thicknesses (4–4.5 m) are lower and compatible with measured

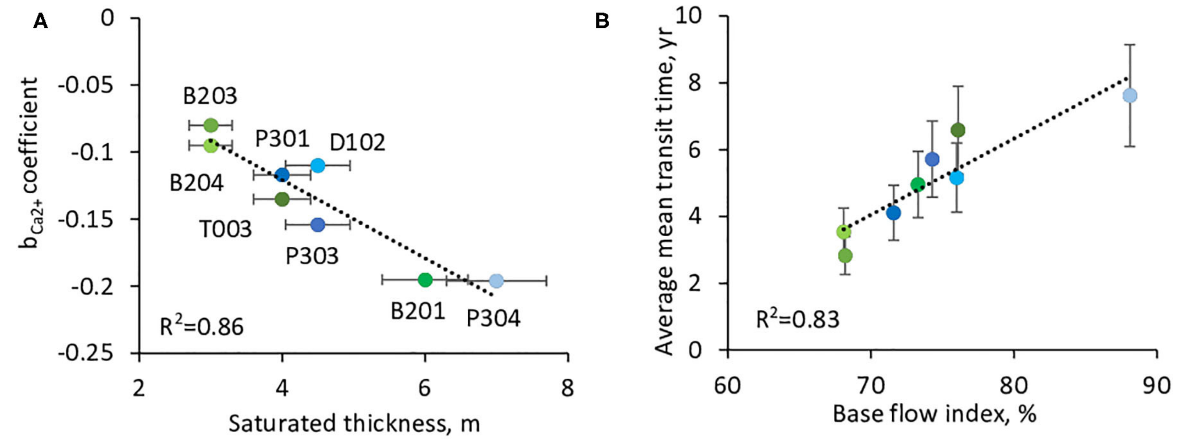

FIGURE 11 | Relations between water storage capacity, b_{ca2+} coefficient and average mean transit times. **(A)** Relationship between the b_{ca2+} coefficient of C-Q relations and the estimated saturated thicknesses. **(B)** Relationship between the modeled average mean transit times and the base flow index (BFI) of watersheds.

mean regolith thicknesses (4–6 m) on the watersheds. No regolith thickness measurements are available in P304, but the higher water storage determined by the hydrogeochemical modeling is consistent with the dampened hydrologic behavior and the higher base flow index in P304 (Safeeq and Hunsaker, 2016).

Little data are available for a direct comparison of modeled results in the Bull watersheds. However, the lower water storage and saturated thickness inferred from the geochemical modeling over three Bull watersheds (T003, B203, and B204) are consistent with previous studies in the region (e.g., Hubbert et al., 2001; Klos et al., 2018; O'Geen et al., 2018). By investigating plant-accessible water in mountain ecosystems, Klos et al. (2018) concluded that regolith thickness and water-storage capacity decrease with increasing elevation in the higher parts of the Sierra Nevada. Measured regolith thicknesses along the SSCZO elevation gradient (**Figure 1**) also show a trend of decreasing thickness from 2000 to 2700 m, with mean regolith thickness decreasing from 5 to 1.5 m between Providence and Short Hair (Short Hair on **Figure 1**; O'Geen et al., 2018). The lowest saturated thicknesses estimated by the hydrogeochemical modeling were located in the B203 and B204 watersheds, and corresponded to the lowest base flow indexes. Our modeling results using reactive-transport approaches and C-Q relations are therefore consistent with several independent estimates from hydrologic, geophysical and isotopic studies.

The Control of CZ Structure on Hydrogeochemical Behavior in Headwater Catchments

The principal contribution of our study is to determine how CZ structure controls hydrogeochemical behavior and C-Q relations in headwater watersheds (**Figure 12**). We found that mean stream concentrations and heights of C-Q relations (a_{Ca2+} coefficient) are primarily controlled by regolith mineralogy and mean transit times of stream water (**Figures 6B**, **10**). The control of regolith geochemistry on stream chemistry is consistent with previous studies conducted at the KREW (Hunsaker and Johnson, 2017). Additionally, hydrogeochemical modeling indicates that the degree of chemodynamic behavior (b_{Ca2+} coefficient) is mainly controlled by the seasonal variability of mean transit times during dry periods (**Figure 10**). This seasonal variability itself is controlled by the geomorphologic features governing the water-storage capacity. Watersheds with thinner saturated thicknesses, a larger stream network and shorter subsurface flow lines have limited storage capacity and show limited variability of water transit times and chemostatic behaviors (e.g., B204, B203 in **Figure 12**). Watersheds with thicker saturated thicknesses and a more limited stream network have larger storage capacity and show higher variability of mean transit times and more chemodynamic behavior (e.g., B201, P304 in **Figure 12**).

The combination of chemostatic behavior with high mean stream water concentrations was not observed (section Hydrology and C-Q Relations), and this is explained by the fact that chemostatic behavior is caused by an absence of significant water storage, preventing the presence of waters with long transit times and high concentrations. This scheme is also consistent with the variability of water discharge and the base flow index (BFI, **Table 2**). The chemostatic watersheds clearly have hydrologic characteristics pointing to an absence of large water storage, with a high seasonal variability of water discharge and low BFI (**Table 2**). The chemodynamic watersheds show the opposite hydrologic characteristics, with low seasonal variability of stream discharge and a higher BFI (**Table 2**).

One of the important takeaways from this study is that the CZ structure in headwater watersheds matters more than their watershed areas for the understanding of hydrogeochemical behavior. For example, B203 has a watershed area that is 2.5 times the area of P304 (**Table 2**), however, its CZ structure with a thin saturated thickness, short subsurface flow lines and fast transit times generates low stream water concentrations and chemostatic behavior. P304 has higher water storage and longer transit times that generate high stream water concentrations and

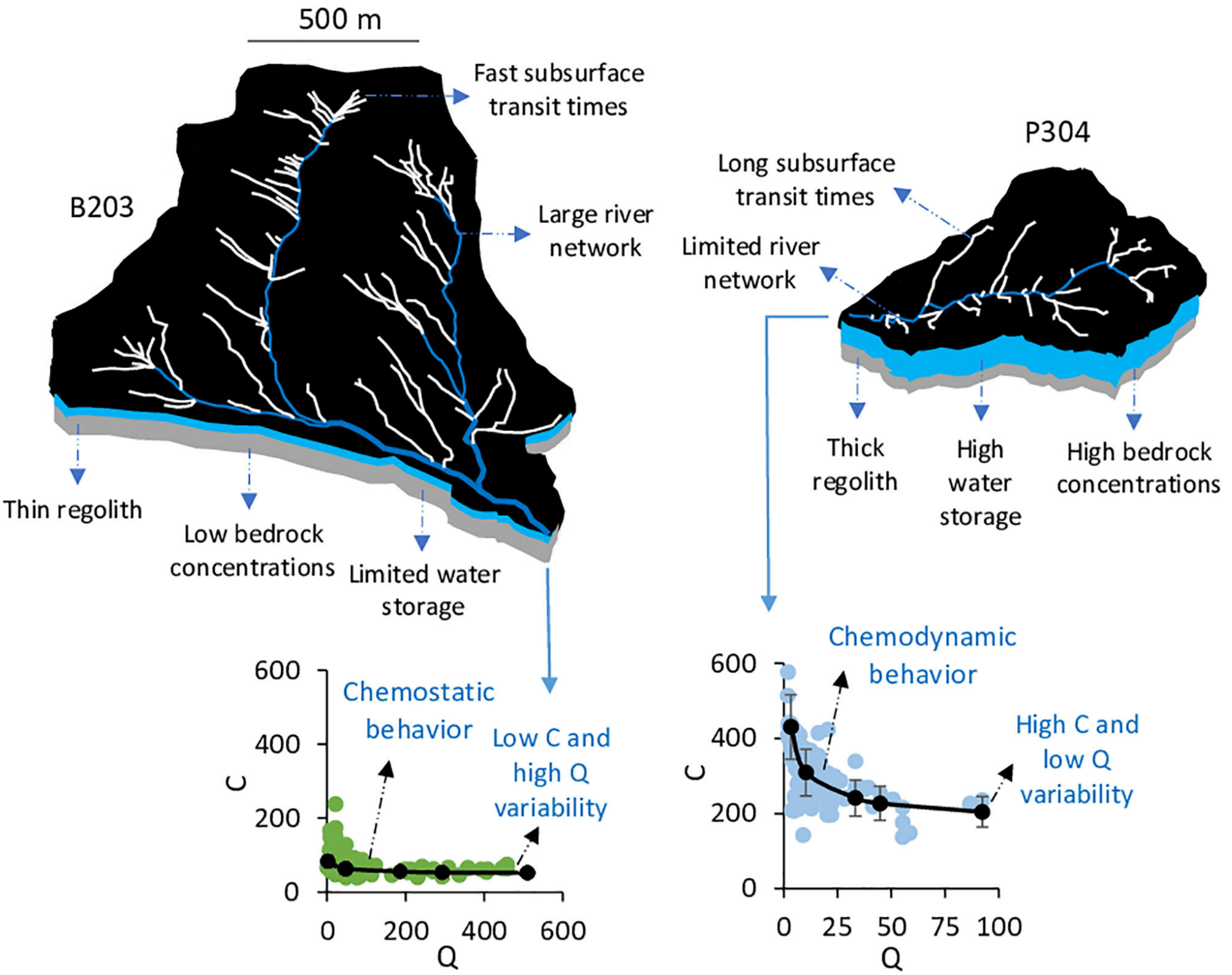

FIGURE 12 | Summary diagram of the CZ structures acquired through long-term processes that control the C-Q relations and hydrogeochemical behavior of watersheds. Thin regolith, large river network, fast subsurface transit times, limited water storage and low bedrock concentrations enhance low mean concentrations and chemostatic behavior for the stream waters. In contrast, thick regolith, limited stream networks, slow subsurface transit times, high water storage and high bedrock concentrations enhance high mean concentrations and chemodynamic behavior for the streamwaters.

chemodynamic behavior. These results suggest that the analysis and modeling of C-Q relations should not be done solely with surface-area-normalized stream discharge (e.g., Wymore et al., 2017; Zhi et al., 2019), as stream water chemistry is primarily controlled by the CZ structure and the distribution of subsurface flow lines, and not by watershed surface areas. At this stage, this point applies only for small headwater watersheds where our approach has been tested. The application of surface-area-normalized data cannot be evaluated with our study for larger watersheds (e.g., Moatar et al., 2017).

Since CZ structure constrains the shapes of C-Q relations, our study opens the possibility of estimating CZ attributes from existing C-Q data where the rich set of field investigations that we had are not available. For example, while combining data on regolith mineralogy with C-Q data from stream waters, the reactive-transport modeling of C-Q relations can be used to estimate water storage and water transit times. This point has implications for using C-Q relations as a tool to estimate water-storage and drought resistance.

We underline that these applications and implications hold when interpreting solutes in stream water with an important lithogenic origin, a strong C-MTT slope, and negative C-Q relations (C tend to decrease with Q, i.e., Ca^{2+}, H_4SiO_4, …). Different strategies could be developed for other species with positive C-Q relations (C tend to increase with Q, i.e., NO_3^-, SO_4^{2-}; Moatar et al., 2017). We expect that species with positive C-Q relations would not be explained in this way by the variability of transit times in the subsurface. Modeling positive C-Q relations could potentially be used to explore other processes in watersheds, such as remobilization processes from channels and soils, or interactions with the vegetation. This needs to be clearly tested in future studies with a specific focus on positive C-Q relations.

Nature and Magnitude of Mixing Processes

A number of recent studies have debated the extent to which C-Q relations are controlled by mixing processes between different water sources (Liu et al., 2017; Torres et al., 2017; Zhi et al., 2019). In our study, the mixing of different subsurface waters occurs when subsurface flow lines reach the stream network (**Figure 2**). No mixing with deep groundwater or with tributary streams was needed to explain the chemical variability. The variability of transit times within the regolith and the mixing of different subsurface flow lines connected to the stream is sufficient to explain the C-Q relations. Our results support that at the small scale of headwater watersheds (0–2 km^2), stream chemistry and its variability are primarily controlled by the lateral flows within the regolith and the CZ structure controlling the architecture of the subsurface flow lines. The importance of lateral flows has been also highlighted in the modeling of geomorphologic evolution of hills (Brantley et al., 2017).

At lower elevations in the Sierra Nevada and for larger watersheds (500–2,000 km^2), an influence from deep groundwater has been identified from the interpretation of C-Q relations from river waters (Liu et al., 2017). The magnitude of the deep-groundwater influence tends to increase when the elevation decreases and the river size increases (Liu et al., 2017). For major rivers, the mixing between different waters can be important when different tributaries draining contrasting lithologies are merged (Torres et al., 2017). Our results and the comparison with previous studies suggest that the nature and magnitude of mixing processes affecting C-Q relations depend to the river order from which water samples are coming. Complexity and contributions of mixing processes appear to increase from headwater streams to large-scale rivers.

In this study, we did not address the potential mixing of different waters coming from different vertical layers in the regolith. Vertically-averaged regolith properties, as used in this study, permit reduced computation times and the number of parameters in the model; however, this modeling approach cannot show the role of different regolith layers (i.e., superficial soil, soil base, lower saprolith) in the acquisition of C-Q relations. A potential improvement of our modeling strategy in future studies is a more detailed description of the CZ vertical heterogeneity and its incorporation in our modeling approach. This would imply that we either consider 2D cross-sections rather than 1D subsurface flow lines, or that we consider multiple subsurface flow lines distributed vertically with mixing between them. However, it is worth noting that this increase in model complexity would significantly increase the amount of field data needed to constrain the regolith physical, geochemical, and hydrologic properties for all the regolith layers in the KREW. In addition, our study did not evaluate the effect of direct input of snowmelt waters into the streams.

Implications for Water Resources From Headwater Watersheds

This study, which was conducted along an elevation gradient of eight watersheds, has implications for understanding the impact of droughts and hydrologic changes in a warmer climate. Presently, higher-elevation watersheds generate a greater fraction of runoff from the Sierra Nevada (Harrington and Bales, 1998; Meixner et al., 2004; Rice et al., 2011; Hunsaker et al., 2012). Our modeling results showed that higher-elevation watersheds (i.e., B203, B204) with thinner regolith and dilute stream chemistry have lower water-storage capacity and shorter water-transit times than the mid-elevation watersheds (i.e., P301, P303, P304). These results imply that in a warming climate with decreasing snowpacks, higher-elevation watersheds may not have sufficient storage capacity in the regolith to compensate for the water that is currently stored in snowpack during winter. Higher temperatures are also expected to produce larger flood events during the winter, followed by longer and drier summers with less runoff available for downstream users. This scenarios of the future hydrologic response in the Sierra Nevada is consistent with previous studies investigating changes in runoff (Hunsaker et al., 2012), vegetation (Goulden and Bales, 2014) and flooding (Das et al., 2013). More broadly, mountain watersheds that experienced Pleistocene glaciations have been scoured by glacial and periglacial processes (Ackerer et al., 2016; Callahan et al., 2019), resulting in thinner regolith and potentially lower water-storage capacities. The CZ structure, which is acquired through long-term processes, may not be adaptable to the rapid changes in climate and snowpack that are currently being observed. This will change the hydrologic behavior of mountain watersheds and have implications for downstream storage capacity and operations.

CONCLUSION

Detailed geomorphologic analysis, characterization of C-Q relations and reactive-transport modeling from a unique elevation gradient determined how CZ structure controls hydrogeochemical behavior of watersheds. Our results indicate that (1) CZ attributes and structure are key determinants of C-Q relations (2) mean stream water concentrations and heights of C-Q relations are primarily controlled by the regolith mineralogy and mean transit times of subsurface water, and (3) the degree of chemodynamic behavior is very sensitive to the water-storage in watersheds. Watersheds with thinner regolith, larger stream networks and limited water storage have faster transit times along subsurface flow lines and show stream chemistry with limited seasonal variability (i.e., chemostatic behavior). In contrast, watersheds with thicker regolith, smaller stream networks and larger water storage have longer transit times along subsurface flow lines and exhibit greater chemical variability (i.e., chemodynamic behavior). No mixing with deep groundwater was needed to explain the chemical variability of stream water. Independent estimates of mean transit times and water-storage from other isotopic, hydrologic and geophysical studies were consistent with our results inferred from the modeling of C-Q relations. This study opens the possibility to estimate CZ characteristics such as water-storage capacity and mean transit times in headwater watersheds by using quantitative modeling of C-Q relations.

DATA AVAILABILITY STATEMENT

All datasets generated for this study are included in the article/**Supplementary Material**.

AUTHOR CONTRIBUTIONS

JA performed the majority of the research presented in this manuscipt. CS was involved for the reactive-transport modeling. FL was involved for the chemical data and interpretation of C-Q relations. RBar was involved for the using of ArcGIS and DEM interpretation. MS was involved for the using of ArcGIS and DEM interpretation as well along with hydrometeorological data from KREW. AO'G was involved for regolith data, regolith thickness data, and mineralogical data. CH was involved for KREW data. RBal was involved for manuscript reading and re-writing and KREW data. All authors contributed to the article and approved the submitted version.

FUNDING

This study was supported by the U.S. National Science Foundation (NSF) through the Southern Sierra Critical Zone Observatory (EAR-0725097). This research was also supported by the long-term collaborations with the Pacific Southwest Research Station and the U.S Forest Service. CS was supported by the Watershed Function Science Focus Area at Lawrence Berkeley National Laboratory funded by the U.S. Department of Energy, Office of Science, Biological and Environmental Research under Contract No. DE-AC02-05CH11231.

SUPPLEMENTARY MATERIAL

The Supplementary Material for this article can be found online at: https://www.frontiersin.org/articles/10.3389/frwa.2020.00023/full#supplementary-material

REFERENCES

Ackerer, J., Chabaux, F., Lucas, Y., Clément, A., Fritz, B., Beaulieu, E., et al. (2018). Monitoring and reactive-transport modeling of the spatial and temporal variations of the Strengbach spring hydrochemistry. *Geochim. Cosmochim. Acta* 225, 17–35. doi: 10.1016/j.gca.2018.01.025

Ackerer, J., Chabaux, F., Van der Woerd, J., Viville, D., Pelt, E., Kali, E., et al. (2016). Regolith evolution on the millennial timescale from combined U–Th–Ra isotopes and in situ cosmogenic 10Be analysis in a weathering profile (Strengbach watershed, France). *Earth Planet. Sci. Lett.* 453, 33–43. doi: 10.1016/j.epsl.2016.08.005

Ackerer, J., Jeannot, B., Delay, F., Weill, S., Lucas, Y., Fritz, B., et al. (2020). Crossing hydrological and geochemical modeling to understand the spatiotemporal variability of water chemistry in an elementary watershed (Strengbach, France). *Hydrol. Earth Syst. Sci.* 24, 3111–3133. doi: 10.5194/hess-24-3111-2020

Ameli, A. A., Beven, K., Erlandsson, M., Creed, I. F., McDonnell, J. J., and Bishop, K. (2017). Primary weathering rates, water transit times, and concentration-discharge relations: A theoretical analysis for the critical zone. *Water Resour. Res.* 53, 942–960. doi: 10.1002/2016WR019448

Bales, R. C., Goulden, M. L., Hunsaker, C. T., Conklin, M. H., Hartsough, P. C., O'Geen, A. T., et al. (2018). Mechanisms controlling the impact of multi-year drought on mountain hydrology. *Sci. Rep.* 8:690. doi: 10.1038/s41598-017-19007-0

Bales, R. C., Hopmans, J. W., O'Geen, A. T., Meadows, M., Hartsough, P. C., Kirchner, P., et al. (2011). Soil moisture response to snowmelt and rainfall in a Sierra Nevada mixed-conifer forest. *Vadose Zone J.* 10, 786–799. doi: 10.2136/vzj2011.0001

Bart, R., and Hope, A. (2014). Inter-seasonal variability in baseflow recession rates: the role of aquifer antecedent storage in central California watersheds. *J. Hydrol.* 519, 205–213. doi: 10.1016/j.jhydrol.2014.07.020

Bateman, P. C., and Busacca, A. J. (1983). *Millerton Lake Quadrangle, Westcentral Sierra Nevada, California – Analytic Data, US Geological Survey Professional Paper, Vol. 1261*. Reston, VA: US Geological Survey. doi: 10.3133/pp1261

Bateman, P. C., and Lockwood, J. P. (1976). *Shaver Lake Quadrangle, Westcentral Sierra Nevada, California – Analytic Data. US Geological Survey Professional Paper, Vol. 774-D*. Reston, VA: US Geological Survey. doi: 10.3133/pp774D

Brantley, S. L., Lebedeva, M. I., Balashov, V. N., Singha, K., Sullivan, P. L., and Stinchcomb, G. (2017). Toward a conceptual model relating chemical reaction fronts to water flow paths in hills. *Geomorphology* 277, 100–117. doi: 10.1016/j.geomorph.2016.09.027

Callahan, R. P., Ferrier, K. L., Dixon, J., Dosseto, A., Hahm, W. J., Jessup, B. S., et al. (2019). Arrested development: Erosional equilibrium in the southern Sierra Nevada, California, maintained by feedbacks between channel incision and hillslope sediment production. *GSA Bulletin* 131, 1179–1202. doi: 10.1130/B35006.1

Chorover, J., Derry, L. A., and McDowell, W. H. (2017). Concentration-Discharge Relations in the Critical Zone: Implications for Resolving Critical Zone Structure, Function, and Evolution. *Water Resour. Res.* 53, 8654–8659. doi: 10.1002/2017WR021111

Chorover, J., Troch, P. A., Rasmussen, C., Brooks, P. D., Pelletier, J. D., Breshears, D. D., et al. (2011). How water, carbon, and energy drive critical zone evolution: The Jemez–Santa Catalina Critical Zone Observatory. *Vadose Zone J.* 10, 884–899. doi: 10.2136/vzj2010.0132

Das, T., Maurer, E. P., Pierce, D. W., Dettinger, M. D., and Cayan, D. R. (2013). Increases in flood magnitudes in California under warming climates. *J. Hydrol.* 501, 101–110. doi: 10.1016/j.jhydrol.2013.07.042

Diamond, J. S., and Cohen, M. J. (2018). Complex patterns of watershed solute–discharge relationships for coastal plain rivers. *Hydrol. Processes* 32, 388–401. doi: 10.1002/hyp.11424

Gérard, F., Clement, A., and Fritz, B. (1998). Numerical validation of a Eulerian hydrochemical code using a 1D multisolute mass transport system involving heterogeneous kinetically controlled reactions. *J. Contam. Hydrol.* 30, 201–216. doi: 10.1016/S0169-7722(97)00047-8

Godsey, S. E., Kirchner, J. W., and Clow, D. W. (2009). Concentration–discharge relationships reflect chemostatic characteristics of US watersheds. *Hydrol. Processes* 23, 1844–1864. doi: 10.1002/hyp.7315

Goulden, M. L., Anderson, R. G., Bales, R. C., Kelly, A. E., Meadows, M., and Winston, G. C. (2012). Evapotranspiration along an elevation gradient in California's Sierra Nevada. *J. Geophys. Res.* 117:G3. doi: 10.1029/2012JG002027

Goulden, M. L., and Bales, R. C. (2014). Mountain runoff vulnerability to increased evapotranspiration with vegetation expansion. *Proc. Natl. Acad. Sci.* 111, 14071–14075. doi: 10.1073/pnas.1319316111

Harrington, R., and Bales, R. C. (1998). Modeling ionic solute transport in melting snow. *Water Resour. Res.* 34, 1727–1736. doi: 10.1029/98WR00557

Herndon, E. M., Dere, A. L., Sullivan, P. L., Norris, D., Reynolds, B., and Brantley, S. L. (2015). Landscape heterogeneity drives contrasting concentration–discharge relationships in shale headwater watersheds. *Hydrol. Earth Syst. Sci.* 19, 3333–3347. doi: 10.5194/hess-19-3333-2015

Herndon, E. M., Steinhoefel, G., Dere, A. L., and Sullivan, P. L. (2018). Perennial flow through convergent hillslopes explains chemodynamic solute behavior in a shale headwater watershed. *Chem. Geol.* 493, 413–425. doi: 10.1016/j.chemgeo.2018.06.019

Holbrook, W. S., Riebe, C. S., Elwaseif, M., L., Hayes, J., Basler-Reeder, K., Harry, D. L., et al. (2014). Geophysical constraints on deep weathering and water storage potential in the Southern Sierra Critical Zone Observatory. *Earth Surface Processes Landforms* 39, 366–380. doi: 10.1002/esp.3502

Hubbert, K. R., Beyers, J. L., and Graham, R. C. (2001). Roles of weathered bedrock and soil in seasonal water relations of Pinus jeffreyi and Arctostaphylos patula. *Can. J. Forest Res.* 31, 1947–1957. doi: 10.1139/x01-136

Hunsaker, C. T., and Johnson, D. W. (2017). Concentration-discharge relationships in headwater streams of the S ierra N evada, C alifornia. *Water Resour. Res.* 53, 7869–7884. doi: 10.1002/2016WR019693

Hunsaker, C. T., Whitaker, T. W., and Bales, R. C. (2012). Snowmelt runoff and water yield along elevation and temperature gradients in California's southern sierra nevada 1. *J. Am. Water Res. Association* 48, 667–678. doi: 10.1111/j.1752-1688.2012.00641.x

Jessup, B. S., Jesse Hahm, W., Miller, S. N., Kirchner, J. W., and Riebe, C. S. (2011). Landscape response to tipping points in granite weathering: The case of stepped topography in the Southern Sierra Critical Zone Observatory. *Appl. Geochem.* 26, S48–S50. doi: 10.1016/j.apgeochem.2011.03.026

Johnson, D. W., Hunsaker, C. T., Glass, D. W., Rau, B. M., and Roath, B. A. (2011). Carbon and nutrient contents in soils from the Kings River Experimental Watersheds, Sierra Nevada Mountains, California. *Geoderma* 160, 490–502. doi: 10.1016/j.geoderma.2010.10.019

Kim, H., Dietrich, W. E., Thurnhoffer, B. M., Bishop, J. K., and Fung, I. Y. (2017). Controls on solute concentration-discharge relationships revealed by simultaneous hydrochemistry observations of hillslope runoff and stream flow: The importance of critical zone structure. *Water Resour. Res.* 53, 1424–1443. doi: 10.1002/2016WR019722

Klos, P. Z., Goulden, M. L., Riebe, C. S., Tague, C. L., O'Geen, A. T., Flinchum, B. A., et al. (2018). Subsurface plant-accessible water in mountain ecosystems with a Mediterranean climate. *Wiley Interdiscipl. Rev.* 5:e1277. doi: 10.1002/wat2.1277

Lackey, J. S., Cecil, M. R., Windham, C. J., Frazer, R. E., Bindeman, I. N., and Gehrels, G. E. (2012). The Fine Gold intrusive suite: the roles of basement terranes and magma source development in the Early Cretaceous Sierra Nevada batholith. *Geosphere* 8, 292–313. doi: 10.1130/GES00745.1

Li, L., Bao, C., Sullivan, P. L., Brantley, S., Shi, Y., and Duffy, C. (2017). Understanding watershed hydrogeochemistry: 2. Synchronized hydrologic and geochemical processes drive stream chemostatic behavior. *Water Res. Res.* 53, 2346–2367. doi: 10.1002/2016WR018935

Liu, F., Conklin, M. H., and Shaw, G. D. (2017). Insights into hydrologic and hydrochemical processes based on concentration-discharge and end-member mixing analyses in the mid-Merced R iver B asin, S ierra N evada, C alifornia. *Water Resour. Res.* 53, 832–850. doi: 10.1002/2016WR019437

Liu, F., Hunsaker, C., and Bales, R. C. (2013). Controls of streamflow generation in small watersheds across the snow–rain transition in the Southern Sierra Nevada, California. *Hydrol. Processes* 27, 1959–1972. doi: 10.1002/hyp.9304

Liu, Y. B., Gebremeskel, S., De Smedt, F., Hoffmann, L., and Pfister, L. (2003). A diffusive transport approach for flow routing in GIS-based flood modeling. *J. Hydrol.* 283, 91–106. doi: 10.1016/S0022-1694(03)00242-7

Lucas, Y., Chabaux, F., Schaffhauser, T., Fritz, B., Ambroise, B., Ackerer, J., et al. (2017). Hydrogeochemical modeling (KIRMAT) of spring and deep borehole water compositions in the small granitic Ringelbach watershed (Vosges Mountains, France). *Appl. Geochem.* 87, 1–21. doi: 10.1016/j.apgeochem.2017.10.005

Meixner, T., Gutmann, C., Bales, R., Leydecker, A., Sickman, J., Melack, J., et al. (2004). Multidecadal hydrochemical response of a Sierra Nevada watershed: sensitivity to weathering rate and changes in deposition. *J. Hydrol.* 285, 272–285. doi: 10.1016/j.jhydrol.2003.09.005

Moatar, F., Abbott, B. W., Minaudo, C., Curie, F., and Pinay, G. (2017). Elemental properties, hydrology, and biology interact to shape concentration-discharge curves for carbon, nutrients, sediment, and major ions. *Water Resour. Res.* 53, 1270–1287. doi: 10.1002/2016WR019635

Musolff, A., Schmidt, C., Selle, B., and Fleckenstein, J. H. (2015). Catchment controls on solute export. *Adv. Water Resour.* 86, 133–146. doi: 10.1016/j.advwatres.2015.09.026

Ngo, V. V., Delalande, M., Clément, A., Michau, N., and Fritz, B. (2014). Coupled transport-reaction modeling of the long-term interaction between iron, bentonite and Callovo-Oxfordian claystone in radioactive waste confinement systems. *Appl. Clay Sci.* 101, 430–443. doi: 10.1016/j.clay.2014.08.020

O'Geen, A. T., Safeeq, M., Wagenbrenner, J., Stacy, E., Hartsough, P., Devine, S., et al. (2018). Southern sierra critical zone observatory and kings river experimental watersheds: a synthesis of measurements, new insights, and future directions. *Vadose Zone J.* 17:81. doi: 10.2136/vzj2018.04.0081

Reis, F. D. A., and Brantley, S. L. (2019). The impact of depth-dependent water content on steady state weathering and eroding systems. *Geochim. Cosmochim. Acta* 244, 40–55. doi: 10.1016/j.gca.2018.09.028

Rice, R., Bales, R. C., Painter, T. H., and Dozier, J. (2011). Snow water equivalent along elevation gradients in the Merced and Tuolumne River basins of the Sierra Nevada. *Water Resour. Res.* 47:8. doi: 10.1029/2010WR009278

Safeeq, M., Grant, G. E., Lewis, S. L., and Tague, C. L. (2013). Coupling snowpack and groundwater dynamics to interpret historical streamflow trends in the western United States. *Hydrol. Processes* 27, 655–668. doi: 10.1002/hyp.9628

Safeeq, M., and Hunsaker, C. T. (2016). Characterizing runoff and water yield for headwater watersheds in the southern Sierra Nevada. *J. Am. Water Res. Association* 52, 1327–1346. doi: 10.1111/1752-1688.12457

Steefel, C. I., Appelo, C. A. J., Arora, B., Jacques, D., Kalbacher, T., Kolditz, O., et al. (2015). Reactive transport codes for subsurface environmental simulation. *Comp. Geosci.* 19, 445–478. doi: 10.1007/s10596-014-9443-x

Storck, P., Bowling, L., Wetherbee, P., and Lettenmaier, D. (1998). Application of a GIS-based distributed hydrology model for prediction of forest harvest effects on peak stream flow in the Pacific Northwest. *Hydrol. Process* 12, 889–904.

Sullivan, P. L., Stops, M. W., Macpherson, G. L., Li, L., Hirmas, D. R., and Dodds, W. K. (2019). How landscape heterogeneity governs stream water concentration-discharge behavior in carbonate terrains (Konza Prairie, USA). *Chem. Geol.* 527:118989. doi: 10.1016/j.chemgeo.2018.12.002

Tardy, Y., and Fritz, B. (1981). An ideal solid solution model for calculating solubility of clay minerals. *Clay Minerals* 16, 361–373. doi: 10.1180/claymin.1981.016.4.05

Tian, Z., Hartsough, P. C., and O'Geen, A. T. (2019). Lithologic, climatic and depth controls on critical zone transformations. *Soil Sci. Soc. Am. J.* 83, 437–447. doi: 10.2136/sssaj2018.03.0120

Torres, M. A., Baronas, J. J., Clark, K. E., Feakins, S. J., and West, A. J. (2017). Mixing as a driver of temporal variations in river hydrochemistry: 1. Insights from conservative tracers in the Andes-Amazon transition. *Water Res. Res.* 53, 3102–3119. doi: 10.1002/2016WR019733

Visser, A., Thaw, M., Deinhart, A., Bibby, R., Safeeq, M., Conklin, M., et al. (2019). Cosmogenic isotopes unravel the hydrochronology and water storage dynamics of the Southern sierra critical zone. *Water Resour. Res.* 55, 1429–1450. doi: 10.1029/2018WR023665

Wymore, A. S., Brereton, R. L., Ibarra, D. E., Maher, K., and McDowell, W. H. (2017). Critical zone structure controls concentration-discharge relationships and solute generation in forested tropical montane watersheds. *Water Resour. Res.* 53, 6279–6295. doi: 10.1002/2016WR020016

Zhi, W., Li, L., Dong, W., Brown, W., Kaye, J., Steefel, C., et al. (2019). Distinct source water chemistry shapes contrasting concentration-discharge patterns. *Water Resour. Res.* 55, 4233–4251. doi: 10.1029/2018WR024257

Conflict of Interest: The authors declare that the research was conducted in the absence of any commercial or financial relationships that could be construed as a potential conflict of interest.

frontiers in Water

ORIGINAL RESEARCH
published: 10 November 2020
doi: 10.3389/frwa.2020.578677

Trace Element Export From the Critical Zone Triggered by Snowmelt Runoff in a Montane Watershed, Provo River, Utah, USA

Hannah N. Checketts[1], Gregory T. Carling[1]*, Diego P. Fernandez[2], Stephen T. Nelson[1], Kevin A. Rey[1], David G. Tingey[1], Colin A. Hale[1], Brian N. Packer[1], Cameron P. Cordner[1], Dylan B. Dastrup[1] and Zachary T. Aanderud[3]

[1] Department of Geological Sciences, Brigham Young University, Provo, UT, United States, [2] Department of Geology & Geophysics, University of Utah, Salt Lake City, UT, United States, [3] Department of Plant & Wildlife Sciences, Brigham Young University, Provo, UT, United States

Edited by:
Carl I. Steefel,
Lawrence Berkeley National
Laboratory, United States

Reviewed by:
Alissa M. White,
University of Arizona, United States
Kalyana Babu Nakshatrala,
University of Houston, United States

***Correspondence:**
Gregory T. Carling
greg.carling@byu.edu

Specialty section:
This article was submitted to
Water and Critical Zone,
a section of the journal
Frontiers in Water

Received: 30 June 2020
Accepted: 23 October 2020
Published: 10 November 2020

Citation:
Checketts HN, Carling GT, Fernandez DP, Nelson ST, Rey KA, Tingey DG, Hale CA, Packer BN, Cordner CP, Dastrup DB and Aanderud ZT (2020) Trace Element Export From the Critical Zone Triggered by Snowmelt Runoff in a Montane Watershed, Provo River, Utah, USA. Front. Water 2:578677. doi: 10.3389/frwa.2020.578677

The Critical Zone is an important source of trace elements to headwater streams during the snowmelt runoff period, yet the mechanisms of trace element release are poorly characterized. To evaluate changes in water chemistry in response to snowmelt, we measured trace element and major ion concentrations at three sites in the upper Provo River in northern Utah, USA, over a 5-year period spanning years with below-and above-average discharge. We also sampled snowpack, ephemeral streams, and soil water to investigate trace element sources. The river drains siliciclastic bedrock above the upper site, carbonate rocks between the upper and middle sites, and volcanic rocks between the middle and lower sites, with minimal anthropogenic impacts in the watershed. Concentrations of specific trace metals (Be, Al, Cu, and Pb) and rare earth elements (represented by La and Y) increased during snowmelt runoff each year at all three sites, with decreasing concentrations from upstream to downstream. In contrast, major ion concentrations, including Ca^{2+} and SO_4^{2-}, were similar year–round at the upper site and were diluted during snowmelt at the lower sites, with increasing concentrations from upstream to downstream. The snowmelt runoff period (April–June) accounted for >84% of the annual trace element loading, with most trace element inputs occurring above the upper sampling site. Concentration–discharge (C–Q) relationships revealed variations in solute behavior from upstream to downstream. For example, at the upstream site the trace elements had a slight positive slope in log C–log Q space, while Ca^{2+} and SO_4^{2-} had zero slope. At the downstream sites, the trace elements had a strong positive slope and Ca^{2+} and SO_4^{2-} had a negative slope. Trace element concentrations were relatively low in snowpack but elevated in ephemeral streams and soil water, suggesting that flushing of shallow soils by snowmelt causes increased trace element concentrations with positive C–Q relationships in the upper part of the river. Trace element loads propagate downstream where concentrations are diluted by groundwater inputs from carbonate bedrock. Our results demonstrate that soil water flushing in the Critical Zone at the headwaters of mountain streams is an important control on downstream water chemistry.

Keywords: trace elements, concentration-discharge (C-Q) relationships, snowmelt, soil water, ephemeral stream, alpine hydrology, the critical zone

INTRODUCTION

Snowmelt–fed river systems exhibit seasonal changes in water chemistry, with increased fluxes of trace elements during snowmelt runoff (Shafer et al., 1997; Rember and Tefrey, 2004; Ogendi et al., 2007; Carling et al., 2015). The seasonal changes in water chemistry of snow dominated watersheds may be detrimental to water supplies impacting up to one–sixth of the world's population (Barnett et al., 2008). The mechanisms for transferring solutes from the watershed to mountain streams are not well-understood, especially for soil–vs. rock–derived solutes and over seasonal timeframes (Brooks et al., 2015). Further, the transfer of solutes along longitudinal profiles from headwater streams to higher order rivers is under-studied as most research has focused on a single site within a river system (Godsey et al., 2009).

The Critical Zone, extending from shallow soils to deeper permeable bedrock, is the primary source of solutes to stream systems (Chorover et al., 2017). The Critical Zone releases solutes to groundwater by weathering of bedrock and soils through seasonally dynamic deep- and shallow-flow paths. The composition of soils in montane watersheds is typically a mixture of weathered bedrock and aeolian dust, which provides allochthonous trace elements that alter snowpack and soil composition (Carling et al., 2012; Munroe, 2014; Reynolds et al., 2014). Shallow groundwater following quick flow paths more likely contains a soil-like water chemistry signature rich in dissolved organic matter (DOM), mineral colloids, and trace elements not found in the local bedrock, while deeper groundwater following long flow paths more likely resembles the chemistry of weathered bedrock (Chorover et al., 2017). The relative fraction of water inputs from shallow vs. deep flow paths changes during hydrologic events, such as snowmelt runoff, thereby altering stream water chemistry (Brooks et al., 2015).

The water chemistry response to changing discharge is often investigated using concentration–discharge (C–Q) plots. C–Q relationships provide information on solute availability and sources within a watershed (Williams, 1989; Evans and Davies, 1998; Godsey et al., 2009; Lloyd et al., 2016). The C–Q slope may reveal chemostatic behavior (no change in concentration with discharge), flushing (increasing concentrations with increased discharge), or dilution (decreasing concentrations with increased discharge) (Creed et al., 2015). While numerous studies have investigated C–Q relationships for major ions, suspended sediments, and nutrients, relatively few have examined C–Q relationships for trace elements (Trostle et al., 2016; Mcintosh et al., 2017). Trace element C–Q relationships, which often demonstrate flushing behavior, are useful for describing flow pathways, colloid transport, and hydrologic connectivity during snowmelt runoff (Aguirre et al., 2017).

The purpose of our study is to investigate the mechanisms for transferring trace elements from the Critical Zone to an alpine stream. Specific objectives are to: (1) characterize changes in water chemistry in response to increasing discharge during snowmelt runoff; (2) evaluate C–Q relationships for chemostatic or chemodynamic behavior; (3) characterize changes in C–Q patterns from upstream to downstream across a longitudinal transect in a nested catchment; and (4) identify sources of trace elements and major ions in the watershed. The upper Provo River watershed in the Uinta Mountains of northern Utah was selected for this study because it is a relatively pristine snowmelt-dominated montane watershed with a network of real-time water quality, snowpack, and discharge measurements. The Provo River supplies drinking water to over half of Utah's population. Our study builds on previous work investigating natural and anthropogenic sources of trace elements to the river system (Carling et al., 2015) and mercury/DOM dynamics in the upper Provo River (Packer et al., 2020).

MATERIALS AND METHODS

Upper Provo River Watershed Study Area

The upper Provo River watershed is primarily fed by high elevation snowmelt from the Uinta Mountains. Three established monitoring locations in the watershed are located (from upstream to downstream) at Soapstone, Woodland, and Hailstone (**Figure 1**). The watershed covers 675 km^2 and receives supplemental water diverted from the Duchesne River watershed (104 km^2) above the Soapstone site and Weber River watershed (589 km^2) above the Hailstone site (**Figure 1**). The upper Provo River extends ∼50 km with a vertical drop of 1,000 m, from 2,900 m asl at Trial Lake to 1,900 m asl at Jordanelle Reservoir. The geology of the upper part of the watershed above Soapstone consists of interbedded siliciclastic rocks (mainly quartz arenite with minor interbedded shales) (Condie et al., 2001; Dehler et al., 2006) overlain by surficial glacial and alluvial deposits (**Figure 1**). Shallow, weakly developed soils with a thin loess cap cover much of the alpine area of the watershed (Munroe et al., 2015). The lower part of the watershed contains Paleozoic carbonate rocks between Soapstone and Woodland and Tertiary volcanic rocks between Woodland and Hailstone. The watershed is mostly undeveloped except for small roads and campgrounds at the top of the watershed and a minor amount of agricultural land use at the bottom of the watershed.

Stream discharge in the upper Provo River is dominated by snowmelt with most runoff occurring during the months of April

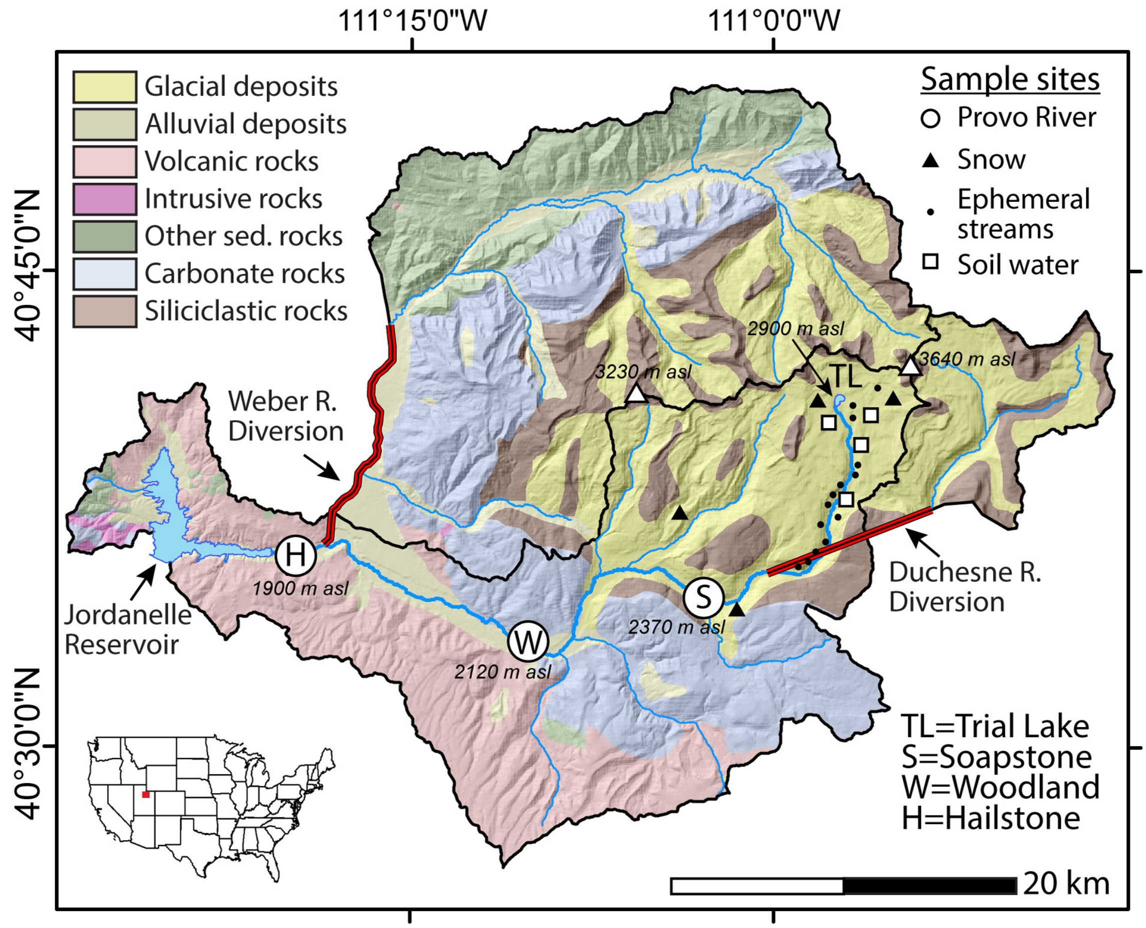

FIGURE 1 | Simplified geologic map of the upper Provo River watershed (northern Utah, USA) showing sample locations, the Duchesne and Weber River diversions, and Jordanelle Reservoir. The upper Provo River watershed receives water from the Duchesne River above the Soapstone site and Weber River above the Hailstone site. Modified after Packer et al. (2020).

through June (**Figure 2**). The higher elevations above Soapstone receive the most snowfall while the lower elevation portions of the watershed are drier. Discharge increases between the Soapstone and Woodland sites due to inputs from groundwater and other tributaries. Likewise, discharge increases between the Woodland and Hailstone sites due to groundwater inputs and transbasin diversions from the Weber River watershed (**Figure 1**). At peak discharge, the river is fed by ∼80% snowmelt and 20% groundwater based on mixing calculations using conductivity measurements (Carling et al., 2015).

River, Ephemeral Stream, Soil Water, and Snowpack Sample Collection

To characterize seasonal trends in water chemistry, we sampled the Provo River at Soapstone, Woodland, and Hailstone (**Figure 1**) during water years 2014–2018 with increased sampling frequency during the snowmelt runoff period (April through June). Each site was sampled ∼20 times per year during 2016, 2017, and 2018. Additionally, Soapstone was sampled eight times per year in 2014 and 2015 and Hailstone was sampled six times in 2015. Near peak runoff in 2016 (June 1–2), we conducted an intensive diel sampling event at Soapstone with hourly samples collected over a 24-h period to measure changes in water chemistry in response to hourly changes in discharge.

To evaluate water chemistry of potential inputs to the Provo River, we sampled ephemeral snowmelt streams during May 2016 ($n = 8$), May/June 2017 ($n = 14$), and May 2018 ($n = 5$). Ephemeral streams, which appeared as small rivulets during the snowmelt season, were sampled opportunistically in the upper part of watershed above Soapstone (**Figure 1**). The samples primarily represent snowmelt water that has interacted with soil water and shallow groundwater. Field blanks ($n = 3$) were collected along with ephemeral stream samples.

For river and ephemeral stream samples, multiple bottles were used for different chemical analyses. For trace elements and major cations, water was collected in a 125 mL LDPE bottle and filtered in the laboratory within ∼6 h of collection using a polypropylene syringe and 0.45 µm PES syringe filter. The filtered sample was amended to 2.4% v/v trace metal grade HNO_3. To avoid sample contamination, filtering was done in a

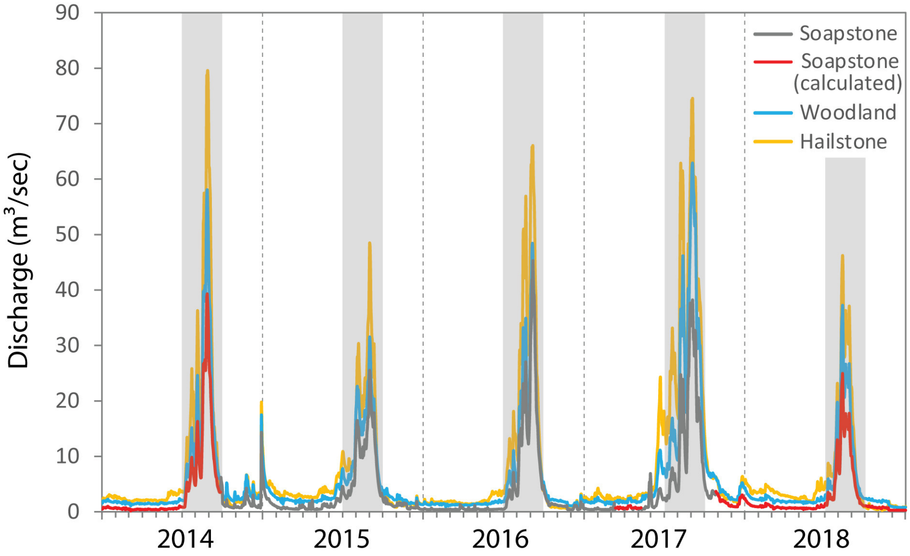

FIGURE 2 | Daily discharge at Soapstone, Woodland and Hailstone sites on the upper Provo River for water years 2014–2018. Vertical dashed lines indicate the beginning of the water year on 1 October and the gray boxes indicate the 3-month snowmelt runoff period (April–June) each year. For Soapstone, missing values (in red) were calculated by regression with Woodland data.

laminar flow hood and all materials that contacted the sample were acid washed with 10% HCl and rinsed with Milli–Q water. Field blanks ($n = 66$) were processed each sampling day by pouring Milli–Q water into a clean LDPE bottle and treating the blank water in the same manner as a sample. Samples for major anions (F^-,Cl^-, NO_3^-, and SO_4^{2-}) and HCO_3^- were collected in 1 L HDPE bottles and stable isotopes of water ($\delta^{18}O$ and δ^2H) were collected in 30 mL amber glass vials with polyseal caps. The major anion samples were filtered in the laboratory using a 0.45 µm acetate filter in a plastic vacuum filtration unit, while HCO_3^-, $\delta^{18}O$, and δ^2H were measured on unfiltered aliquots.

To compare with ephemeral stream sample chemistry, we collected a total of eight shallow soil water samples during the snowmelt period over 2 years using different methods due to the difficulty of obtaining sufficient volume from the clay–rich soils. In 2017, we collected two soil water samples using UMS tension lysimeters. In 2018, we collected one sample using an Eijkelkamp MacroRhizon sampler and five samples by centrifuging wet soils. All samples were filtered using a 0.45 µm PES syringe filter into a LDPE bottle for analysis of trace elements and major cations. There was insufficient volume for other analyses.

To compare snow chemistry with river chemistry, we sampled snowpack at maximum accumulation (prior to snowmelt) each spring from 2014 through 2018 in the upper watershed (**Figure 1**). Snow was sampled at five sites in 2014, one site in 2015, six sites in 2016, and two sites in 2017 and 2018. The sites were carefully selected in flat, wind-protected areas within clearings in the coniferous forest beyond the canopy drip edge, with consistent locations year-to-year. At each site, three snow pits were excavated to collect separate full–depth snow samples ($n = 48$). A complete snow column (except the bottom ~10 cm near the ground) was collected behind the snow pit face using a clean acrylic tube following established methods (Carling et al., 2012). Snow was transferred from the tube to a clean 2 L fluorinated high-density polyethylene (FLPE) bottle. Field blanks ($n = 7$) were collected each sampling day by pouring Milli–Q water through the sampling tubes into a sample bottle and treating the water in the same manner as a snow sample. After melting samples in the lab, the water was subsampled for trace elements and major cations, major anions, and stable isotopes as described above for the other water samples.

Laboratory Analysis of Water Samples

Water samples (river, ephemeral streams, soil water, and snow) were analyzed for metals and major cations, major anions, alkalinity, and stable isotopes of water ($\delta^{18}O$ and δ^2H). Trace element and major cation concentrations were measured using an Agilent 7500ce quadrupole inductively coupled plasma mass spectrometer (ICP–MS). Concentrations were measured for the following elements: Ag, Al, As, B, Ba, Be, Ca, Cd, Ce, Co, Cr, Cs, Cu, Dy, Er, Eu, Fe, Gd, Ho, K, La, Li, Lu, Mg, Mn, Mo, Na, Nd, Ni, Pb, Pr, Rb, Sb, Se, Sm, Sr, Tb, Th, Ti, Tl, U, V, Y, Yb, and Zn. The detection limit (DL) was determined as the standard deviation of all blanks analyzed throughout each run. A USGS standard reference sample (T−205) and NIST standard reference material (SRM 1643e) were analyzed multiple times in each run together with the samples as a continuing calibration verification. The long-term reproducibility for T−205 and SRM 1643e shows that our results are accurate within 10% for most elements. Major anions (F^-, Cl^-, NO_3^-, and SO_4^{2-}) were analyzed on filtered samples using a Dionex ICS−90 ion chromatograph (IC). Alkalinity, assumed to be HCO_3^-, was measured on unfiltered samples by acid titration. Stable isotopes of water ($\delta^{18}O$ and δ^2H) were measured on unfiltered samples using a Los Gatos Research

Liquid Water Isotope Analyzer (LWIA—24d). All measurements were made relative to Vienna Standard Mean Ocean Water (VSMOW), with a precision of 0.4‰ and 1.0‰ for δ^{18}O and δ^2H, respectively.

Data Quality Control

For data quality control, we checked for elements with high background in field blanks and elements with detection limit issues. For most elements, concentrations were near or <DL in all field blank samples (including blanks for river, ephemeral stream, and snow samples). Two exceptions were B and Zn, which showed measurable values in nearly all field blank samples and thus were excluded from the working dataset. Ag, Cd, Cs, Sc, and Tl were excluded from this study because of insufficient concentrations (<DL) across sample types. For those elements with measurable concentrations in most sample types, occurrences of <DL were set to ½ DL to allow for subsequent calculations.

Charge balances calculated using cation (K^+, Na^+, Ca^{2+}, and Mg^{2+}) concentrations from the ICP–MS, anion (F^-, Cl^-, NO_3^-, and SO_4^{2-}) concentrations from the IC, and HCO_3^- concentrations from titration were within an acceptable range of ±5% for 221 out of 239 river and ephemeral stream samples. The remaining 18 samples were charge balanced by slightly adjusting HCO_3^- concentrations. Raw data for all river, ephemeral stream, soil water, and snow samples, including field blanks and charge balance calculations, are provided in the **Supplementary Tables 1–5**.

Stream Discharge Data and Solute Loads

Stream discharge measurements were used to develop C–Q relationships and calculate solute loads. Stream discharge data were obtained from the US Geological Survey (USGS) gauging stations at Woodland (USGS 10154200) and Hailstone (USGS 10155000). For the Soapstone site, discharge data were obtained from the iUTAH (innovative Urban Transitions and Arid region Hydro-sustainability) project using 15-min water level measurements (iUTAH GAMUT Working Group, 2019) converted to discharge with a stream rating curve (iUTAH Cyberinfrastructure Team, 2017). Discharge values at Soapstone were missing for most of water year 2014 and all of water year 2018, with interspersed missing days between 2015 and 2017. Given the strong relationship between discharge at the Soapstone and Woodland sites (R^2 value of 0.94 over 3 years of overlapping daily data), periods of missing data at Soapstone were interpolated by linear regression on Woodland discharge data using the equation (with units of m^3/s): Soapstone discharge = 0.6868 (Woodland discharge) − 0.5777. The regression equation was similar considering all data or considering only data collected during baseflow and the rising or falling limbs of the hydrograph (**Supplementary Figure 1**). Negative values were replaced with a nominal value of 0.3 m^3/s. The measured and calculated daily discharge values are shown in **Figure 2** and provided in the **Supplementary Tables 1–5**. The calculated discharge values were used in subsequent C–Q analysis and load calculations. The best-fit slope of the log C–log Q relationship was determined by regression for each solute at Soapstone, Woodland, and Hailstone, where a slope of zero represents chemostatic behavior, a positive slope represents flushing, and a negative slope represents dilution (Godsey et al., 2009; Creed et al., 2015).

Daily, seasonal, and annual trace element and major ion loads were calculated using the USGS LOADEST (LOAD ESTimator) program (Runkel et al., 2004). LOADEST uses nine regression models to calculate the adjusted maximum likelihood estimation (AMLE) of load, assuming a normal distribution in the model residuals, and automatically selects the model with the lowest Aikake information criterion (AIC). The inputs included concentrations of trace elements and major ions and discharge at Soapstone, Woodland, and Hailstone.

RESULTS

Snowmelt Dominated Stream Hydrograph

Stream discharge in the upper Provo River was variable throughout our 5-year study period (**Figure 2**). Water years 2014 and 2016 had near-average annual discharge (103 and 96% of the long-term mean), while 2017 was above average (155% of the long-term mean) and 2015 and 2018 were below average (85 and 72% of the long-term mean) based on nearly 70 years of data at the Hailstone site. Peak discharge was higher in 2014 relative to 2017, but the snowmelt runoff period was much longer during 2017 extending from March through July compared with April through June for other years. Discharge typically increased between Soapstone and Woodland and between Woodland and Hailstone, during low flow periods and during snowmelt runoff.

Contrasting Response of Trace Elements and Major Ions to Snowmelt Runoff

Specific trace elements and major ions showed contrasting behavior over time in the upper Provo River (**Figure 3**). We focused on specific trace elements (Be, Al, Cu, Pb, La, and Y) and major ions (Ca^{2+} and SO_4^{2-}) that showed contrasting trends relative to discharge. We used the trace metals Be, Al, Cu, and Pb because they represent potential water quality impairments and are elevated in atmospheric deposition to the Uinta Mountains (Reynolds et al., 2010; Munroe, 2014; Dastrup et al., 2018; Goodman et al., 2019). In particular, Al concentrations commonly exceed state water quality standards in the upper Provo River (Boyd, 2017). La and Y are representative of the rare earth elements in our dataset and Ca^{2+} and SO_4^{2-} are representative of the major ions. Raw data for all trace elements and major ions at Soapstone, Woodland, and Hailstone are provided in the **Supplementary Tables 1–5**.

Trace element concentrations increased with discharge, with year-to-year variability for some elements depending on total discharge (**Figure 3**). Concentrations were typically highest at Soapstone, intermediate at Woodland, and lowest at Hailstone. For Be, La, and Y, peak concentrations were similar each year in response to snowmelt runoff. In contrast, maximum Al, Cu, and Pb concentrations were variable in response to the amount of discharge, with the highest concentrations occurring in 2017 coincident with the highest discharge. The lowest peak concentrations of Al were measured in 2016 with average

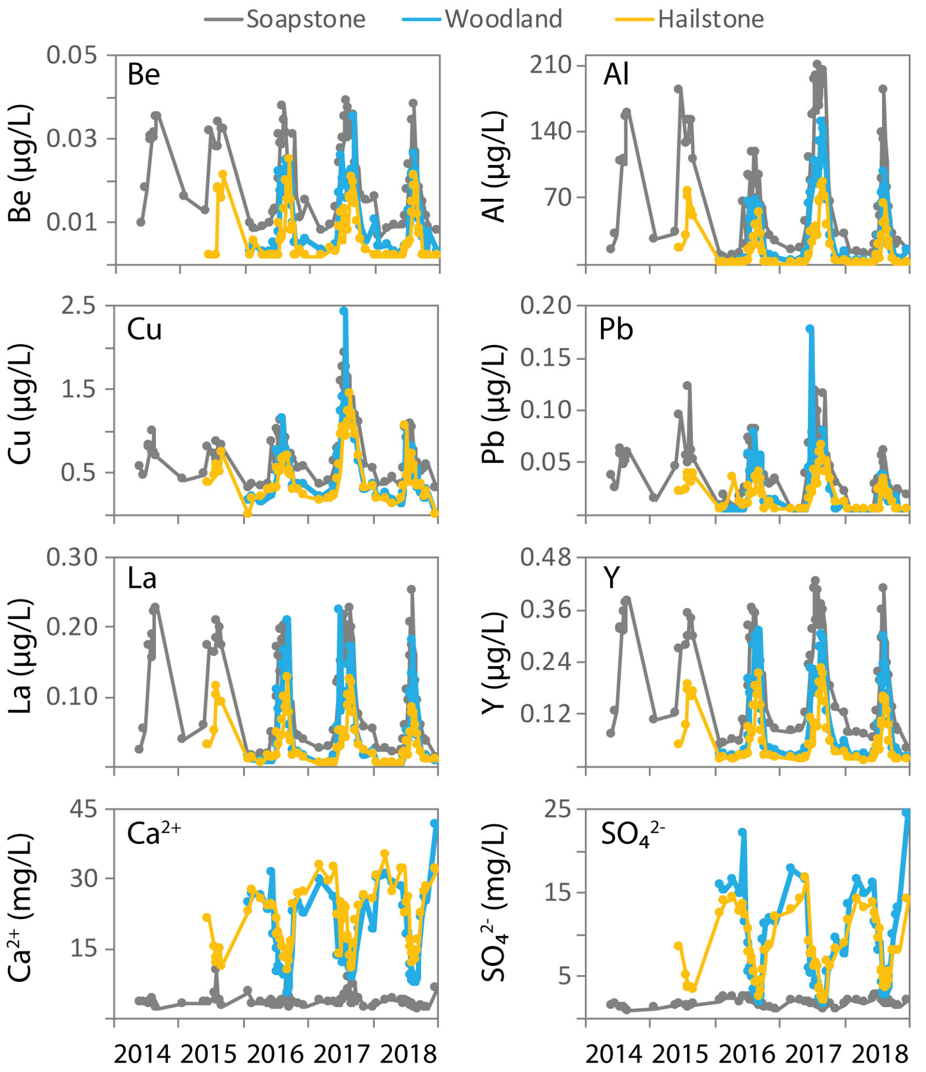

FIGURE 3 | Time-series concentrations of selected trace elements (Be, Al, Cu, Pb, La, and Y) and major ions (Ca^{2+} and SO_4^{2-}) at Soapstone, Woodland, and Hailstone for the period 2014–2018.

discharge, while the lowest peak concentrations of Cu were measured in 2015 and 2018 with the lowest discharge. Peak concentrations of Pb were moderate in 2015 and low in 2018.

Major ion concentrations showed dramatically different trends relative to the trace elements, with increasing concentrations from upstream to downstream (**Figure 3**). At Soapstone, Ca^{2+} and SO_4^{2-} concentrations were similar throughout the entire 5-year sampling period, with minimal change in response to discharge. At Woodland and Hailstone, major ion concentrations varied in response to discharge. Specifically, Ca^{2+} and SO_4^{2-} concentrations were relatively high during low-flow periods and decreased during snowmelt runoff each year, nearly matching the low concentrations observed at Soapstone. For major ions and trace elements, the seasonal and year-to-year variability were much larger than measurement errors (in the range of ±10%).

Concentration–Discharge Relationships for Trace Elements and Major Ions

Concentration–discharge (C–Q) plots showed positive slopes for trace elements and either no slope or negative slopes for the major ions (**Figure 4**). For the trace elements, the slopes of the log C–log Q relationships were less steep at Soapstone relative to Woodland and Hailstone. For example, the log C–log Q slope for be increased from 0.31 at Soapstone to 0.62 and Woodland and 0.61 at Hailstone. The steepest slopes were found for Al, which increased from 0.59 at Soapstone to >1 at Woodland and Hailstone. For the major ions, in contrast, the slopes were near zero at Soapstone and negative at Woodland and Hailstone. For example, the slope was −0.09 at Soapstone and decreased to −0.63 at Woodland and −0.35 at Hailstone. For each of these solutes, C–Q data were included for all years of the study period for each site.

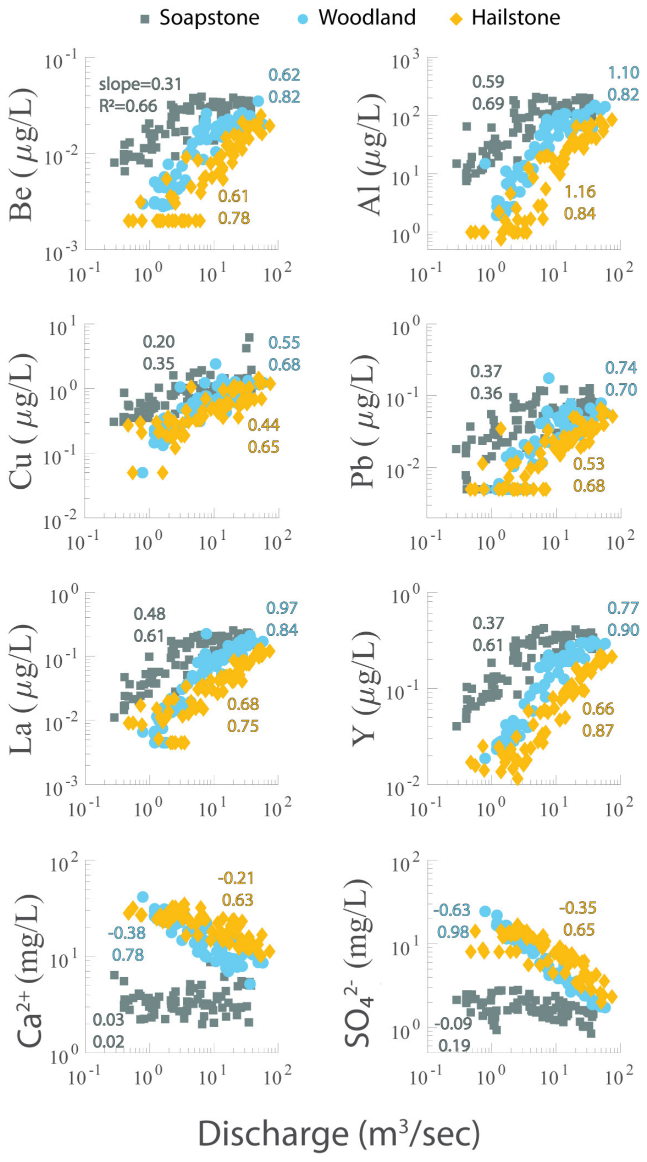

FIGURE 4 | Concentration-discharge (C–Q) plots on a log-log scale for selected trace elements (Be, Al, Cu, Pb, La, and Y) and major ions (Ca^{2+} and SO_4^{2-}) from Soapstone, Woodland, and Hailstone with data from multiple years. The slope of the best fit line and R^2 value are shown for each data series.

The C–Q relationships were more robust at Woodland and Hailstone (higher R^2 values) relative to Soapstone (lower R^2 values) for all solutes. At Woodland and Hailstone, R^2 values ranged from 0.63 to 0.98. At Soapstone, R^2 values ranged from 0.35 to 0.69 for trace elements and were <0.2 for the major ions.

Stable isotopes of water ($\delta^{18}O$ and δ^2H) showed small changes relative to discharge (**Figure 5**). Both isotopes were slightly depleted from low flow to high flow. Notably, the values were similar at Soapstone, Woodland, and Hailstone.

Annual Solute Loads Dominated by Snowmelt Runoff

Solute loading was dominated by the snowmelt runoff period (April–June) each year, with the upper watershed (above Soapstone) contributing a majority of trace elements and the lower watershed (below Soapstone) contributing a majority of major ions (**Tables 1**, **2**). Trace element loads at Soapstone were nearly as high (Be, Cu, Pb) or similar (Al, La, Y) as the loads further downstream at Hailstone, whereas the major ion loads at Soapstone were only a small fraction (<15%) of the loads at Hailstone (**Table 1**). The 3-month snowmelt runoff period accounted for 84–99% of the annual trace element loads compared with only 67–86% of the annual discharge at Soapstone, Woodland, and Hailstone. For the major ions, the snowmelt runoff period accounted for 75–89% of the annual load at Soapstone and 37–71% of the annual load at Woodland and Hailstone (**Table 2**).

Solute Concentrations in Snow, Soil Water, and Ephemeral Streams

Solute concentrations were variable across snow, soil water, ephemeral stream, and river samples (**Figure 6**). For the trace elements, concentrations were highest in soil water and ephemeral stream samples. Concentrations of Be, Cu, La, and Y were similar in soil water and ephemeral streams, while concentrations of Al and Pb were much higher in soil water. Trace element concentrations were lower in baseflow samples (defined as the period July–March) relative to snowmelt runoff samples (April–June) at Soapstone, Woodland, and Hailstone. For the major ions, in contrast, concentrations were low in soil water and ephemeral streams and high in the river samples during baseflow and were higher during baseflow relative to snowmelt runoff. For all solutes, concentrations in snowpack were low relative to the other sample types. There is some uncertainty in the concentration ranges within each sample type (**Figure 6**) because of spatial variability across the landscape for snowpack or ephemeral streams and the difficulty of collecting representative soil water samples. However, even with the uncertainty, the differences were so large between snow and soil water or ephemeral streams that the interpretations likely would not change even with additional sampling.

DISCUSSION

Trace Element Flushing From the Critical Zone During Snowmelt Runoff

Trace element concentrations in the upper Provo River increased during snowmelt runoff each year, suggesting that these elements are sourced from shallow flow paths that are activated by snowmelt in the watershed. The increased concentrations likely result from soil water flushing based on C–Q relationships, elevated concentrations in soil water, and increased DOM concentrations during the snowmelt period (**Supplementary Figure 2**). The C–Q relationships depend on material availability, with positive slopes demonstrating that high discharge events provide new sources of trace elements through

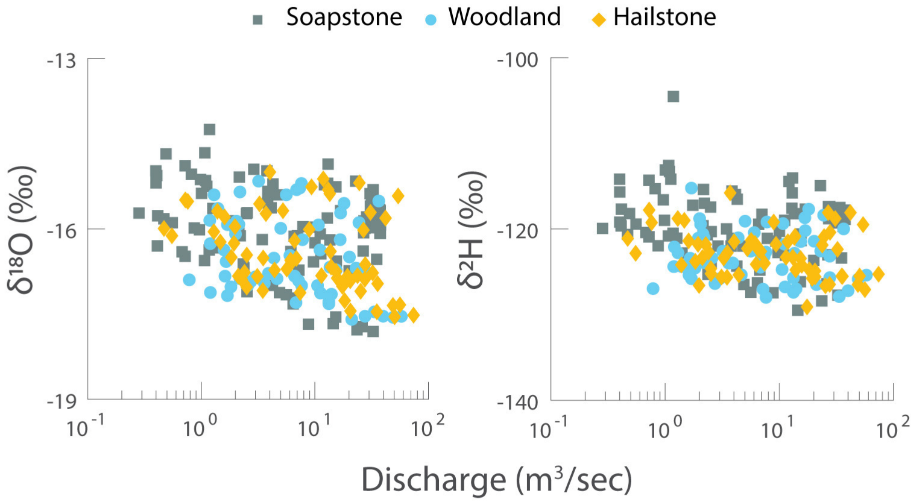

FIGURE 5 | Stable isotopes of water ($\delta^{18}O$ and $\delta^{2}H$) vs. discharge for Soapstone, Woodland, and Hailstone with data from multiple years. Note the linear scale for the y-axis and log scale for the x-axis.

TABLE 1 | Annual solute loads at Soapstone, Woodland, and Hailstone.

Location	Water year	Be (kg)	Al (t)	Cu (kg)	Pb (kg)	La (kg)	Y (kg)	Ca^{2+} (t)	SO_4^{2-} (t)
Soapstone	2016	3.3	13.8	121	8.4	19.6	33.9	529	198
Soapstone	2017	4.0	21.6	183	9.5	24.4	43.2	688	209
Soapstone	2018	1.6	5.8	60	2.7	9.2	17.4	256	154
Woodland	2016	3.2	12.2	132	9.5	24.1	37.2	1,993	924
Woodland	2017	5.6	26.6	279	12.8	33.0	61.7	3,873	1,266
Woodland	2018	2.0	6.4	72	3.7	11.6	20.8	2,262	996
Hailstone	2016	3.6	12.2	165	11.7	23.4	37.6	3,603	1,339
Hailstone	2017	6.0	19.3	348	14.5	27.2	53.8	6,971	2,027
Hailstone	2018	1.7	5.1	81	3.4	8.2	15.4	3,658	1,357

Units are kg or metric tons (t).

TABLE 2 | Fraction of annual solute load and discharge during snowmelt runoff (April–June).

Location	Water year	Be	Al	Cu	Pb	La	Y	Ca^{2+}	SO_4^{2-}	Discharge
Soapstone	2016	0.93	0.97	0.92	0.95	0.96	0.95	0.89	0.85	0.86
Soapstone	2017	0.86	0.92	0.86	0.89	0.90	0.88	0.83	0.75	0.77
Soapstone	2018	0.88	0.94	0.85	0.92	0.94	0.91	0.77	0.78	0.76
Woodland	2016	0.95	0.98	0.93	0.97	0.98	0.96	0.55	0.42	0.77
Woodland	2017	0.86	0.92	0.84	0.87	0.93	0.90	0.55	0.42	0.73
Woodland	2018	0.89	0.96	0.85	0.93	0.96	0.92	0.44	0.37	0.67
Hailstone	2016	0.98	0.99	0.95	0.97	0.98	0.98	0.71	0.59	0.83
Hailstone	2017	0.92	0.96	0.87	0.91	0.93	0.92	0.61	0.51	0.73
Hailstone	2018	0.92	0.98	0.84	0.90	0.95	0.92	0.51	0.45	0.67

flushing, as observed in other studies (Trostle et al., 2016). Positive C–Q slopes for Be, Al, Cu, Pb, La, and Y reflect flushing of these elements from soils (**Figure 4**). Soil water contained the highest trace element concentrations relative to snowpack and ephemeral streams, indicating that soil water is the likely source of trace elements (**Figure 6**). Flushed soil water mixes with groundwater and surficial snowmelt to create ephemeral streams, which carry trace elements to the river. Solutes in snowpack likely contribute minimally to observed water chemistry in the upper Provo River. Rather, snowmelt interacts with the soil profile and flushes trace elements from soil water. The major ion C–Q relationships showed chemostatic behavior at Soapstone, with constant concentrations with increasing discharge, and dilution at Woodland and Hailstone. During baseflow, when the river

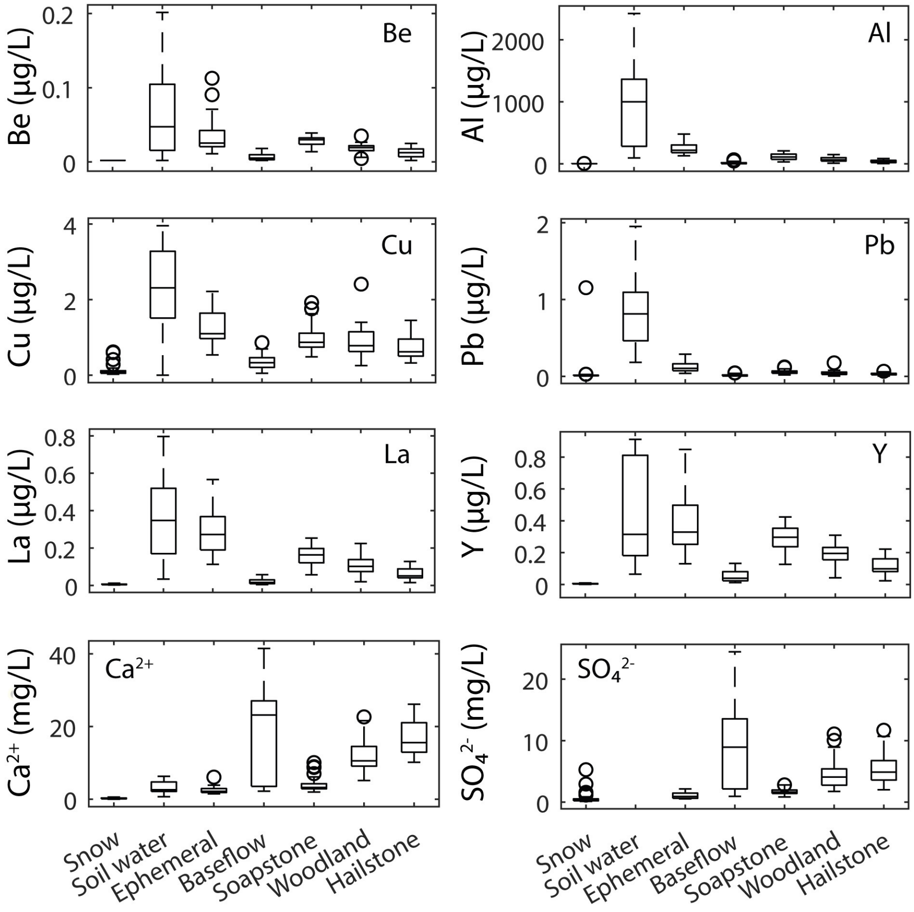

FIGURE 6 | Box plots of trace element (Be, Al, Cu, Pb, La, and Y) and major ion (Ca^{2+} and SO_4^{2-}) concentrations in snowpack ($n = 48$), soil water ($n = 8$), ephemeral streams ($n = 27$), river samples under baseflow conditions (defined as July–March) combined for Soapstone, Woodland, and Hailstone ($n = 77$), and river samples collected during snowmelt runoff (defined as April–June) for Soapstone ($n = 51$), Woodland ($n = 36$), and Hailstone ($n = 40$). Circles represent outliers.

is dominated by groundwater inputs, major ion concentrations increased substantially between Soapstone and Woodland with inputs of solute-rich groundwater from carbonate bedrock. While we did not measure groundwater chemistry as part of our study, previous work in the Provo River watershed (Carling et al., 2015) and the Logan River in northern Utah (Neilson et al., 2018) describes contributions of solute-rich groundwater from carbonate bedrock to rivers during dry-season baseflow. During snowmelt runoff, the major ion concentrations remained low at Soapstone and were diluted at Woodland and Hailstone with the influx of snowmelt-flushed shallow soil water from the upper watershed.

Changing flow paths during the snowmelt season is supported by stable isotopes of water. As shallow flow paths were activated during high discharge, the $\delta^{18}O$ and δ^2H values were more depleted (**Figure 5**). This suggests that isotopically depleted snowmelt entered the river, either as direct inputs or along quick flow paths. The slightly depleted isotopic values transferred downstream from Soapstone to Woodland and Hailstone, highlighted the importance of high elevation recharge to streamflow at lower elevations. Yet the small isotopic changes from low- to high-discharge also demonstrate that high elevation snowmelt dominates shallow soil water and groundwater fluxes to the river, with similar isotopic values at all locations throughout each year. Thus, snowmelt is the primary source of water to the river but the chemistry of snowmelt changes depending on the flow path.

Flushing of shallow soils as a source of trace elements is further supported by elevated DOM concentrations in the upper Provo River during snowmelt (**Supplementary Figure 2**). Trace metal and DOM concentrations are typically correlated in streams, especially during runoff events (Rember and Tefrey, 2004; Hölemann et al., 2005; Kerr et al., 2008; Reynolds et al., 2014; Herndon et al., 2015). Soil water is the main source of DOM in mountain watersheds (Hornberger et al., 1994; Rember and Tefrey, 2004). The most likely source of stream DOM is from the upper soil horizon by degradation of plant material, where DOC is transported from soil water to the river system (Brooks et al., 1999). Probe-measured fluorescent DOM (fDOM) concentrations spiked during the snowmelt runoff period over multiple years at Soapstone and Woodland (**Supplementary Figure 2**). Samples collected for DOM characteristics at Soapstone, Woodland, and Hailstone during 2017 identified the dominance of soil humic and fulvic acid fractions of DOM during snowmelt runoff (Packer et al., 2020). Further analysis of DOM is needed to identify relationships between the complexation of metals with fulvic and humic acids.

Trace element transport from soil water to the stream during snowmelt may be facilitated by both DOM and mineral colloids (Trostle et al., 2016). For example, concentrations of both fDOM and turbidity increased dramatically during snowmelt runoff at Soapstone in 2016 (**Supplementary Figure 3**). The elevated metal concentrations at peak discharge could be related to colloid transport, as observed in other headwater streams (Aguirre et al., 2017). High discharge is typically a driver of total suspended solid concentrations (Rose et al., 2018), of which a fraction may be composed of colloids that pass through a $<0.45\,\mu\text{m}$ filter. Colloids effectively sorb metals and facilitate metal transport, especially Pb (Citeau et al., 2003). Sorbed metals can move more quickly through soils due to size exclusion (Grolimund et al., 1998), which explains why a flux of metals often precedes peak discharge and why metals in particular are flushed, while other solute concentrations remain chemostatic. The presence of colloid-bound metals is supported by our previous research comparing water chemistry above and below Jordanelle Reservoir, with decreasing concentrations of "dissolved" metals likely due to settling in the reservoir (Carling et al., 2015). The relative amount transported by DOM or colloids during snowmelt deserves further attention but was beyond the scope of this study.

Trace element fluxes from soil water at the top of the watershed dominate the trace element loads at the bottom of the watershed. The annual trace element loads were controlled by annual discharge, with the largest loads occurring in 2017 (above average discharge) and the smallest loads occurring in 2018 (below average discharge). Most trace element loading occurred during the short window of snowmelt runoff, with >84% of the loads of Be, Al, Cu, Pb, La, and Y occurring during April–June each year (**Table 2**). The fraction of trace element loading during snowmelt runoff was greater than the fraction of discharge occurring over the same period, highlighting the importance of shallow flow paths for contributing trace elements to the river. The trace element loads at Soapstone were nearly equal to the loads at Hailstone (**Table 1**), demonstrating that trace element inputs at the top of the watershed dominate the total trace element load for the river and that the trace elements are effectively transported downstream. Although trace element concentrations decreased from upstream to downstream (**Figure 3**), the loads remained similar, suggesting that trace elements are diluted but not removed during transport. It is also possible that trace elements are lost from the river due to settling or other processes, such that trace elements in the additional water at downstream sites makes up for the trace elements lost during transport.

Major ion loading is controlled by groundwater inputs in the lower part of the watershed, with loads of Ca^{2+} and SO_4^{2-} increasing substantially from upstream to downstream (**Table 1**). At Soapstone, most major ion loading occurred during snowmelt runoff, but the loads were small compared to Woodland and Hailstone, where only about half of the loading occurred during snowmelt runoff (**Table 2**). At the downstream sites, groundwater contributions during baseflow dominated the major ion loads. Although baseflow contributed only ∼30% of the annual discharge at Woodland and Hailstone, the major ion concentrations in groundwater were high enough to account for ∼50% of the annual loading. The loads of Ca^{2+} and SO_4^{2-} doubled between Woodland and Hailstone due to contributions from the Weber River diversion.

Changes in Solute Concentration–Discharge Relationships From Upstream to Downstream

Trace element concentrations decreased from Soapstone to Woodland and Hailstone (**Figure 3**) but the slope of the C–Q relationship was steeper at the downstream sites (**Figure 4**). This suggests that water from the upper reaches of the watershed exerts a greater influence on downstream water chemistry during periods of high discharge relative to baseflow even as trace elements are diluted or removed from upstream to downstream. In other words, trace elements in soils at the top of the watershed are flushed with snowmelt tens of kilometers downstream to cause a steeper slope in the C–Q relationships. The slug of water from Soapstone increases trace element concentrations but also dilutes the major ion chemistry of the river downstream and Woodland and Hailstone, causing the negative slope for Ca^{2+} and SO_4^{2-} in C–Q space (**Figure 4**).

For many solutes, chemostasis is expected to develop with increasing stream order as flows accumulate downstream (Creed et al., 2015). However, across our transect of three sites, the C–Q relationships trended toward more chemodynamic behavior with flushing of trace elements or dilution of major ions (**Figure 4**). Further downstream, below Jordanelle Reservoir, water chemistry is generally chemostatic owing to long holding times in the reservoir (Carling et al., 2015). The emergent C–Q patterns in the upper watershed highlight the importance of comparing C–Q relationships at multiple sites along a river. Investigating the water chemistry only at Soapstone would result in interpretation of chemostatic or slight flushing behavior during snowmelt runoff, yet the C–Q relationships at Woodland and Hailstone reveal a more dynamic system. The C–Q relationships at Woodland and Hailstone are affected by water and solutes inherited from upstream at Soapstone, such that the groundwater–dominated river during baseflow is overwhelmed by snowmelt water from the upper watershed during the runoff period. Solute concentrations converge at the three sites at high discharge. The snowmelt water from shallow flow paths (soil water) causes dilution of the solute–rich groundwater at Woodland and Hailstone while simultaneously causing a much steeper slope in the trace element C–Q relationships. Under baseflow conditions, trace element concentrations decrease more rapidly from upstream to downstream, likely due to longer residence in the stream allowing for increased biogeochemical processing between the sites.

Solute Sources Within the Critical Zone During Snowmelt Runoff

The increase in dissolved metal and rare earth element concentrations and loads during snowmelt deserves further discussion given the limited source of these elements in local bedrock at the upper part of the watershed. The bedrock geology in the Uinta Mountains above the Soapstone site is dominated by siliciclastic rocks with relatively low concentrations of trace elements such as Be, Al, Cu, Pb, La, and Y (Munroe, 2014; Munroe et al., 2020). Alpine soils in the periglacial zone of the Uintas contain ~50–80% dust, with elevated trace element concentrations in soils relative to bedrock (Munroe et al., 2020). The concentrations of dust–derived metals, including Cu and Pb, increased dramatically in Uinta Mountain lake sediments after the year 1870, implying that dust–derived material increased as a result of anthropogenic activities (Reynolds et al., 2010). Similarly, others studies have shown that dust contributes elevated trace element concentrations to northern Utah snowpack (Carling et al., 2012; Reynolds et al., 2014; Dastrup et al., 2018; Goodman et al., 2019). Dust deposited to snowpack during winter or directly to the landscape during summer accumulates over time in soils and adds trace metals and rare earth elements to the soil profile, as observed in the Uintas and other locations (Vázquez-Ortega et al., 2015; Mcintosh et al., 2017; Munroe et al., 2020). The minerals in dust slowly weather from soils, contributing to elevated trace element concentrations in soil water (**Figure 6**) that is released during the snowmelt pulse. It is also possible that weathered material from the interbedded shales within siliciclastic rocks in the upper watershed are a source of metals due to their composition of micas and plagioclase minerals with relatively high metal concentrations (Condie et al., 2001; Myer, 2008). However, the shale would likely contribute metals during the baseflow period with deeper groundwater flow paths rather than during the snowmelt season.

The major ions (Ca^{2+} and SO_4^{2-}) are dominated by inputs from carbonate bedrock weathering in the lower portions of the watershed and soils and dust in the upper part of the watershed (**Figure 1**). Particularly, between the Soapstone and Woodland sites, groundwater in carbonate rocks contributes large amounts of major ions to groundwater and cause higher total solute concentrations at Woodland and Hailstone relative to Soapstone (Carling et al., 2015). In the upper watershed above Soapstone, weathering of siliciclastic sedimentary rocks (Condie et al., 2001) contribute low concentrations of major ions that is matched by concentrations from soil water during the snowmelt runoff period to maintain chemostasis.

Additional work is needed to quantify solute contributions from dust vs. bedrock in the upper Provo River watershed. This could be accomplished by developing watershed-scale solute mass balances over multiple years, better characterizing groundwater chemistry and fluxes, and investigating biogeochemical processing of solutes during transport. Our data could be used to constrain watershed models of solute transport, such as the Soil & Water Assessment Tool (SWAT), to determine the fate of dust-derived solutes in the watershed by coupling with modules to consider metals (Meng et al., 2018). Currently, we are using $^{87}Sr/^{86}Sr$ ratios to quantify Sr can Ca^{2+} inputs from dust and bedrock and to track the fate of dust-derived solutes through the watershed, which is described in an upcoming paper. The additional sampling, modeling work, and isotopic measurements are part of an ongoing, long-term project.

CONCLUSIONS

The Critical Zone is the primary source of solutes to rivers, with inputs of trace elements and major ions changing with discharge. We demonstrate the importance of shallow flow paths activated during snowmelt runoff for flushing trace elements from soil water in the upper Provo River watershed of northern Utah. Trace metal (Be, Al, Cu, and Pb) and rare earth element (represented by La and Y) concentrations increased dramatically during the snowmelt runoff period, with loads from the upper watershed propagating downstream. Snowmelt flushing of soils in the upper watershed plays an important role in controlling trace element chemistry of the river, accounting for most of the annual trace element loading. Given the low concentrations of trace elements in the siliciclastic bedrock at the top of the watershed, trace elements in soils are likely sourced from aeolian dust. Thus, metals and rare earth elements in dust represent an important control on river chemistry. Trace element transport is likely facilitated by a combination of dissolved organic matter and mineral colloids.

Major ion fluxes, in contrast, are controlled by water-rock interactions along groundwater flow paths in the carbonate bedrock at the lower elevations in the watershed. Major ion concentrations and loads were low at the upper site and increased substantially downstream with groundwater inputs from carbonate rocks. Only about half of the Ca^{2+} and SO_4^{2-} loads occurred during snowmelt runoff, with the other half coming from groundwater during baseflow. During the snowmelt runoff period, water from the upper watershed diluted major ion concentrations in the lower part of the watershed, resulting in similar concentrations longitudinally from upstream to downstream.

Concentration–discharge relationships revealed unique patterns for trace elements and major ions along the longitudinal transect of three sites. Concentration–discharge plots showed flushing behavior for trace elements and either chemostatic behavior or dilution for the major ions. For the trace elements, there was a weak flushing behavior at the upstream site and much stronger flushing behavior at the downstream sites. Major ion concentrations were chemostatic at the upstream site and diluted at the downstream sites. These relationships are contrary to expectations because chemostatic behavior should develop as flows accumulate downstream. This observation highlights the importance of characterizing concentration–discharge at multiple locations in a river for better understanding water quality in response to changing discharge.

Our findings highlight the importance of the Critical Zone for controlling water chemistry in montane watersheds, with snowmelt–driven soil water flushing dominating the annual trace element loads. Understanding flow paths during snowmelt and baseflow is necessary for determining impacts on water quality. The flux of trace elements during snowmelt may exert a larger control on river chemistry, and at larger scales, than previously thought. In particular, trace element inputs from aeolian dust to montane soils may be an important, yet overlooked, source of potentially harmful elements to river systems.

DATA AVAILABILITY STATEMENT

The datasets generated for this study can be found in the **Supplementary Material** and in HydroShare with the following DOIs: soil water and ephemeral stream data (https://doi.org/10.4211/hs.b5f8b9a80fa44d9b869a4d1604f8df2b), river chemistry (https://doi.org/10.4211/hs.1825ac7f0cd94f4d950929600729f36d), and snow chemistry (https://doi.org/10.4211/hs.20891fd47c3d4be28d723950ff415671).

AUTHOR CONTRIBUTIONS

HC performed field and laboratory work, data analysis, and wrote the first draft of the paper. GC directed the research, secured funding, and wrote the final draft. DF, SN, and ZA co-advised students and helped with writing. KR and DT directed field and laboratory work. CH, BP, and CC assisted with field and laboratory work and performed data analysis. All authors contributed to the article and approved the submitted version.

FUNDING

This work was supported by the U.S. National Science Foundation grants EAR−1521468, EAR-2012093, and OIA−1208732. Any opinions, findings, and conclusions or recommendations expressed are those of the authors and do not necessarily reflect the views of the National Science Foundation.

ACKNOWLEDGMENTS

We thank Natalie Barkdull, Greta Hamilton, Andrew Luymes, and Andrew Bentz for help in the field and laboratory.

SUPPLEMENTARY MATERIAL

The Supplementary Material for this article can be found online at: https://www.frontiersin.org/articles/10.3389/frwa.2020.578677/full#supplementary-material

REFERENCES

Aguirre, A. A., Derry, L. A., Mills, T. J., and Anderson, S. P. (2017). Colloidal transport in the gordon gulch catchment of the boulder creek CZO and its effect on C-Q relationships for silicon. *Water Resour. Res.* 53, 2368–2383. doi: 10.1002/2016WR019730

Barnett, T. P., Pierce, D. W., Hidalgo, H. G., Bonfils, C., Santer, B. D., Das, T., et al. (2008). Human-induced changes in the hydrology of the western United States. *Science* 319, 1080–1083. doi: 10.1126/science.1152538

Boyd, A. E. (2017). *2018 Water Quality Implementation Report. Prepared for Wasatch County & Utah Division of Water Quality*, Park City, UT, 68.

Brooks, P. D., Chorover, J., Fan, Y., Godsey, S. E., Maxwell, R. M., Mcnamara, J. P., et al. (2015). Hydrological partitioning in the critical zone: recent advances and opportunities for developing transferable understanding of water cycle dynamics. *Water Resour. Res.* 51, 6973–6987. doi: 10.1002/2015WR017039

Brooks, P. D., Mcknight, D. M., and Bencala, K. E. (1999). The relationship between soil heterotrophic activity, soil dissolved organic carbon (DOC) leachate, and catchment-scale DOC export in headwater catchments. *Water Resour. Res.* 35, 1895–1902. doi: 10.1029/1998WR900125

Carling, G. T., Fernandez, D. P., and Johnson, W. P. (2012). Dust-mediated loading of trace and major elements to Wasatch Mountain snowpack. *Sci. Total Environ.* 432, 65–77. doi: 10.1016/j.scitotenv.2012.05.077

Carling, G. T., Tingey, D. G., Fernandez, D. P., Nelson, S. T., Aanderud, Z. T., Goodsell, T. H., et al. (2015). Evaluating natural and anthropogenic trace element inputs along an alpine to urban gradient in the provo river, Utah, USA. *Appl. Geochem.* 63, 398–412. doi: 10.1016/j.apgeochem.2015.10.005

Chorover, J., Derry, L. A., and Mcdowell, W. H. (2017). Concentration-discharge relations in the critical zone: implications for resolving critical zone structure, function, and evolution. *Water Resour. Res.* 53, 8654–8659. doi: 10.1002/2017WR021111

Citeau, L., Lamy, I., Van Oort, F., and Elsass, F. (2003). Colloidal facilitated transfer of metals in soils under different land use. *Colloids Surf. A.* 217, 11–19. doi: 10.1016/S0927-7757(02)00554-X

Condie, K. C., Lee, D., and Farmer, G. L. (2001). Tectonic setting and provenance of the Neoproterozoic Uinta Mountain and Big Cottonwood groups, northern Utah: constraints from geochemistry, Nd isotopes, and detrital modes. *Sediment. Geol.* 141–142, 443–464. doi: 10.1016/S0037-0738(01)00086-0

Creed, I. F., Mcknight, D. M., Pellerin, B. A., Green, M. B., Bergamaschi, B. A., Aiken, G. R., et al. (2015). The river as a chemostat: fresh perspectives on dissolved organic matter flowing down the river continuum. *Canad. J. Fish. Aquat. Sci.* 72, 1272–1285. doi: 10.1139/cjfas-2014-0400

Dastrup, D. B., Carling, G. T., Collins, S. A., Nelson, S. T., Fernandez, D. P., Tingey, D. G., et al. (2018). Aeolian dust chemistry and bacterial communities in snow are unique to airshed locations across northern Utah, USA. *Atmos. Environ.* 193, 251–261. doi: 10.1016/j.atmosenv.2018.09.016

Dehler, C. M., Porter, S. M., De Grey, L. D., Sprinkel, D. A., and Brehm, A. (2006). The neoproterozoic uinta mountain group revisited: a synthesis of recent work on the red pine shale and related undivided clastic strata, northeastern Utah. *Soc. Sediment. Geol.* 86:151. doi: 10.2110/pec.07.86.0151

Evans, C., and Davies, T. D. (1998). Causes of concentration/discharge hysteresis and its potential as a tool for analysis of episode hydrochemistry. *Water Resour. Res.* 34, 129–137. doi: 10.1029/97WR01881

Godsey, S. E., Kirchner, J. W., and Clow, D. W. (2009). Concentration–discharge relationships reflect chemostatic characteristics of US catchments. *Hydrol. Process* 23, 1844–1864. doi: 10.1002/hyp.7315

Goodman, M. M., Carling, G. T., Fernandez, D. P., Rey, K. A., Hale, C. A., Bickmore, B. R., et al. (2019). Trace element chemistry of atmospheric deposition along the Wasatch Front (Utah, USA) reflects regional playa dust and local urban aerosols. *Chem. Geol* 530:119317. doi: 10.1016/j.chemgeo.2019.119317

Grolimund, D., Elimelech, M., Borkovec, M., Barmettler, K., Kretzschmar, R., and Sticher, H. (1998). Transport of *in situ* mobilized colloidal particles in packed soil columns. *Environ. Sci. Technol.* 32, 3562–3569. doi: 10.1021/es980356z

Herndon, E. M., Dere, A. L., Sullivan, P. L., Norris, D., Reynolds, B., and Brantley, S. L. (2015). Landscape heterogeneity drives contrasting concentration-discharge relationships in shale headwater catchments. *Hydrol. Earth Syst. Sci.* 19, 3333–3347. doi: 10.5194/hess-19-3333-2015

Hölemann, J. A., Schirmacher, M., and Prange, A. (2005). Seasonal variability of trace metals in the Lena river and the southeastern Laptev sea: impact of the spring freshet. *Glob. Planet. Change* 48, 112–125. doi: 10.1016/j.gloplacha.2004.12.008

Hornberger, G., Bencala, K., and Mcknight, D. (1994). Hydrological controls on dissolved organic carbon during snowmelt in the Snake river near Montezuma, Colorado. *Biogeochemistry* 25, 147–165. doi: 10.1007/BF00024390

iUTAH Cyberinfrastructure Team (2017). *Discharge Rating Curve at Provo River Near Soapstone Basin Aquatic Site (PR_ST_BA)*. HydroShare. Available online at: http://www.hydroshare.org/resource/d14c319e607140bb607183fe607146b607143b93302994

iUTAH GAMUT Working Group (2019). *iUTAH GAMUT Network Quality Control Level 1 Data at Provo River Near Soapstone Basic Aquatic (PR_ST_BA)*. HydroShare. Available online at: https://www.hydroshare.org/resource/e640b621cb649b604d620a952cf156459a156729/

Kerr, S. C., Shafer, M. M., Overdier, J., and Armstrong, D. E. (2008). Hydrologic and biogeochemical controls on trace element export from northern Wisconsin wetlands. *Biogeochemistry* 89, 273–294. doi: 10.1007/s10533-008-9219-2

Lloyd, C. E. M., Freer, J. E., Johnes, P. J., and Collins, A. L. (2016). Using hysteresis analysis of high-resolution water quality monitoring data, including uncertainty, to infer controls on nutrient and sediment transfer in catchments. *Sci. Total Environ.* 543, 388–404. doi: 10.1016/j.scitotenv.2015.11.028

Mcintosh, J. C., Schaumberg, C., Perdrial, J., Harpold, A., Vázquez-Ortega, A., Rasmussen, C., et al. (2017). Geochemical evolution of the critical zone across variable time scales informs concentration-discharge relationships: Jemez river basin critical zone observatory. *Water Resour. Res.* 53, 4169–4196. doi: 10.1002/2016WR019712

Meng, Y., Zhou, L., He, S., Lu, C., Wu, G., Ye, W., et al. (2018). A heavy metal module coupled with the SWAT model and its preliminary application in a mine-impacted watershed in China. *Sci. Total Environ.* 613–614, 1207–1219. doi: 10.1016/j.scitotenv.2017.09.179

Munroe, J. S. (2014). Properties of modern dust accumulating in the Uinta Mountains, Utah, USA, and implications for the regional dust system of the Rocky mountains. *Earth Surf. Process. Landf.* 39, 1979–1988. doi: 10.1002/esp.3608

Munroe, J. S., Attwood, E. C., O'keefe, S. S., and Quackenbush, P. J. M. (2015). Eolian deposition in the alpine zone of the Uinta Mountains, Utah, USA. *CATENA* 124, 119–129. doi: 10.1016/j.catena.2014.09.008

Munroe, J. S., Norris, E. D., Olson, P. M., Ryan, P. C., Tappa, M. J., and Beard, B. L. (2020). Quantifying the contribution of dust to alpine soils in the periglacial zone of the Uinta mountains, Utah, USA. *Geoderma* 378:114631. doi: 10.1016/j.geoderma.2020.114631

Myer, C. A. (2008). *Sedimentology, stratigraphy, and organic geochemistry of the Red Pine Shale, Uinta Mountains, Utah: a prograding deltaic system in a mid-Neoproterozoic interior seaway* (All Graduate Theses and Dissertations). Utah State University, Logan, UT, United States.

Neilson, B. T., Tennant, H., Stout, T. L., Miller, M. P., Gabor, R. S., Jameel, Y., et al. (2018). Stream centric methods for determining groundwater contributions in karst mountain watersheds. *Water Resour. Res.* 54, 6708–6724. doi: 10.1029/2018WR022664

Ogendi, G. M., Hannigan, R. E., and Farris, J. L. (2007). Association of dissolved organic carbon with stream discharge and dissolved metals concentrations in black shale-draining streams. *Dev. Environ. Sci.* 5, 247–272. doi: 10.1016/S1474-8177(07)05012-7

Packer, B. N., Carling, G. T., Veverica, T. J., Russell, K. A., Nelson, S. T., and Aanderud, Z. T. (2020). Mercury and dissolved organic matter dynamics during snowmelt runoff in a montane watershed, Provo River, Utah, USA. *Sci. Total Environ.* 704:135297. doi: 10.1016/j.scitotenv.2019.135297

Rember, R. D., and Tefrey, J. H. (2004). Increased concentrations of dissolved trace metals and organic carbon during snowmelt in rivers of the Alaskan arctic. *Geochem. Cosmochim. Acta* 68, 477–489. doi: 10.1016/S0016-7037(03)00458-7

Reynolds, R. L., Goldstein, H. L., Moskowitz, B. M., Bryant, A. C., Skiles, S. M., Kokaly, R. F., et al. (2014). Composition of dust deposited to snow cover in the Wasatch Range (Utah, USA): Controls on radiative properties of snow cover and comparison to some dust-source sediments. *Aeol. Res.* 15, 73–90. doi: 10.1016/j.aeolia.2013.08.001

Reynolds, R. L., Mordecai, J. S., Rosenbaum, J. G., Ketterer, M. E., Walsh, M. K., and Moser, K. A. (2010). Compositional changes in sediments of subalpine lakes, Uinta Mountains (Utah): evidence for the effects of human activity on atmospheric dust inputs. *J. Paleolimnol.* 44, 161–175. doi: 10.1007/s10933-009-9394-8

Rose, L. A., Karwan, D. L., and Godsey, S. E. (2018). Concentration–discharge relationships describe solute and sediment mobilization, reaction, and transport at event and longer timescales. *Hydrol. Process* 32, 2829–2844. doi: 10.1002/hyp.13235

Runkel, R. L., Crawford, C. G., and Cohn, T. A. (2004). "Load estimator (LOADEST): a fortran program for estimating constituent loads in streams and rivers," in *U.S. Geological Survey Techniques and Methods Book, Vol. 4,* (Reston, VT: USGS) 69.

Shafer, M. M., Overdier, J. T., Hurley, J. P., Armstrong, D., and Webb, D. (1997). The influence of dissolved organic carbon, suspended particulates, and hydrology on the concentration, partitioning and variability of trace metals in two contrasting Wisconsin watersheds (U.S.A.). *Chem. Geol.* 136, 71–97. doi: 10.1016/S0009-2541(96)00139-8

Trostle, K. D., Ray Runyon, J., Pohlmann, M. A., Redfield, S. E., Pelletier, J., Mcintosh, J., et al. (2016). Colloids and organic matter complexation control trace metal concentration-discharge relationships in Marshall Gulch stream waters. *Water Resour. Res.* 52, 7931–7944. doi: 10.1002/2016WR019072

Vázquez-Ortega, A., Perdrial, J., Harpold, A., Zapata-Ríos, X., Rasmussen, C., Mcintosh, J., et al. (2015). Rare earth elements as reactive tracers of biogeochemical weathering in forested rhyolitic terrain. *Chem. Geol.* 391, 19–32. doi: 10.1016/j.chemgeo.2014.10.016

Williams, G. P. (1989). Sediment concentration versus water discharge during single hydrologic events in rivers. *J. Hydrol.* 111, 89–106. doi: 10.1016/0022-1694(89)90254-0

Conflict of Interest: The authors declare that the research was conducted in the absence of any commercial or financial relationships that could be construed as a potential conflict of interest.

ORIGINAL RESEARCH
published: 23 November 2020
doi: 10.3389/frwa.2020.578602

From Patch to Catchment: A Statistical Framework to Identify and Map Soil Moisture Patterns Across Complex Alpine Terrain

Anna L. Hermes[1,2]*, *Haruko M. Wainwright*[3], *Oliver Wigmore*[2,4,5], *Nicola Falco*[3], *Noah P. Molotch*[2,6] and *Eve-Lyn S. Hinckley*[1,2]

[1] Environmental Studies Program, University of Colorado at Boulder, Boulder, CO, United States, [2] Institute of Arctic and Alpine Research, University of Colorado at Boulder, Boulder, CO, United States, [3] Lawrence Berkeley National Laboratory, Earth and Environmental Sciences Division, Berkeley, CA, United States, [4] Antarctic Research Centre, Victoria University of Wellington, Wellington, New Zealand, [5] Earth Lab, Cooperative Institute for Research in Environmental Sciences, University of Colorado at Boulder, Boulder, CO, United States, [6] Department of Geography, University of Colorado at Boulder, Boulder, CO, United States

Climate warming in alpine regions is changing patterns of water storage, a primary control on alpine plant ecology, biogeochemistry, and water supplies to lower elevations. There is an outstanding need to determine how the interacting drivers of precipitation and the critical zone (CZ) dictate the spatial pattern and time evolution of soil water storage. In this study, we developed an analytical framework that combines intensive hydrologic measurements and extensive remotely-sensed observations with statistical modeling to identify areas with similar temporal trends in soil water storage within, and predict their relationships across, a 0.26 km^2 alpine catchment in the Colorado Rocky Mountains, U.S.A. Repeat measurements of soil moisture were used to drive an unsupervised clustering algorithm, which identified six unique groups of locations ranging from predominantly dry to persistently very wet within the catchment. We then explored relationships between these hydrologic groups and multiple CZ-related indices, including snow depth, plant productivity, macro- (10^2->10^3 m) and microtopography ($<10^0$-10^2 m), and hydrological flow paths. Finally, we used a supervised machine learning random forest algorithm to map each of the six hydrologic groups across the catchment based on distributed CZ properties and evaluated their aggregate relationships at the catchment scale. Our analysis indicated that ~40–50% of the catchment is hydrologically connected to the stream channel, lending insight into the portions of the catchment that likely dominate stream water and solute fluxes. This research expands our understanding of patch-to-catchment-scale physical controls on hydrologic and biogeochemical processes, as well as their relationships across space and time, which will inform predictive models aimed at determining future changes to alpine ecosystems.

Keywords: hydrology, critical zone, topography, random forest, Niwot Ridge LTER, Rocky Mountains, Colorado

OPEN ACCESS

Edited by:
Jon Chorover,
University of Arizona, United States

Reviewed by:
Luca Brocca,
National Research Council (CNR), Italy
Ty Ferre,
University of Arizona, United States

***Correspondence:**
Anna L. Hermes
anna.hermes@colorado.edu

Specialty section:
This article was submitted to Water and Critical Zone, a section of the journal Frontiers in Water

Received: 30 June 2020
Accepted: 12 October 2020
Published: 23 November 2020

Citation:
Hermes AL, Wainwright HM, Wigmore O, Falco N, Molotch NP and Hinckley E-LS (2020) From Patch to Catchment: A Statistical Framework to Identify and Map Soil Moisture Patterns Across Complex Alpine Terrain. Front. Water 2:578602. doi: 10.3389/frwa.2020.578602

INTRODUCTION

Alpine regions are essential sources of fresh water to lower elevation ecosystems and ∼50% of people around the globe (Winkler, 2019). In addition, they are also some of the most vulnerable to climate change (Buytaert et al., 2011; Seidl et al., 2011; Ernakovich et al., 2014). Many researchers have shown that alpine areas are already warming and predict that they may experience the highest levels and impacts of warming well before other ecosystems (e.g., Bradley, 2004; Cannone et al., 2007; Pepin et al., 2015; Winkler, 2019). These impacts include changes to the timing, amount, and quality of water exported from alpine catchments (Barnett et al., 2005; Horton et al., 2006; Tague, 2009; Schneeberger et al., 2015), among others.

Water export from the alpine zone is controlled both by sources—including, in some cases, glaciers (Cannone et al., 2008), and precipitation, primarily as snow (Bales and Harrington, 1995; Bales et al., 2006)—and their mediation by the critical zone (CZ; Tague and Grant, 2009; Penna et al., 2011; Yang et al., 2014; Baraer et al., 2015; Brooks et al., 2015; Winnick et al., 2017). Many past studies have focused on determining the effects of a warming climate on the distribution of snowpack (Ishida et al., 2018; Smith and Bookhagen, 2018) as well as the timing and rate of snowmelt that feeds the CZ (Magnusson et al., 2012; Musselman et al., 2017; Jennings and Molotch, 2020). An important next step is to delve into how the physical structure of the CZ determines patterns of water storage and routing within alpine catchments; this is baseline knowledge required to predict changes to alpine water balances as well as ecological and biogeochemical functions.

Multiple scales of the CZ affect patterns of alpine water storage and routing. In particular, topographical features, both at macro- (10^2->10^3 m) and micro-scales (<10^0-10^2 m) play important roles. At the macro-scale, the characteristics of complex relief, including hillslope position, aspect, and slope, which interact with winds to influence snow accumulation and redistribution (Winstral et al., 2002). At the micro-scale, freeze-thaw processes produce morphological features, such as patterned ground, nivation depressions, and solifluction lobes and terraces that affect snow depth, water storage, and hydrologic connectivity (Russell, 1933; Matsuoka et al., 2005; Wainwright et al., 2015, 2017). At still finer, sub-meter scales, soil properties and vegetation influence infiltration rates (see Hinckley et al., 2014b; Brooks et al., 2015). When combined, these characteristics of the CZ create areas of like hydrologic behavior, characterized by both the quantity and rate of change of soil water storage.

Mapping areas of like hydrologic behaviors across alpine catchments is an important step toward understanding the aggregate effects of patch-scale processes. For example, mapping the spatial distribution of hydrologic behaviors aids in quantifying the temporal stability of soil water storage (Lee and Kim, 2019) and water transit time distributions (Harman, 2015). These are both key factors that complicate hillslope modeling studies (Kirchner, 2016; Guio Blanco et al., 2018) and efforts to quantify chemical export from the CZ (Ward et al., 2019). Furthermore, different hydrologic behaviors may map to important ecosystem control points (Bernhardt et al., 2017)—areas that support continuously or periodically high rates of biogeochemical cycling (Darrouzet-Nardi and Bowman, 2011; Knowles et al., 2015; Chen et al., 2020). Finally, patch-scale variability in snowmelt and soil moisture affects plant phenology and physiology (Bjorkman et al., 2018; Winkler et al., 2018) and results in catchment-scale spatial patterns of plant community composition and productivity (Seastedt, 2020) and responses to change (Suding et al., 2015; Winkler et al., 2016). Thus, the capacity to identify and predict the spatial organization of distinct hydrologic behaviors is relevant not only to understanding how alpine systems will change under a warmer climate, but also to addressing outstanding questions in hydrology and CZ science more broadly. This capacity has remained a challenge, however, because of limitations in our approach to connect point-scale hydrologic observations to broader scales, which is necessary for understanding catchment processes such as water and chemical export.

Previous analytical approaches have included a combination of terrain-derived topographic indices and other CZ-related properties to predict hydrologic states. For example, Western et al. (1999) used the upslope flow accumulation area and potential radiation indices to determine soil moisture values, finding that these variables were useful for prediction at different points in time. Williams et al. (2009) applied a similar approach to show that both static (e.g., slope, aspect, soil texture) and dynamic (e.g., snowmelt) properties controlled soil moisture spatiotemporal variability. More recently, Oroza et al. (2018) were able to accurately predict soil water storage over multiple years, relying on high-resolution soil moisture sensor network data from the Southern Sierra Critical Zone Observatory. Moving beyond prediction of point-scale surface soil moisture measurements, terrain-derived indices have also been used to identify areas of connected saturation or hydrologic connectivity to stream channels (Ali et al., 2013) and explain subsurface flow variability (Bachmair and Weiler, 2012). Combined, these studies demonstrate analytical approaches that connect multiple scales of physical properties with observations to explain spatiotemporal variability in soil water storage across landscapes.

Another set of analytical approaches extrapolate hydrologic, biogeochemical, and ecological measurements beyond the locations of field observations by combining point measurements, topographic indices, and statistical models. At Hubbard Brook Experimental Forest, Gillin et al. (2015) extrapolated soil hydropedons across a catchment with

---

Abbreviations: CI, Convergence index; CIr, Range in convergence index over 5 m; CZ, Critical zone; D, Dry; D-D, Dry cluster, Dry hydrologic group; D-MD, Dry cluster, Moist-to-dry hydrologic group; D-WM, Dry cluster, Wet-to-moist hydrologic group; DEM, Digital elevation model; DTM, Digital terrain model; FA, Flow accumulation; GNSS, Global navigation satellite system; mNDVI, Maximum normalized difference vegetation index measured; MPI, Morphometric protection index; MSD, Maximum snow depth measured; OD2C, Overland distance to channel; OOB, Out-of-bag error estimate; PC, Principal component; PCA, Principal component analysis; Slope-L, Local slope; Slope-M, Macro slope; SWFA, Snow-weighted flow accumulation; TPI, Topographic position index; TPIr, Range in topographic position index over 20 m; TWI, Topographic wetness index; UAV, Unmanned aerial vehicle; VD2C, Vertical distance to channel; W, Wet; W-RD, Wet cluster, Rapid dry-down hydrologic group; W-W, Wet cluster, Wet hydrologic group; W-VW, Wet cluster, Very wet hydrologic group; WS, Wind shelter.

topographic wetness index, topographic position index, and bedrock-weighted upslope accumulation area using a multinomial logistic regression model. Another study by Wainwright et al. (2015) mapped carbon fluxes across arctic ice wedge polygons using high-resolution transects of geophysical and topographic metrics and support vector machine learning. Similarly, tower-based net ecosystem productivity, soil chamber CO_2 flux measurements, and topographic indices were combined to calculate regions of a catchment that were either strong carbon sources or sinks (Emanuel et al., 2011). Falco et al. (2019) developed a new data fusion and machine learning approach that assimilated remote sensing and surface geophysical measurements to categorize plant communities and estimate soil moisture distributions across a lower montane-floodplain landscape in Colorado. This set of predictive modeling studies demonstrates a movement toward harnessing on the ground observations, remotely-sensed data, and statistical approaches to map integrated CZ processes at broader spatial scales.

Our study builds on these previous efforts to address this gap in our ability to connect point- or patch-scale hydrologic observations to broader spatial scales. We addressed three primary research questions: (1) Are there unique temporal trends, or hydrologic behaviors, in soil water storage across an alpine catchment? (2) Which CZ-related properties explain these different behaviors? and (3) What are the spatial scales that dictate the pattern of these hydrologic behaviors across an alpine catchment? To address these questions, we developed an analytical framework that integrates existing statistical approaches to (1) identify unique hydrologic behaviors from intensive *in situ* soil moisture observations, (2) explore CZ-related drivers of these behaviors, and then (3) map the occurrence and spatial pattern of behaviors across a study catchment. We apply this framework to an alpine system in the Colorado Rocky Mountains where physical properties of the CZ clearly exert control over hydrologic patterning at multiple scales. Developing this predictive capability to move from patch-scale measurements to catchment-scales is extremely valuable in alpine landscapes, due to their complexity, fragility, and societal importance as sources of fresh water.

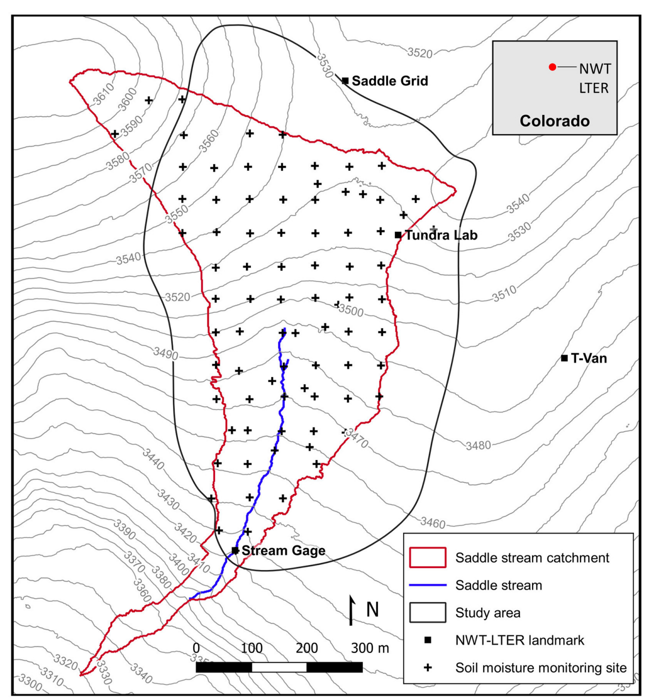

FIGURE 1 | Headwater catchment (Saddle stream) of North Boulder Creek within the Niwot Ridge (NWT) Long-term Ecological Research (LTER) site in the Colorado Rocky Mountain Front Range. Repeat soil moisture measurements occurred at 84 locations (black "+") and were combined with UAV-derived observations over the study area (black outline). Gray lines show 10 m elevation contours. The catchment outline and contours were derived from a 1 m digital terrain model (National Ecological Observatory Network, 2018).

MATERIALS AND METHODS

Study Area

We focused our research at the Niwot Ridge Long-term Ecological Research (NWT-LTER) site (40.05 N, 105.59 W), a high elevation, mountainous, alpine tundra ecosystem in the Colorado Rocky Mountains, U.S. This region, broadly, is part of the traditional territories of the Cheyenne, Ute, and Arapaho Peoples. The mean annual temperature is −4.1°C (Greenland and Losleben, 2001), although the annual minimum temperature has increased ∼0.43°C per decade from 1953 to 2008, with the largest increases during July (McGuire et al., 2012). There is some evidence of spring warming (March–June) and winter cooling (October, December; McGuire et al., 2012). Annual precipitation is ∼1,000 mm and long-term records at Niwot Ridge show that precipitation has increased by 60 mm per decade (Kittel et al., 2015). The majority (∼80%) of precipitation falls as snow during winter and spring and localized convective rainstorms occur in the summer (Greenland and Losleben, 2001). Strong westerly winds redistribute snow, and topography dictates spatial patterns in snow accumulation and melt (Litaor et al., 2008). In turn, snow heterogeneity influences biogeochemical process rates (Darrouzet-Nardi and Bowman, 2011), solute transport (Perrot et al., 2014), and alpine plant community distributions (May and Webber, 1982; Caine, 1995). Snowmelt and streamflow typically peak during late May-June, and streamflow stops by late November (Williams and Caine, 2001). This climatology normally restricts the growing season to 1–3 snow-free months.

We used a 0.26 km^2 headwater catchment within the North Boulder Creek Watershed as a study area (**Figure 1**). Ranging ∼3,330 to 3,610 m in elevation, the study catchment is primarily south-facing, with east and west hillslopes. The upper portion of the catchment is alpine tundra, which transitions downslope to sub-alpine forest. A seasonally intermittent stream bifurcates the catchment and stream flow has been recorded since 1999 (Caine et al., 2020). Soils are typically ≤2 m deep and are categorized as Cryochrepts and Cryumbrepts, with some Cryorthents in areas without biota (Burns, 1980). Solifluction deposits, characterized by hummocks, turf- and stone-banked lobes and terraces, and ephemeral ponds are found throughout the catchment (Benedict, 1970); they are the dominant microtopographical features.

Point-Scale Characterization of Near Surface Hydrology

During the summer of 2017, we established a grid of 84 monitoring locations across the study catchment. The locations were on roughly a 60 m × 60 m grid to maximize the spatial extent of monitoring across the landscape (**Figure 1**). We surveyed positions of monitoring locations to within 0.05 m using a GNSS rover receiver/antenna (Septentrio Altus APS3G) with dual band L1/L2 GPS and GLONASS functionality. Rover positions were differentially post-processed against base station observations from the five closest 1 second Continuously Operating Reference Stations (CORS) operated by the National Geodetic Survey (station codes: STBT, TMGO, P041, EC01, COFC). Two locations were marked by hand-held consumer grade GPS to 5 m accuracy. At each monitoring location, a 0.3 m × 0.3 m plot was established, with the northeast corner of the plot aligned with the surveyed point.

We measured surface soil moisture as a proxy for soil water storage. Repeat soil moisture surveys occurred weekly to biweekly with survey start dates on July 3, July 10, July 18, July 24, August 1, August 7, August 24, and September 8, 2017. The surveys began during late snowmelt, captured summer rainfall mid-July and August, and ended before snowfall recommenced in late September (**Figure 3**). Each survey took 2–4 days to complete. We measured soil moisture to 0.05 m depth five times within each 0.3 m × 0.3 m plot using a Delta-T Devices Ltd. SM-150 Soil Moisture Sensor. The five measurements captured fine-scale heterogeneity within plots, but we report soil moisture as plot averages. A site-specific calibration converted raw instrument voltages to volumetric soil moisture, which resulted in values >1.0 v/v for some locations (**Supplementary Materials**, Delta-T Devices Ltd. SM-150 Soil Moisture Sensor User Manual, v. SM150-UM-1.2, September 2016).

High-Resolution Characterization of Landscape-Scale Properties

As part of a related study we completed weekly multispectral (red, green, blue, near infrared) photogrammetric surveys of the study catchment with an unmanned aerial vehicle (UAV). These flights were coordinated with our soil moisture surveys. Eight flights between June–August 2017 characterized spatial patterns of snow accumulation and depth and plant productivity (Wigmore and Molotch, 2018). Multispectral imagery collected at 0.03 m spatial resolution was used to derive 0.05 m orthomosaics and 0.10 m digital elevation models (DEM) using a Structure from Motion workflow (Westoby et al., 2012; Fonstad et al., 2013; Wigmore et al., 2019). Maximum snow depth (MSD) measured (21st June 2017) was calculated through DEM differencing against a snow free DEM (14th August 2017; Bühler et al., 2016; Webb et al., 2020) and accuracy assessed against extensive field-based snow depth measurements. From the multispectral surveys we calculated the Normalized Difference Vegetation Index (NDVI) for each date, which we use here as a proxy for plant productivity. We took this multi-temporal series and returned the maximum NDVI value for each pixel across the series, which is reported as max NDVI and is used as an index of peak productivity for the survey period.

We derived a 1 m digital terrain model (DTM) from publicly available LiDAR survey data. We downloaded raw .laz point cloud tiles over our area of interest from a National Ecological Observatory Network (NEON) aerial LiDAR survey of Niwot Ridge completed on September 4, 2017 (National Ecological Observatory Network, 2018). NEON point clouds are already classified by land cover/terrain features (e.g., ground, vegetation, building etc.); however, we re-classified the point cloud in ENVI LiDAR to better account for local terrain parameters and identify structures, low shrubs, trees, and bare ground. We calculated a 1 m DTM from the ground classified points and smoothed it to 5, 10, 20, 30, 65, and 100 m scales in *MATLAB* (v. 9.5.0.1033004, R2018b, Update 2) using the *smooth2a* function (Reeves, 2020).

We used the 1 m DTM to calculate a wide range of topographic indices. Topographic index calculations are detailed in the **Supplementary Materials**. In brief, we calculated: slope (both local, L, and macro, M), aspect, northness, eastness, flow accumulation (FA), topographic position index (TPI), the range in TPI across 20 m (TPIr), topographic wetness index (TWI), wind shelter (WS), convergence index (CI), the range in CI across 5 m (CIr), morphometric protection index (MPI), overland distance to channel network (OD2C), and vertical distance to channel network (VD2C; **Supplementary Table 1**). Slope, aspect, FA, TWI, and TPI indices were examined at a number of spatial scales (1, 5, 10, 20, 30, 65, 100, 200, and 300 m). We transformed indices that were strongly skewed to better approximate normal distributions or at least increase dispersion (**Supplementary Table 1**). All indices were scaled to account for differing means. Average topographic index values were extracted at the 84 soil moisture monitoring locations using either a 1, 5, or 10 m buffer radius around each location's GPS point. Topographic indices were visually inspected using *QGIS* (v. 3.12 Bucuresti). Collectively, we refer to the UAV-derived snow and NDVI layers and DTM-derived topographic indices as "CZ indices."

Statistical Analyses

We combined multiple statistical methods into a data analytical framework, which allowed us to (1) identify unique hydrologic behaviors from intensive *in situ* observations, (2) explore physical drivers with extensive remotely sensed parameters, (3) and map behaviors across broader spatial scales (**Figure 2**). The framework began with an unsupervised agglomerative hierarchical cluster analysis to identify groups of locations with like hydrologic behaviors within the study catchment. To cluster the locations, we included each location's time series of soil moisture; importantly, we included missing values for some monitoring locations due to snow cover. We calculated a Euclidean distance matrix and then used the *hclust* function in the base *stats R* package using a *ward.D2* linkage method. This method minimizes within-group variance (Murtagh and Legendre, 2014), which was found to be most representative for grouping locations based on related studies in mountainous ecosystems (Devadoss et al., 2020). We visualized cluster separation using a dendrogram and a plot of the total within sum of squares for each increasing cluster number (Hastie et al., 2009). We named clusters of locations, "hydrologic groups," which represented unique hydrologic behaviors.

We then used a suite of univariate and multivariate statistical analyses to identify CZ indices that had differences across hydrologic groups. First, we removed highly co-variate CZ indices that had a Pearson correlation coefficient $\geq \pm 0.8$, which was particularly useful for determining optimal micro- and macrotopographical spatial scales in our study catchment. Second, we reduced CZ indices to a final subset that differentiated at least two hydrologic groups using pairwise Wilcox tests with Bonferroni p-value adjustments ($p < 0.1$ significance threshold), visual examination of boxplots, and principal components analysis (PCA) and principal component (PC) biplots. The PCA analysis was primarily used as a visualization tool to understand the relationships among CZ indices and between hydrologic groups.

We used a supervised machine learning classification approach to extrapolate the hydrologic groups across the study catchment. We selected Breiman's (2001) random forest classification algorithm, which generates a large number of decision trees with bootstrapped sample data, and each tree is trained with a random selection of predictor variables. We selected random forest, because it does not assume underlying data distributions, avoids data overfitting, produces strong results compared to other machine learning-based classification methods, and performs well without substantial tuning (Breiman's, 2001; Liaw and Wiener, 2002; Cutler et al., 2007; Hastie et al., 2009; James et al., 2013). Furthermore, CZ indices seemed to separate hydrologic groups in a rule-based fashion.

We developed two random forest models: one with six hydrologic groups and the other with three. For both, we used the *randomForest* algorithm in the *randomForest R* package (v 4.6-14; Liaw and Wiener, 2002) to classify hydrologic groups using a suite of CZ indices as predictor variables. We used a grid-search approach to tune the number of predictor variables included in each tree and test the effect of different numbers of trees per forest. We selected the combination of hyperparameters that minimized "out-of-bag" (OOB) error and maximized Cohen's kappa coefficient (Cohen, 1960). Both models had a single

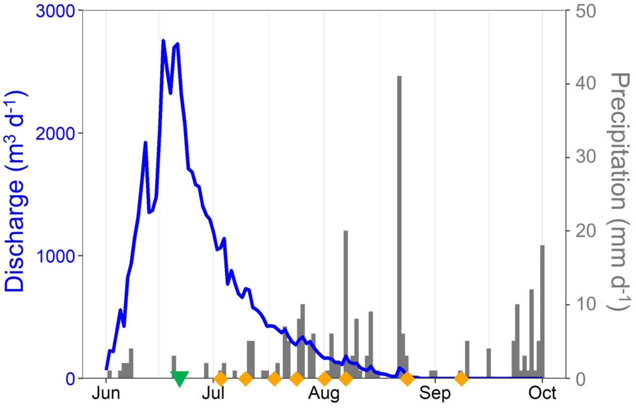

FIGURE 3 | Summer 2017 climatology for the NWT Saddle stream catchment depicting stream discharge (blue line; Caine et al., 2020), precipitation (gray bars; Morse et al., 2020), date of our maximum snow depth UAV survey (green inverted triangle), and soil moisture surveys (yellow diamonds).

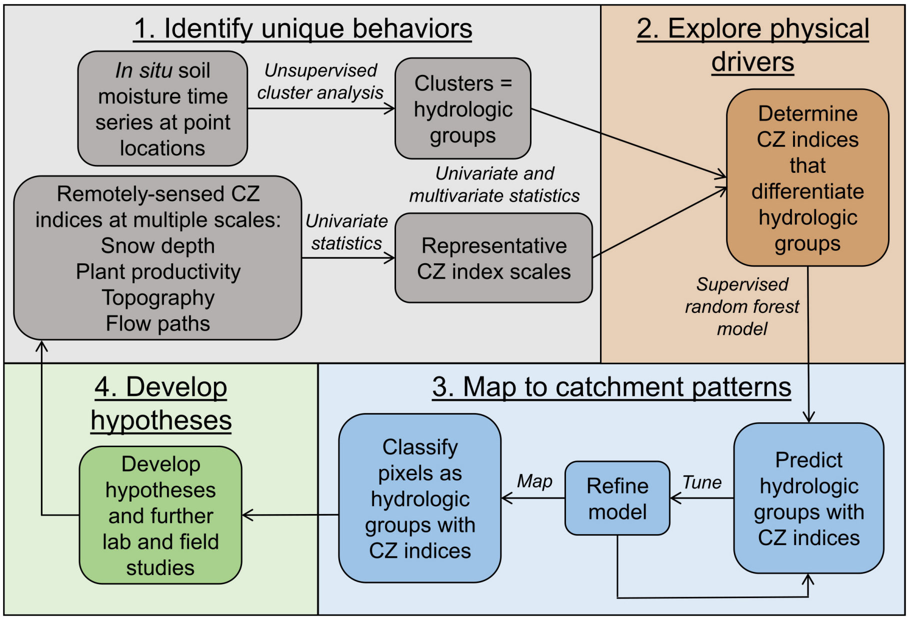

FIGURE 2 | Analytical framework used to (1) identify unique hydrologic behaviors and landscape patterns from field observations, (2) explore critical zone (CZ) physical drivers underpinning groups of hydrologic behaviors, (3) map hydrologic behaviors beyond point scales, and (4) develop further hypotheses and studies.

observation per terminal node and bootstrapped samples without replacement, which produces less bias with unbalanced classes (Boehmke and Greenwell, 2020). The six-group model had one predictor variable per tree and 500 trees, while the three-group model used nine predictor variables and 250 trees. We performed leave-one-out cross-validation (LOOCV) to assess overall model accuracy and class-specific balanced accuracy (Kuhn, 2008; James et al., 2013). We also calculated the local variable importance, which is the increase in the percent of times a site was misclassified when a CZ index was permuted. Though local importance calculations are often noisy, they provided some indication of which indices best separated groups (Touw et al., 2013).

We then applied the random forest models to distributed CZ index maps to classify a hydrologic group for every pixel in the study area. We compared predicted maps to spatial patterns of hydrologic features observed during field surveys and high-resolution multispectral imagery across the study catchment to qualitatively evaluate model performance. Lastly, we calculated the areal extent of each hydrologic group across our study area. All statistical analyses were conducted in *R*, v. 4.0.0 (R Core Team, 2017).

RESULTS

Growing Season Climatology and Soil Moisture Observations

Measurements collected in summer 2017 captured late snow melt, rainfall, and dry-down. The earliest UAV survey, June 21, occurred during peak streamflow (June 16–June 23; **Figure 3**) and measured a maximum snow depth of 4.8 m and median snow depth of 1.1 m (**Supplementary Figure 1**). During our first three soil moisture surveys (July 3, July 10, July 18), snow was still present at 12, 7, and 2 monitoring sites, respectively. Frequent convective thunderstorms began mid-July, and cumulative monthly rainfall peaked in August at 0.11 m (surveys 5–7; **Figure 3**). The catchment was completely snow-free by August 14, as shown by the high-resolution UAV imagery surveys. Between the 7th and 8th soil moisture surveys, precipitation was <0.001 m, and surveys ended before snowfall began again in late September (**Figure 3**).

Soil moisture measurements reflected these seasonal patterns in snowmelt and rainfall. Overall, median soil moisture was highest for surveys 1, 6, and 7 at $\sim$0.3 v/v (**Figure 4A**). It was lowest for surveys 3 and 8, near 0.1 v/v. The widest range in soil moisture, $\sim$1.1 v/v, was during the first two surveys. By the final survey, 80% of sites had dried to < 0.2 v/v. Despite these overall trends, every survey had a wide range in soil moisture values with coefficients of variation across the catchment $\sim$50 to 110.

Unsupervised Hierarchical Cluster Analysis of Soil Moisture

Our unsupervised hierarchical cluster analysis revealed that monitoring locations assembled into two main clusters. The plot of within-sum-of-squares by cluster number showed an "elbow" at two clusters (**Supplementary Figure 2**). The locations in the first cluster had lower median soil moisture overall than the locations in the second cluster, and so we named them "DRY" (D) and "WET" (W), respectively. The D cluster locations exhibited a decline in soil moisture between surveys 1–3 in response to snowmelt, and then an increase in soil moisture later in the study period in response to summer rainfall events (**Figure 4A**). Locations in the W cluster had either wet (> 0.4 v/v) or very wet (≥ 0.8 v/v) soil moisture conditions during the first two surveys.

Using a dendrogram, we subdivided the D and W clusters into six groups of locations with common soil moisture quantities and temporal trends over the observed period (**Supplementary Figure 3**). We summarize the relationships between the two clusters and six hydrologic groups in **Table 1** and **Figure 4B**. The first D group we named "dry" (D-D) since it had soil moisture $\leq$0.2 v/v during surveys 1-3. This group's median soil moisture peaked at $\sim$0.3 v/v during surveys 6-7 and coincident with maximum summer rainfall (**Figure 3**). We named the second group "wet-to-moist" (D-WM). Median soil moisture was highest during the first survey at 0.5 v/v and then peaked again during surveys 6-7, similar to the D-D group. The third group, "moist-to-dry" (D-MD), had soil moisture values in between the D-D and D-WM groups. The fourth group, "rapid dry-down" (W-RD), had median soil moisture at 1.1 v/v which decreased approximately linearly to 0.13 v/v over the eight field surveys. The final two groups were either "persistently wet" (W-W; 0.4–1.0 v/v) or "persistently very wet" (W-VW; $\geq$ 0.8 v/v) until the last survey. We note that for each hydrologic group, its range in soil moisture values overlapped with one or more other groups (shaded areas, **Figure 4A**).

Relationships Between CZ Indices and Soil Moisture-Derived Hydrologic Groups

Critical zone indices were first narrowed by linear correlation analysis. We started with 47 CZ indices representing snow, plant productivity, macrotopography, microtopography, and flow accumulation patterns. Twenty-eight indices were highly co-variate with either the same index calculated at a different spatial resolution or another index representing similar topographic patterns (**Supplementary Table 1**). For example, we calculated slope at 1, 5, 10, 20, 30, 65, and 100 m scales, but all scales except 1 and 65 m had Pearson correlation coefficients $\geq \pm 0.8$. Thus, these two scales were retained to represent local slope and macro-slope, respectively. In another example, CI was highly correlated with TPI-30 m ($r = 0.9$) and so CI was removed.

With the 19 remaining CZ indices, we aimed to hone the CZ indices to a set that separated as many hydrologic groups as possible in univariate or multivariate space. Pairwise Wilcox tests determined that 11 CZ indices (MSD, mNDVI, OD2C, VD2C, CIr, TPIr, SWFA, TWI-1 m, TWI-10 m, TPI-300 m, and northness) had significant differences across one or more hydrologic groups (**Supplementary Table 2**). Four pairs of hydrologic groups could not be statistically separated by CZ indices, but five CZ indices (elevation, MPI, WS, slope-L, slope-M) did show trends toward differences when CZ indices were visualized using boxplots (**Figure 5**; **Supplementary Table 2**). While some CZ index values, such

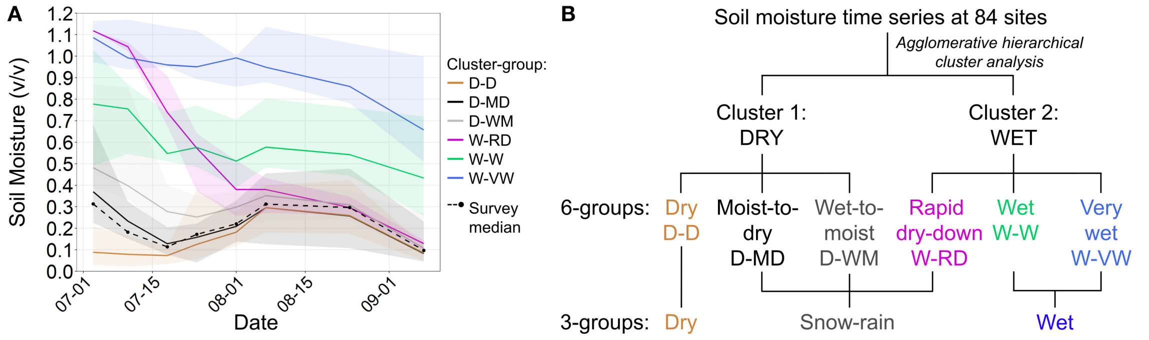

FIGURE 4 | Soil moisture cluster analysis results. **(A)** Time series' of the overall soil moisture median (dashed black line) for each survey (black dots), and median (solid lines) and range (shaded area) in soil moisture for each of the six hydrologic groups. **(B)** Schematic of the relationships between clusters and hydrologic groups. Names and abbreviations correspond to those in **Table 1**.

TABLE 1 | Soil moisture clusters and hydrologic groups.

Cluster	6-group model	Abbreviation	Locations per group	3-group model	Important CZ indices[a]
DRY	Dry	D-D	33	Dry	**MSD, TWI-10m, mNDVI,** slope-L, **TPI-300m**
DRY	Moist-to-dry	D-MD	22	Snow-rain	**MSD,** TPIr, North, **MPI, mNDVI**
DRY	Wet-to-moist	D-WM	14	Snow-rain	North, WS, **SWFA,** Elevation, VD2C
WET	Rapid dry-down	W-RD	4	Snow-rain	**MSD**, TPIr
WET	Persistently wet	W-W	7	Wet	**TWI-10m,** North, **OD2C, TPIr**
WET	Persistently very wet	W-VW	4	Wet	**CIr,** TWI-1m, MSD, **Slope-L, OD2C**

[a] *Top CZ indices based on local importance calculations from the six-group random forest model. Indices in bold text were also important in the three-group model.*

as slope-L and mNDVI, were more of a continuum across hydrologic groups (e.g., local slope or mNDVI), others clearly isolated one or more of them (e.g., OD2C, CIr; **Figure 5**).

Our PCA analysis showed relationships among CZ indices and hydrologic group separation in multivariate space. The first principal component (PC1) explained 28% of the CZ index variance and generally separated the D cluster from the W-W and W-VW groups (**Figure 6A**). The D cluster tended to have higher TPI-300 m, elevation, OD2C, and VD2C, while the W-W and W-VW groups had higher mNDVI, CIr, TWI-10 m, and TPIr. The second principal component axis (PC2) generally separated the D cluster from the W-RD group (**Figure 6A**) and explained 20% of overall variance. Plotting the first and third principal components (PC3), which explained an additional 15% of overall variance, further separated the D-D group from most others with higher TPI-300 m and slope, lower WS and SWFA, and was more south-facing (low northness index) compared with the rest of the groups (**Figure 6B**). Despite these patterns in PCA biplot space, no one group completely separated from the others, and the first three principal components only explained 63% of overall variance.

Spatial Organization of Hydrologic Groups Across the Catchment

We used random forest models to classify hydrologic groups across the study catchment using CZ indices as predictor variables. The six-group model included all 16 CZ indices and had an overall accuracy of 52.4% (**Table 2**). Some hydrologic group classifications were more accurate than others. Individual group balanced accuracy rates ranged from 49 to 80%. We reclassified our six hydrologic groups into three to increase sample numbers per group for random forest classification exercises. Locations classified as D-D remained the same across models, but locations classified into the D-MD, D-WM, and W-RD groups were combined into a "snow-rain" group (**Table 1**, **Figure 4B**). The remaining W-W and W-VW groups were combined into an overall "wet" group. The three-group random forest model had substantially improved overall accuracy at 71.4% and snow-rain group class balanced accuracy of 72% (**Table 3**). The wet group still had lower balanced accuracy than the others at 66%.

Local importance calculations identified CZ indices underpinning each of the two main clusters (**Table 1**). Important CZ indices for the W cluster included CIr, TPIr, MSD, northness, OD2C, slope-L, TWI-1 m, and TWI-10 m,

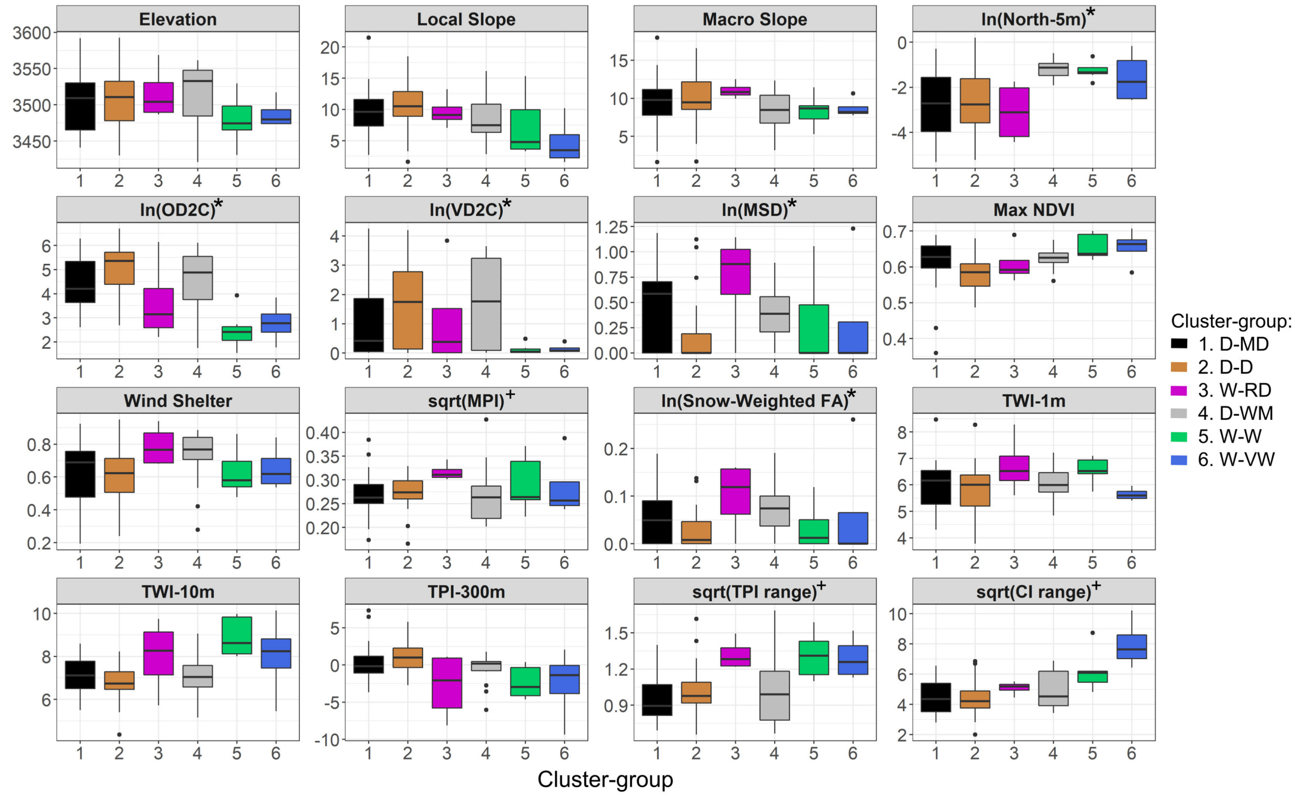

FIGURE 5 | Hydrologic groups by CZ indices. Local slope and macro slope are in degrees. OD2C, overland distance to channel (meters); VD2C, vertical distance to channel (meters); MSD, maximum snow depth (meters); max NDVI, maximum normalized difference vegetation index; MPI, morphometric protection index; FA, flow accumulation; TWI, topographic wetness index, where higher values indicate flow accumulation; TPI, topographic position index, where "0" represents flat areas, while positive values are topographic highs and negative values are topographic lows; and CI, convergence index. "*", indicates the index was transformed by natural log (ln) and "+" indicates the index was transformed by square root (sqrt).

all of which represent microtopography or flow accumulation patterns. In contrast, CZ indices that differentiated the D cluster included mNDVI, WS, MPI, SWFA, northness, TPI-300 m, elevation, TPIr, and TWI-10 m. These indices represent snow accumulation and melt patterns driven by macrotopography and flow paths.

We then applied both the six- and three-group random forest models to distributed CZ index maps to classify each pixel in the study catchment (**Figure 7**). For the six-group model, the D-D group was mapped throughout the study area and encompassed the highest proportion of total area at 58.3% (**Table 2**). The upper portion of the catchment was mostly classified as a D-MD and D-WM zone (**Figure 7A**). These two groups made up 27.2 and 9.7% of the study area, respectively (**Table 2**). The middle area of the catchment was classified as the overall W cluster (W-RD, W-W, and W-VW; **Figure 7A**), with isolated patches of the W-W and W-VW groups also found along the eastern flank of the catchment. The W cluster accounted for ∼5% of the total study area (**Table 2**). For the three-group model, the study area was classified as 46% dry, 51% snow-rain, and 3% wet (**Table 3**). The dry and snow-rain groups generally mapped to broad zones across the study area, with wet patches intermingling with the snow-rain group in the eastern half of the catchment (**Figure 7B**).

Despite some uncertainty related to the six- and three-group maps, the spatial patterns of groups mirrored field observations of key hydrologic and topographic features across the study area (compare **Figures 7**, **8**). In the upper portion of the catchment, mostly classified as D-MD and D-WM groups, snow caught between stone-banked solifluction terraces and accumulated in a wide "saddle" between two knolls. The saddle area had broad areas of wet and moist meadow plant communities, captured as W-W and W-VW groups. Eastern and western flanks of the catchment were predominated by dry meadow plant communities, captured as the D-D group in our models. Mid-catchment, a snow field persists every year until mid-August, adjacent to a broad zone of highly productive shrub and wet meadow plant communities. This area was classified as the W-RD, W-W, and W-VW groups. From this mid-catchment snow field and wet meadow, the stream channel emerged, and continued into sub-alpine forest in the lower portion of the catchment. Throughout the catchment, we observed seeps and ephemeral ponds in areas of local microtopographic variability, which were largely captured as D-MD, W-W, and W-VW groups.

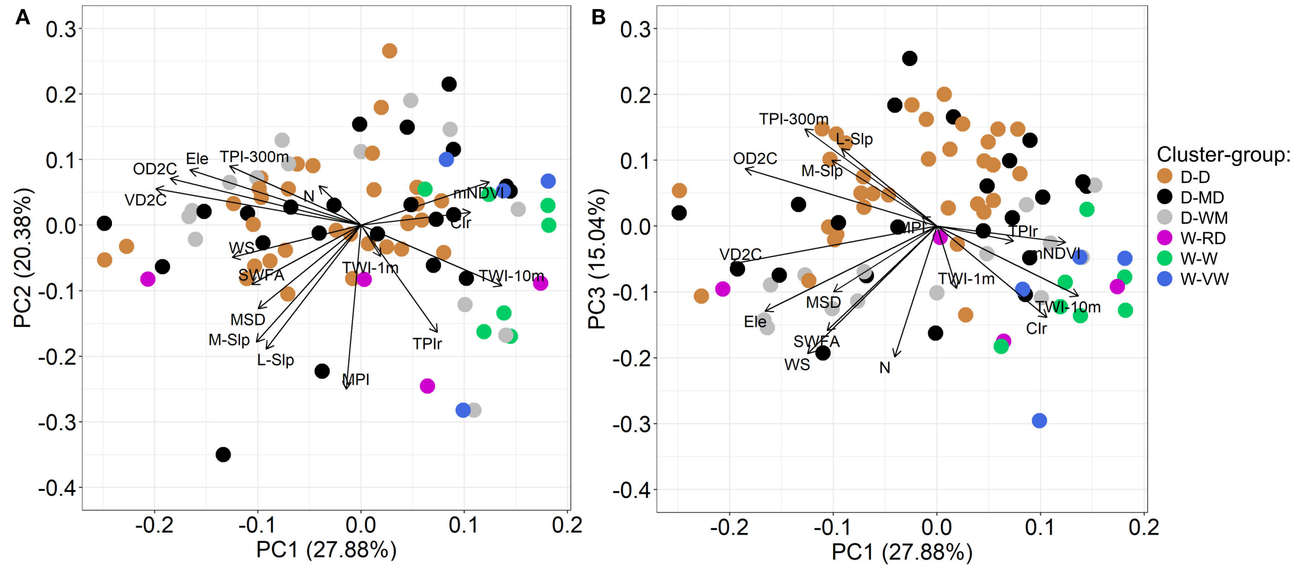

FIGURE 6 | CZ index principal component analysis (PCA) biplots showing **(A)** PC1 vs. PC2 and **(B)** PC1 vs. PC3. Vector lengths are proportional to the variance of each CZ index, and the angle between vectors represents the correlation between CZ indices. Points are colored by hydrologic group. The x- and y-axes provide the percent variance explained by each PC.

TABLE 2 | Confusion matrix and accuracy for the six-group random forest model[a].

		Predicted Hydrologic Group						Group accuracy[c]	% Study Area
		1	2	3	4	5	6		
Actual hydrologic group[b]	**1 D-MD**	9	10	0	3	0	0	0.61	27.2
	2 D-D	4	28	0	1	0	0	0.80	58.3
	3 W-RD	2	1	0	0	1	0	0.49	1.5
	4 D-WM	4	1	0	6	3	0	0.66	9.7
	5 W-W	1	0	0	3	1	2	0.54	3.0
	6 W-VW	1	1	1	0	1	0	0.49	0.3
Overall accuracy								52.4%	

[a] *Each number in the matrix represents the number of times a site was predicted into a hydrologic group compared to its actual hydrologic group during leave-one-out cross-validation.*
[b] *Abbreviations as defined in **Table 1**.*
[c] *Group balanced accuracy.*

TABLE 3 | Confusion matrix and accuracy for the three-group random forest model[a].

		Predicted hydrologic group			Group accuracy[c]	% Study area
		1	2	3		
Actual Hydrologic Group	**1 Dry**	22	11	0	0.80	45.7
	2 S-R[b]	3	34	3	0.72	50.9
	3 Wet	0	7	4	0.66	3.4
Overall accuracy					71.4%	

[a] *Each number in the matrix represents the number of times a site was predicted into a hydrologic group compared to its actual hydrologic group during leave-one-out cross-validation.*
[b] *S-R = "Snow-Rain" group.*
[c] *Group balanced accuracy.*

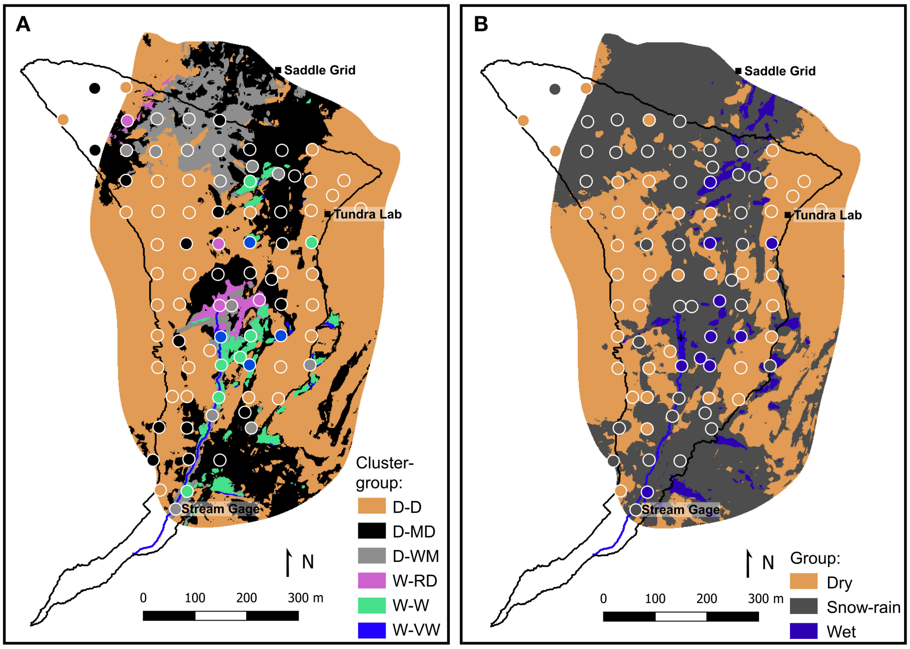

FIGURE 7 | Predictions for the six- **(A)** and three- **(B)** hydrologic group random forest models. Colors reflect pixel-by-pixel hydrologic group classifications compared to observed classifications (dots).

DISCUSSION

Alpine Hydrologic Patterns Driven by Physical Properties of the Critical Zone

In this study, we used a hierarchical cluster analysis to identify six unique hydrologic behaviors, or the quantity and time evolution of soil moisture, across an alpine catchment at Niwot Ridge. Multiple scales of CZ properties drove the differences among these six groups, affecting patterns in water routing, storage, and potentially export to the stream channel. Notably, macrotopography and snow accumulation and melt across broad zones within the catchment created a continuum from drier sites to those more influenced by snow and snowmelt. For example, sites in the driest group, D-D, were found on hillslope summits or shoulders (high TPI-300 m, higher slope values; **Figures 5**, **6**), which had high wind scour (lower WS values), low to no snow accumulation (low MSD; **Figure 5**), and were distant from the stream channel (higher OD2C and VD2C). These sites also tended to be south-facing, consistent with prior evidence that equator-facing slopes have higher solar radiation, and, thus, lower snow accumulation and soil moisture (Hinckley et al., 2014b; Pelletier et al., 2018). Water limitation characterizes the D-D areas, making them less likely to contribute to catchment export of water and solutes.

In contrast to the D-D group, the D-MD, D-WM, and W-RD groups reflected differences in the timing and duration of snow and snowmelt. The D-MD group was found along snowmelt flow paths (**Figures 5**, **7A**), reflecting early snowmelt patterns across the study area; these areas also supported higher plant productivity than the D-D group, as shown by mNDVI measurements (**Figure 5**). The D-WM group, which mapped to a broad zone in the upper catchment, reflected an area of delayed snowmelt. These sites had higher wind shelter and were more north-facing than the D-D and D-MD groups. The W-RD group, with the highest MSD measured and highest morphometric protection on average, largely coincided with the persistent snow field mid-catchment. This group had a proximal source of snowmelt throughout the spring and summer, and, hence, was saturated during the first survey. Together, the physical drivers of the D-D to W-RD groups are consistent with prior work showing that wind interacts with macrotopography to drive snow accumulation and re-distribution patterns across Niwot Ridge (Winstral et al., 2002; Erickson et al., 2005; Litaor et al., 2008; Jepsen et al., 2012) and in mountainous regions globally (Grünewald et al., 2013).

Our research demonstrates that multiple scales of topography play a role in defining areas of soil water storage. We found that the W-W and W-VW groups were driven by a combination of macrotopography, microtopography, and hydrological flow paths. Both of these groups were in areas of lower macrotopographic position (lower TPI-300 m and slope relative to the DRY cluster groups; **Figure 6**). However, the W-W group was closer to stream channels (lower OD2C) or along flow paths (higher TWI) compared to the W-VW group (**Figure 5**). Sites in the W-VW group, in contrast, had lower local slope and were in areas of microtopographic change on the order of 5 m (higher CIr values; **Figure 5**). These differences suggest that those areas characterized by the W-W group follow the stream network and may contribute to catchment export, while the W-VW group is associated with areas of water storage (longer residence

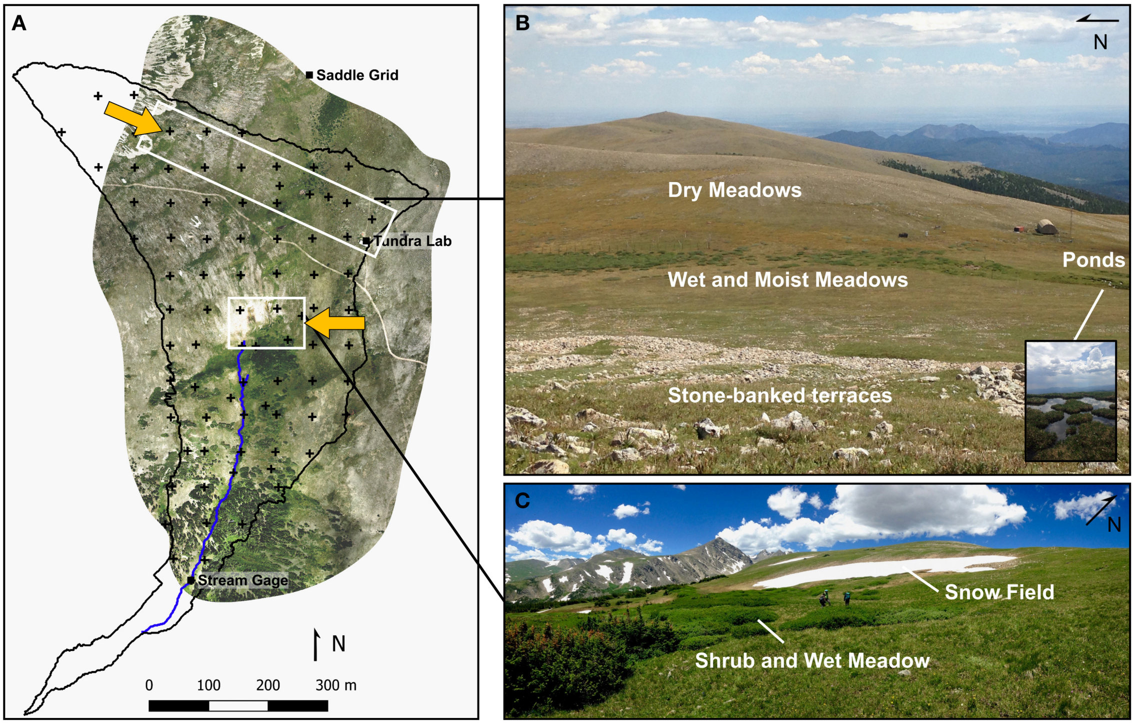

FIGURE 8 | Key features across the study catchment from field-based observations. **(A)** UAV-derived orthomosaic (14th August, 2017) of the snow-free study area with boxes showing approximate locations represented by **(B)** a photo looking east from a western knoll in the upper catchment with image of ponds (inset) and **(C)** a photo looking west across a central shrub and wet meadow with a snow field in the distance. Yellow arrows on **(A)** indicate view direction of **(B,C)**.

time), such as solifluction lobes, terraces, and ephemeral ponds (Benedict, 1970; Harris, 1977; Mercer, 2018). Areas in the W-VW group may have a number of functions: acting as biogeochemical reactors on the landscape, due to storage of water and material, or contribute to groundwater recharge depending on subsurface structure, including the presence of permafrost layers (Leopold et al., 2008; Mercer, 2018; Knowles et al., 2019).

Based on the results of this study and others, we propose a conceptual model of CZ influence on landscape hydrology in regions influenced by snow and ice. At high latitudes, the CZ is predominated by microtopographic features. For example, across great swaths of arctic tundra, microtopographic ice wedge polygons (∼ 5–20 m) affect near surface soil moisture, permafrost, microbial activity, carbon fluxes, and vegetation (Zona et al., 2011; Hubbard et al., 2013; Wainwright et al., 2015; Dafflon et al., 2016; Taş et al., 2018). On the other end of the continuum, the CZ is predominated by macrotopographic features. For example, Hinckley et al. (2014a,b) found that hydrologic response and the fate of atmospheric nitrogen deposition in the montane were consistent within north- and south-facing aspects, but that the opposing hillslope aspects differed greatly, demonstrating nearly binary behavior when compared to one another. Here, we illustrate that alpine tundra sits between the arctic and montane endmembers: macrotopography dictates broad zones of snow accumulation and melt, as well as hydrological flow paths, while microtopography influences patches of water storage. We predict that this patch-to-zone structure of the CZ results in the heterogeneous patterns of hydrologic connectivity (Ronayne et al., 2012), biogeochemistry (Darrouzet-Nardi and Bowman, 2011), and plant community composition (Spasojevic et al., 2013; Opedal et al., 2015) that complicate our understanding of these sensitive but critical environments. Additional studies across multiple years and in other alpine regions are warranted to confirm this conceptual model.

A Dialogue Between Datasets and Predictions

Our random forest statistical classification models were strongly informed by our field observations, monitoring, and empirical data. Visual inspection of topographic features during field surveys informed initial topographic index selection and scales of interest. In addition, they led to the calculation of new indices, including CIr and TPIr, to capture solifluction lobe and terrace features. We also observed areas of persistent snowpack, ephemeral or subsurface flow paths, and surface ponding, indicating locations of extended water storage. These field observations aided in validating our random forest maps. For example, our six- and three-group random forest models were evaluated on their successful prediction of observed upper- and mid-catchment wet and moist meadows, ponds, extent of dry meadows, and isolated wet patches (**Figure 7** compared to **Figure 8**). The three-group map presents predictions for broad spatial patterns in dry-to-wet areas, while the six-group map provides insight into patch-scale patterns that reflect more nuanced hydrologic dynamics. As posed by Blöschl et al. (2019), our study shows that employing multiple approaches to characterize alpine hydrology leads to a stronger understanding of how physical drivers affect patterns of hydrologic dynamics across space.

In turn, our random forest predictions identified gaps in our understanding of alpine hydrology, pointing to future field-based research needs in alpine CZ science (**Figure 2**, box 4). Although all of our groups had some degree of separation based on CZ indices, wide variance in most CZ index values (**Figure 5**), the incomplete separation of groups in multidimensional space, relatively low explanatory power of principal components (**Figure 6**), and high single-group error rates in our random forest models (**Tables 2**, **3**) suggests that hydrologic groups may be affected by additional factors that we did not include in our analysis. First, our study did not include sub-meter-scale CZ properties specifically related to soils. Several studies reinforce the importance of soil texture indices for predicting patterns in soil moisture (Williams et al., 2009; Oroza et al., 2018). Other soil characteristics, such as porosity, mineralogy, and organic matter content are important for vertical infiltration rates and lateral flow paths in the alpine (e.g., Quinton et al., 2005; Yang et al., 2014). Stone-banked lobes and terraces may also affect surface soil moisture, similar to the importance of rock-related metrics in defining hydropedologic units in the Hubbard Brook Experimental Forest (Gillin et al., 2015) or explaining subsurface flow variability (Bachmair and Weiler, 2012).

Second, while the regularly spaced grid of monitoring sites enabled broad characterization of the landscape and allowed us to extrapolate hydrologic groups across the area, it yielded few samples of wet patches and zones (**Table 1**). As a result, it was difficult to predict W groups accurately. When W-W and W-VW groups were combined for the three-group model, wet group balanced accuracy improved from ∼50 to 66%, but this was still higher error than for the "dry" and "snow-rain" groups (**Tables 2**, **3**). The W-W and W-VW group were mostly misclassified as one another or as W-RD, D-WM, or D-MD groups, which suggests that we did not include some mechanisms that may more clearly differentiate these groups. Our results highlight a need for more rigorous study of wet areas within alpine landscapes to better understand the mechanisms underlying persistent wetness. For example, we do not know whether wet areas stay wet because they continually receive snowmelt or rather that they are areas fed locally by melting subsurface ice lenses and/or permafrost (e.g., Leopold et al., 2008; Knowles et al., 2019).

Third, subsurface characterization will be critical for developing predictive capacity related to quantifying stream flow and chemical export from the CZ. Characterizing subsurface heterogeneity has long been identified as a missing link in developing a unified theory of watershed hydrology (Troch et al., 2008), and our study indicates that the alpine is no exception. We could not physically measure soil moisture under the stone-banked terraces in the upper western portion of the catchment, nor in a broad shrub zone mid-catchment (**Figure 8**). Yet, we heard water percolating through the terraces and the broad shrub zone appeared saturated throughout most of the summer season. We know little about subsurface flow in these areas. These two unmeasured areas of the alpine may be important for water transport or storage, respectively, with important implications for water delivery to lower elevations. More broadly, characterizing surface water-groundwater interactions would inform the hydrologic connectivity between our hydrologic groups (Liu et al., 2004; Williams et al., 2015; Mercer, 2018).

Additionally, we believe that estimation error associated with predicting the W-RD group may be due to the lack of characterization of the subsurface CZ structure. This group was found in broad areas of steep relief with snow accumulation (i.e., the snowfield in the middle of the catchment; **Figure 8**) and in the upper western part of the catchment, where the stone-banked terraces intermix with meadows. These sites were mostly misclassified as the D-MD function, suggesting that the physical drivers of these two groups are similar. Although obviously influenced by snowmelt supply, the W-RD function may reflect subsurface properties at play. Our predicted maps can guide future acquisition of intensive geophysical datasets, such as ground-penetrating radar, as well as tracer studies to determine patterns of hydrologic connectivity at hillslope-to-catchment scales. In summary, our data analysis framework capitalized on the combination of intensive field observations, extensive remotely-sensed CZ indices, and the strength of machine learning models. However, continuing the dialogue between targeted data collection and building predictive frameworks is critical for extending our efforts beyond mapping soil water storage patterns (**Figure 2**).

Our analytical framework provides a strategy for condensing multiple and complex data streams into a process-oriented understanding of within catchment functions. This approach is increasingly important as technology enables observations with higher spatiotemporal resolutions and for longer durations. For example, unmanned aerial vehicles, such as those used in this and prior studies, offer sub-meter-scale observations (Wigmore et al., 2019), commercially available high-resolution (3 m) satellite images provide broad spatial coverage (Planet Team, 2017), and *in situ* soil moisture sensor arrays yield real-time sub-hourly data feeds and long-term monitoring (e.g., Demand et al., 2009; Oroza et al., 2018). Our unsupervised cluster analysis distilled many observations into clear and related soil moisture behaviors, and similar approaches identified characteristic time series of plant productivity in mountainous regions (Devadoss et al., 2020). In turn, our machine learning-derived maps could be used to design sensor array placement in new locations or targeted process oriented transect studies (e.g., Wainwright et al., 2015).

Implications of Soil Moisture Patterns for Biogeochemical and Ecological Processes

Our approach to identify and predict hydrologic groups allowed us to begin exploring their relationships within a catchment, as well as their potential effects on biogeochemical processes, plant productivity, and stream water and solute fluxes. Both our six- and three-group random forest predictions indicated that ∼40–55% of the catchment is hydrologically active early in the summer growing season (**Tables 2**, **3**). Areas classified as the D-MD, D-WM, and W-RD groups (∼40% of the study area) are expected to contribute significantly to water fluxes and the fluxes of solutes stored in snowpack (e.g., inorganic N; Williams et al., 2015), mobilized from shallow soils (e.g., dissolved organic carbon), or produced from carbonic acid weathering (Winnick et al., 2017). As temperatures warm and soil moisture saturation decreases during the growing season, these areas develop optimal conditions for soil respiration (Knowles et al., 2015), soil N transformation rates (Chen et al., 2020), and plant growth (**Supplementary Figure 1**). We would expect that D-MD, D-WM, and W-RD groups then "prime" soils for mobilization of solutes in response to snowmelt and convective rainstorms later in the season, but future hydrologic modeling studies are needed to test this hypothesis. While their biogeochemical activity appears to be activated by warming temperatures and declining soil moisture, we predict that their primary role in the catchment is as export control points (Bernhardt et al., 2017); they accumulate and then contribute much of the water, solute, and nutrient fluxes from the terrestrial ecosystem when hydrologically connected to the channel.

Although we estimated that the W-W and W-VW groups are only ∼3% of the study area, these sites may be disproportionately important in net ecosystem or catchment processes. Encompassing the riparian zones along the stream channel and areas accumulating snowmelt, these groups align with the "activated control points" typology outlined by Bernhardt et al. (2017). When warming temperatures cause thawing, these areas exhibit high soil respiration rates relative to other areas (Knowles et al., 2015, 2019). Consistent with prior research on Niwot Ridge (Bowman and Fisk, 2001; Seastedt, 2020), the wetter areas also had the highest mNDVI (**Supplementary Figure 1**). However, since these areas had the highest predictive uncertainty, further study is warranted to better understand their biogeochemical process rates, subsurface weathering dynamics, and surface-subsurface hydrologic connectivity.

We classified the other half of the study area as the D-D group. Dry areas have high rates of net N mineralization and nitrification early in the summer season (June-July) and again during August-September (Chen et al., 2020). These biogeochemical processes are stimulated by higher soil moisture during early snowmelt and summer rains. However, the overall low antecedent soil moisture conditions at dry sites prior to rains suggest that they are unlikely to contribute to streamflow, similar to the findings of Penna et al. (2011) in the Italian Alps. Low soil moisture also limits plant productivity; these areas had the lowest mNDVI on average (**Supplementary Figure 1**), consistent with previous studies on Niwot Ridge (for review, see Bowman and Fisk, 2001). However, these drier areas host the highest plant species richness of alpine plant communities (Seastedt and Vaccaro, 2001; Litaor et al., 2008; Seastedt, 2020). Our findings suggest that while the D-D group may be important areas for local nutrient cycling and plant species diversity, they are less important for ecosystem- or catchment-scale processes; thus, we do not designate them as control points. We do note, however, that D-D group areas may be more hydrologically relevant during early snowmelt—a period of time that our measurements did not capture.

Our observations and random forest predictions reflect only one growing season's hydrology in one alpine catchment, but we can consider our findings in the context of long-term climate data and predictions for the region. We suggest that, broadly, the spatial patterns of the different hydrologic groups will be robust to change, since these patterns are driven by the physical template of the landscape. This idea is similar to Williams et al. (2009)—patterns in soil moisture respond to both static (i.e., topography and soils) and dynamic (i.e., snowpack) CZ controls. However, we might expect some shifts in the spatial extent of groups, since over the long term, winter precipitation is increasing (Kittel et al., 2015) but spring and summer are warming (McGuire et al., 2012). Earlier but slower snowmelt (Musselman et al., 2017) may shift more areas to behave like an expanded D-MD group, with early influence of snowmelt, a slower dry-down period, and longer dry conditions prior to summer precipitation. This shift reinforces the importance of summer rains for stimulating microbial activity and plant growth under conditions of temperature stress (Harpold, 2016; Winkler et al., 2016; Chen et al., 2020). Nutrient losses to the channel may increase, since alpine plant productivity may be limited by photoperiod despite early snowmelt and warmer spring temperatures (Ernakovich et al., 2014). The W-W and W-VW areas may experience increases in subsurface thawing with warming summer temperatures, enhancing the hydrologic connectivity of these zones to other areas of the landscape and shifting their role, for example, from activated to transport control points (Bernhardt et al., 2017), important for conveying water and solutes to the channel (e.g., Barnes et al., 2014).

CONCLUSIONS

Our intensive soil moisture observations clustered into six hydrologic groups, characterized by similar quantities and temporal trends in soil moisture over the alpine growing season. Interestingly, we found that multiple scales of topography were at play in differentiating these groups, and these scales of topography interacted to manifest as broad zones or isolated patches of like soil moisture behaviors across the landscape. We expect hydrologic groups may shift in response to changes in snowmelt predicted for the region (Musselman et al., 2017; Jennings and Molotch, 2020), which may affect the roles of different patches or zones as ecosystem control points (Bernhardt et al., 2017). Our study illustrates the novel insights that can be provided by applying an analysis framework that links intensive on-the-ground field observations with empirical evidence, topography-derived terrain indices, and extensive aerial imagery from UAVs. Our framework combined the exploratory nature of hierarchical cluster analysis to identify unique hydrologic behaviors in our observations with the power of machine learning algorithms to predict them across a landscape. This approach yielded a detailed snapshot of hydrologic dynamics and connectivity across space, which will aid in informing targeted, process-based field and modeling studies in this and other sensitive alpine CZ systems.

DATA AVAILABILITY STATEMENT

The datasets presented in this study can be found in online repositories as follows. The original soil moisture measurements presented in this study are publicly available and can be found here: Hermes, A. 2019. Soil moisture and temperature surveys for Saddle Stream Network, 2017 ver 1. Environmental Data Initiative. https://doi.org/10.6073/pasta/caaa4da3a6ab7a4949a8afb3c0df6c14. Restrictions apply to the UAV-derived datasets presented in this article. These datasets are currently embargoed on the Environmental Data Initiative. Requests to access the datasets should be directed to Oliver Wigmore, oliver.wigmore@vuw.ac.nz.

We also analyzed existing publicly available datasets, which can be found here: Caine, T.N., Morse J., and Niwot Ridge LTER (2020). Streamflow data for Saddle stream, 1999 - ongoing. ver 3. Environmental Data Initiative. https://doi.org/10.6073/pasta/5947b3ce4f706470b83da7c4afa4a875 (accessed 2020-05-26).

Morse, J., Losleben, M., and Niwot Ridge LTER (2020). Precipitation data for Saddle chart recorder, 1981 - ongoing. ver 10. Environmental Data Initiative. https://doi.org/10.6073/pasta/21e69431d63e97ffb2d311bb35793eb1 (accessed 2020-05-26). National Ecological Observatory Network (2018).

Data Products: NEON_D13_NIWO_DP1_448000_4433000_classified_point_cloud,NEON_D13_NIWO_DP1_448000_4434000_classified_point_cloud,NEON_D13_NIWO_DP1_449000_4433000_classified_point_cloud,NEON_D13_NIWO_DP1_449000_4434000_classified_point_cloud,NEON_D13_NIWO_DP1_450000_4433000_classified_point_cloud,NEON_D13_NIWO_DP1_450000_4434000_classified_point_cloud. Provisional data downloaded from http://data.neonscience.org on 17 October 2018. Battelle, Boulder, CO, USA.

AUTHOR CONTRIBUTIONS

AH collected soil moisture observations, performed statistical analyses, and contributed to the original manuscript. HW advised statistical analyses and edited the original manuscript. OW collected unmanned aerial vehicle datasets, advised statistical analyses, and edited the original manuscript. NF advised statistical analyses and edited the original manuscript. NM edited the original manuscript. E-LH advised field observations and statistical analyses and contributed to the original manuscript. All authors contributed to the article and approved the submitted version.

FUNDING

This research was supported by the Niwot Ridge LTER program (NSF DEB—1637686). HW and NF were supported by the U.S. Department of Energy, Office of Science, Office of Biological and Environmental Research, Earth and Environmental Systems Sciences Division under Award Number DE-AC02-05CH11231, as part of the Watershed Function Scientific Focus Area. OW was supported in part through funding from the University of Colorado 2016 Innovative Seed Grant, and the University of Colorado Earth Lab Grand Challenge, in association with NM. GNSS survey equipment was provided by the GAGE Facility, operated by UNAVCO, Inc. with support from the National Science Foundation and the National Aeronautics and Space Administration under NSF Cooperative Agreement EAR-1724794.

ACKNOWLEDGMENTS

We thank Youchao Chen, Cara Lauria, and the Mountain Research Station staff and field technicians for logistical and field assistance, and Brian Ebel contributed helpful insight into methods for hydrologic characterization. We acknowledge that this research occurred within traditional territories inhabited by the Ute, Cheyenne, and Arapaho Peoples and that our approach presented in this article is only one way of knowing a landscape.

SUPPLEMENTARY MATERIAL

The Supplementary Material for this article can be found online at: https://www.frontiersin.org/articles/10.3389/frwa.2020.578602/full#supplementary-material

REFERENCES

Ali, G., Birkel, C., Tetzlaff, D., Soulsby, C., Mcdonnell, J. J., and Tarolli, P. (2013). A comparison of wetness indices for the prediction of observed connected saturated areas under contrasting conditions. *Earth Surf. Process. Landforms* 39, 399–413. doi: 10.1002/esp.3506

Bachmair, S., and Weiler, M. (2012). Hillslope characteristics as controls of subsurface flow variability. *Hydrol. Earth Syst. Sci.* 16, 3699–3715. doi: 10.5194/hess-16-3699-2012

Bales, R. C., and Harrington, R. F. (1995). Recent progress in snow hydrology. *Rev. Geophys.* 33, 1011–1020. doi: 10.1029/95RG00340

Bales, R. C., Molotch, N. P., Painter, T. H., Dettinger, M. D., Rice, R., and Dozier, J. (2006). Mountain hydrology of the western United States. *Water Resour. Res.* 42:W08432. doi: 10.1029/2005WR004387

Baraer, M., McKenzie, J., Mark, B. G., Gordon, R., Bury, J., Condom, T., et al. (2015). Contribution of groundwater to the outflow from ungauged glacierized catchments: a multi-site study in the tropical Cordillera Blanca, Peru. *Hydrol. Process.* 29, 2561–2581. doi: 10.1002/hyp.10386

Barnes, R. T., Williams, M. W., Parman, J. N., Hill, K., and Caine, N. (2014). Thawing glacial and permafrost features contribute to nitrogen export from Green Lakes Valley, Colorado Front Range, USA. *Biogeochemistry* 117, 413–430. doi: 10.1007/s10533-013-9886-5

Barnett, T. P., Adam, J. C., and Lettenmaier, D. P. (2005). Potential impacts of a warming climate on water availability in snow-dominated regions. *Nature* 438, 303–309. doi: 10.1038/nature04141

Benedict, J. B. (1970). Downslope soil movement in a Colorado alpine region: rates, processes, and climatic significance. *Arctic Alpine Res.* 2, 165–226. doi: 10.1080/00040851.1970.12003576

Bernhardt, E. S., Blaszczak, J. R., Ficken, C. D., Fork, M. L., Kaiser, K. E., and Seybold, E. C. (2017). Control points in ecosystems: moving beyond the hot spot hot moment concept. *Ecosystems* 20, 665–682. doi: 10.1007/s10021-016-0103-y

Bjorkman, A. D., Myers-Smith, I. H., Elmendorf, S. C., Normand, S., Ruger, N., Beck, P. S. A., et al. (2018). Plant functional trait change across a warming tundra biome. *Nature* 562, 57–62. doi: 10.1038/s41586-018-0563-7

Blöschl, G., Bierkens, M. F., Chambel, A., Cudennec, C., Destouni, G., Fiori, A., et al. (2019). Twenty-three unsolved problems in hydrology (UPH) - a community perspective. *Hydrol. Sci. J.* 64, 1141–1158. doi: 10.1080/02626667.2019.1620507

Boehmke, B., and Greenwell, B. (2020). *Hands-on Machine Learning with R. Chapman and Hall/CRC Press*, 488. Available online at: https://bradleyboehmke.github.io/HOML/

Bowman, W. D., and Fisk, M. C. (2001). *Ch. 9 Primary Production, in Structure and Function of an Alpine Ecosystem*. eds W. D. Bowman, and T.R. Seastedt. New York, NY: Oxford University Press, 15–31.

Bradley, R. S. (2004). Projected temperature changes along the American cordillera and the planned GCOS network. *Geophys. Res. Lett.* 31:L16210. doi: 10.1029/2004GL020229

Breiman, L. (2001). Random forests. *Mach. Learn.* 45, 5–32. doi: 10.1023/A:1010933404324

Brooks, P. D., Chorover, J., Fan, Y., Godsey, S. E., Maxwell, R. M., McNamara, J. P., et al. (2015). Hydrological partitionaing in the critical zone: recent advances and opportunities for developing transferable understanding of water cycle dynamics. *Water Resour. Res.* 51, 6973–6987. doi: 10.1002/2015WR017039

Bühler, Y., Adams, M. S., Bösch, R., and Stoffel, A. (2016). Mapping snow depth in alpine terrain with unmanned aerial systems (UASs): potential and limitations. *Cryosphere* 10, 1075–1088. doi: 10.5194/tc-10-1075-2016

Burns, S. F. (1980). Alpine soil distribution and development, Indian Peaks, Colorado Front Range. (Ph.D. dissertation). University of Colorado, Boulder.

Buytaert, W., Cuesta-Camacho, F., and Tobón, C. (2011). Potential impacts of climate change on the environmental services of humid tropical alpine regions. *Glob. Ecol. Biogeogr.* 20, 19–33. doi: 10.1111/j.1466-8238.2010.00585.x

Caine, N. (1995). Snowpack influences on geomorphic processes in Green Lakes Valley, colorado front range. *Geogr. J.* 161, 55–68. doi: 10.2307/3059928

Caine, T. N., Morse, J., and the Niwot Ridge, L. T. E. R. (2020). Streamflow Data for Saddle stream, 1999-Ongoing. ver 3. *Environmental Data Initiative*. doi: 10.6073/pasta/5947b3ce4f706470b83da7c4afa4a875

Cannone, N., Diolaiuti, G., Guglielmin, M., and Smiraglia, C. (2008). Accelerating climate change impacts on alpine glacier forefield ecosystems in the European Alps. *Ecol. Appl.* 18, 637–648. doi: 10.1890/07-1188.1

Cannone, N., Sgorbati, S., and Guglielmin, M. (2007). Unexpected impacts of climate change on alpine vegetation. *Front. Ecol. Environ.* 5, 360–364. doi: 10.1890/1540-9295(2007)5[360:UIOCCO]2.0.CO;2

Chen, Y., Wieder, W. R., Hermes, A. L., and Hinckley, E.-L. S. (2020). The role of physical properties in controlling soil nitrogen cycling across a tundra-forest ecotone of the Colorado Rocky Mountains, U.S.A. *Catena* 186:104369. doi: 10.1016/j.catena.2019.104369

Cohen, J. A. (1960). Coefficient of agreement for nominal scales. *Educ. Psychol. Meas.* 20, 37–46. doi: 10.1177/001316446002000104

Cutler, D., Edwards, T., Beard, K., Cutler, A., Hess, K., Gibson, J., et al. (2007). Random forests for classification in ecology. *Ecology* 88, 2783–2792. doi: 10.1890/07-0539.1

Dafflon, B., Hubbard, S., Ulrich, C., Peterson, J., Wu, Y., Wainwright, H., et al. (2016). Geophysical estimation of shallow permafrost distribution and properties in an ice-wedge polygon-dominated Arctic tundra region. *Geophysics* 81, WA247–WA263. doi: 10.1190/geo2015-0175.1

Darrouzet-Nardi, A., and Bowman, W. D. (2011). Hot spots of inorganic nitrogen availability in an alpine-subalpine ecosystem, Colorado Front Range. *Ecosystems* 14, 848–863. doi: 10.1007/s10021-011-9450-x

Demand, D., Blume, T., and Weiler, M. (2009). Spatio-temporal relevance and controls of preferential flow at the landscape scale. *Hydrol. Earth Syst. Sci*. 23, 4869–4889. doi: 10.5194/hess-23-4869-2019

Devadoss, J., Falco, N., Dafflon, B., Wu, Y., Franklin, M., Hermes, A., et al. (2020). Remote sensing-informed zonation for understanding snow, plant, and soil moisture dynamics within a mountain ecosystem. *Remote Sens.* 12:2733. doi: 10.3390/rs12172733

Emanuel, R. E., Riveros-Iregui, D. A., McGlynn, B. L., and Epstein, H. E. (2011). On the spatial heterogeneity of net ecosystem productivity in complex landscapes. *Ecosphere* 2, 1–13. doi: 10.1890/ES11-00074.1

Erickson, T. A., Williams, M. W., and Winstral, A. (2005). Persistence of topographic controls on the spatial distribution of snow in rugged mountain terrain, Colorado, United States. *Water Resour. Res* 41:04014. doi: 10.1029/2003WR002973

Ernakovich, J. G., Hopping, K. A., Berdanier, A. B., Simpson, R. T., Kachergis, E. J., Steltzer, H., et al. (2014). Predicted responses of arctic and alpine ecosystems to altered seasonality under climate change. *Glob. Chang. Biol.* 20, 3256–3269. doi: 10.1111/gcb.12568

Falco, N., Wainwright, H., Dafflon, B., Léger, E., Peterson, J., Steltzer, H., et al. (2019). Investigating microtopographic and soil controls on a mountainous meadow plant community using high-resolution remote sensing and surface geophysical data. *J. Geophys. Res. Biogeosci.* 124, 1618–1636. doi: 10.1029/2018JG004394

Fonstad, M. A., Dietrich, J. T., Courville, B. C., Jensen, J. L., and Carbonneau, P. E. (2013). Topographic structure from motion: a new development in photogrammetric measurement. *Earth Surf. Process. Landforms* 38, 421–430. doi: 10.1002/esp.3366

Gillin, C. P., Bailey, S. W., McGuire, K. J., and Gannon, J. P. (2015). Mapping of hydropedologic spatial patterns in a steep headwater catchment. *Soil Sci. Soc. Am. J.* 79, 440–453. doi: 10.2136/sssaj2014.05.0189

Greenland, D., and Losleben, M. (2001). Ch. 2 climate in structure and function of an alpine ecosystem. eds W. D. Bowman, and T. R. Seastedt. New York, NY: Oxford University Press, 15–31.

Grünewald, T., Stötter, J., Pomeroy, J. W., Dadic, R., Moreno Banos, I., Marturià, J., et al. (2013). Statistical modelling of the snow depth distribution in open alpine terrain. *Hydrol. Earth Syst. Sci.* 17, 3005–3021. doi: 10.5194/hess-17-3005-2013

Guio Blanco, C. M., Brito Gomez, V. M., Crespo, P., and Lieb, M. (2018). Spatial prediction of soil water retention in a Páramo landscape: methodological insight into machine learning using random forest. *Geoderma* 316, 100–114. doi: 10.1016/j.geoderma.2017.12.002

Harman, C. J. (2015). Time-variable transit time distributions and transport: Theory and application to storage-dependent transport of chloride in a watershed. *Water Resour. Res.* 51, 1–30. doi: 10.1002/2014WR015707

Harpold, A. A. (2016). Diverging sensitivity of soil water stress to changing snowmelt timing in the Western U.S. *Adv. Water Resour.* 92, 116–129. doi: 10.1016/j.advwatres.2016.03.017

Harris, C. (1977). Engineering properties, groundwater conditions, and the nature of soil movement on a solifluction slope in north Norway. *Q. J. Eng. Geol. Hydrogeol.* 10, 27–43. doi: 10.1144/GSL.QJEG.1977.010.01.02

Hastie, T., Tibshirani, R., and Friedman, J. (2009). *The Elements of Statistical Learning: Data Mining, Inference, and Prediction, 2nd Edn*. New York, NY: Springer.

Hinckley, E.-L. S., Barnes, R. T., Anderson, S. P., Williams, M. W., and Bernasconi, S. M. (2014a). Nitrogen retention and transport differ by hillslope aspect at the rain-snow transition of the Colorado Front Range. *J. Geophys. Res. Biogeosci.* 119, 1281–1296. doi: 10.1002/2013JG002588

Hinckley, E.-L. S., Ebel, B. A., Barnes, R. T., Anderson, R. S., Williams, M. W., and Anderson, S. P. (2014b). Aspect control of water movement on hillslopes near the rain-snow transition of the Colorado Front Range. *Hydrol. Process.* 28, 74–85. doi: 10.1002/hyp.9549

Horton, P., Schaefli, B., Mezghani, A., Hingray, B., and Musy, A. (2006). Assessment of climate-change impacts on alpine discharge regimes with climate model uncertainty. *Hydrol. Process.* 20, 2091–2109. doi: 10.1002/hyp.6197

Hubbard, S. S., Gangodagamage, C., Dafflon, B., Wainwright, H., Peterson, J., Gusmeroli, A., et al. (2013). Quantifying and relating land-surface and subsurface variability in permafrost environments using LiDAR and surface geophysical datasets. *Hydrogeol. J.* 21, 149–169. doi: 10.1007/s10040-012-0939-y

Ishida, K., Ercan, A., Trinh, T., Kavvas, M. L., Ohara, N., Carr, K., et al. (2018). Analysis of future climate change impacts on snow distribution over mountainous watersheds in Northern California by means of a physically-based snow distribution model. *Sci. Total Environ.* 645, 1065–1082. doi: 10.1016/j.scitotenv.2018.07.250

James, G., Witten, D., Hastie, T., and Tibshirani, R. (2013). *An Introduction to Statistical Learning with Applications in R*. New York, NY: Springer, 436.

Jennings, K. S., and Molotch, N. P. (2020). Snowfall fraction, cold content, and energy balance changes drive differential response to simulated warming in an alpine and subalpine snowpack. *Front. Earth Sci.* 8:186. doi: 10.3389/feart.2020.00186

Jepsen, S. M., Molotch, N. P., Williams, M. W., Rittger, K. E., and Sickman, J. O. (2012). Interannual variability of snowmelt in the Sierra Nevada and Rocky Mountains, United States: examples from two alpine watersheds. *Water Resour. Res.* 48:W02529. doi: 10.1029/2011WR011006

Kirchner, J. W. (2016). Aggregation in environmental systems-Part 2: Catchment mean transit times and young water fractions under hydrologic nonstationarity. *Hydrol. Earth Syst. Sci.* 20, 299–328. doi: 10.5194/hess-20-299-2016

Kittel, T. G. F., Williams, M. W., Chowanski, K., Hartman, M., Ackerman, T., Losleben, M., et al. (2015). Contrasting long-term alpine and subalpine precipitation trends in a mid-latitude North American mountain system, Colorado Front Range, USA. *Plant Ecol. Diversity*. 8, 607–624. doi: 10.1080/17550874.2016.1143536

Knowles, J. F., Blanken, P. D., Lawrence, C. R., and Williams, M. W. (2019). Evidence for non-steady-state carbon emissions from snow-scoured alpine tundra. *Nat. Commun.* 10:1306. doi: 10.1038/s41467-019-09149-2

Knowles, J. F., Blanken, P. D., and Williams, M. W. (2015). Soil respiration variability across a soil moisture and vegetation community gradient within a snow-scoured alpine meadow. *Biogeochemistry* 125, 185–202. doi: 10.1007/s10533-015-0122-3

Kuhn, M. (2008). Building predictive models in R using the caret package. *J. Stat. Softw.* 28, 1–26. doi: 10.18637/jss.v028.i05

Lee, E., and Kim, S. (2019). Seasonal and spatial characterization of soil moisture and soil water tension in a steep hillslope. *J. Hydrol.* 568, 676–685. doi: 10.1016/j.jhydrol.2018.11.027

Leopold, M., Lewis, G., Dethier, D., Caine, N., and Williams, M. W. (2008). Using geophysical methods to study the shallow subsurface of a sensitive alpine environment, Niwot Ridge, Colorado Front Range, U.S.A. *Arct. Antarct. Alp. Res* 40, 519–530. doi: 10.1657/1523-0430(06-124)[LEOPOLD]2.0.CO;2

Liaw and Wiener, M. (2002). Classification and regression by randomForest. *R News* 2, 18-22.

Litaor, M. I., Williams, M., and Seastedt, T. R. (2008). Topographic controls on snow distribution, soil moisture, and species diversity of herbaceous alpine vegetation, Niwot Ridge, Colorado. *J. Geophys. Res* 113:2008. doi: 10.1029/2007JG000419

Liu, F., Williams, M. W., and Caine, N. (2004). Source waters and flow paths in an alpine catchment, Colorado Front Range, United States. *Water Resour. Res.* 40:W09401. doi: 10.1029/2004WR003076

Magnusson, J., Jonas, T., Ló Pez-Moreno, I., and Lehning, M. (2012). Snow cover response to climate change in a high alpine and half-glacierized basin in Switzerland. *Hydrol. Res.* 41, 230–240. doi: 10.2166/nh.2010.115

Matsuoka, N., Ikeda, A., and Date, T. (2005). Morphometric analysis of solifluction lobes and rock glaciers in the Swiss Alps. *Permafr. Periglac. Process.* 16, 99–113. doi: 10.1002/ppp.517

May, D. E., and Webber, P. J. (1982). "Spatial and temporal variation of the vegetation and its productivity on Niwot Ridge, Colorado," in Ecological Studies in the Colorado alpine, a festschrift for John W. Marr. Occasional paper number 37. Institute of Arctic and Alpine Research, University of Colorado Boulder. Colorado, 35–62.

McGuire, C. R., Nufio, C. R., Bowers, M. D., and Guralnick, R. P. (2012). Elevation-dependent temperature trends in the Rocky Mountain Front Range: changes over a 56- and 20-year record. *PLoS ONE* 7:e44370. doi: 10.1371/journal.pone.0044370

Mercer, J. J. (2018). Insights into Mountain Wetland Resilience to Climate Change: an Evaluation of the Hydrological Processes Contributing to the Hydrodynamics of Alpine Wetlands in the Canadian Rocky Mountains. (Ph. D. dissertation). University of Saskatchewan Saskatoon.

Morse, J., Losleben, M., and Ridge, N. (2020). *Precipitation data for Saddle chart recorder, 1981 - ongoing. ver 10. Environmental Data Initiative.* doi: 10.6073/pasta/21e69431d63e97ffb2d311bb35793eb1

Murtagh, F., and Legendre, P. (2014). Ward's hierarchical agglomerative clustering method: Which algorithms implement Ward's Criterion? *J. Classificat.* 31, 274–295. doi: 10.1007/s00357-014-9161-z

Musselman, K. N., Clark, M. P., Liu, C., Ikeda, K., and Rasmussen, R. (2017). Slower snowmelt in a warmer world. *Nat. Clim. Chang.* 7, 214–219. doi: 10.1038/nclimate3225

National Ecological Observatory Network. (2018). Data Products: NEON_D13_NIWO_DP1_448000_4433000_classified_point_cloud, NEON_D13_NIWO_DP1_448000_4434000_classified_point_cloud, NEON_D13_NIWO_DP1_449000_4433000_classified_point_cloud, NEON_D13_NIWO_DP1_449000_4434000_classified_point_cloud, NEON_D13_NIWO_DP1_450000_4433000_classified_point_cloud, NEON_D13_NIWO_DP1_450000_4434000_classified_point_cloud. (Battelle, Boulder, CO). Available online at: http://data.neonscience.org (accessed October 17, 2018).

Opedal, O. H., Armbruster, W. S., and Graae, B. J. (2015). Linking small-scale topography with microclimate, plant species diversity and intra-specific trait variation in an alpine landscape. *Plant Ecol. Divers*. 8, 305–315. doi: 10.1080/17550874.2014.987330

Oroza, C. A., Bales, R. C., Stacy, E. M., Zheng, Z., and Glaser, S. D. (2018). Long-term variability of soil moisture in the Southern Sierra: measurement and prediction. *Vadose Zone J.* 17, 1–9. doi: 10.2136/vzj2017.10.0178

Pelletier, J. D., Barron-Gafford, G. A., Gutiérrez-Jurado, H., Hinckley, E.-L. S., Istanbulluoglu, E., Mcguire, L. A., et al. (2018). Which way do you lean? Using slope aspect variations to understand critical zone processes and feedbacks. *Earth Surf. Process. Landforms* 43, 1133–1154. doi: 10.1002/esp.4306

Penna, D., Tromp-Van Meerveld, H. J., Gobbi, A., Borga, M., and Dalla Fontana, G. (2011). The influence of soil moisture on threshold runoff generation processes in an alpine headwater catchment. *Hydrol. Earth Syst. Sci.* 15, 689–702. doi: 10.5194/hess-15-689-2011

Pepin, N., Bradley, R. S., Diaz, H. F., Baraer, M., Caceres, E. B., Forsythe, N., et al. (2015). Elevation-dependent warming in mountain regions of the world. *Nat. Clim. Chang.* 5, 424–430. doi: 10.1038/nclimate2563

Perrot, D., Molotch, N. P., Williams, M. W., Jepsen, S. M., and Sickman, J. O. (2014). Relationships between stream nitrate concentration and spatially distributed snowmelt in high-elevation catchments of the western U.S. *Water Resour. Res.* 50, 8694–8713. doi: 10.1002/2013WR015243

Planet Team. (2017). *Planet Application Program Interface: In Space for Life on Earth, Planet.* San Francisco, CA. Available online at: https://api.planet.com

Quinton, W. L., Shirazi, T., Carey, S. K., and Pomeroy, J. W. (2005). Soil water storage and active-layer development in a sub-alpine tundra hillslope, southern Yukon Territory, Canada. *Permafr. Periglac. Processs* 16, 369–382. doi: 10.1002/ppp.543

R Core Team. (2017). *R: A Language and Environment for Statistical Computing*. (Vienna, Austria: R Foundation for Statistical Computing). Available online at: https://www.R-project.org.

Reeves, G. (2020). *smooth2a* MATLAB Central File Exchange. Available online at: https://www.mathworks.com/matlabcentral/fileexchange/23287-smooth2a (accessed May 21, 2020).

Ronayne, M. J., Houghton, T. B., and Stednick, J. D. (2012). Field characterization of hydraulic conductivity in a heterogeneous alpine glacial till. *J. Hydrol.* 458–459, 103–109. doi: 10.1016/j.jhydrol.2012.06.036

Russell, R. J. (1933). Alpine land forms of western united states. *Bull. Geol. Soc. Am.* 44, 927–950. doi: 10.1130/GSAB-44-927

Schneeberger, K., Dobler, C., Huttenlau, M., and Stötter, J. (2015). Assessing potential climate change impacts on the seasonality of runoff in an Alpine watershed. *J. Water Clim. Chang.* 6, 263–277. doi: 10.2166/wcc.2014.106

Seastedt, T. R. (2020). "Patterns and controls on the productivity and plant diversity of alpine ecosystems," in *Encyclopedia of the World's Biomes*, eds M. I. Goldstein and D. A. DellaSala (Elsevier), 265–274. doi: 10.1016/B978-0-12-409548-9.11787-7

Seastedt, T. R., and Vaccaro, L. (2001). Plant species richness, productivity, and nitrogen and phosphorus limitations across a snowpack gradient in alpine tundra. *Arct. Antarct. Alp. Res.* 33, 100–106. doi: 10.1080/15230430.2001.12003410

Seidl, R., Rammer, W., and Lexer, M. J. (2011). Climate change vulnerability of sustainable forest management in the Eastern Alps. *Clim. Chang.* 106, 225–254. doi: 10.1007/s10584-010-9899-1

Smith, T., and Bookhagen, B. (2018). Changes in seasonal snow water equivalent distribution in High Mountain Asia (1987 to 2009). *Sci. Adv.* 4:e1701550. doi: 10.1126/sciadv.1701550

Spasojevic, M. J., Bowman, W. D., Humphries, H. C., Seastedt, T. R., and Suding, K. N. (2013). Changes in alpine vegetation over 21 years: Are patterns across a heterogeneous landscape consistent with predictions? *Ecosphere* 4, 1–18. doi: 10.1890/ES13-00133.1

Suding, K., Farrer, E., King, A., Kueppers, L., and Spasojevic, M. J. (2015). Vegetation change at high elevation: scale dependence and interactive effects on Niwot Ridge. *Plant Ecol. Divers.* 8, 713–725. doi: 10.1080/17550874.2015.1010189

Tague, C., and Grant, G. E. (2009). Groundwater dynamics mediate low-flow response to global warming in snow-dominated alpine regions. *Water Resour. Res.* 45:W07421. doi: 10.1029/2008WR007179

Tague, C. L. (2009). Assessing climate change impacts on alpine stream-flow and vegetation water use: mining the linkages with subsurface hydrologic processes. *Hydrol. Process.* 23, 1815–1819. doi: 10.1002/hyp.7288

Taş, N., Prestat, E., Wang, S., Wu, Y., Ulrich, C., Kneafsey, T., et al. (2018). Landscape topography structures the soil microbiome in arctic polygonal tundra. *Nat. Commun.* 9:777. doi: 10.1038/s41467-018-03089-z

Touw, W. G., Bayjanov, J. R., Overmars, L., Backus, L., Boekhorst, J., Wels, M., et al. (2013). Data mining in the life sciences with Random Forest: a walk in the park or lost in the jungle? *Brief. Bioinformatics* 14, 315–326. doi: 10.1093/bib/bbs034

Troch, P. A., Carrillo, G. A., Heidbüchel, I., Rajagopal, S., Switanek, M., Volkmann, T. H. M., et al. (2008). Dealing with landscape heterogeneity in watershed hydrology: a review of recent progress toward new hydrological theory. *Geograph. Compass* 3, 375-392. doi: 10.1111/j.1749-8198.2008.00186.x

Wainwright, H. M., Dafflon, B., Smith, L. J., Hahn, M. S., Curtis, J. B., Wu, Y., et al. (2015). Identifying multiscale zonation and assessing the relative importance of polygon geomorphology on carbon fluxes in an Arctic tundra ecosystem. *J. Geophys. Res. Biogeosci.* 120, 788–808. doi: 10.1002/2014JG002799

Wainwright, H. M., Liljedahl, A. K., Dafflong, B., Ulrich, C., Peterson, J. E., Gusmerolia, A., et al. (2017). Mapping snow depth within a tundra ecosystem using multiscale observations and Bayesian methods. *Cryosphere* 11, 857–975. doi: 10.5194/tc-11-857-2017

Ward, A. S., Kurz, M. J., Schmadel, N. M., Knapp, J. L. A., Blaen, P. J., Harman, C. J., et al. (2019). Solute transport and transformation in an intermittent, headwater mountain stream with diurnal discharge fluctuations. *Water* 11:2208. doi: 10.3390/w11112208

Webb, R. W., Wigmore, O., Jennings, K., Fend, M., and Molotch, N. P. (2020). Hydrologic connectivity at the hillslope scale through intra-snowpack flow paths during snowmelt. *Hydrol. Process* 34, 1616–1629. doi: 10.1002/hyp.13686

Western, A. W., Grayson, R. B., Blöschl, G., Willgoose, G. R., and McMahon, T. A. (1999). Observed spatial organization of soil moisture and its relation to terrain indices. *Water Resour. Res.* 35, 797–810. doi: 10.1029/1998WR900065

Westoby, M. J., Brasington, J., Glasser, N. F., Hambrey, M. J., and Reynolds, J. M. (2012). "Structure-from-motion" photogrammetry: a low-cost, effective tool for geoscience applications. *Geomorphology* 179, 300–314. doi: 10.1016/j.geomorph.2012.08.021

Wigmore, O., Mark, B. G., McKenzie, J., Baraer, M., and Lautz, L. (2019). Sub-metre mapping of surface soil moisture in proglacial valleys of the tropical Andes using a multispectral unmanned aerial vehicle. *Remote Sens. Environ.* 222, 104–118. doi: 10.1016/j.rse.2018.12.024

Wigmore, O., and Molotch, N. P. (2018). "Assessing spatiotemporal variability in mountain ecosystem productivity with multispectral unmanned aerial systems," in *American Geophysical Union Fall Meeting,* (Washington, DC: AGU). Available online at: https://agu.confex.com/agu/fm18/meetingapp.cgi/Paper/461222 (accessed June 28, 2020).

Williams, C. J., McNamara, J. P., and Chandler, D. G. (2009). Controls on the temporal and spatial variability of soil moisture in a mountainous landscape: the signature of snow and complex terrain. *Hydrol. Earth System Sci.* 13, 1325–1336. doi: 10.5194/hess-13-1325-2009

Williams, M. W., and Caine, N. (2001). Ch. 5 hydrology and hydrochemistry in structure and function of an alpine ecosystem. eds. W. D. Bowman, and T. R. Seastedt (New York, NY: Oxford University Press), 75–98.

Williams, M. W., Hood, E., Molotch, N. P., Caine, N., Cowie, R., and Liu, F. (2015). The 'teflon basin' myth: hydrology and hydrochemistry of a seasonally snow-covered catchment. *Plant Ecol. Divers.* 8, 639–661. doi: 10.1080/17550874.2015.1123318

Winkler, D. E. (2019). Contemporary human impacts on alpine ecosystems: the direct and indirect effects of human-induced climate change and land use. *Encyclopedia of the World's Biomes*. 1, 574–580. doi: 10.1016/B978-0-12-409548-9.11879-2

Winkler, D. E., Butz, R. J., Germino, M. J., Reinhardt, K., and Kueppers, L. M. (2018). Snowmelt timing regulates community compositoin, phenology, and physiological performance of alpine plants. *Front. Plant Sci.* 9:1140. doi: 10.3389/fpls.2018.01140

Winkler, D. E., Chapin, K. J., and Kueppers, L. M. (2016). Soil moisture mediates alpine life form and community productivity responses to warming. *Ecology* 97, 1553–1563. doi: 10.1890/15-1197.1

Winnick, M. J., Carroll, R. W. H., Williams, K. H., Maxwell, R. M., Dong, W., and Maher, K. (2017). Snowmelt controls on concentration-discharge relationships and the balance of oxidative and acid-base weathering fluxes in an alpine catchment, East River, Colorado. *Water Resour. Res.* 53, 2507–2523. doi: 10.1002/2016WR019724

Winstral, A., Elder, K., and Davis, R. E. (2002). Spatial snow modeling of wind-redistributed snow using terrain-based parameters. *J. Hydrometerol.* 3, 524–538. doi: 10.1175/1525-7541(2002)003<;0524:SSMOWR>;2.0.CO;2

Yang, F., Zhang, G. L., Yang, J. L., Li, D. C., Zhao, Y. G., Liu, F., et al. (2014). Organic matter controls of soil water retention in an alpine grassland and its significance for hydrological processes. *J. Hydrol.* 519, 3010–3027. doi: 10.1016/j.jhydrol.2014.10.054

Zona, D., Lipson, D. A., Zulueta, R. C., Oberbauer, S. F., and Oechel, W. C. (2011). Microtopographic controls on ecosystem functioning in the Arctic coastal plain. *J. Geophys. Res*. 116:G00I08. doi: 10.1029/2009JG001241

Conflict of Interest: The authors declare that the research was conducted in the absence of any commercial or financial relationships that could be construed as a potential conflict of interest.

The reviewer TF declared a past co-authorship with one of the authors NM to the handling editor.

ORIGINAL RESEARCH
published: 25 November 2020
doi: 10.3389/frwa.2020.562298

Geochemical Controls on Release and Speciation of Fe(II) and Mn(II) From Hyporheic Sediments of East River, Colorado

Wenming Dong*, **Amrita Bhattacharyya**, **Patricia M. Fox**, **Markus Bill**, **Dipankar Dwivedi**, **Sergio Carrero**, **Mark Conrad** and **Peter S. Nico***

Earth and Environment Sciences Area, Lawrence Berkeley National Laboratory, Berkeley, CA, United States

Edited by:
Alexis Navarre-Sitchler,
Colorado School of Mines,
United States

Reviewed by:
Ruben Kretzschmar,
ETH Zürich, Switzerland
John Bargar,
Stanford University, United States

***Correspondence:**
Wenming Dong
wenmingdong@lbl.gov
Peter S. Nico
psnico@lbl.gov

Specialty section:
This article was submitted to
Water and Critical Zone,
a section of the journal
Frontiers in Water

Received: *15 May 2020*
Accepted: *21 October 2020*
Published: *25 November 2020*

Citation:
Dong W, Bhattacharyya A, Fox PM, Bill M, Dwivedi D, Carrero S, Conrad M and Nico PS (2020) Geochemical Controls on Release and Speciation of Fe(II) and Mn(II) From Hyporheic Sediments of East River, Colorado. Front. Water 2:562298.
doi: 10.3389/frwa.2020.562298

Hyporheic zones act as critical ecological links between terrestrial and aquatic systems where redox-sensitive metals of iron (Fe) and manganese (Mn) significantly impact nutrient cycling and water quality. However, the geochemical controls on the release and speciation of Fe(II) and Mn(II) in these biogeochemical hotspots are still poorly understood. Here we conducted batch incubation experiments and analyzed Fe K-edge extended X-ray absorption fine structure (EXAFS) spectroscopy data using sediment samples from a hyporheic zone of the East River floodplain in Colorado to understand the production, release and speciation of Fe(II) and Mn(II) in groundwater. Our results indicate that the production and release of Fe(II) and Mn(II) vary with sediment reducing conditions and subsurface positions, and the rates were determined either by a zero- or first-order rate equation. The sediments with higher Fe(II) production did not necessarily result in higher release of dissolved Fe(II), and $\geq$97% Fe(II) is accumulated in solid phase. We found that the majority of Fe(II) exists as siderite ($FeCO_3$), Fe(II)-natural organic matter (NOM) complexes and ferrosmectite, and the equilibrium concentrations of dissolved Fe(II) are controlled primarily by siderite solubility, and enhanced greatly by formation of strong Fe(II)-NOM complexes as dominant aqueous Fe(II) species. By contract, dissolved Mn(II) increases slowly and linearly, and an equilibrium concentration was not reached during the incubation period, and the roles of rhodochrosite ($MnCO_3$) and Mn(II)-NOM complexes are insignificant. Furthermore, we reviewed and calibrated the literature reported binding constants (log K) of Fe(II)-NOM complexes which successfully predicted our experimental data. This work reveals that siderite and dissolved NOM are the controlling phases in release and speciation of dissolved Fe(II), and the finding is expected to be applicable in many hyporheic zones and subsurface environments with similar geochemical conditions.

Keywords: hyporheic zone, dissolved Fe(II), dissolved Mn(II), siderite, natural organic matter (NOM), complexation, extended X-ray absorption fine structure (EXAFS) spectroscopy

INTRODUCTION

River hyporheic zones are defined as regions of sediment beneath and alongside a streambed where mixing and bidirectional exchange of shallow groundwater and river water occurs. These zones perform important ecological functions by linking terrestrial and aquatic systems within watersheds and have been recognized as hotspots for biological activity and cycling of metals and nutrients (Boulton et al., 1998; Gomez et al., 2012; Boano et al., 2014; Dwivedi et al., 2018; Saup et al., 2019). The interaction of nutrient-rich groundwater and oxygen-rich stream water results in distinct redox gradients (Dwivedi et al., 2018) which significantly impact the export of redox-sensitive metals from hyporheic zone to the local watershed, thereby influencing the overall nutrient cycling and water quality (Bryant et al., 2020).

Redox reactions of iron (Fe) and manganese (Mn), often accompanied by dissolution-precipitation processes, widely influence the biogeochemical cycles of nutrients (e.g., carbon, nitrogen, sulfur, oxygen, and phosphorous) as well as the transport of contaminants such as uranium, chromium, and polychlorinated biphenyls (PCBs) in many subsurface aquifers (Lovley, 1991, 1997). Toxic metalloids (e.g., arsenic and selenium) associated with Fe/Mn mineral assemblies could also be simultaneously released into groundwater (Lovley, 1991; Pedersen et al., 2006; Rowland et al., 2007; Park et al., 2018). In addition, soluble Fe(II) and Mn(II) species in groundwater gets re-oxidized and precipitated as insoluble Fe(III) and Mn(III/IV) oxides during transport, thereby changing the porosity and permeability of sediment, clogging water pathway as well as staining water supply systems.

The production and release of Fe(II) and Mn(II) are critically important geochemical processes in hyporheic zones. Dissimilatory metal reduction can convert highly insoluble Fe(III) and Mn(III/IV) (oxyhydr)oxides to more soluble Fe(II) and Mn(II) species in oxygen-limited environments (Lovley, 1991, 1997; Cooper et al., 2006; Hyun et al., 2017). Their release rates, extent and speciation are not yet fully understood, and could be controlled by site-specific geochemical factors such the solubility of metal minerals under neutral and alkaline conditions [e.g., siderite ($FeCO_3$), rhodochrosite ($MnCO_3$) and pyrite (FeS_2); Coleman et al., 1993; Zachara et al., 1998; Jensen et al., 2002; Wan et al., 2019] or formation of metal complexes with natural organic matter (NOM) in NOM-rich environments (Daugherty et al., 2017). Siderite has been considered as an important reduced phase of iron(II) mineral and end product of bacterial respiration in anaerobic environments (Coleman et al., 1993) as well as in laboratory studies (Zachara et al., 1998). NOM can influence mineral solubility and metal speciation via formation of strong metal complexes (Tipping, 2002; Dong et al., 2010; Daugherty et al., 2017), and serve as an electron donor for microbial metal reduction (Lovley, 1991, 1997; Cooper et al., 2006; Kenwell et al., 2016; Hyun et al., 2017; Bryant et al., 2020). However, the impact of NOM on release and speciation of Fe(II) and Mn(II) in hyporheic zones is still not well-understood.

The East River floodplain, located in the upper Colorado River Basin, has been developed as a community headwaters testbed for the U.S. Department of Energy (DOE) to explore how mountainous watersheds retain and release water, nutrients, carbon and metals, and how they respond to early snowmelt, drought, and other disturbances (Hubbard et al., 2018). It consists of multiple river meanders with a distinctive fluvial progression and is representative of other headwater systems (Kenwell et al., 2016; Dwivedi et al., 2018). The East River flow is fed predominantly by snowmelt in late spring to early summer, with middle to late-summer monsoon (Winnick et al., 2017; Hubbard et al., 2018). A reactive transport modeling study (Dwivedi et al., 2018) indicated that dissolved oxygen (DO) and nitrate (NO_3^-) decreased quickly along the intrameander flow paths while Fe(II) concentration increased. It further confirmed that the interactions of river water and groundwater resulted in distinct redox gradients and geochemical conditions. However, there is a knowledge gap in understanding the geochemical controls on the release of these redox active metals and their speciation in the hyporheic sediments and groundwater of East River. To address these questions, we conducted (1) laboratory batch incubation experiments to determine the production, release rates and extent of Fe(II) and Mn(II) using the depth- and redox-distributed sediment samples from East River hyporheic sediments, (2) synchrotron-based bulk Fe K-edge extended X-ray absorption fine structure (EXAFS) spectroscopy to identify the major Fe species associated with sediments, (3) geochemical modeling to explore the geochemical controls on the release and speciation of Fe(II) and Mn(II), with an emphasis on the impact of Fe(II)-NOM complexation on siderite dissolution.

MATERIALS AND METHODS

Site Description and Sediment Characterization

Sediment samples were collected from a meandering reach of the East River located near Gothic, Colorado (**Figure 1**). Detailed descriptions of the field site and sediment sampling have been reported previously (Dwivedi et al., 2018; Fox et al., 2020). The watershed geology includes a diverse suite of Paleozoic and Mesozoic sedimentary rocks. In particular, the floodplain site consists of the Mancos Shale, a relative young Cretaceous Shale bedrock overlain by glacial moraine and alluvial sediment deposits. The Mancos is an agglomeration of an array of marine black shale with regions of elevated metal, metalloid, and pyrite content (Morrison et al., 2012; Kenwell et al., 2016). The four sediment samples (MCP1S, MCP1D, MCP3S, and MCP3D) used in this study were collected at ∼30–45 cm and 60–75 cm depth using a 5-cm diameter soil core sampler directly adjacent to two existing wells, MCP1 and MCP3 along a transect across Meander C (**Figure 1**) on September 22, 2016. Here "S" denotes shallow depth 30–45 cm and "D" denotes deep depth 60–75 cm. These samples represent the variation of naturally reducing zones within the meander C (Dwivedi et al., 2018). MCP3 is located in the anoxic zone with more Fe-reducing conditions, while MCP1 is located in the suboxic zone with relatively less Fe-reducing conditions. The deep sample (60–75 cm) has more Fe-reducing conditions than the shallow samples. At the time of sampling, the water table was ∼80 cm (MCP1) and 90 cm (MCP3) below

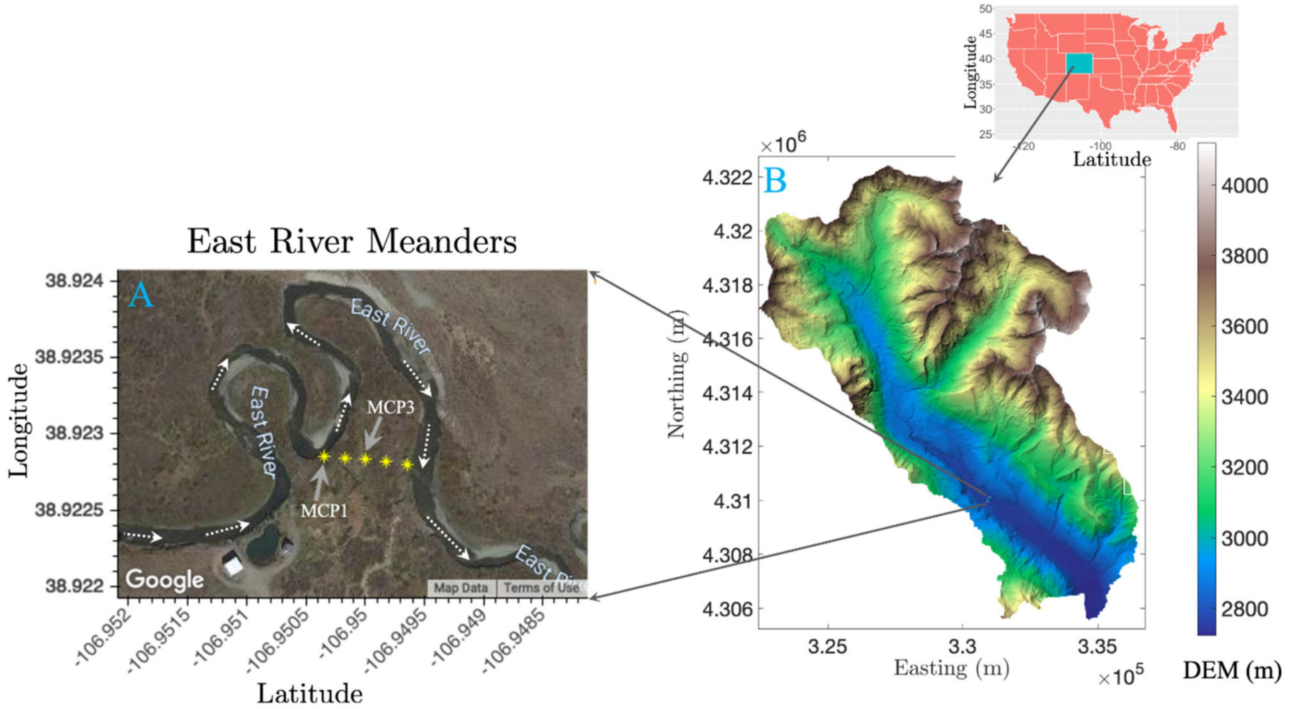

FIGURE 1 | Map showing core sampling locations of MCP1 and MCP3 from the meander C floodplain transect **(A)**, and a digital elevation map (DEM) of the East River watershed in Colorado **(B)**.

ground surface and the river discharge was nearing baseflow conditions during a water year characterized as average (Hubbard et al., 2018). However, the water table varies seasonally with river discharge, and portions of the floodplain can become completely saturated due to overbank flow during spring snowmelt (May–July). The samples were sealed into Mylar bags with oxygen absorbers immediately after sampling in order to preserve its redox status, shipped in a cooler with ice packs to the laboratory and stored at 4°C until further use. Note that the samples were stored ~6 months in Mylar bags in a 4°C refrigerator before our incubation experiments. Each sediment was homogenized and sieved through a 2-mm sieve in an anaerobic glovebox. Typical groundwater composition at the two locations is shown in **Supplementary Table 1**.

Moisture content was measured by drying a portion of sample at 105°C until a constant mass was achieved. A subsample of ≤2-mm fraction was air-dried at room temperature and ball-milled to fine powder for chemical and mineralogy analyses. Total carbon (TC) and total inorganic carbon (TIC) were analyzed using a Shimadzu TOC-V_{CPH} analyzer equipped with a solid sample module (SSM-5000A). Total organic carbon (TOC) was obtained from the difference between TC and TIC. The iron (Fe) and manganese (Mn) contents from their free (oxyhydr)oxides were determined by extracting finely ground samples with sodium salt solution of citrate (0.3 M), bicarbonate (0.1 M), and dithionite (0.1 M) (CBD-extractable Fe and Mn) at 80°C on duplicate samples (Sparks, 1996). Total Fe(II) was extracted with 1 M HCl for 24 h and analyzed by ferrozine assay (Stookey, 1970). The mineralogical composition of powdered samples was analyzed by X-ray diffraction (XRD) using Rigaku SmartLab® diffractometer. The diffractometer was equipped with a theta-theta goniometer and a rotating sample holder using Cu ($\lambda k\alpha 1 = 1.5406$ Å and $\lambda k\alpha 2 = 1.5444$ Å) cathode. The data were collected from 2° to 90° of 2θ with a 0.02 °2θ step-size and count times of 2 s per step using a Kα radiation tube (40 kV, 40 mA). The diffraction patterns were analyzed using the software Match (Putz and Brandenburg, 2011) extended with the PDF2 mineral database.

Artificial River Water

Artificial river water was synthesized based on the annual average water chemistry of Pump House stream water, which is located nearby meander C. The artificial river water chemistry is provided in **Table 1**. ACS analytical-grade chemicals were dissolved in Milli-Q water (18.2 MΩ·cm) and the water was sparged gently with air for ~3 days to ensure equilibrium with atmospheric $CO_2(g)$ and $O_2(g)$. The pH was adjusted with small amount of HCl/NaOH until to achieve a final pH of 8.2 ± 0.1. After equilibrium, the water was filtered with 0.2 µm Corning filter system (polystyrene, sterile) in order to remove any possible microbes. Note that the concentrations of cations and anions in artificial river water (**Table 1**) are similar and comparable to those of the groundwater at the MCP1 and MCP3 wells (**Supplementary Table 1**). The major difference is that the artificial river water was manipulated with a relatively higher $[NO_3^-] = 40\,\mu M$ and saturated with atmospheric O_2 for

TABLE 1 | The concentrations of major cations and anions in artificial river water.

Cation	Concentration, μM	Anion	Concentration, μM
Na^+	72.0	Cl^-	25.0
K^+	15.0	NO_3^-	40.0*
Mg^{2+}	270.0	SO_4^{2-}	500.0
Ca^{2+}	1141.0	HCO_3^-	2100.7

**Actual river water $[NO_3^-]$ = 5.5 μM, higher $[NO_3^-]$ = 40 μM used for monitoring its concentration change during incubation period.*

evaluating the rapid deoxygenation and denitrification processes in hyporheic zones (Dwivedi et al., 2018).

Batch Incubation Experiments

Batch incubation experiments were conducted in duplicate in an anaerobic glovebox (~2% H_2 and ~98%N_2) under ambient temperature (~ 22.5°C). All materials and tools used were either autoclaved or purchased as sterile. All preparation and processing procedures were conducted in an anaerobic glovebox unless otherwise stated. First, field-wet sediment samples (15.0 g dry weight equivalent) and the artificial river water (135 mL) were mixed in 160-mL serum bottles. The bottles were then sealed with thick rubber stoppers and aluminum crimp caps, and the headspace was immediately purged with N_2 to remove atmospheric O_2 and CO_2. The approach of mixing air saturated artificial river water with sediment mimics the process of fresh surface stream water infiltrating into anaerobic sediments. The bottles were then wrapped with aluminum foil and placed on a rotary shaker (VWR Orbital Shaker 5000). Aliquots of samples were taken at pre-selected time intervals within 57 days' incubation for chemical analyses. During sampling, we turned the bottles upside down, inserted a 25-gauge needle with 10-mL syringe, swirled vigorously, and ~ 5 mL slurry samples were taken for analyses. The nominal inner diameter of 260 μm of 25 gauge needles helps to successfully capture the reactive fine fraction (clay, silt, and fine sand) of sediment. Immediately, a 0.2 mL aliquot of the slurry sample was injected in 2-mL Eppendorf tube containing 1.8 mL of 1 M HCl, vortexed briefly and then allowed the sediment to settle for 24 h. The supernatant was analyzed for total Fe(II). The remaining slurry sample was centrifuged at 14,000 rpm for 5 min and then filtered with 0.2 μm Supor® membrane syringe filters (Pall Life Science). The filtrates were immediately split into three portions: 0.5 mL acidified (2% HNO_3) for metal analysis, 0.5 mL for anion analysis, and the remaining filtrate for dissolved organic carbon (DOC) analysis. At the end of the incubation (57 days), larger samples were collected and filtered as described above for measurement of pH and Fe(II) concentrations, and headspace gas samples were collected for CO_2 and $\delta^{13}C$ analysis. Prior to each sampling point, nitrogen gas (N_2) was injected first with the same volume of sample to be taken. A sediment-free control experiment was also conducted. DOC was analyzed as non-purgeable organic carbon (NPOC) using a Shimadzu TOC-V_{CPH} analyzer. Dissolved metal and anions were analyzed using inductively coupled plasma mass spectrometry (ICP-MS) (Elan DRC II, PerkinElmer) and ion chromatography (IC) (Dionex ICS-2100, Thermo Scientific), respectively. The pH values were measured using an Orion 8104BNUWP Ross Ultra pH electrode. Fe(II) was analyzed using the ferrozine assay at 562 nm (Stookey, 1970). The concentrations and the carbon isotope ratios ($\delta^{13}C_{VPDB}$) of headspace CO_2 were analyzed using a headspace autosampler (Gilson, Villiers-le-Bel, France) connected to a Trace gas preconcentrator interfaced to Micromass JA Series Isoprime isotope ratio mass spectrometer (Micromass, Manchester, UK). CO_2 concentrations were determined using the m/z 44 (CO_2) peak area.

Iron Speciation by X-Ray Absorption Spectroscopy

Iron oxidation state and chemical coordination environment of the sediment samples were determined using Fe K-edge extended X-ray absorption fine structure (EXAFS) (7,112 eV) at beamline 4-3 at the Stanford Synchrotron Radiation Light Source, at Menlo Park, CA, under ring operating conditions of 3 GeV with a current of 450 mA. EXAFS data were processed and analyzed using the Sixpack and Athena software packages (Ravel and Newville, 2005; Webb, 2005). Linear combination fitting (LCF) of spectra was performed in Athena in k^3-weighted k-space between $k = 2$ and 12, using the following end-members: siderite ($FeCO_3$), 2-and 6-line ferrihydrite [$Fe(OH)_3 \cdot nH_2O$], goethite (α-FeOOH), lepidocrocite (γ-FeOOH), ferrosmectite (Fe-containing clays), and Fe(II)-NOM. Details of Fe(II)-NOM preparation and characterization are provided in Daugherty et al. (2017). These references were chosen based on their likelihood to be present in our experimental samples. The fits were optimized such that the sum of the contributing Fe phases would be 1. Compounds were only included in the fit if the fractional contribution was >0.05. Additional details for the LCF-EXAFS analysis are presented in the **Supplementary Material**.

Kinetic and Geochemical Modeling

The kinetics of total Fe(II) production, dissolved Fe(II) and Mn, and DOC were simulated using the data analysis of Origin 8.1 with user defined kinetic rate equations. The geochemical computer code PHREEQC (Parkhurst and Appelo, 2004) was applied for modeling of dissolved Fe(II) and Mn(II) species and the solubilities of relevant minerals including siderite ($FeCO_3$), rhodochrosite ($MnCO_3$), amorphous ferrous hydroxide ($Fe(OH)_2$) and pyrite (FeS) under our incubation experimental conditions. Pyrite is included because it was identified as an important Fe(II) mineral in deep sediments from East River hillslope and floodplain (Kenwell et al., 2016; Dwivedi et al., 2018; Wan et al., 2019). The relevant geochemical reactions and thermodynamic constants (Stumm and Morgan, 1996; Langmuir, 1997) used are given in **Supplementary Table 2**.

RESULTS

Sediment Characterization and Redox Variations

The CBD-extractable Fe and Mn, Fe(II), and TIC/TOC are provided in **Table 2**. The CBD-extractable Fe (214–436 μmol/g) and Mn (3.5–6.5 μmol/g) represent the Fe and Mn present in

TABLE 2 | Characterization of hyporheic sediment samples.

Sample ID	MCP1S	MCP1D	MCP3S	MCP3D
Depth, cm	30–45	60–75	30–45	60–75
Moisture content, wt %[a]	15.5	46.6	15.5	34.4
TOC, wt %	1.43 ± 0.02	1.75 ± 0.01	1.47 ± 0.01	1.70 ± 0.04
TIC, wt %	0.03[b]	0.03[b]	0.03[b]	0.47 ± 0.03
CBD-extractable Fe, μmol/g[a]	213.6 ± 0.9	219.5 ± 0.8	436.0 ± 0.9	189.7 ± 0.9
CBD-extractable Mn, μmol/g[a]	5.3 ± 0.9	6.5 ± 0.1	5.8 ± 0.1	3.5 ± 0.1
Total Fe(II), μmol/g	16.1 ± 0.4	16.0 ± 0.5	21.3 ± 0.4	32.6 ± 0.6
Quartz, wt %	65.2	61.3	58.5	55.6
Phyllosilicate clays, wt %	26.2	24.6	24.3	18.9
Plagioclase, wt %	11.7	14.2	14.5	21.2
Titanite, wt %	n.d.	n.d.	2.6	1.5
Calcite, wt %	n.d.	n.d.	n.d.	2.7
Dolomite, wt %	n.d.	n.d.	n.d.	0.2

[a] *Datasets are available through the East River Watershed, CO, USA: Watershed Function SFA (Fox et al., 2019).*

[b] *≈Detection limit. n.d., not detectable.*

all "free" (oxyhydr)oxide and may server as sources for microbial reduction (Lovley, 1991, 1997; Cooper et al., 2006; Hyun et al., 2017). Similarly, total Fe(II) content serves as an indicator of the Fe-reducing conditions of the samples. As expected, MCP3 has higher Fe(II) content than MCP1 which is consistent with observations of high dissolved Fe(II) in groundwater at MCP3 (Dwivedi et al., 2018).

Deep sediments (60–75 cm) have similar TOC content ≈ 1.7% while the shallow sediments (30–45 cm) have TOC ≈ 1.5% (**Table 2**). TIC is much higher in MCP3D (0.47%) than in the other three samples (≤0.03%) which is in agreement with the contents of calcite and dolomite determined by XRD method. Organic carbon can serve as a major electron donor for microbial metal reduction (Lovley, 1991, 1997; Hyun et al., 2017), but also can complex with metals (Daugherty et al., 2017). TIC is a potential sink of metal-carbonates, also can be dissolved in aqueous phase as alkaline pH buffer (Stumm and Morgan, 1996). XRD analysis (**Table 2**) shows that the samples are composed of mostly quartz (55–65%), phyllosilicate clays (19–26%), and plagioclase (12–21%), with minor titanite (1.5–2.6%) for MCP3, and MCP3D contains detectable calcite (2.7%) and dolomite (0.2%).

Distribution of Fe Phases in Sediments

LCF of bulk Fe K-edge EXAFS provides semi-quantitative information regarding the different Fe forms present in the sediment samples (**Figure 2**, **Supplementary Figure 1**, **Table 3**). Irrespective of the meander location or depth, the majority of Fe species is composed of ferrihydrite (25–41%), ferrosmectite (20–45%), and Fe(II)-NOM complexes (23–32%), along with siderite (2–8%) as a minor component. Low values of R-factor and reduced chi-square indicate the goodness of the LCF fits.

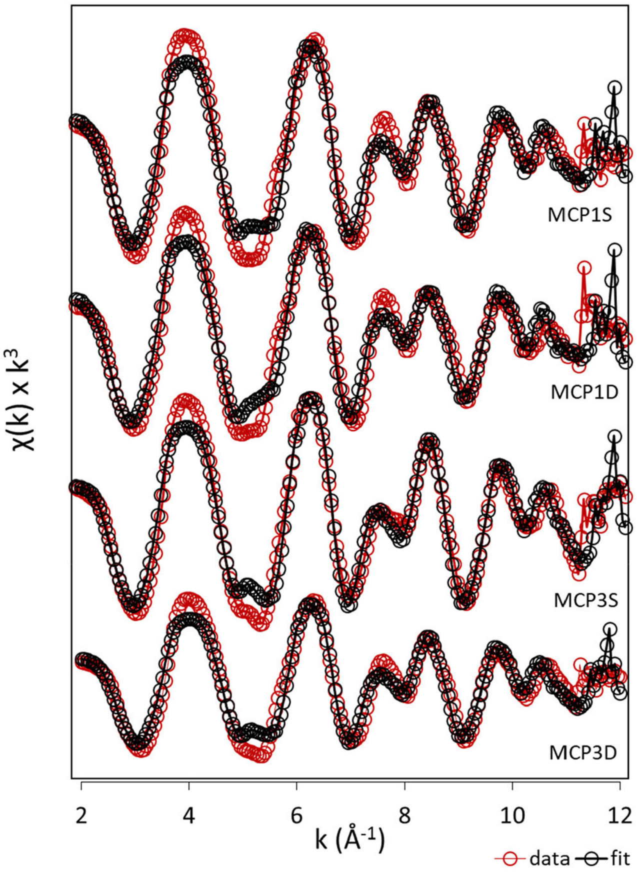

FIGURE 2 | EXAFS analysis. k^3-weighted EXAFS spectra and fits of sediment samples collected from MCP1 and MCP3 wells at shallow (S) and deep (D) zones (top to bottom). Red and black dotted lines indicate the experimental and fitted Fe K-edge EXAFS spectra, respectively.

TABLE 3 | Linear combination fit (LCF) analysis results for Fe K-edge EXAFS spectra of sediment samples collected from MCP1 and MCP3 wells at shallow (S) and deep (D) zones.

Sediment	Ferrihydrite	Ferrosmectite	Siderite	Fe(II)-NOM	R-factor	Reduced chi-square
	% contribution				(%)	(χ^2)
MCP1S	25.0	44.2	7.5	23.3	0.06	0.29
MCP1D	41.3	20.2	6.6	31.9	0.05	0.24
MCP3S	30.9	44.5	1.7	22.9	0.03	0.22
MCP3D	34.3	36.1	6.5	23.2	0.05	0.28

The percentage of Fe species is based on linear combination fitting of Fe EXAFS spectra using the following phases: siderite ($FeCO_3$), 2-and 6-line ferrihydrite [$Fe(OH)_3 \cdot nH_2O$], goethite (α-FeOOH), lepidocrocite (γ-FeOOH), ferrosmectite (Fe-containing clays), and Fe(II)-NOM. The compounds with a fractional contribution >0.05 were included in the fit and their relative distribution has been summarized in the table.

Kinetics of Total Fe(II) Production

Nitrate concentrations decreased rapidly from the initial 40 μM to ∼4 μM within the first day (**Supplementary Figure 2**), then reduced further to ≤3 μM after 3 days for all sediments which is

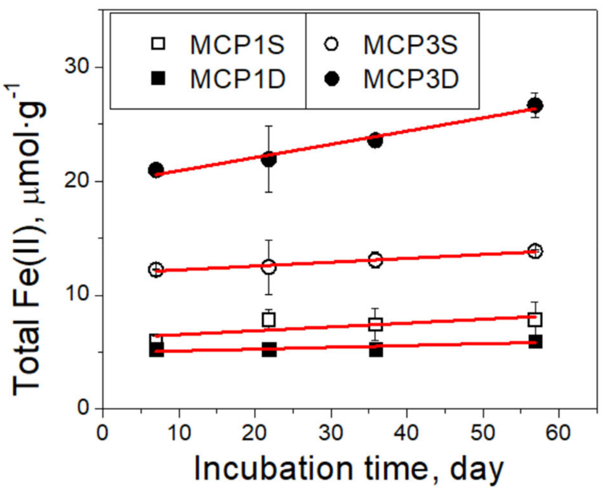

FIGURE 3 | Kinetics of total Fe(II) production over time in incubation experiments. Black symbols are the experimental data, and red lines are the fitted results with the zero-order rate (Equation 2). The error bars represent one standard deviation from duplicate experiments.

consistent with the nitrate concentrations observed in the nearby river water. It suggests that dissolved oxygen (DO) was depleted within the first day of incubation, because DO is energetically more favorable to accept electrons than nitrate, Fe(III) and sulfate (Froelich et al., 1979; Luu and Ramsay, 2003), i.e., reduction potential: dissolved O_2 > nitrate > Mn(IV) > Fe(III) > sulfate. More details about interactions of DO with sediments are provided in **Supplementary Material**. With a rapid depletion of DO and nitrate, dissimilatory Fe(III) reduction became the dominant mechanism resulting in Fe(II) production (Lovley, 1991, 1997; Lovley et al., 1998; Lovley and Blunt-Harris, 1999) (**Figure 3**).

Total Fe(II) production (μmol g^{-1} sediment) increased linearly over incubation time (**Figure 3**). It can be described by a zero-order rate equation,

$$\frac{d[Fe\ (II)]_t^{total}}{dt} = k_0 \tag{1}$$

where k_0 is the overall zero-order rate constant (μmol·g^{-1}·day^{-1}). It can be integrated to yield

$$C_t^{total\ Fe(II)} = C_0^{total\ Fe(II)} + k_0 t \tag{2}$$

where $C_0^{total\ Fe(II)}$ is the initial total Fe(II) content (μmol·g^{-1}) at $t = 7$ day, and $C_t^{total\ Fe(II)}$ is total Fe(II) content at $t > 7$ day. The data before 7 days are not used in order to avoid any potential perturbation caused by DO and nitrate. Equation (2) fits the experimental data well (red lines in **Figure 3**). The fitted rate constants and other parameters are provided in **Table 4A**. It shows the production rate constant k_0 (μmol·g^{-1}·day^{-1}): MCP3D (0.12) > MCP3S (0.034) ≈ MCP1S (0.034) > MCP1D (0.0159), with $C_0^{\text{total Fe(II)}}$ existed at 7 days: MCP3D (19.8 μmol·g^{-1}) > MCP3S (11.9 μmol·g^{-1}) > MCP1S (6.2 μmol·g^{-1}) > MCP1D (5.0 μmol·g^{-1}). The trend is in good agreement with the total sediment Fe(II) in **Table 2**, indicating that the reduction rates are highly dependent on the Fe-reducing conditions and subsurface positions.

Release Rates and Extent of Dissolved Fe(II)

Dissolved Fe(II) showed an initial drop during the first day of incubation due to the oxidation by DO introduced from the artificial river water, increased thereafter, and reached near-constant equilibrium concentrations after ~3 weeks (**Figure 4**). The experimental kinetic and equilibrium data can be simulated by a pseudo first-order rate equation (Langmuir, 1997)

$$\frac{d[Fe\ (II)]_t^{aq}}{dt} = k_1(C_{eq} - C_t) \tag{3}$$

where k_1 is the overall first-order rate constant (day^{-1}). C_{eq} is the equilibrium concentration (μM) of dissolved Fe(II), and C_t is the concentration (μM) of dissolved Fe(II) at incubation time t. This can be integrated to yield

$$C^t = C_{eq} - \left(C_{eq} - C_0\right) \exp(-k_1 t) \tag{4}$$

where C_0 is the initial concentration (μM) of dissolved Fe(II) at time $t = 1$ day. Here we selected the initial time at $t = 1$ day because dissolved Fe increased steadily after day 1. The fitted rate constants and parameters are given in **Table 4B**, and the fitted lines (red) are shown in **Figure 4**.

Our observation shows that the release extent [i.e., equilibrium concentration (C_{eq})] of dissolved Fe(II) varies with Fe-reducing conditions and positions (**Table 4B**). Specifically, MCP3 sediments released more dissolved Fe(II) than MCP1. This result is expected because MCP3 sediments were collected from the middle of the meander with greater Fe-reducing conditions, while MCP1 from near the river bank where relatively lower Fe-reducing conditions exist (Dwivedi et al., 2018). However, **Figure 4** shows that the shallow sediments (30–45 cm) released more dissolved Fe(II) than the deep sediments (60–75 cm) which is contrary to our expectation that shallow sediments will have a lower Fe-reducing potential compared to that of the deep sediment. For example, MCP3S released the highest concentration of dissolved Fe(II), contrary to what we observe in **Figure 3** where MCP3D contains the highest total Fe(II) production, indicating that higher total Fe(II) did not necessarily result in higher dissolved Fe(II). Although the release of dissolved Fe(II) is expected to be controlled by the equilibrium process, the release rates (k_1) in **Table 4B** could be useful for predicting the kinetic release of dissolved Fe(II) when systems are under non-equilibrium conditions due to groundwater table changes during drought and wet seasons or other disturbances (Hubbard et al., 2018).

Mn(II) Release Kinetics

Because of the very low solubility of Mn(III/IV) oxides, dissolved Mn can be considered as Mn(II) species resulting from reductive

TABLE 4 | Fitted kinetic parameters of total Fe(II) production (A), and release of dissolved Fe (B), dissolved Mn (C), and DOC (D).

	$C_0^{\text{total Fe(II)}}$, μmol·g^{-1}		k_0 (μmol·g^{-1}·day^{-1})	R^2	Chi^2
(A) TOTAL Fe(II) PRODUCTION					
MCP1S	6.2 ± 0.4		0.034 ± 0.009	0.534	1.1
MCP1D	5.0 ± 0.2		0.0159 ± 0.003	0.667	0.13
MCP3S	11.9 ± 0.1		0.034 ± 0.004	0.963	0.04
MCP3D	19.8 ± 0.5		0.12 ± 0.01	0.960	0.50
	$C_0^{\text{dissolved Fe(II)}}$, μM	**$C_{eq}^{\text{dissolved Fe(II)}}$, μM**	**k_1 (day^{-1})**	**R^2**	**Chi^2**
(B) DISSOLVED Fe(II)					
MCP1S	1.4 ± 0.6	13.1 ± 0.9	0.09 ± 0.03	0.968	0.70
MCP1D	2.0 ± 0.4	6.5 ± 0.4	0.032 ± 0.008	0.912	0.22
MCP3S	10.2 ± 3.0	43.6 ± 0.3	0.15 ± 0.05	0.974	0.85
MCP3D	13.5 ± 1.5	19.5 ± 1.3	0.07 ± 0.05	0.549	4.5
	$C_0^{\text{dissolved Mn}}$, μM,		**$k_0 \times 10^3$ (μM·day^{-1})**	**R^2**	**Chi^2**
(C) DISSOLVED Mn					
MCP1S	5.3 ± 0.3		0.25 ± 0.01	0.992	0.90
MCP1D	0.8 ± 0.7		0.25 ± 0.02	0.955	5.7
MCP3S	14.34 ± 0.08		0.280 ± 0.002	0.980	0.036
MCP3D	5.3 ± 0.2		0.070 ± 0.006	0.962	0.37
	C_0^{DOC}, mM	**C_{eq}^{DOC}, mM**	**$k_1 \times 10^3$ (day^{-1})**	**R^2**	**Chi^2**
(D) DOC					
MCP1S	0.53	0.90	3.7 ± 1.5	0.967	0.007
MCP1D	0.31	0.55	3.0 ± 0.7	0.932	0.001
MCP3S	0.50	0.97	0.9 ± 0.6	0.604	0.02
MCP3D	0.33	1.01	0.9 ± 0.4	0.823	0.004

R^2 is the correlation coefficient. Chi^2 is the sum of the squares of the deviations of the theoretical curve from the experimental points.

dissolution of Mn(III/IV) oxides (Stone, 1987; Lovley, 1991; Gounot, 1994). Dissolved Mn increased slowly and linearly, and a steady state of concentration was not reached over the 57-day incubation period (**Figure 5**). The zero-order rate laws (Equations 1, 2) can be applied to describe the Mn release kinetics well (red lines in **Figure 5**). The fitted parameters are given in **Table 4C**. MCP3S released the highest Mn concentrations (14–30 μM) with a rate of 0.28 μM·day^{-1}, whereas MCP3S released the highest dissolved Fe(II) as well (**Figure 4**). MCP1S and MCP1D both have the same release rate of 0.25 μM·day^{-1}, but MCP1S releases more Mn (5.3–20 μM) than MCP1D (0.8–15 μM) due to its higher initial dissolved Mn concentration. The release rate is only 0.070 μM·day^{-1} for MCP3D with an initial concentration of 5.3 μM. The very slow release rate of Mn in strongly Fe-reducing MCP3D can be attributed to either available reducible Mn being limited or inhibited by strong reduction of Fe(III).

DOC Release Kinetics and Decomposition

DOC concentrations increase rapidly and reach a relatively steady state within 24 h of incubation, with slight fluctuations during the first 3 weeks (**Supplementary Figure 3**). The data have been successfully fitted with a first-order rate (Equation 4) and the fitted parameters summarized in **Table 4D**. Equilibrium DOC concentrations range from 0.55 to 1.01 mM across samples. For all samples, the partial pressure of CO_2 (p_{CO2}) in headspace increased over the course of the 57-day incubation, with a concomitant decrease in $\delta^{13}C$ for headspace CO_2 and aqueous pH (**Table 5**), indicating that some sediment OC was mineralized. For example, p_{CO2} in the headspace MCP3S increased to $10^{-2.0}$ atm from an initial $10^{-3.4}$ atm, and aqueous pH decreased to 7.45 from an initial 8.2. The $\delta^{13}C$ values of headspace CO_2 range from −18.3 to −21.1‰. These values are higher than $\delta^{13}C$ values from the soil organic C (−25 to −27‰) (Fox et al., 2020) and lower than those values from soil carbonate (−10 to 4‰) (Montanez, 2013), suggesting that a high proportion of the CO_2 produced during the experiment comes from microbially decomposed sediment organic C.

DISCUSSION

Geochemical Reactions Controlling Fe(II) Release

Our experimental observation indicates that the majority of Fe(II) production exists as insoluble Fe(II) species since the total Fe(II) (**Figure 3**) is significantly higher than the dissolved Fe(II)

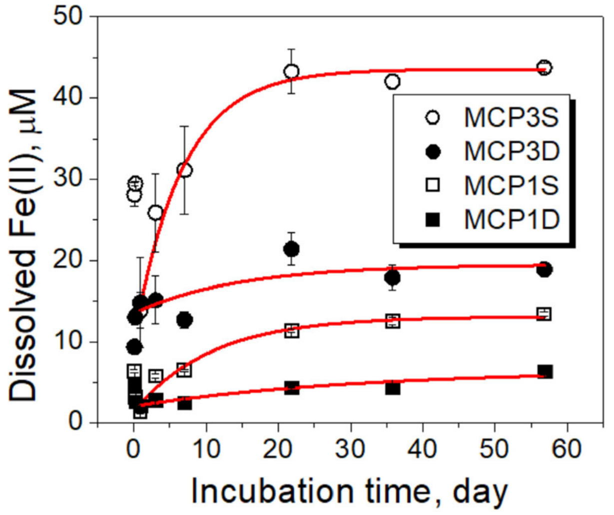

FIGURE 4 | Dissolved Fe(II) concentrations over time during incubation experiments. Black symbols are the experimental data, and red lines are the fitted results with the first-order rate (Equation 4). The error bars represent one standard deviation from duplicate experiments.

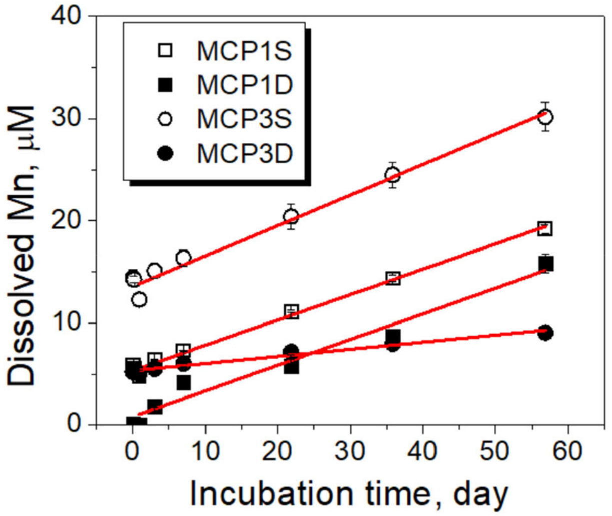

FIGURE 5 | Kinetics of dissolved Mn over time during sediment incubation experiments. Black symbols are the experimental data, and red lines are the fitted results with the zero rate (Equation 2). The error bars represent one standard deviation from duplicate experiments.

(**Figure 4**), with the amount of dissolved Fe(II) only 0.5–3% of total Fe(II) after 57 days of incubation (**Table 5**). Furthermore, sediments with highest initial or accumulated total Fe(II) do not necessarily release more Fe(II) to groundwater. The fact that dissolved Fe(II) reaches a near-constant concentration after ∼3 weeks (**Figure 4**), while total Fe(II) concentrations (**Figure 3**) continue to increase, suggests that over longer time periods, dissolved Fe(II) concentrations are controlled by an equilibrium process rather than through the continued reduction of Fe(III) to Fe(II).

Our LCF of bulk Fe EXAFS spectroscopy analysis (**Figure 2** and **Table 3**) suggests that siderite and NOM are the primary phases of Fe(II) in sediments along with a significant contribution of Fe from Fe-containing clays. Other studies also reported siderite as the end product under alkaline condition (Coleman et al., 1993; Zachara et al., 1998), and Fe(II)-NOM complexes as the primary reduced phase in NOM-rich environment (Daugherty et al., 2017). Under the aqueous pH (7.5–8.2) and DOC concentrations (0.5–1.1 mM) in these experiments, we hypothesize the release of dissolved Fe(II) is primarily controlled by siderite solubility, which is enhanced by Fe(II) complexation with dissolved NOM. These processes can be described by the following reactions:

$$FeCO_3\,(s) + 2H^+ = Fe\,(II)\,(aq) + CO_2\,(aq) + H_2O, \quad (5)$$

$$Fe\,(II)\,(aq) + L^- = Fe\,(II)\,L(aq), \quad (6)$$

Where L^- represents the reactive ligands or binding sites from dissolved NOM.

Siderite Solubility vs. Dissolved Fe(II) Without Dissolved NOM

In order to verify our hypotheses, we first calculated the solubility of siderite in absence of dissolved NOM [i.e., without considering the role of aqueous Fe(II) complexation with NOM] under our experimental conditions of pH and p_{CO2} (**Table 5**). The relevant thermodynamic reactions and constants are listed in **Supplementary Table 2** and the experimental concentrations of coexisting ions are given in **Supplementary Table 3**. The results are compared with the concentrations of experimentally dissolved Fe(II) in **Figure 6**. The solubilities of pyrite (FeS_2) and amorphous $Fe(OH)_2$ are also presented in **Figure 6**. It is apparent that pyrite and amorphous $Fe(OH)_2$ are not phase controlling minerals. The concentrations of dissolved Fe(II) are closely related to the predicted solubility of siderite, which increases with decrease of pH. However, the predicted Fe(II) concentrations underpredict the experimental Fe(II) concentrations in all cases, accounting for 31, 52, 32, and 30% for MCP1S, MCP1D, MCP3S, and MCP3D, respectively (**Figure 7**), indicating that the solubility of siderite alone cannot describe the release of dissolved Fe(II) without considering the effect of Fe(II)-NOM complexes.

Enhanced Solubility of Siderite by Dissolved NOM

In order to evaluate the impact of dissolved NOM on siderite solubility, we need to know (i) the concentrations of the reactive ligands (L) from dissolved NOM, and (ii) the binding constants (log K) for Fe(II) complexation with L. NOM can be grouped into humic substance (HS) and non-humic substances. Dissolved HS is operationally defined as humic acid (HA) and fulvic acid (FA) based on their solubility at pH = 2 (Schnitzer and Khan, 1972). HA and FA are the most reactive components of NOM

TABLE 5 | Concentrations of total Fe(II), dissolved Fe(II), dissolved Mn and DOC, and pH, p_{CO2} and $\delta^{13}C$ values of CO_2 at incubation time = 57 day.

Sediment	Total Fe(II), $\mu mol \cdot g^{-1}$	Dissolved Fe(II), μM	Dissolved Mn, μM	DOC, mM	pH	log p_{CO2}	CO_2 $\delta^{13}C_{VPDB}$(‰)
MCP1S	7.8 ± 1.6	13.4 ± 0.3	19.2 ± 0.4	0.90 ± 0.03	8.05 ± 0.05	−2.67 ± 0.01	−20.1 ± 0.1
MCP1D	6.0 ± 0.5	6.4 ± 0.5	15.8 ± 0.9	0.55 ± 0.05	8.15 ± 0.05	−2.69 ± 0.05	−18.3 ± 0.1
MCP3S	13.86 ± 0.09	43.8 ± 0.5	30.2 ± 1.4	0.97 ± 0.02	7.45 ± 0.05	−2.04 ± 0.01	−21.1 ± 0.1
MCP3D	26.6 ± 1.1	18.9 ± 0.8	9.1 ± 0.4	1.01 ± 0.04	8.05 ± 0.05	−2.82 ± 0.01	−18.8 ± 0.5
No sediment	n.d.	<2	<0.1	ND	8.20 ± 0.05	−3.4	−9.2

n.d., not detectable.

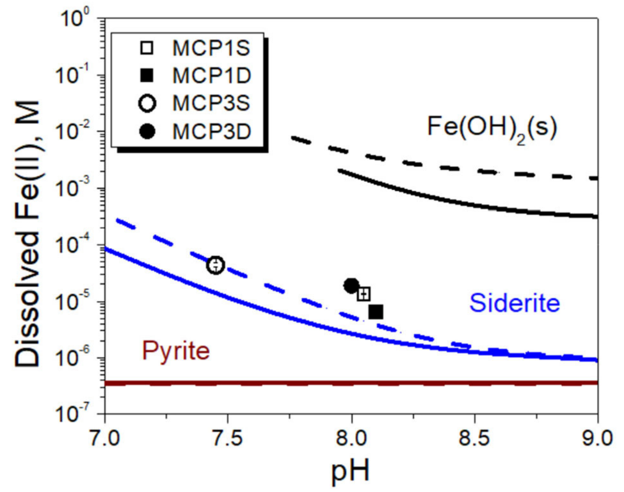

FIGURE 6 | Dissolved Fe(II) concentrations (symbols) vs. solubilities of amorphous $Fe(OH)_2(s)$, siderite and pyrite in the absence of Fe(II)-NOM complex (solid lines calculated at $p_{CO2} = 10^{-2.0}$ atm and dashed lines calculated at $p_{CO2} = 10^{-2.7}$ atm).

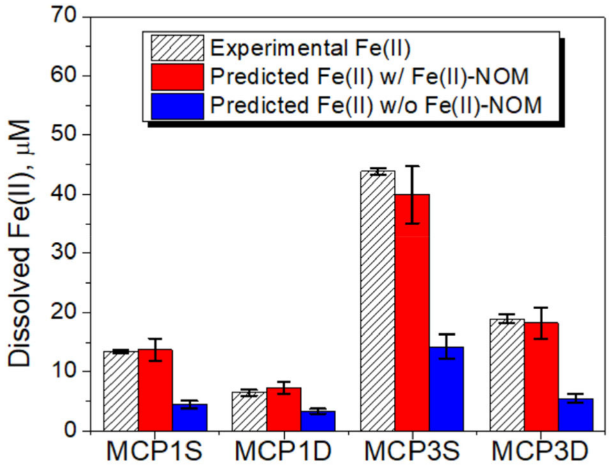

FIGURE 7 | Dissolved Fe(II) concentrations vs. predicted siderite solubility with and without including Fe(II)-NOM complexes. The error bars represent one standard deviation from duplicate experiments.

which are responsible for complexing metals via their acidic carboxylic and phenolic groups (Schnitzer and Skinner, 1966; Tipping, 2002; Daugherty et al., 2017). The contribution of non-humic substances on metal complexation is negligible due to their weak binding strength. However, the fraction of HS in DOC ranges from 30 to 70% (Dilling and Kaiser, 2002; Spencer et al., 2012; Kida et al., 2018) with a mean value of ∼50% in surface and subsurface waters (Suffet and MacCarthy, 1988; Herbert and Bertsch, 1995). By assuming ∼50% of DOC in **Table 5** is from HA and FA, we can calculate the concentrations of acidic functional groups as the reactive binding sites (L). According to the definition of the International Humic Substances Society (IHSS), the carboxylic content is the charge density (mmol/g C) at pH 8.0 and the phenolic content is the charge density (mmol/g C) between pH 8.0 and pH 10.0. Since our incubation experiment was conducted at pH ≤ 8.2, the carboxyls are considered as the major binding sites (Ritchie and Perdue, 2003; Rosario-Ortiz, 2014). Based on the nineteen HAs and FAs from IHSS, the carboxylic groups are estimated to have a mean value of 10.4 mmol/g C, with a mean value of the proton binding constant log $K = 4.1$ (**Supplementary Table 4**). Based on these assumptions, L concentrations from DOC can be estimated as

$$[L] = [DOC] \times 12 g/mol \times 50\% \times 10.4 \times 10^{-3} mol/g\ C = 0.0624\ [DOC] \quad (7)$$

where [DOC] is the concentration of DOC in mol/L.

It is a challenge to select an appropriate log K value for Fe(II)-L complexes because the literature reported values are conditional constants, and vary over many orders of magnitude due to different experimental conditions and methodologies applied (Schnitzer and Skinner, 1966; Rose and Waite, 2003; Yamamoto et al., 2010; Fujisawa et al., 2011; Catrouillet et al., 2014). After a literature review, the log K-values for Fe(II)-L complexes from Rose and Waite (2003) are selected and corrected for the difference of experimental conditions. The original log K values vary from 6.6 to 10.2 (**Supplementary Table 5**) for Fe(II) with twelve extracted HAs and FAs. We modified their values by correcting the effects of the binding site density and ionic strength. The corrected log K values are given in **Table 6**. More details on log K corrections and a literature review are provided in **Supplementary Material**. In addition, log K values

TABLE 6 | Original and corrected binding constants (log K) for 1:1 complexes between metals(II) and the carboxylic acid groups (L) in NOM.

NOM source	Reaction	log K range		log K	pH	I (M)	Method	References
HAs & FAs from 12 soils & SRFA	Fe(II) + L = Fe(II)-L	Original	6.6–10.2		8.1	0.7	Complexation kinetics	Rose and Waite, 2003
		Corrected[a]	5.6–8.8	5.6[c]	8.1	0		This work
HAs & FAs from peat & lake water	Mn(II) + L = Fe(II)-L	Original	3.7–4.3		8.0	0.02	Gel Complexometry	Mantoura et al., 1978
		Corrected[b]	3.9–4.5	4.2[c]	8.0	0		This work
HAs & FAs from peat & lake water	Ca(II) + L = Fe(II)-L	Original	3.2–3.4		8.0	0.02	Gel Complexometry	Mantoura et al., 1978
		Corrected[b]	3.4–3.6	3.5[c]	8.0	0		This work
HAs & FAs from peat & lake water	Mg(II) + L = Fe(II)-L	Original	3.1–3.5		8.0	0.02	Gel Complexometry	Mantoura et al., 1978
		Corrected[b]	3.3–3.7	3.5[c]	8.0	0		This work

NOM, natural organic matter; HAs, humic acids and FAs, fulvic acids; SRFA, Suwannee River fulvic acid.

[a] *The original value was corrected for the binding site concentration and ionic strength.*

[b] *The original value was corrected for the ionic strength only.*

[c] *log K used in this work.*

for coexisting metals of Mn(II), Ca(II), and Mg(II) with NOM are also selected from Mantoura et al. (1978) because of similar pH 8.0. The original log K-values given in **Table 6** for Mn(II), Ca(II), and Mg(II) have also been converted into binding sites based values from their original molecular weight based values (Mantoura and Riley, 1975; Mantoura et al., 1978).

Given the corrected log K-values in the range of 5.6–8.8 for Fe(II)-L (**Table 6**), we first evaluated these values for simulating the solubility of siderite, while using the mean log K values of Mn(II)-L, Ca(II)-L, and Mg(II)-L and the concentrations of coexisting ions provided in **Supplementary Table 3** and the relevant thermodynamic reactions and constants listed in **Supplementary Table 2**. We found log K = 5.6 for Fe(II)-L best describes the equilibrium concentrations of dissolved Fe(II) (**Figure 7**) for all samples, with an overall average 100% (± 5%) agreement. The log K = 5.6 is also in agreement with those reported by Fujisawa et al. (2011) (log K = 5.3–5.6 at pH 3.6). These results clearly demonstrate that dissolved NOM can significantly enhance the solubility of siderite by forming strong Fe(II)-NOM complex, and affected by pH as well as p_{CO_2}.

Influence of NOM on Dissolved Fe(II) Species

Predicted distribution of dissolved Fe(II) species indicate that Fe(II)-NOM complex is the major Fe(II) species in all samples and comprised of 54–70% of total dissolved Fe(II) species (**Figure 8**). The remaining inorganic species (30–46%) are mostly composed of free Fe^{2+} (20–25%), $FeCO_3$(aq) (2.5–14%) and $FeHCO_3^+$ (5–10%) along with a minor percentage of $FeSO_4$ (∼1%). More detailed prediction of siderite solubility and Fe(II) species at a pH range of 7.5–9.0 is provided in **Supplementary Figure 4**.

Geochemical Controls on Mn(II) Release

Similar to Fe(II), the potential phase controlling Mn(II) release could be rhodochrosite ($MnCO_3$) at alkaline conditions (Jensen et al., 2002). We calculated the solubility of rhodochrosite in the same manner as for siderite, i.e., with and without including Mn(II)-NOM complex, and compared with the dissolved Mn(II) concentrations at 57-days (**Figure 9**). The results show that all samples are oversaturated regarding the solubility of rhodochrosite for the Mn(II) concentrations after 3 weeks of incubation. The dissolution and precipitation of rhodochrosite ($MnCO_3$) are reported to be very slow processes, and precipitation may not occur within 57 days even when oversaturated (Pingitore et al., 1988; Jensen et al., 2002), indicating that other mechanisms or processes controlled Mn(II) release. We hypothesize that the dissolved Mn(II) occurs either via continuous microbial reduction of Mn(III/IV) oxides (Stone, 1987; Lovley, 1991; Gounot, 1994; Lloyd, 2003) or through the co-release of adsorbed or co-precipitated Mn(II) during dissolution of other minerals (e.g., Fe-oxides; Pingitore et al., 1988; Gounot, 1994). Reduction of Mn(IV) oxides by Fe(II) could be another potential mechanism for Mn(II) release (Siebecker et al., 2015), which shows how intricately linked the Fe/Mn redox cycles can be in these hyporheic zones.

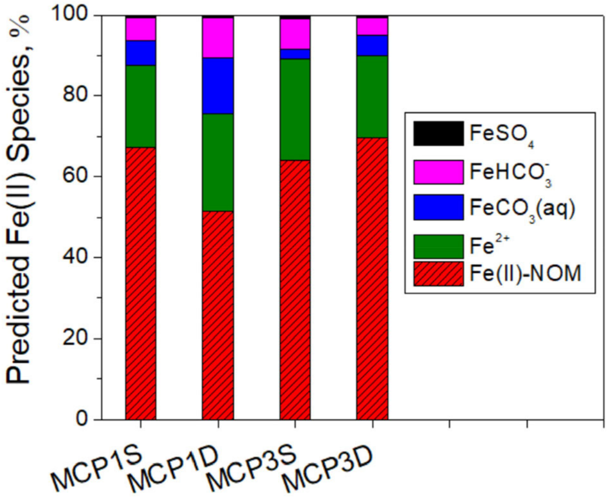

FIGURE 8 | Predicted distribution (%) of dissolved Fe(II) species including Fe(II)-NOM complexes.

Unlike Fe(II)-NOM, predicted Mn(II)-NOM is a minor species (3–7%) due to the weaker binding strength between Mn(II) and NOM (**Table 6**). Dissolved Mn(II) speciation is dominated by inorganic species of free Mn^{2+} (34–58%),

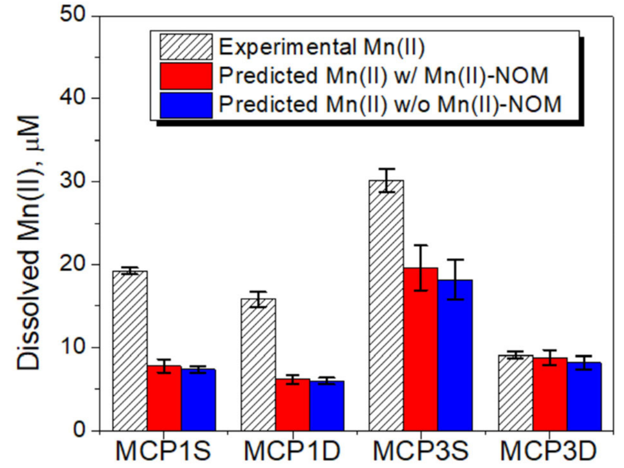

FIGURE 9 | Dissolved Mn(II) concentrations vs. predicted rhodochrosite solubility with and without including Mn(II)-NOM complex. The error bars represent one standard deviation from duplicate experiments.

$MnCO_3(aq)$ (17–52%), $MnHCO_3^+$ (10–16%), and $MnSO_4$ (1–2%). Therefore, unlike for Fe(II), dissolved NOM has little influence on Mn(II) species distribution and solubility.

CONCLUSIONS

Prediction of the release and speciation of Fe and Mn are crucially important in hyporheic zones for understanding their impact on nutrient cycling and water quality in East River watershed. To our knowledge, this work is the first study which reports siderite and dissolved NOM as the controlling phases for Fe(II) release from hyporheic sediments of the upper Colorado River basin.

Our results reveal that the release rates, extent and speciation of dissolved Fe(II) and Mn(II) are highly dependent on the site-specific geochemical conditions. While precipitation and dissolution of siderite and NOM are predicted to be the controlling processes for Fe(II) release under neutral and alkaline environments, the role of Fe(II)-NOM aqueous complexes are not well evaluated and rarely included in reactive geochemical transport models due to the lack of reliable and applicable Fe(II)-NOM complexation constants in literature. In this work, we calibrated the log K values of 1:1 Fe(II)-NOM complexes from Rose and Waite (2003). The calibrated log K values successfully predicted our experimental data, and expected to be applicable for geochemical modeling in many East River hyporheic zones and other subsurface aquifers with similar geochemical conditions. However, further study on NOM complexation with Fe(II) and other co-existing metals is truly needed to improve our current understanding on the binding models and strength under *in-situ* environmental conditions due to the challenges and uncertainties associated with characterization of NOM composition and their reactive binding sites as well as methodologies for determining metal-NOM complexation.

DATA AVAILABILITY STATEMENT

All datasets generated for this study are included in the article/**Supplementary Material**, and the kinetics datasets are publicly available through the East River Watershed. CO, USA: Watershed Function SFA (Dong et al., 2020).

AUTHOR CONTRIBUTIONS

PN conceptualized the project and designed the research. WD conducted the incubation experiments, geochemical modeling, and prepared the original draft. AB conducted EXAFS measurements and LCF analysis. PF conducted samples preparation and characterization. DD conducted field sampling and mapping. SC conducted XRD analysis. MB and MC conducted the CO_2 $\delta^{13}C_{VPDB}$(‰) and p_{CO2} analysis. All authors participated in the review, editing, and revision of the manuscript.

FUNDING

This work was supported as part of the Watershed Function Scientific Focus Area program at Lawrence Berkeley National Laboratory, supported by the U.S. Department of Energy, Office of Science, Office of Biological and Environmental Research, Subsurface Biogeochemical Research Program, through Contract No. DE-AC02-05CH11231 between Lawrence Berkeley National Laboratory and the U.S. Department of Energy. Synchrotron work was performed at beamline 4-3 of the Stanford Synchrotron Radiation Lightsource, SLAC National Accelerator Laboratory which is supported by the U.S. Department of Energy, Office of Basic Energy Sciences under Contract No. DE-AC02-76SF00515.

ACKNOWLEDGMENTS

We thank Harry Beller and Patrick Sorensen at Lawrence Berkeley National Lab for providing experimental suggestions and assistance.

SUPPLEMENTARY MATERIAL

The Supplementary Material for this article can be found online at: https://www.frontiersin.org/articles/10.3389/frwa.2020.562298/full#supplementary-material

REFERENCES

Boano, F., Harvey, J. W., Marion, A., Packman, A. I., Revelli, R., Ridolfi, L., et al. (2014). Hyporheic flow and transport processes: mechanisms, models, and biogeochemical implications. *Rev. Geophys.* 52, 603–679. doi: 10.1002/2012RG000417

Boulton, A. J., Findlay, S., Marmonier, P., Stanley, E. H., and Valett, H. M. (1998). The functional significance of the hyporheic zone in streams and rivers. *Ann. Rev. Ecol. Syst*. 29, 59–81. doi: 10.1146/annurev.ecolsys.29.1.59

Bryant, S. R., Sawyer, A. H., Briggs, M. A., Saup, C. M., Nelson, A. R., Wilkins, M. J., et al. (2020). Seasonal manganese transport in the hyporheic zone of a snowmelt-dominated river (East River, Colorado, USA). *Hydrogeol. J*. 28, 1323–1341. doi: 10.1007/s10040-020-02146-6

Catrouillet, C., Davranche, M., Dia, A., Bouhnik-Le Coz, M., Marsac, R., Pourret, O., et al. (2014). Geochemical modeling of Fe(II) binding to humic and fulvic acids. *Chem. Geol*. 372, 109–118. doi: 10.1016/j.chemgeo.2014.02.019

Coleman, M. L., Hedrick, D. B., Lovley, D. R., White, D. C., and Pye, K. (1993). Reduction of Fe(III) in sediments by sulfate-reducing bacteria. *Nature* 361, 436–438. doi: 10.1038/361436a0

Cooper, D. C., Picardal, F. F., and Coby, A. J. (2006). Interactions between microbial iron reduction and metal geochemistry: effect of redox cycling on transition metal speciation in iron bearing sediments. *Environ. Sci. Technol*. 40, 1884–1891. doi: 10.1021/es051778t

Daugherty, E. E., Gilbert, B., Nico, P. S., and Borch, T. (2017). Complexation and redox buffering of iron(II) by dissolved organic matter. *Environ. Sci. Technol*. 51, 11096–11104. doi: 10.1021/acs.est.7b03152

Dilling, J., and Kaiser, K. (2002). Estimation of the hydrophobic fraction of dissolved organic matter in water samples using UV photometry. *Water Res*. 36, 5037–5044. doi: 10.1016/S0043-1354(02)00365-2

Dong, W., Fox, P. M., Bhattacharyya, A., Bill, M., and Nico, P. S. (2020). *Kinetics Data of Iron(II), Manganese(II), Dissolved Organic Carbon and Nitrate from Batch Incubation Experiments Using Hyporheic Sediments from the East River Watershed, Colorado*. Watershed Function SFA.

Dong, W., Liang, L., Brooks, S., Southworth, G., and Gu, B. (2010). Roles of dissolved organic matter in the speciation of mercury and methylmercury in a contaminated ecosystem in Oak Ridge, Tennessee. *Environ. Chem*. 7, 94–102. doi: 10.1071/EN09091

Dwivedi, D., Steefel, C. I., Arora, B., Newcomer, M., Moulton, J. D., Dafflon, B., et al. (2018). Geochemical exports to river from the intrameander hyporheic zone under transient hydrologic conditions: East River mountainous watershed, Colorado. *Water Res. Res*. 54, 8456–8477. doi: 10.1029/2018WR023377

Fox, P. M., Bill, M., Heckman, K., Conrad, M., Anderson, C., Keiluweit, M., et al. (2019). *Geochemical Characterization of Floodplain Sediments from Meander C and O in the East River Watershed, CO, USA*. Watershed Function SFA.

Fox, P. M., Bill, M., Heckman, K., Conrad, M., Anderson, C., Keiluweit, M., et al. (2020). Shale as a source of organic carbon in floodplain sediments of a mountainous watershed. *J. Geophy. Res. Biogeosci*. 125:e2019JG005419. doi: 10.1029/2019JG005419

Froelich, P. N., Klinkhammer, G. P., Bender, M. L., Luedtke, N. A., Heath, G. R., Cullen, D., et al. (1979). Early oxidation of organic-matter in pelagic sediments of the eastern equatorial Atlantic - suboxic diagenesis. *Geochim. Cosmochim. Acta* 43, 1075–1090. doi: 10.1016/0016-7037(79)90095-4

Fujisawa, N., Furubayashi, K., Fukushima, M., Yamamoto, M., Komai, T., Ootsuka, K., et al. (2011). Evaluation of the iron(II)-binding abilities of humic acids by complexometric titration using colorimetry with ortho-phenanthroline. *Humic Subst. Res*. 8, 1–6.

Gomez, J. D., Wilson, J. L., and Cardenas, M. B. (2012). Residence time distributions in sinuosity-driven hyporheic zones and their biogeochemical effects. *Water Resourc. Res*. 48:W09533. doi: 10.1029/2012WR012180

Gounot, A. M. (1994). Microbial oxidation and reduction of manganese - consequences in groundwater and applications. *FEMS Microbiol. Rev*. 14, 339–349. doi: 10.1111/j.1574-6976.1994.tb00108.x

Herbert, B. E., and Bertsch, P. M. (eds.). (1995). *Characterization of Dissolved and Colloidal Organic Matter in Soil Solution: A Review*. Madison, WI: SSSA, 63–68.

Hubbard, S. S., Williams, K. H., Agarwal, D., Banfield, J., Beller, H., Bouskill, N., et al. (2018). The East River, Colorado, watershed: a mountainous community testbed for improving predictive understanding of multiscale hydrological-biogeochemical dynamics. *Vadose Zone J*. 17, 1–25. doi: 10.2136/vzj2018.03.0061

Hyun, J. H., Kim, S. H., Mok, J. S., Cho, H., Lee, T., Vandieken, V., et al. (2017). Manganese and iron reduction dominate organic carbon oxidation in surface sediments of the deep Ulleung Basin, East Sea. *Biogeosciences* 14, 941–958. doi: 10.5194/bg-14-941-2017

Jensen, D. L., Boddum, J. K., Tjell, J. C., and Christensen, T. H. (2002). The solubility of rhodochrosite ($MnCO_3$) and siderite ($FeCO_3$) in anaerobic aquatic environments. *Appl. Geochem*. 17, 503–511. doi: 10.1016/S0883-2927(01)00118-4

Kenwell, A., Navarre-Sitchler, A., Prugue, R., Spear, J. R., Hering, A. S., Maxwell, R. M., et al. (2016). Using geochemical indicators to distinguish high biogeochemical activity in floodplain soils and sediments. *Sci. Total Environ*. 563, 386–395. doi: 10.1016/j.scitotenv.2016.04.014

Kida, M., Fujitake, N., Suchewaboripont, V., Poungparn, S., Tomotsune, M., Kondo, M., et al. (2018). Contribution of humic substances to dissolved organic matter optical properties and iron mobilization. *Aquatic Sci*. 80:26. doi: 10.1007/s00027-018-0578-z

Langmuir, D. (1997). *Aqueous Environmental Geochemistry*. New Jersey, NJ: Prentice-Hall, Inc.

Lloyd, J. R. (2003). Microbial reduction of metals and radionuclides. *FEMS Microbiol. Rev*. 27, 411–425. doi: 10.1016/S0168-6445(03)00044-5

Lovley, D. R. (1991). Dissimilatory Fe(III) and Mn(IV) reduction. *Microbiol. Rev*. 55, 259–287. doi: 10.1128/MMBR.55.2.259-287.1991

Lovley, D. R. (1997). Microbial Fe(III) reduction in subsurface environments. *FEMS Microbiol. Rev*. 20, 305–313. doi: 10.1111/j.1574-6976.1997.tb00316.x

Lovley, D. R., and Blunt-Harris, E. L. (1999). Role of humic-bound iron as an electron transfer agent in dissimilatory Fe(III) reduction. *Appl. Environ. Microbiol*. 65, 4252–4254. doi: 10.1128/AEM.65.9.4252-4254.1999

Lovley, D. R., Fraga, J. L., Blunt-Harris, E. L., Hayes, L. A., Phillips, E. J. P., and Coates, J. D. (1998). Humic substances as a mediator for microbially catalyzed metal reduction. *Acta Hydrochim. Hydrobiol*. 26, 152–157. doi: 10.1002/(SICI)1521-401X(199805)26:3<152::AID-AHEH152>3.0.CO;2-D

Luu, Y. S., and Ramsay, J. A. (2003). Review: microbial mechanisms of accessing insoluble Fe(III) as an energy source. *World J. Microbiol. Biotechnol*. 19, 215–225. doi: 10.1023/A:1023225521311

Mantoura, R. F. C., Dickson, A., and Riley, J. P. (1978). The complexation of metals with humic materials in natural waters. *Estuarine Coast. Mar. Sci*. 6, 387–408. doi: 10.1016/0302-3524(78)90130-5

Mantoura, R. F. C., and Riley, J. P. (1975). The use of gel-filtration in study of metal binding by humic acids and related compounds. *Anal. Chim. Acta* 78, 193–200. doi: 10.1016/S0003-2670(01)84765-6

Montanez, I. P. (2013). Modern soil system constraints on reconstructing deep-time atmospheric CO2. *Geochim. Cosmochim. Acta* 101, 57–75. doi: 10.1016/j.gca.2012.10.012

Morrison, S. J., Goodknight, C. S., Tigar, A. D., Bush, R. P., and Gil, A. (2012). Naturally occurring contamination in the Mancos Shale. *Environ. Sci. Technol*. 46, 1379–1387. doi: 10.1021/es203211z

Park, J. H., Kim, S. J., Ahn, J. S., Lim, D. H., and Han, Y. S. (2018). Mobility of multiple heavy metalloids in contaminated soil under various redox conditions: effects of iron sulfide presence and phosphate competition. *Chemosphere* 197, 344–352. doi: 10.1016/j.chemosphere.2018.01.065

Parkhurst, D. L., and Appelo, C. J. (2004). *User's Guide to PHREEQC (Version 2) – A Computer Program for Speciation, Batch-Reaction, One-Dimensional Transport, and Inverse Geochemical Calculations*, *2 Edn.* Denver, CO: US Geological Survey.

Pedersen, H. D., Postma, D., and Jakobsen, R. (2006). Release of arsenic associated with the reduction and transformation of iron oxides. *Geochim. Cosmochim. Acta* 70, 4116–4129. doi: 10.1016/j.gca.2006.06.1370

Pingitore, N. E., Eastman, M. P., Sandidge, M., Oden, K., and Freiha, B. (1988). The coprecipitation of manganese(II) with calcite - an experimental-study. *Mar. Chem*. 25, 107–120. doi: 10.1016/0304-4203(88)90059-X

Putz, H., and Brandenburg Gbr, K. (2011). "*Match! - Phase Identification from Powder Diffraction, Crystal Impact*". Bonn.

Ravel, B., and Newville, M. (2005). ATHENA, ARTEMIS, HEPHAESTUS: data analysis for X-ray absorption spectroscopy using IFEFFIT. *J. Synchrotron Radiat*. 12, 537–541. doi: 10.1107/S0909049505012719

Ritchie, J. D., and Perdue, E. M. (2003). Proton-binding study of standard and reference fulvic acids, humic acids, and natural organic matter. *Geochim. Cosmochim. Acta* 67, 85–96. doi: 10.1016/S0016-7037(02)01044-X

Rosario-Ortiz, F. (ed.). (2014). *Advances in the Physicochemical Characterization of Dissolved Organic Matter: Impact on Natural and Engineered Systems*. Boulder, CO: American Chemical Society; University of Colorado. doi: 10.1021/bk-2014-1160

Rose, A. L., and Waite, T. D. (2003). Kinetics of iron complexation by dissolved natural organic matter in coastal waters. *Mar. Chem*. 84, 85–103. doi: 10.1016/S0304-4203(03)00113-0

Rowland, H., Pederick, R. L., Polya, D. A., Pancost, R. D., Van Dongen, B. E., et al. (2007). The control of organic matter on microbially mediated iron reduction and arsenic release in shallow alluvial aquifers, Cambodia. *Geobiology* 5, 281–292. doi: 10.1111/j.1472-4669.2007.00100.x

Saup, C. M., Bryant, S. R., Nelson, A. R., Harris, K. D., Sawyer, A. H., Christensen, J. N., et al. (2019). Hyporheic zone microbiome assembly is linked to dynamic water mixing patterns in snowmelt-dominated headwater catchments. *J. Geophys. Res. Biogeosci*. 124, 3269–3280. doi: 10.1029/2019JG005189

Schnitzer, M., and Khan, S. U. (1972). *Humic Substances in Environment*. New York, NY: Marcel Dekker.

Schnitzer, M., and Skinner, S. I. M. (1966). Organo-metallic interactions in soils: 5. stability constants of Cu2+, Fe2+ and Zn++ fulvic acid complexes. *Soil Sci.* 102:361. doi: 10.1097/00010694-196612000-00002

Siebecker, M., Madison, A. S., and Luther, G. W. (2015). Reduction kinetics of polymeric (soluble) manganese(IV) oxide (MnO2) by ferrous iron (Fe2+). *Aquatic Geochem*. 21, 143–158. doi: 10.1007/s10498-015-9257-z

Sparks, D. L. (ed.). (1996). *Mehtods of Soil Analysis. Part3. Chemical Methods-SSSA Book Series: 5*. Madison, WI: Soil Science Society of America and American Society of Agronom. doi: 10.2136/sssabookser5.3

Spencer, R. G. M., Butler, K. D., and Aiken, G. R. (2012). Dissolved organic carbon and chromophoric dissolved organic matter properties of rivers in the USA. *J. Geophys. Res. Biogeosci*. 117:G03001. doi: 10.1029/2011JG001928

Stone, A. T. (1987). Microbial metabolites and the reductive dissolution of manganese oxides - oxalate and pyruvate. *Geochim. Cosmochim. Acta* 51, 919–925. doi: 10.1016/0016-7037(87)90105-0

Stookey, L. L. (1970). Ferrozine - a new spectrophotometric reagent for iron. *Anal. Chem*. 42, 779–781. doi: 10.1021/ac60289a016

Stumm, W., and Morgan, J. J. (1996). *Aquatic Chemistry*. New York, NY: John Wiley & Song, Inc.

Suffet, I. H., and MacCarthy, P. (eds.). (1988). *Aquatic Humic Substances*. Washington DC: American Chemical Society.

Tipping, E. (2002). *Cation Binding by Humic Substances*. Cambridge: Cambridge University Press.

Wan, J., Tokunaga, T. K., Williams, K. H., Dong, W., Brown, W., Henderson, A. N., et al. (2019). Predicting sedimentary bedrock subsurface weathering fronts and weathering rates. Sci. *Rep*. 9:17198. doi: 10.1038/s41598-019-53205-2

Webb, S. M. (2005). SIXpack: a graphical user interface for XAS analysis using IFEFFIT. *Phys. Scripta* T115, 1011–1014. doi: 10.1238/Physica.Topical.115a01011

Winnick, M. J., Carroll, R. W. H., Williams, K. H., Maxwell, R. M., Dong, W., and Maher, K. (2017). Snowmelt controls on concentration-discharge relationships and the balance of oxidative and acid-base weathering fluxes in an alpine catchment, East River, Colorado. *Water Res. Res*. 53, 2507–2523. doi: 10.1002/2016WR019724

Yamamoto, M., Nishida, A., Otsuka, K., Komai, T., and Fukushima, M. (2010). Evaluation of the binding of iron(II) to humic substances derived from a compost sample by a colorimetric method using ferrozine. *Bioresour. Technol*. 101, 4456–4460. doi: 10.1016/j.biortech.2010.01.050

Zachara, J. M., Fredrickson, J. K., Li, S. M., Kennedy, D. W., Smith, S. C., and Gassman, P. L. (1998). Bacterial reduction of crystalline Fe3+ oxides in single phase suspensions and subsurface materials. *Am. Mineral.* 83, 1426–1443. doi: 10.2138/am-1998-11-1232

Conflict of Interest: The authors declare that the research was conducted in the absence of any commercial or financial relationships that could be construed as a potential conflict of interest.

frontiers in Water

ORIGINAL RESEARCH
published: 08 December 2020
doi: 10.3389/frwa.2020.577511

Hydrogeochemical Dynamics and Response of Karst Catchment to Rainstorms in a Critical Zone Observatory (CZO), Southwest China

Caiqing Qin [1,2], ***Hu Ding*** [1*], ***Si-Liang Li*** [1,3,4], ***Fu-Jun Yue*** [1], ***Zhong-Jun Wang*** [5] ***and Jie Zeng*** [6]

[1] Institute of Surface-Earth System Science, School of Earth System Science, Tianjin University, Tianjin, China, [2] Department of Earth & Environmental Science, School of Human Settlements and Civil Engineering, Xi'an Jiaotong University, Xi'an, China, [3] State Key Laboratory of Environmental Geochemistry, Institute of Geochemistry, Chinese Academy of Sciences, Guiyang, China, [4] Puding Karst Ecosystem Observation and Research Station, Chinese Academy of Sciences, Puding, China, [5] Department of Water Environment, China Institute of Water Resources and Hydropower Research, Beijing, China, [6] Institute of Earth Sciences, China University of Geosciences (Beijing), Beijing, China

Edited by:
Carl I. Steefel,
Lawrence Berkeley National Laboratory, United States

Reviewed by:
Kalyana Babu Nakshatrala,
University of Houston, United States
Reza Soltanian,
University of Cincinnati, United States

***Correspondence:**
Hu Ding
dinghu@tju.edu.cn

Specialty section:
This article was submitted to Water and Critical Zone, a section of the journal Frontiers in Water

Received: *29 June 2020*
Accepted: *23 October 2020*
Published: *08 December 2020*

Citation:
Qin C, Ding H, Li S-L, Yue F-J, Wang Z-J and Zeng J (2020) Hydrogeochemical Dynamics and Response of Karst Catchment to Rainstorms in a Critical Zone Observatory (CZO), Southwest China. Front. Water 2:577511. doi: 10.3389/frwa.2020.577511

Karst water is vital for local drinking and irrigation but is susceptible to contamination. Hydrochemistry, which is highly related to carbonate weathering in karst catchments, can affect water quality and respond rapidly to climate change. In order to explore hydrogeochemical sources, dynamics, and their responses to rainstorms, rainwater, throughfall, hillslope runoff, surface water, and groundwater were sampled synchronously during rainstorms at a karst Critical Zone Observatory (CZO), Southwest China. Results showed that the total dissolved solids (TDS) concentration in throughfall increased by 30.1 ± 8.0% relative to rainwater, but both throughfall and rainwater contributed little to TDS in surface water and groundwater compared with terrestrial sources. Hydrochemistry in surface water and groundwater was diluted by rainstorms but displayed chemostatic responses with different intensities to increasing discharge. This is possibly regulated by hydrogeological conditions, available sources of various solutes, and the difference between solute concentrations before and after rainstorms. Ca^{2+} and Mg^{2+} dynamics were mainly regulated by carbonate weathering, gypsum dissolution, and gypsum-induced dedolomitization (geological sources), which also affect Ca^{2+}, Mg^{2+}, and SO_4^{2-} in deep confined groundwater draining a gypsum stratum. For HCO_3^-, CO_2 from respiration and microbiologic activities is one dominant contributor, especially for spring. The chemostatic behaviors of NO_3^-, Cl^-, and K^+ were related to agricultural activities, especially in surface water. These controls on hydrochemistry may already exist as hillslope runoff occurs, which has be further demonstrated by principle component analysis (PCA). The heterogeneous permeability of epikarst can affect the mixture of groundwater from different sources and flowing pathways, enabling hydrochemistry at different hydrogeological conditions to display discrepant responses to rainstorms. The epikarst aquifer with high permeability is susceptible to changes in external environment, such as rainstorms and agricultural activities, increasing the potential risk of water environment problems (chronic pollution of nitrogen and high hardness of water) during a certain period. Drinking water safety thus deserves consideration in the agricultural karst catchment.

Keywords: hydrochemistry, high-resolution data, rainstorms, chemical weathering, chemostatic behavior, karst catchment

INTRODUCTION

Karst landforms cover 2.2 × 10^7 km^2 and are scattered around the world, especially in Southeast Asia, South America, and the Mediterranean coasts (Yuan and Cai, 1988; Ford and Williams, 2007). Southeast Asia is the largest continuous karst region, centered on Southwest China (Zhao and Seip, 1991). Comprised of chemically soluble rocks with large passages or network of conduits and caves inside, karst aquifers are very permeable and can store and transport large amounts of water, supplying drinking and irrigation water to ∼25% of the world's population (Ford and Williams, 2007). However, the increasing water demand (residential, industrial, and agricultural use) can cause water shortage and water quality degradation. Additionally, the special hydrogeological conditions (high permeable soil/rock systems with caves and fractures inside) of karst systems benefit water and solutes migration, making the CO_2-H_2O-$CaCO_3$ system sensitive to hydrological changes (Yuan and Zhang, 2008; Beaulieu et al., 2012), and making karst aquifers vulnerable to contamination (Kačaroglu, 1999). Researching karstic hydrochemical dynamics during rainfall storms is conducive to understanding the transfer of contaminants and solutes and their responses to climate change.

Intense carbonate weathering and mixing of "new" and "old" water can alter solute concentrations in karst water (Gabet et al., 2006; Basu et al., 2010). Solute concentrations also normally show distinct seasonal patterns due to hydrological variations and some biogeochemical processes (Han and Liu, 2004; Lang et al., 2006; Zhong et al., 2020). Therefore, hydrogeochemical behaviors in karst catchments need to be demonstrated by high-resolution information that can capture key processes. High-frequency field campaigns during rainstorms are thus necessary to analyze the dynamic response of chemical compositions to hydrological variations and its potential effects on water quality as well as public health. The dynamic behaviors and corresponding controls of hydrochemistry in river and/or groundwater have been reported (Koger et al., 2018; Piazza et al., 2018; Correa et al., 2019). However, there are few studies conducting high-frequency sampling to analyze hydrochemistry in both surface water and groundwater in karst regions of Southwest China. Additionally, rainwater, one important source of surface and ground water, also plays a significant role in hydrochemical dynamics (Polkowska et al., 2005; Ma et al., 2017). But most research only pays attention to sources of solutes in rainwater (Han and Liu, 2006; Lu et al., 2011; Wu et al., 2012; Zhang et al., 2012; Rao et al., 2017; Zhou et al., 2019); the dynamic variation of hydrochemistry among different waters (rainwater, throughfall, hillslope runoff, surface water, and groundwater) are rarely explored during rainstorms. Rainwater may play a more important role in karst catchments than non-karst systems, since the acidic rainwater may also dissolve carbonate minerals and then alter the hydrochemistry as well. Analyzing hydrochemistry of different water bodies in spatial profile can offer comprehensive information to understand hydrogeochemical dynamics in Earth's Critical Zone. This is necessary for modeling the migration processes of hydrochemistry and better implementing cost-effective water quality management in karst catchment.

Against this background, high-frequency sampling for surface water and spring was conducted during rainstorms at a karst catchment in Southwest China. Rainwater, throughfall, hillslope runoff, and well water were also synchronously collected, to analyze (1) the dynamic response of surface water and groundwater to rainstorms and corresponding controls and (2) the dynamic variations of hydrochemistry among different water bodies at a catchment scale and corresponding controls.

MATERIALS AND METHODS

Study Area

Chenqi catchment (26°15′20′′-26°16′9′′N, 105°46′3′′-105°46′50′′E), with an area of 1.25 km^2, is a karst Critical Zone Observatory (CZO) located in Puding, Guizhou province, Southwest China (**Figure 1**). This CZO has been investigated for ∼40 years in the aspect of hydrogeological structure, hydrological connectivity, soil characteristics, and other fundamental information (Chen et al., 2005, 2018; Cheng et al., 2019; Zhang et al., 2019; Liu M. et al., 2020). It is an agricultural karst catchment where irrigation and drinking water are both supplied by karst water. Under the influence of a subtropical monsoonal climate, the annual mean rainfall is 1,140 mm, over 80% of which falls in the wet season. Average monthly air temperature is highest in August (24°C) but lowest in December (7°C). Average monthly humidity ranges from 74 to 78%.

The elevation of this catchment decreases from east of 1,520 m to west of 1,320 m (outlet). Carbonate rocks dominate the lithology, over which Quaternary soils are unevenly distributed. Limestone is the dominant geological strata in the higher elevation area with 150–200 m thickness, and the underlying layer is impermeable marlite strata (Zhang et al., 2019). Soil is thin (mean < 50 cm) in hills but thicker (40–100 cm) in valley depressions. Deciduous broad-leaved forest and scrub-grassland, occupying 83% of total land use, grow mainly on the mountains. Agricultural paddy and dry land are spread in valley depressions, accounting for about 3 and 14% of the catchment area, respectively (Qin et al., 2020). The catchment outlet is in the valley depression surrounded by scattered hills. There are three

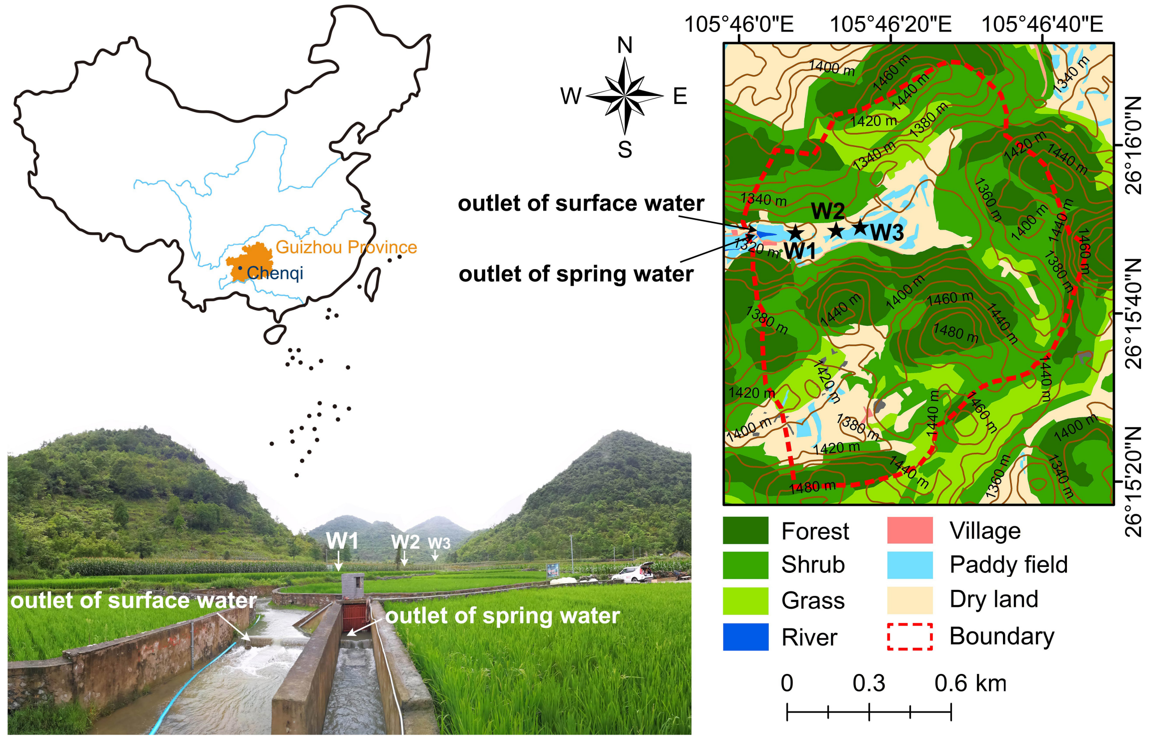

FIGURE 1 | Location of the study area and sampling sites. W1, W2, and W3 refer to three observation wells.

observation wells with different depth distributed in depression (**Figure 1**). The depth (below the ground surface) of well W1 and well W3 are 20 and 12 m, respectively. The permeability of aquifer around W1 is low (most resistivity > 1,000 Ωm) but that around W3 is high (most resistivity < 100 Ωm) (Chen et al., 2018). The well W2 (depth > 20 m) is fed by deep confined spring draining gypsum stratum and scarcely suffers outside disturbance. The 3-wells can thus reflect the circumstances at different depth in the karst structure.

Sampling and Measurement

High-frequency sampling was conducted at the outlet of spring (SP) and surface water (SU) during rainstorms from June 11 to 17, 2018 (**Figure 1**). Well water samples of W2 were synchronously collected at the outlet through a drain line. Well water at different depths of W1 and W3 were sampled before (B), during (D), after (A) and on the fourth days (F) after the rainstorms. Meanwhile, rainwater (RA), throughfall (TH), and hillslope runoff (HI) were also collected on surrounding hills.

At the sampling time, water temperature (T), dissolved oxygen (DO), electrical conductivity (EC), and pH were measured in the field by a portable multiple parameter sensor (WTW, Multi 3630 IDS). All water samples were collected in duplicate in dry and clean bottles that were rinsed twice beforehand with *in-situ* water and stored in darkness at 4°C until analysis. One part was used for measuring HCO_3^- concentration through acid titration with 0.02 mol L^{-1} HCl. The other was filtered through 0.22 µm filters to measure major ions (Ca^{2+}, Mg^{2+}, Na^+, K^+, SO_4^{2-}, Cl^-, NO_3^-) by the Ion Chromatography (Thermo Scientific, Dionex Aquion). Blank test and sample duplicates were conducted during analytical processes to perform quality assurance and control. The blank was lower than the method detection limits and the relative standard deviation (RSD) of above analyses were all within 5%.

Total dissolved solids (TDS) were calculated by the sum of eight ions measured above. The bracket "[]" was used to symbolize the concentration of solutes, e.g., Ca^{2+} concentration is simply described as $[Ca^{2+}]$. To more accurately compare solute concentrations within this study or between different researches, discharge-weighted concentration (DWC) of solutes was calculated as follows:

$$\mathrm{DWC} = \frac{\sum (Q_i \times C_i)}{\sum Q_i} \tag{1}$$

where Q_i is the discharge at timestep i and C_i is the synchronous concentration of solutes.

RESULTS

During the sampling period, two considerable rainstorms occurred continuously, with amounts of 30.4 mm on June 11 and 24 mm on June 12 (**Figure 2**). The pH value of rainwater here is 6.27 ± 0.03, which increases by 0.44 in throughfall (**Supplementary Table 1**). Ion concentrations in rainwater are low and follow the order of $[HCO_3^-]$ (109 µmol L^{-1}) > $[SO_4^{2-}]$

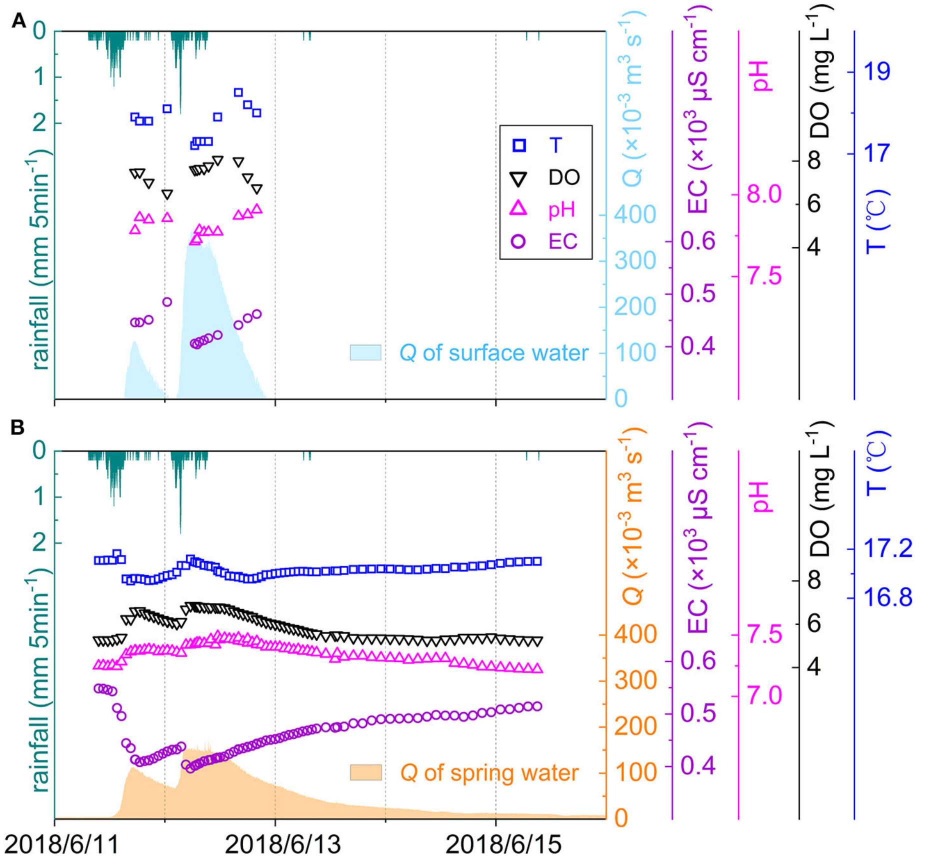

FIGURE 2 | Time series of rainfall, discharge (*Q*), and water quality parameters of surface water **(A)** and spring water **(B)**.

(79.8 μmol L^{-1}) > [Ca^{2+}] (46.3 μmol L^{-1}) > [NO$_3^-$] (30.7 μmol L^{-1}) > [Mg^{2+}] (7.87 μmol L^{-1}) > [K$^+$] (3.57 μmol L^{-1}) > [Na$^+$] (2.76 μmol L^{-1}) > [Cl$^-$] (2.40 μmol L^{-1}) (**Supplementary Table 1**). The first four ions dominate chemical compositions, accounting for 94.1%. After passing through the vegetation canopy, [NO$_3^-$] decreases by 9.13 ± 6.13 μmol L^{-1} but other ions increase with different degrees. The TDS concentration in TH is slightly higher than that in RA (24.2 vs. 18.6 mg L^{-1}). Both RA and TH show lower total cation charge (TZ$^+$ = 2[Ca^{2+}] + 2[Mg^{2+}] + [Na$^+$] + [K$^+$]) than total anion charge (TZ$^-$ = [HCO$_3^-$] + 2[SO$_4^{2-}$] + [NO$_3^-$] + [Cl$^-$]). The net inorganic charge balance (NICB = [TZ$^+$ $^-$ TZ$^-$] / [TZ$^+$ + TZ$^-$] * 100%) in RA is even <-10% (**Figure 3**).

During rainstorms, discharge varied from 0.4 × 10^{-3} to 179.5 × 10^{-3} m^3 s^{-1} at SP outlet and from 0 to 378.1 × 10^{-3} m^3 s^{-1} at SU outlet, and high discharge normally accompanied high DO and low EC (**Figure 2**). SU samples have higher DO and pH but lower EC compared with SP samples, and all of them have small coefficient of variation (CV < 10%) (**Supplementary Table 1**). TDS in SU and SP range from 331 to 397 mg L^{-1} and from 345 to 475 mg L^{-1}, respectively. The DWC of ions in SU follow the order of [HCO$_3^-$] (3,371 μmol L^{-1}) > [Ca^{2+}] (1,804 μmol L^{-1}) > [Mg^{2+}] (362 μmol L^{-1}) > [SO$_4^{2-}$] (333 μmol L^{-1}) > [NO$_3^-$] (321 μmol L^{-1}) > [Cl$^-$] (73.4 μmol L^{-1}) > [Na$^+$] (35.5 μmol L^{-1}) > [K$^+$] (33.5 μmol L^{-1}) (**Supplementary Table 1**). In SP, the DWC of HCO$_3^-$, Ca^{2+}, and Mg^{2+} are higher than that in SU, at 3,812, 2,053, and 436 μmol L^{-1}, respectively. While the DWC of NO$_3^-$, Cl$^-$, and K$^+$ in SP are lower than that in SU, at 217, 61.0, and 21.8 μmol L^{-1}, respectively. Except NO$_3^-$, parameters have higher CV in SP than in SU (**Supplementary Table 1**). The NICB of both SU and SP samples are within ±10% (**Figure 3**).

The water levels in W1 and W3 fluctuated by 1.6 and 3.7 m, respectively (**Supplementary Figure 1**). All ion concentrations in W1 have relatively small spatial variations in vertical profiles and temporal variations among the four sampling campaigns [before (B), during (D), after (A), and on the fourth days (F) after the rainstorms], as reflected by their CV in **Supplementary Table 1** and box plots in **Figure 4**. In vertical profiles of W3, however, ion concentrations normally fluctuate more widely, except the third sampling (A) when almost all ions have the minimum CV. The mean ion concentrations in W1 follow the order of [HCO$_3^-$] (4,434 μmol L^{-1}) > [Ca^{2+}] (2,355 μmol L^{-1}) > [SO$_4^{2-}$] (1,743 μmol L^{-1}) > [Mg^{2+}] (1,385 μmol L^{-1}) > [Cl$^-$] (122 μmol L^{-1}) > [K$^+$] (98.4 μmol L^{-1}) > [Na$^+$] (68.9 μmol L^{-1}) > [NO$_3^-$] (64.3 μmol L^{-1}) (**Supplementary Table 1**). In W3, the mean [Ca^{2+}], [Na$^+$], [NO$_3^-$], and [Cl$^-$] are higher, at 2,672, 81.9, 526, and 199 μmol L^{-1}, respectively. But [Mg^{2+}], [HCO$_3^-$], [SO$_4^{2-}$], and [K$^+$] are lower, at 653, 3,819, 1,114, and 33.0 μmol L^{-1},

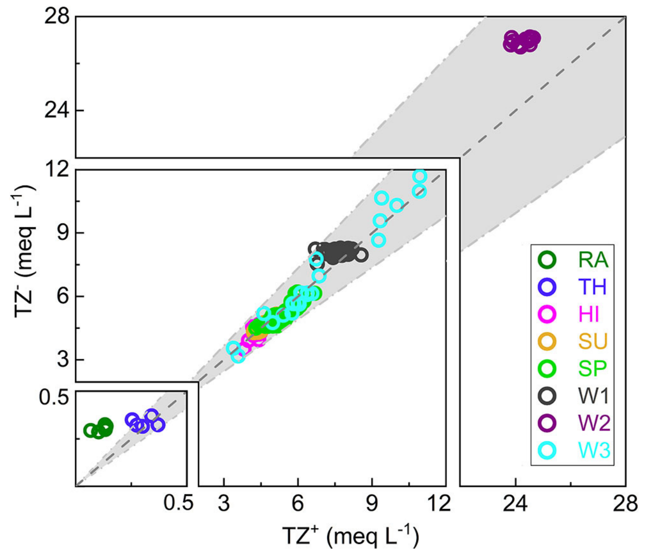

FIGURE 3 | The correlation between total cation charge ($TZ^+ = 2[Ca^{2+}] + 2[Mg^{2+}] + [Na^+] + [K^+]$) and total anion charge ($TZ^- = [HCO_3^-] + 2[SO_4^{2-}] + [NO_3^-] + [Cl^-]$). The light gray zone stands for that the net inorganic charge balance ($NICB = [TZ^+ - TZ^-] * 100/ [TZ^+ + TZ^-]$) is within ±10. RA, TH, HI, SU, and SP refer to rainwater, throughfall, hillslope runoff, surface water, and spring water, respectively. W1, W2, and W3 refer to three observation wells.

respectively. The water velocity of W2 flowing from the drain pipeline was almost unchanged. All ion concentrations in W2 are relatively stable at different depths or moments throughout the whole rainstorms, following the order of $[SO_4^{2-}]$ (11,560 μmol L^{-1}) $>[Ca^{2+}]$ (8,003 μmol L^{-1}) $>$ $[Mg^{2+}]$ (3,952 μmol L^{-1}) $>$ $[HCO_3^-]$ (3,766 μmol L^{-1}) $>$ $[Na^+]$ (262 μmol L^{-1}) $>$ $[K^+]$ (66.4 μmol L^{-1}) $>$ $[Cl^-]$ (39.6 μmol L^{-1}) $>$ $[NO_3^-]$ (10.3 μmol L^{-1}) (**Supplementary Table 1**).

DISCUSSIONS

Dynamic Responses of Surface Water and Groundwater to Rainstorms

Solute concentrations normally vary inversely with discharge, which can be well reflected by power-law function (Godsey et al., 2009; Musolff et al., 2015; Zimmer et al., 2019; Ackerer et al., 2020). To demonstrate relationships between concentrations and discharge, power-law function was adopted as follows:

$$C_i = aQ_i^b \tag{2}$$

where C_i and Q_i are instantaneous solute concentrations (C) and discharge (Q) at timestep i. The exponent "b" is an indicator reflecting the sensitivity of solute concentrations to discharge variation (Godsey et al., 2009). When $b = -1$, solute fluxes (the product of C and Q) equal the constant "a" and the dilution effect occurs; when b is near-zero, chemostatic behavior occurs; when $b > 0$, the flushing effect arises. In this study, the C-Q fitting curves generate "b" closer to 0 for HCO_3^-, Ca^{2+}, and Mg^{2+} than other ions (**Figure 5**), indicating that there are more supplementary inputs alleviating dilution of increasing discharge, resulting in stronger chemostatic response (Clow and Mast, 2010). Except NO_3^- and Na^+, other ions all exhibit weaker chemostatic behavior in SP than SU (**Figure 5**). This observation may be largely related to their initial concentrations at or before the beginning of rainstorms (low discharge). In this catchment, there is no flow in ground surface at no-rain days, but the discharge at the spring outlet occurs almost all the time.

During low-flow periods, most groundwater is retained in underground networks (Zhang et al., 2019) and has enough time to interact with carbonates, leading to the accumulation of solutes and products. At the early stage of rainstorms, rainwater infiltrates into epikarst initially and is intercepted in the aquifer (Williams, 2008), mixing with "old" water in soil or matrix. This process usually accompanies the dissolution of soil CO_2. As rainstorms go on, rainfall is enough to generate hillslope runoff and surface runoff, and "old" water is extruded and gradually replaced by the percolating "new" water. At this stage, the dominant pathway of underground flow is likely to change from matrix to conduit after saturating epikarst aquifer; the supplementary sources of solutes in spring can be quickly mobilized by the increasing discharge along pathways (Qin et al., 2020); the excess infiltration water would quickly pass through conduits and flow out at the outlet (Trček, 2007). This process can shorten the available time for both spring transportation and fluid-rock interaction (Tipper et al., 2006; Chen et al., 2018), generating differences on the transportation of both fluid and solutes (Bakalowicz, 2005; Bowes et al., 2005). Therefore, solute concentrations in SP decrease with increasing discharge and are gradually close to that in SU, and the effect of increasing discharge on solute concentrations is smaller in SU than SP. At the end of rainstorms, most available proximal sources near to or even within the flow pathways have been flushed. Hillslope runoff and surface runoff gradually decrease until they stop; spring runoff also decreases but normally maintains low discharge with slow velocity due to the recharge of matrix flow. Throughout the complete rainstorm, flow velocity, pathways, and the time for transportation and water-rock interaction all have been changing, leading to variations of sources and its contributions to solutes.

As highlighted by Thompson et al. (2011), the interpretation of $b \approx 0$ might be incomplete when the concentration variability is small. The ratio of CV of concentrations to CV of discharge (CV_C/CV_Q) is an alternative metric to statistically assess chemostatic behavior (Thompson et al., 2011; Musolff et al., 2015; Duncan et al., 2017; Zimmer et al., 2019), which could be calculated as follows:

$$\frac{CV_C}{CV_Q} = \frac{\mu_Q \sigma_C}{\mu_C \sigma_Q} \tag{3}$$

where μ and σ represent the mean and the standard deviation of concentrations (μ_C and σ_C) and discharge (μ_Q and σ_Q), respectively. The condition of $-0.2 < b < 0.2$ and $CV_C/CV_Q < 1$ is deemed a criterion of chemostatic behavior (Thompson et al., 2011; Zimmer et al., 2019). A $CV_C/CV_Q > 1$ indicates a relatively bigger variability in concentration than discharge,

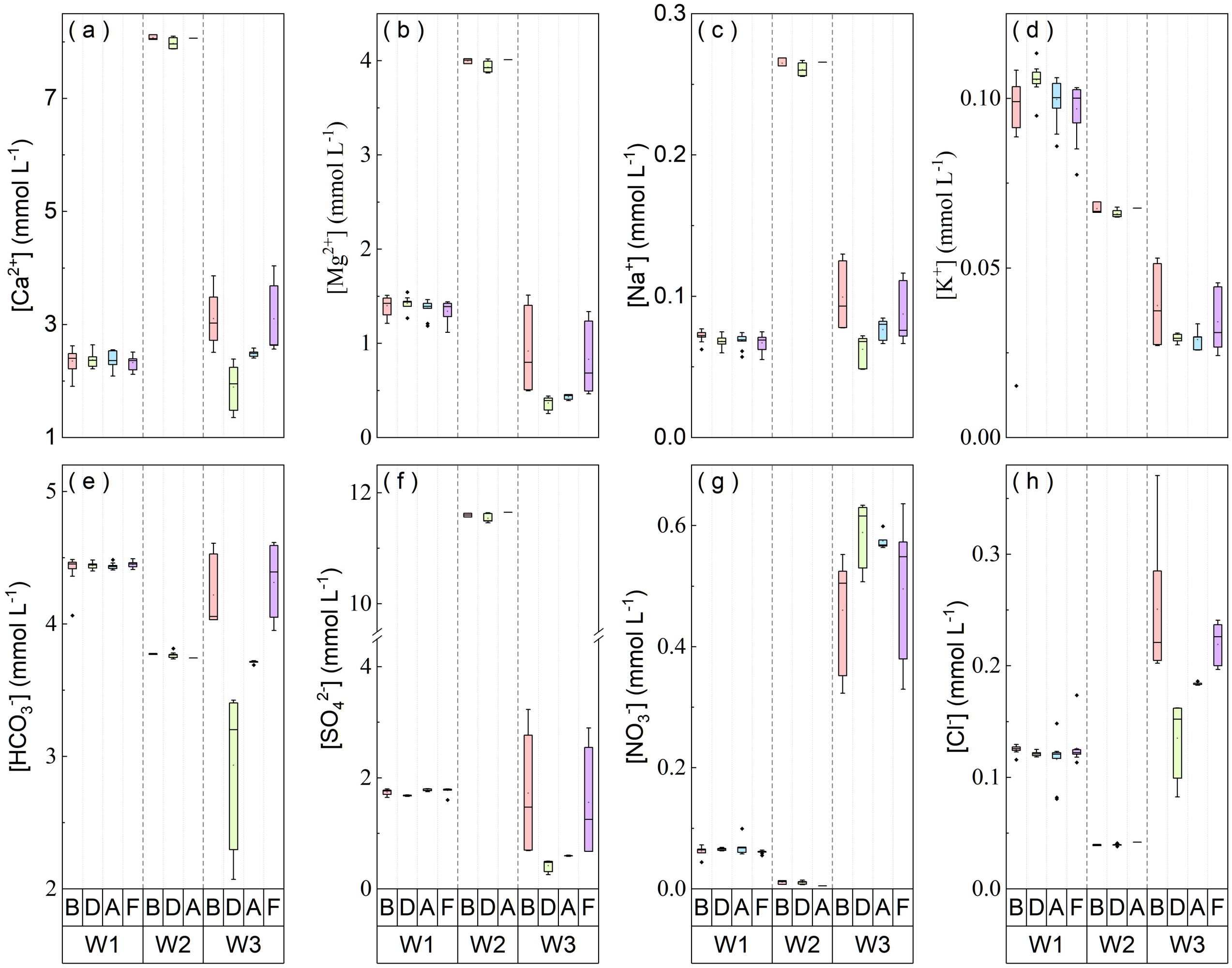

FIGURE 4 | The variation of ion concentrations in water collected from three observation wells before **(B)**, during **(D)**, after **(A)**, and on the fourth days **(F)** after the rainstorms. W1, W2, and W3 refer to three observation wells. Each box plot corresponds to an individual depth-profile.

which is usually referred to as "chemodynamic" (Musolff et al., 2015). According to the export regime classification system proposed by Musolff et al. (2015), plot of *b* vs. CV_C/CV_Q can be used to intuitively categorize and compare various solutes in catchment or between catchments (**Figure 6**). HCO_3^-, Ca^{2+}, and Mg^{2+} in both SU and SP have near-zero *b* values and low CV_C/CV_Q ratios ($<< 1$), indicating chemostatic behaviors. The three ions in Yu River (Liu J. et al., 2020) and Xijiang River (Zhong et al., 2018) display similar export regime with this study, but their chemostatic behaviors are relatively weaker. Conversely, there are scenes of $b > 0$ for the three ions in the Bode River of central Germany (Musolff et al., 2015) and Ca^{2+} in SU of Los Alamos (Koger et al., 2018), showing an enrichment trend. This phenomenon indicates their large potential supplements with increasing discharge. Other ions in this study display weaker chemostatic behavior, especially Na^+ and NO_3^- in SU and Na^+, SO_4^{2-} and NO_3^- in SP, implying that the pool of these ions is more susceptible to dilution, which is mainly due to their slower release or lower quantities along flowing pathways (Qin et al., 2020). SO_4^{2-} in SP is more sensitive to hydrological variation than that in SU. This is similar to the results from Los Alamos (Koger et al., 2018) and signifies that the potential sources of SO_4^{2-} in SP could be more quickly mobilized by increasing discharge. Overall, the dynamic response of hydrochemistry to rainstorms or climate change is largely controlled by regional hydrogeological properties (e.g., porosity, thickness, and hydraulic conductivity). It may differ between different conditions and needs to be analyzed using detailed local information. In this study, chemostatic is the predominant export regime of solutes in SU and SP.

During rainstorms, hydrochemistry in 3-wells respond differently to rainstorms, which is quicker in W3. This is mainly attributed to the higher permeability of epikarst around W3 (Chen et al., 2018). In the epikarst with better permeability, the relative proportion of vertical flow from infiltration replenishment increases and the lateral flow from "old" water

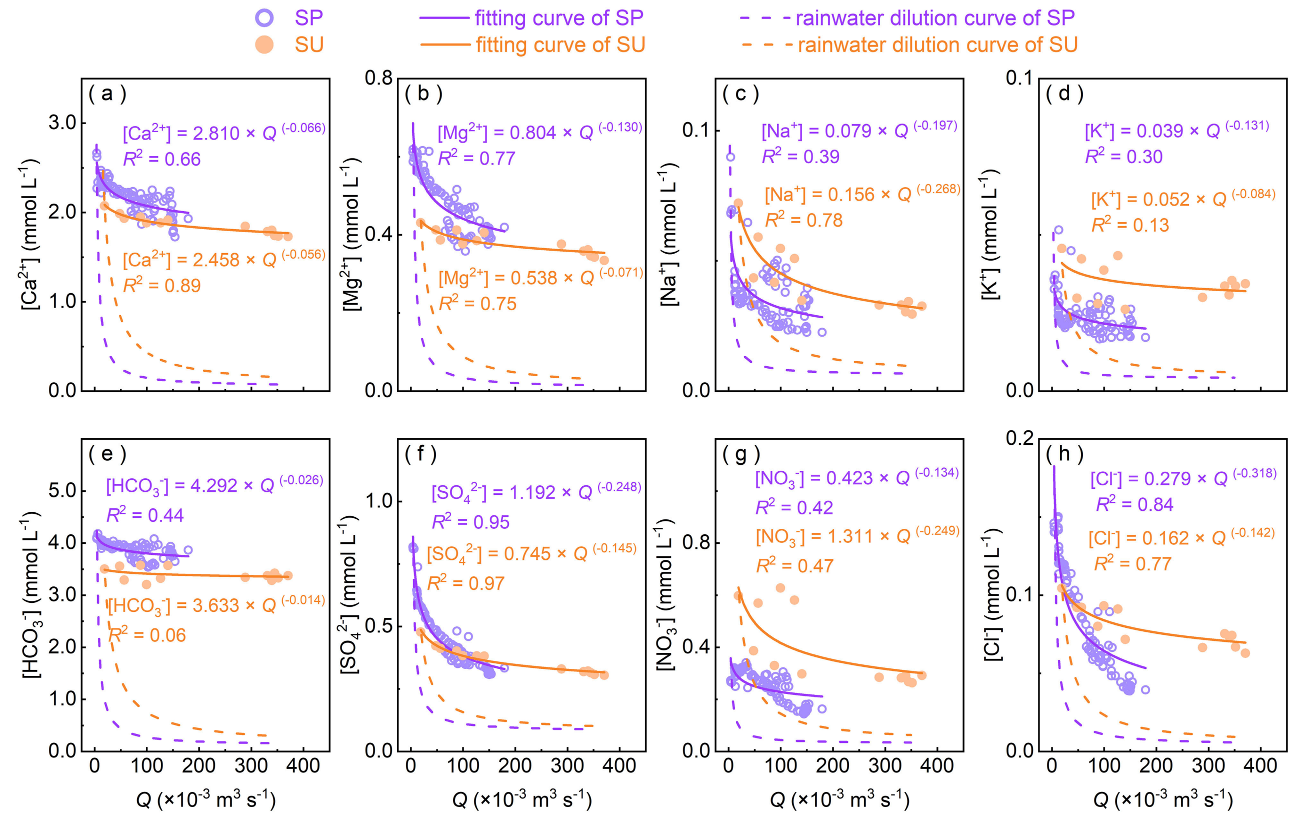

FIGURE 5 | Power-law relationships ($C = a\,Q^b$) between concentration (C) of major ions and discharge (Q). Rainwater dilution curves denote ideal conditions that ions are purely diluted by local rainwater. SU and SP refer to surface water and spring water, respectively.

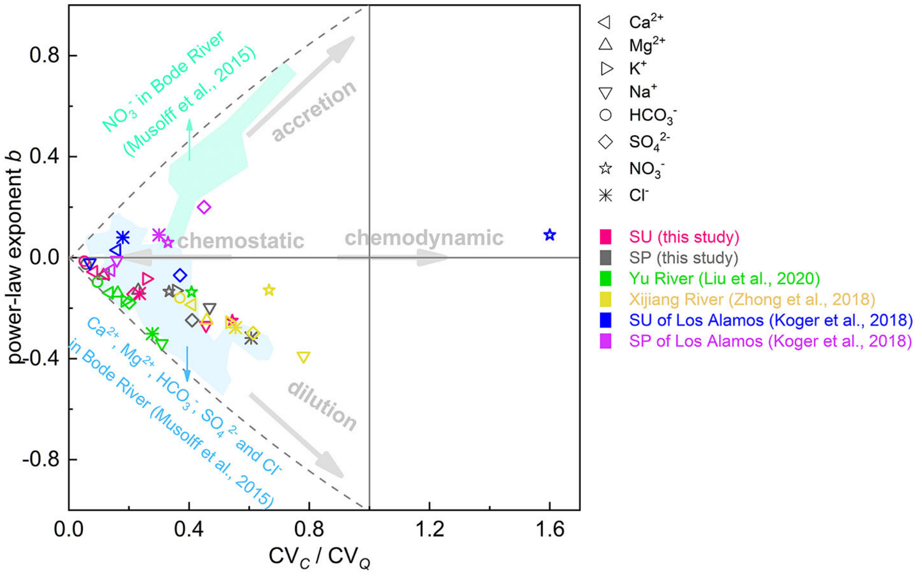

FIGURE 6 | Plot of b (the power-law exponent of $C=aQ^b$) vs. CV$_C$/CV$_Q$ (the ratio of CV of concentrations to CV of discharge) for ions in different catchments. SU and SP refer to surface water and spring water, respectively. The shadow areas classify corresponding zones of ions in Bode River catchment (Musolff et al., 2015).

is gradually extruded out with the ongoing rainstorms (Zhang et al., 2019). At the second sampling (D), large inputting water in W3 diluted solute concentrations, excluding [NO$_3^-$], which may be affected by fertilizer application and some biological processes (Yue et al., 2020). The highest CV of [HCO$_3^-$] in W3 at this time is possibly caused by the variation of dissolved soil

CO_2 and soil respiration during infiltration processes (Qin et al., 2020). At the third sampling (A), the relative ratio of vertical flow to lateral flow might remain constant or infiltration water might dominate discharge, leading to small profile variation for solute concentrations in W3. At the fourth sampling (F), water level and chemistries in W3 nearly restored to the situation before the rainstorms. The permeability of epikarst normally weakens with increasing depth (Ford and Williams, 2007). W2 is a deep confined well fed by groundwater draining a gypsum stratum and not susceptible to changes in external environment (e.g., occurrences of rainstorms and agricultural activities) (Qin et al., 2019). Therefore, its hydrological environment is stable with smaller [NO_3^-] and lower CV of most ions. [SO_4^-] in W2 is approximately an order of magnitude higher than that in other 2-wells; [Ca^{2+}] and [Mg^{2+}] are also higher. It is thus reasonable to deduce the existence of gypsum dissolution and gypsum-induced dedolomitization around W2. Overall, the heterogeneous permeability of epikarst can affect the mixture of groundwater from different sources and flowing pathways, eventually enabling hydrochemistry in groundwater at different hydrogeological

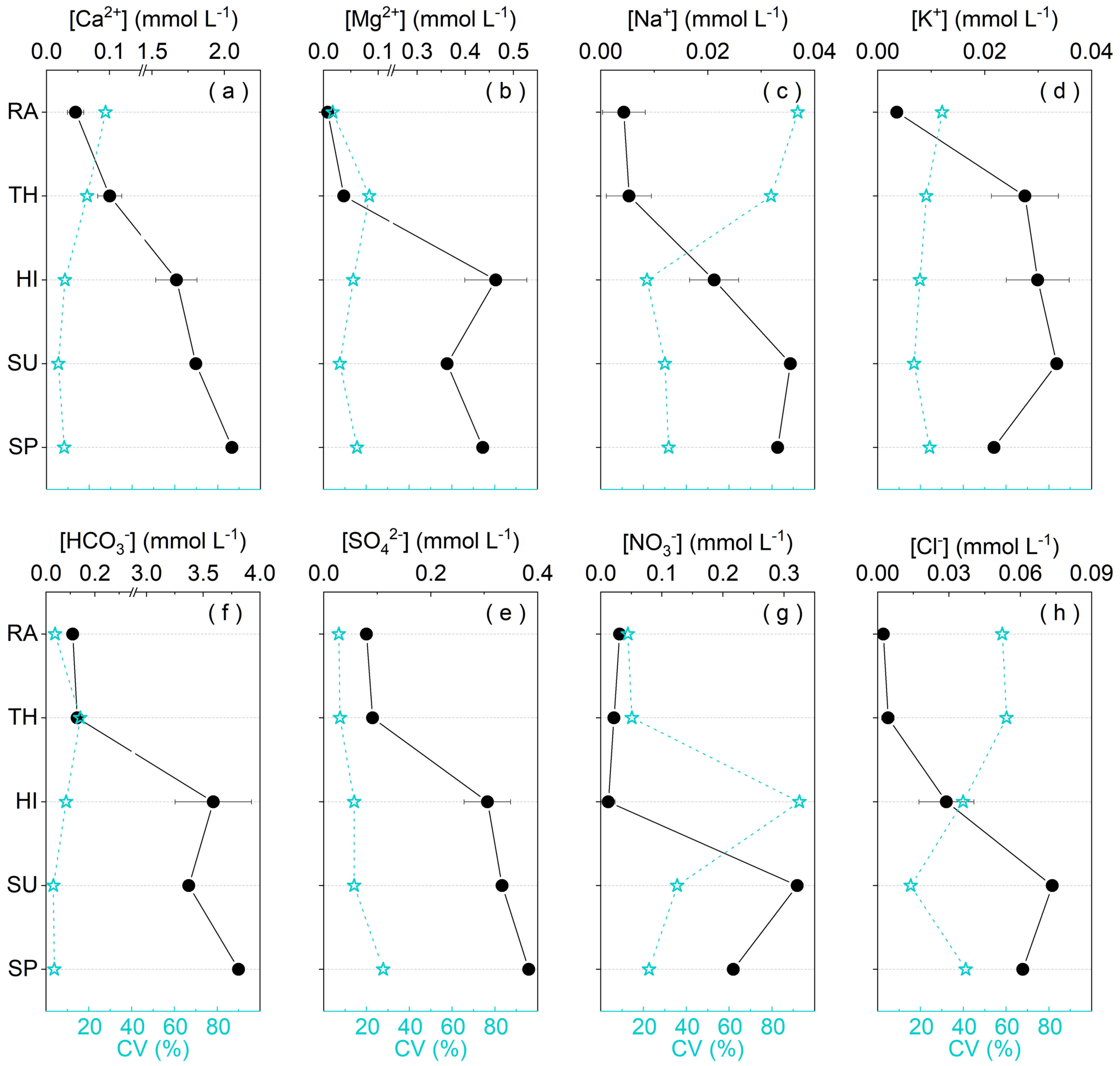

FIGURE 7 | The dynamic changes of ion concentrations among different spatial levels and corresponding CV during the rainstorms. In this figure, ion concentrations in rainwater (RA), throughfall (TH), and hillslope runoff (HI) are mean values with standard deviation. Discharge-weighted concentrations (DWC) are shown for surface water (SU) and spring (SP).

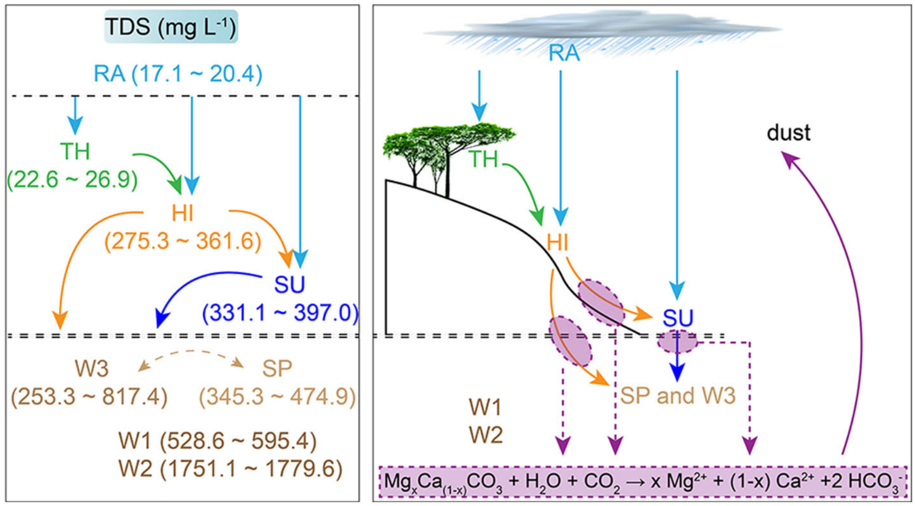

FIGURE 8 | Schematic diagram showing the possible transport processes of TDS and waters among different spatial levels.

conditions to display discrepant responses to rainstorms or discharge variations.

Dynamic Variations of Hydrochemistry Among Different Spatial Levels

The pH value of RA in this study is higher than that of other karst or forest regions in Southwest China, e.g., Guiyang of 4.5 (Han and Liu, 2006) and Chongqing of 4.75 (Ma et al., 2017), but it is lower than that of some areas in Northwestern China, e.g., Alxa Desert Plateau of 7.6 (Rao et al., 2017) and Urumqi River Valley of 7.0 (Zhao et al., 2008). This is most likely attributed to active carbon circulation and intense carbonate weathering within this karst depression (Qin et al., 2020). These processes can release some alkaline products (e.g., $CaCO_3$ and $MgCO_3$) into the atmosphere, neutralizing rainwater acidity (Tang and Han, 2019). $[SO_4^{2-}]$ and $[Ca^{2+}]$ in RA are much lower than that a decade ago (Wu et al., 2012), indicating that acid deposition has decreased after implementing environmental protection policies. This may also account for the higher pH in RA in this study than before. But $[SO_4^{2-}]$ and $[NO_3^-]$ in RA of this study are higher than that in Central Tibetan Plateau (Li et al., 2007), Eastern Tien Shan (Zhao et al., 2008), and Xisha Islands of South China Sea (Xiao et al., 2016), so there is still the possibility of anthropogenic emissions (NO_x, NH_3, and SO_x).

Migration processes of water among different spatial levels of Earth's Critical Zone can alter ion concentrations to different degrees (**Figure 7**). The variations of chemical compositions after passing through the vegetation canopy are mainly ascribed to (1) the adsorption of NO_3^- by vegetation (Polkowska et al., 2005); (2) the volatilization of HNO_3 after increasing its exposed area in vegetation surface; (3) the dissolution of $Ca^{2+}$and K^+ transported from roots to leaves through transpiration and respiration; and (4) the flushing of atmospheric particulates that contain ions (Ca^{2+}, Mg^{2+}, SO_4^{2-}, and K^+) and accumulate in vegetation surface during dry deposition. In karst regions, some weathering products could be released to ambient atmosphere with dust and pedogenesis processes (Lü et al., 2017). This possibly also affects $Ca^{2+}$and Mg^{2+} in RA and TH in this karst catchment, as demonstrated by **Supplementary Figure 2**. However, NH_4^+, one dominant ion in rainwater originating mainly from NH_3 emission of agricultural soil (Zeng et al., 2019), was not measured or considered when calculating TZ^+ and NICB in this study. This should be responsible for the imbalance of net inorganic charge. The better NICB in TH than in RA indirectly means that the vegetation canopy may intercept some NH_4^+ from RA. All these hydrochemical variations above are also the causes of the elevation of pH in TH relative to RA. Solutes in rivers are mostly derived from rock weathering, atmosphere, and anthropogenic inputs (Gaillardet et al., 1999; Qin et al., 2019). In this study, most solute concentrations in SU and SP are much higher than that in RA and TH (**Figure 7**), indicating little contributions of atmospheric sources compared with terrestrial sources. Carbonate weathering is one major source for this catchment (**Supplementary Figure 2**). $[Ca^{2+}]$, $[Mg^{2+}]$, and $[HCO_3^-]$ in HI are far higher than that in RA and TH but closer to that in SU and SP (**Figure 7**), indicating that the contribution of carbonate weathering and CO_2 dissolution may already exist when hillslope runoff occurs. Their relative contribution ratios are different from that generated during surface and underground processes, as illustrated in **Figure 8**. Additionally, $[Ca^{2+}]$, $[Mg^{2+}]$, and $[HCO_3^-]$ in SP are higher than that in SU (**Figure 7**). One possible explanation is that during the infiltration of flow through epikarst and the spring transportation within an underground conduit, there is dissolution of more soil CO_2 and intense carbonate weathering (Qin et al., 2020). In this agricultural karst depression, NO_3^- characterizes nitrification and owns large input from reductive nitrogen fertilizer and manure (Yue et al., 2020). Cl^- is deemed to have similar source area or transport pathways with NO_3^- (Qin et al., 2020). K^+ can also accumulate in soil surface after the application of potash fertilizer due to cation exchange and relative high contents in biomass (Boy et al., 2008). Therefore, NO_3^-, Cl^-, and K^+ all have potential

TABLE 1 | Varimax rotated component matrix for physic-chemical parameters in water at different spatial levels.

Parameters	PC1	PC2	PC3	PC4	Extraction
Ca^{2+}	0.992				0.709
Na^+	0.970				0.995
SO_4^{2-}	0.969				0.829
EC	0.963				0.909
Mg^{2+}	0.927				0.992
K^+		0.887			0.932
T		0.815			0.996
DO		−0.808			0.975
NO_3^-			0.885		0.906
Cl^-			0.854		0.915
pH				0.896	0.990
HCO_3^-				0.797	0.872
Eigenvalues	5.087	2.666	1.746	1.552	
Variance (%)	42.394	22.215	14.551	12.935	
Cumulative (%)	42.394	64.609	79.160	92.095	

Extraction method, principal component analysis; Rotation method, Varimax with Kaiser normalization. Here we only show loadings with high scores (>0.7).

agricultural sources and might be intercepted by epikarst during infiltration processes, leading to lower concentrations in SP than in SU (**Figure 7**). Overall, the difference of hydrochemistry among different water bodies is related to the double properties of agriculture and karst in this depression catchment.

In order to acquire descriptive statistics and explore interactive effects among physic-chemical parameters, principle component analysis (PCA) was performed with varimax rotation. The Kaiser-Meyer-Olkin (KMO) Measure of Sampling Adequacy and Bartlett's Test of Sphericity were conducted and generated a value of 0.738 with the significance of <0.001, indicating the suitability of the dataset for PCA. As shown in **Table 1**, there are four components (PC, eigenvalues >1), totally explaining 92.095% of the variation. PC1 explains 42.394% of the total variance and has high positive loading values (>0.9) of Ca^{2+}, Na^+, SO_4^{2-}, EC, and Mg^{2+}. This indicates that these parameters may follow an alike trend that is possibly due to same controls or sources areas or transit pathways. According to the common properties of these parameters, PC1 could be attributed to geological origins. This also indirectly reflects that EC is mainly controlled by Ca^{2+}, Mg^{2+}, and SO_4^{2-}. The main geological source of SO_4^{2-} is gypsum dissolution. PC2 can explain 18.56% of the total variance and includes two positive loadings (K^+ and T) and one negative loading (DO), indicating that temperature and dissolved oxygen may exert positive and negative influences on the eluviation of K^+, respectively. PC2 could be partially attributed to the influence of the mixing of soil and natural factors. NO_3^- and Cl^- are two positive loadings of PC3 that can explain 14.551% of the variance and is likely to denote agricultural contributions. Additionally, PC4 can only explain 12.935% variance by pH and HCO_3^-, and HCO_3^- owns a loading of <0.8. Because HCO_3^- is mostly contributed by soil CO_2 that is controlled by respiration and microbiologic activities (Qin et al., 2020), we conclude that PC4 is mainly contributed by biological sources.

Despite the differences of hydrochemical concentrations and controlling factors among different spatial levels, all waters show the dominance of HCO_3^- and Ca^{2+} in ions (except W2 draining a gypsum stratum) (**Supplementary Figure 3**), reflecting the characteristics of karst water. It is worth noting that Chenqi catchment has continual agricultural activities (e.g., fertilization and herding), so topsoil can store or accumulate NO_3^- and Cl^-. As a rainstorm occurs, water head of groundwater varies with hydrology, regulating nutrient exchange between matrix flow and conduit flow. Because the transportation from conduits to matrix is faster than that from matrix to conduits (Li et al., 2008), there is potential chronic pollution on karst groundwater in this agricultural catchment. Additionally, the accumulation of Ca^{2+} and Mg^{2+} in karst groundwater can elevate hardness of water. Both can deteriorate regional water quality during a certain period.

CONCLUSIONS

Rainwater, throughfall, hillslope runoff, surface water, spring, and well water at different hydrogeological conditions were collected synchronously during rainstorms to analyze the dynamic responses of hydrochemistry and its variation at different spatial levels at a karst Critical Zone Observatory (CZO), Southwest China. In this karst depression, pH and TDS in rainwater are 6.71 ± 0.03 and 18.6 ± 1.17 mg L^{-1}, respectively. After passing through the vegetation canopy, pH increases by 0.4, and most ion concentrations also have increments with different degrees (except $[NO_3^-]$ which decreases by 4.1–54.0%). Chemical compositions in rainwater and throughfall could be affected by both anthropogenic emission (NO_x, NH_3, and SO_x) and some weathering products (Ca^{2+} and Mg^{2+}) released to ambient atmosphere with dust. Wet deposition generally contributes little to hydrochemistry in surface water and groundwater. The influences of CO_2 dissolution and carbonate weathering on hydrochemistry already exist when hillslope runoff occurs, but their relative contribution ratios are different from that generated during surface and underground processes. Throughout the whole rainstorms, TDS in surface water and spring are 331–397 mg L^{-1} and 345–475 mg L^{-1}. Hydrochemistry in surface water and spring displays chemostatic responses with different intensities to discharge variations, possibly controlling by available sources and the difference between solute concentrations before and after rainstorms. Carbonate weathering contributes most to Ca^{2+} and Mg^{2+}, gypsum dissolution and gypsum-induced dedolomitization also regulate Ca^{2+}, Mg^{2+}, and SO_4^{2-} in deep confined well water draining a gypsum stratum. Soil CO_2 from respiration and microbiologic activities is one biological source of HCO_3^-. Agricultural activities are responsible for the chemostatic behavior of NO_3^-, Cl^-, and K^+, especially in surface water. All these were further demonstrated by principle component analysis (PCA). Epikarst aquifer with low permeability is insensitive to changes in external environment (e.g., occurrences of rainstorms and agricultural activities). High permeability can enhance the response of epikarst aquifer to hydrological variations, deteriorating regional water quality (potential chronic pollution of nitrogen and high hardness of water) during a certain period. Optimal measures of water protection are necessary in agricultural karst catchment.

DATA AVAILABILITY STATEMENT

The original contributions presented in the study are included in the article/**Supplementary Materials**, further inquiries can be directed to the corresponding author/s.

AUTHOR CONTRIBUTIONS

CQ, S-LL, HD, and F-JY designed the research objectives and interpreted the data and prepared the manuscript. CQ, Z-JW, and JZ carried out the field and laboratory work. All authors discussed the results and commented on the manuscript.

FUNDING

This study was jointly funded by the National Key R&D Program of China (grant number 2016YFA0601002) and the National Natural Science Foundation of China (grant numbers 41571130072 and 41861144026).

ACKNOWLEDGMENTS

We thank Susan Waldron and Xi Chen for their discussions and suggestions. We also thank Sen Xu, Yu-Chong Fu, teachers in Puding Karst Ecosystem Observation and Research Station for their help in sensor installation and data collection.

SUPPLEMENTARY MATERIAL

The Supplementary Material for this article can be found online at: https://www.frontiersin.org/articles/10.3389/frwa.2020.577511/full#supplementary-material

REFERENCES

Ackerer, J., Steefel, C., Liu, F., Bart, R., Safeeq, M., O'Geen, A., et al. (2020). Determining how critical zone structure constrains hydrogeochemical behavior of watersheds: learning from an elevation gradient in California's Sierra Nevada. *Front. Water* 2:23. doi: 10.3389/frwa.2020.00023

Bakalowicz, M. (2005). Karst groundwater: a challenge for new resources. *Hydrogeol. J.* 13, 148–160. doi: 10.1007/s10040-004-0402-9

Basu, N. B., Destouni, G., Jawitz, J. W., Thompson, S. E., Loukinova, N. V., Darracq, A., et al. (2010). Nutrient loads exported from managed catchments reveal emergent biogeochemical stationarity. *Geophys. Res. Lett.* 37:L23404. doi: 10.1029/2010GL045168

Beaulieu, E., Goddéris, Y., Donnadieu, Y., Labat, D., and Roelandt, C. (2012). High sensitivity of the continental-weathering carbon dioxide sink to future climate change. *Nat. Clim. Change* 2, 346–349. doi: 10.1038/nclimate1419

Bowes, M. J., House, W. A., Hodgkinson, R. A., and Leach, D. V. (2005). Phosphorus-discharge hysteresis during storm events along a river catchment: the River Swale, UK. *Water Res.* 39, 751–762. doi: 10.1016/j.watres.2004.11.027

Boy, J., Valarezo, C., and Wilcke, W. (2008). Water flow paths in soil control element exports in an Andean tropical montane forest. *Eur. J. Soil Sci.* 59, 1209–1227. doi: 10.1111/j.1365-2389.2008.01063.x

Chen, H. Y., Chen, B. Y., and Chen, B. (2005). Lithologic characteristics of Houzhai karst small valley, Puding, Guizhou Province. *Guizhou Geol.* 22, 284–288 (in Chinese).

Chen, X., Zhang, Z., Soulsby, C., Cheng, Q., Binley, A., Jiang, R., et al. (2018). Characterizing the heterogeneity of karst critical zone and its hydrological function: an integrated approach. *Hydrol. Process.* 32, 2932–2946. doi: 10.1002/hyp.13232

Cheng, Q., Chen, X., Tao, M., and Binley, A. (2019). Characterization of karst structures using quasi-3D electrical resistivity tomography. *Environ. Earth Sci.* 78:285. doi: 10.1007/s12665-019-8284-2

Clow, D. W., and Mast, M. A. (2010). Mechanisms for chemostatic behavior in catchments: Implications for CO_2 consumption by mineral weathering. *Chem. Geol.* 269, 40–51. doi: 10.1016/j.chemgeo.2009.09.014

Correa, A., Breuer, L., Crespo, P., Celleri, R., Feyen, J., Birkel, C., et al. (2019). Spatially distributed hydro-chemical data with temporally high-resolution is needed to adequately assess the hydrological functioning of headwater catchments. *Sci. Total Environ.* 651, 1613–1626. doi: 10.1016/j.scitotenv.2018.09.189

Duncan, J. M., Welty, C., Kemper, J. T., Groffman, P. M., and Band, L. E. (2017). Dynamics of nitrate concentration-discharge patterns in an urban watershed. *Water Resour. Res.* 53, 7349–7365. doi: 10.1002/2017WR020500

Ford, D., and Williams, P. (2007). *Karst Hydrogeology and Geomorphology*. Chichester: John Wiley & Sons.

Gabet, E. J., Edelman, R., and Langner, H. (2006). Hydrological controls on chemical weathering rates at the soil-bedrock interface. *Geology* 34, 1065–1068. doi: 10.1130/G23085A.1

Gaillardet, J., Dupre, B., Louvat, P., and Allegre, C. J. (1999). Global silicate weathering and CO_2 consumption rates deduced from the chemistry of large rivers. *Chem. Geol.* 159, 3–30. doi: 10.1016/S0009-2541(99)00031-5

Godsey, S. E., Kirchner, J. W., and Clow, D. W. (2009). Concentration-discharge relationships reflect chemostatic characteristics of US catchments. *Hydrol. Process.* 23, 1844–1864. doi: 10.1002/hyp.7315

Han, G., and Liu, C.-Q. (2004). Water geochemistry controlled by carbonate dissolution: a study of the river waters draining karst-dominated terrain, Guizhou Province, China. *Chem. Geol.* 204, 1–21. doi: 10.1016/j.chemgeo.2003.09.009

Han, G., and Liu, C. Q. (2006). Strontium isotope and major ion chemistry of the rainwaters from Guiyang, Guizhou Province, China. *Sci. Total Environ.* 364, 165–174. doi: 10.1016/j.scitotenv.2005.06.025

Kačaroglu, F. (1999). Review of groundwater pollution and protection in karst areas. *Water Air Soil Pollut.* 113, 337–356. doi: 10.1023/A:1005014532330

Koger, J. M., Newman, B. D., and Goering, T. J. (2018). Chemostatic behaviour of major ions and contaminants in a semiarid spring and stream system near Los Alamos, NM, USA. *Hydrol. Process.* 32, 1709–1716. doi: 10.1002/hyp.11624

Lang, Y.-C., Liu, C.-Q., Zhao, Z.-Q., Li, S.-L., and Han, G.-L. (2006). Geochemistry of surface and ground water in Guiyang, China: water/rock interaction and pollution in a karst hydrological system. *Appl. Geochem.* 21, 887–903. doi: 10.1016/j.apgeochem.2006.03.005

Li, C., Kang, S., Zhang, Q., and Kaspari, S. (2007). Major ionic composition of precipitation in the Nam Co region, Central Tibetan Plateau. *Atmos. Res.* 85, 351–360. doi: 10.1016/j.atmosres.2007.02.006

Li, G. Q., Loper, D. E., and Kung, R. (2008). Contaminant sequestration in karstic aquifers: experiments and quantification. *Water Resour. Res.* 44:W02429. doi: 10.1029/2006WR005797

Liu, J., Zhong, J., Ding, H., Yue, F. J., Li, C., Xu, S., et al. (2020). Hydrological regulation of chemical weathering and dissolved inorganic carbon biogeochemical processes in a monsoonal river. *Hydrol. Process.* 34, 2780–2792. doi: 10.1002/hyp.13763

Liu, M., Han, G., and Zhang, Q. (2020). Effects of agricultural abandonment on soil aggregation, soil organic carbon storage and stabilization: Results from observation in a small karst catchment, Southwest China. *Agric. Ecosyst. Environ.* 288:106719. doi: 10.1016/j.agee.2019.106719

Lü, P., Han, G., and Wu, Q. (2017). Chemical characteristics of rainwater in karst rural areas, Guizhou Province, Southwest China. *Acta Geochim.* 36, 572–576. doi: 10.1007/s11631-017-0238-3

Lu, X., Li, L. Y., Li, N., Yang, G., Luo, D., and Chen, J. (2011). Chemical characteristics of spring rainwater of Xi'an city, NW China. *Atmos. Environ.* 45, 5058–5063. doi: 10.1016/j.atmosenv.2011.06.026

Ma, M., Sun, T., Li, D. K., and Wang, D. Y. (2017). Dynamics of the water quality in a broad-leaf evergreen forest at different spatial levels on Jinyun mountain. *Environ. Sci.* 38, 5056–5062. doi: 10.13227/j.hjkx.201704208

Musolff, A., Schmidt, C., Selle, B., and Fleckenstein, J. H. (2015). Catchment controls on solute export. *Adv. Water Resourc.* 86, 133–146. doi: 10.1016/j.advwatres.2015.09.026

Piazza, G. A., Dupas, R., Gascuel-Odoux, C., Grimaldi, C., Pinheiro, A., and Kaufmann, V. (2018). Influence of hydroclimatic variations on solute concentration dynamics in nested subtropical catchments with heterogeneous landscapes. *Sci. Total Environ.* 635, 1091–1101. doi: 10.1016/j.scitotenv.2018.03.394

Polkowska, Z., Astel, A., Walna, B., Małek, S., Medrzycka, K., Górecki, T., et al. (2005). Chemometric analysis of rainwater and throughfall at several sites in Poland. *Atmos. Environ.* 39, 837–855. doi: 10.1016/j.atmosenv.2004.10.026

Qin, C., Li, S.-L., Waldron, S., Yue, F.-J., Wang, Z.-J., Zhong, J., et al. (2020). High-frequency monitoring reveals how hydrochemistry and dissolved carbon respond to rainstorms at a karstic critical zone, Southwestern China. *Sci. Total Environ.* 714:136833. doi: 10.1016/j.scitotenv.2020.136833

Qin, C., Li, S. L., Yue, F. J., Xu, S., and Ding, H. (2019). Spatiotemporal variations of dissolved inorganic carbon and controlling factors in a small karstic catchment, Southwestern China. *Earth Surf. Process. Landf.* 44, 2423–2436. doi: 10.1002/esp.4672

Rao, W., Han, G., Tan, H., Jin, K., Wang, S., and Chen, T. (2017). Chemical and Sr isotopic characteristics of rainwater on the Alxa Desert Plateau, North China: implication for air quality and ion sources. *Atmos. Res.* 193, 163–172. doi: 10.1016/j.atmosres.2017.04.007

Tang, Y., and Han, G. (2019). Seasonal variation and quality assessment of the major and trace elements of atmospheric dust in a typical karst city, Southwest China. *Int. J. Environ. Res. Public Health* 16:325. doi: 10.3390/ijerph16030325

Thompson, S. E., Basu, N. B., Lascurain, J. Jr., Aubeneau, A., and Rao, P. S. C. (2011). Relative dominance of hydrologic versus biogeochemical factors on solute export across impact gradients. *Water Resour. Res.* 47:WOOJ05. doi: 10.1029/2010WR009605

Tipper, E. T., Bickle, M. J., Galy, A., West, A. J., Pomies, C., and Chapman, H. J. (2006). The short term climatic sensitivity of carbonate and silicate weathering fluxes: insight from seasonal variations in river chemistry. *Geochim. Cosmochim. Acta* 70, 2737–2754. doi: 10.1016/j.gca.2006.03.005

Trček, B. (2007). How can the epikarst zone influence the karst aquifer hydraulic behaviour? *Environ. Geol.* 51, 761–765. doi: 10.1007/s00254-006-0387-x

Williams, P. W. (2008). The role of the epikarst in karst and cave hydrogeology: a review. *Int. J. Speleol.* 37, 1–10. doi: 10.5038/1827-806X.37.1.1

Wu, Q., Han, G., Tao, F., and Tang, Y. (2012). Chemical composition of rainwater in a karstic agricultural area, Southwest China: the impact of urbanization. *Atmos. Res.* 111, 71–78. doi: 10.1016/j.atmosres.2012.03.002

Xiao, H., Xiao, H., Zhang, Z., Wang, Y., Long, A., and Liu, C. (2016). Chemical characteristics and source apportionment of atmospheric precipitation in Yongxing Island. *China Environ. Sci.* 36, 3237–3244 (in Chinese).

Yuan, D., and Cai, G. (1988). *The Science of Karst Environment*. Chongqing: Chongqing Publishers. p. 1–332 (in Chinese).

Yuan, D., and Zhang, C. (2008). Karst dynamics theory in China and its practice. *Acta Geosci. Sin.* 29, 355–365 (in Chinese).

Yue, F. J., Li, S. L., Waldron, S., Wang, Z. J., Oliver, D. M., Chen, X., et al. (2020). Rainfall and conduit drainage combine to accelerate nitrate loss from a karst agroecosystem: Insights from stable isotope tracing and high-frequency nitrate sensing. *Water Res.* 186:116388. doi: 10.1016/j.watres.2020.116388

Zeng, J., Yue, F.-J., Wang, Z.-J., Wu, Q., Qin, C.-Q., and Li, S.-L. (2019). Quantifying depression trapping effect on rainwater chemical composition during the rainy season in karst agricultural area, southwestern China. *Atmos. Environ.* 218:116998. doi: 10.1016/j.atmosenv.2019.116998

Zhang, X., Jiang, H., Zhang, Q., and Zhang, X. (2012). Chemical characteristics of rainwater in northeast China, a case study of Dalian. *Atmos. Res.* 116, 151–160. doi: 10.1016/j.atmosres.2012.03.014

Zhang, Z., Chen, X., Cheng, Q., and Soulsby, C. (2019). Storage dynamics, hydrological connectivity and flux ages in a karst catchment: conceptual modelling using stable isotopes. *Hydrol. Earth Syst. Sci.* 23, 51–71. doi: 10.5194/hess-23-51-2019

Zhao, D., and Seip, H. M. (1991). Assessing effects of acid deposition in Southwestern China using the magic model. *Water Air Soil Pollut.* 60, 83–97. doi: 10.1007/BF00293967

Zhao, Z., Tian, L., Fischer, E., Li, Z., and Jiao, K. (2008). Study of chemical composition of precipitation at an alpine site and a rural site in the Urumqi River Valley, Eastern Tien Shan, China. *Atmos. Environ.* 42, 8934–8942. doi: 10.1016/j.atmosenv.2008.08.003

Zhong, J., Li, S. L., Ibarra, D. E., Ding, H., and Liu, C. Q. (2020). Solute production and transport processes in Chinese monsoonal rivers: implications for global climate change. *Global Biogeochem. Cycles* 34:e2020GB006541. doi: 10.1029/2020GB006541

Zhong, J., Li, S. L., Liu, J., Ding, H., Sun, X. L., Xu, S., et al. (2018). Climate variability controls on CO_2 consumption fluxes and carbon dynamics for monsoonal rivers: evidence from Xijiang river, Southwest China. *J. Geophys. Rese. Biogeosci.* 123, 2553–2567. doi: 10.1029/2018JG004439

Zhou, X., Xu, Z., Liu, W., Wu, Y., Zhao, T., Jiang, H., et al. (2019). Chemical composition of precipitation in Shenzhen, a coastal mega-city in South China: influence of urbanization and anthropogenic activities on acidity and ionic composition. *Sci. Total Environ.* 662, 218–226. doi: 10.1016/j.scitotenv.2019.01.096

Zimmer, M. A., Pellerin, B., Burns, D. A., and Petrochenkov, G. (2019). Temporal variability in nitrate-discharge relationships in large rivers as revealed by high-frequency data. *Water Resour. Res.* 55, 973–989. doi: 10.1029/2018WR023478

Conflict of Interest: The authors declare that the research was conducted in the absence of any commercial or financial relationships that could be construed as a potential conflict of interest.

frontiers in Water

ORIGINAL RESEARCH
published: 11 December 2020
doi: 10.3389/frwa.2020.600409

Groundwater–Stream Connectivity Mediates Metal(loid) Geochemistry in the Hyporheic Zone of Streams Impacted by Historic Mining and Acid Rock Drainage

Beth Hoagland[1]*, *Alexis Navarre-Sitchler*[1], *Rory Cowie*[2] and *Kamini Singha*[1]

[1] Department of Geology and Geological Engineering, Colorado School of Mines, Golden, CO, United States, [2] Alpine Water Resources, Limited Liability Company (LLC), Silverton, CO, United States

OPEN ACCESS

Edited by:
Dipankar Dwivedi,
Lawrence Berkeley National Laboratory, United States

Reviewed by:
Alessandra Marzadri,
University of Trento, Italy
Alberto Bellin,
University of Trento, Italy

***Correspondence:**
Beth Hoagland
hoagland@mines.edu

Specialty section:
This article was submitted to Water and Critical Zone, a section of the journal Frontiers in Water

Received: *29 August 2020*
Accepted: *29 October 2020*
Published: *11 December 2020*

Citation:
Hoagland B, Navarre-Sitchler A, Cowie R and Singha K (2020) Groundwater–Stream Connectivity Mediates Metal(loid) Geochemistry in the Hyporheic Zone of Streams Impacted by Historic Mining and Acid Rock Drainage. Front. Water 2:600409. doi: 10.3389/frwa.2020.600409

High concentrations of trace metal(loid)s exported from abandoned mine wastes and acid rock drainage pose a risk to the health of aquatic ecosystems. To determine if and when the hyporheic zone mediates metal(loid) export, we investigated the relationship between streamflow, groundwater–stream connectivity, and subsurface metal(loid) concentrations in two ∼1-km stream reaches within the Bonita Peak Mining District, a US Environmental Protection Agency Superfund site located near Silverton, Colorado, USA. The hyporheic zones of reaches in two streams—Mineral Creek and Cement Creek—were characterized using a combination of salt-tracer injection tests, transient-storage modeling, and geochemical sampling of the shallow streambed (<0.7 m). Based on these data, we present two conceptual models for subsurface metal(loid) behavior in the hyporheic zones, including (1) well-connected systems characterized by strong hyporheic mixing of infiltrating stream water and upwelling groundwater and (2) poorly connected systems delineated by physical barriers that limit hyporheic mixing. The comparatively large hyporheic zone and high hydraulic conductivities of Mineral Creek created a connected stream–groundwater system, where mixing of oxygen-rich stream water and metal-rich groundwater facilitated the precipitation of metal colloids in the shallow subsurface. In Cement Creek, the precipitation of iron oxides at depth (∼0.4 m) created a low-hydraulic-conductivity barrier between surface water and groundwater. Cemented iron oxides were an important regulator of metal(loid) concentrations in this poorly connected stream–groundwater system due to the formation of strong redox gradients induced by a relatively small hyporheic zone and high fluid residence times. A comparison of conceptual models to stream concentration–discharge relationships exhibited a clear link between geochemical processes occurring within the hyporheic zone of the well-connected system and export of particulate Al, Cu, Fe, and Mn, while the poorly connected system did not have a notable influence on metal concentration–discharge trends. Mineral Creek is an example of a hyporheic system that serves as a natural dissolved metal(loid) sink, whereas poorly connected systems such as Cement Creek may require a combination of subsurface remediation of sediments and mitigation of upstream, iron-rich mine drainages to reduce metal export.

Keywords: hyporheic zone, metal(loid)s, acid rock drainage (ARD), concentration-discharge (C-Q) relationships, tracer test experiments, Bonita Peak Mining District

INTRODUCTION

Over 64,000 inactive metal mines persist in the United States and contribute high metal loads to streams and groundwater, damaging aquatic ecosystems (Nordstrom, 2011; Hudson-Edwards, 2016; Horton and San Juan, 2020). In watersheds impacted by historic mining activity, chemical weathering of minerals containing high metal content can occur at rates three times as fast as natural weathering rates (Alpers et al., 2007). Some of these metal(loid)s, such as arsenic (As), copper (Cu), and manganese (Mn), are commonly found in high concentrations downstream of hard-rock mines. They pose a well-documented risk to human and aquatic health (Smedley and Kinniburgh, 2002), and their toxicity and concentration are highly sensitive to changes in pH and redox conditions of streams and groundwater (Smedley and Kinniburgh, 2002; Borch et al., 2010). Mixing of oxic stream water and sub-oxic, shallow groundwater within the hyporheic zone can rapidly change the geochemical conditions of the shallow subsurface over space and time (e.g., Bencala, 2011; Boano et al., 2014). Unlike the fate of organic carbon or nutrients, which are the focus of many hyporheic studies to date, the behavior of metal(loid)s in mine-impacted hyporheic zones are complicated by reactions with sediments, such as sorption/desorption (Harvey and Fuller, 1998), storage *via* complexation with organic matter (Findlay et al., 2003), surface redox chemistry, or (co)precipitation/dissolution reactions. Furthermore, redox gradients that form as a result of fluid exchange across the groundwater–surface water boundary (Kasahara and Hill, 2007) are often facilitated by diverse microbial metabolisms and can control the fate and form of nutrients (Findlay et al., 2003; Fischer et al., 2005). However, the role of groundwater–surface water connectivity in mediating the toxicity and mobility of redox-sensitive metal(loid)s is not well-quantified and could have important implications for our estimates of metal fluxes from mine-impacted watersheds (Gandy et al., 2007).

Hydrological parameters such as permeability, transient storage zone area, fluid exchange rate, and residence time influence hyporheic zone characteristics (e.g., Miller et al., 2006; Boano et al., 2014). These parameters vary seasonally as a function of changing temperature (Weber et al., 2010), discharge (Wondzell, 2006), and microbial processes (Saup et al., 2019). Seasonal changes in stream discharge and subsurface saturation may, in turn, affect the kinetics of metal(loid) release from the hyporheic zone, given that abiotic and biotic process rates are hypothesized to be inherently different in areas characterized by variable fluid saturation and redox chemistry compared to permanently oxic or anoxic environments (Borch et al., 2010). In an abandoned mine system, for example, the delivery of As *via* groundwater and the residence time of As in the hyporheic zone were greater in the summer and led to the saturation of sediment sorption sites and a resulting decrease in As storage (Brown et al., 2007). Similarly, seasonal fluctuations in discharge and groundwater levels in marine and estuarine environments influenced the speciation of metal(loid)s *via* interactions with sediments such as sorption, complexation, and precipitation (Howard et al., 1995; Fattorini et al., 2008). These previous studies suggest an important link between streamflow, hyporheic area and mass transfer rates, and metal(loid) redox chemistry.

In addition to the influence of streamflow on the physical and geochemical conditions of the hyporheic zone, previous studies have highlighted that streambed characteristics and mixing conditions within the hyporheic zone regulate microbial community composition (e.g., Feris et al., 2004; Danczak et al., 2016; Nelson et al., 2019) and trace metal concentrations (e.g., Benner et al., 1995; Harvey and Fuller, 1998; Nagorski and Moore, 1999; Gandy et al., 2007). Systems such as the East River near Crested Butte, CO, USA, where highly permeable, gravel-dominated streambed sediments control groundwater–stream mixing, were characterized by high levels of dissolved oxygen at depth, microbial homogenization, and seasonal variability in metal concentrations in the shallow subsurface (Nelson et al., 2019; Saup et al., 2019). Furthermore, increased mixing depth and supply of dissolved organic carbon caused respiration of Mn-oxides in the East River during spring snowmelt, whereas a small and well-oxygenated hyporheic zone caused Mn-oxide accumulation during baseflow conditions (Bryant et al., 2020). In contrast, the Colorado River near Rifle, CO, USA, had fine sediments and a low influx of surface water into the hyporheic zone, which reduced mixing, promoted redox stratification, and created a unique hyporheic microbiome (Danczak et al., 2016; Nelson et al., 2019). Given the potential influence of hyporheic zone connectivity on microbial processes and sediment–water interactions, we hypothesized that the degree of groundwater–surface water connection will influence whether the hyporheic zone serves as a source or sink of trace metal(loid)s.

The behavior of solutes in the hyporheic zone can be reflected at the reach or catchment scale in how solute concentrations respond to changes in streamflow, also known as concentration–discharge (CQ) relationships, yet few studies directly link hyporheic processes to stream export of major ions (Hoagland et al., 2017; Singley et al., 2017) and even fewer investigate hyporheic influences on trace metal export. Specific to trace metals, Sherrell and Ross (1999) linked metal(loid)–Q relationships to changing flow-path contributions to the stream, where anthropogenic sources of metals were accessed at high flow and in-stream processes aided metal removal at low flow. In other catchments, a link between metal concentrations and stream discharge was difficult to identify (Nagorski et al., 2003), or metal–discharge relationships were attributed to the formation of inorganic colloids (Trostle et al., 2016). These previous studies suggest that in-stream chemical dynamics, including processes occurring in the hyporheic zone, may mediate the response of trace metal(loid)s to stream discharge and overall metal(loid) export from disturbed watersheds.

The headwaters of the Animas River in southwestern Colorado are an ideal location to study the relationship between stream–groundwater connectivity, metal(loid) export, and stream discharge. This site is home to ∼1,500 abandoned gold and silver mines (Buxton et al., 1997) and the site of the Bonita Peak Mining District, a US Environmental Protection Agency (EPA) Superfund site (**Figure 1**). The primary purpose of the Superfund site is to investigate the potential impacts of contaminated soil, groundwater, and surface waters on aquatic and human health. Bedrock weathering and abandoned mine adits contribute diffuse subsurface and surface flows of metal-laden waters to the Animas River headwaters and have led to the development of several water sources with elevated metal concentrations (Guerard et al., 2004). The headwaters of the Animas River gained publicity in August 2015 when an accidental breach of a tunnel connected to the legacy Gold King Mine led to the release of ∼11 million liters of acidic mine drainage into surface waters that persisted as far as San Juan River in New Mexico (∼200 km downstream) (Rodriguez-Freire et al., 2016). Dissolved metals associated with the Gold King Mine spill were hypothesized to have rapidly immobilized in the headwaters *via* adsorption onto streambed sediments and precipitation of Fe-oxyhydroxide minerals (Rodriguez-Freire et al., 2016; Saup et al., 2017). Although the Gold King Mine spill contributed a slug of metals to the system over a short period of time, numerous historic mines or mining-related sources contribute diffuse loads upwards of 20.4 million liters per day to the Animas River headwaters (USEPA, 2016). Furthermore, the three streams that comprise the headwaters—Cement Creek, Mineral Creek, and the Upper Animas River—exhibit wide seasonal variations in streamflow and pH. For example, pH and discharge (Q) measurements in 2019 at the US Geological Survey monitoring stations (sites 09358550 and 09359019) ranged from winter lows of pH ∼3.5 and Q ∼0.3 m^3 s^{-1} to summer highs of pH ∼6.4 and Q ∼14.8 m^3 s^{-1} in Cement Creek, whereas pH ranged from winter lows of pH 4.8 and Q ∼0.4 m^3 s^{-1} to summer highs of pH 7.4 and Q ∼33.7 m^3 s^{-1} in Mineral Creek (USGS, 2020).

The goal of this study was to understand how stream–hyporheic–groundwater connectivity influences dissolved metal(loid) concentrations and mobilization in streams impacted by mining activities. To address this goal, we investigated two reaches in the Bonita Peak Mining District downstream of redox-sensitive metal(loid) sources: (a) Cement Creek, a low-pH system with extensive ferricrete formation, located downstream of the Gold King Mine, and (b) Mineral Creek, a circumneutral pH stream without ferricrete precipitates, located downstream of the Koehler Tunnel (**Figure 1C**). At both sites, we conducted salt-tracer injection tests at high and at low flow, collected seasonal water samples, and compiled historical sediment and water data to constrain the timing of metal(loid) release or storage in the hyporheic zone.

METHODS

Hydrogeologic Setting and Site Selection

The headwaters of the Animas River, located in the San Juan Mountains of southwestern Colorado, USA, are characterized by a complex geologic and mining history. The three tributaries that comprise the headwaters—Cement Creek, Mineral Creek, and the Upper Animas River—connect south of Silverton, Colorado, to form the Animas River (**Figure 1B**), which serves as a primary drinking and agricultural water source for communities in southwestern Colorado, northern New Mexico, and southeastern Utah. The tributaries and town of Silverton lie almost completely within the Silverton caldera and are underlain by highly mineralized and faulted terrain that formed as a result of volcanotectonic and hydrothermal alteration events that occurred from 35 to 10 Ma (Yager and Bove, 2007). Metal-rich sulfide minerals formed during the mid- to late-Tertiary supported a gold and silver mining industry in this region beginning in the late 1800's and lasting for over a century (Yager and Bove, 2007). The history of mining in combination with natural sulfide weathering has led to low-pH and Fe-rich groundwater and streams in the Animas River headwaters (e.g., Guerard et al., 2004).

Given the complex terrain and geology of the Animas headwater catchments, careful consideration was taken when choosing stream reaches of interest. Based on historical data collected by the US Geological Survey and the Animas River Stakeholders Group, we identified a ∼1.2-km stream reach in Mineral Creek and a ∼1.8-km stream reach in Cement Creek located downstream of trace metal sources (**Figure 1C**). Mine drainage with elevated concentrations of metal(loid)s, such as arsenic, aluminum, copper, manganese, and zinc, discharges from Koehler Tunnel at the headwaters of Mineral Creek and from the Henrietta, Joe and John, and Lark Mines into the headwaters of Prospect Gulch, which eventually drains into Cement Creek (**Figure 1C**). Other major contributors of metals to Cement Creek include the Natalie/Occidental Mine, the American Tunnel, the Red and Bonita Mine, and the Mogul Mine (**Figure 1C**), all of which are mines prioritized by the EPA Superfund site. In addition to their location downstream of mine drainages, we selected reaches with the same stream gradient (∼0.03 km/km) to control for potential effects of stream gradient on hyporheic exchange flows (e.g., Hester and Doyle, 2008) and with similar drainage areas (24.6 and 23.1 km^2 for Cement Creek and Mineral Creek reaches, respectively). Furthermore, the topographical divide Mineral Creek and Cement Creek constitutes the southern lobe of the Red Mountain acid–sulfate alteration system, which contains silver, lead, and copper mined from breccia-pipe chimney deposits (Bove et al., 2007). Both sites

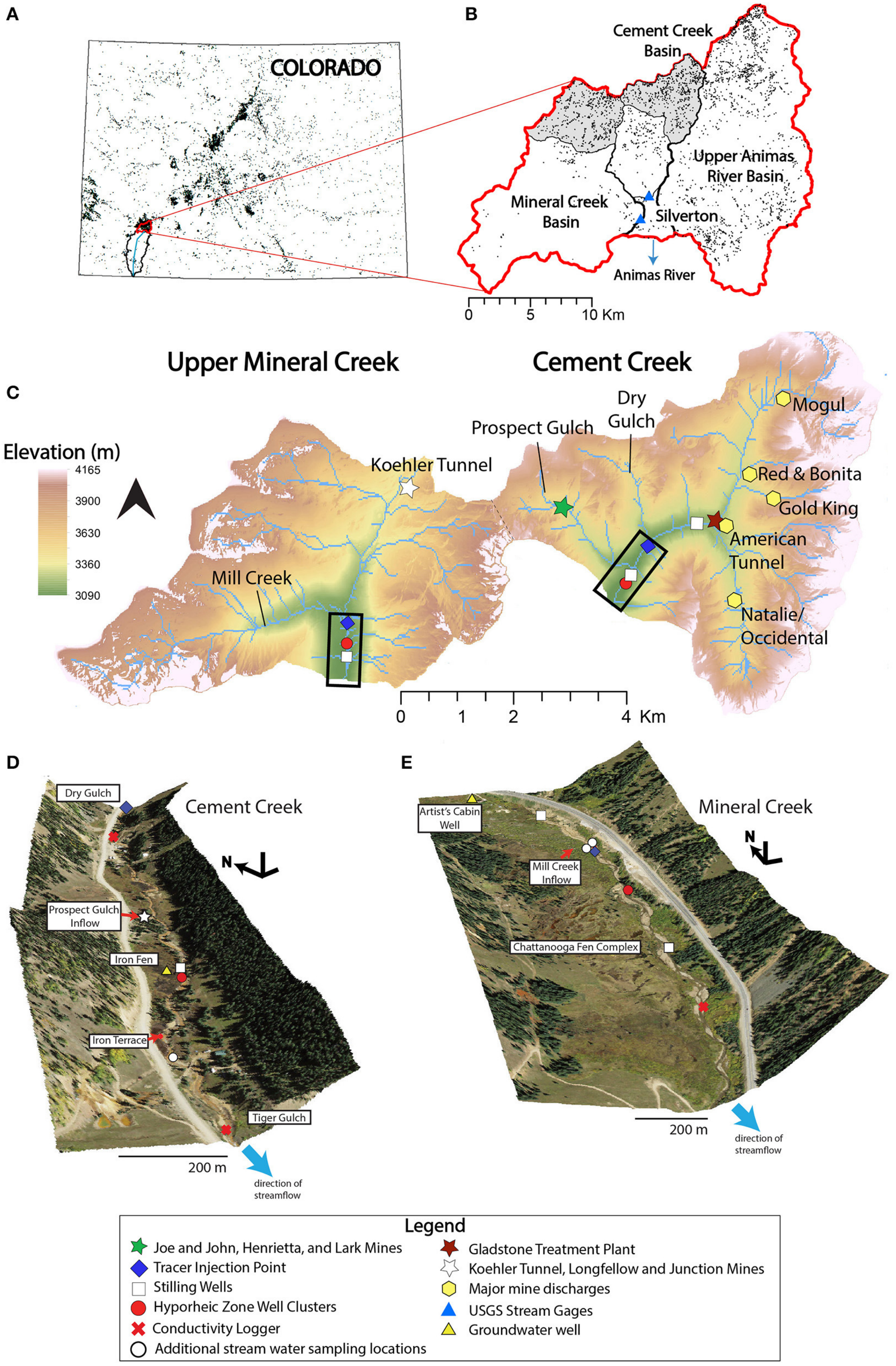

FIGURE 1 | The upper Mineral Creek and Cement Creek study areas are located at **(A)** the headwaters of the Animas River watershed in **(B)** the Bonita Peak Mining District north of Silverton, in the San Juan Mountains of southwestern Colorado. The study areas and the locations of the redox-sensitive metal sources are

(Continued)

FIGURE 1 | highlighted in **(C)** and denoted in **(B)** by the gray-shaded regions within the greater Cement Creek and Mineral Creek basins. Black points on subplots **(A,B)** represent all mine-related features in the state of Colorado and the Animas River headwaters (Horton and San Juan, 2020). The tracer study reaches are outlined by black boxes and are located downstream of trace metal(loid) sources at the headwaters of Mineral Creek and the headwater of the Prospect Gulch tributary. The blue triangles in **(B,D)** represent stream gages managed by the US Geological Survey at Cement Creek (Gage #09358550) and Mineral Creek (Gage #09359010). The white circles in **(D,E)** represent additional stream water sampling sites. Detailed views of the tracer test reaches [as outlined by the black boxes in **(C)**] are highlighted for **(D)** Cement Creek at Prospect Gulch and **(E)** Mineral Creek at Chattanooga Fen and presented at a 65° viewing angle. Elevation above mean sea level is mapped for **(C)** using the Shuttle Radar Topography Mission 30-m digital elevation model. Aerial imagery for **(D,E)** is from the USDA National Agriculture Imagery Program dated September 20, 2017.

contain iron-rich groundwater wetlands, or iron fens (Chimner et al., 2010), along the banks.

The Mineral Creek stream reach is located within the 0.07-km^2 Chattanooga fen complex (**Figure 1E**) and will be referred to as the "MC-Fen" site throughout the remainder of the text. The MC-Fen is a rare and sensitive ecosystem characterized by low pH (∼3.4), high dissolved Fe concentrations, and unique vegetation including *Sphagnum* mosses, *Carex* sedges, and bog birch (Chimner et al., 2010). By definition, fens are groundwater-fed wetlands, and the iron fens in the Silverton area predate mining activity by thousands of years (Chimner et al., 2010). The water table in the fen is shallow, fluctuating between 0 and 40 cm below ground level (bgl) (Chimner et al., 2010). The MC-Fen is located ∼2.8 km downstream of the first trace metal(loid) source, which includes two draining abandoned mines, Koehler Tunnel and Junction Mine, and one abandoned dry mine, Longfellow Mine (**Figure 1**). Prior to remediation efforts in the early 2000's, flows from the Koehler Tunnel constituted nearly 50% of flow entering the head of the stream and contained elevated concentrations of copper, lead, zinc, and arsenic (Runkel and Kimball, 2002; Walton-Day et al., 2007; Runkel et al., 2009b). In 2003, a bulkhead was installed in the Koehler Tunnel, reducing surface drainage from 11.7 to <0.3 L/s (Runkel et al., 2009a). Although these efforts significantly reduced metal loads, the Koehler Tunnel and Junction Mine and the Longfellow Mine have been identified by the Bonita Peak Mining District Superfund as primary sources of mining-related contamination to the watershed, where waste rock samples exceeded the human health risk-based level for arsenic (Smith, 2018).

The second trace metal(loid) source includes several abandoned mines, including the Henrietta Mine, Joe and John Mine, and Lark Mine, located at the head of the Prospect Gulch tributary, which flows into Cement Creek. The Gladstone Treatment Plant, managed by the US EPA and located at the upstream end of the Cement Creek study reach, treats discharge from the Gold King Mine adit with lime (CaO) to raise the pH and trigger the precipitation of metals out of solution. However, the pH downstream of the plant at the outlet of Cement Creek remains low ($\sim 3 < \text{pH} < \sim 4.5$), which is likely a result of several other draining mines such as the Mogul Mine or Red and Bonita Mine (**Figure 1C**) that contribute low pH and metal-rich water to Cement Creek and do not undergo treatment (USGS, 2020). Historic data show dissolved aluminum, copper, and zinc concentrations as high as ∼18,500, 285, and 7,280 µg/L, respectively, in Cement Creek downstream of the Prospect Gulch inflow (Johnson et al., 2007). Recently, the Bonita Peak Mining District Superfund identified the Henrietta Mine as a priority contamination source as a result of elevated aqueous concentrations of Al, Cd, Cu, Pb, and Zn and high sediment-As concentrations (USEPA, 2017). We investigated Cement Creek along a reach extending from the Gladstone Treatment Plant to ∼600 m downstream of Prospect Gulch (referred to throughout the remainder of the text as CC-PG; **Figure 1D**). Metal-rich groundwater in the Cement Creek catchment can discharge into the stream along this reach *via* several flow paths, including direct discharge from upslope mine drainages, natural seeps and springs, or diffuse subsurface discharge through iron fens and streambanks. Furthermore, the mine drainages can comprise a notable portion of total streamflow in Cement Creek during baseflow conditions (Cowie and Roberts, 2020). Cement Creek, including within the study area, is characterized by abundant ferricrete deposits along the stream channel and banks. Ferricrete deposits form when reducing acidic groundwater, containing high concentrations of iron, interacts with the atmosphere or oxygenated surface water and causes the precipitation of amorphous iron oxyhydroxides that, in turn, cement clastic sedimentary conglomerates (Guerard et al., 2004; Walton-Day et al., 2007). These ferricrete deposits serve as a long-term sink of metals and contain solid-phase concentrations as high as ∼300 ppm As, ∼350 ppm Cu, and 350 ppm Pb (Wirt et al., 2007).

Field Instrumentation

Stream gages were installed at MC-Fen on May 20, 2019 and CC-PG on July 18, 2019 (**Figures 1D,E**). Water and barometric pressure were measured every 15 min at each gage using pressure transducers (HOBO U20) and corrected to water level with a staff plate. A rating curve was built for each site based on 12 flow measurements at Cement Creek and 11 flow measurements at Mineral Creek using a HACH flow meter (**Supplementary Figure 1**). The rating curve at Mineral Creek was supplemented with eight additional measurements collected from a nearby stream gage managed by the US Forest Service (Mineral Creek below Mill Creek; **Figure 1E**). Given the spatial variability in alpine rainfall events, we include data from a NOAH-II All-Weather Precipitation Gauge (ETI Instrument Systems) installed by the US EPA and managed by the Mountain Studies Institute.[1] Discharge measurements were compared to 10-min precipitation measurements from the Gladstone Treatment Plant weather station (**Figure 1C**). Water levels were summed for daily measurements following corrections for evaporative losses. Snow water equivalent data were obtained

---

[1] www.mountainstudies.org

from the Snowpack Telemetry Network (SNOTEL) monitoring site (#629) located downstream of MC-Fen (USDA, 2020).

A cluster of three hyporheic zone monitoring wells was installed in the streambed at each site to determine vertical hydraulic gradients, perform slug tests, and sample porewater chemistry (**Figures 1D,E**; described in "Section continuous salt-tracer injection tests"). The wells were installed on July 18, 2019 in CC-PG and May 21, 2019 in MC-Fen and constructed from PVC with a 19-mm inner diameter and a 0.2-mm slotted screen comprising the bottom 10 cm of each well. The hyporheic zone monitoring wells at Cement Creek (37.88049, −107.66814) extended to depths of 28, 44, and 58 cm (**Figure 1D**), and the wells at Mineral Creek (37.86970, −107.72387) extended to depths of 20, 40, and 68 cm (**Figure 1E**). To determine the vertical hydraulic gradient, manual water level measurements were made with a water level tape in each well prior to the high and low flow tracer tests at each site (described below). Slug tests were performed in the monitoring wells, and hydraulic conductivity was estimated according to Bouwer and Rice (1976).

To compare temporal variations in average linear velocities for CC-PG and MC-Fen, thermal probes were installed adjacent to the well clusters in each stream reach. The Thermochron temperature logging iButtons (Model #DS 1922L-F5) recorded stream-water temperature and streambed temperatures at 10- and 40-cm depths every 15 min with a precision of 0.0625°C. Our primary focus of these measurements was twofold: (a) explore the effects of ferricrete precipitates on average linear velocity of the stream infiltrating into the subsurface of Cement Creek and (b) determine when, during the year, the streams were gaining or losing. Thermal probes were constructed by drilling out three 2 × 24-mm holes in a wooden stake and adhering iButtons into the holes with epoxy. The thermal probes were deployed from July 19, 2019 to October 19, 2019 in Cement Creek and May 24, 2019 to October 10, 2019 in Mineral Creek; however, data gaps exist for portions of these time series due to iButton damage during removal of the thermal probes and instances when the stream temperature iButton was not submerged. All temperature data were filtered using a bandpass filter, resampled, and processed in MATLAB according to the temperature time-series analysis developed by Hatch et al. (2006). We calculated average linear velocities into the sediment based upon the amplitude ratio (V_{Ar}) and phase shift ($V_{\Delta\phi}$) between the shallow and the deep thermal signals and assuming parameters for a saturated, sandy streambed (Hatch et al., 2006, 2010). These parameters included porosity ($\eta = 0.35$), fluid and sediment densities ($\rho_{\mathrm{f}} = 997\,\mathrm{kg\,m}^3$ and $\rho_{\mathrm{s}} = 2{,}650\,\mathrm{kg\,m}^3$), fluid and sediment heat capacities ($c_{\mathrm{f}} = 4{,}180\,\mathrm{J\,kg}^{-1}\,{}^{\circ}\mathrm{C}^{-1}$ and $c_{\mathrm{s}} = 800\,\mathrm{J\,kg}^{-1}\,{}^{\circ}\mathrm{C}^{-1}$), thermal dispersivity ($\beta \sim 0.001\,\mathrm{m}$), and thermal conductivity ($\lambda_0 = 1.58\,\mathrm{W\,m}^{-1}\,{}^{\circ}\mathrm{C}^{-1}$) (Hatch et al., 2010). Based on field observations of sand-sized grains between streambed cobbles, we assumed that these parameters for a sandy streambed would be representative of the two sites but acknowledge that there are likely heterogeneities in these parameters along the reaches. Negative linear velocities indicate losing conditions (i.e., stream water infiltrates into the streambed), whereas positive linear velocities indicate gaining stream conditions (i.e., groundwater discharges into the stream).

Continuous Salt-Tracer Injection Tests

Continuous injection salt-tracer tests were conducted to quantify mass transfer parameters and hyporheic zone area. Two tracer tests were conducted at Mineral Creek during baseflow (September) and high flow (July/August) and were compared to high and low flow tracer tests conducted in Cement Creek. During each tracer test, a saltwater solution (∼240 g/L NaCl) was injected into the stream at a constant rate for a period of 4 h. The injection rate was determined based on stream discharge at the time of the tracer test (**Supplementary Table 1**). Prior to the baseflow tracer test, the stream discharge in MC-Fen ($Q \sim 0.12\ \mathrm{m}^3\ \mathrm{s}^{-1}$) was similar to the discharge measured prior to the low flow tracer test in Cement Creek ($Q \sim 0.15\ \mathrm{m}^3\ \mathrm{s}^{-1}$), and the specific conductivity was ∼450 and 1,090 µs/cm at MC-Fen and CC-PG, respectively. Prior to the high flow tracer test, the stream discharge in MC-Fen and CC-PG were 2.2 and 1.1 $\mathrm{m}^3\ \mathrm{s}^{-1}$, respectively, and the specific conductivity was ∼120 and 440 µs/cm, respectively (**Supplementary Table 1**). Specific conductivity was measured every minute during the tracer test using fluid electrical conductivity loggers (HOBO U-24, Onset Computing). One conductivity logger was deployed upstream of the saltwater injection point to measure background fluid conductivity, and three conductivity loggers were deployed downstream (200, 475, and 680 m in MC-Fen; **Figures 1D,E**) of the tracer mixing zone. Based on previous estimates of approximate mixing zone lengths of 25 times the stream width (Day, 1977), the loggers at 225 m in MC-Fen and 185 m in CC-PG were launched at these locations to ensure adequate mixing of the stream and the tracer.

Stream water samples for analysis of Cl^-, SO_4^{2-}, and Na^+ concentrations were collected during the arrival of the tracer 200 m downstream of the MC-Fen injection point and 700 m downstream of the CC-PG injection point. The timing of grab-sample collection was based upon continuous conductivity measurements using a handheld meter (Orion Star A325). Samples were collected during the arrival of the tracer, every 30 min during the breakthrough curve plateau, and during the recession of the tracer until stream conductivity returned to background conditions. The samples were collected in Whatman vials, filtered (<0.2 µm, Nylon), and frozen until analysis using ion chromatography for anions (Dionex ICS-2100) and cations (Dionex ICS-1100).

Transport parameters were determined at high and low flow for both study reaches using the one-dimensional transport with inflow and storage (OTIS) model (Runkel, 1998) coupled with the parameter estimation (PEST) model (Doherty, 2010). OTIS compartmentalizes the system into the main stream channel and the transient storage zone and operates under the primary assumptions that (a) mass is conserved, (b) solute concentration only varies in the longitudinal direction, and (c) transient storage is the only physical process affecting solute concentration in the transient storage zone (Runkel, 1998). The models were constrained using conductivity time-series data, measured Cl^- concentrations, and stream discharge measurements. Air bubbles near the conductivity sensor led to noise in the sensor measurements. To remove the noise, the conductivity time-series data were filtered using the robust locally weighted scatterplot smoothing (RLOWESS) filter and *smoothdata* function in MATLAB using a 10-min window. The data were then sampled every 10 min to reduce the dataset size prior to importing into PEST. The models then solved for the best-fit area of hyporheic fluid exchange (A_s), rate of mass transfer between the stream and hyporheic zone (α), dispersion coefficient (D), lateral inflows (q_{lat}), and concentration of lateral inflows (c_{lat}).

Additional metrics were calculated to allow for direct comparison of the two stream reaches by normalizing the model estimates to stream characteristics such as discharge and cross-sectional area. Storage zone residence time (T_{sto}), which gives the average time a water molecule remains in transient storage, was calculated from the modeled parameters,

$$T_{sto} = \frac{A_s}{A\alpha} \tag{1}$$

where A is the stream area. We also calculated the hydraulic retention factor (R_h) as

$$R_h = \frac{A_s}{Q}, \tag{2}$$

which represents the storage-zone residence time relative to the hydraulic turnover length (e.g., discharge, Q) (Morrice et al., 1997; Wondzell, 2006) and the average distance a molecule travels before entering the storage zone (L_s),

$$L_s = \frac{u}{\alpha} \tag{3}$$

where u is the stream water velocity as well as the proportion of the median travel time resulting from transient storage (F_{med}),

$$F_{\mathrm{med}} \cong \left[1 - e^{-L(\alpha/u)}\right] \frac{A_s}{A + A_s} \tag{4}$$

which quantifies the movement of the tracer into the storage zone relative to the total mass transport (Runkel, 2002). Furthermore, we can determine the relative importance of transient storage and advective velocity using the Damkohler index (Da) as follows:

$$Da = \frac{\propto \left(1 + \frac{A}{A_s}\right) L}{u} \tag{5}$$

where L is the reach length (Wagner and Harvey, 1997). The experimental Da also reflects if the model estimates for transient storage zone parameters are reasonable (Wagner and Harvey, 1997). Da on the order of 1 indicates minimum uncertainty in α and A_s (Wagner and Harvey, 1997).

Stream, Groundwater, and Hyporheic Zone Sampling

Independent of the tracer tests, water samples were collected from the stream channel near the hyporheic zone well clusters at Mineral Creek ($n = 8$) and at Cement Creek ($n = 10$) from February to November 2019, when weather conditions allowed. Shallow groundwater samples were collected from a private well in Mineral Creek (referred to herein as the Artist's Cabin well, $n = 1$; **Figure 1E**) and from a shallow well (120 cmbgl) installed in the iron fen adjacent to the hyporheic zone well clusters in Cement Creek ($n = 3$; **Figure 1D**). One sample was collected from a fen wetland pool in the Chattanooga Fen complex at Mineral Creek (**Figure 1E**). Two samples from the Koehler Tunnel discharge and one from Prospect Gulch inflow near Cement Creek (**Figure 1C**) were collected for comparison to historical data.

The hyporheic zone was sampled directly twice during high flow (June 2019 and 2020) and once during low flow conditions (September 2019) from the hyporheic zone well clusters installed at MC-Fen and CC-PG (**Figures 1D,E**). The wells settled for 2–4 weeks before the first sampling event. Prior to collecting the water samples, each shallow well was purged at a low flow rate until the measurements of pH, temperature, and specific conductivity stabilized (USEPA, 2010). After these measurements stabilized, water samples were collected for analysis of total and dissolved metals, major anions, and total organic carbon (described below). Ferrous iron (Fe^{2+}) and dissolved oxygen (DO) were measured immediately in the field using a portable spectrophotometer (HACH DR1900). Fe^{2+} was determined using 1,10-phenathroline reagent (HACH Method 8146), and DO was determined using AccuVac Ampules (HACH Method 8166).

During each sampling campaign, measurements of pH, conductivity, and temperature were made using an Orion Star A325. The alkalinity measurements were made in the field using a field kit (HACH Model AL-DT). All water samples were collected according to standard methods (Clesceri et al., 1999). Total metals (unfiltered) and dissolved metals (defined here as $<0.2\,\mu m$) were collected in acid-washed polypropylene sample bottles and acidified to pH < 2 with trace-metal-grade nitric acid. Samples for major anions were collected in Whatman vials and filtered to $<0.2\,\mu m$ (Nylon). Total organic carbon (TOC) samples were collected in amber glass vials (combusted at 400°C) and preserved with hydrochloric acid to pH < 2. All samples were kept on ice in the field and frozen (e.g., anion and metal samples) or refrigerated (e.g., TOC samples) within 6 h of sample collection.

Geochemical Analyses and Calculations

The stream, groundwater, and hyporheic zone water samples were analyzed for total and dissolved metals, including Al, As, B, Ba, Be, Ca, Cd, Cu, Cr, Fe, K, Li, Mg, Mn, Mo, Na, Ni, P, S, Sb, Se, Si, Sn, Sr, Ti, Tl, V, and Zn, using an inductively coupled plasma-optical emission spectrometer (ICP-OES, Perkin-Elmer Optima 5,300 DV) at Colorado School of Mines (Mines). Major anions (Br^-, Cl^-, F^-, NO_2^-, NO_3^-, SO_4^{2-}, and PO_4^{3-}) were analyzed using ion chromatography (Dionex ICS-2100) with an IonPac AS-11 analytical column (2 × 250 mm) at Mines. The TOC samples were analyzed by a Shimadzu TC-Analyzer at the Mines Advanced Water Technology Center.

Mineral saturation indices were calculated for stream and hyporheic zone water samples using PHREEQC with the WATEQ4F database (Ball and Nordstrom, 1987; Parkhurst and

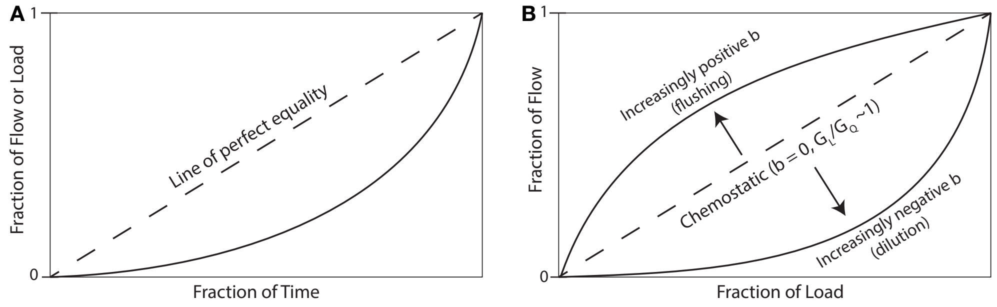

FIGURE 2 | Schematics of **(A)** Lorenz curves and **(B)** dual Lorenz curves for load *versus* flow, as modified from Jawitz and Mitchell (2011) and Gall et al. (2013). The shape of the curves are determined by the Gini coefficient for load and discharge, where perfect equality is $G = 0$ and perfect inequality is $G = 1$, and can be used to indirectly evaluate concentration-discharge relationships.

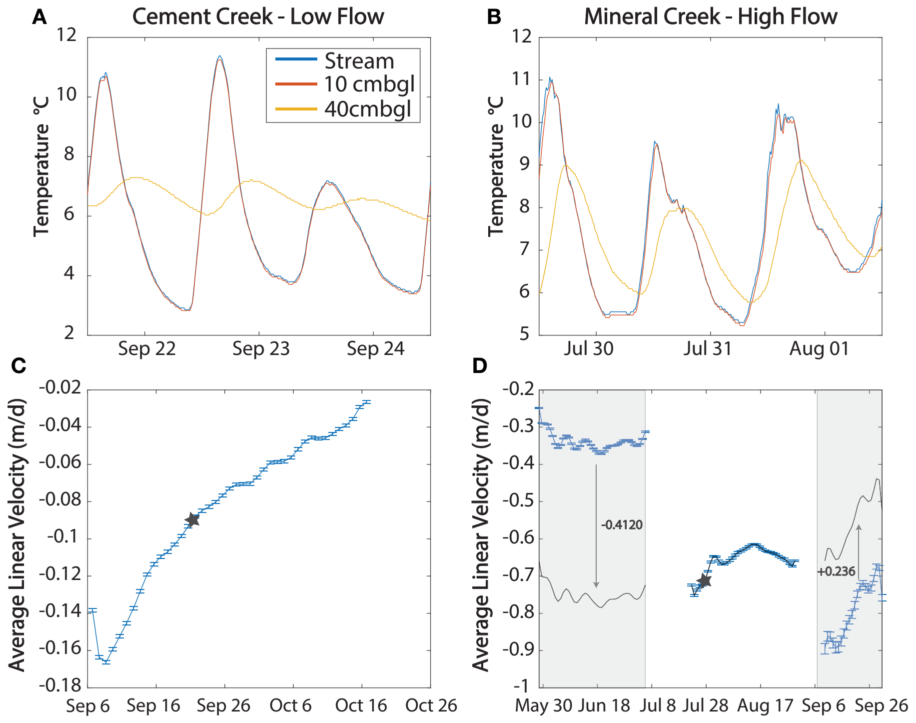

FIGURE 3 | Temperature time-series data for **(A)** Cement Creek–Prospect Gulch during the low-flow tracer test and **(B)** Mineral Creek–Chattanooga Fen during the high-flow tracer test, as well as average linear velocity estimates based on amplitude ratios (V_{Ar}) (Hatch et al., 2006) for **(C)** Cement Creek and **(D)** Mineral Creek in 2019. Data are not presented for the high-flow tracer test in Cement Creek due to temperature sensor damage and loss of data. The black stars indicate the average linear velocity at the approximate time of the tracer tests. Note that the thermal sensors were removed from Mineral Creek on September 26, before the tracer test was completed on September 28. The blue dashed lines represent uncertainty in the average linear velocity estimates. Negative velocities indicate water fluxes from the stream into the subsurface (e.g., losing stream conditions). The gray-shaded areas in **(D)** indicate high uncertainty velocity estimates given that the estimates were calculated only from stream temperature and 10 cmbgl temperature sensors due to damage of the 40 cmbgl temperature sensor. Values on plot **(D)** represent the offset used to correct the Mineral Creek average linear velocity estimates in the shaded regions to the estimates made for the July–August data. We subtracted 0.412 m/day from all velocity estimates measured from May 30 to July 7 and added 0.236 m/day to all estimates made in September, assuming that the measurements made during these time periods were offset from the low uncertainty velocity estimates measured from July 8 through August.

Appelo, 2013). The dissolution reaction and associated solubility product for schwertmannite was added to the database (Bigham et al., 1990). We calculated saturation indices for minerals previously identified using x-ray diffraction in Cement Creek and Mineral Creek (Vincent et al., 2007; Wirt et al., 2007; Yager and Bove, 2007) and using measurements from this study of pH, temperature, alkalinity, DO, and dissolved concentrations of major ions and trace metal(loid)s. All water samples were charge-balanced using chloride for geochemical modeling; however, the charge balance error was less than 5% for all samples, except the

Mineral Creek 40 cmbgl samples for high and low flow in 2019 (<10%) and several samples collected in 2020 (<20%).

Compilation of Historic Data and CQ Analysis

To determine the influence of variable streamflow on solute fluxes, we compiled historical streamflow and geochemical data for locations nearby the MC-Fen and CC-PG sampling locations. Data were compiled for redox-sensitive elements, including total and dissolved concentrations of Al, As, Cu, Fe, Mn, and SO_4^{2-}. Four samples of stream chemistry and streamflow were compiled from recent US EPA reports (USEPA, 2016, 2017) for MC-Fen. For the CC-PG reach, a total of 10 geochemical samples and corresponding streamflow measurements were compiled from Johnson et al. (2007) and one from a US EPA report (site no. CC27) (USEPA, 2017). These historic data were combined with the samples collected for this study in 2019 to assess concentration–discharge relationships for MC-Fen (total sample count of 10) and CC-PG (total sample count of 20).

A CQ analysis was performed using the compiled datasets for the MC-Fen and CC-PG locations (using historic and new data) to assess potential influences of hyporheic processes on metal(loid) export. A power-law slope (b) was calculated by plotting the concentrations (C) of each redox-sensitive element against the corresponding discharge (Q) in log–log space (e.g., Godsey et al., 2009). The coefficient of variation of each redox-sensitive element (CV_C) was normalized to the coefficient of variation of the discharge (CV_Q) to determine the variability in concentration with respect to discharge (Thompson et al., 2011; Musolff et al., 2015). The use of b alone to interpret chemostatic behavior, when concentration is invariant with changes in discharge, can be misleading because concentration variability could be high even in cases where $b < \pm 0.1$ (Thompson et al., 2011; Musolff et al., 2015). Chemostatic solute behavior is defined here as $b \leq \pm 0.1$ and $CV_C / CV_Q \leq 0.2$. We characterize solutes as moderately chemodynamic when $0.2 < CV_C / CV_Q \leq 1$ and chemodynamic when $CV_C / CV_Q > 1.0$. Gini coefficients, which are a measure of inequality, were calculated to determine the temporal inequality of loads (G_L) and discharge (G_Q) for Lorenz curves, which relate the cumulative proportion of a variable [in this case, streamflow (Q) or solute load (C)] and the cumulative proportion of the population (in this case, time; **Figure 2A**) (Jawitz and Mitchell, 2011). For example, chemostatic behavior would result in load inequality (G_L) controlled primarily by discharge inequality (G_Q) because variability in concentration is low compared to variability in discharge and thus $G_L / G_Q \approx 1$ (**Figure 2B**).

RESULTS AND DISCUSSION

Physical Characteristics of Streambed Determine Stream–Groundwater Connectivity

Transport modeling of the tracer test data, in combination with measurements of hydraulic conductivity and average linear velocities, elucidate the physical controls on the hyporheic zone at Mineral Creek and Cement Creek. According to temperature time-series data, both stream reaches were losing (e.g., negative average linear velocities) during all time periods observed (**Figure 3**); however, the stream velocity into the subsurface was greater at MC-Fen (−0.7 to −0.5 m/day, **Figure 3D**) compared to CC-PG (−0.16 to −0.03 m/day; **Figure 3C**). Vertical hydraulic gradients (dh / dz) measured in the hyporheic zone well clusters also reflected losing stream conditions, where hydraulic heads were greater in the shallower well-compared to the deep well at both sites (**Supplementary Table 2**). The lower linear velocity at CC-PG was consistent with the lower hydraulic conductivity at depth ($\sim 4 \times 10^{-5}$ m/s at low flow and 8×10^{-5} at high flow in the 39 cmbgl well) compared to the higher linear velocities and hydraulic conductivity at depth in the MC-Fen reach ($\sim 9 \times 10^{-5}$ m/s at low flow and 1×10^{-4} at high flow in the 63 cmbgl well) based on slug test data (**Supplementary Table 3**).

The physical differences in average linear velocities and hydraulic conductivity of the streambeds in the MC-Fen and CC-PG reaches influenced the hyporheic storage and mass transfer rates between the stream and the transient storage zones. Model estimates of mass transfer parameters using PEST with OTIS and the tracer data (**Supplementary Figure 2**) measured at the hyporheic zone well clusters (e.g., 200 m downstream of the injection site for MC-Fen and 700 m downstream of the injection site for CC-PG) indicated that hyporheic storage (A_s) and the proportion of solute storage in the hyporheic zone compared to the stream (A_s / A) were greater at high flow and low flow in MC-Fen compared to CC-PG (**Table 1**, **Supplementary Figures 3**, **4**). Thus, the smaller hyporheic zone areas of 0.1 m^2 at low flow and 0.4 m^2 at high flow for CC-PG were consistent with low average linear velocities and less permeable sediments, whereas the larger hyporheic zone areas of 0.6 m^2 at low flow and 1.8 m^2 at high flow for MC-Fen were associated with high average linear velocities and more permeable sediments. It is important to note that we observed surface-flow contributions from hillslope tributaries to MC-Fen that likely caused a variable discharge along the reaches investigated and caused a lag between the measured and the modeled breakthrough curves for the low flow tracer tests. To minimize this lag, the stream discharge in OTIS was adjusted for the low flow tracer test to improve model fits (**Table 1**). The root mean square error of the data-model fit was relatively low for all simulations (∼11 to 43; **Table 1**), indicating that model estimates were representative of the breakthrough curves. However, the mass transfer rate (α) was less sensitive to model output than A_s, and estimates of α were similar across site and flow regime ($0.001 < \alpha < 0.005\ s^{-1}$).

Cement Creek as a Model of Poorly Connected Groundwater–Stream Systems

In the CC-PG well cluster, the dissolved concentrations of Cl^-, Li^+, and Ca^{2+} varied with depth during high flow in 2019, as indicated by the high coefficients of variation (CV) for these solutes (111, 56.6, and 23.4%, respectively; **Table 2**). Furthermore, the percent difference between high flow and low flow in dissolved concentrations of Li^+, Ca^{2+}, and Na^+ for the stream and shallowest well (23 cmbgl), and dissolved Cl^- for the shallowest well only, was greater compared to the middle

TABLE 1 | One-dimensional transport with inflow and storage with parameter estimation (PEST) model constraints, model outputs, and calculated transient storage zone parameters [data were filtered prior to entry into PEST using a robust locally weighted smoothing filter (RLOWESS)].

Stream reach	Field measurements			Model inputs		Model estimates and RMSE						Calculated					
	Measured discharge $m^3\ s^{-1}$	u $m\ s^{-1}$	pH	Adjusted discharge[a] $m^3\ s^{-1}$	A m^2	$Q_{lat\text{-}in}$[b] $m^3\ s^{-1}\ m^{-1}$	$C_{lat\text{-}in}$	A_s m^2	D $m^2\ s^{-1}$	α s^{-1}	RMSE[c]	A_s / A	Da	T_{sto} h	R_h^d $s\ m^{-1}$	L_s m	F_{med} %
Mineral Creek at Chattanooga	0.12	0.14	6.5	0.20	0.86	9.0×10^{-7}	46	0.60	0.2	0.004	42.5	0.70	2.9	2.8	3.00	55	40.6
	2.2	1.0	6.8	n.a.	2.2	1.0×10^{-4}	8.3	1.8	0.1	0.005	10.5	0.82	0.9	2.7	0.82	200	30.4
Cement Creek at Prospect Gulch	0.18	0.45	3.9	0.26	0.62	9.7×10^{-6}	49	0.10	0.8	0.001	23.6	0.16	0.1	2.7	0.36	450	11.8
	1.3	0.68	5.2	n.a.	1.6	5.0×10^{-6}	25	0.40	0.09	0.001	17.1	0.25	0.1	4.1	0.36	680	14.2

u, stream velocity; A, stream cross-sectional area; Q_{lat-in}, discharge of lateral inflows; C_{lat-in}, concentration of lateral inflows; A_s, transient storage zone cross-sectional area; D, dispersion; α, mass transfer rate; Da, Damkohler number; T_{sto}, storage zone residence time; R_h, hydraulic retention factor; L_s, average distance a solute travels before entering the storage zone; F_{med}, median travel time resulting from transient storage.

[a] *For both low-flow model runs, the discharge was adjusted to account for a lag in the arrival time of the modeled breakthrough curve.*

[b] *The boundary condition for $Q_{lat-out}$ ($m^3\ s^{-1}\ m^{-1}$) was set to 0.*

[c] *Root mean square error (RMSE) = $\sqrt{\frac{\sum_{i=1}^{n}(residual)^2}{\#\ of\ observations}}$.*

[d] *Hydraulic retention factor (R_h) was calculated using the adjusted discharge values, when applicable.*

TABLE 2 | Average, standard deviation, and coefficient of variation for dissolved concentrations of conservative elements as a function of depth in the hyporheic zone well clusters.

Site	Solute	High flow 2019			Low flow 2019			High flow 2020		
		Average[a]	Standard deviation	Coefficient of variation (%)	Average[a]	Standard deviation	Coefficient of variation (%)	Average[a]	Standard deviation	Coefficient of variation (%)
Cement Creek	Cl	16.4	18.2	111	5.84	2.59	44.4	9.72	3.22	33.1
	Li	2.16	1.22	56.6	2.31	0.11	4.67	0.84	0.51	60.5
	Ca	2.65	0.62	23.4	3.69	0.49	13.4	1.92	0.62	32.0
	Na	78.2	8.93	11.4	111	10.5	9.46	82.9	19.6	23.6
Mineral Creek	Cl	20.8	1.14	5.49	17.5	2.10	12.0	22.1	3.05	13.8
	Li	<0.7	NA	NA	<0.7	NA	NA	0.68[b]	0.16	23.4
	Ca	0.34	0.05	13.7	2.10	0.05	2.38	0.36	0.06	16.6
	Na	59.5	9.09	15.3	210	16.8	7.97	52.20	7.22	13.8

[a] *Average dissolved concentrations are reported in units of μM for Cl, Li, and Na and units of mM for Ca.*

[b] *Duplicate Li analyses on Mineral Creek samples indicated a high error (±1 ppm) on Li values.*

and deep wells (39 and 53 cmbgl, respectively) (**Figures 4A,B**). The invariability of water chemistry in the middle and deep wells compared to the chemical variability in the shallow well in response to flow suggests a disconnect between the shallow and the deeper two wells. This disconnect is also reflected in the dissolved oxygen concentrations as a function of depth in the CC-PG wells. While the pH varied by only ∼1 pH unit with depth (**Figure 4C**), the dissolved oxygen concentrations decreased from ∼9 mg/L in the stream to ∼2 mg/L in the deepest well (**Figure 4D**). Furthermore, a fourfold difference in dissolved oxygen concentrations in the shallow well (23 cmbgl) between low flow (3.7 mg/L) and high flow conditions (7.6 mg/L) is consistent with model results from OTIS, where the hyporheic mixing of oxygenated stream water and shallow groundwater was limited to an area (A_s) of ~ 0.1 m^2 during low flow and ~ 0.4 m^2 during high flow (**Table 1**). Given that (a) dissolved Ca^{2+}, Na^+, and Li^+ in the middle and deep wells changed minimally in response to changing stream discharge (percent difference between high flow and low flow of 1.1–18%), (b) dissolved Ca^{2+}, Na^+, Li^+, and Cl^- in the stream and shallowest well did change in response to variable stream discharge and fluctuations in hyporheic area (percent difference of 26–1,310%), and (c) the middle well was characterized by low hydraulic conductivity and low dissolved oxygen, a physical disconnect between hyporheic mixing that occurs above the middle well and groundwater below the middle well was indicated.

We propose that the physical disconnect between hyporheic mixing and groundwater in CC-PG occurs as a result of ferricrete precipitation at the approximate location of the middle well and the estimated maximum area of hyporheic mixing (40 cm^2). Hyporheic mixing would facilitate the penetration of oxygenated waters to this depth, where it would mix with reducing groundwaters and trigger the precipitation of minerals that compose ferricrete (Wirt et al., 2007). The potential of ferricrete deposits to serve as a barrier between stream water and groundwater is consistent with previous observations that the reduced permeability from ferricrete cementation of clastic sediments decreases the flow of groundwater near streams and influences streambed geomorphology (Vincent et al., 2007; Wirt et al., 2007).

Mineral Creek as a Model of Well-Connected Groundwater–Stream Systems

In comparison to CC-PG, the MC-Fen system was characterized by a larger hyporheic storage area (**Table 1**), higher average linear velocities (**Figure 3**), and higher hydraulic conductivity (**Supplementary Table 3**). The behavior of conservative solutes in the subsurface of MC-Fen also differed from CC-PG. The coefficient of variation as a function of depth for dissolved concentrations of Cl^-, Na^+, and Ca^{2+} in the MC-Fen wells under high flow and low flow conditions was $\leq$15% (compared to $\leq$111% for CC-PG; **Table 2**). Similarly, the percent differences in dissolved Ca^{2+}, Na^+, and Cl^- were within 10, 15, and 34%, respectively, of each other with depth, and pH (6.2–7.3 pH) and dissolved oxygen (6.4–10 mg/L) exhibited no identifiable trend with depth (**Figure 4**). The dissolved concentrations of Li^+ were below detection limits in all samples. While the shallow and deep wells in the CC-PG system were disconnected, both the shallow well chemistry and the deep well chemistry at MC-Fen responded to flow, where an increase in flow resulted in a decrease in conservative solute concentrations at all depths (**Table 2**, **Supplementary Figure 6**). This behavior indicates that groundwater and surface water were well-connected at this site, and this connection facilitated the homogenization of chemistry in the hyporheic zone. Chemical homogenization at MC-Fen was consistent with observations from the East River, where intermittent surface water infiltration and high hydraulic conductivities homogenized the subsurface water chemistry (Nelson et al., 2019; Saup et al., 2019).

Metal(loid) Behavior in the Hyporheic Zone at CC-PG and MC-Fen

Here we focus on how differences in subsurface mixing processes (as highlighted by the conservative element behavior) influence dissolved metal–sediment interactions in the shallow subsurface at CC-PG and MC-Fen. Although the metal sources at these two sites—Koehler Tunnel and Prospect Gulch—had dissolved and total concentrations of Al, Fe, Mn, and Zn that were the same order of magnitude (**Table 4**), the average dissolved concentrations of these elements were at least one order of magnitude greater in the stream at CC-PG compared to those in the stream at MC-Fen (**Table 3**). The metal(loid) concentrations in this study were consistent with measurements of seeps, springs, and draining mines in Prospect Gulch made by the US EPA from 2016 to 2018 (**Table 3**) and previous water quality surveys by the US EPA at Koehler Tunnel in 2016 and 2017 (**Table 3**). Furthermore, the dissolved Al, As, Fe, Mn, Pb, and Zn concentrations were several orders of magnitude greater in a wetland pool in the Chattanooga Fen adjacent to MC-Fen than in the Koehler Tunnel, but these concentrations were not reflected in the stream at MC-Fen. The following sections highlight how a well-connected groundwater–stream system influences the relatively low dissolved Al, Fe, and Mn concentrations in Mineral Creek, while a poorly connected groundwater–stream system influences the relatively high Al, Fe, and Mn concentrations in CC-PG.

Ferricrete Is an Important Regulator of Metal Concentrations at CC-PG

The stream and the shallow groundwater at CC-PG were poorly connected, and a ferricrete layer at depth limited the areal extent of the hyporheic zone. The low average linear velocities facilitated low dissolved oxygen fluxes into the subsurface (8.0 g/m^2/h $O_{2(aq)}$ at low flow and 109 g/m^2/h $O_{2(aq)}$ at high flow in 2020), which resulted in a steep decrease in oxygen (**Figure 4D**) and correspondingly steep metal concentration gradients (**Figure 5**). Furthermore, the dissolved and total metal concentrations were within error for nearly all samples and metals, which was likely due to the stable and acidic pH at all depths and over time (**Figure 4C**). Notable partitioning between dissolved and total Fe and Al in the deeper two wells (i.e., in and below the ferricrete layer) was only observed for the 2020 high flow sampling event (**Figures 5A,I**) and for Mn at low flow, indicating the limited precipitation of Al, Fe, and Mn particulates or colloids. Dissolved

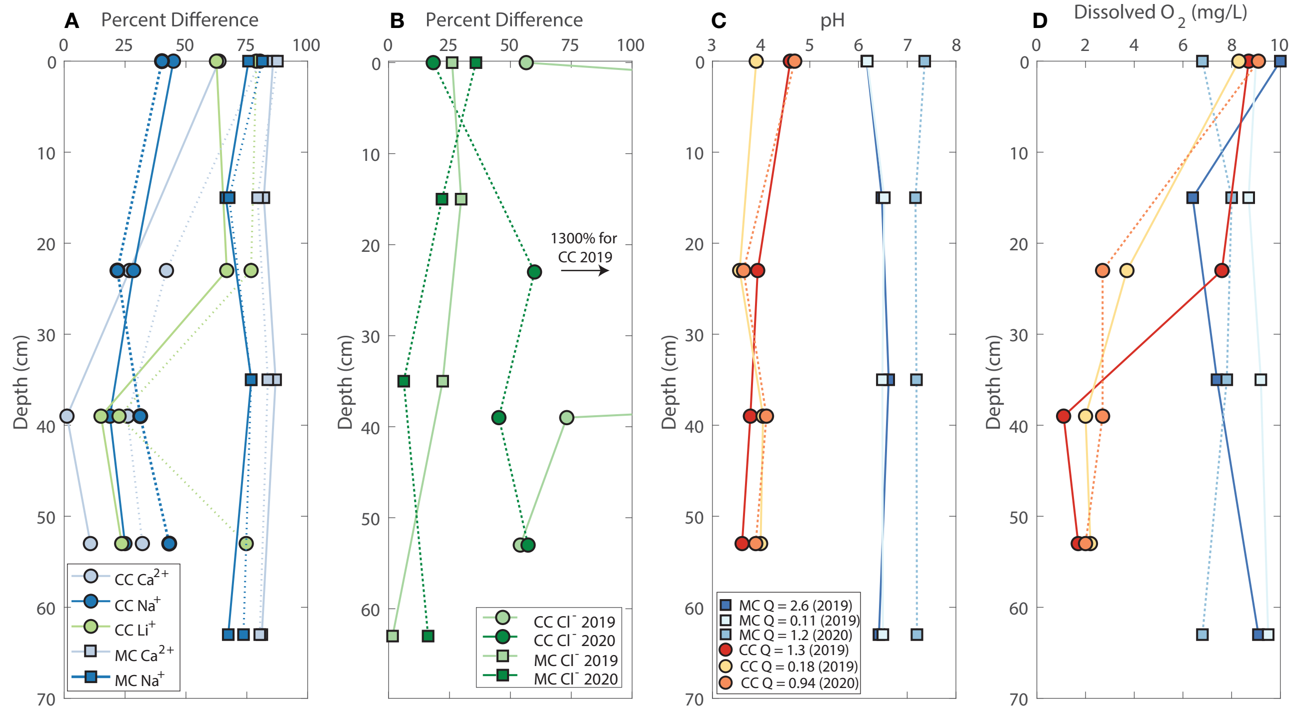

FIGURE 4 | Percent difference between high flow in 2019 and low flow in 2019 (solid lines), as well as high flow in 2020 and low flow in 2019 (dashed lines), in the dissolved concentrations of **(A)** Ca^{2+}, Na^+, and Li^+, and **(B)** Cl^-. Field measurements are included for all sampling times of **(C)** pH and **(D)** dissolved oxygen. The discharges corresponding to these sampling times are included in the legend of **(C)**. The data points at depth represent the mid-point of the 10-cm screened interval. The 0-cm depth represents concentrations or measurements in the stream.

concentrations of Mn, SO_4^{2-}, and Cu, which were sensitive to changes in streamflow in the stream and shallowest well but were insensitive to changes in streamflow near the ferricrete layer and the deepest well, further highlight the disconnect between the shallow hyporheic zone and groundwater at this site. Metals such as Al and Fe, which increased in dissolved and total concentration with depth until the ferricrete layer and did not change in response to streamflow in the shallowest well, reflect that processes other than stream water infiltration and hyporheic mixing regulated these metal concentrations (**Figures 5A,I**).

According to saturation index calculations (**Table 5**) and Eh–pH diagrams (**Figure 6**), the Al and Fe concentrations were buffered by several minerals commonly identified in acid rock drainage environments, such as alunite (Wirt et al., 2007; Yager and Bove, 2007), jurbanite (Anthony and McLean, 1976), and Fe-bearing minerals that typically form ferricrete, such as ferrihydrite, goethite, and schwertmannite (Stanton et al., 2007; Wirt et al., 2007). For dissolved Al, waters were at or near equilibrium (defined here as $SI < \pm 0.5$) with respect to jurbanite and alunite (**Table 4**). Furthermore, most samples at low flow and at high flow were near equilibrium between $AlSO_4^+$ and jurbanite on the Eh–pH diagram, based on the pH measured during sampling and Eh calculated from the Fe^{2+} / Fe^{3+} redox couple (**Figure 6**). Although all samples, except for the stream at low flow, were calculated to be oversaturated ($SI > \pm 0.5$) with respect to ferrihydrite, goethite, and schwertmannite (**Table 5**), the Eh–pH diagram calculations show samples near equilibrium between the schwertmannite and $FeOH^{2+}$ or Fe^{2+} species boundary when the iron concentrations are high (dashed line in **Figure 6A**). Although the measured pH and calculated Eh levels do not plot directly on this boundary, the equilibrium constants can vary with crystallinity and the age of iron oxide minerals (Schwertmann, 1991), where a change in the equilibrium constant toward a more soluble, freshly precipitated form of iron oxide would shift the position of the dashed line in **Figure 6A** up toward the plotted data. Thus, we posit that schwertmannite dissolution likely plays a role in buffering iron concentrations in the shallow subsurface of CC-PG, particularly at high flow (**Figure 6A**). This observation is consistent with the measured increase in dissolved As concentrations with depth at high flow, which may occur as a result of decreased Fe-oxide sediment surfaces and desorption (Smedley and Kinniburgh, 2002). These calculations suggest that Al- and Fe-bearing minerals regulate dissolved Fe and Al concentrations, as well as sorption of metal(loid)s such as arsenic, with depth in the subsurface at Cement Creek.

The small hyporheic zone at CC-PG (**Table 1**), facilitated by low linear velocities (**Figure 3**) and a physical disconnect between shallow groundwater and the stream, results in less movement of stream water through the hyporheic zone. For example, the average distance a solute travels in Cement Creek before entering the storage zone (L_s) was 450 and

TABLE 3 | Stream chemistry for the samples collected in 2019 adjacent to the hyporheic zone well clusters and used in CQ analysis[a].

Site name	Sampling date	Filter fraction	pH	Discharge[b]	Al	As	Co	Cu	Fe	Mn	Ni	Pb	Zn^{213c}	SO_4^{2-d}
				m^3/s	μM	μM	μM	μM	μM	μM	μM	μM	μM	mM
Cement Creek at hyporheic zone well cluster	5/24/19	Unfiltered	4	0.47[b]	116	0.21	0.28	1.36	178	71.4	0.14	0.07	33	NA
		<0.2 μm			131	<0.11	0.33	1.56	188	81.9	0.19	0.1	37.5	NA
	6/21/19	Unfiltered	3.3	3.8[b]	34.9	<0.11	0.08	1.03	51.1	12.9	<0.02	0.07	9.53	NA
		<0.2 μm			23.7	<0.11	0.08	1.06	25.7	13.2	<0.02	0.03	10.1	0.79
	8/1/2019[e]	<0.2 μm	5.2	0.99	31.1	0.22	0.15	0.48	85.4	42.5	0.12	0.05	16.6	NA
	8/7/19	Unfiltered	5.1	0.75	62.6	0.17	0.24	0.62	102	47.5	<0.02	0.08	17.9	2.51
		<0.2 μm			43.7	0.29	0.23	0.57	93.3	48	<0.02	0.08	18.4	NA
	8/8/19	Unfiltered	5	0.78	64.8	0.27	0.24	0.77	98.3	45.6	<0.02	0.1	18.1	2.52
		<0.2 μm			52.9	0.27	0.24	0.7	89.8	46.1	<0.02	0.02	18.2	NA
	11/11/19	Unfiltered	4.1	0.19	171	0.49	0.45	0.5	260	146	0.26	0.12	44.9	NA
		<0.2 μm			176	0.39	0.45	0.49	254	153	0.25	0.09	46.4	5.15
	6/10/20	Unfiltered	4.7	0.94	43.1	0.3	NA	0.89	73.7	28.9	0.12	< 0.02	16.9	NA
		<0.2 μm			32.8	0.19	NA	0.49	48.7	16.9	0.09	< 0.02	9.7	1.71
Mineral Creek at hyporheic zone well cluster	5/24/19	Unfiltered	7.1	0.99	4.46	0.14	<0.02	0.38	4.69	2.13	<0.02	0.12	6.28	NA
		<0.2 μm			1.27	<0.11	<0.02	0.18	0.73	1.59	<0.02	<0.02	5.07	NA
	9/6/19	Unfiltered	7.5	0.24	0.64	0.19	<0.02	<0.09	0.43	0.8	<0.02	0.08	3.2	NA
		<0.2 μm			0.23	0.18	<0.02	<0.09	0.08	0.75	<0.02	0.05	3.23	NA
	11/11/19	Unfiltered	7.3	0.07	0.63	0.39	<0.02	<0.09	0.31	0.53	<0.02	<0.02	4.04	NA
		<0.2 μm			0.53	0.2	0.02	<0.09	0.13	0.54	<0.02	0.03	4.23	3.54
	6/9/20	Unfiltered	7.4	1.2	3.15	0.17	NA	0.2	3.6	1.05	0.04	0.05	2.5	NA
		<0.2 μm			0.67	0.14	NA	<0.09	0.58	0.57	0.04	0.04	1.55	0.36
Detection limit					0.04	0.11	0.02	0.09	0.03	0	0.02	0.02	0.04	0.46

[a] *Four additional stream samples are included in this table, with chemistry from the shallow wells collected on the same date. These include stream samples from Cement Creek collected on 7/31/19 and 9/21/19, when discharge was 1.00 and 0.12 m^3 s^{-1}, respectively, and samples from Mineral Creek collected on 6/20/19 and 9/27/19, when discharge was 3.13 and 0.12 m^3 s^{-1}, respectively.*

[b] *These discharge values were measured upstream at the CCSG1 stilling well, given that these samples were collected prior to the installation of the stilling well near Prospect Gulch.*

[c] *213 represents the wavelength of measurement for ICP-OES (in nm).*

[d] *SO_4^{2-} was measured for filtered samples only.*

[e] *Not used in concentration–discharge analysis.*

680 m, and the median travel time resulting from transient storage (F_{med}) was 12 and 14% at high flow and at low flow, respectively. This indicates that water in the shallow subsurface has more time to react before being replenished with new infiltrating stream water, which allows for more reaction time with subsurface sediments. Thus, we conclude that poorly connected systems with a small hyporheic zone facilitate the formation of strong redox and metal concentration gradients and enhance metal–sediment interactions (**Figure 7A**).

Connected Stream–Groundwater System Facilitates Colloid and Precipitate Formation

Unlike for CC-PG, where metal concentrations were predominantly in the dissolved phase (<0.2 μm), the total metal concentrations (unfiltered) in the wells of MC-Fen were several orders of magnitude greater than the dissolved concentrations of Al, Cu, Fe, and Mn at all depths within the hyporheic zone (**Figures 5C,D,H,K**). Furthermore, dissolved oxygen penetrated to a depth of at least 70 cm (**Figure 4D**), dissolved oxygen fluxes were two orders of magnitude greater (170 and 110 g/m^2/h $O_{2(aq)}$ at high flow and at low flow, respectively) compared to CC-PG, and dissolved Al, Cu, Fe, and Mn concentrations remained low as a function of depth (**Figure 5**). Saturation indices and stability diagrams indicate that the waters were oversaturated with respect to minerals such as goethite, $Fe(OH)_{3(a)}$, and manganite, as well as alunite during high flow in 2019 (**Table 5**, **Figure 6B**, **Supplementary Figure 7**). The formation of metal colloids and precipitates would decrease dissolved metal concentrations relative to the conservative elements, which were invariable as a function of depth (**Figure 4**, **Supplementary Figure 6**). Higher concentrations of Al, Cu, Fe, and Mn in unfiltered samples compared to filtered samples indicate the presence of some colloidal and precipitated metals, consistent with the deep penetration of oxygen in the subsurface (**Figure 4D**). We posit that the mixing of metal-rich groundwater with oxygen-rich stream water in the hyporheic zone of MC-Fen, facilitated by high linear velocities and a large hyporheic area, triggers the precipitation of metal oxides in the subsurface (**Figure 7B**). Furthermore, the higher total metal concentrations with depth at high flow compared to those at low flow (**Figure 5**) suggest that colloid and precipitate formation is enhanced at high flow when the groundwater level is higher (**Supplementary Table 2**) and the hyporheic zone is larger (**Table 1**).

TABLE 4 | Groundwater, metal(loid) source, and iron fen trace metal(loid) and sulfur chemistry, including historical data from Koehler Tunnel and Prospect Gulch collected by the Environmental Protection Agency.

Sample site	Sampling date	Filter fraction	pH	Dissolved oxygen	Fe^{2+}	Al	As	Co	Cu	Fe	Mn	Ni	Pb	SO_4^{2-}	Zn^{213}
				mg/L	mg/L	uM	uM	uM	uM	uM	uM	uM	uM	mM	uM
CC-PG well[e]	6/21/19	Unfiltered	3.6	1.6	2.75	240	0.36	0.28	<0.09	445	33	0.21	0.09	NA	6.4
		<0.2 μm				230	0.39	0.28	<0.09	442	33.3	0.22	0.06	3.94*	6.51
	7/31/19[a]	Unfiltered	3.3	3.9	> 3	58.9	0.26	0.22	0.74	37.8	37.8	0.03	0.16	NA	15.2
		<0.2 μm				50.4	0.22	0.22	0.69	30.9	38.1	0.03	0.20	2.54*	15.2
	9/21/19[a]	Unfiltered	3.6	4.5	> 3	571	0.31	1.3	0.09	414	38.7	1.1	0.53	NA	16.2
		<0.2 μm				547	0.35	1.24	0.09	422	37.5	1.06	0.47	3.54	15.1
Prospect Gulch	6/10/20	Unfiltered	3.6	NA	NA	95.8	0.27	NA	3.44	88.8	4.29	0.13	0.25	NA	10.6
		<0.2 μm				94.2	0.23	NA	3.49	87.3	4.27	0.12	0.25	0.69	10.6
	2016–2018 (mean of data collected by the EPA)[b]	Unfiltered	4.6 *(1.5)*	NA	NA	166	0.6	5.48	2.251	523	21.1	0.24	0.28	1.29	43.3
						252[d]	*1.76*	*23.1*	*6.16*	*1,486*	*55.7*	*0.42*	*0.58*	*1.8*	*96.5*
		<0.2 μm		NA	NA	151	0.53	0.56	7.03	464	19	0.25	0.27	NA	41.2
						237	*1.81*	*1.58*	*21.8*	*1,345*	*47.1*	*0.39*	*0.6*		*91.2*
Chatt-Fen	9/28/19	Unfiltered	4.2	NA	NA	20,650	<0.11	0.49	203	8,300	32,630	<0.02	26.6	NA	4,740
		<0.2 μm				19,910	<0.11	0.48	205	7,790	30,380	<0.02	14.2	2.10	4,560
Artist's Cabin well[e]	9/29/19	Unfiltered	6.5	NA	NA	<0.04	0.23	<0.02	<0.09	0.38	0.07	<0.02	0.03	NA	0.36
		<0.2 μm				<0.04	<0.11	<0.02	<0.09	0.28	0.03	<0.02	0.03	1.71	0.34
Koehler Tunnel	9/29/19	<0.2 μm	3.2	NA	NA	200	0.74	0.71	25.5	189	205	0.78	0.23	9*	202
	6/11/20	Unfiltered	5.5	NA	NA	63.1	0.86	NA	12.4	122	36	0.27	0.15	NA	54.8
		<0.2 μm				36.6	0.38		11.8	104	36.1	0.29	0.07	1.87	55.1
	2016–2017 [mean of data collected by the Environmental Protection Agency (EPA)][c]	Unfiltered	4.3 *(1.3)*	NA	NA	189	1.33	NA	18.7	300	196	0.85	0.31	NA	176
						96.3	*0.43*		*9.17*	*140*	*120*	*0.59*	*0.06*		*101*
		<0.45 μm				150	0.32	NA	17.9	202	189	0.85	0.18	2	173
						133	*0.13*		*9.37*	*178*	*122*	*0.57*	*0.12*	*1.3*	*105*
Detection limit						0.04	0.11	0.02	0.09	0.03	0	0.02	0.02	0.04	0.46

[a] *Corresponds to the date of a hyporheic zone well cluster sampling event.*

[b] *Average across 42 samples from seeps, springs, and draining mines along Prospect Gulch measured by the EPA in 2016–2018 (Cowie and Roberts, 2020).*

[c] *Average across three samples collected by the EPA from the Koehler Tunnel discharge on June 28, 2016 and July 11 and September 27, 2017.*

[d] *Italicized values represent the standard deviation of historical measurements made by the EPA.*

[e] *Depth of sample from CC-PG well was 1.1 m; depth for sample from Artist's Cabin well was 10 m.*

**Presented as sulfur measured using an inductively coupled plasma-optical emission spectrometer at a wavelength of 181 nm.*

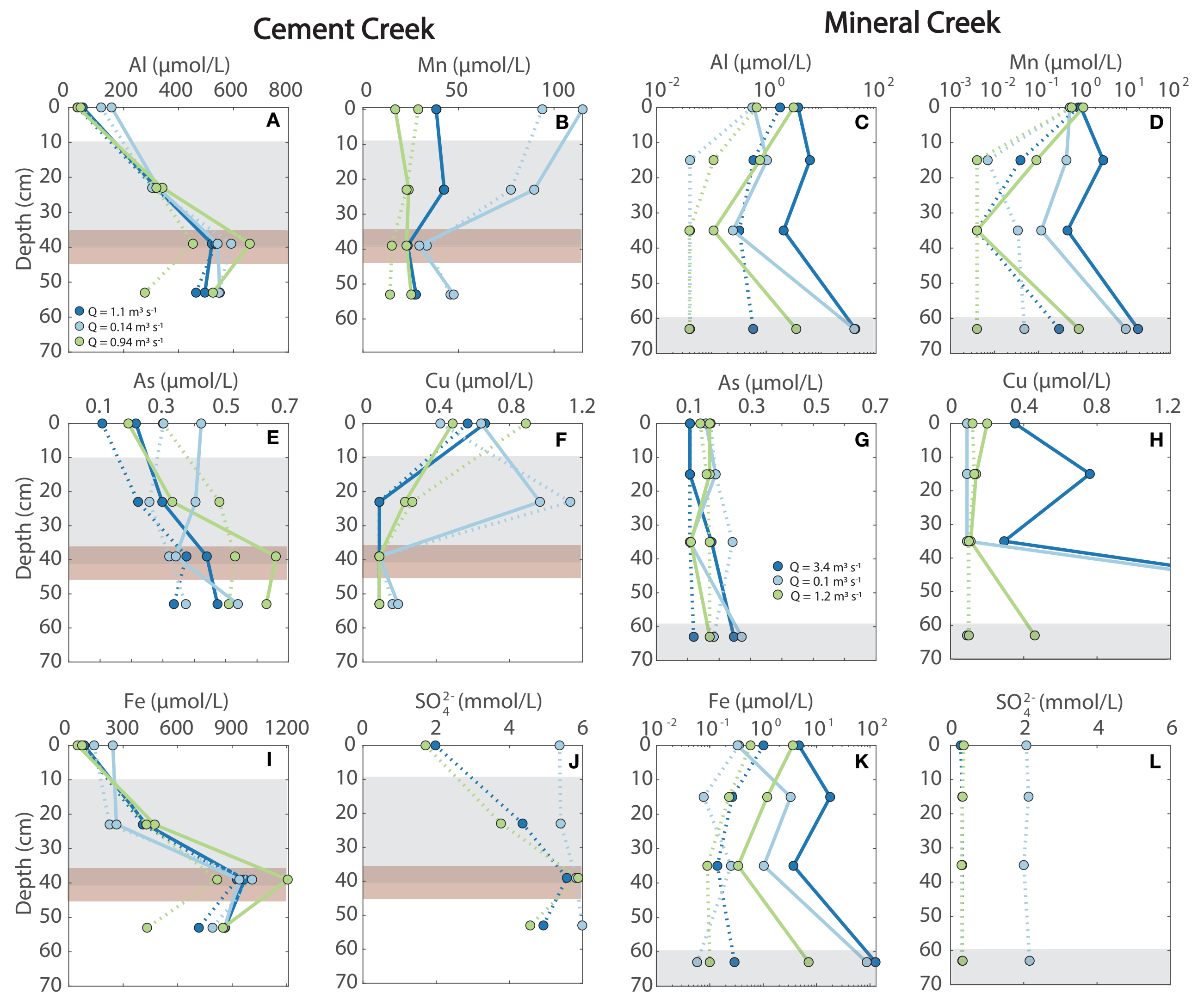

FIGURE 5 | Hyporheic zone chemistry in the CC-PG **(A,B,E,F,I,J)** and MC-Fen **(C,D,G,H,K,L)** well clusters. The colors represent different sampling events and associated stream discharge (Q), the dashed lines represent dissolved (<0.2 µm) concentrations, and the solid lines represent total metal(loid) concentrations (e.g., unfiltered). Note the difference in x-axis range for the Al, Mn, and Fe subplots for Mineral Creek. The deepest data points on the Cement Creek plots represent shallow groundwater chemistry sampled from a nearby well (**Figure 1D**). The shaded red bar represents the low hydraulic conductivity barrier between groundwater and hyporheic mixing zone. The gray-shaded regions represent the range of the hyporheic extent (relative to ground surface) modeled in one-dimensional transport with inflow and storage. The white area from 0 cm to the top of the gray-shaded area represents the hyporheic extent at low flow and the gray-shaded area represents the hyporheic extent at high flow, where the hyporheic extent at high flow for Mineral Creek extends off the plot to a depth of 180 cm. The arrows in **(D,H)** represent total Cu concentrations at 68-cm depth in Mineral Creek (corresponding data in **Supplementary Table 5**).

Stream Concentration–Discharge Relationships Linked to Hyporheic Zone Processes

Seasonal changes in streamflow influenced the hyporheic zone area and mass transfer rates for the Mineral Creek and Cement Creek reaches (as noted in "Section 3.1.4") as well as the subsurface metal(loid) interactions with sediments ("Section metal(loid) behavior in the hyporheic zone at CC-PG and MC-Fen"). During the period of investigation (February 2019 to May 2020), flow varied from 0.2 to ∼7.8 m^3 s^{-1} at MC-Fen and from 0.2 to ∼3.3 m^3 s^{-1} at CC-PG (**Figure 8**). Streamflow reached as high as ∼7.8 m^3 s^{-1} at MC-Fen following melt of snowpack ∼180% above that recorded on May 1 of the 2018 water year (according to SNOTEL site #713) (USDA, 2020). Although the high snowpack followed a period of extreme to exceptional drought that began in January 2018 (NIDIS, 2020), the annual streamflow variability follows a pattern similar to what we observed in 2019, where discharge was greatest following late spring snowmelt and lowest in late summer throughout the winter.

The variability in flow between spring snowmelt, late summer monsoon season, and winter baseflow conditions leads to marked

TABLE 5 | Saturation indices calculated in PHREEQ-C using stream and hyporheic zone water chemistry.

Site	Depth[a] (cm)	Flow regime	CB (%)[b]	Amorphous Fe-oxide[c]	Manganite	K-Jarosite	Schwertmannite	Goethite	Alunite	Jurbanite	Al-oxide	Gypsum	Barite
Cement Creek	0	High flow 2019	−0.63	1.74	1.47	3.36	15.7	6.95	0.42	−0.33	−3.49	−1.32	0.15
	23		2.77	1.33	−0.70	5.89	14.9	6.87	0.88	0.00	−4.13	−0.93	0.01
	39		2.36	1.48	−5.99	6.54	16.7	6.88	0.11	0.11	−4.65	−0.82	−0.43
	53		4.05	1.08	−0.96	5.52	13.9	6.39	−1.38	−0.12	−5.34	−0.89	−0.25
	0	High flow 2020	3.00	2.16	−4.75	3.95	18.7	7.26	0.97	−0.10	−3.24	−1.41	0.17
	23		−0.33	0.99	−6.44	4.92	13.0	6.32	−1.70	−0.26	−5.30	−1.04	0.08
	39		−21.8	2.06	−5.53	7.28	20.4	7.44	1.64	0.38	−3.84	−0.89	0.20
	53		−17.7	1.42	−6.26	5.77	15.8	6.82	−0.27	−0.06	−4.58	−0.98	−0.07
	0	Low flow	0.53	0.04	−0.40	2.28	6.02	5.29	−4.13	−0.75	−6.29	−0.63	0.08
	23		−0.96	1.32	0.31	5.06	14.7	6.65	0.45	0.13	−4.31	−0.70	0.26
	39		−1.41	2.00	0.03	7.33	20.3	7.24	0.99	0.39	−4.33	−0.76	−0.22
	53		3.86	1.75	0.03	6.71	18.6	6.98	0.31	0.26	−4.61	−0.79	−0.09
Mineral Creek	0	High flow 2019	2.89	1.79	3.21	−3.29	9.92	6.93	2.69	−1.14	−0.56	−2.63	0.39
	15		−0.52	1.49	2.46	−5.06	6.55	6.63	1.46	−1.84	−0.69	−2.51	0.34
	35		−8.52	1.13	1.42	−6.28	3.14	6.43	−0.08	−2.72	−0.94	−2.72	−0.04
	63		2.12	1.24	2.84	−5.15	4.78	6.57	1.09	−2.14	−0.77	−2.49	0.28
	0	High flow 2020	−15.8	2.35	5.25	−4.75	10.7	7.55	−1.84	−3.90	−0.95	−2.59	−0.43
	15		7.68	2.01	5.22	−5.49	8.53	7.10	−2.06	−3.69	−1.27	−2.44	−0.37
	35		0.28	1.34	2.99	−7.18	3.08	6.62	−3.26	−4.36	−1.51	−2.57	−0.76
	63		3.20	1.32	2.94	−7.32	2.92	6.62	−3.50	−4.41	−1.54	−2.47	−0.66
	0	Low flow	4.74	1.22	2.78	−3.01	6.51	6.45	2.66	−1.13	−1.12	−1.18	0.44
	20		−0.67	0.88	1.58	−5.27	2.63	6.10	−0.83	−2.57	−1.88	−1.20	0.51
	40		−9.58	1.38	2.22	−3.44	6.91	6.58	−0.51	−2.40	−1.91	−1.11	0.56
	70		1.71	0.71	2.33	−5.52	1.42	5.95	−0.67	−2.54	−1.89	−1.18	0.52

[a] *Depths represent the mid–point of a 10-cm-long screen.*

[b] *Charge balance.*

[c] *The chemical formulas for the minerals are as follows: amorphous iron oxide [$Fe(OH)_{3(a)}$], manganite [$MnO(OH)$], K-Jarosite [$KFe_3^{+3}(OH)_6(SO_4)_2$], schwertmannite [$Fe_8O_8(OH)_6(SO_4)\cdot nH_2O$], goethite [$Fe^{3+}O(OH)$], alunite [$KAl_3(SO_4)_2(OH)_6$], jurbanite [$AlSO4\cdot 5H_2O$], Al-oxide [$Al(OH)_{3(a)}$], gypsum ($CaSO_4$), and barite ($BaSO_4$).*

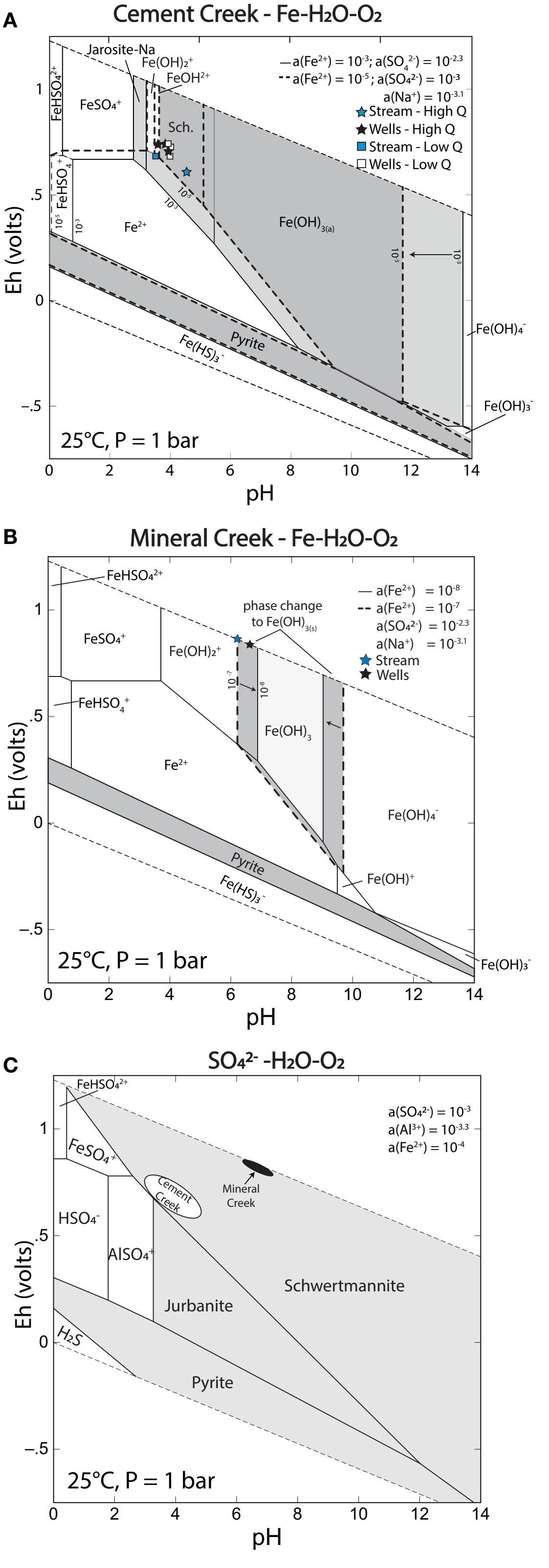

FIGURE 6 | Eh–pH diagrams calculated in Geochemist's Workbench for Fe at **(A)** Cement Creek and **(B)** Mineral Creek and for **(C)** SO_4^{2-} at Mineral Creek *(Continued)*

FIGURE 6 | and Cement Creek. Points on the stability diagrams represent the Eh and the pH of stream and hyporheic well cluster samples collected in 2019. Eh was calculated assuming that Fe^{2+} / Fe^{3+} was the dominant redox couple for Cement Creek and assuming that O_2 / O(0) was the dominant redox couple for Mineral Creek. The dashed lines represent contours for diagrams calculated using different molar concentrations of Fe for the range of concentrations measured in the streams and the wells.

differences in seasonal water chemistry in the Bonita Peak Mining District and is reflected in stream CQ relationships. First, the ratio of the load and discharge Gini coefficients (G_L / G_Q) for total and dissolved solutes at MC-Fen was nearly all 1 ± 0.2 (except for dissolved Ca and Fe), whereas the G_L / G_Q values for solutes at CC-PG were as low as 0.5–0.6 for metals such as As, Fe, and Al. This indicates that load inequality is dominated by discharge inequality at MC-Fen (i.e., relatively low variability in concentration compared to variability in discharge), whereas the load inequality is greater than the discharge inequality at CC-PG (i.e., high variability in concentration compared to discharge variability). We posit that this difference could be related to the fact that a greater number of draining mines with temporally heterogeneous flow contributions are located upstream of the Cement Creek reach, while the only large draining mine above the Mineral Creek reach is the Koehler Tunnel, which is bulkheaded and had minimal discharge during this study. Second, all solutes in both stream systems were moderately chemodynamic ($1.0 > CV_C / CV_Q > 0.2$) to chemodynamic ($b > \pm0.1$, $CV_C / CV_Q > 1.0$), and no solutes exhibited a purely chemostatic behavior with low concentration variability ($b < \pm0.1$, $CV_C / CV_Q < 0.2$). Cu and Pb in CC-PG and Mn and Pb in the MC-Fen were the only trace metal(loid)s with power-law slopes for dissolved species less than ±0.1 (**Table 6**), which indicates a chemostatic behavior. While the increase in flow dilutes all other metal concentrations, additional sources of Cu, Mn, and Pb that are only accessed at high flow may contribute to the stream channel to counteract dilution.

CQ trends for major elements (i.e., Ca^{2+}, Cl^-, Mg^{2+}, Na^+, SO_4^{2-}) were characterized by negative power law slopes at both CC-PG and MC-Fen, whereas power law slopes were positive for the redox-sensitive metals Fe, Al, Cu, and Mn at MC-Fen (i.e., $b > 0.1$, flushing behavior) and negative at CC-PG (i.e., $b < -0.1$, dilution behavior) (**Figure 9A** and **Supplementary Figure 8**, **Table 6**). The difference in trace metal(loid) power law slopes appears to be linked to differences in how metals are exported from the catchment at these two sites. In general for MC-Fen, the power law slopes for total Fe, Al, Cu, and Mn concentrations with dissolved, colloidal, and particulate material (unfiltered samples) were higher than the power law slopes of dissolved concentrations (filtered samples, <0.2 μm for our samples and <0.45 μm for historical data) (**Figure 9A**, **Table 6**). In contrast, the power law slopes for total and dissolved concentrations of these same metal(loid)s at CC-PG were similar (**Figure 9A**), indicating that metal transport in the dissolved phase is relatively more important at CC-PG

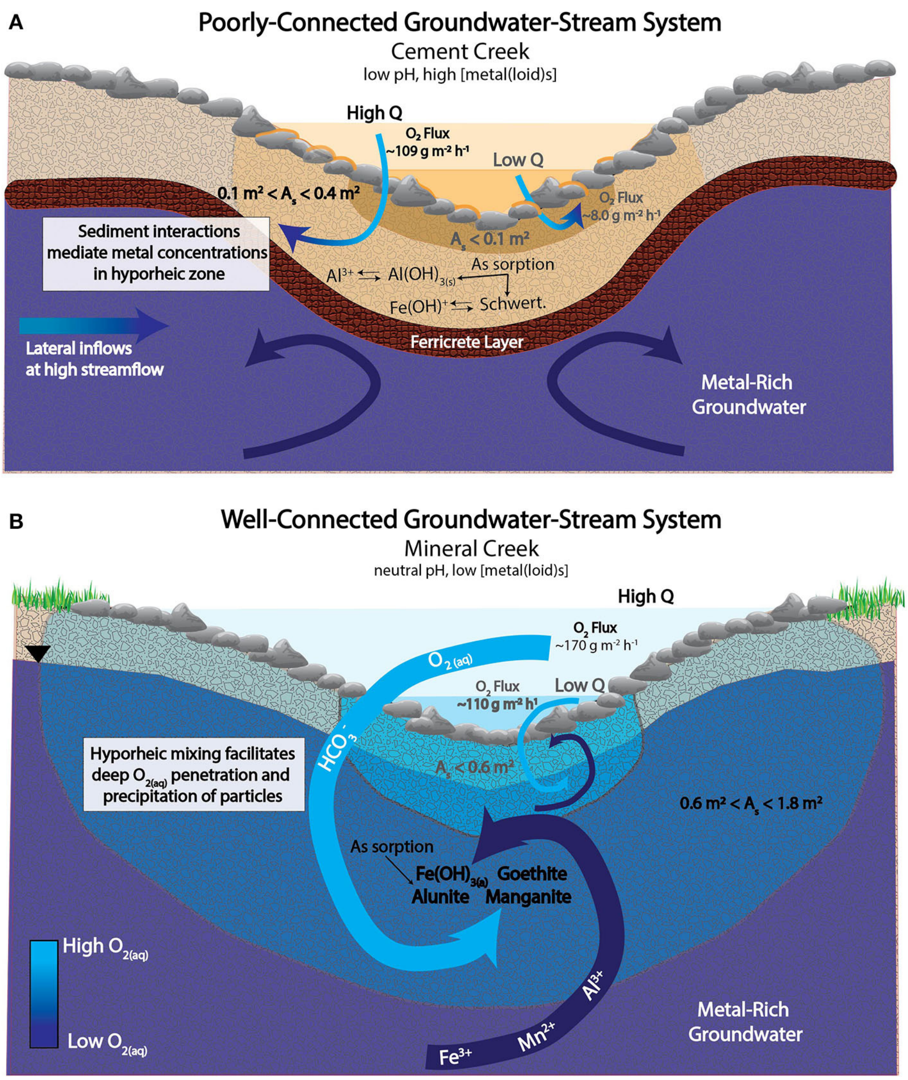

FIGURE 7 | Conceptual model for **(A)** a poorly connected stream–groundwater system at Cement Creek and **(B)** a well-connected groundwater–stream system at Mineral Creek. The color of the arrows corresponds to oxygen concentration, where light blue represents oxygenated waters and dark blue represents waters with low dissolved oxygen concentrations. The text in gray denotes low flow, and the text in black denotes high flow oxygen and transient storage conditions. The transient storage areas (A_S) for the poorly connected and well-connected conceptual models are bounded by one-dimensional transport with inflow and storage model estimates. The exchange rate was the same order of magnitude at high and low flow for both systems ($\alpha \sim 0.001$–0.005 s^{-1}).

compared to MC-Fen. We also observe a separation between MC-Fen and CC-PG when comparing the power law slopes to the ratio of dissolved-to-total metal concentrations (**Figure 9B**). Positive power law slopes were correlated with low concentration ratios of Al, Cu, Fe, and Mn at MC-Fen, suggesting that the flushing CQ behavior at MC-Fen may be linked to the accumulation of colloids and particulates in the subsurface during baseflow conditions that are accessed and transported to the stream at high flow. A relationship between flushing CQ behavior and concentration ratio was previously observed by Trostle et al. (2016), who found that metals, such as Al, with steeper, positive power law slopes were characterized by a lower ratio of dissolved-to-colloidal form of the metal, and thus these metals were more influenced by colloidal transport. In contrast, a correlation between negative power law slopes and high dissolved-to-total concentration ratios for CC-PG (**Figure 9B**) indicates that metals are transported primarily in the dissolved phase, and an additional source of colloidal or particulate metals is not contributing metals to the stream under high flow conditions.

Our findings indicate a link between stream–groundwater connectivity in the hyporheic zone (i.e., well-connected vs. poorly connected systems) and stream metal(loid) export at high flow and low flow. In the connected groundwater–stream system of Mineral Creek, colloids and particulates formed as a result of groundwater–surface water mixing in the hyporheic zone. For

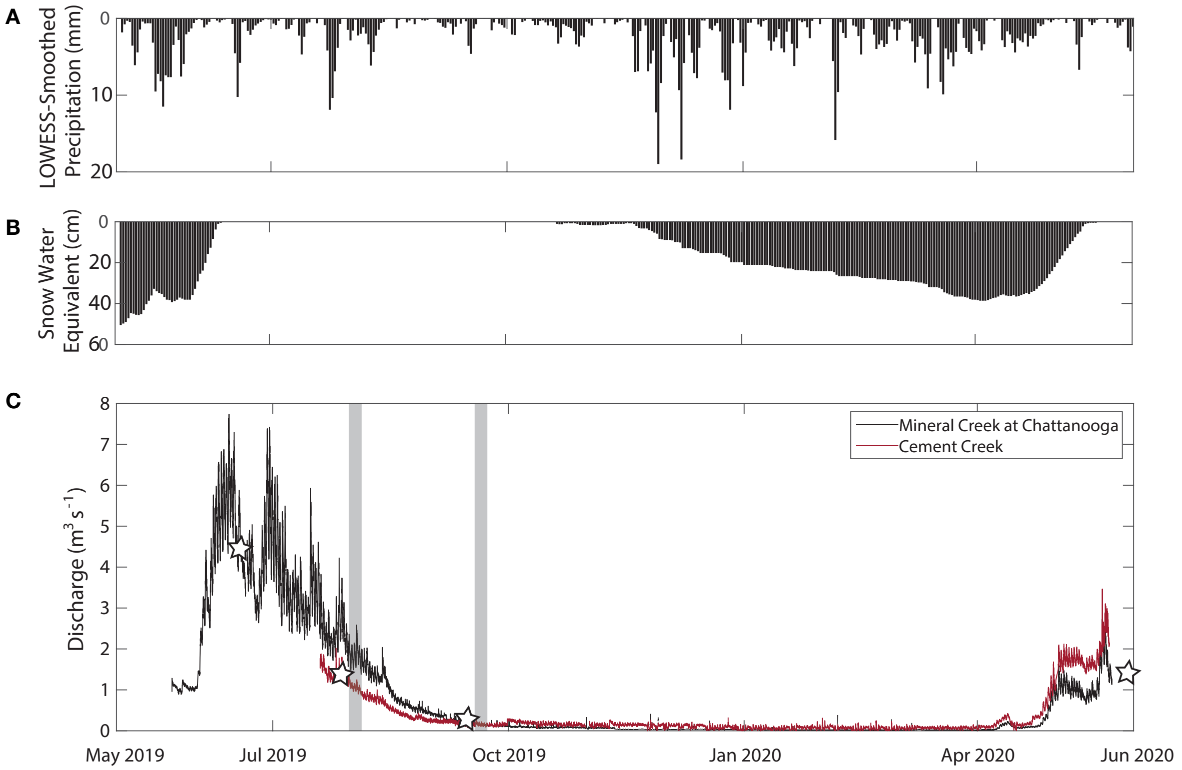

FIGURE 8 | (A) Precipitation from the Gladstone Treatment Plant smoothed using a RLOWESS filter with a filtering window of 3 days, **(B)** snow water equivalent data from the Mineral Creek SNOTEL site (USDA, 2020), and **(C)** hydrographs for the stilling wells installed in Mineral Creek near Chattanooga Fen and Cement Creek downstream of Prospect Gulch. The gray-shaded bars represent the period during which tracer tests were completed at high and low flows. The stars represent times of hyporheic zone well sampling.

Mineral Creek near Chattanooga Fen, the increase in hyporheic zone area at high flow compared to low flow (**Table 1**), the increase in total metal concentrations in the wells at high flow compared to low flow (**Figure 5**), and the lower concentration ratios of dissolved-to-total metals compared to CC-PG indicate that the flushing CQ behavior of Al, Cu, Fe, and Mn at high flow is linked to colloid and particle generation in the well-mixed hyporheic zone. Given the lack of stream–groundwater connection (**Figure 7A**), the small hyporheic area (**Table 1**), and the difference in dissolved metal concentrations in the stream and the hyporheic zone (**Figure 5**), we posit that the dilution-driven trends at CC-PG are not strongly influenced by hyporheic processes. The relatively greater influence of hyporheic processes on whole-stream mass transport at MC-Fen compared to CC-PG is further supported by calculations based on mass transfer estimates from the tracer test data. For example, the proportion of median travel time for a solute in the hyporheic zone (F_{med}) was lower for CC-PG compared to MC-Fen, indicating that reactions occurring within the hyporheic zone of CC-PG will have less influence on the metal concentrations in the stream (**Table 1**).

Potential Implications for Remediation

The contrast between hyporheic zone processes at these two sites located downstream of acid mine drainage has potential implications for approaches to remediation. The enhanced hyporheic mixing and invariant dissolved metal concentrations with depth at MC-Fen indicate that the initial concentrations of metal(loid)s in the infiltrating stream water are important. Given that the metal(loid) concentrations in the stream are well-mixed with the shallow subsurface, streams such as Mineral Creek would benefit from treatment of the stream itself. Furthermore, dissolved metal contributions to MC-Fen from upwelling groundwater or inflows from metal-rich iron fens are inhibited by precipitation of colloidal and particulate metals in the hyporheic zone. Although these colloidal and particulate metals may be supplied to the stream at high flow (**Figure 9A**), dissolved metals are naturally attenuated in the subsurface by mixing in the hyporheic zone at MC-Fen.

Dissolved metal(loid)s at depth in Cement Creek were not as sensitive to changes in streamflow as they were at Mineral Creek, and the small hyporheic zone at this site did not naturally remediate metals at CC-PG *via* surface water–groundwater mixing. The change in metal(loid) concentrations with depth was rather controlled by interactions with subsurface sediments. We posit that high Fe loads from metal-rich mine drainages in the upper portion of the Cement Creek watershed have contributed to ferricrete precipitation and the clogging of hyporheic pore spaces, which limits groundwater–surface water exchange and, in

TABLE 6 | Power law slopes (*b*) for concentration–discharge relationships for Mineral Creek and Cement Creek at two locations, including the standard error of the slope (s_b), coefficients of variation (CV), and Gini coefficients for concentration (G_L) normalized to the Gini coefficient for discharge (G_Q).

Filter size	Solute	Cement Creek–Prospect Gulch						Mineral Creek–Chattanooga Fen					
		n[a]	b[b]	s_b	CV_C / CV_Q[c]	G_L / G_Q[d]	R^2	n	b	s_b	CV_C / CV_Q	G_L / G_Q	R^2
Filtered (<0.2 and <0.45 μm)	As	18	−0.6	0.19	0.53	0.5	0.4	10	−0.33	0.19	0.70	1.2	0.1
	Al	18	−0.9	–	0.75	0.9	0.7	10	0.31	0.2	0.71	1.1	0.4
	Cu	18	0.06	0.17	0.55	1.2	0.0	10	0.22	0.11	0.46	1.2	0.4
	Fe	18	−0.9	–	0.75	0.5	0.7	10	0.53	0.32	1.03	1.3	0.4
	Mn	18	−0.4	0.37	0.92	0.9	0.2	10	0.10	0.15	0.51	1.0	0.1
	Pb	17	0.07	0.15	0.53	0.7	0.0	10	−0.08	0.11	0.32	0.9	0.1
	SO_4	17	−0.6	0.14	0.49	0.6	0.7	8	−0.64	0.17	1.03	0.9	0.7
	Zn	18	−0.3	0.3	0.78	0.7	0.3	10	−0.18	0.11	0.44	0.9	0.2
	Ca	18	−0.3	0.31	0.79	0.9	0.2	10	−0.60	0.11	0.85	0.6	0.7
	Cl	15	−0.6	0.43	0.84	0.9	0.2	8	−0.22	0.12	0.55	1.0	0.3
	Mg	18	−0.4	0.14	0.43	0.7	0.6	10	−0.28	0.06	0.42	0.9	0.7
	Si	18	−0.5	0.26	0.71	0.7	0.2	10	−0.13	0.15	0.55	1.0	0.1
Unfiltered	As	18	−0.4	0.12	0.42	0.8	0.5	10	−0.28	0.14	0.60	1.0	0.3
	Al	18	−0.9	–	0.79	0.6	0.7	10	0.55	0.22	0.76	1.1	0.4
	Cu	18	0.06	0.16	0.50	1.1	0.0	10	0.34	0.15	0.57	1.2	0.5
	Fe	18	−0.8	–	0.72	0.6	0.7	10	0.82	0.22	0.79	1.1	0.6
	Mn	18	−0.4	0.37	0.90	0.9	0.1	10	0.21	0.14	0.48	1.0	0.2
	Pb	17	0.28	0.26	0.63	1.3	0.2	10	0.19	0.2	0.70	1.1	0.1
	Zn	18	−0.3	0.29	0.75	0.8	0.3	10	−0.10	0.12	0.43	0.9	0.1
	Ca	18	−0.4	0.3	0.76	0.8	0.2	9	−0.55		0.79	0.8	0.7
	Mg	18	−0.5	0.11	0.40	0.6	0.7	9	−0.23	0.07	0.36	1.0	0.7
	Si	18	−0.6	–	0.72	0.6	0.2	9	−0.15	0.12	0.44	1.0	0.2

[a] *Number of observations.*

[b] *Power law slopes, s_b, and R^2 determined with MATLAB nlmfit function.*

[c] *Coefficient of variation calculated as the standard deviation divided by the mean of all samples.*

[d] *Gini coefficients calculated in R using "ineq" package.*

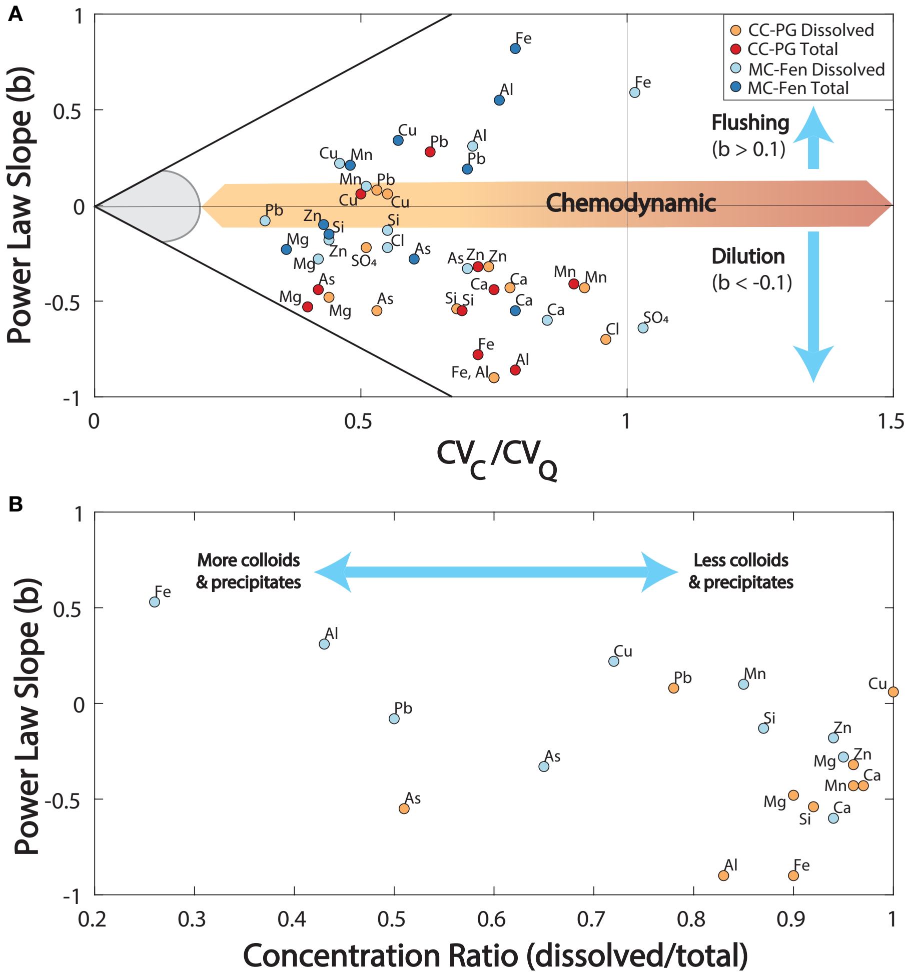

FIGURE 9 | (A) CV_C / CV_Q and power law slopes for redox-sensitive metals and major elements for the tracer study reaches and **(B)** power law slopes vs. the ratio of dissolved (<0.2 or <0.45 μm) and total (unfiltered) samples.

turn, concentrates toxic metal(loid)s in the shallow subsurface. We suggest that subsurface reactive barriers or removal of contaminated sediments will restore the ecosystem services provided by the hyporheic zone and help remove naturally occurring metals discharging from metal-rich groundwater to the stream, as well as anthropogenic metals infiltrating from the stream into the hyporheic zone. However, direct restoration of hyporheic sediments will not be effective unless iron loading from upstream draining mines is also reduced. Flow reduction from draining mines will decrease iron contributions to Cement Creek, which may, reduce ferricrete precipitation and clogging of the hyporheic zone. Even though Fe is not considered as toxic a metal as As, Al, Cd, or Zn, which are the primary foci of remediation efforts in the Bonita Peak Mining District, our study suggests that treatment of Fe is equally important given the effect it has on the physical structure of the hyporheic zone at Cement Creek.

The transient storage model OTIS, in combination with geochemical data from the hyporheic zone well clusters, highlighted distinct differences in metal fate and transport at Mineral and Cement Creeks, yet the parameters estimated in OTIS do not necessarily capture the full complexity of physical and chemical processes occurring in the hyporheic zone, particularly for highly advective streams such as Mineral Creek. Future work could implement multi-rate mass transfer models (e.g., Fang et al., 2020), physical and advective models that consider channel morphology (e.g., Cardenas and Wilson, 2007; Marzadri et al., 2012, 2013; Boano et al., 2014), or coupled reactive transport-hyporheic models (Zarnetske et al., 2012; Trauth et al., 2014) to understand finer-scale processes affecting the metal dynamics in poorly connected and well-connected stream–groundwater systems.

CONCLUSIONS

The goal of this study was to determine how the hyporheic zone influences metal export in streams impacted by acid mine drainage. By comparing the hydrogeochemical properties of two streams in the Animas River headwaters of southwestern Colorado, we discovered differences in how the form and function of the hyporheic zone influence the concentrations of redox-sensitive metal(loid)s in mine-impacted and acid rock drainage streams. The key findings highlighted in this study include:

(i) The stream system with low average linear velocities and less permeable sediments (Cement Creek) was characterized by relatively small hyporheic zone areas at low flow and high flow, whereas the system with high average linear velocities and more permeable sediments (Mineral Creek) was characterized by relatively large hyporheic areas that were sensitive to changes in stream discharge.

(ii) Mass transfer rates from OTIS modeling and conservative element behavior in the well clusters reflected the degree of connection between the stream and the groundwater in the hyporheic zone. Mineral Creek represented a well-connected groundwater–stream system, facilitated by a large hyporheic storage area and invariable conservative element concentrations as a function of depth. Cement Creek represented a poorly connected groundwater–stream system, where hyporheic area and low hydraulic conductivities were limited by ferricrete precipitation. Conservative element concentrations were insensitive to changes in streamflow in the deep subsurface compared to the stream and shallow subsurface.

(iii) Saturation indices and Eh–pH diagrams indicated that Al and Fe were buffered by mineral equilibria at Cement Creek, and the sediment–dissolved metal(loid) interactions in this poorly connected system were a more important regulator of metal concentrations than physical mixing of water within the hyporheic zone. Colloid and particulate precipitation in Mineral Creek were due to the extensive mixing of oxygen-rich stream water and metal-rich groundwater in the hyporheic zone.

(iv) Differences in groundwater–stream connectivity at these two sites impacted stream metal(loid) export, as highlighted by concentration–discharge relationships. Positive power law slopes were linked to colloidal and particulate metal formation in the hyporheic zone at Mineral Creek. The poorly connected groundwater–stream system of Cement Creek was less important for overall stream metal(loid) export, and negative chemodynamic power law slopes reflect the influence of hillslope flow contributions on CQ rather than in-stream processes.

These differences in hyporheic zone characteristics and groundwater–stream connectivity can inform localized approaches to treatment. Even though Mineral Creek was downstream and adjacent to metal-rich sources (i.e., a mine drainage and iron fen), the neutral pH and low metal concentrations in the stream reflected the pH and the metal concentrations in the hyporheic zone. Thus, streams such as this with geochemically well-mixed hyporheic zones already benefit from the natural attenuation of metals in the subsurface, such that remediation efforts could focus on stream water treatment. The small hyporheic zone and poorly connected groundwater–stream system at Cement Creek did not attenuate metals in the subsurface and did not appear to influence stream metal(loid) export. Metals such as Fe and Al concentrated in the subsurface as a result of interactions with metal-laden sediments. Poorly connected systems such as these would benefit from remediation of the shallow subsurface and removal or treatment of sediments.

DATA AVAILABILITY STATEMENT

The original contributions presented in the study are included in the article/**Supplementary Materials**, further inquiries can be directed to the corresponding author/s.

AUTHOR CONTRIBUTIONS

BH designed, led the field experiments, data collection, laboratory analyses, data processing/modeling, and the writing of this manuscript. RC contributed to site selection and field sampling. RC, AN-S, and KS contributed to the editing and data analysis within this manuscript. AN-S, KS, and BH acquired funding to carry out this project. All authors contributed to the article and approved the submitted version.

FUNDING

Financial support for this study was provided by the National Science Foundation Earth Sciences Postdoctoral Fellowship program [grant no. 1806718]. Any opinions, findings, and conclusions or recommendations expressed in this material are those of the authors and do not necessarily reflect the views of the National Science Foundation.

ACKNOWLEDGMENTS

We would like to acknowledge the extensive help with field work provided by Kendall Wnuk, Jackie Randell, Ariel Rickel, Sawyer McFadden, and Luke Jacobsen at the Colorado School of Mines, Nate Rock at Mountain Studies Institute, and Stefan Klingler from the University of Tubingen. Additional thanks go to Rob Runkel with the US Geological Survey and Peter Butler with the Animas River Stakeholders Group for an introduction to the field area and help in identifying field sites. We would like to acknowledge and thank Lisa Merrill and Andrew Breibart at the Bureau of Land Management, as well as Benerito Martinez and Lewis Sovocool at the US Forest Service, for help with the permitting process and for access to the site.

SUPPLEMENTARY MATERIAL

The Supplementary Material for this article can be found online at: https://www.frontiersin.org/articles/10.3389/frwa.2020.600409/full#supplementary-material

Streamflow data for Mineral and Cement Creek referenced in this paper can be found on Hydroshare: https://doi.org/10.4211/hs.c9ef6ecde25640d4bd4c7a9c50575016.

REFERENCES

Alpers, C. N., Nordstrom, D. K., Verosub, K. L., and Helm-Clark, C. (2007). Paleomagnetic determination of pre-mining metal-flux rates at the Iron Mountain Superfund Site, Northern California. *Eos Trans. Jt. Assem. Suppl. Abstr.* 88, AGU-10194685.

Anthony, J. W., and McLean, W. J. (1976). Jurbanite, a new post-mine aluminum sulfate mineral from San Manuel, Arizona. *Am. Min.* 61, 1–4.

Ball, J. W., and Nordstrom, D. K. (1987). *User's Manual for WATEQ4F, With Revised Thermodynamic Data Base and Text Cases for Calculating Speciation of Major, Trace, and Redox Elements in Natural Waters*. U.S. Geological Survey. doi: 10.3133/ofr91183

Bencala, K. E. (2011). "Stream-groundwater interactions," in *Treatise on Water Science*, ed. P. Wilderer (Oxford: Academic Press), 537–546. doi: 10.1016/B978-0-444-53199-5.00115-9

Benner, S. G., Smart, E. W., and Moore, J. N. (1995). Metal behavior during surface-groundwater interaction, silver bow Creek, Montana. *Environ. Sci. Technol.* 29, 1789–1795. doi: 10.1021/es00007a015

Bigham, J. M., Schwertmann, U., Carlson, L., and Murad, E. (1990). A poorly crystallized oxyhydroxysulfate of iron formed by bacterial oxidation of Fe(II) in acid mine waters. *Geochim. Cosmochim. Acta* 54, 2743–2758. doi: 10.1016/0016-7037(90)90009-A

Boano, F., Harvey, J. W., Marion, A., Packman, A. I., Revelli, R., Ridolfi, L., et al. (2014). Hyporheic flow and transport processes: mechanisms, models, and biogeochemical implications. *Rev. Geophys.* 52, 603–679. doi: 10.1002/2012RG000417

Borch, T., Kretzschmar, R., Skappler, A., Van Cappellen, P., Ginder-Vogel, M., Voegelin, A., et al. (2010). Biogeochemical redox processes and their impact on contaminant dynamics. *Environ. Sci. Technol.* 44, 15–23. doi: 10.1021/es9026248

Bouwer, H., and Rice, R. C. (1976). A slug test for determining hydraulic conductivity of unconfined aquifers with completely or partially penetrating wells. *Water Resour. Res.* 12, 423–428. doi: 10.1029/WR012i003p00423

Bove, D. J., Mast, M., Dalton, J., Wright, W., and Yager, D. (2007). "Chapter E3: Major styles of mineralization and hydrothermal alteration and related solid- and aqueous-phase geochemical signatures," in *US Geological Survey Professional Paper 1651*, vol. 1, eds S. E. Church, P. von Guerard and S. E. Finger (Reston, VA).

Brown, B. V., Valett, H. M., and Schreiber, M. E. (2007). Arsenic transport in groundwater, surface water, and the hyporheic zone of a mine-influenced stream-aquifer system. *Water Resour. Res.* 43, 1–14. doi: 10.1029/2006WR005687

Bryant, S. R., Sawyer, A. H., Briggs, M. A., Saup, C. M., Nelson, A. R., Wilkins, M. J., et al. (2020). Seasonal manganese transport in the hyporheic zone of a snowmelt-dominated river (East River, Colorado, USA). *Hydrogeol. J.* 28, 1323–1341. doi: 10.1007/s10040-020-02146-6

Buxton, H. T., Nimich, D. A., von Guerard, P., Church, S. E., Frazier, A., Gray, J. R., et al. (1997). A science-based, watershed strategy to support effective remediation of abandoned mine lands. in *Proceedings of the Fourth International Conference on Acid Rock Drainage* (Vancouver, BC), 1869–1880.

Cardenas, M. B., and Wilson, J. L. (2007). Exchange across a sediment-water interface with ambient groundwater discharge. *J. Hydrol.* 346, 69–80. doi: 10.1016/j.jhydrol.2007.08.019

Chimner, R. A., Lemly, J. M., and Cooper, D. J. (2010). Mountain fen distribution, types and restoration priorities, San Juan Mountains, Colorado, USA. *Wetlands* 30, 763–771. doi: 10.1007/s13157-010-0039-5

Clesceri, L. S., Greenberg, A., and Eaton, A. (1999). *Standards for the Examination of Water and Wastewater, 20th ed.* Washington, DC: American Public Health Association.

Cowie, R., and Roberts, S. (2020). *Bonita Peak Mining District 2016-2018 Seeps, Springs, and Draining Mines Characterization Report*. Denver, CO: U.S. Environmental Protection Agency, 1–481.

Danczak, R. E., Sawyer, A. H., Williams, K. H., Stegen, J. C., Hobson, C., and Wilkins, M. J. (2016). Seasonal hyporheic dynamics control coupled microbiology and geochemistry in colorado river sediments. *J. Geophys. Res. Biogeosci.* 121, 2976–2987. doi: 10.1002/2016JG003527

Day, T. J. (1977). Field procedures and evaluation of a slug dilution gauging method in mountain streams. *J. Hydrol.* 16, 113–133.

Doherty, J. (2010) *PEST, Model-Independent Parameter Estimation—User Manual*. 5th Edn. Brisbane: Watermark Numerical Computing.

Fang, Y., Chen, X., Velez, J. G., Zhang, X., Duan, Z., Hammond, G. E., et al. (2020). A multirate mass transfer model to represent the interaction of multicomponent biogeochemical processes between surface water and hyporheic zones (SWAT-MRMT-R 1.0). *Geosci. Model Dev.* 13, 3553–3569. doi: 10.5194/gmd-13-3553-2020

Fattorini, D., Notti, A., Di Mento, R., Cicero, A. M., Gabellini, M., Russo, A., et al. (2008). Seasonal, spatial and inter-annual variations of trace metals in mussels from the adriatic sea: a regional gradient for arsenic and implications for monitoring the impact of off-shore activities. *Chemosphere* 72, 1524–1533. doi: 10.1016/j.chemosphere.2008.04.071

Feris, K. P., Ramsey, P. W., Frazar, C., Rillig, M., Moore, J. N., Gannon, J. E., et al. (2004). Seasonal dynamics of shallow-hyporheic-zone microbial community structure along a heavy-metal contamination gradient. *Appl. Environ. Microbiol.* 70, 2323–2331. doi: 10.1128/AEM.70.4.2323-2331.2004

Findlay, S. E. G., Sinsabaugh, R. L., Sobczak, W. V., and Hoostal, M. (2003). Metabolic and structural response of hyporheic microbial communities to variations in supply of dissolved organic matter. *Limnol. Oceanogr.* 48, 1608–1617. doi: 10.4319/lo.2003.48.4.1608

Fischer, H., Kloep, F., Wilzcek, S., and Pusch, M. T. (2005). A river's liver: microbial processes within the hyporheic zone of a large lowland river. *Biogeochemistry* 76, 349–371. doi: 10.1007/s10533-005-6896-y

Gall, H. E., Park, J., Harman, C. J., Jawitz, J. W., and Rao, P. S. C. (2013). Landscape filtering of hydrologic and biogeochemical responses in managed catchments. *Landsc. Ecol.* 28, 651–664. doi: 10.1007/s10980-012-9829-x

Gandy, C. J., Smith, J. W. N., and Jarvis, A. P. (2007). Attenuation of mining-derived pollutants in the hyporheic zone: a review. *Sci. Total Environ.* 373, 435–446. doi: 10.1016/j.scitotenv.2006.11.004

Godsey, S. E., Kirchner, J. W., and Clow, D. W. (2009). Concentration-discharge relationships reflect chemostatic characteristics of US catchments. *Hydrol. Process.* 23, 1844–1864. doi: 10.1002/hyp.7315

Guerard, P., Von Church, S. E., Yager, D. B., and Besser, J. M. (2004). "Chapter B: The animas river watershed, San Juan County, Colorado," in *US Geological Survey Professional Paper 1651*, vol. 1, eds S. E. Church, P. von Guerard and S. E. Finger (San Juan County, Colorado).

Harvey, J. W., and Fuller, C. C. (1998). Effect of enhanced manganese oxidation in the hyporheic zone on basin-scale geochemical mass balance. *Water Resour. Res.* 34, 623–636. doi: 10.1029/97WR03606

Hatch, C. E., Fisher, A. T., Revenaugh, J. S., Constantz, J., and Ruehl, C. (2006). Quantifying surface water-groundwater interactions using time series analysis of streambed thermal records: method development. *Water Resour. Res.* 42, 1–14. doi: 10.1029/2005WR004787

Hatch, C. E., Fisher, A. T., Ruehl, C. R., and Stemler, G. (2010). Spatial and temporal variations in streambed hydraulic conductivity quantified with time-series thermal methods. *J. Hydrol.* 389, 276–288. doi: 10.1016/j.jhydrol.2010.05.046

Hester, E. T., and Doyle, M. W. (2008). In-stream geomorphic structures as drivers of hyporheic exchange. *Water Resour. Res.* 44:5810. doi: 10.1029/2006WR005810

Hoagland, B., Russo, T. A., Gu, X., Hill, L., Kaye, J., Forsythe, B., et al. (2017). Hyporheic zone influences on concentration-discharge relationships in a headwater sandstone stream. *Water Resour. Res.* 53, 4643–4667. doi: 10.1002/2016WR019717

Horton, J., and San Juan, C. A. (2020). *Prospect- and mine-related features from U.S. Geological Survey 7.5- and 15-minute topographic quadrangle maps of the United States. U.S. Geol. Surv. data release* ver. 5.0. doi: 10.5066/F78W3CHG

Howard, A. G., Comber, S. D. W., Kifle, D., Antai, E. E., and Purdie, D. A. (1995). Arsenic speciation and seasonal changes in nutrient availability and micro-plankton abundance in southampton water, U.K. *Estuar. Coast. Shelf Sci.* 40, 435–450. doi: 10.1006/ecss.1995.0030

Hudson-Edwards, K. (2016). Tackling mine wastes. *Science* 352, 288–290. doi: 10.1126/science.aaf3354

Jawitz, J. W., and Mitchell, J. (2011). Temporal inequality in catchment discharge and solute export. *Water Resour. Res.* 47, 1–16. doi: 10.1029/2010WR010197

Johnson, B. R. H., Wirt, L., Manning, A. H., Leib, K. J., Fey, D. L., Douglas, B., et al. (2007). *In cooperation with the bureau of land management geochemistry of surface and ground water in Cement Creek from Gladstone to Georgia Gulch* *and in Prospect Gulch*. San Juan County, Colorado: U.S. Geological Survey. doi: 10.3133/ofr20071004

Kasahara, T., and Hill, A. R. (2007). Lateral hyporheic zone chemistry in an artificially constructed gravel bar and a re-meandered stream channel, Southern Ontario, Canada. *J. Am. Water Resour. Assoc.* 43, 1257–1269. doi: 10.1111/j.1752-1688.2007.00108.x

Marzadri, A., Tonina, D., and Bellin, A. (2012). Morphodynamic controls on redox conditions and on nitrogen dynamics within the hyporheic zone: application to gravel bed rivers with alternate-bar morphology. *J. Geophys. Res. Biogeosci.* 117, 1–14. doi: 10.1029/2012JG001966

Marzadri, A., Tonina, D., and Bellin, A. (2013). Effects of stream morphodynamics on hyporheic zone thermal regime. *Water Resour. Res.* 49, 2287–2302. doi: 10.1002/wrcr.20199

Miller, M. P., McKnight, D. M., Cory, R. M., Williams, M. W., and Runkel, R. L. (2006). Hyporheic exchange and fulvic acid redox reactions in an alpine stream/wetland ecosystem, Colorado front range. *Environ. Sci. Technol.* 40, 5943–5949. doi: 10.1021/es060635j

Morrice, J. A., Valett, H. M., Dahm, C. N., and Campana, M. E. (1997). Alluvial characteristics, groundwater-surface water exchange and hydrological retention in headwater streams. *Hydrol. Process.* 11, 253–267. doi: 10.1002/(SICI)1099-1085(19970315)11:3<253::AID-HYP439>3.0.CO;2-J

Musolff, A., Schmidt, C., Selle, B., and Fleckenstein, J. H. (2015). Catchment controls on solute export. *Adv. Water Resour.* 86, 133–146. doi: 10.1016/j.advwatres.2015.09.026

Nagorski, S. A., and Moore, J. N. (1999). Arsenic mobilization in the hyporheic zone of a stream. *Hydrogeochem. Water Chem.* 35, 3441–3450. doi: 10.1029/1999WR900204

Nagorski, S. A., Moore, J. N., McKinnon, T. E., and Smith, D. B. (2003). Geochemical response to variable streamflow conditions in contaminated and uncontaminated streams. *Water Resour. Res.* 39:1247. doi: 10.1029/2001WR001247

Nelson, A. R., Sawyer, A. H., Gabor, R. S., Saup, C. M., Bryant, S. R., Harris, K. D., et al. (2019). Heterogeneity in hyporheic flow, pore water chemistry, and microbial community composition in an alpine streambed. *J. Geophys. Res. Biogeosci.* 124, 3465–3478. doi: 10.1029/2019JG005226

NIDIS (2020). North American Drought Monitor (NADM). *Natl. Integr. Drought Inf. Syst*. Available online at: https://www.drought.gov/drought/data-gallery/north-american-drought-monitor-nadm (accessed April 1, 2020).

Nordstrom, D. K. (2011). Mine waters: acidic to circmneutral. *Elements* 7, 393–398. doi: 10.2113/gselements.7.6.393

Parkhurst, D. L., and Appelo, C. A. J. (2013). PHREEQC (Version 3)-A computer program for speciation, batch-reaction, one-dimensional transport, and inverse geochemical calculations. *Model. Tech. B* 6:497. doi: 10.3133/tm6A43

Rodriguez-Freire, L., Avasarala, S., Ali, A. M. S., Agnew, D., Hoover, J. H., Artyushkova, K., et al. (2016). Post gold king mine spill investigation of metal stability in water and sediments of the animas river watershed. *Environ. Sci. Technol.* 50, 11539–11548. doi: 10.1021/acs.est.6b03092

Runkel, R. (1998). *One-Dimensional Transport with Inflow and Storage: A Solute Transport Model for Streams and Rivers*. Denver, CO: U.S. Geological Survey.

Runkel, R. L. (2002). A new metric for determining the importance of transient storage. *J. North Am. Benthol. Soc.* 21, 529–543. doi: 10.2307/1468428

Runkel, R. L., Bencala, K. E., Kimball, B. A., Walton-day, K., and Verplanck, P. L. (2009a). A comparison of pre- and post-remediation water quality. *Hydrol. Process.* 23, 3319–3333. doi: 10.1002/hyp.7427

Runkel, R. L., and Kimball, B. A. (2002). Evaluating remedial alternatives for an acid mine drainage stream: application of a reactive transport model. *Environ. Sci. Technol.* 36, 1093–1101. doi: 10.1021/es0109794

Runkel, R. L., Kimball, B. R., Steiger, J. I., and Walton-day, K. (2009b). Geochemical data for upper Mineral Creek, Colorado, under existing ambient conditions and during an experimental pH modification, August 2005. *U. S. Geol. Surv. Data Ser.* 442:41. doi: 10.3133/ds442

Saup, C. M., Bryant, S. R., Nelson, A. R., Harris, K. D., Sawyer, A. H., Christensen, J. N., et al. (2019). Hyporheic zone microbiome assembly is linked to dynamic water mixing patterns in snowmelt-dominated headwater catchments. *J. Geophys. Res. Biogeosci.* 124, 3269–3280. doi: 10.1029/2019JG005189

Saup, C. M., Williams, K. H., Rodríguez-Freire, L., Cerrato, J. M., Johnston, M. D., and Wilkins, M. J. (2017). Anoxia stimulates microbially catalyzed metal release from animas river sediments. *Environ. Sci. Process. Impacts* 19, 578–585. doi: 10.1039/C7EM00036G

Schwertmann, U. (1991). Solubility and dissolution of iron oxides. *Plant Soil* 130, 1–25. doi: 10.1007/BF00011851

Sherrell, R. M., and Ross, J. M. (1999). Temporal variability of trace metals in New Jersey Pinelands streams: relationships to discharge and pH. *Geochim. Cosmochim. Acta* 63, 3321–3336. doi: 10.1016/S0016-7037(99)00254-9

Singley, J. G., Wlostowski, A. N., Bergstrom, A. J., Sokol, E. R., Torrens, C. L., Jaros, C., et al. (2017). Characterizing hyporheic exchange processes using high-frequency electrical conductivity-discharge relationships on subhourly to interannual timescales. *Water Resour. Res.* 53, 4124–4141. doi: 10.1002/2016WR019739

Smedley, P. L., and Kinniburgh, D. G. (2002). A review of the source, behaviour and distribution of arsenic in natural waters. *Appl. Geochem.* 17, 517–568. doi: 10.1016/S0883-2927(02)00018-5

Smith, C. (2018). *Interim Remedial Actions Bonita Peak Mining District Superfund.* San Juan County, Colorado; Denver, CO: U.S. Environmental Protection Agency.

Stanton, M., Yager, D., Fey, D., and Wright, W. (2007). "Chapter E14: Formation and geochemical significance of iron bog deposits," in *US Geological Survey Professional Paper 1651*, vol. 2, eds S. E. Church, P. von Guerard and S. E. Finge (Reston, VA), 693–718.

Thompson, S. E., Basu, N. B., Lascurain, J., Aubeneau, A., and Rao, P. S. C. (2011). Relative dominance of hydrologic versus biogeochemical factors on solute export across impact gradients. *Water Resour. Res.* 47, 1–20. doi: 10.1029/2010WR009605

Trauth, N., Schmidt, C., Vieweg, M., Maier, U., and Fleckenstein, J. H. (2014). Hyporheic transport and biogeochemical reactions in pool-riffle systems under varying ambient groundwater flow conditions. *J. Geophys. Res. Biogeosci.* 119, 910–928. doi: 10.1002/2013JG002586

Trostle, K. D., Runyon, J. R., Pohlmann, M. A., Redfield, S. E., Pelletier, J., McIntosh, J., et al. (2016). Colloids and organic matter complexation control trace metal concentration-discharge relationships in Marshall Gulch stream waters. *Water Resour. Res.* 52, 7931–7944. doi: 10.1002/2016W.R.019072

USDA (2020). SNOwpack TELemetry Network (SNOTEL). *Nat. Resour. Conserv. Serv*. Available online at: https://www.nrcs.usda.gov/wps/portal/nrcs/detail/co/snow/?cid=nrcs144p2_063325 (accessed April 20, 2020).

USEPA (2010). *Low stress (low flow) purging and sampling procedure for the collection of groundwater samples from monitoring wells*. North Chelmsford, MA: US Environmental Protection Agency. 30.

USEPA (2016). *One year after the Gold King Mine Incident: A Retrospective of EPA's Efforts to Restore and Protect Impacted Communities*. U.S. Environmental Protection Agency. Available online at: https://www.epa.gov/sites/production/files/2016-08/documents/mstanislausgkm1yrreportwhole8-1-16.pdf

USEPA (2017). *Sampling Activities Report: 2017 Sampling Events, Bonita Peak Mining District Site San Juan/La Plata Counties, Colorado Final*. Denver, CO: U.S. Environmental Protection Agency.

USGS (2020). National Water Information System data available on the World Wide Web (USGS Water Data for the Nation). *U.S. Geol. Surv.* Available online at: https://waterdata.usgs.gov/co/nwis/uv/?site_no=09358550&agency_cd=USGS (accessed April 4, 2020).

Vincent, K. R., Church, S. E., and Wirt, L. (2007). "Chapter E16: Geomorphology of cement creek and its relation to ferricrete deposits," in *US Geological Survey Professional Paper 1651*, Vol. 2, eds S. E. Church, P. von Guerard and S. E. Finger (Reston, VA), 747–772.

Wagner, B. J., and Harvey, J. W. (1997). Experimental design for estimating parameters of rate-limited mass transfer: analysis of stream tracer studies. *Water Resour. Res.* 33, 1731–1741. doi: 10.1029/97WR01067

Walton-Day, K., Paschke, S. S., Runkel, R. L., and Kimball, B. A. (2007). "Chapter E24: Using the OTIS solute-transport model to evaluate remediation scenarios in cement creek and the upper animas river," in *US Geological Survey Professional Paper 1651*, Vol. 2, eds S. E. Church, P. von Guerard and S. E. Finger (Reston, VA), 979–1028.

Weber, F. A., Hofacker, A. F., Voegelin, A., and Kretzschmar, R. (2010). Temperature dependence and coupling of iron and arsenic reduction and release during flooding of a contaminated soil. *Environ. Sci. Technol.* 44, 116–122. doi: 10.1021/es902100h

Wirt, L., Vincent, K. R., Verplanck, P. L., Yager, D. B., Church, S. E., and Fey, D. L. (2007). "Chapter E17: Geochemical and hydrologic processes controlling formation of ferricrete, in *US Geological Survey Professional Paper 1651*, Vol. 2, eds S. E. Church, P. von Guerard and S. E. Finger.

Wondzell, S. M. (2006). Effect of morphology and discharge on hyporheic exchange flows in two small streams in the cascade mountains of Oregon, USA. *Hydrol. Process.* 20, 267–287. doi: 10.1002/hyp.5902

Yager, D. B., and Bove, D. J. (2007). "Chapter E1: Geologic framework," in *US Geological Survey Professional Paper 1651*, Vol. 2, eds S. E. Church, P. von Guerard and S. E. Finger (Reston, VA), 111–137.

Zarnetske, J. P., Haggerty, R., Wondzell, S. M., Bokil, V. A., and González-Pinzón, R. (2012). Coupled transport and reaction kinetics control the nitrate source-sink function of hyporheic zones. *Water Resour. Res.* 48, 1–15. doi: 10.1029/2012WR011894

Conflict of Interest: RC was employed by company Alpine Water Resources, LLC.

The remaining authors declare that the research was conducted in the absence of any commercial or financial relationships that could be construed as a potential conflict of interest.

frontiers
in Water

ORIGINAL RESEARCH
published: 01 February 2021
doi: 10.3389/frwa.2020.575216

Combining Uranium, Boron, and Strontium Isotope Ratios ($^{234}U/^{238}U$, $\delta^{11}B$, $^{87}Sr/^{86}Sr$) to Trace and Quantify Salinity Contributions to Rio Grande River in Southwestern United States

Sandra Garcia[1], *Pascale Louvat*[2], *Jerome Gaillardet*[2], *Syprose Nyachoti*[1] *and Lin Ma*[1]*

[1] Department of Geological Sciences, University of Texas at El Paso, El Paso, TX, United States, [2] Institut de Physique du Globe de Paris, Paris, France

Edited by:
Carl I. Steefel,
Lawrence Berkeley National Laboratory, United States

Reviewed by:
John Neil Christensen,
Lawrence Berkeley National Laboratory, United States
Thai Phan,
University of Waterloo, Canada
Nathaniel R. Warner,
Pennsylvania State University (PSU), United States

****Correspondence:***
Lin Ma
lma@utep.edu

Specialty section:
This article was submitted to Water and Critical Zone, a section of the journal Frontiers in Water

Received: *22 June 2020*
Accepted: *31 December 2020*
Published: *01 February 2021*

Citation:
Garcia S, Louvat P, Gaillardet J, Nyachoti S and Ma L (2021) Combining Uranium, Boron, and Strontium Isotope Ratios ($^{234}U/^{238}U$, $\delta^{11}B$, $^{87}Sr/^{86}Sr$) to Trace and Quantify Salinity Contributions to Rio Grande River in Southwestern United States. Front. Water 2:575216. doi: 10.3389/frwa.2020.575216

In semi-arid to arid regions, both anthropogenic sources (urban and agriculture) and deeper Critical Zone (groundwater with long flow paths and water residence times) may play an important role in controlling chemical exports to rivers. Here, we combined two anthropogenic isotope tracers: uranium isotope ratios ($^{234}U/^{238}U$) and boron isotope ratios ($\delta^{11}B$), with the $^{87}Sr/^{86}Sr$ ratios to identify and quantify multiple solute (salinity) sources in the Rio Grande river in southern New Mexico and western Texas. The Rio Grande river is a major source of freshwater for irrigation and municipal uses in southwestern United States. There has been a large disagreement about the dominant salinity sources to the Rio Grande and particularly significant sources are of anthropogenic (agriculture practices and shallow groundwater flows, groundwater pumping, and urban developments) and/or geological (natural groundwater upwelling) origins. Between 2014 and 2016, we collected monthly river samples at 15 locations along a 200-km stretch of the Rio Grande river from Elephant Butte Reservoir, New Mexico to El Paso, Texas, as well as water samples from agricultural canals and drains, urban effluents and drains, and groundwater wells. Our study shows that due to the presence of localized and multiple salinity inputs, total dissolved solids (TDS) and isotope ratios of U, B, and Sr in the Rio Grande river show high spatial and temporal variability. Several agricultural, urban, and geological sources of salinity in the Rio Grande watershed have characteristic and distinguishable U, Sr, and B isotope signatures. However, due to the common issue of overlapping signatures as identified by previous tracer studies (such as $\delta^{18}O$, δD, $\delta^{34}S$), no single isotope tracer of U, Sr, or B isotopes was powerful enough to distinguish multiple salinity sources. Here, combining the multiple U, Sr, and B isotope and elemental signatures, we applied a multi-tracer mass balance approach to quantify the relative contributions of water mass from the identified various salinity end members along the 200-km stretch of the Rio Grande during different river flow seasons. Our results show that during irrigation (high river flow) seasons, the Rio Grande had uniform chemical and isotopic compositions, similar to the Elephant Butte reservoir where water is stored and well-mixed, reflecting the dominant contribution from shallow Critical Zone in headwater regions in temperate southern Colorado and northern New Mexico.

In non-irrigation (low flow) seasons when the river water is stored at Elephant Butte reservoir, the Rio Grande river at many downstream locations showed heterogeneous chemical and isotopic compositions, reflecting variable inputs from upwelling of groundwater (deeper CZ), displacement of shallow groundwater, agricultural return flows, and urban effluents. Our study highlights the needs of using multi-tracer approach to investigate multiple solutes and salinity sources in rivers with complex geology and human impacts.

Keywords: uranium isotopes, boron isotopes, strontium isotopes, Rio Grande watershed, river salinity, mass balance, salinity contribution

INTRODUCTION

The Critical Zone, extending from surface vegetation and shallow soils to deeper permeable bedrock, provides chemical constituents to rivers and controls water quality (Brantley et al., 2006). Chemical fluxes to river systems may originate in soils via physical and biogeochemical processes as well as water-bedrock (saprolite) interactions in the shallow Critical Zone. However, these processes may have a limited role in exporting solutes to rivers in semi-arid to arid regions due to low amounts of rainfall and soil moisture. The deeper Critical Zone with long ground water flow paths and travel times may serve as an important solute contributor to river systems in these regions. Natural processes from the deeper Critical Zone such as upwelling of saline groundwater and dissolution of evaporites can significantly increase the salinity of arid rivers (e.g., Allison et al., 1990; Meybeck, 2003; Phillips et al., 2003; Hogan et al., 2007; Szynkiewicz et al., 2015a). Furthermore, human activities, such as dam construction, agricultural practices (e.g., irrigation, fertilizer/pesticide applications), groundwater pumping, and urbanization, have significantly modified the hydrologic cycle with respect to both water quantity and quality (e.g., Chetelat and Gaillardet, 2005; Lyons et al., 2012; National Research Council, 2012; Chen et al., 2014). Elevated salinity of rivers is an increasing concern for sustainable water management, especially for semi-arid to arid regions (Ghassemi et al., 1995; Postel, 1999; Johnson et al., 2001; Farber et al., 2004). While identifying sources of salinity in arid rivers is essential for the development of effective remediation strategies, it still remains a challenging task due to the lack of effective geochemical tools to distinguish multiple salinity sources of natural and human origins. Previous salinity tracers (e.g., major elemental concentrations and ratios, light stable isotope ratios such as $\delta^{34}S$, $\delta^{18}O$, and δD) have shown overlapping signatures for multiple salinity end members (e.g., Szynkiewicz et al., 2011, 2015b).

In this study, we explored the potential of combining uranium, boron and strontium isotopic tracers ($^{234}U/^{238}U$, $\delta^{11}B$, $^{87}Sr/^{86}Sr$) to distinguish and quantify contributions from anthropogenic and natural processes that lead to salt loads in a semi-arid portion of the Rio Grande as well as in shallow groundwater aquifers. In particular, uranium isotope ratios ($^{234}U/^{238}U$) can be a potentially effective tracer in identifying salinity inputs from agricultural activities due to the high contents of natural U in phosphorous fertilizers and their distinctive secular equilibrium activity ratio (1.0) in fertilizers (e.g., Zielinski et al., 1995, 1997, 2000). Boron isotope ratios ($\delta^{11}B$) are useful in distinguishing urban salinity sources due to its high concentration in municipal wastewater and characteristic isotope ratios (e.g., Chetelat and Gaillardet, 2005). Strontium isotope ratios ($^{87}Sr/^{86}Sr$) have been shown to be effective in distinguishing water-rock interaction from various types of sedimentary and crystalline rocks (e.g., Brown et al., 2010). Despite that there may be overlapping signatures of single isotope tracer of U, B, and Sr for different salinity sources, our study aims at demonstrating that a multiple-isotope (U, B, and Sr) approach is a powerful tool in tracing and quantifying salinity inputs in arid rivers such as groundwater upwelling/pumping, agriculture, and urban activities. This study also highlights the effective use of ($^{234}U/^{238}U$) ratios to trace salinity related to agricultural practices.

Furthermore, our study focused on the Rio Grande river in the Southwestern United States (U.S.), a major river system experiencing high salt loads due to its semi-arid climate, complex in geological settings, and impacts from agriculture and population centers. In this study area, over two million of residents of southern New Mexico and western Texas rely on the Rio Grande for irrigation of cropland and municipal uses. In this region, average total dissolved solids (TDS) of the Rio Grande vary seasonally, remaining at relatively low values (∼500 to 700 mg/L) during the spring-summer irrigation season and often reaching > ∼2,000 mg/L during the fall-winter months when river flow is significantly reduced due to regulation by Elephant Butte Reservoir. The use of water with elevated salinity for irrigation has caused reduction of crop productivity and significant salt loading of soils (Ghassemi et al., 1995; Postel, 1999). Therefore, it has been a pressing issue to understand the origins of the elevated salinity in the semi-arid portions of the Rio Grande. This study improves our understanding of how human activity effects water quality and elemental cycles in a semi-arid river. As the studied region of the Rio Grande watershed faces many of the same water pressures as in other arid regions around the world, our multi-tracer approach has a potential to develop effective environmental tracers for similar river and aquifer systems elsewhere.

RIO GRANDE WATERSHED

General Settings

The Rio Grande is the fifth longest river in the U.S. and among the top twenty of the world. The Rio Grande originates in south-central Colorado and its main water source is from snowmelt in the Rocky Mountains (**Figure 1**; Ellis et al., 1993; Moore et al., 2008). The Rio Grande river water is currently distributed to three states (Colorado, New Mexico, Texas) and two countries (U.S. and Mexico; Water 2025: Preventing Crisis and Conflict in the West, 2005; Alley, 2013). Rapid population growth in this region has led to increasing demand for freshwater (Wong et al., 2012; Sheng, 2013). The Rio Grande river may soon reach tipping points with respect to both freshwater quality and availability under current scenarios of climate changes and population growth (Swetnam and Betancourt, 1998; Phillips et al., 2003, 2011; Seager et al., 2007; Gutzler and Robbins, 2010). Consequently, the U.S. Department of Interior has identified the Rio Grande region as having the highest potential for conflict and crisis among any U.S. river systems.

The studied stretch of the Rio Grande is located in southern New Mexico and western Texas, flowing through the Rio Grande Valley along a series of rift basins filled with alluvial, fluvial, playa and lacustrine sediments (**Figure 1**; Phillips et al., 2003; Szynkiewicz et al., 2011). The climate in the study area is semi-arid to arid, with hot summers (mean air temperature in June ∼28°C) and mild winters (mean air temperature in January ∼8°C). For Elephant Butte reservoir, New Mexico and El Paso, Texas (**Figure 2**), the annual rainfall averages ∼250 and 300 mm, respectively, with most of the rainfall occurring during the late summer months as monsoons (Miyamoto et al., 1995).

Rio Grande Water Uses

In the study area, water from the Rio Grande is mainly used to irrigate ∼193,000 acres of agricultural land (∼800 km^2) within the Hatch and Mesilla Valley irrigation districts (Garfin et al., 2013) (**Figure 1A**). Downstream from El Paso, TX, Rio Grande water is used to irrigate additional agricultural land in the Hueco Basin in Texas and Mexico. Water for irrigation is delivered through an interconnected system of dams, reservoirs, canals, and drains (commonly known as the Rio Grande project). In the study area, the Rio Grande river flows are regulated by Elephant Butte and Caballo Reservoirs, which generally store river water during fall and winter months (November through February, or non-irrigation seasons) and release water to downstream users during spring and summer (March through October, or irrigation seasons). Consequently, Rio Grande river flows vary significantly between irrigation and non-irrigation seasons as a result of considerable human impacts on the local hydrological cycle (Moyer et al., 2013). The river flows at downstream locations are high in spring and summer months but significantly reduced in fall and winter months. At some locations the riverbed can be completely dry for several months. Most of the low flows during non-irrigation seasons have been attributed to seepage from reservoirs, groundwater base flows, irrigation return flows, and effluents from wastewater treatment plants near large cities and population centers (Moore et al., 2008).

Multiple Sources of Solute and Salinity in Rio Grande Watershed

Previous investigations have identified multiple salinity sources to the Rio Grande but there is a general disagreement about which source is dominant. Upwelling of deep groundwater has been suggested as important salinity source at distal ends of alluvial basins where groundwater is inferred to flow upward due to uplifted basement blocks (**Figure 1B**; Moore and Anderholm, 2002; Phillips et al., 2003; Hogan et al., 2007; Moore et al., 2008; Williams et al., 2013). However, in the semi-arid region, the Rio Grande is a losing stream in most of southern New Mexico and western Texas (Driscoll and Sherson, 2016), and in dry years the Rio Grande channel completely dries out for several months during non-irrigation seasons. In addition, intense pumping of the groundwater has led to significant decreases of the groundwater table. These observations raise the question of the importance of the natural upwelling of saline groundwater in these alluvial basins as a dominant mechanism of direct input into the Rio Grande.

Other studies have suggested possible sources of salinity related to agricultural activities (e.g., evapotranspiration from agricultural field and return flows, displacement of shallow groundwater, irrigation use of groundwater, and application of fertilizers), urban/industrial inputs (e.g., point sources of treated or non-treated waste effluents), and shallow geological sources (e.g., dissolution of secondary evaporites in soil zones, and shallow brackish groundwater) (**Figure 1B**; Lippincott, 1939; Haney and Bendixen, 1953; Wilcox, 1957; Ellis et al., 1993; Moore and Anderholm, 2002; Phillips et al., 2003; Witcher et al., 2004; Hogan et al., 2007; Szynkiewicz et al., 2011; Moyer et al., 2013; Driscoll and Sherson, 2016).

Groundwater is another important source of irrigation water in this region particularly in drought years to supplement shortages of Rio Grande surface water. While elevated salinity values in some local groundwater is usually due to long residence time in sedimentary and crystalline bedrock in this region, evapotranspiration associated with agricultural fields has been suggested to increase salinity in irrigation return flows that in turn recharge to shallow groundwater underneath agricultural areas (Walton et al., 1999). It is unclear, however, whether there are additional important salinity inputs to shallow groundwater from other sources such as application of fertilizers on agricultural fields, and urban effluents discharging directly to the Rio Grande or infiltrating to shallow aquifers (**Figure 1B**).

METHODS

Description of Sample Locations

We selected fifteen locations (RG-1 to RG-15) along a ∼200 km-stretch of Rio Grande, from Elephant Butte Reservoir in southern New Mexico to State Highway 273 in the city of El Paso, Texas for river sample collection (**Figure 2**; **Appendix Table 1**). The water in the Elephant Butte reservoir (RG-1) is the source of river water in this region and represents a "baseline" for salinity investigations. Locations RG-2 (Williamsburg) and RG-3 (Percha Dam) have some agricultural activities but less than further downstream locations. RG-2 and 3 are located in an area with many reported natural occurrences of hot springs and geothermal activity (e.g., Williams et al., 2013; Pepin et al., 2015). However, local spa resorts near Location RG-2 may also lead to human-induced discharge of highly saline, geothermal groundwater sourced from artesian wells (Szynkiewicz et al.,

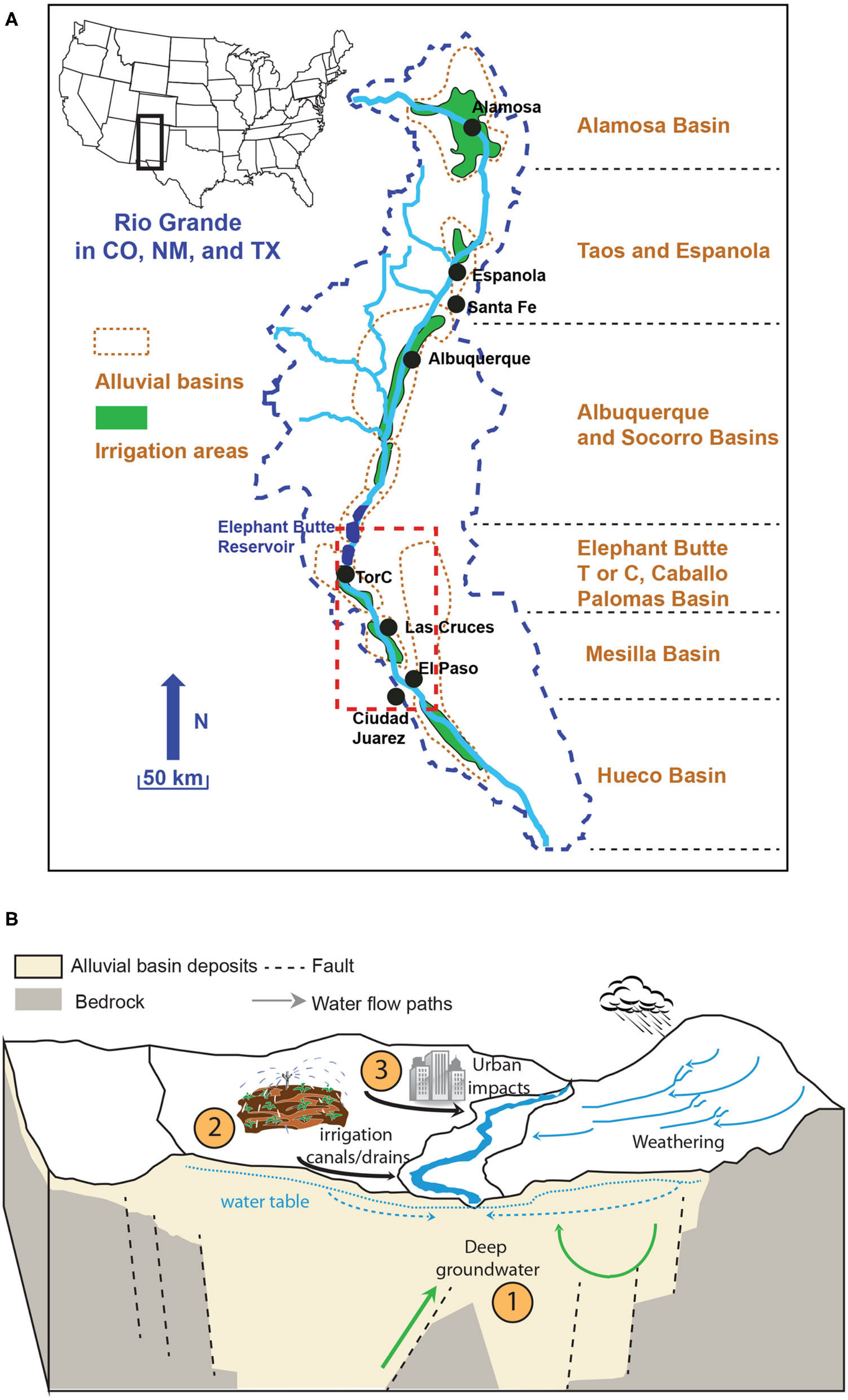

FIGURE 1 | (A) The Rio Grande Watershed in Colorado, New Mexico and Texas (after Phillips et al., 2003; Hogan et al., 2007; Szynkiewicz et al., 2011). Major alluvial basins, cities, and irrigation areas along the river are indicated. Red dashed box indicates the detailed study area shown in **Figure 2**; **(B)** A simplified block model of multiple salinity sources in the Rio Grande Watershed. Natural and anthropogenic processes (numbers highlighted in closed circles) are included: (1) upwelling of deep groundwater and geothermal water; (2) agriculture water; and (3) urban activities. Chemical weathering is also an important process to control solute and salinity input but plays a limited role in semi-arid and arid regions.

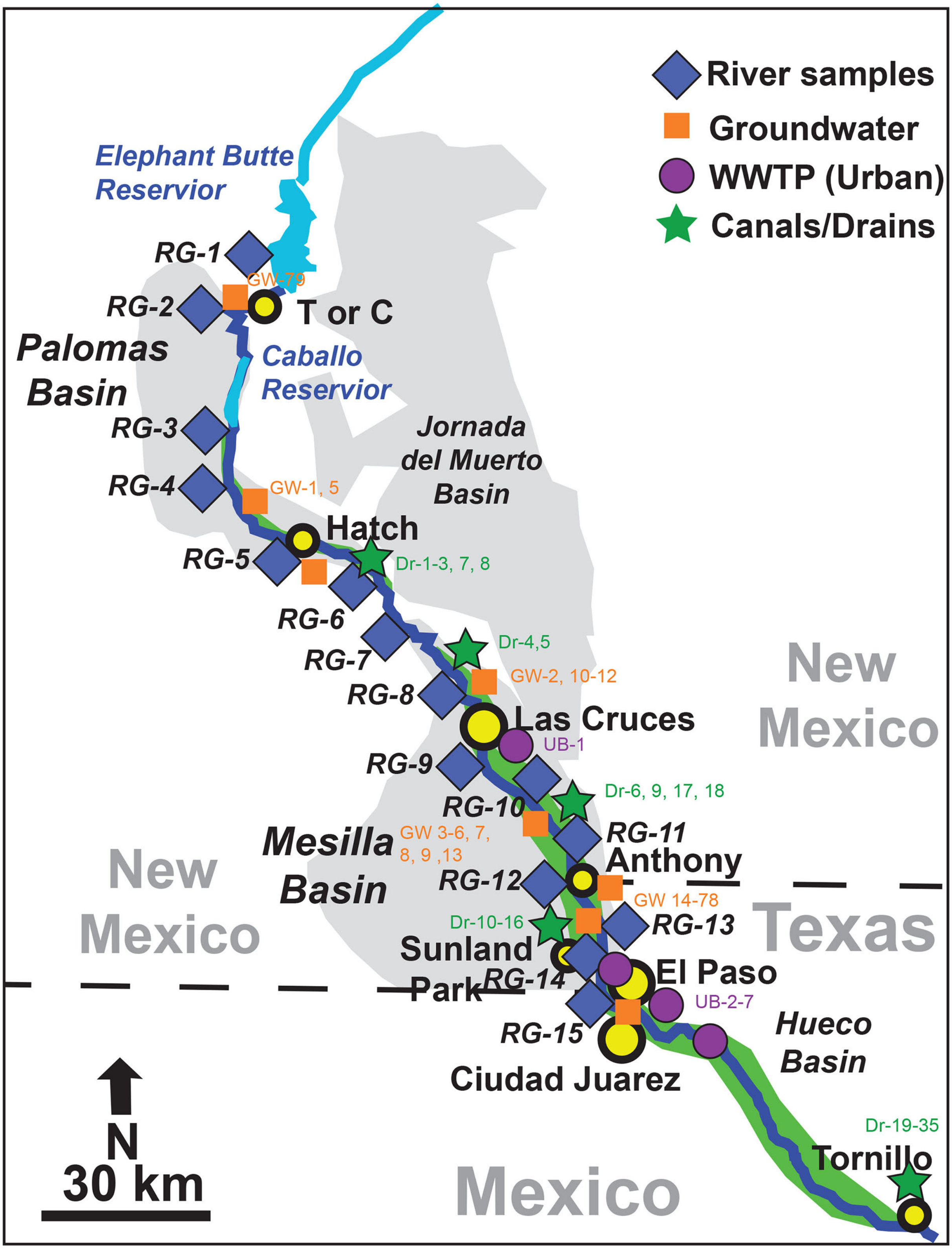

FIGURE 2 | The ∼200 km stretch of the Rio Grande from Elephant Butte reservoir in NM to El Paso, TX. Sample locations for river water, groundwater wells, agricultural canals and drains, and urban water (wastewater treatment plants: WWTP) are indicated. Details of sample location information is in **Appendix Table 1**.

2015b) and there is also effluent inflow into the Rio Grande at RG-2 from a nearby wastewater treatment plant. Locations RG-4 through RG-7 are along the Hatch and Mesilla Valley irrigation districts in the southern Palomas Basin and Mesilla Basin. Locations RG-8 through RG-11 are in close proximity to the city of Las Cruces, a relatively large urban area in southern New Mexico (population ∼100,000) with one WWTP (UB-1) located below RG-8. Locations RG-12 through RG-15 are located between Anthony, New Mexico and El Paso, Texas (population ∼800,000) near the distal end of the Mesilla Basin where plausible upwelling of highly saline groundwater to the Rio Grande has been previously suggested (e.g., Phillips et al., 2003; Hogan et al., 2007). However, there may be also inflow of saline water originating from shallow groundwater of the salt flat intersected by Montoya Drain near El Paso, which conveys return flows to the Rio Grande from nearby irrigation districts (Szynkiewicz et al., 2015b). At these 15 sampling sites, a total of ∼200 river samples were collected monthly between 2014 and 2016 for elemental and isotopic analyses.

In this study, we also sampled 79 groundwater wells (GW-1–GW-79), 7 waste effluents from the cities of Las Cruces (UB-1), Sunland Park (UB-4), and El Paso (UB-2, 3, 5, 6, 7), and 35 irrigation canals/drains (DR-1–DR-35) along the studied stretch of the Rio Grande (**Figure 2**; **Appendix Table 1**). It is noted that due to the nature of population distribution in this region, many of the groundwater, urban, and agricultural samples were from the Messila Basin in the south while samples from the north study area were limited. Available archived samples from Szynkiewicz et al. (2015b) were also included to determine signatures of an agricultural drain near Tornillo, Texas which combines return flows from downstream irrigation districts located below the city of El Paso (**Figure 2**). Two archived samples (Szynkiewicz et al., 2011, 2015b) of shallow saline groundwater from monitoring piezometers near Fabens, Texas, one archived sample from an artesian well with geothermal groundwater near Truth or Consequences, New Mexico, and two shallow groundwater samples from private wells near Anthony, New Mexico were also included for isotope analysis. Finally, several archived samples of commonly used fertilizers in the region were also analyzed for U, B, and Sr isotope composition (Szynkiewicz et al., 2015b).

Water Sample Collection

Water samples were collected into 1L acid washed HDPE Nalgene bottles. Field measurements of pH, temperature, and electric conductivity were taken *in situ* during sample collection using a YSI Professional Plus multimeter, which was calibrated prior to sampling. The samples were stored in a cooler for ∼5–6 h before arrival to the laboratory. In the laboratory, ∼400 mL of each water sample was filtered using a 0.45 μm cellulose acetate filter to remove suspended sediment and particulates, and the filtered water was placed in two 250 mL acid washed HDPE Nalgene bottles. One bottle was acidified with 3 drops of ultrapure concentrated nitric acid for cation and isotope analysis, and the second bottle was archived without acidification for immediate anion analysis. The samples were stored at 4°C in the refrigerator before analysis.

Major and Trace Element Analysis

For major cation concentrations (Na, Ca, Si, K, and Mg), the acidified water sample was analyzed on a Perkin Elmer 5300DV Optical Emission Spectrometer (OES) at University of Texas at El Paso (UTEP). Two water standards (USGS M-210 and NIST 1640a) were analyzed at least 3–5 times during each analytical session to assess analytical precision of cations. The analytical precision was estimated to be better than 10% for major cations.

For major anion concentrations (Cl, SO_4, and NO_3), the non-acidified filtered sample was analyzed using a Dionex ICS-2100 at UTEP. An in-house water standard was measured at least twice during each analytical session to ensure accuracy. In general, the analytical precision of anions for the standards used was better than 12%. A selected number of samples were measured for alkalinity by the titration method. For the rest of samples, their alkalinity values were calculated based on the mass charge balance of the analyzed major chemical species.

A subset of samples was analyzed for trace element concentrations (U, B, and Sr) with a Thermo Fisher Scientific X Series 2 ICP-MS at the Pennsylvania State University Laboratory for Isotopes and Metals in the Environment (LIME). The NIST water standard (NIST 1640a) was used to assess accuracy. Analytical error was between 1 and 11%. In this study, only U, B, and Sr concentrations are reported and discussed. More details of the analytical methods for major and trace elements are reported in Nyachoti (2016) and Garcia (2017).

Uranium Isotope Analysis

Uranium isotopic ratios, $^{234}U/^{238}U$, were measured for a subset of 116 river and other types of water samples at UTEP. A minimum of 50 ng of U was used to carry out U isotope analysis. The volume needed to obtain 50 ng of U was calculated using U concentrations [U] with trace elements analysis carried out at LIME. Samples were evaporated overnight at 90°C in a class-100 clean room. U column chemistry followed a procedure similar to Chabaux et al. (1995).

Purified U samples were analyzed on a Nu Plasma HR MC-ICP-MS at UTEP to determine $^{234}U/^{238}U$ isotopic ratios with the uranium standard (NBL145B) for standard-sample-standard bracketing. The estimated errors (2SE) of the isotope ratios were better than 0.5%. From the measured isotope ratios of $^{234}U/^{238}U$, we calculated ($^{234}U/^{238}U$) activity ratios (here the parenthesis specifies the activity ratio) using decay half-lives of ^{234}U and ^{238}U (Cheng et al., 2000). The USGS rock standard BCR-2 was processed along with column chemistry and measured multiple times to ensure accuracy of measurements: average measured ($^{234}U/^{238}U$) activity ratio is 1.004 ± 0.002 (2SE, $n = 10$), consistent with the expected ($^{234}U/^{238}U$) activity ratio at equilibrium (1.0). The procedure blank for U was ∼30 pg and negligible.

Boron Isotope Analysis

A total of 45 representative water samples (river and other types of water samples) were selected for B isotope analysis at the Institut de Physique du Globe de Paris (IPGP) in France. The measurements were made with the procedure described in Louvat et al. (2010, 2014). The procedure required ∼300 ng of boron and the final solution to be at 200 ng/mL of B for isotope analysis. For samples with high salinity, the sample was diluted with 5 mL of 18 MΩ water to prevent clogging of the column.

The purified B samples were analyzed on a Neptune MC-ICP-MS at IPGP using a direct injection high efficiency nebulization (d-DIHEN) method developed by Louvat et al. (2014) to measure boron isotopic ratios. Each sample was measured three times. The standard reference material SRM 951 was used at the sample concentration for standard-sample bracketing. The boric acid reference material AE121 was measured 8 times to assess accuracy and precision (19.44 ± 0.07%, 2 SD). The North Atlantic Surface Seawater (NASS-5) standard was also processed along with the samples (39.55 ± 0.15%, $N = 2$; in agreement with Louvat et al., 2014).

Strontium Isotope Analysis

A total of 106 river and other types of water samples were selected for $^{87}Sr/^{86}Sr$ isotope analysis at UTEP. Around 25 ml of water samples were evaporated to dryness, the dried samples were re-dissolved in 3.5 N HNO_3 then separated and purified through Sr-Spec resin. The purified samples were measured for $^{87}Sr/^{86}Sr$ ratios on MC-ICP-MS using the standard-sample bracketing method with NIST SRM 987 as the standard bracketing solution (Konter and Storm, 2014). About 200 mg of rock standard BCR2 was acid-digested in HNO_3-HF and HCl-H_3BO_3 then separated through Sr-Spec resin. $^{87}Sr/^{86}Sr$ ratios in BCR2 reported an average value of 0.70502 ± 0.00001 (2σ; $N = 5$) consistent with values reported in the literature (0.70502; Raczek et al., 2003). Blanks for Sr analysis (∼82 pg) are negligible.

RESULTS

Our study focuses on the salinity (TDS) and chemical and isotopic compositions of U, Sr, and B observed in Rio Grande river samples for both irrigation and non-irrigation seasons as well as in different possible salinity end members (groundwater, agricultural water, and urban water). Salinity (TDS values converted from field measurements of electric conductivity) and major elemental concentrations (Na, Ca, Mg, K, Si, Cl, SO_4, and NO_3) from this study are archived at the EarthChem Library (http://dx.doi.org/10.1594/IEDA/111231). Concentrations and isotopic compositions of U, Sr, and B obtained in this study are presented in **Appendix Table 2**.

Water Salinity and Major Chemistry

In general, salinity values in the Rio Grande river in our study area vary both spatially and temporally. Between May 2014 and May 2016, the measured TDS values of the Elephant Butte Reservoir water (EBR: RG-1) showed a narrow range of 450 to 630 mg/L (average: 550 ± 60 mg/L; $n = 15$; **Figure 3**). In contrast, TDS values of the Rio Grande at downstream locations showed much greater variability. More specifically, under high flow conditions from April to July, Rio Grande water (RG-2 to RG-15) had TDS values ranging from ∼450 to 840 mg/L (**Figure 3**). Higher TDS values (e.g., 840 mg/L) were generally observed in close proximity to agricultural areas and large urban centers (e.g., between RG-4 and RG-15). Under low flow conditions from August to March, Rio Grande water below EBR showed a large variability of TDS values from ∼370 to 5000 mg/L (**Figure 3**). The highest TDS values (up to ∼5,000 mg/L) was observed in close proximity to both Truth or Consequences (RG-2) and west El Paso (RG-15). The lowest TDS values (e.g., 370 mg/L) were observed near urban areas (RG-5 and RG-11).

Major elemental concentrations for the Rio Grande river samples between May 2014 and May 2016 (http://dx.doi.org/10.1594/IEDA/111231) were used to calculate water chemistry types and saturation indices (SI) by Nyachoti (2016) and Garcia (2017). The main results are summarized here. The EBR (RG-1) water was largely the Ca-Na-HCO_3-SO_4 type during both irrigation and non-irrigation seasons. The downstream Rio Grande sites during the irrigation seasons were also dominated by the Ca-Na-HCO_3-SO_4 type. During the non-irrigation seasons, the water types at the downstream locations were more variable, including Ca-Na-HCO_3-SO_4 (RG-3, 4, 6), Na-Ca-SO_4-HCO_3 (RG-5, 7, 8), Na-Cl-SO_4 (RG-9, 14, 15), and Na-Cl types (RG-2). These variable water types at downstream locations are mostly related to the contributions of additional Na, Ca, Cl, and SO_4 sources that lead to changes of the Ca-Na-HCO_3-SO_4 type from upstream. According to the calculated SI values (Nyachoti, 2016; Garcia, 2017), all river water samples between May 2014 and May 2016 were saturated with respect to calcite and dolomite and under-saturated with respect to gypsum, halite, and thenardite. The degree of saturation (SI values) for calcite and dolomite increases from RG-1 to RG-15 while the SI values for gypsum and halite show higher values for selected locations (RG-2, 6, 7, and 15).

The salinity of Rio Grande river at downstream locations to RG-1 is impacted by possible salinity end members from geological, agricultural, and urban sources. The groundwater, agricultural canal/drain water, and treated wastewater samples from this study showed highly variable TDS values: 320–16,900, 550–4,300 mg/L, 780–1,554 mg/L, respectively (**Figure 3**). The water types of these end-member samples were also highly variable, mostly overlapping with the water types of the Rio Grande. The groundwater and agricultural canal/ drains had mainly Ca-HCO_3-SO_4, Ca-Na-HCO_3-SO_4, Na-SO_4, and Na-Cl water types, and the dominant water type in the urban wastewater was Ca-Na-Cl-SO_4 (Nyachoti, 2016; Garcia, 2017). It is noted that as a limitation of the study's approach to assess the end member salinity sources, the sample locations for the groundwater, agricultural canal/drain, and wastewater treatment plants are largely restricted to the nature of the distribution of population and agricultural centers that is centered along the river in the southern study area and only with a limited number of sample locations from the northern study area.

Uranium Concentrations and ($^{234}U/^{238}U$) Ratios

Generally, the measured U concentrations in the Rio Grande water samples (∼0.6 to 10 μg/L) are considered to be higher than U concentrations of other major rivers (Chabaux et al.,

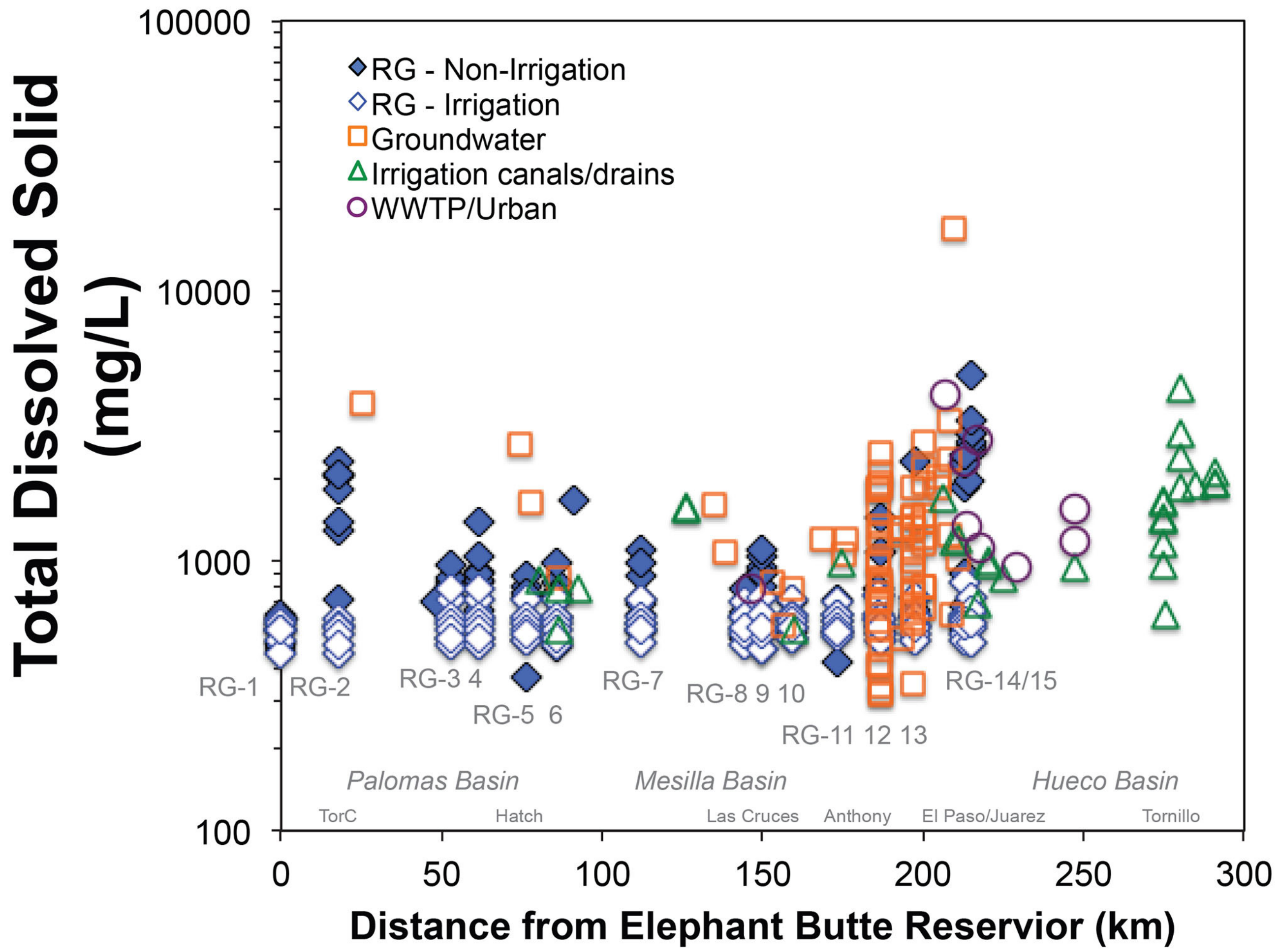

FIGURE 3 | Total dissolved solids (mg/L) in Rio Grande river water, groundwater, agricultural canals and drains, and urban water (wastewater treatment plants: WWTP). The Rio Grande river water is classified into non-irrigation and irrigation seasons. The sample locations are placed with distance (km) from Elephant Butte Reservoir along the Rio Grande. Major cities and alluvial basins are indicated.

2003) and the average U concentration of ocean water (~3 µg/L; Drever, 1997). Similar to the observations of the TDS values, the Rio Grande river water had less variable U concentrations during the irrigation seasons (~2 to 4 µg/L) and large variability during the non-irrigation seasons (~0.6 to 10 µg/L) (**Appendix Table 2**). There is a positive correlation between U and HCO_3 concentrations in Rio Grande river samples (**Figure 4**). Noticeably, elevated U concentrations were observed during non-irrigation seasons mostly near agricultural areas and urban areas in Palomas and Hueco Basin (RG-3, 4, 15; **Figure 5A**). The lowest U concentrations in the Rio Grande were observed during non-irrigation season below the inflows of urban effluents (RG-9 and RG-14) as well as in several agricultural areas in Mesilla Basin (RG-7) (**Figure 5**). This observation is consistent with lower U concentrations measured in the urban effluents in this study (<0.1 to 2 µg/L; **Figure 5A**). By contrast, agricultural drains in this study generally have elevated U concentrations (~2 to 12 µg/L). The groundwater samples showed the most variations in U concentrations among the end-member samples, between <0.1 to 95 µg/L.

During irrigation seasons, the measured $(^{234}U/^{238}U)$ ratios of the Rio Grande river water showed a narrow range between 1.7 and 1.8, similar to the Elephant Butte reservoir water (**Figure 5B**). During non-irrigation season the $(^{234}U/^{238}U)$ ratios of Rio Grande showed much greater variations, with higher ratios (2.0 to 2.5) in locations RG-2, RG-3 and RG-4, in proximity to Truth or Consequences and Caballo Reservoir, and lower ratios (1.5 to 1.6) in locations RG-6, RG-9, RG-14, and RG-15, mostly observed near large agricultural and urban areas (**Figure 5B**). Noticeably, agricultural canals and drains showed characteristically lower $(^{234}U/^{238}U)$ ratios (~1.1 to 1.6) compared to the Rio Grande. The urban wastewater had slightly higher $(^{234}U/^{238}U)$ ratios (1.5 to 1.9) and mostly similar to the Rio Grande river water. The studied groundwater samples showed a large range of $(^{234}U/^{238}U)$ ratios (~1.2 to 2.7). Significantly higher $(^{234}U/^{238}U)$ ratios in groundwater were

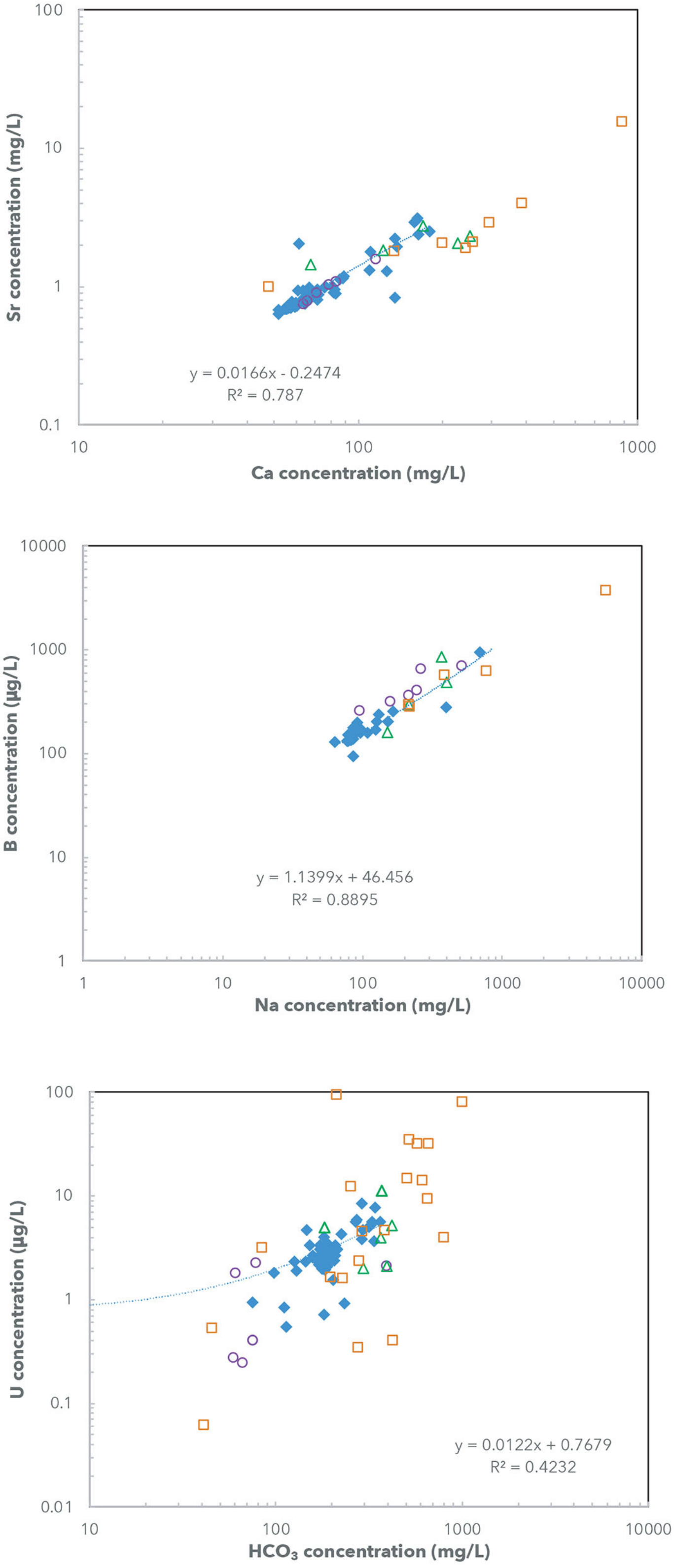

FIGURE 4 | (A) Sr vs. Ca concentrations (mg/L), **(B)** B vs. Na concentrations (µg/L), and **(C)** U vs. HCO_3 concentrations (µg/L), in Rio Grande river water, groundwater, agricultural canals and drains, and urban water (wastewater treatment plants: WWTP). Positive correlations for the Rio Grande river samples are indicated by linear fit lines.

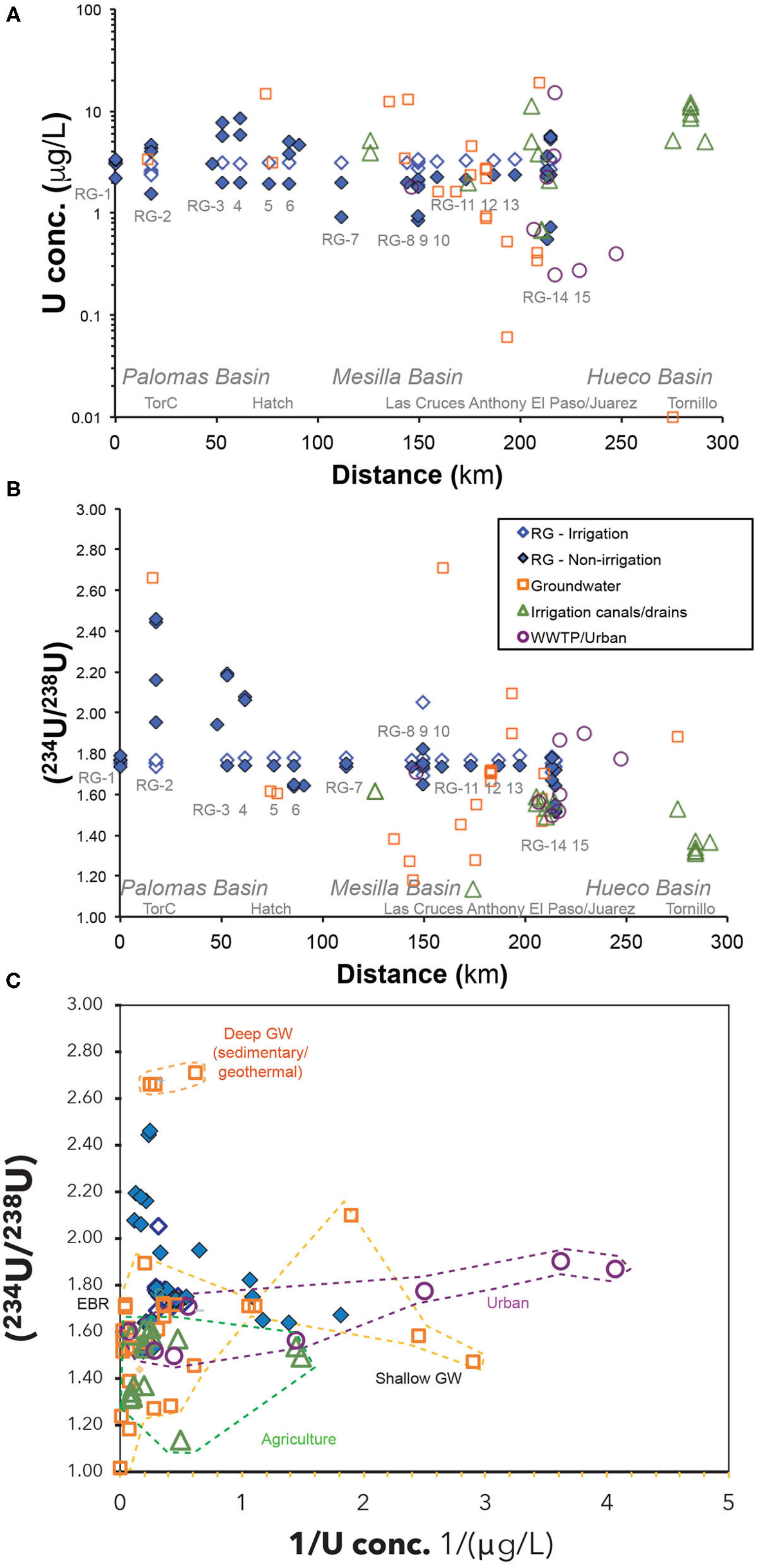

FIGURE 5 | (A) U concentrations and **(B)** activity ratios in the Rio Grande river water, groundwater, agricultural canals and drains, and urban water (waste water treatment plants). The Rio Grande water is classified into non-irrigation and irrigation seasons. The sample locations are placed with distance (km) from Elephant Butte Reservoir along the Rio Grande. **(C)** U activity ratios vs. 1/U concentrations. End members for Elephant Butte Reservoir, shallow groundwater, deep groundwater, agricultural water, and urban water are indicated and outlined.

observed from areas with hot spring and hydrothermal activities such as from Truth or Consequences, NM or Fabens, TX, compared to relatively low ratios generally observed in shallow irrigation wells near agricultural areas along the Rio Grande (**Appendix Table 2**).

Boron Concentrations and $\delta^{11}B$

Both temporal and spatial variability of B concentrations in Rio Grande water samples follows similar trends as observed in U concentrations. There is also a positive correlation between B and Na concentrations (**Figure 4**). More specifically, the Rio Grande river water had limited variation of B concentration during the irrigation seasons (~90 to 200 μg/L) compared to much larger variations (~180 μg/L to 1,000 μg/L) during the non-irrigation season (**Figure 6A**). The groundwater, drain and urban water samples all had higher B concentrations (up to ~3,700 μg/L) compared to the Rio Grande river samples (**Figure 6A**).

The Rio Grande river samples also showed similar spatial and temporal trends of $\delta^{11}B$ values to the measured ($^{234}U/^{238}U$) ratios, with smaller variation during irrigation seasons (+8% to +11%) and larger variation during non-irrigation seasons (+3% to +16%; **Figure 6B**). Urban wastewater had uniquely lower $\delta^{11}B$ values (+4% to +11%) compared to higher values in drains (+9% to +15%). The highest $\delta^{11}B$ values were measured in groundwater (+11% to +30%), with one exception for the geothermal groundwater sample in Truth or Consequences with a significantly lower $\delta^{11}B$ of +6% (**Figure 6B**).

Strontium Concentrations and $^{87}Sr/^{86}Sr$ Ratios

The Rio Grande river samples showed low Sr concentrations during the irrigation seasons (~0.5 to 1.2 mg/L) and higher concentrations during the non-irrigation seasons (~1 to 3 mg/L) (**Figure 7A**). There is a positive correlation between Sr and Ca concentrations in these samples as well (**Figure 4**). The highest Sr concentrations in the Rio Grande water (~2 to 3 mg/L) were observed during non-irrigation season in Locations RG-2, 6, 14, and 15. Noticeably higher Sr concentrations were observed in agricultural drains (~2 to 4 mg/L). The groundwater samples showed the largest variation of Sr concentration, from ~1 to 16 mg/L. The urban effluent samples had Sr concentrations similar to the Rio Grande water (~1 mg/L).

During irrigation seasons, the measured $^{87}Sr/^{86}Sr$ ratios of the Rio Grande showed a narrow range of values (0.710 to 0.711), similar to Elephant Butte reservoir water (**Figure 7B**). In contrast, the $^{87}Sr/^{86}Sr$ ratios of Rio Grande during non-irrigation seasons showed much greater variation, with lower ratios in locations RG-9 and RG-15 (0.709 to 0.711) and higher ratios in locations RG-2 and RG-6 (0.712 to 0.715). Slightly high $^{87}Sr/^{86}Sr$ ratios (0.711–0.712) were observed in agricultural drains in Mesilla Basin, while lower ratios (~0.710) were observed in drains from the Hueco Basin (**Figure 7B**). The urban effluent had similar or slightly lower ($^{87}Sr/^{86}Sr$) ratios (~0.709 to 0.710). The studied groundwater samples showed the most diverse groups of values: much higher ($^{87}Sr/^{86}Sr$) ratios in Palomas Basin (~0.720) compared to low ratios in downstream locations in Mesilla and Hueco Basin (~0.708 to 0.710).

DISCUSSION

Rio Grande Salinity End-Members and U, Sr, and B Isotope Tracers

Previous studies have identified multiple salinity sources of geological, agricultural, and urban origins in the semi-arid Rio Grande watershed of southern New Mexico and western Texas (**Figure 1B**; e.g., Ellis et al., 1993; Phillips et al., 2003; Moyer et al., 2013). Total dissolved solid contents, major element chemistry, and several light stable isotope ratios ($\delta^{18}O$, δH, and $\delta^{34}S$) have been used to attempt to identify and quantify contributions from each possible salinity end-members in the Rio Grande watershed. Several specific processes that have been previously identified, including: (1) natural upwelling of deep saline groundwater at the distal ends of alluvial basins, (2) mixing with saline groundwater in shallow aquifers via faults, (3) agricultural return flows from irrigation canals and drains, and (4) urban streams and discharges of treated or untreated wastewater from urban areas. Indeed, the groundwater, agricultural canals/drains, and urban wastewater samples in this study all show variable but elevated TDS (**Figure 3**) and are justified as potential salinity sources to the Rio Grande. However, accurate identification and quantification for contributions of these salinity end members are difficult due to the general overlapping values of TDS, major element concentrations and elemental ratios, as well as light stable isotope ratios ($\delta^{18}O$, δD, and $\delta^{34}S$) (e.g., Szynkiewicz et al., 2015b). In addition, several major elements (Ca, K, SO_4 or NO_3) or stable isotope ratios ($\delta^{18}O$, δD, and $\delta^{34}S$) may not behave conservatively in the Rio Grande watershed (e.g., Phillips et al., 2003; Szynkiewicz et al., 2015b), undermining their use as salinity tracers to identify the original sources. It is expected that U and Sr isotope ratios may behave conservatively in rivers under oxic conditions, while B isotope ratios may experience modification due to its intrinsic nature as a light stable isotope system. To apply these isotope ratios of trace elements to identify major salinity sources, it is generally expected that these trace elements (U, Sr, and B) mimic the changes of major elements (TDS, or Ca, Mg, K, Na, Cl, SO_4, NO_3) in water. Such an assumption is not easily to validate due to the different geochemical and physical behavior of these different elements. However, the Sr, B, and U concentrations of Rio Grande water samples in this study show a positive trend with respect to the changes of Ca, Na, and HCO_3 concentrations, respectively (especially for Sr and B, **Figure 4**), strongly suggesting that the salinity changes were accompanied by the changes of Sr, B, and U concentrations. Such positive correlations of Sr, B, and U with TDS values support the use of their isotope tracers to identify sources of major elements and salinity in this study.

Characteristics of U, Sr, and B Isotope Ratios in Rio Grande Salinity End Members

Here, we first assess using the U, Sr, and B isotope ratios of groundwater, agricultural, and urban samples to characterize possible salinity end members in the Rio Grande watershed in this study area.

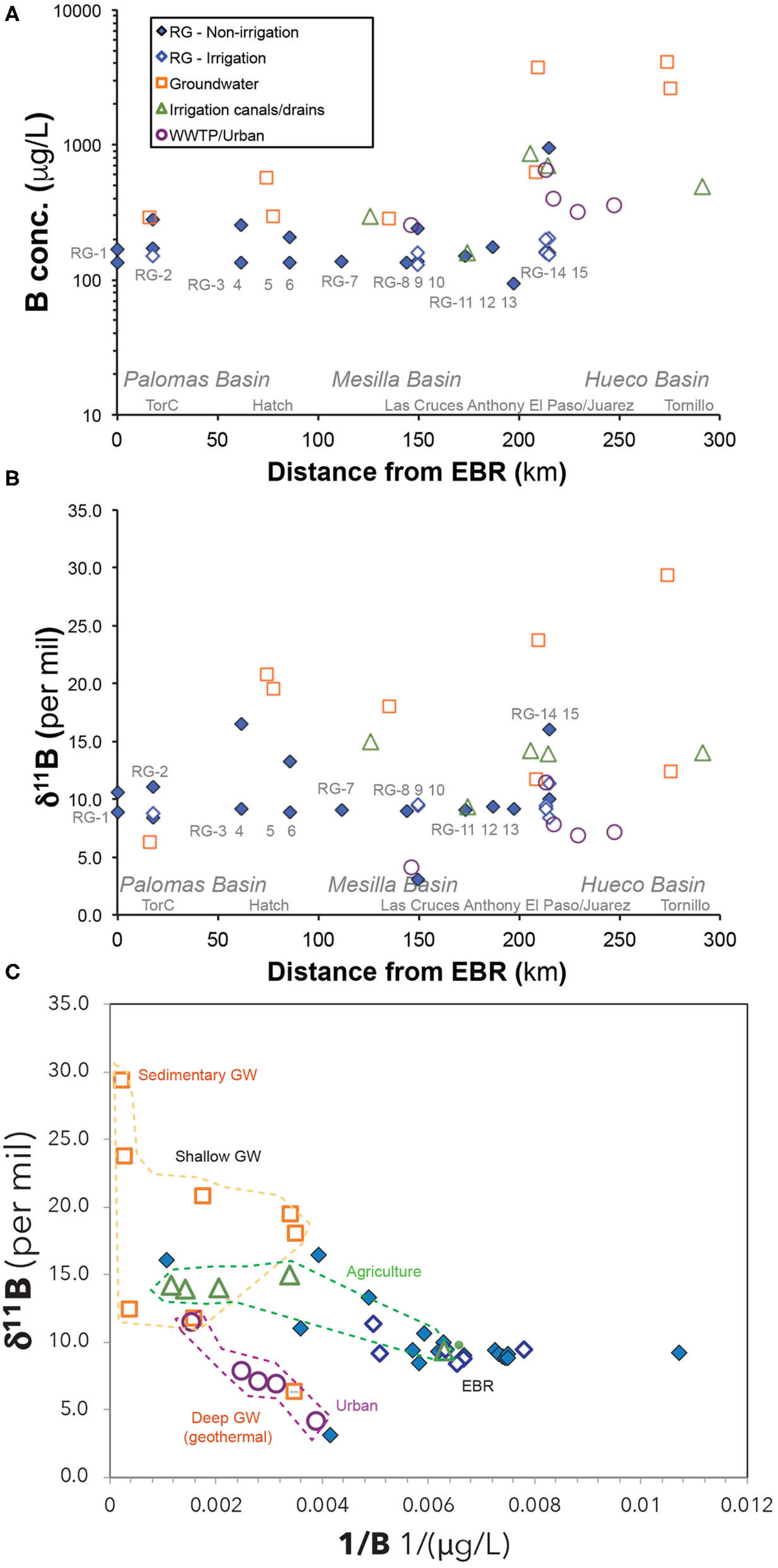

FIGURE 6 | (A) Boron concentrations and **(B)** B isotope ratios in the Rio Grande river water, groundwater, agricultural canals and drains, and urban water (waste water treatment plants). The Rio Grande water is divided into non-irrigation and irrigation seasons. The sample locations are placed with distance (km) from Elephant Butte Reservoir along the Rio Grande. **(C)** B isotope ratios vs. 1/B concentrations. End members for Elephant Butte Reservoir, shallow groundwater, deep groundwater, agricultural water, and urban water are indicated and outlined.

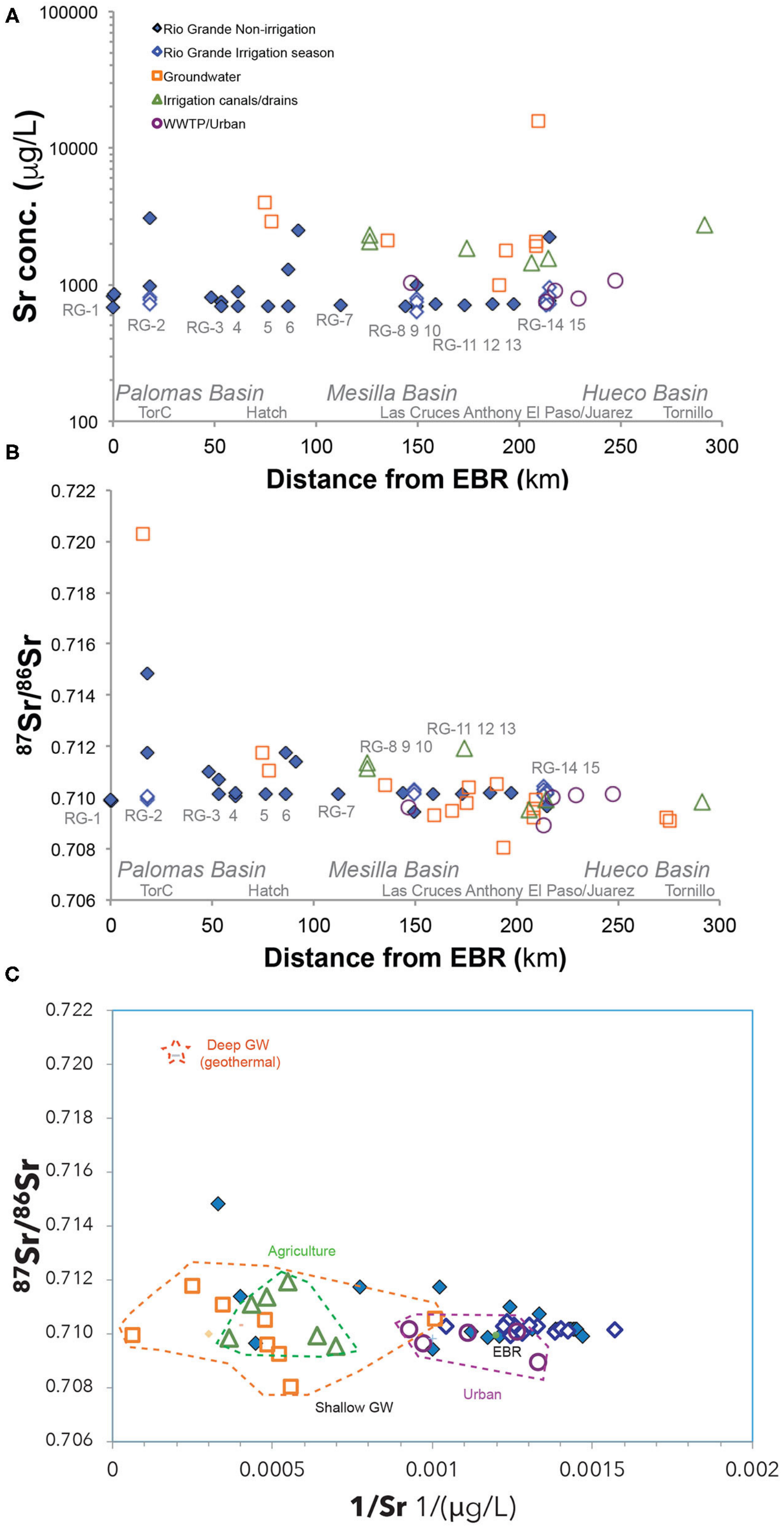

FIGURE 7 | (A) Sr concentrations and **(B)** ^{87}Sr/^{86}Sr isotope ratios in the Rio Grande river water, groundwater, agricultural canals and drains, and urban water (waste water treatment plants). The Rio Grande water is divided into non-irrigation and irrigation seasons. The sample locations are placed with distance (km) from Elephant Butte Reservoir along the Rio Grande. **(C)** ^{87}Sr/^{86}Sr isotope ratios vs. 1/Sr concentrations. End members for Elephant Butte Reservoir, shallow groundwater, deep groundwater, agricultural water, and urban water are indicated and outlined.

Agricultural Salinity Sources to Rio Grande

Palomas Basin, Mesilla Basin, and Hueco Basin host several populated areas in southern New Mexico and western Texas in cities of Hatch, Las Cruces, NM and El Paso, TX with a combined population of more than 1 million, or 2.3 million if the neighboring city of Ciudad Juarez, Mexico is included. The hydrologic cycle (river flow, groundwater flow, surface-ground water interactions) in the Rio Grande region has been extensively impacted by agricultural activities such as irrigation with river and groundwater. Rio Grande water is diverted to an extensive irrigation network of canals to irrigate a large area of agricultural land (193,000 acres in Palomas and Mesilla Basin; **Figure 2**) that is generally parallel to Rio Grande. Agricultural drains return excess irrigation water from the agricultural fields back to Rio Grande. The total length of the canals and drains is >1,700 km for the ~200 km-stretch of Rio Grande (**Figure 2**). Most of the canals and drains are not covered nor lined and significant water loss has been documented as evaporation, transpiration, and leakages to underlying aquifers (Moyer et al., 2013). In addition, during drought periods or low flow seasons of the Rio Grande, groundwater is generally pumped from numerous privately-owned irrigation wells from the alluvial aquifers as a supplement to irrigation water. The exact amount of groundwater pumping is difficult to monitor due to different regulations in New Mexico and Texas. However, the extensive groundwater pumping has led to well-documented declines in groundwater table and cone of depressions in this region.

The agricultural water samples from canals and drains in this study show highly variable salinity of ~700 to 2,800 mg/L (**Figure 3**), with noticeable increases in areas near major irrigation districts in New Mexico. Evaporation and transpiration on agricultural fields has been suggested to account for the increased TDS values (Phillips et al., 2003). The use of brackish to saline groundwater (TDS > 1,000 mg/L) for irrigation is another possible salinity source related to agricultural activities. Agricultural canals and drains in this study show high U concentrations (>10 μg/L) and distinctively low (^{234}U/^{238}U) ratios (~1.1 to 1.6) (**Figure 5**). Similarly, agricultural return flows and shallow groundwater beneath agricultural areas in other geographic regions such as California and Ohio have shown elevated U concentrations (e.g., Mangini et al., 1979; Nolan and Weber, 2015; Lyons et al., 2020). The elevated U concentrations in water from agricultural areas have been suggest as a result of the wide application of phosphorus fertilizers, which are generally enriched in U due to the co-presence of uranium and phosphorus in many phosphorous minerals. If such U in phosphorous minerals is geologically old (>1.25 Ma), then the U released from the phosphorus fertilizers can be inferred at secular equilibrium with a characteristic (^{234}U/^{238}U) ratio = 1 (Zielinski et al., 2000; Szynkiewicz et al., 2015b). Indeed, the agricultural canals and drains in the Rio Grande region show lower (^{234}U/^{238}U) ratios (~1.1 to 1.6) that is consistent with their interactions with fertilizer sourced U with the water flow path from agricultural fields. Consequently, this agricultural water end member could develop the high TDS values from a combination of processes such as evaporation and transpiration during water transport and irrigation on agricultural fields, leaching of soluble salts from agricultural fields, and displacement of shallow saline groundwater beneath the agricultural fields (e.g., Ellis et al., 1993).

The role of an agricultural salinity source to the Rio Grande river has been previously suggested by a series of sulfur isotope studies in this region in which the unusually low δ^{34}S isotope signatures of Rio Grande water were attributed to the fertilizer sourced sulfur isotope end-member (Szynkiewicz et al., 2011, 2015a,b). However, despite its high potential to trace agricultural sourced salinity, an extensive use of sulfur isotopes are limited by two complicating factors: (1) significant overlapping δ^{34}S values among fertilizers, sulfates, and sulfide sources; and (2) non-conservative nature of sulfates at surface or near surface environments (Szynkiewicz et al., 2011; 2015a,b). As highlighted in this study, U isotope systematics could be used as a particularly effective tracer for the agricultural salinity source as the fertilizer (^{234}U/^{238}U) ratio (e.g., ~1.0) is distinctively low compared to other natural (^{234}U/^{238}U) signatures (e.g., groundwater U) and U remains as a conservative tracer in most oxic environments at Earth's surface (Chabaux et al., 2003).

Furthermore, agricultural waters in this study show a characteristic narrow range of δ^{11}B values (~+13.1 ± 2.5%, n = 4) (**Figure 6**). Previous studies have characterized the δ^{11}B values in common types of fertilizers due to their high B contents (Barth, 2000; Chetelat and Gaillardet, 2005). However, previous studies show that fertilizers could have a large range of δ^{11}B values (e.g., −2 to +17%) due to different geological sources of B in fertilizers, consistent with our measurements of fertilizer samples showing even larger δ^{11}B variation (0 to +26%; **Appendix Table 2**). Hence the narrow range of δ^{11}B values observed in the agricultural waters in this study highlights the possibility of several other processes that could modify δ^{11}B values of the fertilizers along the water flow paths from the agricultural fields, such as extensive interactions with clay minerals and/or bio-uptake by crops. Indeed, it is well-known that δ^{11}B values in water can be modified by water-clay interactions since adsorption-desorption processes could impact the coordination of dissolved boron ions and change their isotope signatures (Palmer et al., 1987). Bio-uptake of B also can modify B isotope signatures. These processes in the agricultural fields could be responsible for the observed narrow range of δ^{11}B values in the agricultural water end-members and such a characteristic B isotope signature may be used to identify salinity from agricultural sources. However, additional studies that focus on understanding various processes in agricultural fields could help to develop the uses of B isotope ratios to trace agricultural activities.

^{87}Sr/^{86}Sr ratios of the agricultural water samples show a large range of values (0.709–0.712) that are overlapping with other end member values (**Figure 7**). Several fertilizer samples were analyzed for ^{87}Sr/^{86}Sr ratios in this study and show a large range of Sr ratios (0.709–0.730) that extend beyond the range of the agriculture water values (**Appendix Table 2**). The contribution of Sr from fertilizer sources to the agricultural water samples is thus limited and the overlapping of the agricultural water and river ^{87}Sr/^{86}Sr ratios suggests that the Sr source in the agricultural water is largely contributed by Sr in river water or groundwater that were used for irrigation. Hence, ^{87}Sr/^{86}Sr ratios have a limited resolving agricultural sourced salinity. By contrast, the combination of U and B isotope tracers show high potential to trace the agricultural salinity sources in the Rio Grande watershed.

Urban Salinity Sources to Rio Grande

Urban effluents (urban streams or treated or untreated wastewater discharge) are likely the source of elevated TDS, NO_3, SO_4, Cl, and Na for rivers flowing through large cities (e.g., Chen et al., 2014). Indeed, high concentrations of TDS, NO_3, and SO_4 are observed in urban samples such as the WWTP samples collected from Las Cruces, Sunland Park, and El Paso areas (**Figure 3**; http://dx.doi.org/10.1594/IEDA/111231), consistent with previous observations (Szynkiewicz et al., 2011, 2015a,b). In this study, these urban samples show characteristic high B concentrations (>200 μg/L) and low $\delta^{11}B$ values (−4 to +11%) (**Figure 6**). The low $\delta^{11}B$ signatures reflect addition of isotopically light B present in soaps and detergents from urban sources. Indeed, previous studies have documented that most of industrial B products are mined from two main sources in Turkey and California, USA that have relatively uniform and low $\delta^{11}B$ values of −4 to +4% (e.g., Barth, 2000; Chetelat and Gaillardet, 2005). Consequently, large rivers near highly populated areas (e.g., the Seine river near Paris, France) tend to have low $\delta^{11}B$ (e.g., ∼+5%; Chetelat and Gaillardet, 2005), as a result of urban effluents. Nevertheless, some urban effluent samples from El Paso had higher $\delta^{11}B$ values (e.g., up to 11%, **Figure 6C**), most likely impacted by the high B concentrations from local groundwater used as municipal water sources. The local groundwater may develop high $\delta^{11}B$ signatures due to interactions with sedimentary bedrock of marine origins (also see next section Deep and Shallow Groundwater Components in Rio Grande Watershed).

In contrast to the B isotope signatures, both ($^{234}U/^{238}U$) ratios and $^{87}Sr/^{86}Sr$ ratios of the urban samples show large overlaps with agricultural and groundwater samples (**Figures 5C**, **7C**), suggesting that the U and Sr sources in the urban samples are dominated by river water and local groundwater and have limited resolution to distinguish urban salinity sources. However, it is noted that the U concentrations in these urban end-member samples are unusually low as compared to other types of water samples in this study (**Figure 5C**). Such low U concentrations may indicate that certain artificial processes could remove U from the urban water, such as during the treatment steps of the city wastewater. For example, it is a common approach to purge air into the wastewater to oxidize dissolved Fe phases and to promote precipitation of Fe oxides during the wastewater treatment. It is known that U has high affinity onto amorphous Fe oxides (e.g., Duff et al., 2002) and hence, the removal of Fe-oxides from wastewater could also remove U from the wastewater. If the U removal process is originated from the wastewater treatment step, the unusually low U concentrations could be an additional detectable signature for urban water inputs to the environments.

Deep and Shallow Groundwater Components in Rio Grande Watershed

Unlike the agricultural and urban salinity sources that have several unique and characteristic U or B isotope signatures, the geological salinity sources, as represented by a limited number of groundwater samples in this study, have variable U, Sr, and B isotope signatures due to the presence of multiple groundwater components with different evolution history (**Figures 5–7**). More specifically, the combination of U, B, and Sr isotope tracers shows the presence of three possible groundwater components in the Rio Grande region: (1) deep groundwater with a sedimentary salinity source, (2) deep groundwater with a geothermal salinity source, and (3) shallow groundwater with multiple salinity sources. Below, we discuss the possible U, Sr, and B isotope signatures to identify these groundwater components.

A deep origin of several groundwater samples from Palomas Basin and Mesilla Basin can be inferred from their elevated ($^{234}U/^{238}U$) ratios (up to ∼2.7) (**Figure 5C**). It has been suggested that deep groundwater tend to carry higher ($^{234}U/^{238}U$) ratios than surface water, soil water, and shallow groundwater (Chabaux et al., 2003; Durand et al., 2005). For example, when groundwater flows through a redox front in the aquifer, generally at deeper part of the aquifer, U solubility decreases significantly under reducing conditions (e.g., Langmuir, 1978; Drever, 1997). Due to the enhanced alpha recoil effect from the U-enriched aquifer matrix and long groundwater residence time, groundwater could develop abnormally high ($^{234}U/^{238}U$) ratios, such as up to ∼10 in deep carbonate aquifers of Texas and South Africa (Osmond and Cowart, 1992; Kronfeld et al., 1994). This is in contrast with the moderate degrees of alpha recoil effects in surface water, soil water, and shallow groundwater as U-series disequilibrium are largely controlled by climatic, geological and hydrologic conditions (e.g., Maher et al., 2004, 2006; Robinson et al., 2004; DePaolo et al., 2006; Chabaux et al., 2008; Andersen et al., 2009; Pogge von Strandmann et al., 2010).

The sedimentary origin of these groundwater samples is supported by their $\delta^{11}B$ values. For example, two of these samples (GW-18 and Faben well#1) show characteristic high $\delta^{11}B$ ratios (+24 to +29%; **Figure 6C**) that represent typical values observed in deep sedimentary brines with ancient marine evaporites (e.g., +35 to +40%) (e.g., Spivack and Edmond, 1987; Louvat et al., 2011). These groundwater samples are most likely linked to deeper sedimentary aquifers that are commonly present in the study area. One other deep groundwater sample (GW-79), however, show much lower $\delta^{11}B$ value (+6%) despite of the high ($^{234}U/^{238}U$) ratio, and is most likely linked with a geothermal signature. Indeed, geothermal water is often characterized by lower $\delta^{11}B$ ratios of such as from 0 to +10%, due to the enhanced water-rock interactions in high temperatures that preferentially release light ^{10}B isotopes from aquifer rocks to groundwater (Spivack and Edmond, 1987; Louvat et al., 2011).

The presence of two different origins of deep groundwater (geothermal and sedimentary) is also supported by the $^{87}Sr/^{86}Sr$ ratios in groundwater, which are mainly controlled by types and ages of the source rocks along its flow paths (Blum et al., 1998; Capo et al., 1998; Shand et al., 2009). Two contrasting groups of $^{87}Sr/^{86}Sr$ ratios are observed in the groundwater samples in the study area (**Figure 7B**): 1) a possible geothermal source with links to more radiogenic crystalline basement blocks (e.g., up to 0.720, GW-79), and 2) a sedimentary source with carbonates or sandstone aquifers (e.g., 0.710). Consistent with the discussion of U, B, and Sr isotope tracers, the $\delta^{34}S$ ratios in SO_4 of groundwater waters from this region also suggested the presence of (1) geothermal/hydrothermal groundwater that has a signature from oxidation of hydrothermal sulfide-rich mineralization, and (2) groundwater water with a sedimentary marine signature (Szynkiewicz et al., 2015a,b).

In addition to the presence of two different deep groundwater components (geothermal and sedimentary), a large number of groundwater samples in this study show overlapping U, B, and Sr signatures with Rio Grande water, agricultural water, or urban water (**Figures 5–7**). Many of these groundwater samples were collected from irrigation wells close to Rio Grande in the agricultural fields with no well log information for well depth or screening depth. However, the identification of Rio Grande water U, B, and Sr signatures in these groundwater samples could point them to a shallow groundwater component. Indeed, Rio Grande water is the main recharge water source for shallow aquifers in Mesilla Basin, as a part of a complex surface-groundwater interaction in this region under both natural and human impact conditions (Witcher et al., 2004). Such recharge mainly occurs as leakage from the main river channel, leakage from canals and drains, as well as infiltration from irrigated agricultural fields (Walton et al., 1999; Witcher et al., 2004). Consistent with this inference of shallow groundwater recharge process, many groundwater samples in this study have similar U isotope signatures to Rio Grande water and agricultural water samples. In addition, urban water could also contribute to shallow groundwater through leakages of runoff or infiltration from urban areas, as evidenced by one groundwater sample (GW-19) that has a urban B signature.

Importantly, the shallow groundwater in the Rio Grande region clearly shows signatures of human impacts with agricultural or urban activities. Indeed, recent studies with ^{3}H and ^{14}C tracers have indicated that most of the shallow groundwater systems around the world has shown significant components of young or modern recharge water, suggesting an extensive connection and interaction of surface and groundwater systems (Gleeson et al., 2016; Jasechko, 2016). Our study highlights that such a connection also exists in the semi-arid Rio Grande region: although natural groundwater recharge rate is low due to the semi-arid or arid climate in this region, groundwater recharge could occur as a result of irrigation or urban runoff in Palomas Basin and Mesilla Basin (e.g., Eastoe et al., 2007; Ahadi et al., 2013). Human impacts to the groundwater aquifers in this region hence are not only limited to groundwater extraction, but also may increase groundwater recharge and surface-groundwater interactions.

Characterization of U, Sr, and B Isotope Ratios in Rio Grande Salinity Sources

For each salinity source, the average and standard deviation values for U, Sr, and B isotope ratios and concentrations from the sample group calculated and summarized in **Table 1**. It is clear that the above salinity end members identified with the agricultural, urban, and groundwater samples have overlapping isotopes signatures and no single isotope tracer of U, Sr, or B would be able to distinguish multiple salinity sources. The issues of overlapping signatures in Rio Grande salinity sources are common and have been identified with tracers such as $\delta^{18}O$, δD, $\delta^{34}S$. The overlapping signatures of Rio Grande salinity sources are intrinsically related to the complex nature of surface-groundwater interaction under both natural and managed conditions in Rio Grande watershed.

More specifically, despite that natural groundwater recharge rate is low due to the semi-arid or arid climate in this region, Rio Grande river water is the dominant source of groundwater recharge in alluvial aquifers (shallow groundwater). Both Rio Grande river and shallow groundwater are also the dominant sources of agricultural and urban water uses. The agricultural and urban water uses may also lead to recharge to shallow groundwater aquifers through irrigation or urban runoff. These complex natural and managed hydrological settings generate similar signatures for salinity sources such as shallow groundwater with Rio Grande water, agricultural, and urban water, as evidenced by the large overlaps of $^{87}Sr/^{86}Sr$ isotope ratios (**Figure 7**). However, deep groundwater can be distinguished by their characteristic high $^{87}Sr/^{86}Sr$ ratio. In addition, urban water samples tend to have lower Sr concentrations than groundwater and agricultural water samples. Furthermore ($^{234}U/^{238}U$), ratios and concentrations highlight the characteristics of agricultural and deep groundwater salinity end members (low vs. high $^{234}U/^{238}U$ ratios) and urban water

TABLE 1 | End member values inferred for salinity sources in the Rio Grande Watershed in this study.

	EBR	Agriculture	Deep GW	Shallow GW	Urban
U concentration (μg/L)	3.0 ± 0.5	6.4 ± 4.0	2.99 ± 1.23	13.9 ± 23.3	1.52 ± 1.27
($^{234}U/^{238}U$)	1.76 ± 0.02	1.44 ± 0.15	2.68 ± 0.03	1.57 ± 0.24	1.69 ± 0.17
B concentration (μg/L)	151.4 ± 25.1	450 ± 304	287	1751 ± 1693	448 ± 184
$\delta^{10}B$ (per mil)	9.7 ± 1.2	13.1 ± 2.5	6.27	19.4 ± 6.2	8.5 ± 3.5
Sr concentration (μg/L)	826 ± 90	2,800 ± 880	10,000	3,400 ± 4,400	1,018 ± 295
$^{87}Sr/^{86}Sr$	0.7099 ± 0.0001	0.7103 ± 0.0009	0.7203	0.7101 ± 0.0010	0.7098 ± 0.0005

*End member values were calculated as the average of each sample group. The standard deviation from each group is shown when applicable (**Appendix Table 2**).*

EBR: RG-1 samples, n = 7; Agriculture samples: n = 14; Deep GW: GW-79 (2) and Well#2, n = 3; Shallow GW: all groundwater samples except for the Deep GW (n = 29); Urban: n = 7.

Sr concentration from Deep GW from Williams et al. (2013).

samples (low U concentrations). The B isotope systematics also highlight the resolving power of separating urban water signatures from agricultural and groundwater signatures. Hence, instead of relying on one single tracer, we combine both isotope ratios and elemental concentrations of U, Sr, and B in a multi-tracer approach to systematically identify the characteristic signatures of the complex nature of the salinity sources.

Spatial and Temporal Variability of Rio Grande River Salinity and Contributing End Members

We aim to assessing the spatial and temporal variability of the Rio Grande river salinity for the study period with the above identified U, B, and Sr isotope and elemental signatures of the agricultural, urban, and geological sources. However, during the irrigation (high flow) seasons, the concentrations and isotopic compositions of U, B and Sr in the Rio Grande were very similar to the Elephant Butte reservoir water (**Figures 5–7**). This is in agreement with that during high river flows, the river chemistry mainly reflects the chemistry of upstream reservoirs. In contrast, the Rio Grande showed highly variable U, B and Sr concentrations and isotope ratios during the non-irrigation (low flow) seasons and we hence focus on the Rio Grande during non-irrigation (low flow) seasons from Elephant Butte reservoir to El Paso, TX.

Natural Upwelling of Deep Groundwater in Palomas and Mesilla Basin to Rio Grande

In the Truth or Consequence region, ∼0 to 50 km downstream to the EBR, the Rio Grande river water is characterized by unusually high ($^{234}U/^{238}U$) ratios (up to ∼2.5) as well as moderately low $\delta^{11}B$ ratios (∼+7 per mil) during the non-irrigation seasons. In addition, the $^{87}Sr/^{86}Sr$ ratios in the same river samples during non-irrigation seasons show high radiogenic signatures (up to 0.715), in contrast to the Rio Grande water during irrigation season (0.709 to 0.710). The Truth or Consequence region marks the northern portion of the Palomas Basin with limited human impacts due to the low population and the lack of large agricultural areas (**Figure 2**). In this region, the young alluvial sediments are in generally thin and the uplifted and highly fractured old (Paleozoic to Pre-Cambrian) crystalline basement is close to the surface (Pepin et al., 2015). The impacts of deep groundwater to shallow aquifers and surface environments have been well-documented by the presence of numerous hot springs and geothermal wells in this region (Williams et al., 2013; Pepin et al., 2015). Indeed, U, Sr, and B isotopic systematics all point to the presence of deep groundwater signatures in the Rio Grande river as a result of groundwater upwelling, including high ($^{234}U/^{238}U$) and $^{87}Sr/^{86}Sr$ ratios as well as low $\delta^{11}B$ values of typical geothermal water (**Figures 5–7**).

Impacts of Agricultural Salinity in Palomas Basin and Mesilla Basin

Both U and B isotope ratios of the Rio Grande at ∼50 to 250 km downstream to EBR show very different signatures from those of the northern Palomas Basin, suggesting a change of dominant salinity source as inferred from the non-irrigation river samples (**Figures 5**, **6**). For example, U isotope ratios of Rio Grande river samples decrease rapidly from high to low ratios (from ∼2.5 to ∼1.6), except for locations near Las Cruces and El Paso where several high ($^{234}U/^{238}U$) ratios (∼2.1) are observed (**Figure 5**). Such a decrease of ($^{234}U/^{238}U$) ratios might be related to a reduced geothermal/deep groundwater input as the thickness of the alluvial basin increases when the Rio Grande flows into the center of Palomas Basin. The inferred decrease of natural upwelling of highly saline groundwater in this region should lead to a significant decrease of river salinity if the upwelling of groundwater is the dominant salinity source to the Rio Grande. However, the river salinity in this region only decrease moderately from ∼3,000 mg/L in the northern Palomas Basin to ∼2,500 mg/L in the southern Palomas and Mesilla Basin during the non-irrigation seasons (**Figure 3**). Such an observation suggests that in addition to the groundwater salinity source, other salinity sources are present and responsible the elevated salinity in the Palomas Basin and Mesilla Basin region. The most likely salinity source could be from the agricultural source. Indeed ($^{234}U/^{238}U$), ratios of Rio Grande in this region show values (∼1.6) lower than the dominant irrigation season river samples (∼1.7), consistent with the presence of the fertilizer related salinity source with the characteristic low U isotope signatures (**Figure 5B**). As suggested by other hydrogeological studies in this region (e.g., Ellis et al., 1993; Walton et al., 1999), the inputs of agricultural salinity are due to direct agricultural return flows or displacement of shallow groundwater underneath agricultural fields to drains.

The $\delta^{11}B$ ratios of Rio Grande water in this region first increase to ∼+16 per mil in Palomas Basin and then decrease to ∼+9 per mil in Mesilla Basin (**Figure 6B**). It is noted that the intermediate range of $\delta^{11}B$ values in Rio Grande is mostly similar to the agricultural water end-member, also consistent with the presence of the agricultural sourced salinity in this region.

Several locations along the Rio Grande such as near Lac Cruces, NM or El Paso, TX show relatively higher $\delta^{11}B$ values as well as higher ($^{234}U/^{238}U$) ratios (**Figures 5**, **6**), which could indicate that the salinity sources in the Rio Grande in this region may not be solely from agricultural activities. The addition of salinity from a groundwater source via deep seated faults in the alluvial basin is possible (Witcher et al., 2004; Hiebing et al., 2018). However, many fault zones are not located near the main channel of Rio Grande and these groundwater likely sourced salinity could be the result of artificial groundwater pumping for irrigation and municipal uses, not due to natural upwelling of groundwater similar to the northern Palomas Basin. To summarize, the combination of U and B isotope tracers points to the presence of a large agricultural source of salinity to Rio Grande in Palomas Basin and Mesilla Basin.

Addition of Urban Salinity Sources Near Large Populated Areas

The presence of large urban centers in this region such as cities of El Paso, TX, Las Cruces, NM, and Juarez, Mexico is an important factor when considering processes to modify both water quality and quantity for the Rio Grande. In this region, the common municipal water sources are generally a combination of surface water from the Rio Grande and groundwater withdraw from alluvial aquifers (such as Mesilla and Hueco aquifers; Sheng, 2013). Urban centers are known as important point sources of effluents for rivers. The released urban water (e.g., treated city wastewater or untreated urban runoff) could have certain distinctive chemical compositions and isotopic signatures, as urban water uses generally lead to high concentrations of Cl (product of chlorination), Na and K (exchange ions in water softeners), NO_3 (city waste water), F (fluoridation for public health), and B, Ca, SO_4 (soaps and detergents). High concentrations of major elements such as Cl, Na, K, NO_3, and SO_4 have been observed in urban water samples in this study (http://dx.doi.org/10.1594/IEDA/111231). Here, we focus on using B isotope systematics to identify urban salinity contribution to Rio Grande river. Indeed, Rio Grande river in this study show anomalously low $\delta^{11}B$ values with high B concentrations: ∼+4 per mil near Las Cruces, NM (∼150 km) and ∼+15 per mil near El Paso, TX (∼220 km) (**Figure 7**), consistent with the presence of urban B source in Rio Grande at these locations.

In contrast to the distinctive lower B isotope ratios ($^{234}U/^{238}U$), ratios of the urban water samples show overlapping values (∼1.6 to 2.0) with Rio Grande river water and groundwater samples (**Figure 5**). This observation is consistent with the fact that the municipal water is a combination of river and groundwater and it is inferred that the urban water uses do not modify ($^{234}U/^{238}U$) ratios. Hence ($^{234}U/^{238}U$), ratios are not a resolvable signature for tracing urban source salinity. However, the Rio Grande near the Las Cruces, NM and El Paso, TX areas shows lower U concentrations for certain sampling months (**Figure 5**), most likely reflecting the addition and dilution of U by treated urban wastewater, as we previously identified that the low U concentrations could be an indicative character of urban water end member.

In addition to the urban water end member, the combined U and B isotope systematics also shown that the Rio Grande river near large urban areas such as El Paso, TX is impacted by multiple salinity sources from agricultural and geological sources (**Figures 5–7**). The contribution of geological source has been suggested as upwelling of groundwater as the area is located at the distal end of the Mesilla Basin and groundwater is forced to flow upward due to the thinning of the alluvial deposition on top of the basement rocks (Phillips et al., 2003; Hogan et al., 2007). Geological factor has been identified as a key factor in this area for understanding the contribution of salinity in Rio Grande watershed (Phillips et al., 2003; Hogan et al., 2007). However, it is also possible that the shallow groundwater flows could bring agricultural source of salinity as part of the upwelling process. Indeed ($^{234}U/^{238}U$), ratios in Rio Grande in this area show low values that suggest the contribution of agricultural sources of salinity, instead of high ($^{234}U/^{238}U$) ratios such as observed at the northern Palomas Basin. Hence, the multi-tracer dataset of U, B, and Sr isotope ratios clearly show evidence of multiple salinity sources (geological, agricultural and urban) to the Rio Grande river at the end of the Mesilla Basin.

Quantification of Contributions of Salinity Sources to Rio Grande: A Multi-Isotope (U, B, and Sr) Mass Balance Approach

The multi-tracer dataset of U, B, and Sr isotope ratios highlights the presence of multiple salinity sources in the Rio Grande watershed and that their contributions to Rio Grande river var both spatially and temporally (**Figure 8**). As discussed in previous sections, despite that no single isotope tracers of U, B, and Sr can effectively distinguish the multiple salinity sources, the combination of the isotope tracers and elemental concentrations of U, B, and Sr shows potentials in a multi-tracer approach. Here, we use a mass balance model to quantify the contributions of individual salinity source, as summarized below.

For a given sampling location, the isotopic composition of Rio Grande water ($R_{RioGrande}$) and elemental concentration ($C_{RioGrande}$) for an element (U, Sr, or B) can be calculated as:

$$\begin{aligned} C_{RioGrande} &= C_{EBR}f_{EBR} + C_{deep\_GW}f_{deep\_GW} \\ &\quad + C_{shallow\_GW}f_{shallow\_GW} \\ &\quad + C_{agricultural}f_{agricutural} + C_{urban}f_{urban} \end{aligned} \tag{1}$$

$$\begin{aligned} R_{RioGrande}C_{RioGrande} &= R_{EBR}C_{EBR}f_{EBR} \\ &\quad + R_{deep\_GW}C_{deep\_GW}f_{deep\_GW} \\ &\quad + R_{shallow\_GW}C_{shallow\_GW}f_{shallow\_GW} \\ &\quad + R_{agricultural}C_{agricultural}f_{agricutural} \\ &\quad + R_{urban}C_{urban}f_{urban} \end{aligned} \tag{2}$$

$$f_{EBR} + f_{deep\_GW} + f_{shallow\_GW} + f_{agricutural} + f_{urban} = 1 \tag{3}$$

Here, the f values in the above equations are the relative water mass contribution of salinity sources: Elephant Butte reservoir water (EBR), deep groundwater, shallow groundwater, agricultural water, and urban water. For each salinity source, the characteristic values for U, Sr, and B isotope ratios and concentrations have been discussed and are summarized in **Table 1**. The f values from each salinity source can be constrained by using U, Sr, and B isotope ratios and concentrations in the measured river water sample with a mathematical inverse procedure (e.g., Roy et al., 1999; Chetelat and Gaillardet, 2005; and Engel et al., 2016). Briefly, the above set of equations is over determined for a given water sample because of the number of constraining equations (7 in this case: 3 from U, Sr, B concentrations, 3 from isotope ratios, and 1 from Equation 3) is greater than the number of the unknowns (5: f values for EBR, deep_GW, shallow_GW, agricultural, and urban). In the inversion technique, we can solve the 5 unknowns (f values) by using a Monte Carlo procedure to minimize the difference between the observed and the calculated values in the 7 equations by iteration, considering the uncertainties of measurements R and C (Engel et al., 2016). If the algorithm converges to the preset difference level (e.g., 5%), a solution is found. For this study, the above mass balance approach is applied at 5 selected locations downstream to EBR to El Paso, TX for both irrigation and non-irrigation seasons (**Table 2**). The 5 selected locations are characterized by various geological, agricultural, and urban settings, respectively. The above algorithm was solved

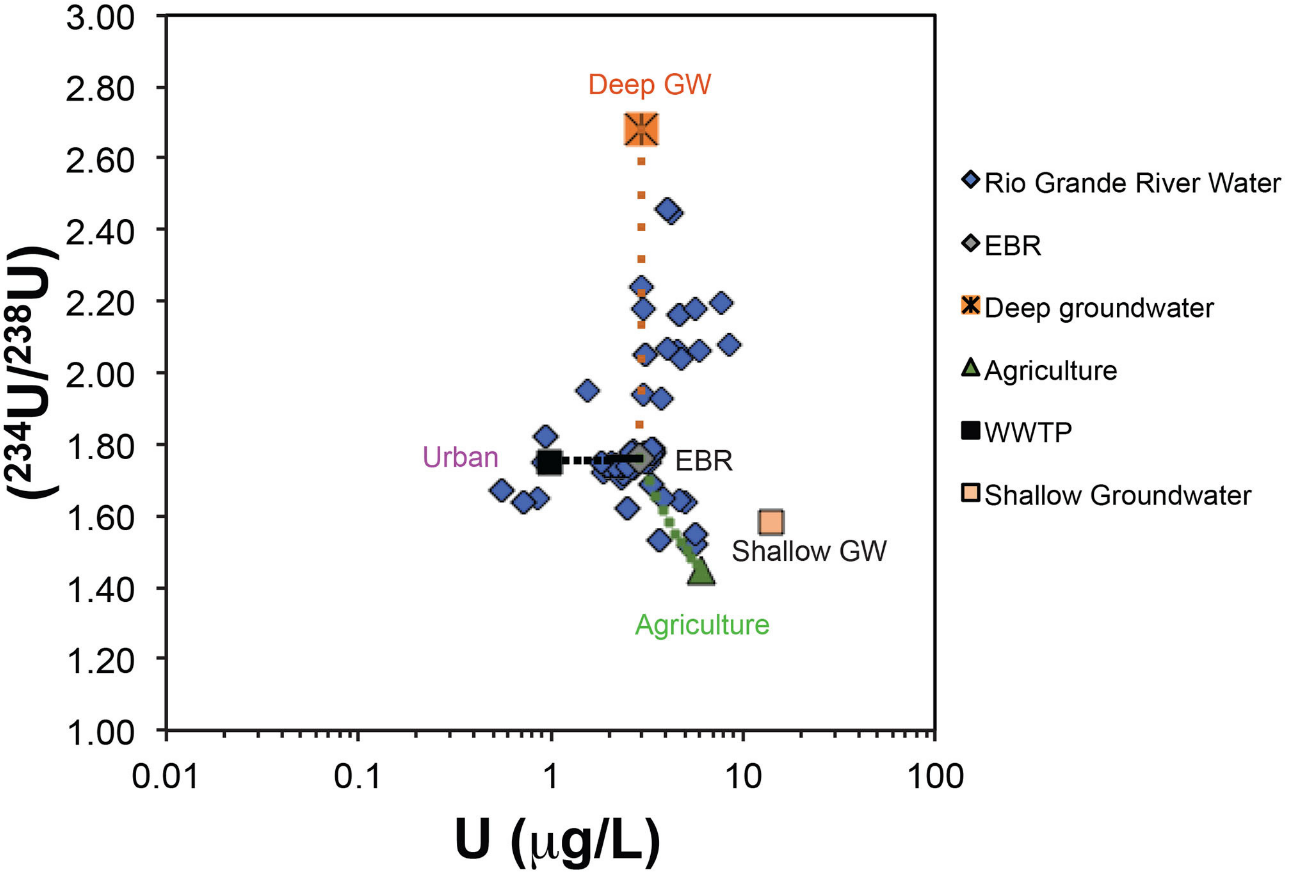

FIGURE 8 | U activity ratios vs. U concentrations in the Rio Grande river during non-irrigation seasons. End member values (**Table 1**) for Elephant Butte Reservoir, shallow groundwater, deep groundwater, agricultural water, and urban water are indicated. Dashed lines indicate the conceptual model of multiple salinity contribution to the Rio Grande water.

100 times and the average f values from the 100 solutions are presented in **Table 2** and **Figure 9**. It is noted that although the f values represent the contribution calculated from U, Sr, and B mass balance, the positive correlation between U, Sr, and B concentrations and the TDS values in these samples supports that the f values also represent the salinity contribution from each end member.

The mass balance quantification shows that during the irrigation (high flow) seasons, salinity at the 5 sampling locations downstream to Elephant Butte reservoir is dominated (>85%) by EBR release water. Only a small fraction of urban signature (∼13%) is observed at RG-15 location next to the city of El Paso (**Table 2**). Small amounts of agricultural, groundwater, and urban (<2%) can be observed at the RB-2 site, which is at the Truth or Consequences area with known upwelling of deep groundwater, small agricultural and urban activities. The Elephant Butte reservoir stores the water coming from the headwater region of the Rio Grande watershed in southern Colorado and Northern New Mexico where climate is temperate and with more precipitation than the southern New Mexico and West Texas. The chemical solutes in EBR are mainly from chemical weathering processes within the Critical Zone in the headwater regions (e.g., Szynkiewicz et al., 2015a).

During the non-irrigation (low flow) seasons, salinity in the Rio Grande is still largely contributed by an EBR type of water (∼40–80%), most likely as the residual EBR flows of the previous irrigation seasons. However, due to the decreased river flow, other salinity signatures can be readily observed at many locations (**Figure 9**), with a significant component of urban signature (8–58%) and a large contribution from shallow groundwater (up to 43%). Agricultural water contribution is low (∼2–4%) and deep groundwater contribution is also low except at the RB-2 location where upwelling of groundwater is documented (∼23%).

Indeed, the above salinity quantification is consistent with the previous notation that upwelling of deep saline groundwater and mixing with groundwater in shallow aquifers may be responsible for salinity increases in certain locations such as at the distal end of the Mesilla Basin, between Locations RG-12 and 15 (Phillips et al., 2003; Witcher et al., 2004; Hogan et al., 2007; Hiebing et al., 2018). Upwelling of geothermal groundwater to shallow aquifers has been also suggested in areas with uplifted basin basements such as in the hot spring district of Truth or Consequences, near Location RG-2 and 3 (Williams et al., 2013).

However, there is no clear evidence for direct connection between the Rio Grande and the deep groundwater via natural

TABLE 2 | Relative water mass contributions (%) to Rio Grande for selected locations for non-irrigation and irrigation seasons.

Site ID	Site Name	Date	f1 (EBR) (%)	f2 (Agriculture) (%)	f3 (Deep GW) (%)	f4 (Shallow GW) (%)	f5 (Urban) (%)
	Non-irrigation (low flow)						
RG-2	RG-2 at WB	26-Feb-15	41.7	2.0	22.8	0.7	32.8
RG-4	RG-4 at NM187	26-Feb-15	64.2	0.0	0.0	0.0	35.7
RG-6	RG-6 at NM 154	26-Feb-15	82.5	4.4	3.4	1.7	8.0
RG-9	RG-9 at NM 359	26-Feb-15	70.7	1.3	0.8	1.0	26.2
RG-15	RG-15 at 273	26-Feb-15	0.0	0.0	0.0	42.6	57.4
	Irrigation (high flow)						
RG-2	RG-2 at WB	16-Jun-15	100.0	0.0	0.0	0.0	0.0
RG-2		18-Sep-15	94.0	1.5	1.0	1.0	2.5
RG-4	RG-4 at NM187	18-Sep-15	100.0	0.0	0.0	0.0	0.0
RG-6	RG-6 at NM 154	18-Sep-15	100.0	0.0	0.0	0.0	0.0
RG-7	RG-7 at RV 185	18-Sep-15	100.0	0.0	0.0	0.0	0.0
RG-8	RG-8 at US 70	18-Sep-15	100.0	0.0	0.0	0.0	0.0
RG-9	RG-9 at NM 359	16-Jun-15	100.0	0.0	0.0	0.0	0.0
RG-9		30-Jul-15	100.0	0.0	0.0	0.0	0.0
RG-9		18-Sep-15	100.0	0.0	0.0	0.0	0.0
RG-11	RG-11 at NM 189	18-Sep-15	100.0	0.0	0.0	0.0	0.0
RG-12	RG-12 at NM 225	18-Sep-15	100.0	0.0	0.0	0.0	0.0
RG-13	RG-13 at TX 259	18-Sep-15	100.0	0.0	0.0	0.0	0.0
RG-14	RG-14 at Racetrack	16-Jun-15	100.0	0.0	0.0	0.0	0.0
RG-14		31-Jul-15	100.0	0.0	0.0	0.0	0.0
RG-14		18-Sep-15	100.0	0.0	0.0	0.0	0.0
RG-15	RG-15 at 273	16-Jun-15	84.5	1.2	0.6	1.0	12.7
RG-15		31-Jul-15	100.0	0.0	0.0	0.0	0.0
RG-15		18-Sep-15	100.0	0.0	0.0	0.0	0.0

upwelling in the most part of the Mesilla Basin. Below Elephant Butte and Caballo Reservoir, the Rio Grande is a losing stream with significant infiltration of surface water to the alluvial aquifers (e.g., Szynkiewicz et al., 2015a,b; Driscoll and Sherson, 2016). During the irrigation season, the Rio Grande surface water is diverted to the large network of irrigation canals. The end points of main agricultural drains are directly connected to the Rio Grande and return the excess irrigation water from the agricultural fields. Therefore, several studies have proposed that agricultural return flows may contribute to river salinity either through use of groundwater with elevated salinity for irrigation, flushing of secondary salts precipitating in soil during dry seasons, and/or high evapotranspiration rates in the agricultural fields (e.g., Ellis et al., 1993; Szynkiewicz et al., 2015b). Our mass balance quantification suggests that the agricultural contribution is present but not significant (at 2–4%). However, a large contribution from shallow groundwater (up to 43%) is documented in this region that may represent the indirect contribution of agricultural water to Rio Grande via infiltration underneath agricultural fields and shallow groundwater flows back to Rio Grande (Walton et al., 1999).

In addition, urban effluents from the cities could be additional sources of salinity since they significantly increase stream flows during the non-irrigation seasons when there is no water release from Elephant Butte and Caballo reservoirs. Indeed, high urban contributions are observed at locations near large cities and towns in the study area (RG-15 is near El Paso, TX as discussed above; RG-2 is near T or C, NM). Note that one WWTP (not sampled in this study) is located ∼3 km upstream from RG-2 and highest NO_3 was mainly observed during non-irrigation season (up to 15 mg/L) when there was no water releases from upstream Elephant Butte reservoir. Additional sources of salinity might be spa resorts from Truth or Consequences that discharge geothermal water directly to the Rio Grande. Indeed, both local groundwater used for municipal supplies and artesian geothermal groundwater from spa resorts have elevated TDS (∼800–4,000 mg/L) due to high concentrations of Na and Cl (∼200–1,200 mg/L).

It is also noted that during non-irrigation seasons, the percentage contribution of EBR is expected to decrease with increasing distance from EBR at downstream locations, due to the addition of other non-EBR types of water sources. However, the calculated EBR contribution in this study increases from RG-2 (∼40%), to RG-4 (∼65%), and RG-6 (∼80%; **Figure 9**). Such an observation may point to the presence of an additional source (or sources) that has similar isotopic composition to the EBR type water but such a source was included in the EBR contribution by the Monte Carlo mass balance model.

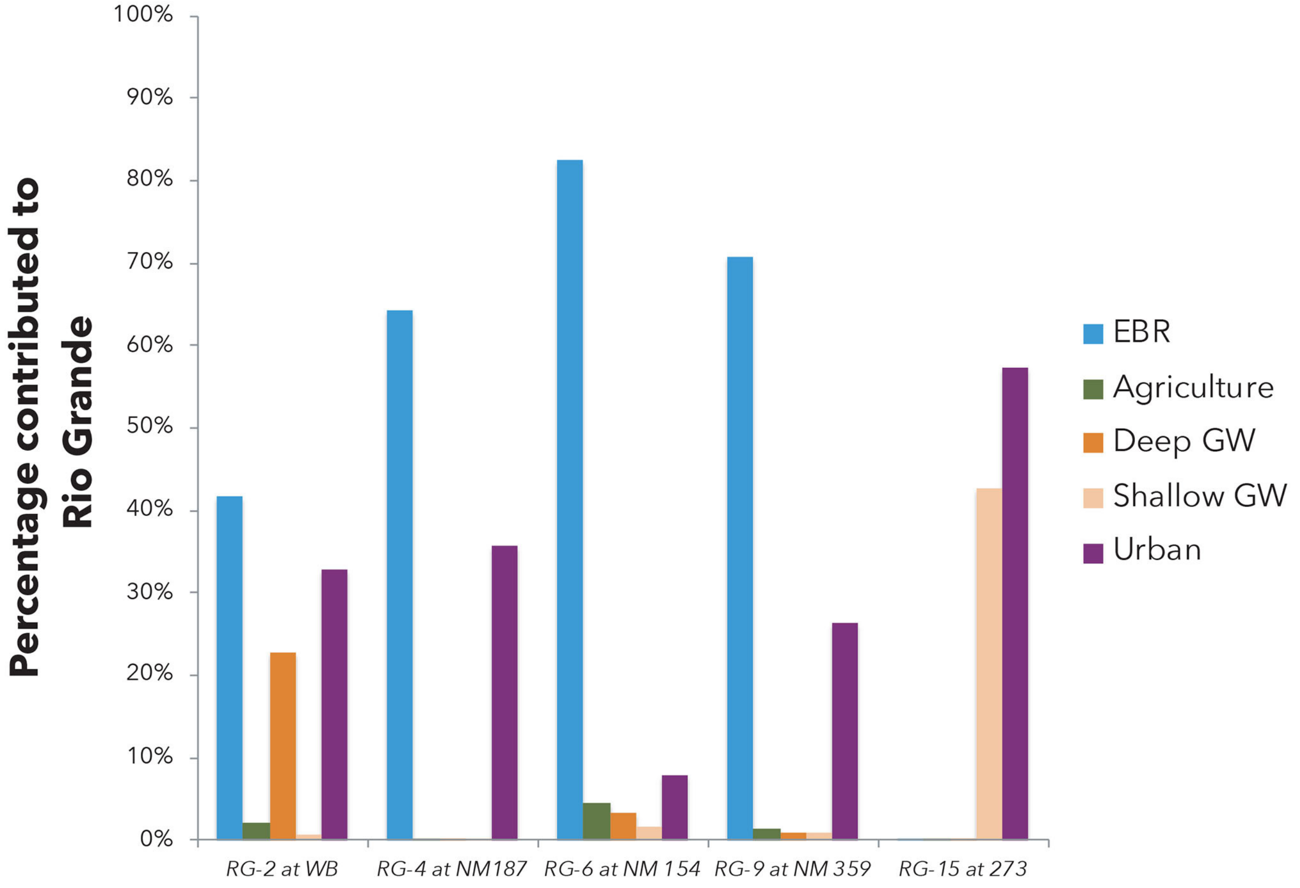

FIGURE 9 | Relative water mass contributions (%) of salinity end members to the Rio Grande river during non-irrigation seasons at the five selected locations downstream to EBR as constrained by the multi-tracer mass balance model.

For example, the seepage of EBR and Caballo reservoirs to shallow aquifers may lead to increased contribution of a shallow groundwater end-member that has "EBR"-like isotope signatures to the Rio Grande at downstream locations (such as at RG-4 and RG-6). The shallow groundwater contribution calculated by the Monte Carlo mass balance model is in fact unusually low at these locations (**Figure 9**), especially at RG-6, which is located at the distal end of the Palomas Basin and expected to receive high groundwater contribution (e.g., at RG-15 location; **Figure 2**). Such inconsistencies of the calculated EBR and shallow groundwater contributions at RG-4 and RG-6 locations point to several limits of the current Monte Carlo mass balance model: (1) the current model cannot solve effectively the end-members with similar or overlapping signatures; (2) the current model does not take into account of river flow discharge that may provide additional constraints on the mass balance model; (3) the current model does not offer sensibility and uncertainty analysis that may help to assess the model results with uncertainties. Future model calculations that may include river discharges, more accurate characterization of salinity end-member and uncertainties will be more useful to address the salinity issues for the complex surface-shallow-deep groundwater system in the Rio Grande watershed.

SUMMARY AND CONCLUSIONS

Our multi-isotope tracer approach (U, Sr, and B) helps to better characterize geologic, agricultural, and urban salinity end members in the semi-arid Rio Grande watershed, thus improves the ability to identify salinity contributions to the Rio Grande river. Generally, the combination of U, Sr, and B isotopes is useful in characterizing multiple groundwater components that carry salts from dissolution of varied bedrock types at different temperatures. In particular, we were able to distinguish two main deep groundwater end members: geothermal and deep brackish to saline groundwater for which chemistry and isotope compositions are controlled by dissolution of sedimentary and hydrothermal deposits, respectively. The U isotopes are useful tracers in distinguishing deep vs. shallow water flow paths, and direct inputs from fertilizers related salinity sources from agricultural fields.

During the irrigation seasons, the chemical and isotope compositions of the Rio Grande appear to be mainly controlled by the water releases from Elephant Butte Reservoir. This is consistent with high stream flows and accompanying dilution effect. The chemical solutes in EBR are mainly from chemical weathering processes within the Critical Zone in the headwater regions.

In contrast, during the non-irrigation season the variable TDS and isotope compositions of U, Sr, and B are consistent with the heterogeneous compositions of multiple end members in shallow groundwater, urban effluents and irrigation return flows. During these low flow seasons, the inputs of salt from these sources appear to be localized due to lack of constant Rio Grande river flows. The Rio Grande surface water is the source of prevailing infiltration into underlying alluvial aquifers. This contradicts previous suggestions that linked the salinity increases in the majority of the Rio Grande river channel with natural upwelling of deep brines. However, we acknowledge that some mixing with deep upwelling water may take place in the Rio Grande shallow alluvial aquifers (Hiebing et al., 2018).

Furthermore, recent studies with ^{3}H and ^{14}C signatures have shown that most of the shallow groundwater systems around the world have significant components of young (modern) recharge, suggesting an interconnectivity between surface and groundwater systems (Gleeson et al., 2016; Jasechko, 2016). In our study, a large number of groundwater samples showed U, Sr, and B signatures that overlap with the Rio Grande surface water, agricultural drains, and urban effluents. Given that these samples were collected from groundwater wells in a close proximity to the Rio Grande and agricultural fields, they likely represent recharge of surface water to shallow groundwater. This recharge most likely occurs through leakage from the main Rio Grande channel and canals/drains, and infiltration of irrigation water (Walton et al., 1999; Witcher et al., 2004). Therefore, human impact in the Rio Grande region is not only limited to groundwater extraction and salt loads from shallow sources, but also increases groundwater recharge with elevated salinity and surface contaminants (e.g., U from fertilizers, NO_3 from urban and agricultural sources).

DATA AVAILABILITY STATEMENT

The datasets presented in this study can be found in online repositories. The names of the repository/repositories and accession number(s) can be found in the article/**Supplementary Material**.

AUTHOR CONTRIBUTIONS

LM and JG directed and initiated the study. SG and SN contributed to conduct U and Sr isotope measurements. SG and PL contributed to B isotope study. All authors contributed to the manuscript writing and data interpretation.

FUNDING

This research was supported by NSF grant EAR-1349091 to LM. SG received NSF international travel support to conduct B isotope analysis at IPGP, France.

ACKNOWLEDGMENTS

We thank Anna Szynkiewicz for insightful comments and discussion on a previous draft. Students who assisted in the field work and data processing/analysis included: M. Hiebing, V. Garcia, C. Reyes, L. Alvarez, E. Sosa, and H. Hernandez. The manuscript benefited significantly from insightful and thoughtful comments and suggestions from three reviewers and effective editorial handling by Dr. Carl Steefel.

SUPPLEMENTARY MATERIAL

The Supplementary Material for this article can be found online at: https://www.frontiersin.org/articles/10.3389/frwa.2020.575216/full#supplementary-material

REFERENCES

Ahadi, R., Samani, Z., and Skaggs, R. (2013). Evaluating on-farm irrigation efficiency across the watershed: a case study of New Mexico's Lower Rio Grande Basin. *Agric. Water Manage.* 124, 52–57. doi: 10.1016/j.agwat.2013.03.010

Alley, W. M. (Ed.). (2013). *Five-Year Interim Report of the United States – Mexico Transboundary Aquifer Assessment Program: 2007 – 2012*. U.S. Geological Survey Open-File Report 2013–1059.

Allison, G. B., Cook, P. G., Barnett, S. R., Walk, G. R., Jolly, I. D., and Hughes, M. W. (1990). Land clearance and river salinisation in the western Murray Basin, Australia. *J. Hydrol.* 119, 1–20. doi: 10.1016/0022-1694(90)90030-2

Andersen, M. B., Erel, Y., and Bourdon, B. (2009). Experimental evidence for 234U−238U fractionation during granite weathering with implications for 234U/238U in natural waters. *Geochim. Cosmochim. Acta* 73, 4124–4141. doi: 10.1016/j.gca.2009.04.020

Barth, S. R. (2000). Boron isotopic compositions of near-surface fluids: a tracer for identification of natural and anthropogenic contaminant sources. *Water Air Soil Pollut.* 124, 49–60. doi: 10.1023/A:1005210226830

Blum, J. D., Gazis, C. A., Jacobson, A. D., and Chamberlain, C. P. (1998). Carbonate versus silicate weathering in the Raikhot watershed within the High Himalayan Crystalline Series. *Geology* 26, 411–414.

Brantley, S. L., White, T. S., White, A. F., Sparks, D., Richter, D., Pregizer, K., et al. (2006). *Frontiers in Exploration of the Critical Zone*. Report of a Workshop Sponsored by the National Science Foundation (NSF), October 24-26, 2005, Newark, DE.

Brown, K. B., McIntosh, J. C., Baker, V., and Gosch, D. (2010). Isotopically-depleted Late Pleistocene groundwater in Columbia River Basalts: evidence for recharge of Glacial Lake Missoula floodwaters? *Geophys. Res. Lett.* 37:L21402. doi: 10.1029/2010GL044992

Capo, R. C., Stewart, B. W., and Chadwick, O. A. (1998). Strontium isotopes as tracers of ecosystem processes: theory and methods. *Geoderma* 82, 197–225. doi: 10.1016/S0016-7061(97)00102-X

Chabaux, F., Bourdon, B., and Riotte, J. (2008). U-series geochemistry in weathering profiles, river waters and lakes. *Radioact. Environ.* 13, 49–104. doi: 10.1016/S1569-4860(07)00003-4

Chabaux, F., Cohen, A. S., O'Nions et, R. K., and Hein, J. R. (1995). 238U-234U-230Th chronometry of Fe-Mn crusts : growth processes and recovery of thorium isotopic ratios of seawater. *Geochim. Cosmoch. Acta* 59, 633–638. doi: 10.1016/0016-7037(94)00379-Z

Chabaux, F., Riotte, J., and Dequincey, O. (2003). U–Th–Ra fractionation during weathering and river transport. *Rev. Mineral. Geochem.* 52, 533–576. doi: 10.2113/0520533

Chen, J.-B., Gaillardet, J., Bouchez, J., Louvat, P., and Wang, Y.-N. (2014). Anthropophile elements in river sediments: overview from the Seine River, France. *Geochem. Geophys. Geosyst.* 15, 4526–4546. doi: 10.1002/2014GC005516

Cheng, H., Edwards, R. L., Hoff, J., Gallup, C. D., Richards, D. A., Asmerom, Y. (2000). The half-lives of U-234 and Th-230. *Chem. Geol.* 169, 17–33.

Chetelat, B., and Gaillardet, J. (2005). Boron isotopes in the Seine River, France: a probe of anthropogenic contamination. *Environ. Sci. Technol.* 39, 2486–2493. doi: 10.1021/es048387j

DePaolo, D. J., Maher, K., Christensen, J. N., and McManus, J. (2006). Sediment transport time measured with U-series isotopes: results from ODP North Atlantic drift site 984. *Earth Planet. Sci. Lett.* 248, 394–410. doi: 10.1016/j.epsl.2006.06.004

Drever, J. I. (1997). *The Geochemistry of Natural Waters: Surface and Groundwater Environments*. |ISBN-10:0132727900. New York, NY: Pearson.

Driscoll, J. M., and Sherson, L. R. (2016). *Variability of Surface-Water Quantity and Quality and Shallow Groundwater Levels and Quality Within the Rio Grande Project Area, New Mexico and Texas, 2009–13*. US Geological Survey.

Duff, M. C., Coughlin, J. U., and Hunter, D. B. (2002). Uranium coprecipitation with iron oxide minerals. *Geochim. Cosmochim. Acta* 66, 3533–3547. doi: 10.1016/S0016-7037(02)00953-5

Durand, S., Chabaux, F., Rihs, S., Duringer, P., and Elsass, P. (2005). U isotope ratios as tracers of groundwater inputs into surface waters: example of the Upper Rhine hydrosystem. *Chem. Geol.* 220, 1–19. doi: 10.1016/j.chemgeo.2005.02.016

Eastoe, C. J., Hibbs, B. J., Olivas, A. G., Hogan, J. F., Hawley, J., and Hutchinson, W. R. (2007). Isotopes in the Hueco Bolson aquifer, Texas (USA) and Chihuahua (Mexico)— local and general implications for recharge sources in alluvial basins. *Hydrogeol. J.* 16:11. doi: 10.1007/s10040-007-0247-0

Ellis, S. R., Levings, G. W., Carter, L. F., Richey, S. F., and Radell, M. J. (1993). Rio Grande Valley, Colorado, New Mexico, and Texas. *Water Resour. Bull.* 29, 617–646. doi: 10.1111/j.1752-1688.1993.tb03230.x

Engel, J., Ma, L., Sak, P., Gaillardet, J., Ren, M., Engle, M., et al. (2016). Quantifying chemical weathering rates along a precipitation gradient on Basse-Terre Island, French Guadeloupe: new insights from U-series isotopes in weathering rinds. *Geochim. Cosmochim. Acta* 195, 29–67. doi: 10.1016/j.gca.2016.08.040

Farber, E., Vengosh, A., Gavrieli, I., Marie, A., Bullen, T., Mayer, B., et al. (2004). The origin and mechanisms of salinization of the Lower Jordan River. *Geochim. Cosmochim. Acta* 68, 1989–2006. doi: 10.1016/j.gca.2003.09.021

Garcia, S. (2017). *Tracing anthropogenic salinity inputs to the semi-arid rio grande river: a multi-isotope tracer (U, S, B, AND SR) approach* [MS thesis] The University of Texas at El Paso, El Paso, TX, United States.

Garfin, G. A., Jardine, R., Merideth, Black, M., and LeRoy, S. (Eds.). (2013). *Assessment of Climate Change in the Southwest United States: A Report Prepared for the National Climate Assessment. A Report by the Southwest Climate Alliance.* Washington, DC: Island Press.

Ghassemi, F., Jakeman, A. J., and Nix, H. A. (1995). *Salinisation of Land and Water Resources: Human Causes, Extent, Management and Case Studies*. Wallingford: CAB International.

Gleeson, T., Befus, K. M., Jasechko, S., Luijendijk, E., and Cardenas, M. B. (2016). The global volume and distribution of modern groundwater. *Nat. Geosci.* 9, 161–167. doi: 10.1038/ngeo2590

Gutzler, D. S., and Robbins, T. O. (2010). Climate variability and projected change in the western United States: regional downscaling and drought statistics. *Climate Dyn.* 37, 835–849. doi: 10.1007/s00382-010-0838-7

Haney, P. D., and Bendixen, T. W. (1953). Effect of irrigation runoff on surface water supplies. *Am. Water Works Assoc. J.* 45, 1160–1171. doi: 10.1002/j.1551-8833.1953.tb20193.x

Hiebing, M., Doser, D., Avila, V. M., and Ma, L. (2018). Geophysical studies of fault and bedrock control on groundwater geochemistry within the southern Mesilla Basin, western Texas and southern New Mexico. *Geosphere* 14, 1912–1934. doi: 10.1130/GES01567.1

Hogan, J., Phillips, F. M., Mills, S. K., Hendrickx, J. M. H., Ruiz, J., Chesley, J. T., et al. (2007). Geologic origins of salinization in semi-arid river: the role of sedimentary basin brines. *Geology* 35, 1063–1066. doi: 10.1130/G23976A.1

Jasechko, S. (2016). Partitioning young and old groundwater with geochemical tracers. *Chem. Geol.* 427, 35–42. doi: 10.1016/j.chemgeo.2016.02.012

Johnson, N., Revenga, C., and Echeverria, J. (2001). Managing water for people and nature. *Science* 292, 1071–1072, doi: 10.1126/science.1058821

Konter, J. G., and Storm, L. P. (2014). High precision 87Sr/86Sr measurements by MC-ICP-MS, simultaneously solving for Kr interferences and mass-based fractionation. *Chem. Geol.* 385, 26–34. doi: 10.1016/j.chemgeo.2014.07.009

Kronfeld, J., Vogel, J. C., and Talma, A. S. (1994). A new explanation for extreme 234U/238U disequilibria in a dolomitic aquifer. *Earth Planet Sci. Lett.* 123, 81–93. doi: 10.1016/0012-821X(94)90259-3

Langmuir, D. (1978). Uranium solution–mineral equilibria at low temperatures with applications to sedimentary ore deposits. *Geochim. Cosmochim. Acta* 42, 547–569. doi: 10.1016/0016-7037(78)90001-7

Lippincott, J. B. (1939). Southwestern border water problems. *Am. Water Works Assoc J.* 31, 1–29. doi: 10.1002/j.1551-8833.1939.tb12350.x

Louvat, P., Bouchez, J., and Paris, G. (2010). MC-ICP-MS isotope measurements with direct injection nebulisation (d-DIHEN): optimisation and application to boron in seawater and carbonate samples. *Geostandards Geoanal. Res.* 35, 75–88. doi: 10.1111/j.1751-908X.2010.00057.x

Louvat, P., Gaillardet, J., Paris, G., and Dessert, C. (2011). Boron isotope ratios of surface waters in Guadeloupe, Lesser Antilles. *Appl. Geochem.* 26, S76–S79. doi: 10.1016/j.apgeochem.2011.03.035

Louvat, P., Moureau, J., Paris, G., Bouchez, J., Noireaux, J., and Gaillardet, J. (2014). A fully automated direct injection nebulizer (d-DIHEN) for MC-ICP-MS isotope analysis: application to boron isotope ratio measurements. *J. Anal. At. Spectrom.* 29, 1698–1707. doi: 10.1039/C4JA00098F

Lyons, W., Berry, R., and Harmon, S. (2012). Why urban geochemistry? *Elements* 8, 417–422. doi: 10.2113/gselements.8.6.417

Lyons, W., Gardner, C., Welch, S., and Israel, S. (2020). Uranium in Ohio, USA surface waters: implications for a fertilizer source in waters draining agricultural lands. *Sci. Rep.* 10:5151. doi: 10.1038/s41598-020-61922-2

Maher, K., DePaolo, D. J., and Lin, J. C. F. (2004). Rates of silicate dissolution in deep-sea sediment: in situmeasurement using U-234/U-238 of pore fluids. *Geochim. Cosmochim. Acta* 68, 4629–4648. doi: 10.1016/j.gca.2004.04.024

Maher, K., Steefel, C. I., DePaolo, D. J., and Viani, B. E. (2006). The mineral dissolution rate conundrum: insights from reactive transport modelling of U isotopes and pore fluid chemistry in marine sediments. *Geochim. Cosmochim. Acta* 70, 337–363. doi: 10.1016/j.gca.2005.09.001

Mangini, A., Sonntag, C., Bertsch, G., and Muller, E. (1979). Evidence for a higher natural uranium content in world rivers. *Nature* 278, 337–339. doi: 10.1038/278337a0

Meybeck, M. (2003). "Global occurrence of major elements in rivers," in *Treatise on Geochemistry*, Vol. 5, ed J. I. Drever (Amsterdam: Elsevier), 207–225.

Miyamoto, S. L., Fenn, B., and Swietlik, D. (1995). *Flow, Salts, and Trace Elements in the Rio Grande: A Review*. College Station, TX: Miscellaneous Publication (1764).

Moore, S. J., and Anderholm, S. K. (2002). *Spatial and Temporal Variations in Streamfl ow, Dissolved Solids, Nutrients, and Suspended Sediment in the Rio Grande Valley Study Unit, Colorado, New Mexico, and Texas, 1993–1995*. U.S. Geological Survey Water-Resources Investigations Report 02–4224.

Moore, S. J., Bassett, R. L., Liu, B., Wolf, C. P., and Doremus, D. (2008). Geochemical tracers to evaluate hydrogeologic controls on river salinization. *Ground Water* 46, 489–501. doi: 10.1111/j.1745-6584.2007.00420.x

Moyer, D., Anderholm, S. K., Hogan, J. F., Phillips, F. M., Hibbs, B. J., Witcher, J. C., et al. (2013). *Knowledge and Understanding of Dissolved Solids in the Rio Grande–San Acacia, New Mexico, to Fort Quitman, Texas, and Plan for Future Studies and Monitoring*. US Geological Survey.

National Research Council (2012). *New Research Opportunities in the Earth Sciences.* Washington, DC: The National Academies Press.

Nolan, J., and Weber, K. A. (2015). Natural uranium contamination in Major US aquifers linked to nitrate. *Environ. Sci. Tech. Lett.* 2, 215–220. doi: 10.1021/acs.estlett.5b00174

Nyachoti, S. (2016). *Application of U and Sr isotopes as salinity and paleo-environmental tracers: insight from the Rio Grande River and pedogenic carbonates in the drylands of the southwest USA. (Chapter 3: Tracing salinity sources in the Lower Rio Grande River using U and Sr isotopes)* [Ph.D. dissertation], The University of Texas at El Paso, El Paso, TX, United States.

Osmond, J. K., and Cowart, J. B. (1992). "Ground water," in *Uranium-Series Disequilibrium*, eds M. Ivanovich and R. S. Harmon. (Oxford: Clarendon Press), 290–334.

Palmer, M. R., Spivack, A. J., and Edmond, J. M. (1987). Temperature and pH controls over isotopic fractionation during adsorption of boron on marine clay. *Geochim. Cosmochim. Acta* 51, 2319–2323. doi: 10.1016/0016-7037(87)90285-7

Pepin, J., Person, M., Phillips, F. M., Kelley, S., Timmons, S., Owens, L., et al. (2015). Deep fluid circulation within crystalline basement rocks and the role of hydrologic windows in the formation of Truth or Consequences, New Mexico low temperature geothermal system. *Geofluids* 15, 139–160. doi: 10.1111/gfl.12111

Phillips, F. M., Emlen Hall, G., and Black, M. (2011). *Reining in the Rio Grande: People, Land, and Water*. Albuquerque, NM: University of New Mexico Press.

Phillips, F. M., Hogan, J., Mills, S., and Hendricks, J. M. H. (2003). "Environmental tracers applied to quantifying causes of salinity in arid-region rivers: Preliminary results from the Rio Grande, southwestern USA," in *Water Resources Perspectives: Evaluation Management, and Policy: Developments in Water Science*, eds A. S. Alsharhan and W. W. Wood (Amsterdam, Elsevier Science), 327–334.

Pogge von Strandmann, P. A. E., Burton, K. W., James, R. H., van Calsteren, P., and Gislason, S. R. (2010). Assessing the role of climate on uranium and lithium isotope behavior in rivers draining a basaltic terrain. *Chem. Geol.* 270, 227–239. doi: 10.1016/j.chemgeo.2009.12.002

Postel, S. (1999). *Pillar of Sand: Can the Irrigation Miracle Last*? New York, NY: Norton.

Raczek, I., Jochum, K. P., and Hofmann, A. W. (2003). Neodymium and strontium isotope data for USGS reference materials BCR-1, BCR-2, BHVO-1, BHVO-2, AGV-1, AGV-2, GSP-1, GSP-2 and eight MPI-DING reference glasses. *Geostand. Newslett.* 27, 173–179. doi: 10.1111/j.1751-908X.2003.tb00644.x

Robinson, L. F., Henderson, G. M., Hall, L., and Matthews, I. (2004). Climatic control of riverine and seawater uranium isotope ratios. *Science* 305, 851–854. doi: 10.1126/science.1099673

Roy, S., Gaillardet, J., and Allegre, C. J. (1999). Geochemistry of dissolved and suspended loads of the Seine River, France: anthropogenic impact, carbonate, and silicate weathering. *Geochim. Cosmochim. Acta* 63, 1277–1292. doi: 10.1016/S0016-7037(99)00099-X

Seager, R., Ting, M. F., Held, I. M., Kushnir, Y., Lu, J., Vecchi, G., et al. (2007). Model projections of an imminent transition to a more arid climate in southwestern North America. *Science* 316, 1181–1184. doi: 10.1126/science.1139601

Shand, P., Darbyshire, D. P. F., Love, A. J., and Edmunds, W. M. (2009). Sr isotopes in natural waters: applications to source characterisation and water–rock interaction in contrasting landscapes. *Appl. Geochem.* 24, 574–586. doi: 10.1016/j.apgeochem.2008.12.011

Sheng, Z. (2013). Impacts of groundwater pumping and climate variability on groundwater availability in the Rio Grande Basin. *Ecosphere* 4, 1–25. doi: 10.1890/ES12-00270.1

Spivack, A. J., and Edmond, J. M. (1987). Boron isotope exchange between seawater and the oceanic crust. *Geochim. Cosmochim. Acta* 51, 1033–1043. doi: 10.1016/0016-7037(87)90198-0

Swetnam, T. W., and Betancourt, J. L. (1998). Mesoscale disturbance and ecological response to decadal climatic variability in the American Southwest. *J. Clim*. 11, 3128–3147.

Szynkiewicz, A., Borrok, D., Ganjegunte, G., Skrzypek, G., Ma, L., Rearick, M., et al. (2015b). Isotopic studies of the Upper and Middle Rio Grande. Part 2 – salt loads and human impacts in south New Mexico and west Texas. *Chem. Geol.* 411, 336–350. doi: 10.1016/j.chemgeo.2015.05.023

Szynkiewicz, A., Borrok, D. M., Skrzypek, G., and Rearick, M. S. (2015a). Isotopic studies of the Upper and Middle Rio Grande. Part 1- Importance of sulfide weathering in the riverine sulfate budget. *Chem. Geol*. 411, 323–335. doi: 10.1016/j.chemgeo.2015.05.022

Szynkiewicz, A., Witcher, J., Modelska, M., Borrok, D. B., and Pratt, L. M. (2011). Anthropogenic sulfate loads in the Rio Grande, New Mexico. *Chem. Geol*. 283, 194–209. doi: 10.1016/j.chemgeo.2011.01.017

Walton, J., Ohlmacher, G., Utz, D., and Kuitanawala, M. (1999). Response of the Rio Grande and shallow groundwater in the Mesilla Bolson to irrigation, climate stress, and pumping. *Environ. Eng. Geosci.* 1, 41–50. doi: 10.2113/gseegeosci.V.1.41

Water 2025: Preventing Crisis and Conflict in the West (2005) U.S. Department of the Interior. Available online at: http://www.usbr.gov/library/ (accessed October 06, 2011).

Wilcox, L. V. (1957). "Analysis of salt balance and salt-burden data on the Rio Grande," in *Problems of the Upper Rio Grande: An Arid Zone River*, ed P. C. Duisberg (Socorro, NM: U.S. Commission for Arid Resource Improvement and Development, Publication no. 1), 39–44.

Williams, A. J., Crossey, L. J., Karlstrom, K. E., Newell, D., Person, M., and Woolsey, E. (2013). Hydrogeochemistry of the Middle Rio Grande aquifer system - fluid mixing and salinization of the Rio Grande due to fault inputs. *Chem. Geol.* 351, 281–298. doi: 10.1016/j.chemgeo.2013.05.029

Witcher, J. C., King, J. P., Hawley, J. W., Kennedy, J. F., Williams, J., Cleary, M., et al. (2004). *Sources of Salinity in the Rio Grande and Mesilla Basin Groundwater*. New Mexico Water Resources Research Institute WRRI Technical Completion Report No. 330.

Wong, C. I., Sharp, J. M., Hauwert, N., Landrum, J., and White, K. M. (2012). Impact of urban development on physical and chemical htdrogeology. *Elements* 8, 429–434. doi: 10.2113/gselements.8.6.429

Zielinski, R. A., Asher-Bolinder, S., and Meier, A. L. (1995). Uraniferous waters of the Arkansas River valley, Colorado, U.S.A.: a fuction of geology and land use. *Appl. Goechem.* 10, 133–144. doi: 10.1016/0883-2927(95)00002-2

Zielinski, R. A., Asher-Bolinder, S., Meier, A. L., Johnson, C. A., and Szabo, B. J. (1997). Natural or fertilizer-derived uranium in irrigation drainage: a case study in southeastern Colorado, U.S.A. *Appl. Geochem.* 12, 9–21. doi: 10.1016/S0883-2927(96)00050-9

Zielinski, R. A., Simmons, K. R., and Orem, W. H. (2000). Use of 234U and 238U isotopes to identify fertilizer-derived uranium in the Florida Everglades. *Appl. Geochem,* 15, 369–383. doi: 10.1016/S0883-2927(99)00053-0

Conflict of Interest: The authors declare that the research was conducted in the absence of any commercial or financial relationships that could be construed as a potential conflict of interest.

frontiers
in Water

ORIGINAL RESEARCH
published: 03 February 2021
doi: 10.3389/frwa.2020.589070

Contrasted Chemical Weathering Rates in Cratonic Basins: The Ogooué and Mbei Rivers, Western Central Africa

Jean-Sébastien Moquet[1,2]*, Julien Bouchez[1], Jean-Jacques Braun[3,4,5], Sakaros Bogning[6], Auguste Paulin Mbonda[7], Sébastien Carretier[3], Vincent Regard[3], Jean-Pierre Bricquet[8], Marie-Claire Paiz[9], Emmanuel Mambela[9] and Jérôme Gaillardet[1]

[1] Université de Paris, Institut de physique du globe de Paris, CNRS, Paris, France, [2] UMR7327 Institut des Sciences de la Terre d'Orléans (ISTO), Université d'Orléans-CNRS/INSU-BRGM, Orléans, France, [3] UMR5563 Géosciences Environnement Toulouse (GET), Université de Toulouse/CNRS/IRD, Toulouse, France, [4] Institut de Recherches Géologiques et Minières/Centre de Recherches Hydrologiques, BP 4110, Yaoundé, Cameroon, [5] International Joint Laboratory DYCOFAC, IRGM-UY1-IRD, BP 1857, Yaoundé, Cameroon, [6] Departement of Earth Sciences, Faculty of Sciences, University of Douala, Douala, Cameroon, [7] National Center for Scientific and Technical Research (CENAREST), Libreville, Gabon, [8] Hydrosciences Montpellier, Montpellier, France, [9] The Nature Conservancy, Libreville, Gabon

OPEN ACCESS

Edited by:
Alexis Navarre-Sitchler,
Colorado School of Mines,
United States

Reviewed by:
Alissa M. White,
University of Arizona, United States
Bryan G. Moravec,
University of Arizona, United States
Richard Wanty,
Colorado School of Mines,
United States

***Correspondence:**
Jean-Sébastien Moquet
jean-sebastien.moquet@
cnrs-orleans.fr

Specialty section:
This article was submitted to
Water and Critical Zone,
a section of the journal
Frontiers in Water

Received: 30 July 2020
Accepted: 10 December 2020
Published: 03 February 2021

Citation:
Moquet J-S, Bouchez J, Braun J-J,
Bogning S, Mbonda AP, Carretier S,
Regard V, Bricquet J-P, Paiz M-C,
Mambela E and Gaillardet J (2021)
Contrasted Chemical Weathering
Rates in Cratonic Basins: The Ogooué
and Mbei Rivers, Western Central
Africa. Front. Water 2:589070.
doi: 10.3389/frwa.2020.589070

Despite the absence of tectonic activity, cratonic environments are characterized by strongly variable, and in places significant, rock weathering rates. This is shown here through an exploration of the weathering rates in two inter-tropical river basins from the Atlantic Central Africa: the Ogooué and Mbei River basins, Gabon. We analyzed the elemental and strontium isotope composition of 24 water samples collected throughout these basins. Based on the determination of the major element sources we estimate that the Ogooué and Mbei rivers total dissolved solids (TDS) mainly derive from silicate chemical weathering. The chemical composition of the dissolved load and the area-normalized solute fluxes at the outlet of the Ogooué are similar to those of other West African rivers (e.g., Niger, Nyong, or Congo). However, chemical weathering rates ($\mathrm{TZ}^{+}_{\mathrm{sil}}$ rate expressed as the release rate of the sum of cations by silicate chemical weathering) span the entire range of chemical weathering intensities hitherto recorded in worldwide cratonic environments. In the Ogooué-Mbei systems, three regions can be distinguished: (i) the Eastern sub-basins draining the Plateaux Batéké underlain by quartz-rich sandstones exhibit the lowest $\mathrm{TZ}^{+}_{\mathrm{sil}}$ rates, (ii) the Northern sub-basins and the Mbei sub-basins, which drain the southern edge of the tectonically quiescent South Cameroon Plateau, show intermediate $\mathrm{TZ}^{+}_{\mathrm{sil}}$ rates and (iii) the Southern sub-basins characterized by steeper slopes record the highest $\mathrm{TZ}^{+}_{\mathrm{sil}}$ rates. In region (ii), higher DOC concentrations are associated with enrichment of elements expected to form insoluble hydrolysates in natural waters (e.g., Fe, Al, Th, REEs) suggesting enhanced transport of these elements in the colloidal phase. In region (iii), we suggest that a combination of mantle-induced dynamic uplift and lithospheric destabilization affecting the rim of the Congo Cuvette induces slow base level lowering thereby enhancing soil erosion, exhumation of fresh primary minerals, and thus weathering rates. The study points out that erosion of lateritic covers in cratonic areas can significantly enhance chemical weathering rates by bringing fresh minerals in contact with meteoric water. The heterogeneity of weathering rates amongst cratonic regions thus need to be considered for reconstructing the global, long-term carbon cycle and its control on Earth climate.

Keywords: chemical weathering, river hydrochemistry, Congo craton, Western Central Africa, Ogooué River basin, regolith rejuvenation

INTRODUCTION

Over geological time scales, chemical weathering acts as a major player of the global biogeochemical cycles of elements in the Earth's Critical Zone. In particular, silicate weathering is known to consume CO_2 through mineral hydrolysis and neutralization of base cations hosted by silicate minerals, and therefore can contribute to regulating the global climate (Berner et al., 1983). Tectonic activity is thought to be a primary driver of chemical weathering (Raymo and Ruddiman, 1992; Herman et al., 2013). Orogenic uplift associated with collision between tectonic plates forms the major world mountain chains, favoring mechanical erosion, and the exposure of fresh primary mineral surfaces to meteoric water and subsequent chemical weathering. This phenomenon has long been suggested to be responsible for the gradual cooling of the Earth over the Cenozoic under the effect of global mountain uplift (Herman et al., 2013; Becker et al., 2018), although this hypothesis is strongly debated (e.g., Godderis, 2010; Willenbring and Von Blanckenburg, 2010; Von Blanckenburg et al., 2015; Norton and Schlunegger, 2017; Caves Rugenstein et al., 2019; Hilton and West, 2020; Penman et al., 2020). By contrast, tectonically quiescent cratonic areas, which represent almost 70% of the continents surface (Artyushkov et al., 2018), have long been considered to be relatively inefficient in terms of chemical weathering compared to erosive, mountainous regions (e.g., Carson and Kirkby, 1972; Stallard, 1985). Indeed, especially in the humid tropics, these low-relief settings favor the formation of deep regolith covers, chemically depleted in base cations and limiting water-bedrock interactions due to slow water percolation from the surface to the bedrock (e.g., Stallard and Edmond, 1987; Braun et al., 2005, 2012; West, 2012; Riebe et al., 2017). While these hot and humid cratonic areas commonly exhibit low silicate weathering rates by comparison with orogenic areas (e.g., Gaillardet et al., 1999b; Moon et al., 2014) they dominate the intertropical regions surface area and, therefore, represent a significant proportion of the global delivery of dissolved matter to the oceans (Milliman and Farnsworth, 2011; Von Blanckenburg et al., 2015). In particular, according to modeling results (Goddéris et al., 2008) the net weathering budget of the intertropical cratonic areas and their role on the long term CO_2 budget may have been underestimated and need to be investigated in more detail to characterize their potential role in the Cenozoic global climate evolution.

River hydrochemical analyses are essential tools for estimating catchment-scale silicate weathering fluxes, through the quantification of the export of silicate-derived dissolved cations (Gaillardet et al., 1999b). River basins draining cratonic areas exhibit contrasted weathering rates (expressed as the drainage-area normalized flux of the sum of cations released by silicate chemical weathering, TZ^+_{sil} rate) from those recorded under boreal conditions (TZ^+_{sil} rate $< 1\,t\ km^{-2}\ yr^{-1}$; Millot et al., 2002; Zakharova et al., 2005, 2007; Pokrovsky et al., 2015) to those measured in India in the Kavery (Pattanaik et al., 2013) and Nethravati (Gurumurthy et al., 2012) basins (TZ^+_{sil} rate $> 15\,t\ km^{-2}\ yr^{-1}$). Various drivers can be invoked to explain this spatial variability. For example, the Nsimi experimental watershed is located in a tectonically quiescent area of the Nyong river basin (South Cameroon Plateau) where swamp environments are widespread. There, organic-rich waters increase the mobilization and transfer of some elements generally considered as immobile (e.g., Al, Fe, Th, Zr) through colloidal transport (Oliva et al., 1999; Viers et al., 2000; Braun et al., 2005, 2012). Such enhancement of weathering in the presence of organic matter has also been reported for boreal Siberian rivers rich in dissolved organic matter and poor in suspended matter (Zakharova et al., 2005, 2007; Pokrovsky et al., 2015, 2016). Indeed, in this type of environment such environments, organo-metal complexes form, leading to the solubilization of Al, Fe, Th, and Zr and thus to the breakdown of silicate minerals (e.g., Oliva et al., 1999; Tamrat et al., 2019). The Kaveri and Nethravati basins drain the Indian craton and exhibit low annual runoff ($<220\,mm\ yr^{-1}$) by comparison with other tropical cratonic areas. In this region, intense monsoons can enhance weathering through strong erosional processes, exposing of felsic granulites and gneissic rocks (Pattanaik et al., 2013; Meunier et al., 2015). In this case, climate and erosion act as dominant drivers of weathering rates. Finally, in the small monolithologic basins of the Mule Hole-India tropical watershed, the presence of minor/accessory minerals (Ca-bearing minerals like epidote and apatite), the dissolution of smectite and calcite, as well as the drainage characteristics of weathering profiles have all been shown to play a key role on weathering budget (Braun et al., 2009; Violette et al., 2010). However, most of the aforementioned work has focused on a local scale (i.e., soil profiles or small watersheds) or, when dealing with weathering fluxes measured at a larger scale, the variability of weathering rates amongst cratonic environments was not considered to be part of the scope of the study.

The existence of sustained uplift due to mantle dynamics or lithospheric destabilization (Cottrell et al., 2004; Jaupart et al., 2007; Hu et al., 2018) in cratonic areas has not been considered yet as a potential driver of Earth denudation. Although much slower and occurring over larger spatial scales than mountain uplift mediated by faulting in collisional tectonic settings (Lamb and Watts, 2010; Flament et al., 2013), mantle-induced dynamic uplift or lithospheric destabilization can lead to lowering of the geomorphological base level that in turn can trigger physical erosion processes (Kusky et al., 2014) as observed for the Southern African Craton (Braun et al., 2014), North China Craton (Zhu et al., 2017) or Brazilian Shield (Rodríguez Tribaldos et al., 2017). Such slow, large-scale mantle and lithospheric dynamics, in conjunction to eustatic changes, have also been shown to control relief as well as erosion and sedimentary processes (Conrad and Husson, 2009; Guillocheau et al., 2015). Presumably, physical erosion processes sustained by mantle induced dynamic uplift or lithospheric destabilization in cratonic settings could lead to significant rock weathering through soil erosion and subsequent increased exposure of "fresh" mineral surfaces—a phenomenon we set out to address in the present study.

The Ogooué River Basin, western Central Africa, is located between the western border of the Congo cuvette and the south of the Cameroun Plateau. This intra-cratonic basin experiences a homogeneous tropical humid climate (Bogning et al., 2018, 2020) and has undergone successive and contrasted uplift phases over the Cenozoic (Guillocheau et al., 2015). The present study provides the opportunity to explore the variability in weathering fluxes and rates in the large Ogooué River Basin (drainage area of ∼ 215,000 km²) as well in the neighboring, smaller Mbei River Basin (drainage area of ∼ 1,800 km^2) with respect to geomorphology, tectonics, and lithology. Based on discrete hydrochemical analyses of the main Ogooué River tributaries, we assess, for the first time, the Ogooué weathering fluxes and their variability throughout the basin. These new constraints allow us to explore the main potential drivers controlling the variability in weathering rates in cratonic areas and to discuss the implications for the long-term evolution of the Earth's climate.

STUDY AREA

The equatorial Ogooué River basin covers ∼215,000 km² (location: between 3°9'S and 2°4'N and between 8°5'E and 14°3E; **Figure 1**). Around 85% of the basin lies within Gabon, 12% in the Republic of Congo and the remaining area in Cameroon and Equatorial Guinea. With an annual discharge of 4,750 $m^3\ s^{-1}$ (Bogning et al., 2018), the Ogooué is the third largest river in terms of annual discharge along the African West Coast after the Congo (∼41,000 $m^3\ s^{-1}$; Laraque et al., 2009) and the Niger (∼6,000 $m^3\ s^{-1}$) rivers (Dai and Trenberth, 2002). In addition to the Ogooué Basin, this study reports on the hydrochemistry of the smaller Mbei River (location: between 0°1'N and 1°1'N and between 10°7'E and 10°4E; **Figure 1**), which is a northern tributary of the Komo River discharging to the Atlantic Ocean around 150 km north of the Ogooué River outlet. The Mbei River is characterized by an annual discharge of ∼60 $m^3\ s^{-1}$ (ORSTOM, 1964; Njutapvoui Fokouop, 2017; data only available for the period 1964–1973) and a drainage area of ∼ 1,800 km^2. According to the Köppen-Geiger classification, the Ogooué and Mbei basins experience a tropical savanna climate. The Ogooué Basin receives around 2,000 mm yr^{-1} in annual precipitation, which leads to a runoff of around 700 mm yr^{-1} (Mahe et al., 2013; Bogning et al., 2018; Kittel et al., 2018). The basin exhibits a bi-modal precipitation regime with wet periods from March to May and from October to December with a maximal monthly rainfall of ∼200 and ∼300 mm $month^{-1}$, respectively. The dry period extends from June to August with a minimum monthly rainfall <15 mm $month^{-1}$ in July. The mean annual temperature is around 24°C and is relatively invariant across the year. In the present work, the study area corresponds to the Ogooué Basin upstream from the Lambaréné station (**Figure 2F**) and covers 206,000 km², representing 96% of the entire Ogooué Basin (**Figure 1**), combined to four Mbei tributaries each covering basin areas <500 km². At the Lambaréné station, the Ogooué River discharge variation follows the rainfall regime of the basin (Mahe et al., 1990). Overall, the seasonal variability in discharge (SV as quantified by the ratio between maximum and minimum monthly discharge; SV = 3.7; **Figure 3**) is relatively low by comparison with other intertropical rivers experiencing a monsoonal regime (e.g., Pacific Peruvian rivers: SV = 6–21; Moquet et al., 2018; Nethravati River: SV = 600–1,100; Gurumurthy et al., 2012). The elevation of the Ogooué basin, as considered in the present study, extends from 914 m.a.s.l (Lolo River sub-basin upstream) to 20 m.a.s.l. (Lambaréné station).

The Ogooué Basin can be separated into three geomorphological domains (**Figure 1**; **Table 1**). The Plateaux Batéké region (Eastern sub-basins) located close to the Congo border is composed of Cenozoic sandstone (pure quartz; Seranne et al., 2008) and is active in terms of dynamic uplift (Guillocheau et al., 2015; Weber et al., 2016). The rest of the basin is underlain by the Archean basement of the Congo craton and by remnants of Proterozoic orogenic belts. The rivers of the Northern sub-basins exclusively drain granitic rocks of the Archean craton whereas the Southern sub-basins are to a significant extent underlain by Paleoproterozoic sedimentary rocks in addition to the typical Archean cratonic rocks (gneiss and undifferencied orthogneiss; Thiéblemont et al., 2009). Some sub-basins in the Northern part (Missanga basin) and in the Southern part (Leyou basin) partly drain Paleoproterozoic volcanic and volcanic sedimentary rocks (Thiéblemont et al., 2009). The southernmost area is characterized by the presence of the Ogoulou-Offoué and Ikoy-Ikobé Faults which produce steeper relief, particularly in the Lopé sub-basin (Weber et al., 2016). The central Ogooué channel flows over Quaternary fluvial sediments laying on the Paleoproterozoic Francevilian metasediments (1,800–1,600 Ma—Seranne et al., 2008; Weber et al., 2016). The Mbei basin is essentially underlain by the Archean craton. Based on Nd radiogenic isotopes measurements, Thiéblemont et al. (2014) show that the whole Ogooué Basin is covered by a homogenous 1–3 meter-thick sandy to clayey lateritic surface cover (dated at around 3,000–2,000 years BP) named "Cover Horizon" inherited from silt- to clay-sized aeolian deposits transported from the Northern part of the Namibia desert.

The study area is essentially covered by rainforest with patchy savanna grassland and is home to a high biodiversity (e.g., Koffi et al., 2011), but has shifted following climate changes over the last 26,000 years (Kim et al., 2010; Oslisly et al., 2013). Approximately 650,000 people live in the Ogooué Basin resulting in a low population density of <3

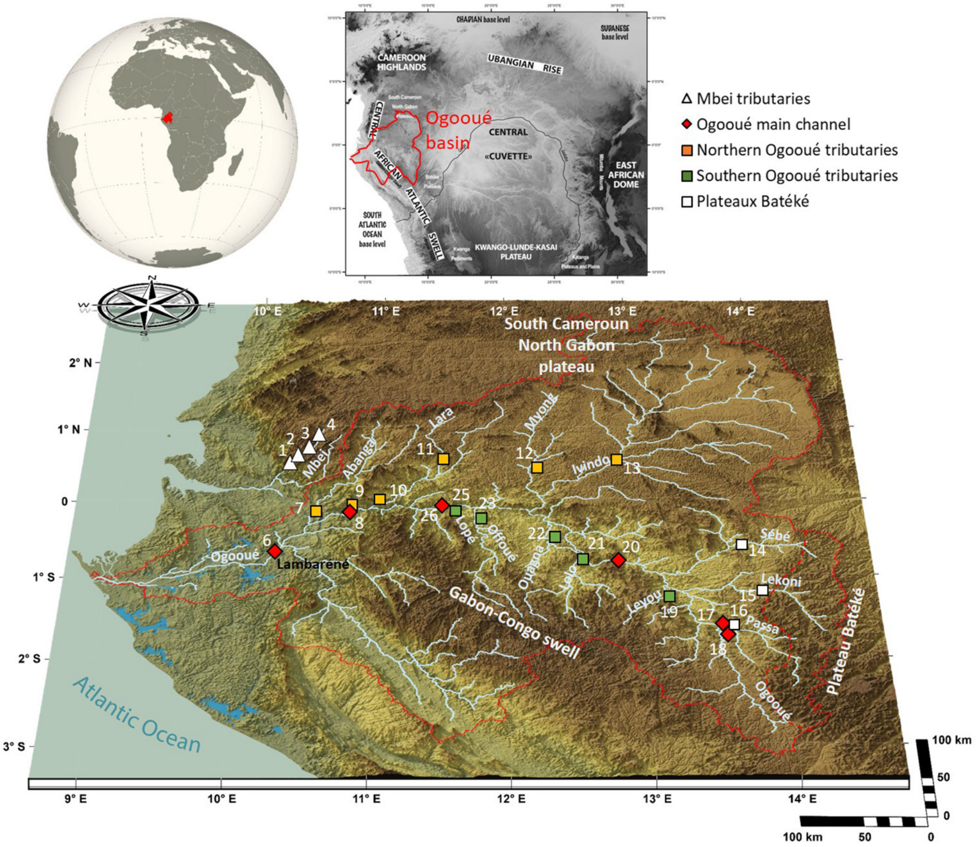

FIGURE 1 | Study area and sampling locations. The regional map of the study area is modified from Guillocheau et al. (2015).

FIGURE 2 | Photos of **(A)** Mbei river tributary 1, **(B)** Ivindo river at Loaloa (a Northern basin), **(C)** Lékoni river at Lakeni (Plateaux Batéké basin), **(D)** Lopé river at Lopé (a Southern basin), **(E)** Ogooué River at Ndjolé, and **(F)** Ogooué River at Lambaréné.

inhabitants km^{-2}, mostly concentrated along the river courses (UNEP, 2010). Uranium and manganese mining activity is reported in the Southern Upper Ogooué area and future dam development may potentially affect river connectivity (Cutler et al., 2020). However, overall the contemporary anthropogenic influence on the Ogooué River system can be assumed as insignificant in terms of chemistry, water flow, and sediment fluxes.

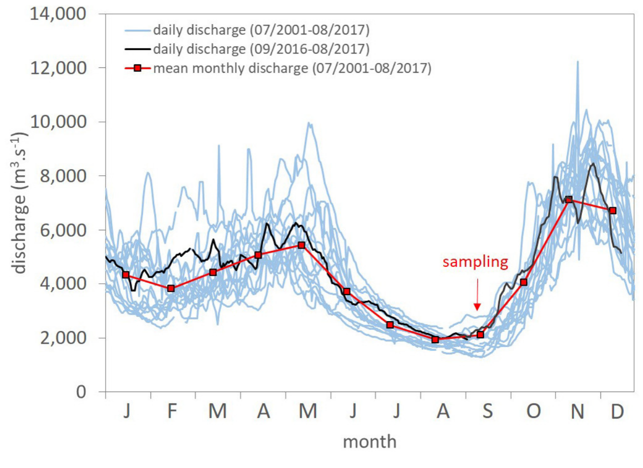

FIGURE 3 | Daily discharge (07/2001 to 08/2017) and mean monthly discharge of the Ogooué River at the Lambaréné station (Bogning et al., 2018). See photo of the Ogooué River at Lambaréné City (**Figure 2F**).

MATERIALS AND METHODS

Sampling and *in-situ* Analyses

Surface water samples were collected at 24 locations in the Ogooué main channel (six samples), Ogooué's tributaries (14 samples), and in the Mbei River tributaries (four samples) in September 2017 (**Figures 1**, **2**; **Table 1**).

Electrical conductivity (normalized to a temperature of 25°C), pH and water temperature were measured *in situ*. We followed the protocol of Bouchez et al. (2012) for water sampling and filtration. Briefly, 10 L of surface water were sampled with a "plastic bag" at the middle of the river course, when possible, or from the bank in a zone of significant water velocity. The plastic bags were filled with a graduated, 5 L bucket and a funnel, both previously rinsed with water from the river being sampled. The bags were rinsed three times with riverine water prior to sampling. The 10 L water samples were transported in a cool box to limit their warming and were filtered 2–10 h later through PES (Millipore) 0.22–μm porosity, pre-weighted filter membranes (142 mm diameter). The filtration unit was filled three times with ~1 L of water sample, each of which was discarded after filtration to pre-condition the filter unit and the membrane. Gloves were used to avoid contamination during the filtration process. The remaining filtered water was splitted into three aliquots: one unacidified aliquot of 30 mL for major anion analyses, one acidified (using three drops of mono-distilled nitric acid to reach a pH ~ 2) aliquot of 1L for cation, trace element, and $^{87}Sr/^{86}Sr$ analyses, and one acidified (using HCl) aliquot of 60 mL stored in an amber glass tube for dissolved organic carbon (DOC) analysis. Alkalinity was determined on the field using the Gran method (Gran, 1950). Note that the filtered water samples ($<0.22\ \mu m$) are considered to reflect primarily a "truly dissolved" fraction, but are likely to include organic and inorganic colloids, depending on the element considered. This is further discussed in section Dynamics of Organic Matter and Colloids.

Analytical Methods

All laboratory procedures and measurements were performed at the PARI (Plateau d'Analyse Haute Résolution) analytical platform of the IPGP (Institut Physique du Globe de Paris). Major cations (Ca^{2+}, Na^+, Mg^{2+}, K^+) and major anions (Cl^-, SO_4^{2-}, and NO_3^-) concentration were determined using ion chromatography (CS16 cationic colomn and AS9HC anionic column—IC5000+DIONEX THERMO). Trace elements were analyzed by Quadrupole-ICP-MS (ICP-QMS 7900 Agilent). For major element concentration, the analytical uncertainty is around 5% (95% confidence interval), and for most trace elements, the analytical uncertainty is <5%. Accuracy was checked using repeated measurements of the river water reference material SLRS-6 (St-Lawrence River water, National Research Council of Canada), with concentration measurements being mostly <10% away from the certified concentrations. DOC concentrations was quantified using a Shimadzu TOC-V CSH with a relative analytical uncertainty <5%. Major element and DOC concentrations are reported in **Table 2** and trace element concentration are reported in **Table 3**.

The TDS (Total Dissolved Solids) concentration corresponds to the sum of the cations (Ca^{2+}, Mg^{2+}, Na^+, and K^+), the anions (HCO_3^-, SO_4^{2-}, and Cl^-) and SiO_2 concentrations, all expressed in mg l^{-1} (**Table 2**).

Isotopic Measurements

The chemical purification of Sr (~200 ng) was performed using extraction chromatography (Sr-SPEC resin; Eichrom) before isotope analysis according to Hajj et al. (2017) with a total blank of <0.5 ng along the Sr separation and MC-ICP-MS measurements procedures. The Sr isotopic composition was measured on a 50 ppb Sr solution within a 0.5 N HNO_3 matrix by MC-ICP-MS (Neptune, ThermoFisher Scientific). Each sample was analyzed three times. The instrumental mass fractionation was corrected for using a $^{86}Sr/^{88}Sr$ ratio of 0.1194. An average internal precision of ± 10 ppm (2σ) was obtained and the quality of the $^{87}Sr/^{86}Sr$ ratio measurements was verified by repeated analysis of the NIST SRM987 standard ($n = 21$; measured value: $^{87}Sr/^{86}Sr = 0.710320 \pm 0.000015$; certified range: $^{87}Sr/^{86}Sr = 0.71034 \pm 0.00026$; accepted NIST SRM987 value: $^{87}Sr/^{86}Sr = 0.71026 \pm 0.00002$; Stein et al., 1997; Swoboda et al., 2008). Uncertainty on the $^{87}Sr/^{86}Sr$ measurements are lower than 0.000043 (95% confidence interval on the three replicates; **Table 2**).

Discrimination of Solute Sources

To discriminate between the different river solutes sources we use a "forward method" (Garrels and MacKenzie, 1972; Moquet et al., 2011), consisting in the application of two calculation steps: atmospheric correction and quantification of the relative roles of silicate and carbonate weathering.

Atmospheric Inputs

In the studied basins, the primary source of Cl^- is precipitation as evaporite rocks are virtually absent from the Ogooué and Mbei basins (Thiéblemont et al., 2009) and because anthropogenic inputs can be considered as negligible (see section Study Area).

TABLE 1 | Main characteristics of the Mbei and Ogooué rivers and their tributaries.

Group	Sampling date	Sample number	River	Location	Sampling site characteristics				Basin characteristics				
					Latitude	Longitude	Sampled site elevation	Annual mean discharge	Basin area	Basin elevation	Mean basin slope	Rainfall	Specific discharge
					Decimal degree		m.a.s.l.	m^3 s^{-1}	km²	m.a.s.l.	%	mm yr^{-1}	mm yr^{-1}
Mbei tributaries	05/09/2017	1	Mbei tributary 1		0.5332	10.2148	139 ± 3	0.36 ± 0.06	13	448	7.9	2,244	890
	05/09/2017	2	Mbei tributary 2	Akelayong	0.5874	10.2541	160 ± 9	0.14 ± 0.02	5	387	7.5	2,244	890
	05/09/2017	3	Mwengue	Akoga	0.8709	10.4961	534 ± 3	2.4 ± 0.68	135	639	1.0	1,957	567
	05/09/2017	4	Binguili	Assok	0.7110	10.3570	526 ± 3	0.36 ± 0.06	13	613	0.8	2,244	890
Ogooué R. main channel	10/09/2017	18	Ogooué	Dam Poubara 2	−1.7728	13.5499	420 ± 3	454 ± 45	8,778	582	0.7	2,663	1,631
	10/09/2017	17	Ogooué	Franceville	−1.6355	13.5314	285 ± 5	781 ± 76	14,944	555	1.0	2,672	1,650
	12/09/2017	20	Ogooué	Lastourville	−0.8096	12.7285	228 ± 3	1,928 ± 233	45,823	493	1.1	2,512	1,328
	13/09/2017	26	Ogooué	Ayem	−0.1037	11.4153	88 ± 3	3,674 ± 726	142,373	502	0.9	2,186	814
	07/09/2017	8	Ogooué	Ndjolé	−0.1827	10.7701	16 ± 3	3,933 ± 818	160,312	497	1.0	2,155	774
	06/09/2017	6	Ogooué	Lambaréné (SEEG)	−0.7139	10.2221	3 ± 3	4,341*	205,585	467	1.2	2,159	666*
Northern Ogooué tributaries	07/09/2017	7	Abanga	Bel_Abanga	−0.2726	10.4847	16 ± 3	139 ± 42	8,265	448	1.3	1,915	531
	07/09/2017	9	Missanga	Ndjolé	−0.1800	10.7687	13 ± 3	8.3 ± 2.4	483	281	3.0	1,933	546
	07/09/2017	10	Okano	Alembé	−0.0591	10.9782	46 ± 3	183 ± 56	11,135	494	1.1	1,902	521
	07/09/2017	11	Lara	Mindzi	0.6034	11.4966	313 ± 5	35 ± 10.4	2,049	590	0.8	1,935	547
	08/09/2017	12	Mvoung	Ovan	0.3136	12.1879	404 ± 3	160 ± 44	8,803	523	0.5	1,967	575
	08/09/2017	13	Ivindo	Loaloa	0.5215	12.8245	462 ± 3	892 ± 252	49,503	549	0.6	1,960	569
Southern Ogooué tributaries	12/09/2017	19	Leyou	Ndoubi	−1.3313	13.0989	293 ± 3	53 ± 5	1,161	592	1.5	2,579	1458
	12/09/2017	21	Lolo	Lolo	−0.6685	12.4929	213 ± 3	258 ± 38	7,582	531	1.6	2,368	1,077
	12/09/2017	22	Ouagna	Wagny	−0.5988	12.3150	201 ± 4	56 ± 10	2,020	394	1.3	2,236	880
	12/09/2017	23	Offoué	Entrance Lopé park	−0.3510	11.7627	183 ± 3	159 ± 36	7,057	493	1.8	2,103	713
	13/09/2017	25	Lopé	Lopé	−0.1102	11.6019	118 ± 3	6.1 ± 1.9	379	322	2.0	1,890	512
Plateaux Batéké	09/09/2017	14	Sébé	Okandja	−0.6176	13.6812	295 ± 3	136 ± 23	4,513	458	0.8	2,287	952
	09/09/2017	15	Lékoni	Akieni	−1.1852	13.8773	387 ± 3	263 ± 25	4,911	537	1.4	2,692	1694
	10/09/2017	16	Passa	Franceville	−1.6294	13.6103	287 ± 3	312 ± 30	5,892	524	1.6	2,682	1,672

*Drainage area and mean slope are based on the SRTM 90 digital elevation model (NASA). For annual discharge values, * represent the measured discharge at Lambaréné station (Bogning et al., 2018) and the other values are deduced from rainfall (Q_{spe} uncertainty = 161 mm yr^{-1}; see section Hydrological and Climate Data for details).*

TABLE 2 | Physico-chemical parameters, major elements concentrations, DOC concentrations, and strontium isotopic ratios ($^{87}Sr/^{86}Sr$) measured in the river dissolved phase (i.e., <0.22 µm) of the Ogooué and Mbei and basins.

Group	sample number	temperature	pH	conductivity	TSS	DOC	Na^+	K^+	Mg^{2+}	Ca^{2+}	Sr^{2+}	F^-	Cl^-	NO_3^-	SO_4^{2-}	HCO_3^-	Si	TDS	TZ^+	TZ^-	NICB	$^{87}Sr/^{86}Sr$	±
		°C		µS cm^{-1}	mg l^{-1}		µmol l^{-1}											mg l^{-1}	meq l^{-1}				10^{-5}
Mbei tributaries	1	22.4	7.22	26	6	1.7	95.9	15.7	28.1	32.6	0.21	6.1	28.3	8.0	8.4	172	210	30.2	233	232	0%	0.72161	1.8
	2	22.2	6.90	20	9	1.1	66.6	12.9	20.4	27.4	0.15	5.3	9.4	8.4	4.1	144	212	26.4	175	176	0%	0.71440	2.3
	3	22.9	6.58	16	21	1.1	63.2	13.8	16.2	24.6	0.13	4.3	12.0	9.4	3.9	122	209	24.7	158	155	1%	0.71709	2.4
	4	21.6	6.75	20	8	1.4	68.6	14.5	19.6	27.1	0.13	8.5	16.3	10.9	4.9	133	195	25.3	177	179	−1%	0.71783	2.3
Ogooué R. main channel	18	27.4	6.93	17	9	2.1	66.1	17.3	16.7	26.0	0.25	7.1	7.9	0.0	3.7	108	205	23.3	169	131	13%	0.71880	1.2
	17	24.8	6.62	18	10	2.3	63.3	15.3	17.4	23.7	0.17	6.6	7.7	0.0	4.2	107	218	23.7	161	129	11%	0.71837	2.6
	20	26.9	6.76	16	30	1.6	44.8	11.2	15.8	20.0	0.11	15.5	8.6	0.0	6.0	88	206	21.5	128	124	1%	0.71752	0.9
	26	27.2	7.10	26	21	2.7	77.0	19.3	28.8	32.6	0.22	7.7	8.3	0.0	9.0	158	255	30.6	219	192	7%	0.71658	4.0
	8	26.5	7.08	26	18	2.7	77.5	20.2	29.2	34.3	0.18	9.0	9.5	0.0	8.5	151	252	30.2	225	187	9%	0.71730	0.5
	6	27.1	7.10	27	9	2.5	80.1	21.7	31.0	35.0	0.21	9.6	10.2	0.0	9.2	175	250	31.8	234	213	5%	0.71765	1.2
Northern Ogooué tributaries	7	24.9	6.82	34	70	2.5	111	24.2	39.6	46.0	0.28	11.8	19.5	0.0	7.2	252	273	39.4	306	298	1%	0.71532	1.5
	9	24.9	6.84	39	29	1.8	88.5	16.8	62.1	56.7	0.33	11.8	25.0	5.4	20.0	248	229	38.5	343	330	2%	0.72012	2.5
	10	25.4	7.18	30	23	4.6	94.3	28.2	35.8	41.8	0.26	10.8	17.6	1.1	12.8	193	240	34.0	278	248	6%	0.71712	0.6
	11	23.9	6.85	20	21	5.0	69.4	15.8	21.6	28.0	0.16	8.2	9.5	1.0	4.7	126	190	23.8	185	154	9%	0.71502	2.7
	12	24.3	6.68	27	19	4.3	91.9	25.7	29.8	39.5	0.21	10.2	12.7	0.0	4.5	193	275	34.6	256	225	6%	0.71691	3.4
	13	26.7	6.32	23	14	11.1	65.1	22.4	27.7	34.4	0.17	7.8	14.2	1.2	21.2	67	188	22.5	212	132	23%	0.71801	1.7
Southern Ogooué tributaries	19	24.2	7.32	48	48	2.0	191	34.0	41.8	63.8	0.48	23.8	11.7	0.0	6.3	362	442	59.1	436	410	3%	0.71347	1.6
	21	27.7	7.52	60	15	1.7	216	40.8	56.9	85.2	0.75	5.1	5.7	0.0	8.0	535	484	73.6	541	561	−2%	0.71250	1.8
	22	28.1	7.62	78	19	2.0	168	40.6	117	137	0.45	26.1	15.3	0.0	15.2	589	390	75.1	715	660	4%	0.71479	2.4
	23	27.2	7.29	47	16	1.7	161	37.4	50.1	57.4	0.38	17.8	12.1	0.0	8.0	343	398	54.7	413	388	3%	0.71970	2.5
	25	25.6	7.23	51	6	2.5	174	44.1	62.3	57.6	0.52	22.5	21.5	0.0	10.5	389	372	57.5	458	454	0%	0.72257	4.3
Plateaux Batéké	14	26.3	6.30	11	19	1.7	32.7	6.37	11.2	15.8	0.00	4.43	5.37	<D.L.	10.2	44	213	18.6	93.2	74.1	11%	-	
	15	26.4	4.63	8	15	0.9	2.13	2.12	2.93	6.26	0.00	1.31	3.02	<D.L.	10.0	0.0	162	11.3	22.6	24.4	−4%	-	
	16	25.6	5.20	5	22	1.2	5.97	3.86	4.24	6.77	0.00	1.27	4.32	2.0	7.0	0.89	155	11.0	31.8	22.5	17%	-	

TSS, DOC, TDS, and NICB stand for "total suspended solid", "dissolved organic carbon," "total dissolved solid," and "normalized inorganic charge balance," respectively. Uncertainty on major elements is <5%.

TABLE 3 | Concentration (in ppb or μg.l^{-1}) of trace elements in the dissolved phase (i.e., <0.22 μm) of the Ogooué and Mbei basins.

Group	Sample number	Li	Be	Al	Ti	V	Cr	Mn	Fe	Co	Ni	Cu	As	Rb	Sr	Y	Nb	Cd	Sn	Cs	Ba
											ppb (μg.l^{-1})										
Mbei tributaries	1	0.580	0.0059	32.2	0.751	0.216	0.160	1.54	40.3	0.031	0.339	0.556	0.017	1.62	14.6	0.060	0.011	0.0008	0.001	0.010	17.7
	2	0.302	0.0041	5.76	0.199	0.144	0.135	3.25	14.9	0.041	7.14	0.313	0.018	1.61	16.5	0.016	0.0003	0.0016	0.000	0.011	25.3
	3	0.289	0.0054	8.53	<blk	0.165	0.104	4.44	22.7	0.051	0.912	0.320	0.007	1.74	12.4	0.020	<blk	0.0024	<blk	0.010	20.4
	4	0.376	0.0058	11.1	<blk	0.128	0.151	3.12	39.3	0.033	0.198	0.286	0.016	1.75	12.0	0.030	<blk	0.0011	0.001	0.012	17.6
Ogooué R. main channel	18	0.517	0.0029	10.1	<blk	0.162	0.125	1.28	27.9	0.021	0.188	0.182	0.081	2.18	15.0	0.0085	0.0049	0.0009	0.001	0.044	10.1
	17	0.521	0.0033	7.39	<blk	0.153	0.133	0.88	13.9	0.017	0.267	0.285	0.046	2.12	16.8	0.0076	0.0018	0.0008	0.001	0.046	13.2
	20	0.450	0.0023	16.8	0.085	0.240	0.190	3.05	15.4	0.019	0.243	0.287	0.049	1.37	11.3	0.0072	<blk	0.0012	0.001	0.015	8.81
	26	0.634	0.0029	14.2	0.277	0.456	0.185	2.06	26.5	0.021	0.401	0.543	0.081	2.25	20.4	0.022	0.0107	0.0064	0.001	0.019	17.1
	8	0.625	0.0051	14.8	0.076	0.432	0.206	1.80	50.8	0.024	0.472	0.440	0.070	2.46	19.5	0.022	<blk	0.0011	0.002	0.020	16.4
	6	0.602	0.0056	10.6	<blk	0.411	0.205	3.13	22.5	0.029	1.71	0.570	0.065	2.66	20.2	0.020	0.0000	0.0007	<blk	0.017	17.6
Northern Ogooué tributaries	7	0.492	0.0030	22.6	0.289	0.375	0.306	1.93	43.1	0.033	0.854	0.507	0.035	3.06	27.8	0.022	<blk	0.0012	<blk	0.014	23.2
	9	1.183	0.0020	5.76	0.026	0.143	0.080	49.9	46.4	0.108	0.568	0.829	0.100	2.49	19.0	0.032	<blk	0.0020	0.000	0.031	9.84
	10	0.616	0.0075	15.8	0.066	0.344	0.255	7.85	58.6	0.077	0.623	0.715	0.046	3.71	26.8	0.037	0.0003	0.0025	0.001	0.024	21.3
	11	0.242	0.0087	31.6	0.053	0.360	0.365	3.83	54.8	0.088	2.82	0.572	0.040	1.93	16.1	0.034	<blk	0.0010	0.000	0.009	16.7
	12	0.442	0.0063	12.5	0.031	0.439	0.335	7.34	55.3	0.077	0.570	0.489	0.033	3.44	23.8	0.023	0.0038	0.0012	<blk	0.038	24.1
	13	0.597	0.0161	110	0.187	0.559	0.851	14.0	125	0.169	1.20	0.773	0.070	2.94	15.0	0.074	0.0081	0.0068	0.001	0.040	16.5
Southern Ogooué tributaries	19	1.688	0.0027	9.85	0.023	0.779	0.11	1.03	24.5	0.022	0.339	0.377	0.019	3.50	47.3	0.013	0.0002	0.0015	0.000	0.020	30.2
	21	0.870	0.0017	4.54	0.004	0.866	0.08	0.41	12.7	0.017	0.245	0.335	0.029	3.74	64.8	0.008	<blk	0.0003	0.000	0.008	49.2
	22	2.501	0.0045	18.2	0.104	0.471	0.13	7.71	51.4	0.042	0.704	0.719	0.255	3.46	54.2	0.009	0.0012	0.0018	<blk	0.018	52.2
	23	1.872	0.0023	14.2	0.0183	0.432	0.11	5.64	23.2	0.030	0.271	0.498	0.093	4.22	40.1	0.011	<blk	0.0009	0.002	0.030	41.5
	25	1.876	0.0018	10.3	0.0467	0.232	0.06	16.7	40.5	0.070	0.425	0.512	0.064	6.30	53.3	0.011	<blk	0.0005	<blk	0.023	29.7
Plateaux Batéké	14	0.629	0.0033	11.6	<blk	0.224	0.09	4.85	17.8	0.039	0.292	0.313	0.079	0.800	5.81	0.013	<blk	0.0011	0.001	0.007	5.33
	15	0.140	0.0082	29.0	<blk	0.118	0.06	5.48	16.3	0.037	0.420	0.149	0.018	0.271	0.889	0.007	<blk	0.0095	<blk	0.007	2.18
	16	0.174	0.0051	19.1	<blk	0.135	0.06	7.95	6.6	0.040	0.218	0.119	0.028	0.491	1.93	0.007	<blk	0.0047	<blk	0.009	3.69

(Continued)

TABLE 3 | Continued

Group	Sample number	La	Ce	Pr	Nd	Sm	Eu	Gd	Tb	Dy	Ho	Er	Tm	Yb	Lu	Th	U
									ppb (μg.l^{-1})								
Mbei tributaries	1	0.101	0.113	0.0187	0.0719	0.0126	0.0061	0.0128	0.0018	0.0101	0.0021	0.0062	0.0011	0.0055	0.0006	0.0063	0.0036
	2	0.0183	0.0352	0.0039	0.0168	0.0036	0.0049	0.0030	0.0004	0.0024	0.0005	0.0014	0.0002	0.0014	0.0002	0.0018	0.0019
	3	0.0221	0.0467	0.0050	0.0221	0.0039	0.0048	0.0041	0.0004	0.0031	0.0006	0.0019	0.0002	0.0021	0.0001	0.0048	0.0027
	4	0.0351	0.0692	0.0083	0.0342	0.0066	0.0046	0.0064	0.0008	0.0049	0.0010	0.0036	0.0004	0.0032	0.0003	0.0059	0.0035
Ogooué R. main channel	18	0.0124	0.0222	0.0025	0.0100	0.0019	0.0023	0.0018	0.0002	0.0012	0.0002	0.0007	0.0001	0.0003	0.0001	0.0012	0.0026
	17	0.00925	0.0191	0.0021	0.0092	0.0018	0.0026	0.0016	0.0002	0.0012	0.0002	0.0008	0.0001	0.0005	0.0001	0.0021	0.0036
	20	0.0127	0.0224	0.0023	0.0098	0.0018	0.0020	0.0013	0.0002	0.0010	0.0002	0.0005	0.0000	0.0006	0.0000	<blk	0.0041
	26	0.0263	0.0582	0.0070	0.0271	0.0054	0.0045	0.0053	0.0007	0.0036	0.0008	0.0022	0.0004	0.0025	0.0003	0.0169	0.0074
	8	0.0366	0.0742	0.0086	0.0354	0.0071	0.0043	0.0060	0.0007	0.0033	0.0006	0.0021	0.0003	0.0019	0.0003	0.0044	0.0100
	6	0.0277	0.0496	0.0063	0.0269	0.0055	0.0045	0.0044	0.0005	0.0032	0.0005	0.0016	0.0001	0.0019	0.0001	0.0033	0.0104
Northern Ogooué tributaries	7	0.0318	0.0714	0.0070	0.0298	0.0057	0.0054	0.0054	0.0006	0.0029	0.0007	0.0021	0.0003	0.0016	0.0003	0.0032	0.0036
	9	0.0488	0.0968	0.0117	0.0488	0.0084	0.0033	0.0085	0.0009	0.0049	0.0010	0.0032	0.0003	0.0025	0.0005	0.0033	0.0142
	10	0.0527	0.112	0.0121	0.0518	0.0095	0.0061	0.0094	0.0011	0.0066	0.0013	0.0037	0.0004	0.0033	0.0006	0.0198	0.0114
	11	0.0392	0.0802	0.0095	0.0382	0.0071	0.0049	0.0073	0.0009	0.0051	0.0011	0.0033	0.0005	0.0032	0.0004	0.0132	0.0045
	12	0.0275	0.0551	0.0068	0.0264	0.0049	0.0050	0.0051	0.0007	0.0042	0.0007	0.0024	0.0003	0.0023	0.0004	0.0097	0.0080
	13	0.0856	0.183	0.0235	0.0972	0.0208	0.0073	0.0171	0.0023	0.0132	0.0025	0.0078	0.0010	0.0070	0.0010	0.0304	0.0149
Southern Ogooué tributaries	19	0.0245	0.0355	0.0045	0.0191	0.0041	0.0059	0.0032	0.0004	0.0017	0.0004	0.0010	0.0001	0.0013	0.0002	0.0023	0.0026
	21	0.0156	0.0223	0.0031	0.0134	0.0029	0.0096	0.0025	0.0002	0.0011	0.0003	0.0008	0.0001	0.0006	0.0001	0.0014	0.0032
	22	0.0209	0.0335	0.0038	0.0158	0.0026	0.0109	0.0026	0.0003	0.0011	0.0003	0.0008	0.0001	0.0007	0.0001	<blk	0.0040
	23	0.0221	0.0416	0.0046	0.0183	0.0026	0.0088	0.0036	0.0002	0.0016	0.0003	0.0008	0.0001	0.0008	0.0001	<blk	0.0026
	25	0.0244	0.0476	0.0050	0.0201	0.0038	0.0058	0.0038	0.0002	0.0017	0.0003	0.0010	0.0001	0.0007	0.0001	0.0044	0.0071
Plateaux Batéké	14	0.0176	0.0347	0.0037	0.0151	0.0026	0.0015	0.0027	0.0004	0.0019	0.0005	0.0012	0.0001	0.0012	0.0001	<blk	0.0036
	15	0.00740	0.0106	0.0012	0.0053	0.0013	0.0007	0.0011	0.0001	0.0012	0.0001	0.0008	<blk	0.0004	0.0001	<blk	0.0023
	16	0.00338	0.0080	0.0011	0.0049	0.0009	0.0010	0.0010	0.0001	0.0008	0.0002	0.0010	0.0000	0.0008	0.0000	0.0002	0.0025

"<blk" refer to values below the blank values concentration.

Therefore, for all water samples, we can apply the following formula to estimate the atmospheric contribution of each solute (X) concentration ($[X_{rain}]$ in μmoles l^{-1}):

$$[X_{rain}] = [Cl^{-}{}_{riv}] \times \left(\frac{X}{Cl^{-}}\right)_{seawater} \tag{1}$$

with X= SO_4^{2-}, Na^+, Ca^{2+}, Mg^{2+}, K^+, and Sr^{2+}, $[Cl^-_{riv}]$ the total Cl^- concentration in the river, and $\left(\frac{X}{Cl^-}\right)_{seawater}$ the X/Cl^- molar ratio of seawater, considered here as the sole source of ions to the rain (Berner and Berner, 1987). Then the concentration of the element X corrected from the atmospheric inputs (annotated $[X^*]$) is calculated as:

$$[X^*] = [X_{riv}] - [X_{rain}] \tag{2}$$

Thereafter, the "*" symbol stands for concentrations corrected from atmospheric inputs.

Contribution of Silicate and Carbonate Weathering

After correction from rainfall inputs, the dissolved load of the rivers is considered to be the result of weathering of silicate and carbonate minerals. The quantitative estimation of the sum of the cations concentrations delivered by silicate weathering ($[TZ^+_{sil}]$ in mg l^{-1}) is:

$$[TZ^+_{sil}] = [Na_{sil}]M_{Na} + [Ca_{sil}]M_{Ca} + [Mg_{sil}]M_{Mg} + [K_{sil}]M_K \tag{3}$$

with $[X_{sil}]$ the concentration of the cation X (with X = Na^+, Ca^{2+}, Mg^{2+} and K^+) derived from silicate weathering (here in μmoles l^{-1}) and M_C the molar mass of the corresponding cation C (in g mol^{-1}).

We consider that all the K^+ and the Na^+ remaining after correction from atmospheric inputs is derived from silicate weathering only:

$$[Na_{sil}] = [Na^*] \tag{4}$$

$$[K_{sil}] = [K^*] \tag{5}$$

The concentrations of Ca^{2+} and Mg^{2+} derived from silicate weathering can then be calculated as:

$$[Ca_{sil}] = [Na^*]\times(Ca/Na)_{sil} \tag{6}$$

$$[Mg_{sil}] = [Na^*]\times(Mg/Na)_{sil} \tag{7}$$

As the Ogooué Basin drains silicate rocks similar to those of the Congo basin (cratonic plutonic and metamorphic lithology) to estimate $[Ca_{sil}]$ and $[Mg_{sil}]$ and thus $[TZ^+_{sil}]$ we used the value of $(Ca/Na)_{sil} = 0.35 \pm 0.15$ and $(Mg/Na)_{sil} = 0.24 \pm 0.12$ (mol/mol) determined by Négrel et al. (1993) and used for the global scale by (Gaillardet et al., 1999b). Note that these values were previously determined based on water geochemistry of rivers draining only the corresponding rock types, and not the rocks themselves, such that this method does not rely on any particular assumption regarding the congruent or incongruent character of weathering reactions.

Without alternative proton sources such as pyrite oxidation (e.g., Calmels et al., 2007; Yu et al., 2020), the main proton sources for mineral hydrolysis is atmospheric / soil CO_2 dissolution in water. Therefore, the estimation of the CO_2 consumption associated with silicate weathering ($CO_{2\ sil}$ in μmoles l^{-1}) can be calculated following the equation:

$$[CO_{2sil}] = [HCO^-_{3\ sil}] \tag{8}$$

$$[HCO^-_{3\ sil}] = [Na^+_{sil}] + [K^+_{sil}] + 2\times[Ca^{2+}_{sil}] + 2\times[Mg^{2+}_{sil}] \tag{9}$$

After estimating the contribution of silicate weathering to the river dissolved load, the remaining dissolved Ca^{2+} and Mg^{2+} is attributed to carbonate weathering, the result in terms of total concentration ($[TZ^+_{carb}]$ in mg l^{-1}) being therefore:

$$[TZ^+_{carb}] = [Ca^* - Ca_{sil}]M_{Ca} + [Mg^* - Mg_{sil}]M_{Mg} \tag{10}$$

From the metrics mentioned above, we can finally calculate the three components of TDS concentration (mg l^{-1}; **Figure 5**):

$$\begin{aligned} [TDS_{rain}] &= [Cl^-_{rain}]M_{Cl} + [SO_4^{2-}{}_{rain}]M_{SO4} \\ &\quad + [Ca^{2+}_{rain}]M_{Ca} + [Na^+_{rain}]M_{Na} \\ &\quad + [Mg^{2+}_{rain}]M_{Mg} + [K^+_{rain}]M_K && (11) \\ [TDS_{sil}] &= [TZ^+_{sil}] + [SiO_2] + [HCO^-_{3\ sil}]M_{HCO3-} && (12) \\ [TDS_{carb}] &= [TZ^+_{carb}] + 2[HCO^-_{3\ carb}]M_{HCO3-} && (13) \end{aligned}$$

Where $[SiO_2]$ is the SiO_2 concentration express in mg l^{-1}, M_{HCO3-} is the HCO_3^- molar mass and

$$[HCO^-_{3\ carb}](\mu moles\ l^{-1}) = (2[Ca_{carb}] + 2[Mg_{carb}]) \tag{14}$$

Note that $[HCO^-_{3\ sil}]$ is entirely derived from CO_2 consumption during silicate weathering while half of the $[HCO^-_{3\ carb}]$ derives from CO_2 consumption and the other half from the carbonate mineral itself. Also, note that here all SiO_2 is assumed to derive from silicate weathering in these calculations. This set of $[TDS_i]$ and $[TZ^+_i]$ (equations 11-13) parameters indicates the concentration of TDS and TZ^+ apportioned to each specific source process i (atmospheric inputs, silicate weathering, and carbonate weathering).

The fluxes (F) and area-normalized fluxes (F_{spe}) were calculated by multiplying the concentrations of TDS, TZ^+_{sil}, and $CO_{2\ sil}$ by the discharge (Q) and the drainage area-normalized discharge (Q_{spe} also named specific discharge), respectively (see the section Hydrological and Climate Data about the calculation of Q and Q_{spe}). For silicate weathering we also calculated the chemical denudation ($D_{\text{chem sil}}$) expressed in m Ma^{-1} using the concentration of solutes (Ca_{sil}, Mg_{sil}, K_{sil}, Na_{sil}, and SiO_2 in mg l^{-1}), expressed as equivalent oxides (CaO, MgO, K_2O, Na_2O, SiO_2 in mg l^{-1}) and using a rock density (d) of 2.7 g cm^{-3} (West et al., 2005; Bouchez and Gaillardet, 2014):

$$D_{\text{chem sil}} = \frac{Q_{spe}}{d}\left([Ca_{sil}]\,(M_{Ca} + M_O) + [Mg_{sil}]\,(M_{Mg} + M_O) + [K_{sil}]\,(2M_K + M_O) + [Na_{sil}]\,(2M_{Na} + M_O) + [SiO_2]\right) \quad (15)$$

with M_O the molar mass of O. This $D_{\text{chem sil}}$ parameter expresses the rate at which silicate weathering processes result in a lowering of the Earth surface.

Hydrological and Climate Data

Drainage areas and mean slopes upstream of the sampling points were extracted from the digital elevation model SRTM 90 (Shuttle Radar Topography Mission; NASA) using ArgGis 10.3 (Esri) and QGis 2.18. The lithological composition for each sub-basin was also extracted from the lithological map of Gabon using ArcGis 10.3 (Esri) (Thiéblemont et al., 2009; see **Supplementary Table 1**).

The daily water discharge of the Ogooué River is available only for the Lambaréné station from Bogning et al. (2018) for the period from July 2001 to August 2017 (**Figure 3**), meaning that the sampling campaign was performed just after the end of the precipitation record used here. Note that according to the discharge record, which does includes the period where water sampling was carried out (September 2017), the discharge pattern of the hydrological year October 2016–September 2017 is very close to the mean pattern observed for the previous 16 years. Therefore, hydrological and precipitation conditions of the year of water sampling can be considered as representative of the longer period used to constrain hydrological fluxes. We calculated an annual discharge over this period to assess an annual solute flux based on the discrete sampling performed in this study.

To calculate the annual discharge of other sampled sites we apply a statistical approach based on a regional polynomial relationship between specific discharge (Q_{spe}) and rainfall (P) as performed by Scherler et al. (2017) to estimate Q_{spe} in ungauged Himalayan rivers. We first calculated the annual mean rainfall received by each studied sub-basin from the TRMM dataset (extracted for the Ogooué Basin over the period 1998–2015 according to the TRMM data–https://gpm.nasa.gov/). The calculated rainfall for these basins ranges from 1,890 to 2,692 mm.yr^{-1}. At the Lambaréné station, $P = 2{,}159$ mm yr^{-1} and Q_{spe} is calculated according to:

$$Q_{spe} = Q/S/1{,}000 \quad (16)$$

with Q the discharge (136 10^9 m^3 yr^{-1}) and S the basin area (205.9 10^3 km^2). At Lambaréné, Q_{spe} is therefore equal to 666 mm yr^{-1} (**Table 1**).

Second, we compiled a new database (**Supplementary Figure 2**; **Supplementary Table 3**) for both specific discharge (Q_{spe}) and rainfall (P) for rivers of western Central Africa (Congo: Becker et al., 2018; Laraque et al., 2020; Cameroun rivers: BVET observatory database/https://mtropics.obs-mip.fr/catalog-m-tropics and Sighomnou, 2004); Atlantic African rivers: (Lienou et al., 2008; Conway et al., 2009). We then fitted a second-order polynomial relationship to the P–Q_{spe} data from rivers submitted to P between 1,500 mm.yr^{-1} and 3,000 mm yr^{-1} ($n = 32$), corresponding to the conditions measured in the Ogooué and Mbei rivers. The equation of the best fit second-order polynomial is:

$$Q_{spe} = 0.00090P^2 - 2.649P + 2304.03\ (R = 0.95;\ RMSE = 161\ mmyr^{-1}) \quad (17)$$

We then applied this relationship to the P-values estimated for each sub-basin of the Ogooué and Mbei basins. We used the RMSE of the fit (161 mm yr^{-1}) as a measure of the uncertainty on these Q_{spe} estimates (see **Supplementary Figure 2**), and propagated this uncertainty in the solute flux calculations (see section Solute Flux Calculation). Note that for the Ogooué River at Lambaréné station, for a rainfall of 2,159 mm yr^{-1}, the simulated Q_{spe} is 780 mm yr^{-1} while the measured Q_{spe} was 666 mm yr^{-1}. The difference between simulated and measured value is therefore 113 mm yr^{-1} (12%) and is lower than the Q_{spe} uncertainty considered (161 mm yr^{-1}).

Solute Flux Calculation

The area-normalized fluxes (hereafter called F_{spe} and "rates" when referring to weathering variables) of each solute was estimated by multiplying the concentration of each solute parameters values by the Q_{spe} value estimated at each sampling sites. To compute the area-normalized fluxes for each sub-region of the study area, we substracted the upstream fluxes (F) where necessary (i.e., samples number 17, 20, 26, 8, 6 along the Ogooué River and sample number 10 on the Okano River).

Our river hydrochemistry dataset features only one sampling date. Therefore, the computed solute fluxes might be affected by significant uncertainty if solute concentrations were to vary along the year. We first note that in other West African rivers like the Nyong (Viers et al., 2000), the Niger (Picouet et al., 2002) and the Congo (Laraque et al., 2009) rivers, the TDS concentration varies only slightly with discharge throughout the year. This chemostatic behavior is observed in numerous rivers in the world from small to large catchments (e.g., Godsey et al., 2009), enabling first-order estimations of annual river dissolved fluxes based on a limited sampling time resolution. Indeed, under such conditions, solute fluxes are mainly controlled by discharge variability rather than by concentration variability, thereby providing confidence to our flux estimates based on only one sampling campaign. However, a systematic bias might exist in our flux estimates since our sole sampling campaign was performed during the dry season, when the highest river solute concentrations are usually measured. Existing hydrochemical time series on the neighboring Congo River helps assessing this bias. Using only the hydrochemical data corresponding to the lowest monthly discharge (August) for the Congo River at Brazzaville (HYBAM database, http://so-hybam.org/), TDS and cations fluxes are +10% and +20%, respectively, higher than flux estimates based on monthly data covering the whole hydrological cycle. However, while informative for assessing the reliability of our flux estimates for the Ogooué and Mbei rivers, we did not consider that our data can be corrected for this bias using constraints from the Congo River, as the specifics of solute concentration-discharge relationships in rivers can be influenced by a variety of processes (Chorover et al., 2017). In particular these relationships can depend on reactive transport processes (e.g., Ameli et al., 2017; Kim et al., 2017), biological effects (e.g., Moatar et al., 2017) or, like in large rivers in hydrological conditions similar to the Ogooué river, on specific patterns of mixing between tributaries (Moquet et al., 2016; Bouchez et al., 2017). Therefore, we took the estimated bias from the Congo River as a measure of uncertainty on the Ogooué and Mbei river solute fluxes associated with the sampling strategy, i.e., ±20% and ±10% for cation and TDS fluxes, respectively.

We calculated the fluxes (F, in 10^3 t y^{-1} or 10^6 mol y^{-1}) for the total dissolved solids (TDS), the total dissolved solids corrected from atmospheric inputs (TDS^*), dissolved silica (express as SiO_2), the cations derived from silicate weathering (TZ^+_{sil}) and for CO_2 consumption associated to silicate weathering ($CO_{2\ sil}$). The corresponding fluxes are called $F\ TDS$, $F\ TDS^*$, $F\ SiO_2$, $F\ TZ^+_{sil}$, and $F\ CO_{2\ sil}$, respectively. The corresponding area-normalized fluxes (also called "specific fluxes" or "rates," equation 16, in t km^{-2} y^{-1} or 10^3 mol km^{-2} y^{-1}) are called $F_{spe}\ TDS$, $F_{spe}\ TDS^*$, $F_{spe}\ SiO_2$, $F_{spe}\ TZ^+_{sil}$, and F_{spe} $CO_{2\ sil}$, respectively (**Table 4**).

Uncertainty Calculation

The uncertainties associated to the calculated flux values (**Tables 1**, **4** and related figures) take into account the propagation of the uncertainty on the major element concentration measurements (5%), a sensitivity test performed on the Ca/Na_{sil} and Mg/Na_{sil} ratios used in the Equations 6 and 7, the uncertainty on the discharge estimate at each sampling location (RMSE = 161 mm yr^{-1}), and the uncertainty associated to our relatively loose sampling time resolution (20%). Note that the propagation of the uncertainty of Ca/Na_{sil} and Mg/Na_{sil} produces asymmetric values and only affects $F\ TDS_{sil}$, $F\ TZ^+_{sil}$, $F\ CO_{2\ sil}$, and $D_{chem\ sil}$. In the text (sections Results and Discussion) and in the **Table 4**, we thus report these fluxes values as "F^{+x}_{-y}" where F is the central estimate, and F^{+x} and F_{-y} the upper and lower bound of the range of estimates, respectively. According to this method, the relative uncertainties on $F\ TDS$, $F\ TDS^*$, $F\ TDS_{sil}$, $F\ TZ^+_{sil}$, $F\ CO_{2\ sil}$, and $D_{chem\ sil}$ range between 11 and 84% (**Table 4**).

RESULTS

In order to ease the presentation of results and the discussion thereof, we divided the samples into five groups which correspond to individual basins, as well as geomorphological and lithological units (**Table 1**; **Figures 1**, **2**): The Mbei tributaries, the Northern Ogooué tributaries, the Plateaux Batéké Ogooué tributaries, the Southern Ogooué tributaries and the Ogooué River main channel. Note that the Ogooué River main channel exhibit intermediate values for all parameters (pH, conductivity, solutes concentration) indicating that its composition simply results from the mixing between the composition of the upstream tributaries inputs.

Physico-Chemical Parameters

The pH of the river water samples range between 4.63 and 7.62 and the conductivity range between 5 and 78 $\mu S\ cm^{-1}$ (**Table 2**). Intermediate values of pH (6.62–7.10) and conductivity (16–27 $\mu S\ cm^{-1}$) were recorded in the Ogooué mainstream. The two lowest values of pH (<5.5) and conductivity (<10 $\mu S\ cm^{-1}$) were recorded in two tributaries draining the Plateaux Batéké (Lékoni and Passa rivers). The highest values (pH > 7.2 and conductivity > 45 $\mu S\ cm^{-1}$) were recorded in the Southern Ogooué tributaries. The other rivers exhibit intermediate values ($6.30 < pH < 7.18$; $11 < conductivity < 34\ \mu S\ cm^{-1}$). Water temperature range between 21.6 and 28.1°C. The lowest temperature values were recorded in the Mbei tributaries (21.6–22.9°C) whereas the Ogooué Basin samples exhibit a narrow temperature range (23.9–28.1°C). No direct relationship between temperature and elevation is observed. The instantaneous SPM (Suspended Particulate Matter) concentration range between 6 and 70 mg l^{-1} (**Table 2**) and its distribution does not display any clear spatial distribution.

Major Elements and Dissolved Organic Carbon

The TDS concentration (and conductivity) are variable throughout the basin and range between 11 and 75 mg l^{-1} (**Table 2**). The highest values (55–75 mg l^{-1}) were recorded in the Southern basins, the lowest values (11–23 mg l^{-1}) are observed in the rivers draining the sandstone region of the Plateaux Batéké, while the other groups (Northern basins, Mbei tributaries, and Ogooué main channel) exhibit intermediate values (21–39 mg l^{-1}).

The total cationic charge (TZ^+, in meq l^{-1}) is generally dominated by Ca^{2+}, Mg^{2+}, and Na^+ in almost equivalent proportion, while the contribution of K^+ to TZ^+ is systematically lower (7 to 12% of TZ^+). The anionic charge (TZ^-, in meq l^{-1}) is generally dominated by HCO_3^- (> 80% of TZ^-). Concentrations of Ca^{2+}, Mg^{2+}, Na^+, K^+, HCO_3^-, and SiO_2 are significantly correlated to the conductivity and to TDS concentration and thus followed the same spatial distribution (**Table 2**). The SiO_2 contribution to TDS concentration range from 86% (Plateaux Batéké) to 31% (Southern basins) and decrease in importance as the TDS concentration increases. Interestingly, dissolved Si concentration is correlated to HCO_3^- concentration ($R = 0.91$; $n = 24$; $p < 0.01$; **Figure 4B**), showing that the alkalinity and, therefore, CO_2 consumption associated with water-rock interactions were likely due to silicate weathering in the Ogooué and Mbei basins. The concentrations of Cl^- and SO_4^{2-} do not follow the same spatial distribution. We did not identify any parameter controlling the SO_4^{2-} concentration distribution;

TABLE 4 | River fluxes and area-normalized fluxes of TDS (Total dissolved solids), TDS*(Total dissolved solids corrected from atmospheric inputs), TZ^{+}_{sil} (cations derived from silicate weathering), SiO_2, and $CO_{2\ sil}$ (CO_2 consumption associated to silicate weathering) in the Ogooué and Mbei Basin, and for the main domains of the Ogooué Basin.

Group	Sample number	Q_{spe}	basin area	Fluxes (*F*)					area-normalized fluxes (F_{spe})					
				TDS	TDS*	TZ^{+}_{sil}	SiO_2	$CO_{2\ sil}$	TDS	TDS*	TZ^{+}_{sil}	SiO_2	$D_{chem\ sil}$	$CO_{2\ sil}$
		$mm\ yr^{-1}$	km²		$10^3\ t\ yr^{-1}$			$10^6 mol\ yr^{-1}$		$t\ km^{-2}\ yr^{-1}$			$m\ Ma^{-1}$	10^3 mol $km^{-2}\ yr^{-1}$
Mbei tributaries	1	890	13	0.35 ± 0.08	0.3 ± 0.07	$0.03^{+0.01}_{-0.01}$	0.15 ± 0.06	$1.29^{+0.56}_{-0.56}$	26.9 ± 11.3	23.2 ± 9.8	$2.17^{+0.93}_{-0.93}$	11.2 ± 4.7	$6.07^{+2.61}_{-2.61}$	99^{+43}_{-43}
	2	890	5	0.12 ± 0.03	0.11 ± 0.02	$0.01^{+0.01}_{-0.01}$	0.057 ± 0.024	$0.60^{+0.26}_{-0.39}$	23.5 ± 9.9	22.2 ± 9.3	$2.52^{+1.1}_{-1.33}$	11.4 ± 4.8	$6.25^{+2.69}_{-2.83}$	119^{+52}_{-77}
	3	567	135	1.89 ± 0.64	1.75 ± 0.59	$0.18^{+0.10}_{-0.10}$	0.96 ± 0.5	$8.15^{+4.36}_{-5.21}$	14 ± 7.3	13 ± 6.7	$1.34^{+0.72}_{-0.77}$	7.1 ± 3.7	$3.93^{+2.10}_{-2.13}$	60^{+32}_{-39}
	4	890	13	0.3 ± 0.06	0.27 ± 0.06	$0.03^{+0.01}_{-0.01}$	0.14 ± 0.06	$1.24^{+0.53}_{-0.64}$	22.5 ± 9.5	20.4 ± 8.6	$2.08^{+0.90}_{-0.99}$	10.4 ± 4.4	$5.61^{+2.42}_{-2.47}$	95^{+41}_{-49}
Ogooué main channel	18	1,631	8,778	333 ± 39	314 ± 37	43^{+15}_{-19}	176 ± 61	$1,928^{+672}_{-1,008}$	37.9 ± 13	35.8 ± 12.3	$4.86^{+1.69}_{-2.14}$	20.1 ± 6.9	$10.4^{+3.63}_{-3.84}$	220^{+77}_{-115}
	17	1,650	14,944	585 ± 68	553 ± 64	69^{+24}_{-30}	323 ± 111	$3,148^{+1,094}_{-1,651}$	39.2 ± 13.4	37 ± 12.7	$4.59^{+1.60}_{-2.01}$	21.6 ± 7.4	$10.71^{+3.72}_{-3.93}$	211^{+73}_{-110}
	20	1,328	45,823	1,306 ± 188	1,209 ± 174	116^{+45}_{-56}	752 ± 275	$5,412^{+2,102}_{-3,225}$	28.5 ± 10.4	26.4 ± 9.6	$2.52^{+0.99}_{-1.21}$	16.4 ± 6	$7.64^{+2.84}_{-2.98}$	118^{+46}_{-70}
	26	814	142,373	3,551 ± 834	3,337 ± 784	419^{+225}_{-227}	1,777 ± 778	$19,469^{+10,487}_{-13,082}$	24.9 ± 10.9	23.4 ± 10.3	$2.94^{+1.58}_{-1.60}$	12.5 ± 5.5	$7.06^{+3.21}_{-3.32}$	137^{+74}_{-92}
	8	774	160,312	3,744 ± 925	3,502 ± 866	448^{+251}_{-247}	1,876 ± 840	$20,759^{+11,550}_{-14,146}$	23.4 ± 10.5	21.8 ± 9.8	$2.79^{+1.56}_{-1.54}$	11.7 ± 5.2	$6.74^{+3.14}_{-3.23}$	129^{+72}_{-88}
	6	666	205,585	4,358 ± 1,090	4,071 ± 1,018	512^{+171}_{-193}	2,061 ± 515	$23,675^{+8242}_{-11,186}$	21.2 ± 5.3	19.8 ± 5.0	$2.49^{+0.83}_{-0.94}$	10 ± 2.5	$5.72^{+1.46}_{-1.61}$	115^{+40}_{-54}
Northern Ogooué tributaries	7	531	8,265	173 ± 62	160 ± 58	20^{+11}_{-13}	72 ± 39	960^{+544}_{-747}	20.9 ± 11.3	19.3 ± 10.4	$2.45^{+1.39}_{-1.55}$	8.7 ± 4.7	$5.45^{+3.02}_{-3.13}$	116^{+66}_{-90}
	9	546	483	10.2 ± 3.6	8.9 ± 3.1	$0.82^{+0.69}_{-0.52}$	3.6 ± 1.9	40^{+31}_{-31}	21 ± 11.2	18.4 ± 9.7	$1.70^{+1.43}_{-1.08}$	7.5 ± 4	$4.35^{+2.47}_{-2.46}$	83^{+65}_{-65}
	10	521	11,135	197 ± 72	178 ± 65	24^{+15}_{-15}	84 ± 45	$1,122^{+677}_{-875}$	17.7 ± 9.6	16 ± 8.7	$2.20^{+1.33}_{-1.39}$	7.5 ± 4.1	$4.77^{+2.69}_{-2.76}$	101^{+61}_{-79}
	11	547	2,049	26.7 ± 9.3	24.9 ± 8.7	$3.4^{+1.9}_{-2.1}$	13 ± 7	161^{+87}_{-122}	13 ± 6.9	12.2 ± 6.4	$1.68^{+0.91}_{-1.04}$	6.2 ± 3.3	$3.84^{+2.09}_{-2.17}$	78^{+43}_{-60}
	12	575	8,803	175 ± 58	165 ± 55	22^{+12}_{-13}	84 ± 43	997^{+551}_{-749}	19.9 ± 10.3	18.8 ± 9.7	$2.46^{+1.38}_{-1.5}$	9.5 ± 4.9	$5.77^{+3.07}_{-3.17}$	113^{+63}_{-85}
	13	569	49,503	633 ± 213	528 ± 177	82^{+58}_{-50}	317 ± 165	$3,707^{+2,505}_{-2,778}$	12.8 ± 6.6	10.7 ± 5.5	$1.66^{+1.16}_{-1.01}$	6.4 ± 3.3	$3.90^{+2.14}_{-2.15}$	75^{+51}_{-56}
Southern Ogooué tributaries	19	1,458	1,161	100 ± 13.1	96.6 ± 12.7	$14.1^{+5.1}_{-6.2}$	45 ± 16	653^{+235}_{-337}	86.1 ± 30.6	83.2 ± 29.5	$12.12^{+4.37}_{-5.33}$	38.7 ± 13.7	$22.51^{+8.11}_{-8.6}$	562^{+203}_{-290}
	21	1,077	7,582	601 ± 107	589 ± 105	86^{+38}_{-44}	237 ± 93	$4,064^{+1,773}_{-2,552}$	79.3 ± 31.1	77.7 ± 30.5	$11.34^{+5.04}_{-5.75}$	31.3 ± 12.3	$20.16^{+8.13}_{-8.71}$	536^{+234}_{-337}
	22	880	2,020	133 ± 29	128 ± 28	14^{+10}_{-8}	42 ± 18	660^{+434}_{-434}	66 ± 28	63.1 ± 26.8	$7.01^{+4.78}_{-3.73}$	20.6 ± 8.7	$13.36^{+6.07}_{-6.16}$	327^{+215}_{-215}
	23	713	7,057	275 ± 74	264 ± 71	38^{+19}_{-21}	120 ± 56	$1,773^{+886}_{-1,214}$	39 ± 18.1	37.4 ± 17.4	$5.39^{+2.67}_{-3.01}$	17 ± 7.9	$11.03^{+5.27}_{-5.5}$	251^{+126}_{-172}
	25	512	379	11.2 ± 4.2	10.5 ± 3.9	$1.5^{+0.9}_{-0.9}$	4.3 ± 2.4	68^{+41}_{-50}	29.4 ± 16.1	27.6 ± 15.1	$3.86^{+2.33}_{-2.38}$	11.4 ± 6.3	$7.77^{+4.42}_{-4.51}$	179^{+109}_{-132}
Plateaux Batéké	14	952	4,513	79.9 ± 16	73.7 ± 14.8	$5.9^{+3.0}_{-3.1}$	55 ± 23	281^{+138}_{-183}	17.7 ± 7.3	16.3 ± 6.7	$1.30^{+0.67}_{-0.68}$	12.2 ± 5	$5.51^{+2.33}_{-2.38}$	62^{+31}_{-40}
	15	1,694	4,911	94.1 ± 10.6	87.4 ± 9.9	$0.30^{+0.10}_{-0.10}$	81 ± 28	$7.62^{+2.63}_{-2.63}$	19.2 ± 6.5	17.8 ± 6.1	$0.06^{+0.02}_{-0.02}$	16.5 ± 5.6	$5.6^{+1.93}_{-1.93}$	$1.6^{+0.5}_{-0.5}$
	16	1,672	5,892	108.5 ± 12.4	97.1 ± 11.1	$1.8^{+0.9}_{-0.7}$	92 ± 31	68^{+34}_{-35}	18.4 ± 6.3	16.5 ± 5.6	$0.3^{+0.14}_{-0.12}$	15.6 ± 5.3	$5.48^{+1.90}_{-1.91}$	12^{+6}_{-6}

(Continued)

TABLE 4 | Continued

Group	Q_{spe}	basin area	Fluxes (*F*)					area-normalized fluxes (F_{spe})					
			TDS	TDS*	TZ^{+}_{sil}	SiO_2	$CO_{2\ sil}$	TDS	TDS*	TZ^{+}_{sil}	SiO_2	$D_{chem\ sil}$	$CO_{2\ sil}$
	mm yr^{-1}	km²		10^3 t yr^{-1}			10^6mol yr^{-1}		t km^{-2} yr^{-1}			m Ma^{-1}	10^3 mol km^{-2} yr^{-1}
Ogooué R. (at Lambaréné station)	666	205,585	4,358 ± 1090	4,071 ± 1018	512^{+171}_{-193}	2,061 ± 515	$23{,}675^{+8{,}242}_{-11{,}186}$	21.2 ± 5.3	19.8 ± 5	$2.49^{+0.83}_{-0.94}$	10 ± 3	$5.72^{+1.46}_{-1.61}$	115^{+40}_{-54}
Northern Tributaries	558	80,239	1214 ± 637	1,064 ± 558	153^{+98}_{-94}	572 ± 300	$6{,}987^{+4{,}395}_{-5{,}303}$	15 ± 8	13 ± 7	$1.9^{+1.23}_{-1.17}$	7 ± 4	$4.39^{+2.41}_{-2.45}$	87^{+55}_{-66}
Southern Tributaries	468	63,471	1,734 ± 1,001	1,656 ± 956	218^{+126}_{-159}	633 ± 365	$10{,}135^{+6{,}330}_{-7{,}895}$	27 ± 16	26 ± 15	$3.44^{+1.98}_{-2.51}$	9 ± 6	$6.05^{+4.89}_{-5.24}$	160^{+100}_{-124}
Plateaux Batéké	1,467	15,317	282 ± 100	258 ± 91	$7.9^{+4}_{-3.9}$	227 ± 81	357^{+175}_{-221}	18 ± 7	16 ± 6	$0.52^{+0.26}_{-0.26}$	14 ± 5	$5.53^{+2.04}_{-2.06}$	23^{+11}_{-14}
Remaining area	858	46,558	1,126 ± 482	1,091 ± 468	133^{+76}_{-69}	626 ± 268	$6{,}196^{+3{,}611}_{-4{,}035}$	24 ± 10	23 ± 10	$2.86^{+1.62}_{-1.49}$	13 ± 6	$7.65^{+3.36}_{-3.45}$	133^{+78}_{-87}

Uncertainty calculation is described in section Uncertainty Calculation.

however, SO_4^{2-} range from 3.7 to 21 μmoles l^{-1} which is small by comparison with the global riverine discharge-weighted average (SO_4^{2-} = 108 μmoles l^{-1}; Burke et al., 2018). The Mbei tributaries, which are located relatively close to the coast (∼150 km), exhibited variable Cl^- concentrations (9–28 μmole l^{-1}). In the Ogooué Basin, the Cl^- concentrations range between 3 and 25 μmole l^{-1} and depend on the basin distance from the sea, as observed in the Congo Basin (Négrel et al., 1993; **Figure 4A**). This observation confirms that Cl^- concentration was mainly controlled by the atmospheric inputs (**Figure 4A**). The highest NO_3^- concentrations (5.4–10.9 μmole l^{-1}) were recorded in all the Mbei tributaries and in one river draining a Northern basin (Missanga at Ndjolé), all corresponding to basins draining the southern Cameroon plateau over catchment areas smaller than 500 km². The other rivers exhibited low NO_3^- concentration (<2 μmole l^{-1}).

The normalized inorganic charge balance ($NICB = \frac{TZ^{+} - TZ^{-}}{TZ^{+} + TZ^{-}}$; note that charges borne by organic matter are not taken into account in this definition of NICB) is smaller than ±10% for most samples. For 5 samples the NICB was within 11% to 23%, which reflected an excess of cationic charge relatively to the anions (**Table 2**). As suggested by the weak but statistically significant correlation between DOC (see below) and NICB (R= 0.63; $N = 24$; $p < 0.01$), as previously reported for Guyana rivers (Sondag et al., 2010), and by the fact that the NICB decreased to 0% when the concentration of "inorganic" solutes increases, the on-average positive NICB is most likely due to the presence of negatively charged dissolved organic matter. Assuming a negative charge of 6 ± 0.5 μeq mg^{-1} of DOC (Dupré et al., 1999), the "corrected" NICB values of less than ±10% for 23 samples and less than ±15% for all samples confirm that the deficit of negative charge relatively to cationic charge is most likely due to the presence of negatively-charged dissolved organic matter.

Dissolved organic carbon concentration ranged between 0.9 and 11 mg l^{-1}. The highest values were recorded in the Northern basins with values ranging from 4.3 to 11 mg l^{-1}, while the other samples exhibited values ranging between 0.9 and 2.7 mg l^{-1}.

Strontium Isotope Ratios

Dissolved $^{87}Sr/^{86}Sr$ ratios range between 0.7125 and 0.7226 over the studied basins (**Table 2**). According to the $^{87}Sr/^{86}Sr$ *vs.* Ca/Na relationship (**Figure 4C**) and the end members determined by Négrel et al. (1993) for crystalline rock types in the Congo Basin, these signatures are distributed between the silicate weathering, evaporite weathering, and rain end members. As no evaporite outcrops are known in the studied area (Thiéblemont et al., 2009), the $^{87}Sr/^{86}Sr$ ratios indicate that in the region major river solutes derive mainly from silicate weathering and atmospheric inputs. The $^{87}Sr/^{86}Sr$ ratios does not display any specific pattern in terms of spatial distribution.

Discrimination of Solute Sources

According to the results of the source discrimination method explained in section Discrimination of Solute Sources, atmospheric inputs to river chemistry in the Ogooué and Mbei basins are low and contribute to <15% of the TDS for most

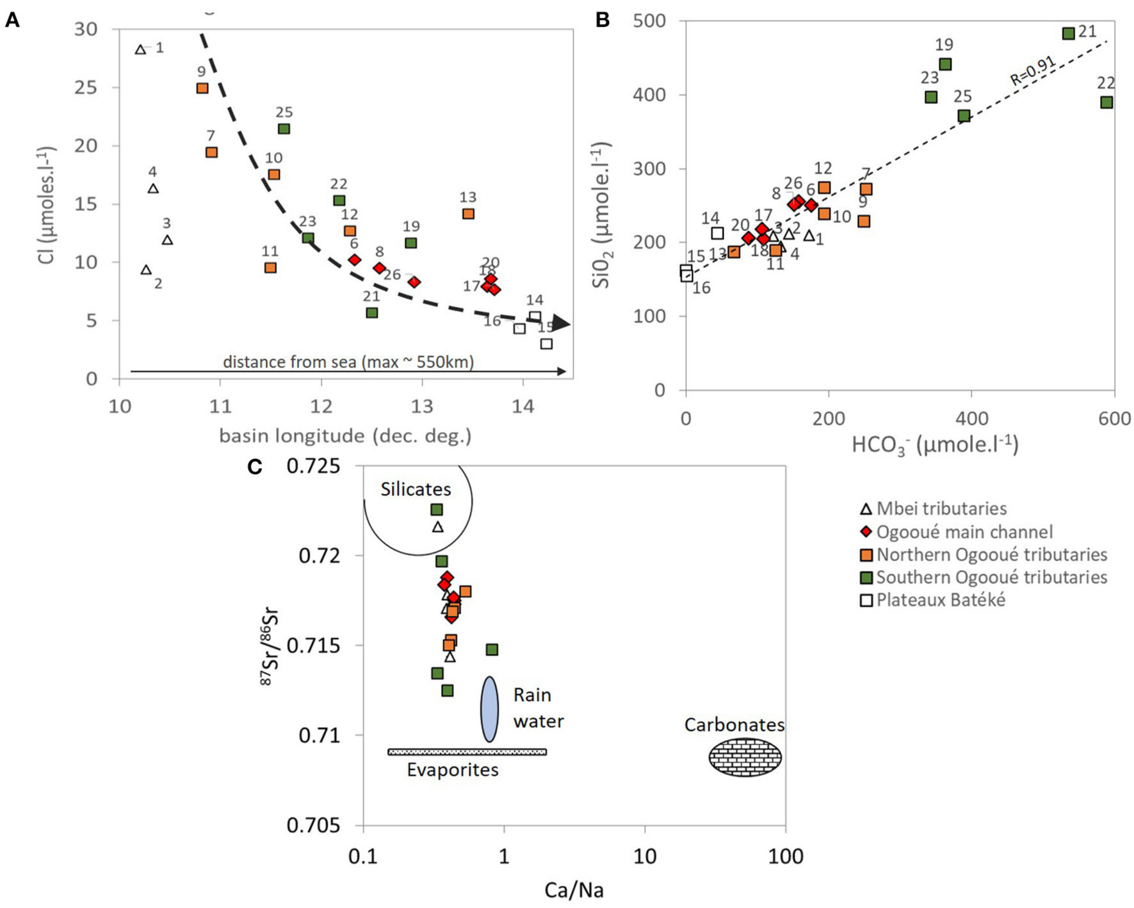

FIGURE 4 | Main characteristics of the dissolved load of the tributaries of the Ogooué and Mbei basins **(A)** Cl^- concentration as function of the centroid basin location. The dotted line represents the decreasing Cl^- concentration from the coast **(B)** SiO_2 vs. HCO_3^-. **(C)** $^{87}Sr/^{86}Sr$ ratio vs. Ca/Na (rock weathering end members defined by Négrel et al., 1993).

of the rivers (**Figure 5**). Interestingly, according to this method, the entirety of river SO_4^{2-} derive from atmospheric inputs. Again, this is consistent with the absence of known evaporite outcrops in the region. The atmospheric contribution to the river budget of other dissolved species is generally lower than 40% with a decreasing impact in the order: Mg^{2+} (40 ± 21%) > K^+ (29 ± 16%) > Ca^{2+} (27 ± 12%) > Na^+ (19 ± 21%) > Sr^{2+} (5 ± 3%). Given the low relative input of rain to the dissolved Sr budget, no attempt was made to correct dissolved $^{87}Sr/^{86}Sr$ ratios from the rain contribution.

The Mg/Na*, Ca/Na*, and HCO_3/Na* molar ratios of the sampled waters are consistent with the silicate end member previously defined for the Congo Basin (Négrel et al., 1993) and used at global scale by Gaillardet et al. (1999b) (**Figure 6**). Together with the strong relationship between HCO_3^- and SiO_2 (**Figure 4B**) and the overall relatively high $^{87}Sr/^{86}Sr$ ratios (**Figure 4C**), this observation confirms that the major solutes in the Ogooué-Mbei basins are mainly sourced from silicate weathering. More quantitatively, source discrimination calculations show that silicate weathering largely dominate the TDS export (by up to 70%; **Figure 5**). Carbonate weathering significantly contribute to TDS only in one Mbei tributary and one Ogooué R. tributary (Ouagna at Wagny). Such low contribution of carbonate weathering to the solute load of the study area is consistent with the lithological map, which displays only sparse carbonate outcrops in the Ogooué and Mbei basins.

Trace Elements

The concentrations of trace elements in the Ogooué and Mbei basins (**Table 3**; **Figure 7**), are generally lower than the global average (Gaillardet et al., 2014). The concentrations of trace alkali and alkaline earth metals (Rb, Cs, Sr, and Ba) in the Ogooué Southern basins are higher than in the Ogooué main channel, and are the lowest in the Plateaux Batéké region. The Northern Ogooué basins and the Mbei tributaries exhibit concentrations similar to those of the Ogooué mainstream. Conversely, transition metals and REE concentrations are generally higher in the Northern basins and in the Mbei tributaries than in Southern and Plateaux Batéké tributaries. For most trace elements, Plateaux Batéké tributaries exhibit the lowest concentrations (exceptions: Al and Cd).

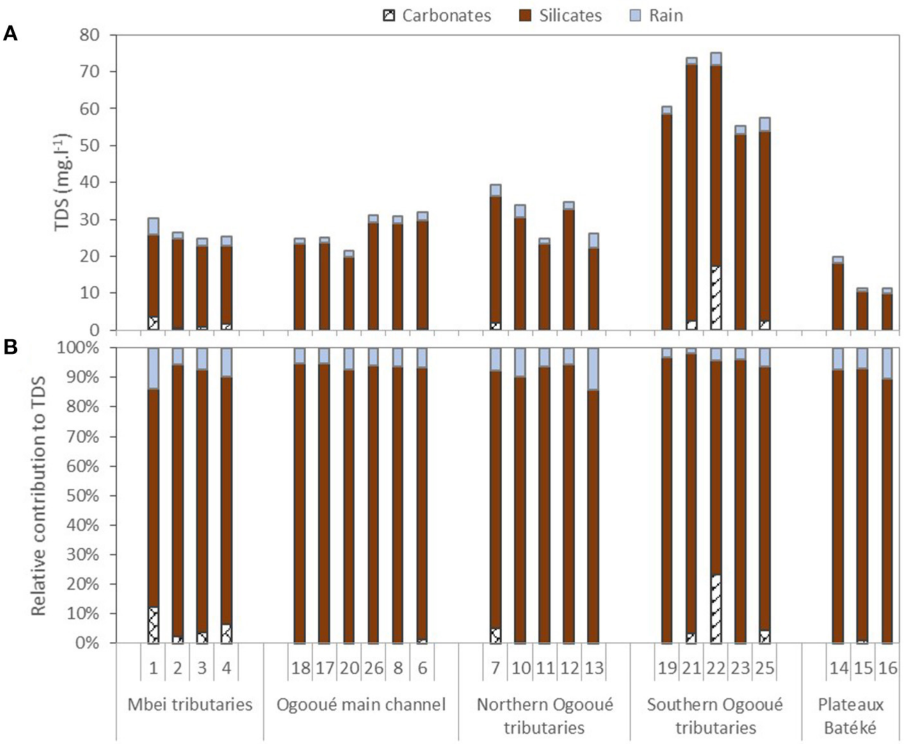

FIGURE 5 | Absolute **(A)** and relative **(B)** contributions of rainfall, carbonate weathering, and silicate weathering to the river TDS for each sampling site of the Ogooué and Mbei basins.

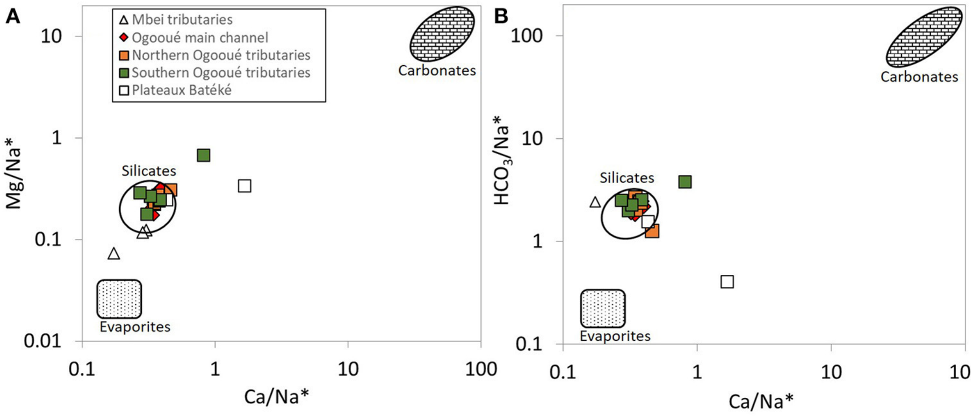

FIGURE 6 | Mixing diagrams indicating the source of solutes to the rivers of the Ogooué and Mbei basins **(A)** Mg/Na* vs. Ca/Na* and **(B)** HCO_3/Na* vs. Ca/Na*. The "*" symbol stands for concentrations corrected from atmospheric inputs (Equation 2). The silicate, carbonate and evaporite end members defined by Gaillardet et al., 1999b are shown for reference.

Based on correlation analysis with other parameters (physico-chemical parameters and concentration of DOC and of major elements) across the sample set, two groups of trace elements can be distinguished. First, elements such as Be, Al, Cr, Fe, Co, Y, most REEs, Zr, Th, and U correlate positively with DOC concentration ($R > 0.5$; $p < 0.01$; **Supplementary Figure 4**; see for example the Fe-DOC relationship in **Figure 8**). In particular, the higher DOC concentration measured in the Northern Ogooué basins corresponds to higher concentration for these elements. Second, other elements such as Li, V, Cu, As, Rb, Sr, Ba, and Eu correlate positively ($R > 0.5$; $p < 0.01$) with conductivity and the concentration of most major elements, and are therefore reflective of release by rock weathering. These elements thus exhibit high concentration in

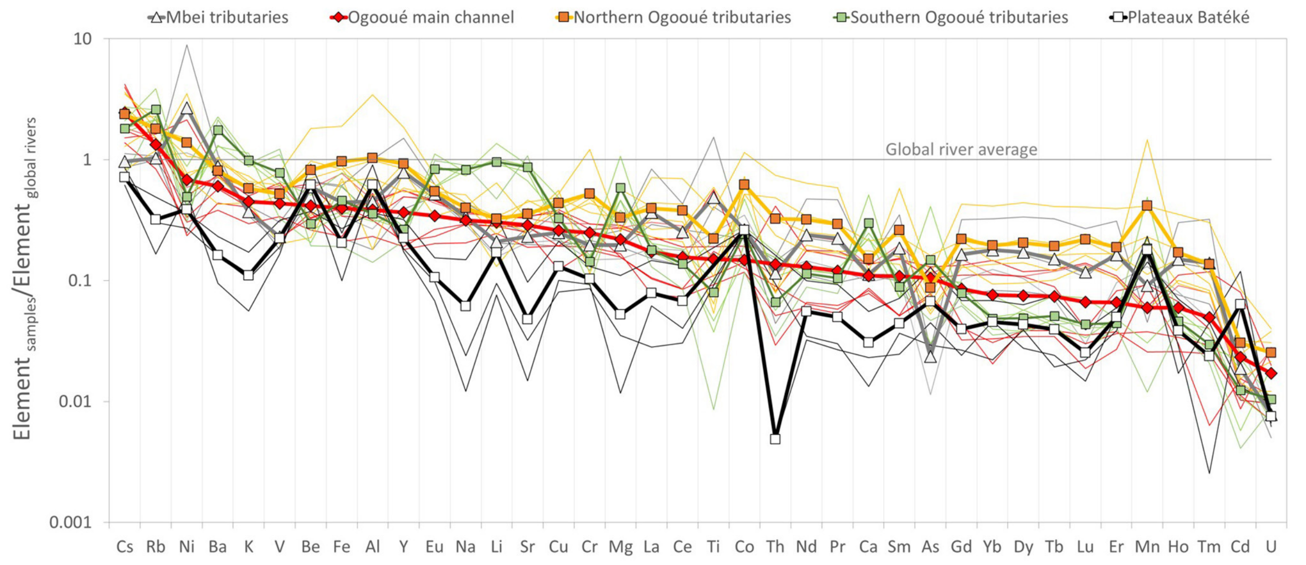

FIGURE 7 | Global average-normalized patterns for the river dissolved load of the Ogooué and Mbei rivers. Plain lines correspond to individual samples, whereas lines with a symbol correspond to average values for each domain defined in **Table 1**. Global river averages are from Gaillardet et al. (2014) for trace elements and from Meybeck (2003) for Na^+, K^+, Mg^{2+}, and Ca^{2+}. Elements are ordered along the y-axis from the highest to lowest values recorded in the Ogooué main channel.

the Southern basins, low concentration in the Plateaux Batéké and intermediate concentration in the other basins. We note that B concentration is strongly correlated to Cl^- concentration (which might point toward a dominantly atmospheric origin of B in the Ogooué–MBei rivers), and that other elements (Ti, Mn, Ni, Nb, Cd, Cs) do not show any significant correlation with the parameters cited above. Interestingly, the elements commonly considered as weakly soluble during weathering (e.g., Al, Fe, REEs+Y) or strongly insoluble (Th, Zr) are correlated to DOC concentration in the Ogooué and Mbei basins, where they exhibit low concentration both in comparison with global rivers (Gaillardet et al., 2014; **Figure 7**) and with other African rivers like the Nyong (Viers et al., 2000), Niger (Picouet et al., 2002), and Congo (Gaillardet et al., 1995) rivers.

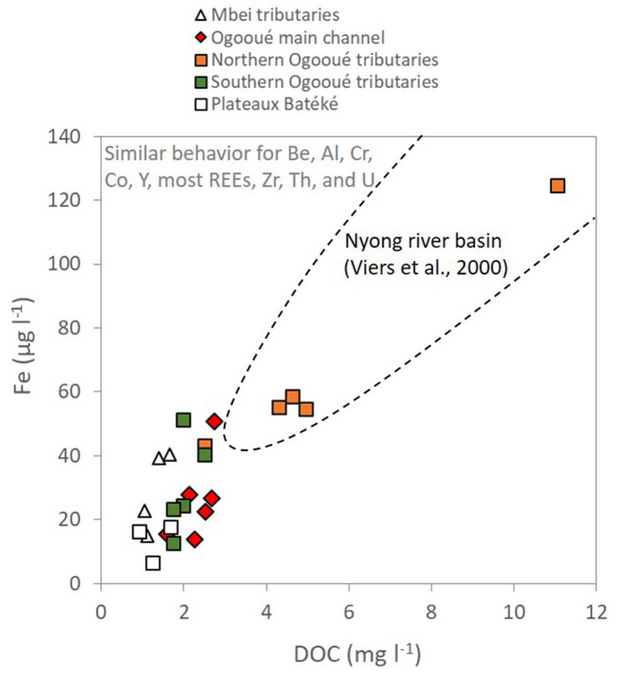

FIGURE 8 | Fe vs. DOC relationship in the Ogooué and Mbei basins. The domain corresponding to the Nyong values (monthly sampling from October 1994 to January 1997; Viers et al., 2000) is added for reference.

Silicate Weathering Fluxes and Associated CO_2 Consumption

Using estimates of Q_{spe} values (specific discharge; see section Hydrological and Climate Data), the TDS and silicate weathering fluxes ($F\ TDS$ and $F\ TZ^+_{sil}$) of the Ogooué and Mbei rivers and their tributaries were calculated. As carbonate weathering is a small contributor to the river dissolved load over the studied area, no attempt was made to estimate the corresponding river dissolved fluxes. At the Lambaréné station, the sampling location closest to the Ogooué outlet, the Ogooué river export a $F\ TDS$ of 4.4 ± 1.1 Mt yr^{-1} including 2.1 ± 0.5 Mt yr^{-1} of $F\ SiO_2$ and $0.5^{+0.2}_{-0.2}$ Mt yr^{-1} of $F\ TZ^+_{sil}$. The corresponding F_{spe} *are* 21 ± 5.3, 10 ± 2.5 and $2.5^{+0.8}_{-0.9}$ t km^{-2} yr^{-1}, respectively, and the $D_{chem\ sil}$ was $5.72^{+1.46}_{-1.61}$ m Ma^{-1} (**Table 4**). Values of the F_{spe} TDS, $F_{spe}\ TZ^+_{sil}$, and $D_{chem\ sil}$ parameters are particularly variable throughout the basin (**Figure 9A**). The highest values ($F_{spe}\ TDS$ = 29 ± 16 to 86 ± 31 t km^{-2} yr^{-1}; $F_{spe}\ TZ^+_{sil} = 3.9^{+2.3}_{-2.4}$ to $12.1^{+4.4}_{-5.3}$ t km^{-2} yr^{-1}; $D_{chem\ sil} = 7.8^{+4.4}_{-4.5}$ to $22.5^{+8.1}_{-8.6}$ m Ma^{-1}) are recorded in the Southern basins, the lowest ones are observed in the Plateaux Batéké tributaries ($F_{spe}\ TDS = 18 \pm 7$ to 19 ± 7 t

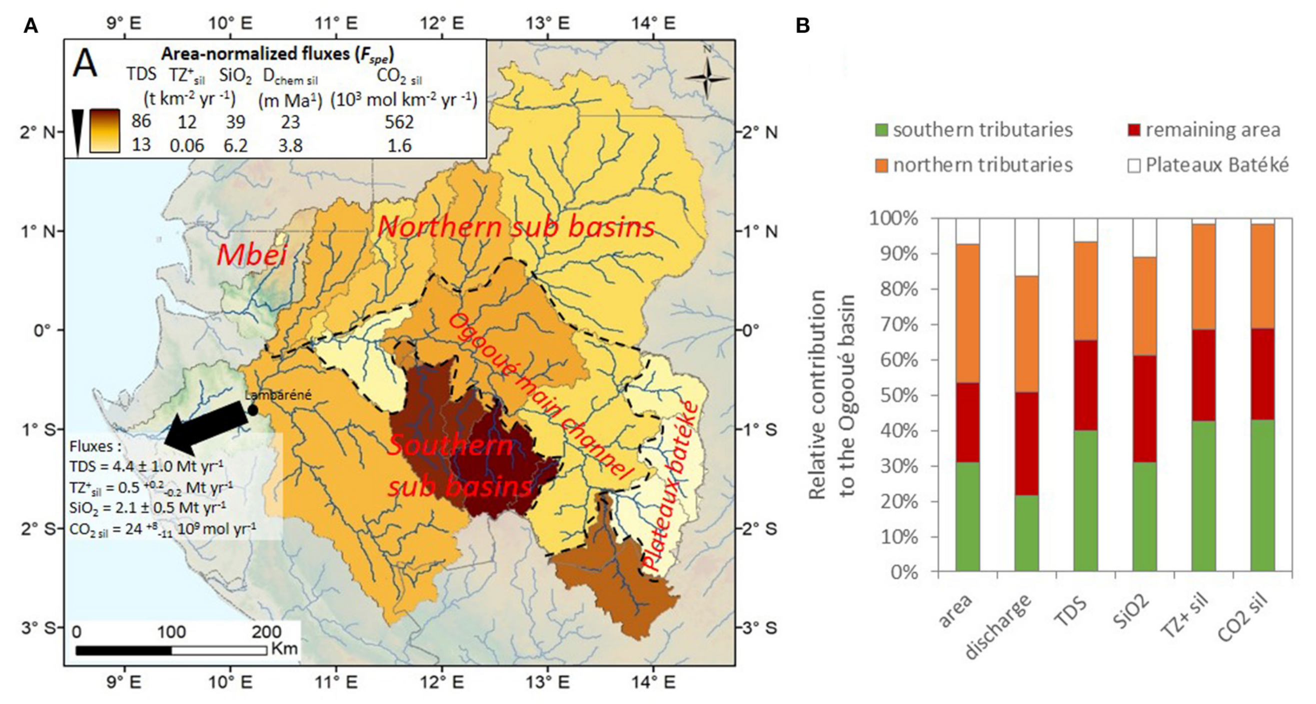

FIGURE 9 | Spatial distribution of weathering fluxes in the Ogooué Basin: **(A)** Color map showing the spatial distribution of specific fluxes (F_{spe}) of TDS, TZ^+_{sil}, SiO_2, and associated $CO_{2\ sil}$ consumption F_{spe} distribution throughout the Ogooué Basin (the darkness of the color is proportional to these rates; the extreme values are reported in the caption). Note that at this scale the basins of the Mbei tributaries are too small to be visible. **(B)** Relative contribution of each region in term of drainage area, discharge and fluxes of TDS, TZ^+_{sil}, SiO_2, and $CO_{2\ sil}$ consumption. The uncertainties are reported in **Table 4**.

km^{-2} yr^{-1}; F_{spe} $TZ^+_{sil} = 0.06^{+0.02}_{-0.02}$ to $1.3^{+0.7}_{-0.7}$ t km^{-2} yr^{-1}; $D_{chem\ sil} = 5.5^{+1.9}_{-1.9}$ to $5.6^{+1.9}_{-1.9}$ m Ma^{-1}), while the other basins exhibit intermediate values (F_{spe} $TDS = 13 \pm 7$ to 39 ± 13 t km^{-2} yr^{-1}; F_{spe} $TZ^+_{sil} = 1.3^{+0.7}_{-0.7}$–$4.9^{+1.7}_{-2.1}$ t km^{-2} yr^{-1}; $D_{chem\ sil} = 3.8^{+2.8}_{-2.2}$–$11^{+5.3}_{-5.5}$ m Ma^{-1}) (**Table 4**; **Figure 9A**). The CO_2 consumption flux associated with silicate weathering ($CO_{2\ sil}$) is 24^{+8}_{-11} 10^9 mol yr^{-1} for the Ogooué Basin, range between $1.6^{+0.5}_{-0.5}$ 10^3 mol km^{-2} yr^{-1} and 562^{+203}_{-290} 10^3 mol km^{-2} yr^{-1}, scaling with F_{spe} TZ^+_{sil} (**Table 4**). Spatially, the Northern basins, the Southern basins and the Plateaux Batéké tributaries contribute to around 28, 40, and 6% of the TDS export from the Ogooué at Lambaréné, respectively (for drainage areas representing 39, 31, and 7% of the total drainage area, respectively). The remaining part of the basin (the Ogooué mainstream and unsampled tributaries; 23% of the Ogooué area) contributes to 26% of the TDS flux (**Figure 9B**).

DISCUSSION

Silicate Weathering Rates in the Ogooué and Mbei Basins, and Comparison With Regional and Global Rates

This study presents the first TDS flux estimates for the Ogooué River. With a TDS flux $F\ TDS = 4.4 \pm 1.1$ 10^6 t yr^{-1}, the Ogooué River contributes to around 4% of the TDS flux for around 7% of the discharge of Western Africa (according to Western Africa TDS flux and discharge estimates of Milliman and Farnsworth, 2011). The Ogooué River area-normalized TDS flux (F_{spe} $TDS = 21 \pm 5$ t km^{-2} yr^{-1}) is lower than the global average (30–50 t km^2 yr^1; Meybeck, 1976, 2003; Milliman and Farnsworth, 2011), partly due to the fact that at the global scale, a large fraction of the river TDS flux is provided by the weathering of carbonate and evaporite rocks, which are not present in the studied area. However, the area-normalized specific fluxes of silicate-derived cationic charge and CO_2 consumption for the whole Ogooué (F_{spe} $TZ^+_{sil} = 2.5^{+0.8}_{-0.9}$ t km^{-2} yr^{-1}; F_{spe} $CO_{2\ sil} = 115^{+40}_{-54}$ 10^3 moles km^{-2} yr^{-1}) are close to the global average (F_{spe} $TZ^+_{sil} = 2.3$ t km^{-2} yr^{-1} and F_{spe} $CO_{2\ sil} = 96$–117 mol km^{-2} yr^{-1}; Gaillardet et al., 1999b; Moon et al., 2014). These numbers challenges the paradigm of cratonic areas being rather inactive in terms of silicate weathering (e.g., Gaillardet et al., 1999b; West, 2012; Moon et al., 2014).

These flux values estimated at the Ogooué outlet result from the mixing of waters derived from regions characterized by a variety of heterogeneous weathering rates. Indeed, the river TDS, TZ^+_{sil}, SiO_2, associated CO_2 consumption F_{spe} and the chemical silicate denudation ($D_{chem\ sil}$) estimated throughout the Ogooué Basin are heterogenous. These estimates cover the whole range of values yet measured in cratonic environments under all latitudes (**Figure 10**). As throughout the Ogooué Basin the area-normalized fluxes of TDS, TZ^+_{sil}, SiO_2 (and associated CO_2

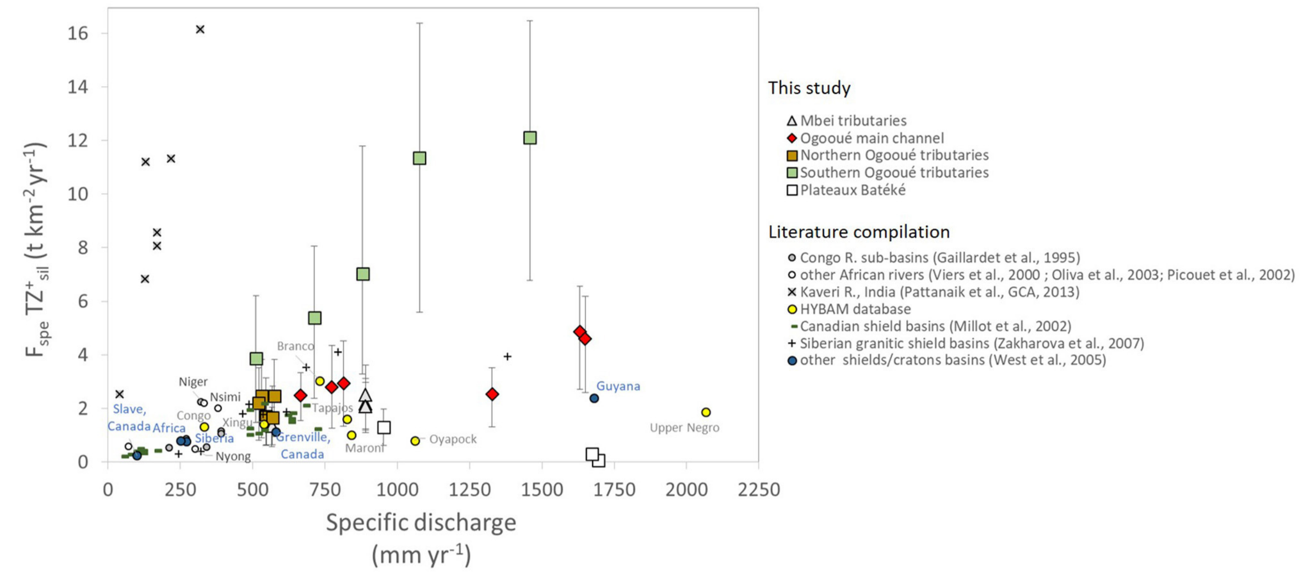

FIGURE 10 | Silicate weathering rate (F_{spe} TZ^+_{sil} in t km^{-2} yr^{-1}) vs. specific discharge (Q_{spe}) for rivers of the Ogooué and Mbei basins, and of other rivers draining cratons at the global scale. The HYBAM database provides major elements fluxes for the Upper Negro, Branco, Xingu, and Tapajos (Moquet et al., 2016), Oyapock and Maroni (Sondag et al., 2010) and Congo (Laraque et al., 2009) for the period 2003–2019. Values of F_{spe} TZ^+_{sil} for the HYBAM stations here correspond to the cation fluxes corrected from the atmospheric inputs, according to the method used in the present study. The remaining cations rate were considered to be only derived from silicate weathering. Error bars reflect uncertainties, the calculation of which is detailed in section Uncertainty Calculation.

consumption) as well as the $D_{chem\ sil}$ are strongly correlated to one another ($R > 0.87$; $p < 0.01$), here we discuss only controls on the values of F_{spe} TZ^+_{sil}. At the global scale, cratonic environments exhibit a large variability in silicate weathering rates (**Figure 10**), ranging from 0.25 t km^{-2} yr^{-1} (Slave River, Canada; West et al., 2002) to 16 t km^{-2} yr^{-1} (Kaveri River, India; Pattanaik et al., 2013). In the Ogooué Basin the lowest values obtained for the Plateaux Batéké (F_{spe} TZ^+ $_{sil} < 1.3^{+0.7}_{-0.7}$ t km^{-2} yr^{-1}) are amongst the lowest silicate weathering rates measured on Earth, lower than or similar to weathering rates recorded in the Siberian craton (Zakharova et al., 2005, 2007; Pokrovsky et al., 2015) and in the Canadian shields (Millot et al., 2002). The highest values obtained for the Southern Ogooué basins (F_{spe} $TZ^+_{sil} = 3.9^{+2.3}_{-2.4}$ to $12.1^{+4.4}_{-5.3}$ t km^{-2} yr^{-1}) are on the order of those measured in the Kaveri Basin (India), a region particularly active in terms of silicate weathering (Gurumurthy et al., 2012; Pattanaik et al., 2013). Interestingly, by comparison with the silicate weathering rates measured in orogenic areas, these values are in the lower range of those recorded in the Andes (F_{spe} $TZ^+_{sil} = 9$–104 t km^{-2} yr^{-1}; Moquet et al., 2011, 2018), in the New Zealand Alps (F_{spe} $TZ^+_{sil} = 2$–187 t km^{-2} yr^{-1}; Moore et al., 2013) but are commensurate to, or higher than those recorded in the Himalayas (mean F_{spe} $TZ^+_{sil} = 5.78$ t km^{-2} yr^{-1}, West et al., 2002), in the European Alps (F_{spe} TZ^+_{sil} = 0.03–11 t km^{-2} yr^{-1}, Donnini et al., 2016) and in the Rocky Mountains of Canada (F_{spe} $TZ^+_{sil} = 0.13$ to 4.3 t km^{-2} yr^{-1}, Millot et al., 2002). The other basins (Northern basins, Mbei tributaries basins) exhibit F_{spe} TZ^+_{sil} values similar to those measured in large tropical rivers like the Amazon tributaries and French Guyana rivers (F_{spe} $TZ^+_{sil} = 0.8$–3.0 t km^{-2} yr^{-1}; Sondag et al., 2010; Moquet et al., 2016; note that these values were updated for the period 2003–2019 from the HYBAM observatory database. These TZ^+_{sil} rates correspond to the cation fluxes corrected from the atmospheric inputs, according to the method performed in the present study. The remaining cation amounts considered to be only derived from silicate weathering because no carbonate and evaporite are present in the considered basins), the Congo (F_{spe} $TZ^+_{sil} = 0.54$–2.3 t km^{-2} yr^{-1}; Négrel et al., 1993; Gaillardet et al., 1995), the Nyong (F_{spe} $TZ^+_{sil} = 0.49$ t km^{-2} yr^{-1}; Viers et al., 2000; Regard et al., 2016) or the Niger (F_{spe} $TZ^+_{sil} = 0.58$ to 2.2 t km^{-2} yr^{-1}; Picouet et al., 2002) rivers.

Among cratonic environments, no direct relationship between specific discharge and silicate weathering intensity is observed, neither at the global scale nor at the scale of the Ogooué Basin (**Figure 10**). The present study shows that the silicate weathering flux calculated at the outlet of the Ogooué Basin does not reflect an intrinsic property of weathering in cratonic areas (i.e., low physical erosion rates associated to low weathering rates; e.g., West, 2012), but results from the mixing of solute fluxes derived from contrasted environments in terms of weathering. In addition, our observations highlight that cratonic areas can be particularly active in terms of weathering, as in the Southern Ogooué Basin, and that the absence of tectonic activity does not necessarily imply slow weathering.

Controlling Factors of Silicate Weathering in the Ogooué Basin and Implications for the Long-Term Carbon Cycle

At the global scale, silicate weathering is controlled by a range of variables like climate, lithology, geomorphology or the presence of organic matter (e.g., Goudie and Viles, 2012) which together influence the rate of exposure of mineral surfaces to water and air, the type of water-mineral interactions, and water flowpaths.

Climate

With all things considered equal, climate is a key driver in differential weathering reaction rates, which can alter reaction temperature (e.g., Oliva et al., 2003) and water availability and potential for weathering (White and Blum, 1995; Maher and Chamberlain, 2014). Due to its equatorial position, the Ogooué Basin is characterized by a relatively constant temperature throughout the year with an average of ∼24°C and is relatively homogenous throughout the basin. Annual rainfall estimates in the basin exhibit a significant spatial variability (from 1,890 to 2,692 mm yr^{-1}) with an estimated specific discharge ranging from 512 to 1,694 (± 161) mm yr^{-1}. Interestingly, amongst the Southern Ogooué tributaries the values of $F_{spe}\ TZ^{+}_{sil}$ calculated significantly ($p < 0.01$) increase with specific discharge suggesting that within this domain rainfall distribution partly controls the $F_{spe}\ TZ^{+}_{sil}$ variability (**Figure 11A**). This is consistent with the observation made at global scale for numerous river basins (e.g., Gaillardet et al., 1999b; West, 2012) that weathering rates increase with precipitation, and thus specific discharge. In this case, weathering rates are controlled by the amount of water available for weathering reactions. Indeed, increased water flow through regolith and rock increases the surface of contact between minerals and water (White and Blum, 1995), and the export flux of solutes when reactions occur near thermodynamic equilibrium (Maher, 2010). However, for a given Q_{spe} value, $F_{spe}\ TZ^{+}_{sil}$ is highly variable throughout the basin (**Figure 11A**). Therefore, at the scale of the whole studied area, climatic parameters (temperature, rainfall or runoff) alone cannot explain the significant variability in silicate weathering rates observed throughout the basin.

Lithology

Lithology is another major factor controlling the Earth surface chemical denudation (e.g., White and Blum, 1995; Hartmann et al., 2014). In the Ogooué Basin, a strong lithological contrast exists between the Plateaux Batéké in the East and the rest of the basin. Plateaux Batéké are composed of Cenozoic sandstone formations, whose mineralogy is dominated by quartz, and which are very poor in soluble elements (e.g., Thiéblemont et al., 2009), whereas the remaining part of the basin is mainly made of plutonic and metamorphic rocks. As already observed in the Congo Basin (Négrel et al., 1993; Gaillardet et al., 1995), this contrast explains the very low major cation content measured in the Ogooué tributaries draining the Plateaux Batéké.

The remaining part of the basin drains the Congo craton mainly composed of Archean and Paleoproterozoic granitic and gneissic rocks. Non-calcareous sedimentary formations (Eburnéen foreland—Francevilien D Group composed of greenish pelite with sandstone and tuffaceous intercalations; Thiéblemont et al., 2009) constitute a more important component of the underlying rocks in the Southern basins than in the Northern basins (see **Supplementary Table 1**). The dissolved Mg/Na* vs. Ca/Na* and HCO_3/Na* vs. Ca/Na* ratios of the studied basins are relatively homogenous (**Figure 6**) and lie within the field of the granitic weathering end member previously defined for the Congo Basin (Négrel et al., 1993). This observation indicates that the river the dissolved major element composition of the Ogooué Basin derives from a relatively homogenous silicate domain. Therefore, other drivers of chemical weathering need to be invoked to explain the latitudinal gradient in chemical weathering rates observed in the Ogooué Basin (**Figure 9**).

Dynamics of Organic Matter and Colloids

The Northern tributaries of the Ogooué Basin drain the southern part of the Cameroon plateau and exhibits characteristics similar to those of the neighboring Nyong Basin: tectonic quiescence, low slopes, and subsequent water stagnation in swamp systems (Viers et al., 1997; Oliva et al., 1999; Braun et al., 2012). In such environments, chemical weathering contributes to around 60-70% of total (physical plus chemical) denudation (Regard et al., 2016), rapid turnover of carbon on hillside soils promote DOC exportation (Nkoue Ndondo et al., 2020), and organic-rich surface waters enhance the mobilization and transfer of insoluble elements such as Al and Fe–and even of highly-charged transition metals such as Th, Ti, and Zr (Braun et al., 2005, 2012). The Northern tributaries exhibit weathering rates similar to those of rivers draining the Cameroon plateau (Nsimi brook, Nyong river, and tributaries; **Figure 10**) and display similar relationships between DOC and concentrations of High Field Strength Elements (Al, Fe, Th, Zr, and REEs) as those observed in these rivers (Olivié-Lauquet et al., 1999; Viers et al., 2000; Braun et al., 2012; **Figure 8**). In such environments, these elements are mainly transported in the stream in the colloidal phase [which is typically composed of a mixture of organic matter and Al and Fe oxy(hydroxides)], operationally included in the dissolved phase in the present study, because of the filter porosity. Such behavior has been shown to be a primary mechanism for these elements to mobilize in many surface and groundwater environments (for example, Pokrovsky et al., 2006; Pourret et al., 2007; Trostle et al., 2016; Vázquez-Ortega et al., 2016). In the Ogooué and Mbei basins, this phenomenon is exemplified by the correlation between the concentrations of these trace elements and DOC concentration (**Figure 8**; **Supplementary Figure 4**). However, these correlations can reveal either that dissolved organo-metal complexes are forming that solubilize Al, Fe, Th, and Zr (e.g., Oliva et al., 1999; Tamrat et al., 2019) and/or that these systems promote the export of colloids composed of organic matter, nanoclays, and Al and Fe oxyhydroxides (e.g., Rose et al., 1998; Olivié-Lauquet et al., 1999; Allard et al., 2004; Guinoiseau et al., 2016). In any case, we emphasize that in the neighboring small river basin of Nsimi, major dissolved cations (Ca^{2+}, Mg^{2+}, K^{+}, and Na^{+}) and SiO_2 are typically transported in the "truly" dissolved phase, i.e., with a size < 5 kD (Viers et al., 1997). The river fluxes of these elements in the Ogooué and Mbei basins thus reflect actually dissolved weathering products, and the intermediate weathering rates calculated in this region are at least partly controlled by the content in dissolved organic matter and associated inorganic colloidal fraction.

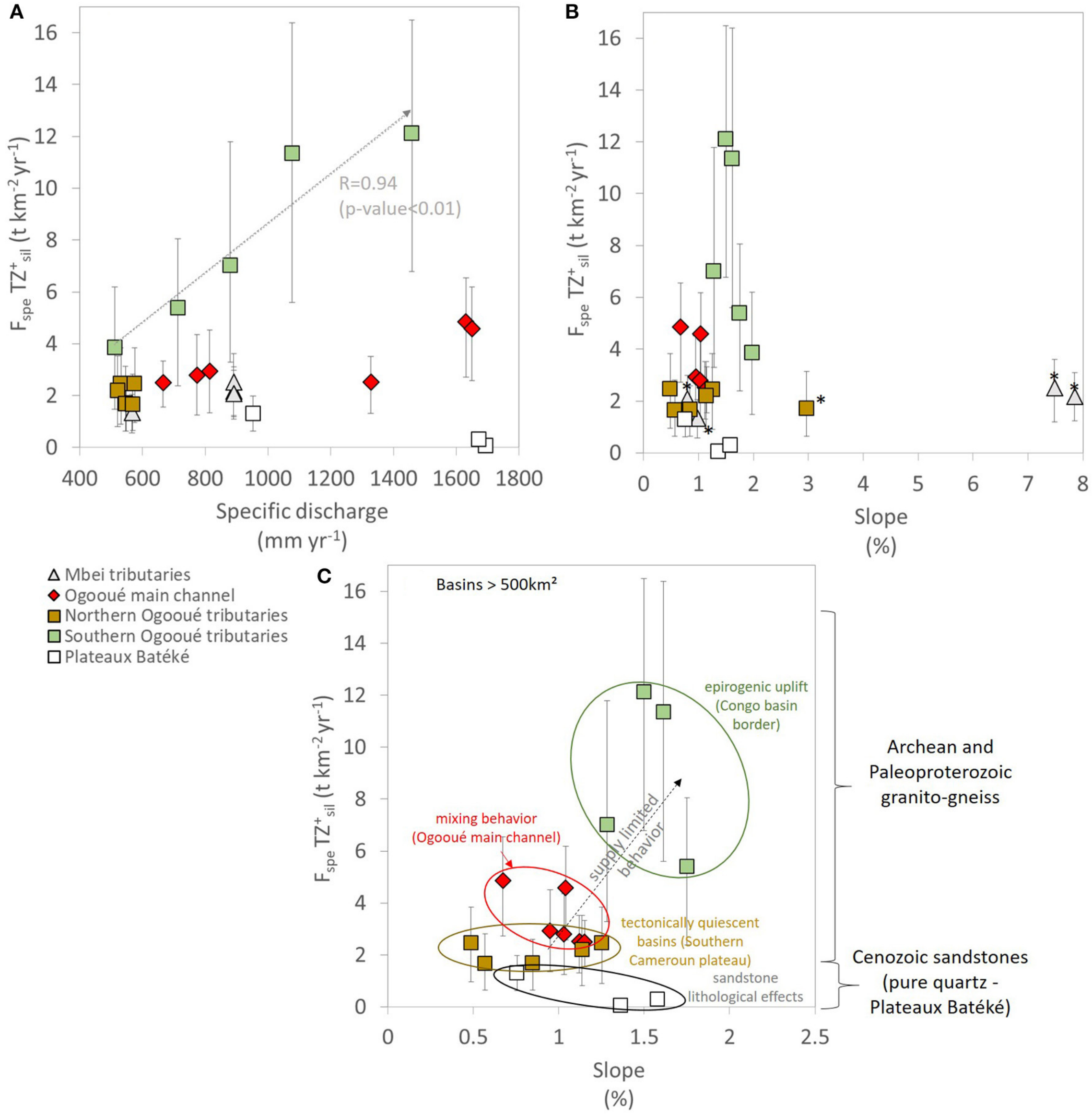

FIGURE 11 | Relationship between silicate weathering rate (F_{spe} TZ^+_{sil} in t km^{-2} yr^{-1}) and **(A)** specific discharge and **(B)** mean basin slope in the Ogooué and Mbei basins. * correspond to the basins which exhibit NO_3^- concentration >5 μmoles l^{-1}. **(C)** Zoom on B only for basins with drainage area >500 km². In panel A, the regression line is reported for Southern Ogooué tributaries for reference (R = 0.94; significant for $p < 0.05$). Error bars reflect uncertainties, the calculation of which is detailed in section Uncertainty Calculation.

The Mbei tributaries and the Missanga River (a small Northern Ogooué tributary) exhibit the highest NO_3^- concentration (from 5.4 to 11 μmoles l^{-1}) of the dataset (**Table 2**; **Figure 11B**). Some of these basins also feature the highest mean slopes of the study area (from 3.0 to 7.9%) and all drain an area <500 km². The other Northern basins exhibit low (<1.2 μmoles l^{-1}) NO_3^- concentrations and low slopes <1.3%. The NO_3^- concentration values recorded in the Mbei and Missanga rivers are within the range recorded in the hillslope piezometers of the experimental Nsimi watershed in the neighboring Nyong Basin (Braun et al., 2005). There, NO_3^- concentrations decrease from 0.75 μmol^{-1} on hillslopes to values <0.12 μmole in downslope swampy areas and in the downstream Nyong River (Viers et al., 1997; Boeglin et al., 2003; Braun et al., 2005). This trend was attributed to the fact that mineralization of organic-rich soil horizons on hillslope favors nitrification, while denitrification occurs in the open water, swampy area (Braun et al., 2005). We suggest that similar processes explain the high NO_3^- concentrations observed in some of the Northern Ogooué basins. Indeed in these small (<500 km²), overall steep basins, hillslope soil processes favoring nitrification would dominate the catchment-scale N cycle, and thus result in high river NO_3^- concentration, while larger and flatter basins would integrate swampy systems where denitrification is active, decreasing NO_3^-

concentration and export fluxes at the outlet. The Missanga stream flows through the suburbs of Ndjolé city, such that its higher NO_3^- concentration can also be attributed to human activities. These observations show that in relatively small basins solute loads do not reflect the same processes as those of larger basins. We thus focus our following discussion of the roles of relief and erosion (section Relief and Erosion) on catchments with drainage areas > 500 km^2, and accordingly exclude from this discussion the data from the Mbei and Missanga rivers.

Altogether, these observations suggest that the presence or absence of flat, swampy areas exert a significant control on the export fluxes of trace elements and nitrate in the Ogooué Basin.

Relief and Erosion

The Southern tributaries of the Ogooué, which exhibit the highest weathering rates of the whole basin, contain DOC concentrations similar to those of rivers draining the Plateaux Batéké, and drain rocks similar to those of the Northern basins. The main characteristic of this region amongst the sub-basins of the Ogooué Basin is the relatively steeper slopes than the Northern sub-basins and the main Ogooué channel (mean slopes = 1.5–2% for the Southern sub-basins; **Table 1**). It is widely acknowledged that in tectonically active areas mountain uplift triggers mechanical erosion, which in turns favors the exposure of "fresh" mineral surfaces to water and reactive gases, providing a potential explanation for the high weathering rates recorded in orogenic regions (Larsen et al., 2014) such as the Himalayas (Raymo and Ruddiman, 1992; France-Lanord et al., 2003), the Andes (Stallard, 1985; Moquet et al., 2011, 2014, 2018; Carretier et al., 2018), or the Australian Alps (Hagedorn and Cartwright, 2009). The Ogooué Basin drains a tectonically inactive area, such that mountain uplift cannot be invoked as a control on weathering rates *via* increased erosion. However, Guillocheau et al. (2015) point out that the Congo Basin borders, which correspond to the Southern and Eastern parts of the Ogooué Basin, have been subjected to active uplift for the past 45 Ma. The origin of this uplift, potentially related to mantle-induced dynamic uplift or lithospheric processes (Guillocheau et al., 2015, 2018), has in particular promoted higher relief in the Atlantic side of the Congo Basin for the past 11.5 Ma. Conversely, the Northern Ogooué tributaries and the Mbei Basin, located in the Southern part of the South Cameroon Plateau, do not undergo such uplift (Weber et al., 2016; Guillocheau et al., 2018). Although little is known about the effects of long-term mantle or lithosphere dynamics on erosion and weathering, and excluding the lithological effect explaining the low weathering rates of the Plateaux Batéké, the North-South gradient in specific weathering fluxes over the Ogooué Basin can be attributed to a southward increase in the intensity of mantle-induced dynamic uplift, or potential to lithospheric destabilization (Cottrell et al., 2004; Jaupart et al., 2007).

As for mountain uplift in tectonically active areas, the most likely process for a positive influence of mantle- or lithosphere-induced dynamic on weathering in tectonically quiescent areas is the enhancement of erosion rates. However, whereas in mountains a tight coupling between erosion and weathering is required to maintain a finite regolith thickness over significant timescales ($>10^3$-10^4 yrs), in tropical cratonic environments mantle uplift would rather sustain regolith rejuvenation (i.e., exposure of deep regolith horizons hosting relatively unweathered primary minerals to water flowpaths in the critical zone) through long-term thinning of the lateritic cover. Regardless of the exact dynamics at play, in both cases erosion remains the main driver for "fresh" material exposure to the Earth surface. Estimates of erosion rates are not available yet for the Ogooué Basin to test this hypothesis, but the steeper slopes of the Southern basins lends support to the following scenario (**Figure 11C**). In the Southern Ogooué basins, higher erosion rates driven by mantle-induced dynamics or by uplift due to lithospheric instability would enhance weathering rates through accrued erosion and thinning of lateritic soils, allowing for an increase in the exposure of "fresh" mineral surfaces to reactive fluids, while in the Northern basins, the absence of uplift inhibits soil erosion and leads to the formation and the preservation of deep lateritic soils. Such scenario would imply that weathering in the Ogooué Basin operates with the "supply-limited" regime (**Figure 11C**), meaning that chemical weathering rates are limited by physical erosion rates (e.g., Riebe et al., 2017).

To our knowledge, this is the first time that an influence of mantle or lithosphere dynamic (also sometimes referred to as "epeirogenic" uplift by geologists) on weathering rates is proposed for cratonic areas. This hypothesis implies that erosion could affect weathering, the global long-term carbon cycle, and climate not only through the formation of the main orogenic belts in collisional contexts (Raymo and Ruddiman, 1992) but also through the slow, large-scale dynamics of the mantle and lithosphere in cratonic areas. Cratonic environments can therefore have a significant role on the continental weathering budgets, and need to be considered carefully when evaluating the global carbon cycle (Goddéris et al., 2008; Carretier et al., 2014). As basin slope alone is an imperfect index for physical erosion, this hypothesis needs to be tested through the comparison of chemical weathering rates with erosion rates. As no sediment gauging program exists in the studied area, alternative approaches such as cosmogenic nuclides (e.g., ^{10}Be, Regard et al., 2016) or/and steady state calculations based on the geochemical composition of river sediments (Gaillardet et al., 1999a; Picouet et al., 2002; Louvat et al., 2008) need to be performed to better characterize the interplay between weathering and erosion in cratonic areas.

CONCLUSION

Cratonic areas located in humid tropical regions have been reported to exhibit low chemical weathering rates due to a "shielding" effect of deep, mature regolith covers. Nevertheless, thanks to their wide aerial extent on intertropical surfaces, cratonic areas represent at the global scale a significant proportion of the dissolved matter delivery to the oceans. Despite this crucial significance, assessment of chemical weathering fluxes and rates in these environments is seldom conducted, and the variability in the intra-cratonic weathering rates–especially in terms of the diversity of geomorphological setting—has generally not been considered to date.

The present study allows us to quantify the chemical weathering budget of the intertropical cratonic basins of the Mbei and the Ogooué basins, Gabon, and to explore the main drivers of weathering in this context. The chemical composition (major and trace element concentration and $^{87}Sr/^{86}Sr$ ratios) of 24 river water samples taken in September 2017 was measured. Solute source discrimination shows that atmospheric inputs account for $<15\%$ of the TDS, while silicate weathering is the main TDS source. Interestingly, the hydrochemical composition of the Ogooué River at the outlet and the whole-basin silicate weathering rate are similar to those of the world average, and similar to (if not higher than) other basins of Western Africa. The significant weathering flux of the Ogooué results from contrasted weathering regimes across the basin, which cover the range of values yet recorded in cratonic basins at the global scale.

In the Ogooué and Mbei basins, three domains, submitted to similar climate, have been identified:

(i) Low weathering rates were recorded in the Plateaux Batéké (Eastern Ogooué tributaries). These low weathering rates, corresponding to the lowest values recorded in cratonic environments at the global scale, are due to a lithological effect associated with the low abundance of chemically-mobile elements in the minerals (i.e., mostly quartz) which compose the underlying Cenozoic sandstones.

(ii) Intermediate weathering rates, comparable to the Ogooué mainstream values, were recorded in the Mbei tributaries and the Northern Ogooué sub-basins. The higher DOC concentrations recorded in the Northern Ogooué sub-basins are associated with elevated concentrations of classically insoluble elements (e.g., Fe, Al, Th, Zr, REEs) suggesting a prominent control of colloidal transport in these basins. In these rivers, our data also show that active nitrification occurs on hillslopes while denitrification is promoted in swamp areas in the valleys.

(iii) The highest weathering rates were recorded in the Southern Ogooué tributaries basins. The rim of the Congo Cuvette drained by these tributaries is submitted to active mantle uplift, which enhances soil erosion, and leads to the dismantlement of soils and to increased availability of fresh mineral surfaces to reactive fluids, thereby promoting higher weathering rates.

In addition to the lithological effect observed in the Plateaux Batéké and to the role of organic matter in Northern basins, the novelty of the present study is to hypothesize that mantle-induced dynamic uplift or lithospheric destabilization in cratonic areas can significantly enhance chemical weathering rates by leading to soil erosion and bringing fresh rocks in contact with meteoric water. As a corollary, the cratonic zones may also host hot-spots of weathering. These Earth surface movements of long spatial (100–1,000 km) and temporal (tens of millions years) wavelengths should be considered, along with the establishment of major orogenic belts linked to plate collision, in models of the global long-term carbon cycle and climate. The drivers of weathering in shield environments thus need deeper investigation to estimate continental weathering budgets and to constrain global-scale, long-term biogeochemical cycles.

DATA AVAILABILITY STATEMENT

The original contributions presented in the study are included in the article/**Supplementary Materials**, further inquiries can be directed to the corresponding author/s.

AUTHOR CONTRIBUTIONS

J-JB, JG, and JB designed the project. J-SM, J-JB, SB, and AM measured *in-situ* data and collected the samples. J-SM and JB performed and coordinated the chemical analyses. SB contributed to the hydroclimate data calculation. SB and J-PB contributed to the hydrological data production. EM contributed to the GIS data compilation. J-SM and JB interpreted the results with the help of J-JB and JG. J-SM wrote the manuscript with the help of JB and J-JB. JG, SC, and VR contributed to the data interpretation and revised the manuscript. M-CP contributed to the study implementation. All authors contributed to the article and approved the submitted version.

FUNDING

This study was supported by the project RALTERAC EC2CO INSU, by the International Joint Laboratory DYCOFAC (Dynamics of the forested ecosystems of Central Africa in a context of global change) and by the Programme Emergences of the City of Paris Chemical weathering of sediments in large tropical floodplains (agreement205DDEEES165). Parts of this work were supported by IPGP multidisciplinary programme PARI and by Paris-IdF region SESAME Grant No. 12015903 and by a grant overseen by the French National Research Agency (ANR) as part of the Investments d'Avenir Programme LabEx VOLTAIRE, 10-LABX-0100.

ACKNOWLEDGMENTS

We especially thank Dr. Aurélie Flore Koumba Pambo for the research authorizations in Gabon, Jean-Grégoire Kayoum driver and photograph during the sampling field, Pr. Marc Benedetti (IPGP) for Dissolved Organic Carbon analyses, Caroline Gorge (IPGP) for the major element analyses, Dr. Pierre Burckel (IPGP) for trace element analyses, D. Thiéblemont (BRGM) for constructive discussions about the Ogooué river Basin geology, G. Mahé (Hydroscience Montpellier) for providing discharge and precipitation data of west African rivers, F. Guillocheau (Géosciences Rennes) for providing the regional topographic map and C. Farnetani (IPGP) for constructive discussions about mantle and lithosphere dynamics in cratons. We also thank ANPN and CIRMF for their support during the field campaign. We thank Alissa M. White, Bryan G. Moravec and Richard Wanty for their constructive recommendations along the review process.

SUPPLEMENTARY MATERIAL

The Supplementary Material for this article can be found online at: https://www.frontiersin.org/articles/10.3389/frwa.2020.589070/full#supplementary-material

REFERENCES

Allard, T., Menguy, N., Salomon, J., Calligaro, T., Weber, T., Calas, G., et al. (2004). Revealing forms of iron in river-borne material from major tropical rivers of the Amazon Basin (Brazil)1 1Associate editor: G. Sposito. Geochim. *Cosmochim. Acta* 68, 3079–3094. doi: 10.1016/j.gca.2004.01.014

Ameli, A. A., Beven, K., Erlandsson, M., Creed, I. F., McDonnell, J. J., and Bishop, K. (2017). Primary weathering rates, water transit times, and concentration-discharge relations: a theoretical analysis for the critical zone. *Water Resour. Res*. 53, 942–960. doi: 10.1002/2016WR019448

Artyushkov, E. V., Korikovsky, S. P., Massonne, H.-J., and Chekhovich, P. A. (2018). Recent crustal uplift of precambrian cratons: key patterns and possible mechanisms. *Russ. Geol. Geophys*. 59, 1389–1409. doi: 10.1016/j.rgg.2018.10.001

Becker, M., Papa, F., Frappart, F., Alsdorf, D., Calmant, S., da Silva, J. S., et al. (2018). Satellite-based estimates of surface water dynamics in the congo river basin. *Int. J. Appl. Earth Obs. Geoinformation* 66, 196–209. doi: 10.1016/j.jag.2017.11.015

Berner, E. K., and Berner, R. A. (1987). *The Global Water Cycle: Geochemistry and Environment*:. ed. I. Prentice-Hall Englewood Cliffs. New Jersey, NJ: Prentice-Hall.

Berner, R. A., Lasaga, A. C., and Garrels, R. M. (1983). The carbonate silicate geochemical cycle and its effect on atmospheric carbon dioxide over the past 100 millions years. *Am. J. Sci*. 283, 641–683. doi: 10.2475/ajs.283.7.641

Boeglin, J.-L., Ndam, J.-R., and Braun, J.-J. (2003). Composition of the different reservoir waters in a tropical humid area: example of the Nsimi catchment (Southern Cameroon). *J. Afr. Earth Sci*. 37, 103–110. doi: 10.1016/S0899-5362(03)00041-1

Bogning, S., Frappart, F., Blarel, F., Niño, F., Mahé, G., Bricquet, J.-P., et al. (2018). Monitoring water levels and discharges using radar altimetry in an ungauged river basin: the case of the ogooué. *Remote Sens*. 10:350. doi: 10.3390/rs10020350

Bogning, S., Frappart, F., Paris, A., Blarel, F., Niño, F., Saux Picart, S., et al. (2020). Hydro-climatology study of the Ogooué River basin using hydrological modeling and satellite altimetry. *Adv. Space Res*. doi: 10.1016/j.asr.2020.03.045

Bouchez, J., and Gaillardet, J. (2014). How accurate are rivers as gauges of chemical denudation of the Earth surface? *Geology* 42, 171–174. doi: 10.1130/G34934.1

Bouchez, J., Gaillardet, J., Lupker, M., Louvat, P., France-Lanord, C., Maurice, L., et al. (2012). Floodplains of large rivers: weathering reactors or simple silos? *Chem. Geol*. 332–333, 166–184. doi: 10.1016/j.chemgeo.2012.09.032

Bouchez, J., Moquet, J.-S., Espinoza, J. C., Martinez, J.-M., Guyot, J.-L., Lagane, C., et al. (2017). River mixing in the Amazon as a driver of concentration-discharge relationships. *Water Resour. Res.* 53, 8660–8685. doi: 10.1002/2017W R02059

Braun, J., Guillocheau, F., Robin, C., Baby, G., and Jelsma, H. (2014). Rapid erosion of the Southern African Plateau as it climbs over a mantle superswell. *J. Geophys. Res. Solid Earth* 119, 6093–6112. doi: 10.1002/2014JB010998

Braun, J.-J., Descloitres, M., Riotte, J., Fleury, S., Barbiéro, L., Boeglin, J.-L., et al. (2009). Regolith mass balance inferred from combined mineralogical, geochemical and geophysical studies: mule hole gneissic watershed, South India. *Geochimica et Cosmochimica Acta* 73, 935–961. doi: 10.1016/j.gca.2008.11.013.

Braun, J.-J., Marechal, J.-C., Riotte, J., Boeglin, J.-L., Bedimo Bedimo, J.-P., Ndam Ngoupayou, J. R., et al. (2012). Elemental weathering fluxes and saprolite production rate in a Central African lateritic terrain (Nsimi, South Cameroon). *Geochim. Cosmochim. Acta* 99, 243–270. doi: 10.1016/j.gca.2012.09.024

Braun, J. J., Ngoupayou, J. R. N., Viers, J., Dupre, B., Bedimo, J. P. B., Boeglin, J. L., et al. (2005). Present weathering rates in a humid tropical watershed : Nsimi, South Cameroon. *Geochim. Cosmochim. Acta* 69, 357–387. doi: 10.1016/j.gca.2004.06.022

Burke, A., Present, T. M., Paris, G., Rae, E. C. M., Sandilands, B. H., Gaillardet, J., et al. (2018). Sulfur isotopes in rivers: insights into global weathering budgets, pyrite oxidation, and the modern sulfur cycle. *Earth Planet. Sci. Lett*. 496, 168–177. doi: 10.1016/j.epsl.2018.05.022

Calmels, D., Gaillardet, J., Brenot, A., and France-Lanord, C. (2007). Sustained sulfi de oxidation by physical erosion processes in the Mackenzie River basin: climatic perspectives. *Geology* 35, 1003–1006. doi: 10.1130/G24132A.1

Carretier, S., Godderis, Y., Delannoy, T., and Rouby, D. (2014). Mean bedrock-to-saprolite conversion and erosion rates during mountain growth and decline. *Geomorphology* 209, 39–52. doi: 10.1016/j.geomorph.2013.11.025

Carretier, S., Goddéris, Y., Martinez, J., Reich, M., and Martinod, P. (2018). Colluvial deposits as a possible weathering reservoir in uplifting mountains. *Earth Surf. Dynam.* 6, 217–237. doi: 10.5194/esurf-6-217-2018

Carson, M. A., and Kirkby, M. J. (1972). *Hillslope Form and Process*. New York, NY: Cambridge University Press.

Caves Rugenstein, J. K., Ibarra, D. E., and von Blanckenburg, F. (2019). Neogene cooling driven by land surface reactivity rather than increased weathering fluxes. *Nature* 571, 99–102. doi: 10.1038/s41586-019-1332-y

Chorover, J., Derry, L. A., and McDowell, W. H. (2017). Concentration-discharge relations in the critical zone: implications for resolving critical zone structure, function, and evolution. *Water Resour. Res*. 53, 8654–8659. doi: 10.1002/2017WR021111

Conrad, C. P., and Husson, L. (2009). Influence of dynamic topography on sea level and its rate of change. *Lithosphere* 1, 110–120. doi: 10.1130/L32.1

Conway, D., Persechino, A., Ardoin-Bardin, S., Hamandawana, H., Dieulin, C., and Mah,é, G. (2009). Rainfall and water resources variability in sub-saharan africa during the twentieth century. *J. Hydrometeorol*. 10, 41–59. doi: 10.1175/2008JHM1004.1

Cottrell, E., Jaupart, C., and Molnar, P. (2004). Marginal stability of thick continental lithosphere. *Geophys. Res. Lett*. 31, L18612. doi: 10.1029/2004GL020332

Cutler, J. S., Olivos, J. A., Sidlauskas, B., and Arismendi, I. (2020). Habitat loss due to dam development may affect the distribution of marine-associated fishes in Gabon, Africa. *Ecosphere* 11:e03024. doi: 10.1002/ecs2.3024

Dai, A., and Trenberth, K. E. (2002). Estimates of freshwater discharge from continents: latitudinal and seasonal variations. *J. Hydrometeorol*. 3, 660–687. doi: 10.1175/1525-7541(2002)003<0660:EOFDFC>2.0.CO;2

Donnini, M., Frondini, F., Probst, J.-L., Probst, A., Cardellini, C., Marchesini, I., et al. (2016). Chemical weathering and consumption of atmospheric carbon dioxide in the Alpine region. *Glob. Planet. Change* 136, 65–81. doi: 10.1016/j.gloplacha.2015.10.017

Dupré, B., Viers, J., Dandurand, J.-L., Polvé, M., Bénézeth, P., Vervier, P., et al. (1999). Major and trace elements associated with colloids in organic-rich river waters: Ultrafiltration of natural and spiked solutions. *Chem. Geol.* 160, 63–80.

Flament, N., Gurnis, M., and Müller, R. D. (2013). A review of observations and models of dynamic topography. *Lithosphere* 5, 189–210. doi: 10.1130/L245.1

France-Lanord, C., Evans, M., Hurtrez, J.-E., and Riotte, J. (2003). Annual dissolved fluxes from Central Nepal rivers: budget of chemical erosion in the Himalayas. *Comptes. Rendus. Geosci*. 335, 1131–1140. doi: 10.1016/j.crte.2003.09.014

Gaillardet, J., Dupré, B., and Allègre, C. J. (1995). A global geochemical mass budget applied to the Congo basin rivers: erosion rates and continental crust composition. *Geochim. Cosmochim. Acta* 59, 3469–3485. doi: 10.1016/0016-7037(95)00230-W

Gaillardet, J., Dupre, B., and Allègre, C. J. (1999a). Geochemistry of large river suspended sediments: silicate weathering or recycling tracer? *Geochim. Cosmochim. Acta* 63, 4037–4051. doi: 10.1016/S0016-7037(99)00307-5

Gaillardet, J., Dupré, B., Louvat, P., and Allègre, C. J. (1999b). Global silicate weathering and CO2 consumption rates deduced from the chemistry of large rivers. *Chem. Geol*. 159, 3–30. doi: 10.1016/S0009-2541(99) 00031-5

Gaillardet, J., Viers, J., and Dupré, B. (2014). "7.7 - trace elements in river waters," in *Treatise on Geochemistry* 2nd *Edn,* eds. H. D. Holland and K. K. Turekian (Oxford: Elsevier), 195–235. Available online at: http://www.sciencedirect.com/science/article/pii/B9780080959757005076.

Garrels, R. M., and MacKenzie, F. T. (1972). A quantitative model for the sedimentary rock cycle. *Mar. Chem*. 1, 27–41. doi: 10.1016/0304-4203(72)90004-7

Godderis, Y. (2010). Mountains without erosion. *Nature* 465, 169–171. doi: 10.1038/465169a

Goddéris, Y., Donnadieu, Y., Tombozafy, M., and Dessert, C. (2008). Shield effect on continental weathering: implication for climatic evolution of the Earth at the geological timescale. *Model. Pedogenesis* 145, 439–448. doi: 10.1016/j.geoderma.2008.01.020

Godsey, S. E., Kirchner, J. W., and Clow, D. W. (2009). Concentration-discharge relationships reflect chemostatic characteristics of US catchments. *Hydrol. Process*. 23, 1844–1864. doi: 10.1002/hyp.7315

Goudie, A. S., and Viles, H. A. (2012). Weathering and the global carbon cycle: geomorphological perspectives. *Earth-Sci. Rev*. 113, 59–71. doi: 10.1016/j.earscirev.2012.03.005

Gran, G. (1950). Determination of the equivalent point in potentiometric titrations. *Acta Chem. Scand*. 4, 559–577. doi: 10.3891/acta.chem.scand.04-0559

Guillocheau, F., Chelalou, R., Linol, B., Dauteuil, O., Robin, C., Mvondo, F., et al. (2015). "Cenozoic landscape evolution in and around the congo basin: constraints from sediments and planation surfaces," in *Geology and Resource Potential of the Congo Basin*, eds. M. J. de Wit, F. Guillocheau, and M. C. J. de Wit (Berlin; Heidelberg: Springer Berlin Heidelberg), 271–313. *doi: 10.1007/978-3-642-29482-2_14*

Guillocheau, F., Simon, B., Baby, G., Bessin, P., Robin, C., and Dauteuil, O. (2018). Planation surfaces as a record of mantle dynamics: the case example of Africa. *Rift. Passive Margins* 53, 82–98. doi: 10.1016/j.gr.2017.05.015

Guinoiseau, D., Bouchez, J., Gélabert, A., Louvat, P., Filizola, N., and Benedetti, M. F. (2016). The geochemical filter of large river confluences. *Chem. Geol*. 441, 191–203. doi: 10.1016/j.chemgeo.2016.08.009

Gurumurthy, G. P., Balakrishna, K., Riotte, J., Braun, J.-J., Audry, S., Shankar, H. N. U., et al. (2012). Controls on intense silicate weathering in a tropical river, southwestern India. *Chem. Geol*. 300–301, 61–69. doi: 10.1016/j.chemgeo.2012.01.016

Hagedorn, B., and Cartwright, I. (2009). Climatic and lithologic controls on the temporal and spatial variability of CO2 consumption via chemical weathering: an example from the Australian Victorian Alps. *Chem. Geol*. 260, 234–253. doi: 10.1016/j.chemgeo.2008.12.019

Hajj, F., Poszwa, A., Bouchez, J., and Guérold, F. (2017). Radiogenic and "stable" strontium isotopes in provenance studies: a review and first results on archaeological wood from shipwrecks. *J. Archaeol. Sci*. 86, 24–49. doi: 10.1016/j.jas.2017.09.005

Hartmann, J., Moosdorf, N., Lauerwald, R., Hinderer, M., and West, A. J. (2014). Global chemical weathering and associated P-release - the role of lithology, temperature and soil properties. *Chem. Geol*. 363, 145–163. doi: 10.1016/j.chemgeo.2013.10.025

Herman, F., Seward, D., Valla, P. G., Carter, A., Kohn, B., Willett, S. D., et al. (2013). Worldwide acceleration of mountain erosion under a cooling climate. *Nature* 504, 423–426. doi: 10.1038/nature12877

Hilton, R. G., and West, A. J. (2020). Mountains, erosion and the carbon cycle. *Nat. Rev. Earth Environ*. 1, 284–299. doi: 10.1038/s43017-020-0058-6

Hu, J., Liu, L., Faccenda, M., Zhou, Q., Fischer, K. M., Marshak, S., et al. (2018). Modification of the western gondwana craton by plume-lithosphere interaction. *Nat. Geosci*. 11, 203–210. doi: 10.1038/s41561-018-0064-1

Jaupart, C., Molnar, P., and Cottrell, E. (2007). Instability of a chemically dense layer heated from below and overlain by a deep less viscous fluid. *J. Fluid Mech*. 572, 433–469. doi: 10.1017/S0022112006003521

Kim, H., Dietrich, W. E., Thurnhoffer, B. M., Bishop, J. K. B., and Fung, I. Y. (2017). Controls on solute concentration-discharge relationships revealed by simultaneous hydrochemistry observations of hillslope runoff and stream flow: the importance of critical zone structure. *Water Resour. Res*. 53, 1424–1443. doi: 10.1002/2016WR019722

Kim, S.-Y., Scourse, J., Marret, F., and Lim, D.-I. (2010). A 26,000-year integrated record of marine and terrestrial environmental change off Gabon, west equatorial Africa. *Palaeogeogr. Palaeoclimatol. Palaeoecol*. 297, 428–438. doi: 10.1016/j.palaeo.2010.08.026

Kittel, C. M. M., Nielsen, K., Tøttrup, C., and Bauer-Gottwein, P. (2018). Informing a hydrological model of the Ogooué with multi-mission remote sensing data. *Hydrol. Earth Syst. Sci*. 22, 1453–1472. doi: 10.5194/hess-22-1453-2018

Koffi, K. G., Hardy, O. J., Doumenge, C., Cruaud, C., and Heuertz, M. (2011). Diversity gradients and phylogeographic patterns in Santiria trimera (Burseraceae), a widespread African tree typical of mature rainforests. *Am. J. Bot*. 98, 254–264. doi: 10.3732/ajb.1000220

Kusky, T. M., Windley, B. F., Wang, L., Wang, Z., Li, X., and Zhu, P. (2014). Flat slab subduction, trench suction, and craton destruction: comparison of the North China, wyoming, and Brazilian cratons. *Tectonophysics* 630, 208–221. doi: 10.1016/j.tecto.2014.05.028

Lamb, S., and Watts, A. (2010). The origin of mountains - implications for the behaviour of Earth's lithosphere. *Curr. Sci*. 99, 1699–1718. Available online at: https://www.jstor.org/stable/24073494

Laraque, A., Bricquet, J.-P., Pandi, A., and Olivry, J.-C. (2009). A review of material transport by the Congo River and its tributaries. *Hydrol. Process*. 23, 3216–3224. doi: 10.1002/hyp.7395

Laraque, A., Moukandi N'kaya, G. D., Orange, D., Tshimanga, R., Tshitenge, J. M., Mahé, G., et al. (2020). Recent budget of hydroclimatology and hydrosedimentology of the congo river in Central Africa. *Water* 12:2613. doi: 10.3390/w12092613

Larsen, I. J., Montgomery, D. R., and Greenberg, H. M. (2014). The contribution of mountains to global denudation. *Geology* 42, 527–530. doi: 10.1130/G35136.1

Lienou, G., Mah,é, G., Paturel, J.-E., Servat, E., Sighomnou, D., Ekodeck, G. E., et al. (2008). Evolution of hydrological regimes in the equatorial area of Cameroon: an impact of climate variability in equatorial Africa? *Hydrol. Sci. J*. 53, 789–801. doi: 10.1623/hysj.53.4.789

Louvat, P., Gislason, S. R., and Allègre, C. J. (2008). Chemical and mechanical erosion rates in Iceland as deduced from river dissolved and solid material. *Am. J. Sci*. 308, 679–726. doi: 10.2475/05.2008.02

Mahe, G., Lerique, J., and Olivry, J.-C. (1990). The ogooue river gabon. discharge reconstruction and evidence of equatorial climatic variations [Le fleuve Ogooue au Gabon. Reconstitution des debits manquants et mise en evidence de variations climatiques a l'equateur]. *Hydrol. Cont*. 5, 105–124

Mahe, G., Lienou, G., Descroix, L., Bamba, F., Paturel, J. E., Laraque, A., et al. (2013). The rivers of Africa: witness of climate change and human impact on the environment. *Hydrol. Process*. 27, 2105–2114. doi: 10.1002/hyp.9813

Maher, K. (2010). The dependence of chemical weathering rates on fluid residence time. *Earth Planet. Sci. Lett*. 294, 101–110. doi: 10.1016/j.epsl.2010.03.010

Maher, K., and Chamberlain, C. P. (2014). Hydrologic regulation of chemical weathering and the geologic carbon cycle. *Science* 343, 1502–1504. doi: 10.1126/science.1250770

Meunier, J. D., Riotte, J., Braun, J. J., Sekhar, M., Chali,é, F., Barboni, D., et al. (2015). Controls of DSi in streams and reservoirs along the Kaveri River, South India. *Sci. Total Environ*. 502, 103–113. doi: 10.1016/j.scitotenv.2014.07.107

Meybeck, M. (1976). Total mineral dissolved transport by world major rivers / Transport en sels dissous des plus grands fleuves mondiaux. *Hydrol. Sci. Bull*. 21, 265–284. doi: 10.1080/02626667609491631

Meybeck, M. (2003). "5.08 – Global occurrence of major elements in rivers," in *Treatise on Geochemistry,* eds H. D. Holland and K. K. Turekian (Oxford: Pergamon), 207–223. Available online at: http://www.sciencedirect.com/science/article/pii/B0080437516051641

Milliman, J. D., and Farnsworth, K. L. (2011). *River Discharge to the Coastal Ocean - A Global Synthesis*. Cambridge: Cambridge University Press

Millot, R., Gaillardet, J., Dupré, B., and Allègre, C. J. (2002). The global control of silicate weathering rates and the coupling with physical erosion: new insights from rivers of the Canadian Shield. *Earth Planet. Sci. Lett*. 196, 83–98. doi: 10.1016/S0012-821X(01)00599-4

Moatar, F., Abbott, B. W., Minaudo, C., Curie, F., and Pinay, G. (2017). Elemental properties, hydrology, and biology interact to shape concentration-discharge curves for carbon, nutrients, sediment, and major ions. *Water Resour. Res*. 53, 1270–1287. doi: 10.1002/2016WR019635

Moon, S., Chamberlain, C. P., and Hilley, G. E. (2014). New estimates of silicate weathering rates and their uncertainties in global rivers. *Geochim. Cosmochim. Acta* 134, 257–274. doi: 10.1016/j.gca.2014.02.033

Moore, J., Jacobson, A. D., Holmden, C., and Craw, D. (2013). Tracking the relationship between mountain uplift, silicate weathering, and long-term CO2 consumption with Ca isotopes: Southern Alps, New Zealand. *Chem. Geol*. 341, 110–127. doi: 10.1016/j.chemgeo.2013.01.005

Moquet, J.-S., Crave, A., Viers, J., Seyler, P., Armijos, E., Bourrel, L., et al. (2011). Chemical weathering and atmospheric/soil CO2 uptake in the Andean and Foreland Amazon basins. *Chem. Geol*. 287, 1–26. doi: 10.1016/j.chemgeo.2011.01.005

Moquet, J.-S., Guyot, J.-L., Morera, S., Crave, A., Rau, P., Vauchel, P., et al. (2018). Temporal variability and annual budget of inorganic dissolved matter in Andean Pacific Rivers located along a climate gradient from northern Ecuador to southern Peru. *Comptes Rendus Geosci*. 350, 76–87. doi: 10.1016/j.crte.2017.11.002

Moquet, J. S., Guyot, J. L., Viers, J., Crave, A., Filizola, N., Sanchez, L. S. H., et al. (2016). Dissolved Amazon River dissolved load: temporal dynamic and annual budget from the Andes to the ocean. *Environ. Sci. Pollut. Res*. 23, 11405–11429. doi: 10.1007/s11356-015-5503-6

Moquet, J. S., Viers, J., Crave, A., Armijos, E., Lagane, C., Lavado, W., et al. (2014). Comparison between silicate weathering and physical erosion rates in Andean basins of Amazon river. *Procedia Earth Planet. Sci*. 10, 275–279. doi: 10.1016/j.proeps.2014.08.061

Négrel, P., Allègre, C. J., Dupré, B., and Lewin, E. (1993). Erosion sources determined by inversion of major and trace element ratios and strontium isotopic ratios in river water: The Congo Basin case. *Earth Planet. Sci. Lett*. 120, 59–76. doi: 10.1016/0012-821X(93)90023-3

Njutapvoui Fokouop, N. (2017). *Régimes des précipitations et relations pluies-niveaux d'eau-débits dans le bassin versant du Komo (Gabon)*. Abomey-Calavi: IRD - Université d'Abomey-Calavi (UAC), BENIN

Nkoue Ndondo, G. R., Probst, J.-L., Ndjama, J., Ndam Ngoupayou, J. R., Boeglin, J.-L., Takem, G. E., et al. (2020). Stable carbon isotopes δ13C as a proxy for characterizing carbon sources and processes in a small tropical headwater catchment: Nsimi, Cameroon. *Aquat. Geochem*. doi: 10.1007/s10498-020-09386-8

Norton, K. P., and Schlunegger, F. (2017). Lack of a weathering signal with increased Cenozoic erosion? *Terra Nova* 29, 265–272. doi: 10.1111/ter.12278

Oliva, P., Viers, J., and Dupré, B. (2003). Chemical weathering in granitic environments. *Chem. Geol*. 202, 225–256. doi: 10.1016/j.chemgeo.2002.08.001

Oliva, P., Viers, J., Dupré, B., Fortuné, J. P., Martin, F., Braun, J. J., et al. (1999). The effect of organic matter on chemical weathering: study of a small tropical watershed: nsimi-zoétélé site, cameroon. *Geochim. Cosmochim. Acta* 63, 4013–4035. doi: 10.1016/S0016-7037(99)00306-3

Olivié-Lauquet, G., Allard, T., Benedetti, M., and Muller, J.-P. (1999). Chemical distribution of trivalent iron in riverine material from a tropical ecosystem: a quantitative EPR study. *Water Res*. 33, 2726–2734. doi: 10.1016/S0043-1354(98)00479-5

ORSTOM (1964). *Régime Hydrologique de la M'Bei Conditions Hydrologiques*. Paris: Service hydrologique.

Oslisly, R., White, L., Bentaleb, I., Favier, C., Fontugne, M., Gillet, J.-F., et al. (2013). Climatic and cultural changes in the west congo basin forests over the past 5000 years. *Philos. Trans. R. Soc. B Biol. Sci*. 368:20120304. doi: 10.1098/rstb.2012.0304

Pattanaik, J. K., Balakrishnan, S., Bhutani, R., and Singh, P. (2013). Estimation of weathering rates and CO2 drawdown based on solute load: Significance of granulites and gneisses dominated weathering in the Kaveri River basin, Southern India. *Geochim. Cosmochim. Acta* 121, 611–636. doi: 10.1016/j.gca.2013.08.002

Penman, D. E., Caves Rugenstein, J. K., Ibarra, D. E., and Winnick, M. J. (2020). Silicate weathering as a feedback and forcing in Earth's climate and carbon cycle. *Earth-Sci. Rev*. 209:103298. *doi: 10.1016/j.earscirev.2020.103298*

Picouet, C., Dupr,é, B., Orange, D., and Valladon, M. (2002). Major and trace element geochemistry in the upper Niger river (Mali): physical and chemical weathering rates and CO2 consumption. *Chem. Geol*. 185, 93–124. doi: 10.1016/S0009-2541(01)00398-9

Pokrovsky, O. S., Manasypov, R. M., Loiko, S., Shirokova, L. S., Krickov, I. A., Pokrovsky, B. G., et al. (2015). Permafrost coverage, watershed area and season control of dissolved carbon and major elements in western Siberian rivers. *Biogeosciences* 12, 6301–6320. doi: 10.5194/bg-12-6301-2015

Pokrovsky, O. S., Manasypov, R. M., Loiko, S. V., Krickov, I. A., Kopysov, S. G., Kolesnichenko, L. G., et al. (2016). Trace element transport in western Siberian rivers across a permafrost gradient. *Biogeosciences* 13, 1877–1900. doi: 10.5194/bg-13-1877-2016

Pokrovsky, O. S., Schott, J., and Dupré, B. (2006). Basalt weathering and trace elements migration in the boreal Arctic zone. Ext. Abstr. Present. 7th Symp Geochem. Earths Surf. GES-7 88, 304–307. *doi: 10.1016/j.gexplo.2005.08.062*

Pourret, O., Dia, A., Davranche, M., Gruau, G., Hénin, O., and Angée, M. (2007). Organo-colloidal control on major- and trace-element partitioning in shallow groundwaters: confronting ultrafiltration and modelling. *Met. Interact. Nat. Org. Matter Watershed-Scale Geochem*. 22, 1568–1582. doi: 10.1016/j.apgeochem.2007.03.022

Raymo, M. E., and Ruddiman, W. F. (1992). Tectonic forcing of late cenozoic mountain building on ocean geochemical cycles. *Geology* 359, 117–122. doi: 10.1038/359117a0

Regard, V., Carretier, S., Boeglin, J.-L., Ndam Ngoupayou, J.-R., Dzana, J.-G., Bedimo Bedimo, J.-P., et al. (2016). Denudation rates on cratonic landscapes: comparison between suspended and dissolved fluxes, and 10Be analysis in the Nyong and Sanaga River basins, south Cameroon. *Earth Surf. Process. Landf*. 41, 1671–1683. doi: 10.1002/esp.3939

Riebe, C. S., Hahm, W. J., and Brantley, S. L. (2017). Controls on deep critical zone architecture: a historical review and four testable hypotheses. *Earth Surf. Process. Landf*. 42, 128–156. doi: 10.1002/esp.4052

Rodríguez Tribaldos, V., White, N. J., Roberts, G. G., and Hoggard, M. J. (2017). Spatial and temporal uplift history of South America from calibrated drainage analysis. *Geochem. Geophys. Geosystems* 18, 2321–2353. doi: 10.1002/2017GC006909

Rose, J., Vilge, A., Olivie-Lauquet, G., Masion, A., Frechou, C., and Bottero, J.-Y. (1998). Iron speciation in natural organic matter colloids. *Colloids Surf. Physicochem. Eng. Asp*. 136, 11–19. doi: 10.1016/S0927-7757(97)00150-7

Scherler, D., DiBiase, R. A., Fisher, G. B., and Avouac, J.-P. (2017). Testing monsoonal controls on bedrock river incision in the Himalaya and Eastern Tibet with a stochastic-threshold stream power model. *J. Geophys. Res. Earth Surf*. 122, 1389–1429. doi: 10.1002/2016JF004011

Seranne, M., Bruguier, O., and Moussavou, M. (2008). U-Pb single zircon grain dating of Present fluvial and Cenozoic aeolian sediments from Gabon: consequences on sediment provenance, reworking, and erosion processes on the equatorial West African margin. *Bull. Société Géologique Fr*. 179, 29–40. doi: 10.2113/gssgfbull.179.1.29

Sighomnou, D. (2004). *Analyse et redéfinition des régimes climatiques et hydrologiques du Cameroun : perspectives d'évolution des ressources en eau*, Tesis Univ. Yaoudé

Sondag, F., Guyot, J. L., Moquet, J. S., Laraque, A., Adele, G., Cochonneau, G., et al. (2010). Suspended sediment and dissolved load budgets of two Amazonian rivers from French Guiana : Maroni and Oyapock rivers. *Hydrol. Process*. 24, 1433–1445. doi: 10.1002/hyp.7603

Stallard, R. F. (1985). "River chemistry, geology, geomorphology, and soils in the amazon and orinoco basins. in *The Chemistry of Weathering. Nato ASI Series (C: Mathematical and Physical Sciences), Vol.* 149. ed J. I. Drever (Dordrecht: Springer,)

Stallard, R. F., and Edmond, J. M. (1987). Geochemistry of the Amazon. 3. weathering chemistry and limits to dissolved inputs. *J. Geophys. Res*. 92, 8293–8302. *doi: 10.1029/JC092iC08p08293*

Stein, M., Starinsky, A., Katz, A., Goldstein, S. L., Machlus, M., and Schramm, A. (1997). Strontium isotopic, chemical, and sedimentological evidence for the evolution of lake lisan and the dead sea. *Geochim. Cosmochim. Acta* 61, 3975–3992. doi: 10.1016/S0016-7037(97)00191-9

Swoboda, S., Brunner, M., Boulyga, S. F., Galler, P., Horacek, M., and Prohaska, T. (2008). Identification of Marchfeld asparagus using Sr isotope ratio measurements by MC-ICP-MS. *Anal. Bioanal. Chem*. 390, 487–494. doi: 10.1007/s00216-007-1582-7

Tamrat, W. Z., Rose, J., Grauby, O., Doelsch, E., Levard, C., Chaurand, P., et al. (2019). Soil organo-mineral associations formed by co-precipitation of Fe, Si and Al in presence of organic ligands. *Geochim. Cosmochim. Acta* 260, 15–28. doi: 10.1016/j.gca.2019.05.043

Thiéblemont, D., Castaing, C., Bouton, P., Billa, M., Brian, J. P., Goujou, J. C., et al. (2009). Carte géologique et des Ressources minérales de la République Gabonaise à 1/1 000 000

Thiéblemont, D., Guerrot, C., Négrel, P., Braucher, R., Bourlès, D. L., and Thiéblemont, R. (2014). Nd-isotope evidence for the distal provenance of the historical (c. <3000BP) lateritic surface cover underlying the Equatorial forest in Gabon (Western Africa). *Aeolian Res*. 15, 177–192. doi: 10.1016/j.aeolia.2014.06.002

Trostle, K. D., Ray Runyon, J., Pohlmann, M. A., Redfield, S. E., Pelletier, J., McIntosh, J., et al. (2016). Colloids and organic matter complexation control trace metal concentration-discharge relationships in Marshall Gulch stream waters. *Water Resour. Res*. 52, 7931–7944. doi: 10.1002/2016WR019072

UNEP (2010). *Africa Water Atlas*. Nairobi, Kenya: Division of Early Warning and Assessment (DEWA). United Nations Environment Programme (UNEP)

Vázquez-Ortega, A., Huckle, D., Perdrial, J., Amistadi, M. K., Durcik, M., Rasmussen, C., et al. (2016). Solid-phase redistribution of rare earth elements in hillslope pedons subjected to different hydrologic fluxes. *Chem. Geol.* 426, 1–18. doi: 10.1016/j.chemgeo.2016.01.001

Viers, J., Dupré, B., Braun, J.-J., Deberdt, S., Angeletti, B., Ngoupayou, J. N., et al. (2000). Major and trace element abundances, and strontium isotopes in the Nyong basin rivers (Cameroon): constraints on chemical weathering processes and elements transport mechanisms in humid tropical environments. *Chem. Geol.* 169, 211–241. doi: 10.1016/S0009-2541(00)00298-9

Viers, J., Dupré, B., Polvé, M., Schott, J., Dandurand, J.-L., and Braun, J.-J. (1997). Chemical weathering in the drainage basin of a tropical watershed (Nsimi-Zoetele site, Cameroon) : comparison between organic-poor and organic-rich waters. *Chem. Geol.* 140, 181–206. doi: 10.1016/S0009-2541(97)00048-X

Violette, A., Goddéris, Y., Maréchal, J.-C., Riotte, J., Oliva, P., Mohan Kumar, M. S., et al. (2010). Modelling the chemical weatheringnext term fluxes at the watershed scale in the Tropics (Mule Hole, South India): Relative contribution of the smectite/kaolinite assemblage versus primary minerals. *Chem. Geol.* 2010, 42–60. doi: 10.1016/j.chemgeo.2010.07.009

Von Blanckenburg, F., Bouchez, J., Ibarra, D. E., and Maher, K. (2015). Stable runoff and weathering fluxes into the oceans over quaternary climate cycles. *Nat. Geosci.* 8, 538–542. doi: 10.1038/ngeo2452

Weber, F., Gauthier-Lafaye, F., Whitechurch, H., Ulrich, M., and El Albani, A. (2016). The 2-Ga eburnean orogeny in gabon and the opening of the francevillian intracratonic basins: a review. *Comptes Rendus Geosci.* 348, 572–586. doi: 10.1016/j.crte.2016.07.003

West, A. J. (2012). Thickness of the chemical weathering zone and implications for erosional and climatic drivers of weathering and for carbon-cycle feedbacks. *Geology* 40, 811–814. doi: 10.1130/G33041.1

West, A. J., Bickle, M. J., Collins, R., and Brasington, J. (2002). Small-catchment perspective on Himalayan weathering fluxes. *Geology* 30, 355–358. doi: 10.1130/0091-7613(2002)030<0355:SCPOHW>2.0.CO;2

West, A. J., Galy, A., and Bickle, M. (2005). Tectonic and climatic controls on silicate weathering. *Earth Planet. Sci. Lett.* 235, 211–228. doi: 10.1016/j.epsl.2005.03.020

White, A. F., and Blum, A. E. (1995). Effects of climate on chemical weathering in watersheds. *Geochim. Cosmochim. Acta* 59, 1729–1747. doi: 10.1016/0016-7037(95)00078-E

Willenbring, J. K., and Von Blanckenburg, F. (2010). Long-term stability of global erosion rates and weathering during late cenozoic cooling. *Nature* 465, 211–214. doi: 10.1038/nature09044

Yu, Z., Yan, N., Wu, G., Xu, T., and Li, F. (2020). Chemical weathering in the upstream and midstream reaches of the yarlung tsangpo basin, southern tibetan plateau. *Chem. Geol.* 559:119906. *doi: 10.1016/j.chemgeo.2020.119906*

Zakharova, E. A., Pokrovsky, O. S., Dupré, B., Gaillardet, J., and Efimova, L. E. (2007). Chemical weathering of silicate rocks in Karelia region and Kola peninsula, NW Russia: Assessing the effect of rock composition, wetlands and vegetation. *Chem. Geol.* 242, 255–277. doi: 10.1016/j.chemgeo.2007.03.018

Zakharova, E. A., Pokrovsky, O. S., Dupré, B., and Zaslavskaya, M. B. (2005). Chemical weathering of silicate rocks in aldan shield and baikal uplift: insights from long-term seasonal measurements of solute fluxes in rivers. *Chem. Geol.* 214, 223–248. doi: 10.1016/j.chemgeo.2004.10.003

Zhu, R., Zhang, H., Zhu, G., Meng, Q., Fan, H., Yang, J., et al. (2017). Craton destruction and related resources. *Int. J. Earth Sci.* 106, 2233–2257. doi: 10.1007/s00531-016-1441-x

Conflict of Interest: The authors declare that the research was conducted in the absence of any commercial or financial relationships that could be construed as a potential conflict of interest.

frontiers in Water

ORIGINAL RESEARCH
published: 17 February 2021
doi: 10.3389/frwa.2021.600649

The Spatiotemporal Evolution of Storm Pulse Particulate Organic Carbon in a Low Gradient, Agriculturally Dominated Watershed

Neal E. Blair[1,2]*, Elmer Arthur Bettis III[3], Timothy R. Filley[4], Jessie A. Moravek[5†], A. N. Thanos Papanicolaou[6‡], Adam S. Ward[7], Christopher G. Wilson[6], Nina Zhou[8†], Breanna Kazmierczak[1] and Jieun Kim[1]

[1] Department of Civil and Environmental Engineering, Northwestern University, Evanston, IL, United States, [2] Department of Earth and Planetary Sciences, Northwestern University, Evanston, IL, United States, [3] Earth and Environmental Sciences, The University of Iowa, Iowa City, IA, United States, [4] Department of Earth, Atmospheric, and Planetary Sciences, Purdue University, West Lafayette, IN, United States, [5] The Environmental Sciences Program, Northwestern University, Evanston, IL, United States, [6] Department of Civil and Environmental Engineering, University of Tennessee, Knoxville, Knoxville, TN, United States, [7] O'Neill School of Public and Environmental Affairs, Indiana University, Bloomington, IN, United States, [8] Biological Sciences, Northwestern University, Evanston, IL, United States

Streams and rivers integrate and transport particulate organic carbon (POC) from an array of aquatic and terrestrial sources. Storm events greatly accelerate the transport of POC. The sequences by which individual POC inputs are mobilized and transported are not well-documented but are predicted to be temporally transient and spatially dependent because of changes in forcing functions, such as precipitation, discharge, and watershed morphology. In this study, the 3rd–4th order agricultural stream network, Clear Creek in Iowa, U.S.A., was sampled at a nested series of stations through storm events to determine how suspended POC changes over time and with distance downstream. Carbon and nitrogen stable isotope ratios were used to identify changes in POC. A temporal sequence of inputs was identified: in-channel algal production prior to heavy precipitation, row crop surface soils mobilized during peak precipitation, and material associated with the peak hydrograph that is hypothesized to be an integrated product from upstream. Tile drains delivered relatively ^{13}C- and ^{15}N-depleted particulate organic carbon that is a small contribution to the total POC inventory in the return to baseflow. The storm POC signal evolved with passage downstream, the principal transformation being the diminution of the early flush surface soil peak in response to a loss of connectivity between the hillslope and channel. Bank erosion is hypothesized to become increasingly important as the signal propagates downstream. The longitudinal evolution of the POC signal has implications for C-budgets associated with soil erosion and for interpreting the organic geochemical sedimentary record.

Keywords: organic carbon, streams, erosion, storms, watershed, agriculture, land use, source-to-sink

OPEN ACCESS

Edited by:
Alexis Navarre-Sitchler,
Colorado School of Mines,
United States

Reviewed by:
Eve-Lyn S. Hinckley,
University of Colorado Boulder,
United States
Joel Moore,
Towson University, United States

***Correspondence:**
Neal E. Blair
n-blair@northwestern.edu
orcid.org/0000-0002-3449-3371

†Present address:
Jessie Moravek,
Department of Environmental Science, Policy, and Management, University of California, Berkeley, Berkeley, CA, United States
Nina Zhou,
Feinberg School of Medicine, Chicago, IL, United States

‡Currently unaffiliated

Specialty section:
This article was submitted to Water and Critical Zone, a section of the journal Frontiers in Water

Received: *30 August 2020*
Accepted: *22 January 2021*
Published: *17 February 2021*

Citation:
Blair NE, Bettis III EA, Filley TR, Moravek JA, Papanicolaou ANT, Ward AS, Wilson CG, Zhou N, Kazmierczak B and Kim J (2021) The Spatiotemporal Evolution of Storm Pulse Particulate Organic Carbon in a Low Gradient, Agriculturally Dominated Watershed. Front. Water 3:600649. doi: 10.3389/frwa.2021.600649

INTRODUCTION

Substantial loss of soil organic carbon (SOC) results from land use associated with agriculture and deforestation (Lal, 2009; Amundson et al., 2015). Initial perceptions were that the loss represented a major net source of CO_2 to the atmosphere (Lal, 2003). Instead, the loss may be part of a landscape-wide sink when C-budgets are broadened to include material that is transported away from the original source, and the reloading of newly exposed C-poor particle surfaces with fresh organic C (Harden et al., 1999; Berhe et al., 2007; Aufdenkampe et al., 2011; Papanicolaou et al., 2015; Doetterl et al., 2016; Wang et al., 2017). Most relevant studies have focused on the landscape itself and its response to the erosion of surface soils. However, waterways provide connectivity between many terrestrial C sources and their eventual sinks. As a result, C-transport within the river corridor may be a critical control in determining whether anthropogenic land use becomes a net source or sink of atmospheric CO_2.

Rivers and their tributaries have been portrayed in descriptions of the C-cycle as both reactors that foster in-channel primary and secondary production, and pipes that transport material (Cole et al., 2007; Bouillon et al., 2009; Raymond et al., 2016). Combined, these two functions produce the biogeochemical spiraling of biogenic elements, including carbon (Newbold et al., 1982; Richey et al., 1990). Rivers also integrate diverse forms of organic C (OC) from in-channel production and the adjacent landscape, and then deliver that mixture to downstream depocenters and ecosystems, such as floodplains, lakes, and the ocean (Blair and Aller, 2012; Wohl, 2017). Particulate OC specifically has been shown to be a mixture of materials with a broad range of ages derived from its sources. Insofar as age often influences reactivity (Blair and Aller, 2012), the downstream fate of POC in terms of whether it is likely to be remineralized to CO_2 or sequestered in depocenters is dependent on integrated mixture composition.

It follows that POC composition changes as it moves downstream because of its interactions with the river corridor. The degree of change per distance traveled, or even the factors that might control that metric, are poorly documented due to a paucity of longitudinal studies. The extent of change is most profound in large watersheds (Hedges et al., 2000; Blair et al., 2004; Aufdenkampe et al., 2007; Leithold et al., 2016). Given sufficient transit and storage time, upland POC can be completely lost to oxidation within river corridor soils and replaced by lower reach primary and secondary production (Bouchez et al., 2010; Blair and Aller, 2012). In contrast, the replacement of upland POC is incomplete in many small, mountainous river systems because of the limited interaction of sediment with the lower reaches of the watershed (Hilton et al., 2011; Galy et al., 2015; Leithold et al., 2016). The upland POC is overprinted by lowland sources but not replaced.

Low temporal-resolution measurements of riverine POC further limit our understanding of the POC transformations (Hope et al., 1994; Galy et al., 2015; Yang et al., 2016; Li et al., 2017). Large storm events in small systems transport significant quantities of sediment and POC within hours to a few days (Dalzell et al., 2005; Jeong et al., 2012; Jung et al., 2012; Gellis, 2013; Rowland et al., 2017). Storms may be responsible for up to 80% of riverine POC transport (Oeurng et al., 2011; Dhillon and Inamdar, 2013, 2014). Temporal resolution on the scale of hours is required for measurements in such situations to capture intra-event changes in POC fluxes and composition. For instance, studies of dissolved OC (DOC) have indicated compositional changes on an hourly time scale during storm events in which aliphatic-rich materials were present at the storm onset and aromatic OC was more prevalent at peak discharge (Wagner et al., 2019). Comparable behavior might occur with POC. Only a small number of high-resolution POC studies that include compositional information exist for either steep-sloped mountainous systems (Jeong et al., 2012; Jung et al., 2012) or lower-gradient settings (Dalzell et al., 2005, 2007; Rowland et al., 2017; Blair et al., 2018; Kim et al., 2020).

Given the combined spatial and temporal limitations of datasets, we are unable to predict in detail how the composition of fluvial POC might evolve in most watersheds as a function of time in response to a storm event or how any response might vary with travel downstream. At the very least, this poses a challenge when designing sampling protocols. More importantly though, it severely limits our ability to interpret the storm pulse compositional "signal" as it moves through the system. A proposed conceptual model based on a storm event in the agricultural stream network of Clear Creek (Iowa, U.S.A.) suggests that a time-resolved sequence of inputs can occur (Kim et al., 2020). The sequence starts with easily suspended in-channel debris including algal material, transitions to surface soils delivered by heavy precipitation, and then culminates with an integrated mixture of sources transported with the rise and fall of the hydrograph. In this study we evaluate the conceptual model over multiple storm events to determine if it is a robust description of POC behavior in the same watershed. The longitudinal behavior is of particular interest because it offers a perspective on how environmental signals are propagated and modified within a watershed (Romans et al., 2016). The results may thus direct future studies concerning the fate of the exported POC.

Clear Creek contributes to the Upper Mississippi River watershed and is part of the U.S. National Science Foundation's Intensively Managed Landscapes Critical Zone Observatory (IML-CZO; Kumar et al., 2018). As such, it is well-poised as an outdoor laboratory to investigate agriculturally induced surface soil erosion (Wilson et al., 2018). Most of the erosion research, which includes both field and modeling studies, has focused on the upland reach where connectivity between hillslopes and the stream channel is high (Wilson et al., 2012; Papanicolaou et al., 2015). We hypothesize the relative importance of surface soil erosion as a direct POC input decreases in the lower reaches due to the interception of eroded materials by lower gradient portions of the landscape adjacent to the Clear Creek channel. To test that hypothesis and the conceptual model described above, suspended sediment samples were collected through storm events at three stations located in the upper, middle and lower reaches of the watershed. Changes in POC composition were monitored using stable isotope ($^{13}C/^{12}C$, $^{15}N/^{14}N$) ratios. Those

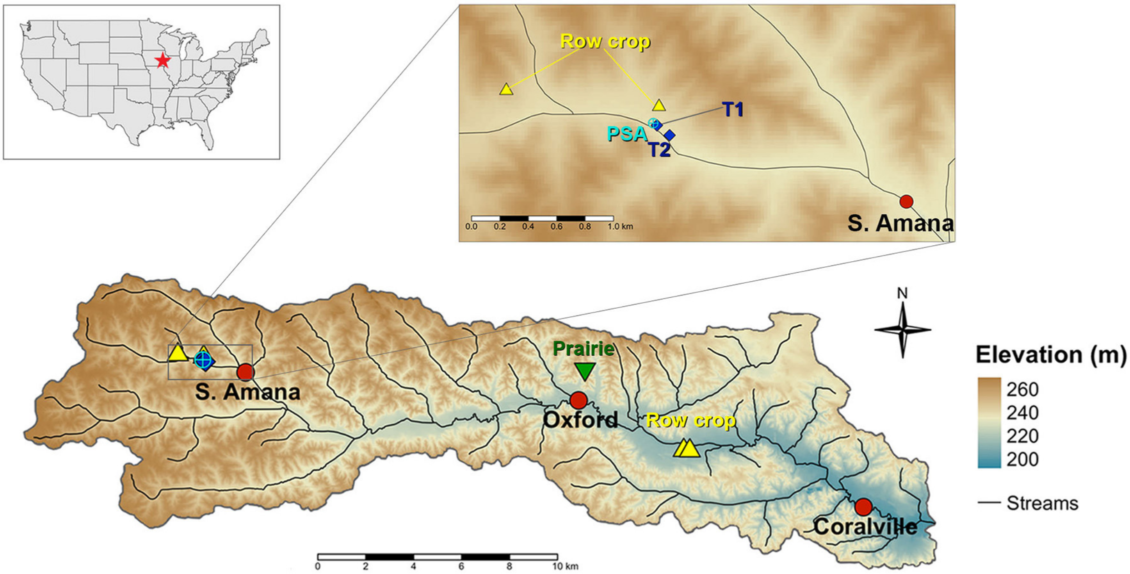

FIGURE 1 | Location of Clear Creek watershed in Iowa, U.S.A. Stream sampling stations are denoted by red circles. Tile drains (T1 and T2) and the alluvial soil core (PSA) are blue symbols. Row crop (yellow triangle) and Prairie (green inverted triangle) are sampling locations for surface soils reported in Hou et al. (2018).

TABLE 1 | Characteristics of Clear Creek subbasins.

Station	Drainage area[a] (km^2)	Elevation (m)[b]	Channel slope (%)[b]	Land cover (%)[c]			
				Corn/soy	Grass	Forest	Developed
S. Amana	26.2	231–278	0.40	83 (76)	8 (19)	1 (0)	6 (5)
Oxford	157.5	213–278	0.21	66 (52)	20 (31)	3 (8)	7 (7)
Coralville	254.3	164–278	0.17	56 (43)	22 (27)	7 (11)	11 (13)

[a] *Davis et al. (2014).*

[b] *Average down-channel slope (rise/run × 100) from headwater to station. Note that these values differ from those in* ***Figure 3****, which are for the segments between sampling stations.*

[c] *Mean % of landscape dedicated to corn-soybean rotation, grasslands, forests, and urban development for 2014–2016 (USDA National Agricultural Statistics Service). The remainder of the landscape is classified as Other crops. Values in parentheses are the land use for floodplains. The interannual range of values is ≤3%.*

measurements were chosen because of their well-demonstrated utility as source indicators (Fry and Sherr, 1984) and small sample size requirements. They also allow direct comparison to previously published elemental and isotopic data from Clear Creek soils that are potential sources of POC (Hou et al., 2018). In addition, tile drains, a ubiquitous hydrologic control and dissolved nutrient transporter in flat agricultural settings (Skaggs et al., 1994), were investigated as a previously unexplored source of POC.

METHODS

Site Description

The 270-km^2 Clear Creek watershed (**Figure 1**; **Table 1**; HUC-10: 0708020904) is in the agriculturally productive loess-mantled Southern Iowa Drift Plain, where the soils rapidly erode when disturbed (Ruhe, 1969; Prior, 1991). Approximately 75% of the annual precipitation (average ~890 mm/year) occurs during the growing season (Wacha et al., 2018). Intense storms at the beginning of the growing season can produce flash floods because of the bare surfaces in the row crop fields and channelization of the stream (Wilson et al., 2012). Erosion rates in Clear Creek fields are high, averaging 20 Mt/ha/yr in some cases (Abaci and Papanicolaou, 2009; Wilson et al., 2016; Wacha et al., 2018). Erosion has been attenuated by the adoption of soil conservation practices in the 1990's (Abaci and Papanicolaou, 2009; Papanicolaou et al., 2015). These include rotations of corn (*Zea mays* L.)—soybean (*Glycine max* L.) crops and no-till, spring shallow-till, and fall deep-till practices. Grassed and forested riparian buffers are often present but range in widths up to 10's of meters.

Soils in the Clear Creek watershed are silty clay to silt loam Mollisols and Alfisols (Hou et al., 2018; Wilson et al., 2018). Conventionally tilled surface soils have SOC contents of ~2 wt% and C/N (wt) ratios of ~10. In contrast, restored prairie site soils had nearly double the SOC content with similar (~11) C/N ratios (Hou et al., 2018). $^{13}C/^{12}C$ ratios reflected the presence or absence of contributions from corn, a C4 plant that expresses an enrichment in ^{13}C (O'Leary, 1981). As a result, tilled row crop soils were significantly enriched in ^{13}C relative to those from the

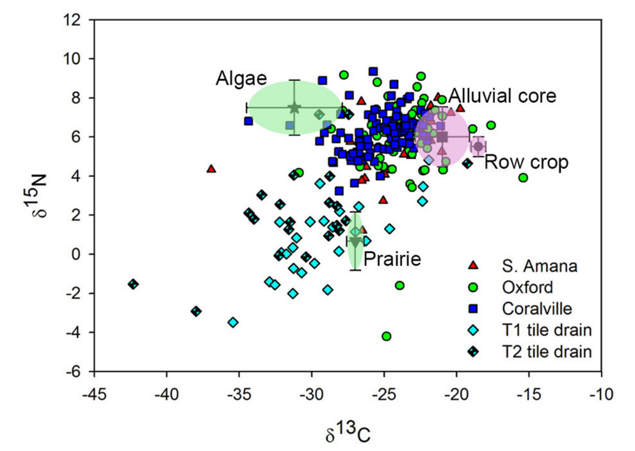

FIGURE 2 | POC $\delta^{13}C$ vs. PN $\delta^{15}N$ for suspended sediments from all events, stations and tile drains, as well as the alluvial soil core. Surface soil ranges are from local row crop fields and restored prairies (Hou et al., 2018). The algal data shown are measurements from suspended sediment filter samples in which algal mat fragments appeared to dominate the organic material.

restored prairie (**Figure 2**; Hou et al., 2018) thereby providing a potential indicator of row crop soil input to Clear Creek. The row crop soils were also enriched in ^{15}N, a potential reflection of fertilizer use, and offering another source tracer.

Three stream sites were sampled to capture material exported from the upper, middle and lower reaches (**Figure 1**; described also by Davis et al., 2014). The upper reach stream site near South Amana has been studied previously in terms of sediment/ POC sources and delivery processes (Wilson et al., 2012; Papanicolaou et al., 2015; Abban et al., 2016; Hou et al., 2018). The middle site is co-located with the U.S. Geological Survey gaging station near Oxford, IA (#05454220) and the lower reach is located near the USGS stream gage (#05454300) in Coralville. The valley cross-section at South Amana is V-shaped (**Figure 3**). The valley cross-sections at Oxford and Coralville are more U- or box-shaped (Yan et al., 2018).

Though corn-soybean fields dominate the landscape overall (∼56%), their greatest concentration is in the upper reach (**Table 1**). The average slope of the upper reach is ∼6%, which enhances surface runoff and erosion, thereby providing significant connectivity between sediment sources and the channel (Abaci and Papanicolaou, 2009; Abban et al., 2016). The channel banks are a secondary source of sediment especially where the stream has been channelized (Sutarto et al., 2014; Papanicolaou et al., 2017). Channel bank erosion becomes proportionately more important downstream. The middle reach is a transition zone where either surface or bank sources can dominate depending on conditions (Abban et al., 2016). Channels are wider and deeper in this reach (Wacha et al., 2018; **Figure 3**) and land cover shifts to more grassland and forest (**Table 1**). The urban areas, while small (7%), are more concentrated in the lower portion of the watershed. Bank erosion is more prevalent in this zone where the banks are higher and steeper, high flows are more sustained, and contributions from surface erosion are minimal due to more impervious surfaces (Papanicolaou et al., 2017).

Sample Collection

Suspended sediment samples were collected shortly before, during and after storm events (**Table 2**; **Figure 4**) using ISCO™ autosamplers equipped with 1-liter bottles. The sampling lines for the in-stream samplers were fixed in the water column and were co-located with water quality monitoring equipment deployed by the Iowa Flood Center. For the tile drain samples, the tubing was affixed to the inside of the tile drain along the bottom of the pipe to sample effluent when water was flowing through the tile. The autosamplers were programmed to collect samples at fixed time intervals, typically every 3 h. The sampling interval was chosen to define the storm peak at the three locations simultaneously while allowing a feasible sample load. For each sample, the autosampler triple-rinsed the sampling line with stream water immediately prior to collection of each sample, then an 800-mL sample was pumped into an open 1-L Nalgene bottle. The sample bottles were capped and frozen immediately after the hydrograph recession.

In addition to in-stream sampling, two tile drains (T1, T2) were located on a farm upstream of the South Amana station (**Figure 1**). Both tile drains were slot-perforated ABS tubing with 8-inch diameter PVC outlets. The slots were ¼″ × 1″ (w × l) spaced 4–6 in number around the diameter and ∼1 inch apart along the length of the tubing.

An intact, 7.6 cm diameter × 2.3 m long soil core (PSA-1) was collected as part of a hillslope erosion study using a Giddings™ coring machine (Yan et al., 2019). The core was at the base of the hillslope ∼15 m from the channel within the South Amana subbasin thus it provides an example of the type of material that is exposed by erosion as the channel meanders (**Figure 1**). The core penetrated into the B soil horizon of a preserved pre-settlement soil profile buried beneath post-settlement alluvial material (Yan et al., 2019). The core was first wrapped in plastic wrap, then aluminum foil, and placed in a cardboard soil core box to preserve integrity and moisture content, then transported to the lab for description and analysis. Air-dried core samples collected in 4–5 cm intervals were lightly crushed with a mortar and pestle to pass through a 1 mm-mesh sieve where roots, stones, and large particulate matter were removed. A subsample was then ground into fine powder using a steel ball mill (Retsch Inc., Haan, Germany).

Water Discharge and Precipitation

Water discharge for the sampling periods at South Amana was determined from a stage-discharge rating curve. Continuous stage measurements at 15-min intervals were collected with a Global Water WL16 Data Logger. The pressure transducer has a ± 0.1% of full scale accuracy at constant temperature and a ± 0.2% accuracy over 1.7 to 21.1°C temperature range. To minimize the effects of waves and water current on the measurements, the pressure transducer was installed within a stilling well. Flow velocity was measured with an Acoustic

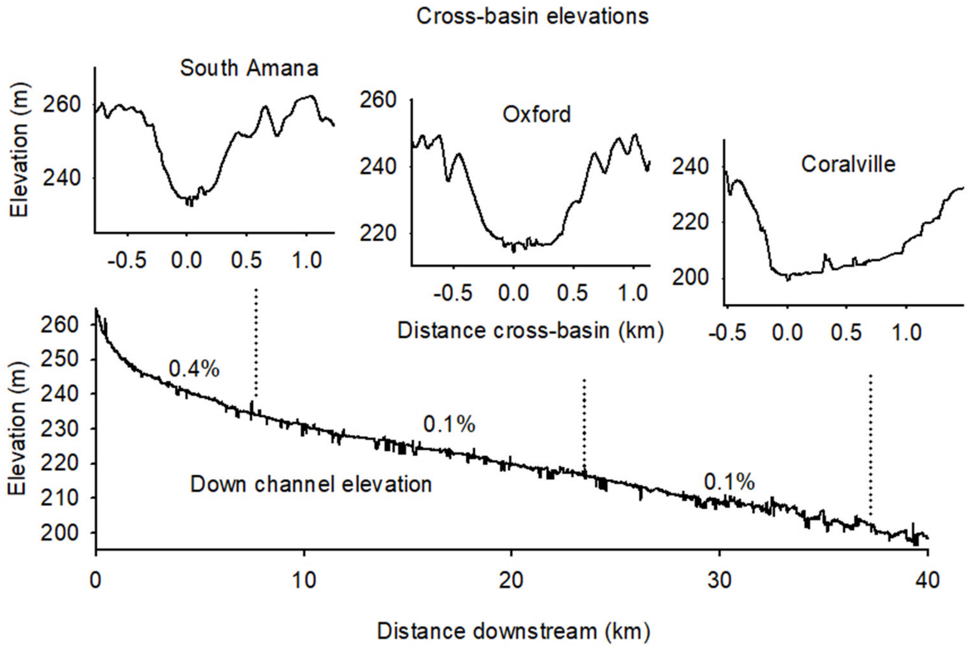

FIGURE 3 | Valley cross-sections at sampling stations (top) and mid-channel elevations as a function of distance from headwaters (bottom). The V-shaped cross-basin profile of the upper reach near Oxford permits a more effective transfer of material from hillslope to channel relative to the box-shape of the lower reach**.** The percent values on the lower graph are the elevational gradients between the headwaters and South Amana, South Amana–Oxford, and Oxford-Coralville.

TABLE 2 | Storm events sampled.

Event ID	Sampling period	Stations sampled[a]	Precipitation (mm)[b]
Oct 2014	10/12–10/22/14	CCO, CCC	134.6
June 6 2015	6/6–6/10/15	SAC, CCO	92.2
June 20 2015	6/20–6/23/15	SAC, CCO, T1, T2	74.9
July 2015	7/28–7/30/15	CCO, CCC, T1, T2	85.8
Oct 2015	10/27–10/30/15	SAC, CCO, CCC, T1, T2	63.5
June 2016	6/24–6/27/16	SAC, CCO, CCC, T1, T2	94.5

[a] *Station locations provided in* ***Figure 1****. SAC, South Amana; CCO, Oxford; CCC, Coralville; T1 and T2, tile drains.*

[b] *Precipitation is for the duration of the sampling period collected at Iowa City.*

Doppler Velocimeter FlowTracker by Sontek every 30 cm along the channel width. The FlowTracker has a velocity range ±0.001–5 m/s and an accuracy ±1% of the measured velocity. During the measurements no bedforms (e.g., dunes) were present that could affect stage estimation as the bed remained near-flat during the development of the curve with minimal effects in changes in Manning's n roughness value. The developed stage–discharge relationship for the South Amana outlet was:

$$Q \quad (\text{discharge}) = 3.645^{*}\text{stage}^{1.814}, \tag{1}$$

where the units of discharge and stage are m^3/s and m, respectively (Abaci and Papanicolaou, 2009). Stream discharge at the Oxford and Coralville stations was retrieved from the USGS website (https://waterdata.usgs.gov/ia/nwis/).

The spatial distribution of daily averaged precipitation for the storm events were derived from quality-controlled, multi-sensor (radar and rain gauge) precipitation estimates obtained from National Weather Service River Forecast Centers (https://water.weather.gov/precip/). The U.S. continental precipitation maps were downloaded and georeferenced in ArcGIS Pro software (version 2.5.1), after which they were clipped to the subbasin areas. Daily precipitation was integrated in each subbasin for each sampling day.

Daily precipitation records for the 2014–2016 period were obtained for Coralville from the NOAA National Centers for Environmental Information (https://www.ncdc.noaa.gov/cdo-web/datasets#GHCND). Hourly precipitation rates for nearby Iowa City (∼6 km SE of Coralville) were obtained from the Iowa State University Iowa Environmental Mesonet (https://mesonet.agron.iastate.edu/).

POC, PN Concentrations, Fluxes, and Stable Isotope Measurements

Particulate organic C and particulate total N concentrations (mass/water volume) were estimated by first measuring suspended sediment concentrations and then determining the %C and %N on a dry weight basis of the sediment. Water samples were thawed shortly before being filtered on pre-weighed 47 mm o.d. glass fiber filters (0.7 micron nominal pore size, Millipore^{TM}). Filters were cleaned before use by roasting at 500°C overnight to remove trace organic matter. Filters and sediment were lyophilized and then weighed. The weights in combination with

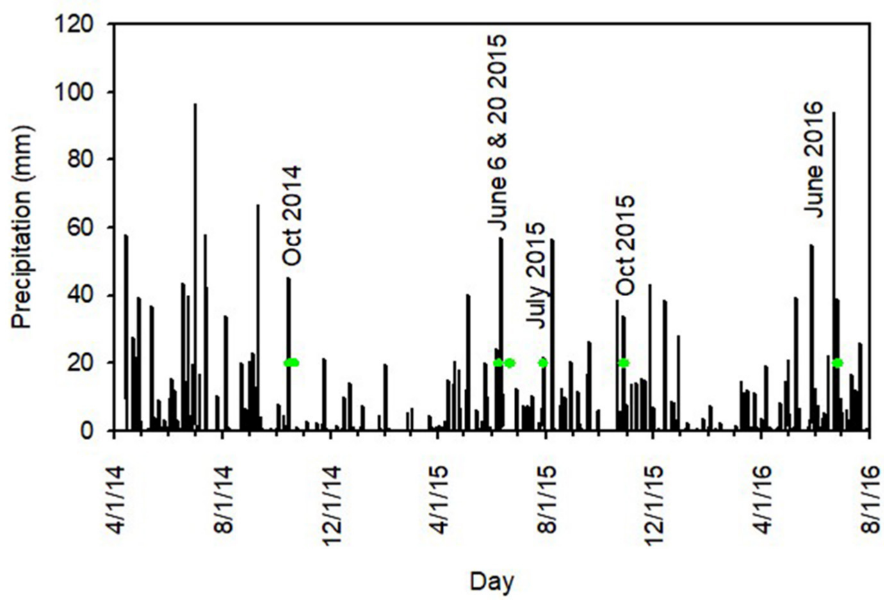

FIGURE 4 | Daily precipitation at Coralville (NOAA NCDC Network GHCND: station US1IAJH0010) for the 2014–2016 period. Horizontal bars are sampling periods in this study.

the measured volumes of filtered water were used to determine sediment concentrations.

The sediment on the filters was fumigated with gaseous HCl for 1–4 days to remove carbonate C. Carbonate removal was verified via transflectance FTIR (Cui et al., 2016) using a Bruker Tensor 37 FTIR [NIR/MIR] equipped with a Hyperion microscope and MCT detectors and monitoring an absorbance peak at 2513 cm^{-1}. Sediment was either analyzed directly on the glass fiber filters, or a small aliquot of the powdered sediment was spread on Aluminum weighing boats. The soil core samples were similarly fumigated with HCl using the method described by Harris et al. (2001).

Decarbonated sediment samples were analyzed for POC and PN contents, as well as their $^{13}C/^{12}C$ and $^{15}N/^{14}N$ ratios using a Costech Elemental Analyzer-Conflo IV interface-Thermo Delta V Plus isotope ratio mass spectrometer (IRMS) combination. This includes those filter samples identified as having captured algal mat fragments. The PSA-1 soil core organic C, PN, and $\delta^{13}C$ and $\delta^{15}N$ stable isotope values were measured using a Sercon Ltd. (Crewe, UK) flash combustion elemental analyzer interfaced to Sercon Ltd. 20/22 IRMS. Isotopic compositions were related to international standards (VPDB, air) through calibrated laboratory reference materials (Coplen, 2011; Leithold et al., 2013) and reported using the $\delta^{13}C$ and $\delta^{15}N$ notations (Craig, 1953). Analytical precision of $\delta^{13}C$ and $\delta^{15}N$ values of the laboratory working standards of NIST 1547 Peach Leaves (NIST, Gaithersburg, MD) and LECO #502-062 soil (ISO Guide 34:2009) was <0.2‰.

POC fluxes at each station were estimated via

$$\text{Flux (g C/s)} = [\text{POC}]\ (\text{g/L})^{*}\text{Q (L/s)}. \tag{2}$$

The total quantity of POC (kg C) that passed the sampling stations was determined by integrating the flux as a function of time over the duration of the sampling period. The integrated quantity of early flush C (see section The POC Components of Storm Responses) was estimated by considering only the time period in which that peak appeared. The $\delta^{13}C$ and $\delta^{15}N$ values of the exported material were calculated via the integration of flux-weighted isotopic signatures over time normalized to the total integrated flux,

$$\delta_{int} = \frac{\int_{t=1}^{t=x} Flux_t \delta_t}{\int_{t=1}^{t=x} Flux_t} \tag{3}$$

where δ_{int} is the flux-weighted integrated isotopic signature. $Flux_t$ and δ_t are the POC flux and isotopic composition at time t.

RESULTS

Precipitation Patterns

Six storm events were captured between October 2014 and June 2016 (**Table 2**; **Supplementary Table 1**; **Figure 4**). The storms were small-to-intermediate in size with precipitation quantities of 28–59 mm (**Figure 4**). June-July storms fell within a cluster of events that were separated by days to several weeks. The October events were preceded by a much drier period 1–2 months long, depending on the year. These observations are consistent with the general pattern of wet springs (June average precipitation ~120 mm) and drier falls (October mean ~75 mm, National Weather Service). In most cases, the precipitation occurred over a 1–2 day period (**Figure 4**).

The spatial coverage of precipitation varied among the events (**Figure 5**). Coverage was relatively uniform (±10 mm) across the

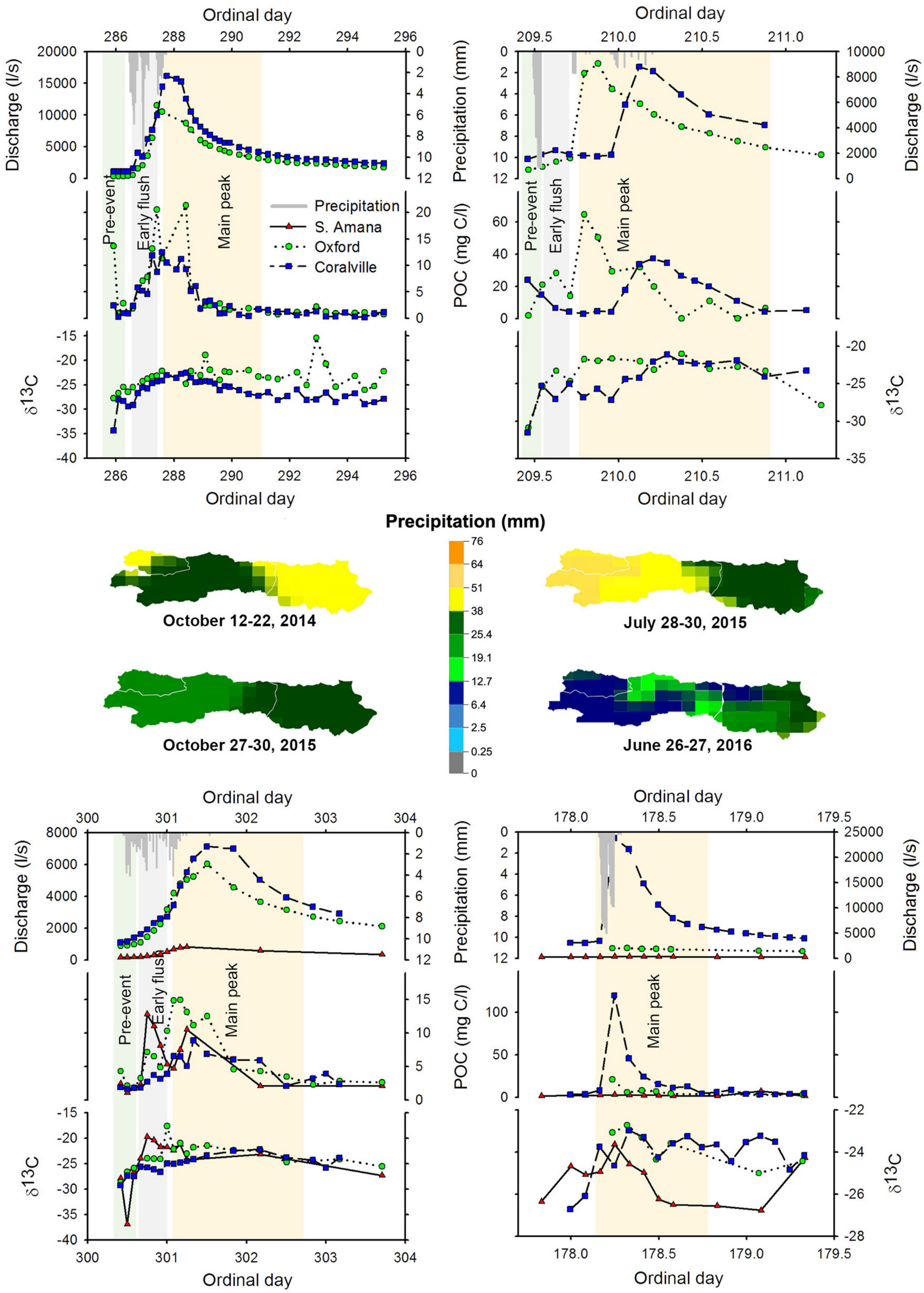

FIGURE 5 | Time series data for storm events at South Amana (▲), Oxford (●), and Coralville (■). Data shown include precipitation in millimeters at Coralville (gray bars), discharge (liters/s), POC (mg C/liter), and POC δ^{13}C. The three phases of POC input (pre-event, early sediment flush, and main peak) are highlighted. Watershed maps depict the spatial coverage of precipitation for the day recording the heaviest rainfall in each event.

watershed in June 2015 and Oct 2015. Precipitation was heavier in the South Amana subbasin (peak precipitation 57 ± 7 mm) than Coralville (32 ± 7 mm; **Figure 5**) during the July 2015 storm. In contrast, the heaviest downfall bypassed South Amana (9.6 ± 3 mm) and fell on Coralville (32 ± 7 mm) in June 2016. The remaining events had patterns that bridged the extremes (**Figure 5**).

Sediment Character and Concentrations

ISCO deployments were done only at Oxford and Coralville in Oct 2014. In 2015–2016, some stations or samples are missing due to equipment failure. The event in October 2015 offers the most complete view of Clear Creek behavior because all stations were in operation throughout the storm. The June 2016 storm yielded the second-best sample coverage, though the beginning of the event was missed at the Oxford station.

Based on visual inspection, sediment color and texture changed throughout events at the three sites. Early sediment tended to be light brown colored, silty in texture, and disaggregated. As discharge increased and sediment concentrations peaked, the sediment transitioned to darker colored, mm-sized fluffy aggregates that were stable to vigorous shaking. Suspended load returned to a lighter colored, siltier material after the sediment concentration peaked. Plant debris, algal mat fragments, and insects were found in some samples. The algal material was the most obvious visually in the pre-storm samples from October.

For the most part, suspended sediment concentrations increased with discharge, which was below flood stage in all cases. In some events, sediment concentrations peaked before water discharge (**Supplementary Table 1**; Oct 2014, July 2015, Oct 2015). Multiple peaks in sediment concentration were often evident within one storm event.

The concentrations of sediment in the tile drain effluent were typically low (∼0.05–0.15 g/l) with occasional spikes (∼0.25 g/l; **Supplementary Table 1**). The spikes in concentration were attributed to run-off into surface inlets.

POC Concentrations, Isotopic Compositions, and Fluxes

POC concentrations in the channel typically paralleled those of the sediment, as expected given the dependence of the POC concentration on that of the sediment (**Figure 5**, **Supplementary Table 1**). However, small pre-event peaks (2.4–24 mg C/l) occurred in three events (Oct 2014, 2015, July 2015) when there was little or no measured increase in sediment. The elevated POC was due to higher %C values (2.6–12.9%) at those times (**Supplementary Table 1**), which was ascribed to algal material in the stream (see section The POC Components of Storm Responses). Tile drain sediment had low %C (<2%), though occasional spikes (3–11%) were observed (**Supplementary Table 1**). POC/PN (C/N) ratios were soil-like (6–18, Hedges and Oades, 1997). Higher values (>12) in C/N during an event are thought to result from the inclusion of plant debris which can have values of 25–400 (Hedges and Oades, 1997; **Supplementary Table 1**).

The cultivation of the C4 plant, corn, provides a sharp contrast in δ^{13}C (∼-10 to −13‰) relative to more ubiquitous C3 plants (∼-25 to −35; O'Leary, 1981; Farquhar, 1983). Not surprisingly, POC δ^{13}C values ranged between purely C3 values and those of mixtures of C3–C4 sources (−15 to −23‰; **Figures 2**, **5**). A consistent ^{13}C-enrichment occurs on the rising limb of the hydrograph (**Figure 5**). Similar ^{13}C-enrichments have been observed in the Sangamon River (Illinois) and the Schwabach River (Germany) and like Iowa, these results were attributed to corn cultivation (Lee et al., 2017; Blair et al., 2018).

The PSA-1 core samples had δ^{13}C values that ranged from ∼-18 to ∼-25‰ reflecting variable mixes of C3 and C4 plant material (**Figure 2**). The organic material at this site is the product of erosional inputs from upslope, inputs from colonizing vegetation (i.e., new soil formation on the alluvial-colluvial deposition), and diagenetic alteration of those inputs (Yan et al., 2019). The isotopic variability indicates changes in the mixtures of plant sources and presumably land use over time. Of most relevance to this study, the wide range of values demonstrates the potential variability in isotopic signatures associated with erosion of alluvial deposits as they are exposed by channel migration.

δ^{15}N values of stream PN were typically positive (+1–9‰, **Figure 2**) and within the range for many soils (Amundson et al., 2003; Fox and Papanicolaou, 2007; Abban et al., 2016; Hou et al., 2018). The PSA-1 core δ^{15}N values were in the nearly identical range. Row crop soils, the alluvial core, and the algal samples were distinctly ^{15}N-enriched relative to the prairie soils (**Figure 2**). The ^{15}N-enriched sources share the characteristic that their N is likely derived from applied fertilizers, whereas the prairie N would be far less so. The common interpretation of the ^{15}N-enrichment in soils is that denitrification selectively converts ^{14}N-nitrate to N_2 thereby concentrating the ^{15}N in the soil pool (Amundson et al., 2003).

Tile drains exported a wide range of δ^{13}C and δ^{15}N values (**Figure 2**). The few values near those of the row crops are interpreted to reflect surface run-off that entered the drains via their surface inlets. The bulk of the samples were depleted in ^{13}C and ^{15}N relative to the stream suspended sediments and the agriculturally dominated sources. The potential origin of the isotopic ratios is discussed later.

POC export from the subbasins varied in response to subbasin area and local rain fall amounts (**Table 3**, **Figure 6**). The 8- to 9-fold higher POC export at Oxford relative to South Amana is commensurate with the 6-fold increase in subbasin area. In contrast, a small decrease (2–17%) was observed between Oxford and Coralville in three of four storm events. It is not clear if these small differences rise above the uncertainty of the estimates, but if they do, they signal a loss of POC between the two stations. The deposition of coarse-grained sediment is one potential mechanism. What can be concluded is that the ∼38% increase in subbasin area between Oxford and Coralville does not lead to a similar net increase in POC flux. This is a potential indicator of the lower erodibility of the landscape in the lowest reach.

The exported δ^{13}C and δ^{15}N values were −25.9 to −22.1 and 4.4–7.5‰, respectively. As discussed previously, the isotopic compositions reflect mixtures of corn and C3 vegetation, as

TABLE 3 | Integrated POC export and isotopic signatures.

Event	Station	Integrated POC export (kg)[a]	Early flush POC (kg)[b]	% Early flush POC	Integrated δ^{13}C[c]	Integrated δ^{15}N[c]
Oct 2014	Oxford	22,074	5,970	27	−23.4	6.2
	Coralville	21,604	3,037	14	−24.0	6.5
July 2015	Oxford	14,397	425	3	−22.1	6.2
	Coralville	11,967	0	0	−23.0	5.8
Oct 2015	S. Amana	714	82	12	−23.6	5.8
	Oxford	6,203	246	4	−22.3	7.2
	Coralville	5,273	176	3	−23.5	7.5
June 2016	S. Amana	95	0	0	−25.9	4.4
	Oxford	780	0	0	−23.8	6.0
	Coralville	34,290	0	0	−24.1	5.5

[a] Total POC exported past station for the duration of sampling.
[b] Integration of early flush POC flux peak.
[c] Integrated flux weighted isotopic signatures of exported material.

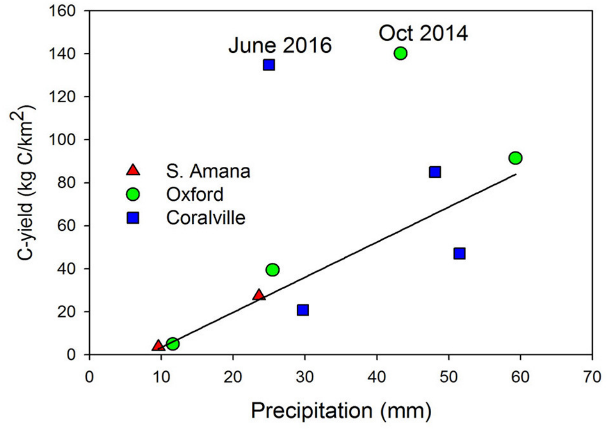

FIGURE 6 | POC yield as a function of precipitation quantity for the three subbasins. Regression excludes the June 2016 (Coralville) and Oct 2014 (Oxford) data points.

well as soils that have experienced varying degrees of fertilizer application and/or denitrification.

X-Q Relationships

Concentration-discharge (C-Q) relationships result from a balance of supply, reaction, transport and dilution of solutes and particulates (Rose et al., 2018). Hysteresis in the C-Q trajectory is common as the result of changing balances between material inputs and losses over the course of storm events. The POC concentration- and δ^{13}C -discharge relationships (X-Q) in this study, which we believe are the first of their kind to be reported, exhibited a range of hysteresis patterns (e.g., clockwise, counterclockwise; Gellis, 2013; Rose et al., 2018) over the different events (**Table 4**). POC-Q trajectories were predominantly clockwise and paralleled those displayed by sediment (not shown). δ^{13}C-Q trajectories in contrast were more variable, and as will be discussed later, likely reflect variations in the arrival times of different POC sources.

To better understand the timing of POC inputs, we focused on the rising limb of the hydrograph, reasoning that the effects of POC supply (as opposed to loss or dilution) would be most obvious for particulates during that period (Rose et al., 2018). The rising limb POC concentration- and δ^{13}C -discharge relationships were parameterized by their slopes obtained from linear regressions. In some situations, and especially at South Amana, linear correlations were poor or non-existent (**Table 4**). POC concentration-Q slopes were statistically significantly for the lower reaches and ranged from 0.0007 to 0.005 mg C-s-l^{-2}. The lower reach δ^{13}C-Q slopes were 0.00004–0.0017‰-s-l^{-1} with a mixture of statistically significant and insignificant values (**Table 4**). X-Q regression values varied among events at individual stations (**Table 4**) and POC-Q slopes appeared to decrease with distance downstream (**Table 4**, **Figure 7**).

DISCUSSION

Inter-storm Variability

No two storm responses were identical in terms of POC temporal or spatial behavior. Multiple factors likely contribute to the variability. Antecedent precipitation and management cycles are two factors known to influence solute and particulate fluxes (Wilson et al., 2012; Davis et al., 2014). Our sampling falls into two general categories in that regard—the wet late spring/early summer following planting and the dry fall seasons following harvest (**Figure 4**). Agricultural field run-off is expected to be more prevalent in the drier fall and in post-harvest fields (Abaci and Papanicolaou, 2009) and evidence is seen for this in Oct 2014 and 2015 when prominent early flush POC peaks attributed to surface erosion occurred (section The POC Components of Storm Responses). Note though that our sampling was less complete in the June-July events thus we can only argue that our results are consistent with the hypothesis that the antecedent conditions have an impact on POC export.

Several end-member scenarios in storm trajectory generated specific responses. When rainfall covers the watershed approximately evenly, the main POC peaks associated with the rise and fall of the hydrograph are nearly contemporaneous with each other at each station because of the small size of the basin (**Figure 5**). This did not happen in July 2015 when

TABLE 4 | X-Q relationships.

		Hysteresis[a]		X-Q slope[b]			
Station	**Event**	**POC**	**δ^{13}C**	**POC**	**r^2 (p)**	**δ^{13}C**	**r^2 (p)**
S. Amana	Oct 2015	8	C	0.006	0.14 (0.25)	0.0075	0.15 (0.23)
S. Amana	June 2016	Complex	CC	0.013	0.56 (0.14)	0.019	0.47 (0.20)
Oxford	Oct 2014	C	Complex	0.001	0.68 (0.006)	0.0003	0.61 (0.01)
Oxford	July 2015	C	Complex	0.005	0.82 (0.01)	0.0006	0.47 (0.13)
Oxford	Oct 2015	C	C	0.002	0.81 (0.00002)	0.001	0.47 (0.01)
Coralville	Oct 2014	C	Complex	0.0007	0.79 (0.0001)	0.0005	0.61 (0.002)
Coralville	July 2015	Complex	CC	0.003	0.56 (0.02)	0.0005	0.28 (0.14)
Coralville	Oct 2015	C	CC	0.0010	0.81 (0.00003)	0.0007	0.71 (0.0003)
Coralville	June 2016	C	Complex	0.006	0.99 (0.0002)	0.00004	0.11 (0.66)

[a] *Hysteresis trajectories abbreviated by: C (clockwise), CC (counterclockwise), 8 (figure 8), Complex (multiple crossovers). Sediment-Q trajectories track those of the POC.*

[b] *Slope of rising limb X-Q relationship. Units for POC-Q and δ^{13}C-Q are mg C-s-l^{-2} and ‰-s-l^{-1}, respectively. Linear regression fit (r^2) and statistical significance (p) are in adjacent columns for each X-Q.*

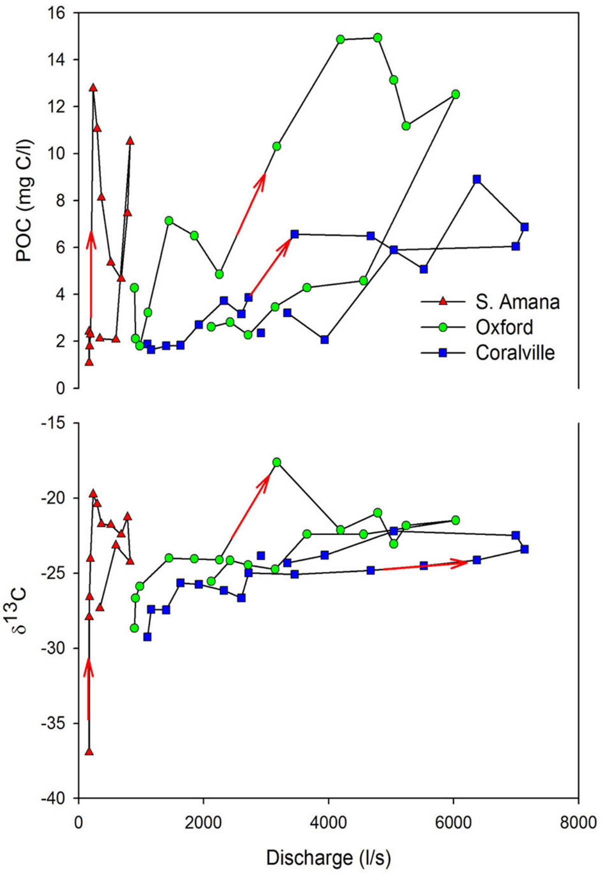

FIGURE 7 | POC concentration (top) and POC δ^{13}C (bottom) as functions of water discharge for the October 2015 event at the sampling stations. The arrows show the direction of the rising limb. The hysteresis is clockwise in all cases in this example except for the POC δ^{13}C at the Coralville (CCC) lower reach location.

the water discharge and POC peaks arrived at Coralville ∼4–5 h after passage in Oxford. In this situation precipitation was heavier in the upper reach (51–64 mm) relative to near Coralville (25–38 mm). It is hypothesized that local inputs in the lower portion of the watershed were muted and that the upland-generated response that traveled downstream dominated the signal at Coralville. In contrast, the lower portion of the watershed received the heaviest rainfall in June 2016. The response in this situation was small POC peaks at South Amana and Oxford, and a much larger POC peak at Coralville. In this case, the upland source was attenuated relative to the local inputs near Coralville. These scenarios aptly illustrate an obvious but important point when understanding the POC composition at a specific time and place—the POC is a mixture of material locally and distally sourced in varying proportions. This observation can explain aspects of X-Q behaviors (section X-Q Relationships).

POC yield, the quantity of exported POC (**Table 3**) normalized to subbasin area (kg C/km^2), has a dependency on precipitation quantity (**Figure 6**). Excluding the two outlier data points (Oxford—Oct 2014, Coralville—June 2016), there is a linear relationship between the POC yield and the precipitation that fell on the subbasin ($r^2 = 0.83$, $p = 0.002$). The outliers, both high POC yields, occurred during storms in which the precipitation was spatially heterogeneous. Localized rainfall if sufficiently intense might have produced such non-linear behavior. We are unaware of similar observations of POC yield and precipitation. The relationship between sediment yield and precipitation is well-established (Kao and Milliman, 2008) however and it is expected to parallel that of POC.

The POC Components of Storm Responses

Surface soils and in-channel sources (algae, vascular plant debris, accumulated sediments, and channel walls) are commonly cited POC inputs to streams and rivers, including those in agricultural watersheds (Griffiths et al., 2012; Abban et al., 2016; Dolph et al., 2017; Le Meur et al., 2017; Rowland et al., 2017; Blair et al., 2018). Previous studies in the South Amana subbasin of Clear Creek identified parallel categories of sediment and POC sources, i.e., algal/detritus, terrestrial, and in-stream (Abaci and Papanicolaou, 2009; Wilson et al., 2012; Abban et al., 2016). The current compilation of past and present data indicate Clear Creek suspended sediment δ^{13}C and δ^{15}N values from the three sampling stations are bracketed by those of algal material, surface soils (row crop, prairie), alluvial deposition, and tile drain suspended sediment (**Figure 2**). This suggests that we have captured the major inputs of POC, or at least the dominant isotopic endmembers. The restored prairie that was sampled in a previous study (Hou et al., 2018) is not likely to be a major source of POC because of its limited area, however as a C3 plant dominated ecosystem it may serve as an isotopic proxy for other C3 vegetative covers, such as forests and pastures. Those sources are important land covers (9–29%), especially along floodplain corridors (**Table 1**).

Algal OC is the first component of the proposed sequence of inputs (Kim et al., 2020). Algal growth is obvious in the eutrophied Clear Creek during the late summer and early autumn, due to ample nutrients from field run-off, periods of low water velocity and low sediment load, and high light availability (Dolph et al., 2017). Abban et al. (2016) estimated that the algal and detrital source contributed ∼10–40% to the Clear Creek POC depending on stream conditions; a finding similar to that observed in an agricultural watershed in Indiana (Dalzell et al., 2005). The most direct evidence that algal POC was captured with the samplers is the visual observation of algal mat debris on some early filters. The combined geochemical measurements eliminate substantial contributions from other potential sources. Elevated POC concentrations were found at the beginning of sample collection in the Oct 2014–2015, and July 2015 at some but not all stations (**Figure 5**). In some cases (e.g., Oxford, Oct 2014; Coralville, July 2015), the %C contents of the materials were higher than typical Clear Creek suspended sediments (8–12 vs. 1–2%), thus arguing against a previously deposited sediment source. ^{13}C-depleted POC ($\delta^{13}C < -25‰$) indicative of C3-autotrophy was observed at the beginning of sampling during the same events (**Figure 5**; Fry and Sherr, 1984; Delong and Thorp, 2006; Abban et al., 2016). Row crop debris in contrast would have a significantly more positive value (>-20‰). Lipid biomarker measurements revealed a high C16-C18 fatty acid/lignin ratio at the onset of the Oct 2015 event indicating that non-vascular plant OC dominates over vascular plant debris (Kim et al., 2020). We argue that for at least certain times and locations, algal production dominates the standing crop of POC in the channel.

The most prominent peaks of POC mirror the behavior of sediment and track the rise and fall of the water discharge (**Figure 5**, **Supplementary Table 1**). Multiple POC peaks, most only partially resolved in time, are prevalent within a storm event. One explanation for the multiple peaks is that they represent inputs of materials that have arrived at different times. These inputs need not be in the same categories outlined earlier but instead may be packets of sediment and POC arriving by different mechanisms or flow paths. Tributary inputs are an example. The challenge is to decode the complex signal within this portion of the storm response.

To begin parsing the signal, we follow the convention of characterizing the first set of peaks that occur on the rising limb of the hydrograph as early flush peaks (Gellis, 2013; **Figure 5**). Early flush peaks of sediment have been attributed to the activation of easily erodible material in channels or on soil surfaces followed by exhaustion of the source (Wilson et al., 2012; Gellis, 2013). Such peaks are most pronounced in the Oct 2014 and 2015 storms (**Figure 5**). A small peak is seen at Oxford in the July 2015 event (**Figure 5**). We argue that the POC is derived predominantly from the erosion of row crop soils driven by precipitation. We propose that the cessation of rainfall turns off the source if exhaustion of the supply of soil does not occur first. The timing in which the peaks occur during rainfall or shortly thereafter is consistent with that premise. Early flush peaks of sediment have been observed previously at South Amana and attributed to precipitation-driven erosion of surface soils based on ^{7}Be measurements (Wilson et al., 2012). They were responsible for 21–67% of the sediment load from the South Amana subbasin, the range being dependent on antecedent conditions (Wilson et al., 2012). The relative importance of the early flush material decreased as successive storms depleted the supply of easily erodible soil thus demonstrating one aspect of the conditional behavior of this source. There also may be a seasonality in the appearance of the early flush material as noted earlier (Abaci and Papanicolaou, 2009). The row crop fields were bare of vegetation but covered by crop debris after early October harvests. This primes the fields for surface erosion (Abaci and Papanicolaou, 2009; Hou et al., 2018; Xu et al., 2019).

The distinctive change in appearance of sediment from largely disaggregated silt at the beginning of storm events to darker-colored, millimeter-scale, stable aggregates at peak sediment concentrations provides visual evidence of an influx of surface soils. Rainfall simulation experiments using Clear Creek soils indicate that such small aggregates (0.2–2 mm) were sufficiently stable to rain-drop impact to be transported off-site (Hou et al., 2018; Wacha et al., 2018). Surface soils (0–5 cm) from Clear Creek fields used for corn-soybean rotations contain SOC with $\delta^{13}C$ values between −16.5 and −19.5‰ (Hou et al., 2018). The stream POC approaches the $^{13}C/^{12}C$ ratios of the corn-soybean soils during the early flush period and afterwards (**Figures 2**, **5**). Lignin phenol biomarker measurements from Oct 2015 early flush samples also indicate that the POC is derived from vascular plants and soils (Kim et al., 2020). The early flush POC bears the expected organic geochemical signatures of a row crop source.

Soil erosion models predict the loss of connectivity between surface soil sources and the channel as the basin area grows and valley morphology changes. Within the V-shaped South Amana subbasin, the sediment delivery ratio (SDR, the sediment yield from an area normalized to gross erosion) decreases from >0.9 for the hillslope scale (<1 km^2) to ∼0.2 for sub-drainage areas of 10–20 km^2 based on a soil erosion model (Abaci and Papanicolaou, 2009). As the watershed widens to a U- shape at Oxford and Coralville, eroded surface soils are more likely to be intercepted by the lower gradient portion of the landscape (Ferro and Minacapilli, 1995; Abaci and Papanicolaou, 2009). Sediment delivery ratios are ∼0.1 based on the model extrapolations, approximately half of what is estimated for South Amana (Abaci and Papanicolaou, 2009). The implication of the model results is that if indeed the early flush peak is from a surface soil source, its contribution to the total POC inventory should decrease longitudinally. This is observed. The early flush POC was 12% of the total flux at South Amana in the Oct 2015 event (**Table 3**; Kim et al., 2020). The contribution to the total POC decreased to

4.0% at Oxford and 3.5% at Coralville. Further evidence of this downstream trend is seen between Oxford and Coralville in Oct 2014 (27% decreasing to 14%) and July 2015 (3 to 0%).

The last series of POC peaks arrive as the stream approaches and passes peak discharge (**Figure 5**). The POC within this series is quantitatively the most important component of the storm response as it is responsible for 73–100% of the total POC flux (**Table 3**). This is a complex region in terms of timing and discharge dependence—peaks occur near the end of the rising limb, near the apex and on the falling limb. The POC is also compositionally complex. C- and N-isotope ratios vary between endmember values as a function of time and location (**Figure 5**, **Supplementary Table 1**). Biomarker measurements of the Oct 2015 event indicate vascular plant, microbial and soil sources (Kim et al., 2020). Diagenetic indicators, such as lignin phenol acid/aldehyde ratios and hydroxy benzoic acids, indicate a range of degradation states within the POC (Kim et al., 2020).

The geochemical indicators are consistent with a partially homogenized mixture of sources that are an integration of upstream inputs. Within this mix would be products of channel wall erosion. Bank erosion can contribute as much as 80% of sediment in Midwestern U.S.A. agricultural watersheds (Lamba et al., 2015). Historical changes in channel meanders and radiochemical studies are evidence that bank erosion is active in Clear Creek (Wilson et al., 2012; Sutarto et al., 2014). Mechanistically, channel wall erosion fits within the context of when the POC peaks appear, i.e., the fluvial entrainment of bank deposits should track the hydrograph as water height and velocity waxes and wanes (Simon et al., 2000; Langendoen and Simon, 2008). The bank deposits in Clear Creek are primarily accumulations of alluvial sediments. As illustrated by the PSA-1 core, this material records a range of POC inputs as land use has evolved (δ^{13}C ∼-25 to −18.5‰, **Figure 2**). Consequently, the erosion of alluvial deposits adds considerable complexity to the stream POC in terms of composition and age. The bank source of POC should increase in importance downstream just as it has been demonstrated for sediments (Sutarto et al., 2014; Papanicolaou et al., 2017).

Tile drains were sampled to determine if they could be an important contribution. The tile drain contribution of water to streams is substantial, with estimates ranging from 15% to over 50% (Schilling et al., 2012; Amado et al., 2017). Tile drain inputs appear to be especially important at baseflow (Schilling and Helmers, 2008). The role of tile drains in the expedited export of solutes, such as N, P, and even DOC, from agricultural landscapes is well-known (Skaggs et al., 1994; Schilling and Helmers, 2008; Ruark et al., 2009; Schilling et al., 2012, 2015; Amado et al., 2017). However, the contribution of sediment from tile drains to streams has been barely studied. In Canada, tile-derived sediment comprised 1 to 8% of the total (overland plus tile) annual sediment load (Coelho et al., 2010). On an event basis, the tile-derived sediment contributions from plot studies in New York contributed between 6 and 46% of the total event load (Klaiber et al., 2020) for similar sized storms. Potential sediment and POC contributions in Clear Creek were estimated via:

$$F = f_w C_{TD}/C_s, \tag{4}$$

where F is the fraction of sediment or POC derived from tile drains; f_w is the fraction of water from tile drains (0.15–0.5); C_{TD} is the concentration of sediment or POC in the tile drain effluent (g/l); and C_s is the concentration in the stream. Using values from the end of sampling periods as the system approached baseflow for the tile drains and the nearest stream site, South Amana, we estimate that ∼4–38% of the suspended sediment in upper Clear Creek and ∼4–16% of the POC could have a tile drain source.

The tile drain δ^{13}C and δ^{15}N values were generally more negative than those of stream sediments or surface soils (**Figure 2**). The source of the ^{13}C- and ^{15}N-depleted materials is unknown, but we offer two hypotheses. In one, the tile drains in the upper reach may be drawing water from late-glacial loess and the material exiting the drains are likely fines derived from it (Skaggs et al., 1994). The POC would be expected to have a C3 plant signature based on paleo-ecological records (Baker et al., 1996). Alternatively, the ^{13}C- and ^{15}N-depletions may signal the presence of microbial communities adapted to an environment in which O_2 is injected into subsurface soils via the drains. Chemoautotrophic ammonia oxidizers are examples of organisms that could generate such isotope effects (Hadas et al., 2009). Regardless of source, the differences between tile drain particulates and the Clear Creek suspended sediment argue against the drains being a major source of POC, even as the system returns to baseflow. During that stage, much of the POC is likely derived from residual material in the channel plus bank failure as the hydrograph recedes (Simon et al., 2000; Langendoen and Simon, 2008).

High resolution mass spectrometric analyses of DOC from nested sites in the Passumpsic River catchment (Vermont, USA) revealed an enrichment of aliphatic molecular structures at storm onset followed by an increase in aromatic functionality at peak discharge (Wagner et al., 2019). The aliphatic and aromatic moieties were attributed to lipid-rich and lignin-derived polyphenolic materials, respectively. This parallels the Clear Creek progression from fatty acid-enrich algal POC to soil and vascular plant sources that have high lignin and hydroxy benzoic acid contents (Kim et al., 2020). This commonality is proposed to be an outgrowth of the reactor-pipe duality of fluvial systems (Cole et al., 2007). Storms not only switch modes from reaction (algal productivity) to transport, but also deliver terrestrial POC (i.e., soils and vascular plant debris) to the channel ensuring the observed change in POC and DOC compositions.

X-Q Relationships

The dependencies of POC concentration and δ^{13}C on discharge provide additional metrics by which to test aspects of our conceptual model. South Amana exhibited poor correlations between POC and discharge, whereas they were significantly correlated at Oxford and Coralville (**Table 4**). Furthermore, the rising limb slope of the POC-Q relationship decreases as one moves from Oxford to Coralville in each event that the slope could be estimated (**Figure 7**, **Table 4**). The observations illustrate the fundamental differences between how POC can behave in the upper and lower reaches. In upland regions, where surface erosion and over-land transport have the potential to be flux limiting, rainfall intensity and duration, not discharge, should be a major control of POC delivery. In contrast, as one moves away from upland sources, stream discharge takes over as the predominant transporting agent. The decrease in slope signals an attenuation of net POC inputs relative to water. Though there may be multiple factors that influence that change, it is consistent with the loss of connectivity between hillslopes and the channel as the valley broadens, as well as transitions in land cover. In essence, the channel may be starved of surface POC inputs from the landscape in the lower reaches because the POC is intercepted by the stream corridor.

The clockwise hysteresis displayed by the POC-Q pair in Clear Creek (**Figure 7**, **Table 4**) is the most frequently observed pattern for sediments in streams and thus it is not surprising that it is seen with POC (Allen, 1974; Gellis, 2013). The delivery of easy-to-mobilize sediment during the rising limb of the hydrograph followed by exhaustion of the source is the most common explanation for the clockwise pattern, though other mechanisms have been invoked for individual systems (Gellis, 2013). Pre-event (algal) and early flush (row crop surface soil) inputs in Clear Creek would certainly contribute to a clockwise pattern. Furthermore, the arrival sequence of local POC inputs followed by broadened (and thus more dilute) peaks with upstream origins could also drive the clockwise pattern.

Changes in POC δ^{13}C values are primarily driven by the mixing of C3 and C4 plant sources. The POC δ^{13}C -Q slope can be viewed as a discharge-driven mixing line between corn (as a surrogate for row crops) and C3 sources. The hysteresis of the POC δ^{13}C -Q relationship is highly variable with few discernable patterns. The cause is unknown but it is reasonable to speculate that spatial patterns in vegetative cover could create a sensitivity to storm track and intensity, and the other previously discussed antecedent and seasonal factors. An illustration of a potential mechanism is provided by POC δ^{13}C exported from the South Amana subbasin during the Oct 2015 and June 2016 events. The rainfall was 24 mm and 10 mm for the respective dates. The Oct 2015 period exhibited a more positive δ^{13}C value (−23.6‰, **Table 3**) than June 2016 (−25.9‰), reflecting a greater row crop soil contribution in the more intense storm. Notably the early flush POC contribution to the total was greater (12 vs. 0%) in Oct 2015 as well. Turning the row crop source on and off, either by rainfall or seasonal vegetative cover, may be the greatest driver of isotopic variability in the system.

The one C-isotope hysteresis pattern that did emerge occurred in the Oct 2015 event (**Figure 7**). A clockwise pattern was observed in the upper part of the watershed where row crops were most concentrated and thus the ^{13}C-enriched (more positive δ^{13}C values) corn signal arrived early as part of the early flush peak. The hysteresis flattened moving downstream, and ultimately became counterclockwise at Coralville. The delayed arrival of upland ^{13}C-enriched POC is likely the driver of the counterclockwise pattern. What may have started out as an early flush peak of POC in the uplands ultimately contributes to the trailing portion of the main peak in the lowlands. This is another illustration of how proximal and distal components combine to create the total storm pulse signal.

CONCLUSIONS

Changing POC compositions were captured as functions of time, location and discharge in Clear Creek in response to passing storms. The nested longitudinal sampling approach employed with a multi-hour sampling frequency allowed us to dissect a storm pulse in unprecedented detail and identify a sequence of inputs (Kim et al., 2020). The analysis of multiple storms allowed us to assess the variability of storm responses. Organic-rich material dominated by algal debris was the first to be mobilized. Small changes in water velocity may have been sufficient to trigger its transport. Generically, any easily suspended POC source, such as vascular plant debris, could be moved at this stage. Eroded surface soils, principally from row crop fields, followed the algal pulse. This source was closely associated with the timing of the precipitation. It also required connectivity between the fields and the channel as illustrated by its diminishing importance with the broadening of the valley's morphology. Both the in-channel and surface soil POC inputs were conditional in the sense that they were dependent on specific environmental conditions. For example, nutrients, light, and low water velocities are requisite conditions for algal growth, thus algal inputs would be expected to be most dominant between storms in eutrophied systems during summer-early fall. Similarly, bare fields shortly after harvest or tillage would be most vulnerable to erosion.

The most complex and ubiquitous POC component is associated with the primary wave of sediment delivered from upstream. As such, it is a mix of materials that accumulates with transport. Based on prior geomorphological and radiochemical studies in Clear Creek and elsewhere, bank erosion is hypothesized to contribute to this mixture. The contribution of bank erosion should increase with a lengthening reach (Sutarto et al., 2014; Lamba et al., 2015; Gellis et al., 2017). Tile drain POC, while projected to be at its greatest importance at or near base flow, is a relatively minor contributor to the temporal series of inputs.

The conceptual model presented here is best fit to small, low gradient, agricultural streams like Clear Creek. Deviations from the model will occur in other systems, such as small, mountainous watersheds, where POC sources and delivery mechanisms differ (Blair et al., 2010; Hilton et al., 2011; Hovius et al., 2011). Nevertheless, we can extract some general principles from our study. A storm-generated pulse can be viewed as a signal that encodes environmental information. Its information content can be altered by interactions within the river corridor as it propagates. At some point the signal may be "shredded" by the trapping and release of alluvial sediment as occurs in active floodplains (Jerolmack and Paola, 2010; Romans et al., 2016). The capture and long-term sequestration of the pulse in downstream depocenters archives the signal's information. Understanding how the signal propagates is thus critical to interpreting those portions of the sedimentological record that are derived from fluvial deposition (Romans et al., 2016). Particulate OC is a particularly useful component to consider from this perspective as its information content is high due to its sensitivity to source and its preservability in sedimentary archives (Castaneda et al., 2009). The Clear Creek data suggest that a temporally resolved portion of the signal, the early flush POC, is progressively lost with propagation and this is hypothesized to be partially due to changing valley geomorphology. A logical question to ask going forward is whether this is a universal response to increasing basin size.

The erosion of bank alluvia, while not the original target in this study, has emerged as a potential focus of future research in terms of its contribution to fluvial POC budgets and geochemical compositions. This is especially relevant now because of the anthropogenic acceleration of alluvial sediment formation and sequestration (Syvitski et al., 2005; Kemp et al., 2020). Erosion of the alluvial deposition injects a mixture of aged POC sources. This adds a level of noise that is expected to grow in importance with increasing reach length. At some point however, the noise becomes the signal, especially in the lower gradient portions of the watershed. The Amazon River system is an endmember example of this phenomenon where geochemical signals generated in the Andes are erased and replaced by its massive floodplain before export to the ocean (Bouchez et al., 2010). The contribution of the lowland reactor has implications for tracking the fate of eroded soil OC from source to sink, and for balancing C ledgers across landscapes. The routing of POC through alluvial deposits lengthens the timescale over which C-budgets must be considered. The quest to ascertain whether soil OC erosion is a net C-source or sink to the atmosphere may need to go through transient alluvial POC traps, such as floodplains.

DATA AVAILABILITY STATEMENT

Original Clear Creek data are archived on the IMLCZO's Clowder database system. A spreadsheet can be downloaded from http://data.imlczo.org/clowder/datasets/5d922de44f0c55584a21a55b. Accession numbers can be found in the **Supplementary Material**.

AUTHOR CONTRIBUTIONS

NB, EB, AP, TF, CW, and AW developed the proposal for this project and oversaw various aspects of the field sample collection, analyses, and data interpretation. JM, NZ, and BK performed the analyses and assisted with data management. JK assisted with data interpretation and manuscript preparation. All authors contributed to the article and approved the submitted version.

FUNDING

Financial support was provided by the U.S. National Science Foundation (NSF) Grant # EAR-1331906 for the Critical Zone Observatory for Intensively Managed Landscapes (IML-CZO), a multi-institutional collaborative effort. A portion of time for Ward, Davis, and Prior was supported by NSF Grant EAR-1360276.

ACKNOWLEDGMENTS

Caroline Davis, Katie Goff, Kara Prior, and Courtney Cappalli assisted with field sampling. Paul Roots, Yue Zeng, Dana Cooperberg, and Koushik Dutta assisted with analyses. Special thanks to Praveen Kumar for his leadership of the IML-CZO project. We thank two reviewers for their detailed constructive comments.

SUPPLEMENTARY MATERIAL

The Supplementary Material for this article can be found online at: https://www.frontiersin.org/articles/10.3389/frwa.2021.600649/full#supplementary-material

REFERENCES

Abaci, O., and Papanicolaou, A. N. T. (2009). Long-term effects of management practices on water-driven soil erosion in an intense agricultural sub-watershed: monitoring and modelling. *Hydrol. Process.* 23, 2818–2837. doi: 10.1002/hyp.7380

Abban, B., Papanicolaou, A. N., Cowles, M. K., Wilson, C. G., Abaci, O., Wacha, K., et al. (2016). An enhanced Bayesian fingerprinting framework for studying sediment source dynamics in intensively managed landscapes. *Water Resour. Res.* 52, 4646–4673. doi: 10.1002/2015wr018030

Allen, J. R. L. (1974). Reaction, relaxation and lag in natural sedimentary systems–general principles, examples and lessons. *Earth Sci. Rev.* 10, 263–342. doi: 10.1016/0012-8252(74)90109-3

Amado, A. A., Schilling, K. E., Jones, C. S., Thomas, N., and Weber, L. J. (2017). Estimation of tile drainage contribution to streamflow and nutrient loads at the watershed scale based on continuously monitored data. *Environ. Monit. Assess.* 189:13. doi: 10.1007/s10661-017-6139-4

Amundson, R., Austin, A. T., Schuur, E. A. G., Yoo, K., Matzek, V., Kendall, C., et al. (2003). Global patterns of the isotopic composition of soil and plant nitrogen. *Glob. Biogeochem. Cycles* 17:1031. doi: 10.1029/2002gb001903

Amundson, R., Berhe, A. A., Hopmans, J. W., Olson, C., Sztein, A. E., and Sparks, D. L. (2015). Soil and human security in the 21st century. *Science* 348. doi: 10.1126/science.1261071

Aufdenkampe, A. K., Mayorga, E., Hedges, J. I., Llerena, C., Quay, P. D., Gudeman, J., et al. (2007). Organic matter in the Peruvian headwaters of the Amazon: compositional evolution from the Andes to the lowland Amazon mainstem. *Org. Geochem.* 38, 337–364. doi: 10.1016/j.orggeochem.2006.06.003

Aufdenkampe, A. K., Mayorga, E., Raymond, P. A., Melack, J. M., Doney, S. C., Alin, S. R., et al. (2011). Riverine coupling of biogeochemical cycles between land, oceans, and atmosphere. *Front. Ecol. Environ.* 9, 53–60. doi: 10.1890/100014

Baker, R. G., Bettis, E. A., Schwert, D. P., Horton, D. G., Chumbley, C. A., Gonzalez, L. A., et al. (1996). Holocene paleoenvironments of northeast Iowa. *Ecol. Monogr.* 66, 203–234. doi: 10.2307/2963475

Berhe, A. A., Harte, J., Harden, J. W., and Torn, M. S. (2007). The significance of the erosion-induced terrestrial carbon sink. *Bioscience* 57, 337–346. doi: 10.1641/b570408

Blair, N. E., and Aller, R. C. (2012). The fate of terrestrial organic carbon in the marine environment. *Annu. Rev. Mar. Sci.* 4, 401–423. doi: 10.1146/annurev-marine-120709-142717

Blair, N. E., Leithold, E. L., and Aller, R. C. (2004). From bedrock to burial: the evolution of particulate organic carbon across coupled watershed-continental margin systems. *Mar. Chem.* 92, 141–156. doi: 10.1016/j.marchem.2004.06.023

Blair, N. E., Leithold, E. L., Brackley, H., Trustrum, N., Page, M., and Childress, L. (2010). Terrestrial sources and export of particulate organic carbon in the

Waipaoa sedimentary system: problems, progress and processes. *Mar. Geol.* 270, 108–118. doi: 10.1016/j.margeo.2009.10.016

Blair, N. E., Leithold, E. L., Papanicolaou, A. N. T., Wilson, C. G., Keefer, L., Kirton, E., et al. (2018). The C-biogeochemistry of a Midwestern USA agricultural impoundment in context: Lake Decatur in the intensively managed landscape critical zone observatory. *Biogeochemistry* 138, 171–195. doi: 10.1007/s10533-018-0439-9

Bouchez, J., Beyssac, O., Galy, V., Gaillardet, J., France-Lanord, C., Maurice, L., et al. (2010). Oxidation of petrogenic organic carbon in the Amazon floodplain as a source of atmospheric CO_2. *Geology* 38, 255–258. doi: 10.1130/g30608.1

Bouillon, S., Abril, G., Borges, A. V., Dehairs, F., Govers, G., Hughes, H. J., et al. (2009). Distribution, origin and cycling of carbon in the Tana River (Kenya): a dry season basin-scale survey from headwaters to the delta. *Biogeosciences* 6, 2475–2493. doi: 10.5194/bg-6-2475-2009

Castaneda, I. S., Werne, J. P., Johnson, T. C., and Filley, T. R. (2009). Late Quaternary vegetation history of southeast Africa: the molecular isotopic record from Lake Malawi. *Palaeogeogr. Palaeoclimatol. Palaeoecol.* 275, 100–112. doi: 10.1016/j.palaeo.2009.02.008

Coelho, B. B., Bruin, A. J., Staton, S., and Hayman, D. (2010). Sediment and nutrient contributions from subsurface drains and point sources to an agricultural watershed. *Air Soil Water Res.* 3, 1–21. doi: 10.4137/ASWR.S4471

Cole, J. J., Prairie, Y. T., Caraco, N. F., McDowell, W. H., Tranvik, L. J., Striegl, R. G., et al. (2007). Plumbing the global carbon cycle: Integrating inland waters into the terrestrial carbon budget. *Ecosystems* 10, 171–184. doi: 10.1007/s10021-006-9013-8

Coplen, T. B. (2011). Guidelines and recommended terms for expression of stable-isotope-ratio and gas-ratio measurement results. *Rapid Commun. Mass Spectrom.* 25, 2538–2560. doi: 10.1002/rcm.5129

Craig, H. (1953). The geochemistry of the stable carbon isotopes. *Geochim. Cosmochim. Acta* 3, 53–92. doi: 10.1016/0016-7037(53)90001-5

Cui, L., Butler, H. J., Martin-Hirsch, P. L., and Martin, F. L. (2016). Aluminium foil as a potential substrate for ATR-FTIR, transflection FTIR or Raman spectrochemical analysis of biological specimens. *Anal. Methods* 8, 481–487. doi: 10.1039/c5ay02638e

Dalzell, B. J., Filley, T. R., and Harbor, J. M. (2005). Flood pulse influences on terrestrial organic matter export from an agricultural watershed. *J. Geophys. Res. Biogeosci.* 110:G02011. doi: 10.1029/2005jg000043

Dalzell, B. J., Filley, T. R., and Harbor, J. M. (2007). The role of hydrology in annual organic carbon loads and terrestrial organic matter export from a midwestern agricultural watershed. *Geochim. Cosmochim. Acta* 71, 1448–1462. doi: 10.1016/j.gca.2006.12.009

Davis, C. A., Ward, A. S., Burgin, A. J., Loecke, T. D., Riveros-Iregui, D. A., Schnoebelen, D. J., et al. (2014). Antecedent moisture controls on stream nitrate flux in an agricultural watershed. *J. Environ. Qual.* 43, 1494–1503. doi: 10.2134/jeq2013.11.0438

Delong, M. D., and Thorp, J. H. (2006). Significance of instream autotrophs in trophic dynamics of the Upper Mississippi River. *Oecologia* 147, 76–85. doi: 10.1007/s00442-005-0241-y

Dhillon, G. S., and Inamdar, S. (2013). Extreme storms and changes in particulate and dissolved organic carbon in runoff: entering uncharted waters? *Geophys. Res. Lett.* 40, 1322–1327. doi: 10.1002/grl.50306

Dhillon, G. S., and Inamdar, S. (2014). Storm event patterns of particulate organic carbon (POC) for large storms and differences with dissolved organic carbon (DOC). *Biogeochemistry* 118, 61–81. doi: 10.1007/s10533-013-9905-6

Doetterl, S., Berhe, A. A., Nadeu, E., Wang, Z. G., Sommer, M., and Fiener, P. (2016). Erosion, deposition and soil carbon: a review of process-level controls, experimental tools and models to address C cycling in dynamic landscapes. *Earth Sci. Rev.* 154, 102–122. doi: 10.1016/j.earscirev.2015.12.005

Dolph, C. L., Hansen, A. T., and Finlay, J. C. (2017). Flow-related dynamics in suspended algal biomass and its contribution to suspended particulate matter in an agricultural river network of the Minnesota River Basin, USA. *Hydrobiologia* 785, 127–147. doi: 10.1007/s10750-016-2911-7

Farquhar, G. D. (1983). On the nature of carbon isotope discrimination in C-4 species. *Aust. J. Plant Physiol.* 10, 205–226.

Ferro, V., and Minacapilli, M. (1995). Sediment delivery processes at basin scale. *Hydrol. Sci. J.* 40, 703–717.

Fox, J. F., and Papanicolaou, A. N. (2007). The use of carbon and nitrogen isotopes to study watershed erosion processes. *J. Am. Water Resour. Assoc.* 43, 1047–1064. doi: 10.1111/j.1752-1688.2007.00087.x

Fry, B., and Sherr, E. B. (1984). Delta-C-13 measurements as indicators of carbon flow in marine and fresh-water ecosystems. *Contrib. Mar. Sci.* 27, 13–47.

Galy, V., Peucker-Ehrenbrink, B., and Eglinton, T. (2015). Global carbon export from the terrestrial biosphere controlled by erosion. *Nature* 521, 204–207. doi: 10.1038/nature14400

Gellis, A. C. (2013). Factors influencing storm-generated suspended-sediment concentrations and loads in four basins of contrasting land use, humid-tropical Puerto Rico. *Catena* 104, 39–57. doi: 10.1016/j.catena.2012.10.018

Gellis, A. C., Fuller, C. C., and Van Metre, P. C. (2017). Sources and ages of fine-grained sediment to streams using fallout radionuclides in the Midwestern United States. *J. Environ. Manage.* 194, 73–85. doi: 10.1016/j.jenvman.2016.06.018

Griffiths, N. A., Tank, J. L., Royer, T. V., Warrner, T. J., Frauendorf, T. C., Rosi-Marshall, E. J., et al. (2012). Temporal variation in organic carbon spiraling in Midwestern agricultural streams. *Biogeochemistry* 108, 149–169. doi: 10.1007/s10533-011-9585-z

Hadas, O., Altabet, M. A., and Agnihotri, R. (2009). Seasonally varying nitrogen isotope biogeochemistry of particulate organic matter in Lake Kinneret, Israel. *Limnol. Oceanogr.* 54, 75–85. doi: 10.4319/lo.2009.54.1.0075

Harden, J. W., Sharpe, J. M., Parton, W. J., Ojima, D. S., Fries, T. L., Huntington, T. G., et al. (1999). Dynamic replacement and loss of soil carbon on eroding cropland. *Glob. Biogeochem. Cycles* 13, 885–901. doi: 10.1029/1999gb900061

Harris, D., Horwath, W. R., and van Kessel, C. (2001). Acid fumigation of soils to remove carbonates prior to total organic carbon or carbon-13 isotopic analysis. *Soil Sci. Soc. Am. J.* 65, 1853–1856. doi: 10.2136/sssaj2001.1853

Hedges, J. I., Mayorga, E., Tsamakis, E., McClain, M. E., Aufdenkampe, A., Quay, P., et al. (2000). Organic matter in Bolivian tributaries of the Amazon River: a comparison to the lower mainstream. *Limnol. Oceanogr.* 45, 1449–1466. doi: 10.4319/lo.2000.45.7.1449

Hedges, J. I., and Oades, J. M. (1997). Comparative organic geochemistries of soils and marine sediments. *Org. Geochem.* 27, 319–361.

Hilton, R. G., Galy, A., Hovius, N., Horng, M. J., and Chen, H. (2011). Efficient transport of fossil organic carbon to the ocean by steep mountain rivers: an orogenic carbon sequestration mechanism. *Geology* 39, 71–74. doi: 10.1130/g31352.1

Hope, D., Billett, M. F., and Cresser, M. S. (1994). A review of the export of carbon in river water–fluxes and processes. *Environ. Pollut.* 84, 301–324. doi: 10.1016/0269-7491(94)90142-2

Hou, T., Berry, T. D., Singh, S., Hughes, M. N., Tong, Y., Thanos Papanicolaou, A. N., et al. (2018). Control of tillage disturbance on the chemistry and proportion of raindrop-liberated particles from soil aggregates. *Geoderma* 330, 19–29. doi: 10.1016/j.geoderma.2018.05.013

Hovius, N., Galy, A., Hilton, R. G., Sparkes, R., Smith, J., Shuh-Ji, K., et al. (2011). Erosion-driven drawdown of atmospheric carbon dioxide: the organic pathway. *Appl. Geochem.* 26, S285–S287. doi: 10.1016/j.apgeochem.2011.03.082

Jeong, J. J., Bartsch, S., Fleckenstein, J. H., Matzner, E., Tenhunen, J. D., Lee, S. D., et al. (2012). Differential storm responses of dissolved and particulate organic carbon in a mountainous headwater stream, investigated by high-frequency, *in situ* optical measurements. *J. Geophys. Res. Biogeosci.* 117:G03013. doi: 10.1029/2012jg001999

Jerolmack, D. J., and Paola, C. (2010). Shredding of environmental signals by sediment transport. *Geophys. Res. Lett.* 37:L19401. doi: 10.1029/2010gl044638

Jung, B. J., Lee, H. J., Jeong, J. J., Owen, J., Kim, B., Meusburger, K., et al. (2012). Storm pulses and varying sources of hydrologic carbon export from a mountainous watershed. *J. Hydrol.* 440, 90–101. doi: 10.1016/j.jhydrol.2012.03.030

Kao, S. J., and Milliman, J. D. (2008). Water and sediment discharge from small mountainous rivers, Taiwan: the roles of lithology, episodic events, and human activities. *J. Geol.* 116, 431–448. doi: 10.1086/590921

Kemp, D. B., Sadler, P. M., and Vanacker, V. (2020). The human impact on North American erosion, sediment transfer, and storage in a geologic context. *Nat. Commun.* 11:6012. doi: 10.1038/s41467-020-19744-3

Kim, J., Blair, N. E., Ward, A. S., and Goff, K. (2020). Storm-induced dynamics of particulate organic carbon in Clear Creek, Iowa: an intensively managed landscape critical zone observatory story. *Front. Water* 2:578261. doi: 10.3389/frwa.2020.578261

Klaiber, L. B., Kramer, S. R., and Young, E. O. (2020). Impacts of tile drainage on phosphorus losses from edge-of-field plots in the Lake Champlain basin of New York. *Water* 12:328. doi: 10.3390/w12020328

Kumar, P., Le, P. V. V., Papanicolaou, A. N. T., Rhoads, B. L., Anders, A. M., Stumpf, A., et al. (2018). Critical transition in critical zone of intensively managed landscapes. *Anthropocene* 22, 10–19. doi: 10.1016/j.ancene.2018.04.002

Lal, R. (2003). Soil erosion and the global carbon budget. *Environ. Int.* 29, 437–450. doi: 10.1016/s0160-4120(02)00192-7

Lal, R. (2009). Challenges and opportunities in soil organic matter research. *Eur. J. Soil Sci.* 60, 158–169. doi: 10.1111/j.1365-2389.2008.01114.x

Lamba, J., Thompson, A. M., Karthikeyan, K. G., and Fitzpatrick, F. A. (2015). Sources of fine sediment stored in agricultural lowland streams, Midwest, USA. *Geomorphology* 236, 44–53. doi: 10.1016/j.geomorph.2015.02.001

Langendoen, E. J., and Simon, A. (2008). Modeling the evolution of incised streams. II: Streambank erosion. *J. Hydraul. Eng. ASCE* 134, 905–915. doi: 10.1061/(asce)0733-9429(2008)134:7(905)

Le Meur, M., Mansuy-Huault, L., Lorgeoux, C., Bauer, A., Gley, R., Vantelon, D., et al. (2017). Spatial and temporal variations of particulate organic matter from Moselle River and tributaries: a multimolecular investigation. *Org. Geochem.* 110, 45–56. doi: 10.1016/j.orggeochem.2017.04.003

Lee, K. Y., van Geldern, R., and Barth, J. A. C. (2017). A high-resolution carbon balance in a small temperate catchment: insights from the Schwabach River, Germany. *Appl. Geochem.* 85, 86–96. doi: 10.1016/j.apgeochem.2017.08.007

Leithold, E. L., Blair, N. E., Childress, L. B., Brulet, B. R., Marden, M., Orpin, A. R., et al. (2013). Signals of watershed change preserved in organic carbon buried on the continental margin seaward of the Waipaoa River, New Zealand. *Mar. Geol.* 346, 355–365. doi: 10.1016/j.margeo.2013.10.007

Leithold, E. L., Blair, N. E., and Wegmann, K. W. (2016). Source-to-sink sedimentary systems and global carbon burial: a river runs through it. *Earth Sci. Rev.* 153, 30–42. doi: 10.1016/j.earscirev.2015.10.011

Li, M. X., Peng, C. H., Wang, M., Xue, W., Zhang, K. R., Wang, K. F., et al. (2017). The carbon flux of global rivers: a re-evaluation of amount and spatial patterns. *Ecol. Indic.* 80, 40–51. doi: 10.1016/j.ecolind.2017.04.049

Newbold, J. D., Mulholland, P. J., Elwood, J. W., and Oneill, R. V. (1982). Organic-carbon spiralling in stream ecosystems. *Oikos* 38, 266–272. doi: 10.2307/3544663

Oeurng, C., Sauvage, S., Coynel, A., Maneux, E., Etcheber, H., and Sanchez-Perez, J. M. (2011). Fluvial transport of suspended sediment and organic carbon during flood events in a large agricultural catchment in southwest France. *Hydrol. Process.* 25, 2365–2378. doi: 10.1002/hyp.7999

O'Leary, M. H. (1981). Carbon isotope fractionation in plants. *Phytochemistry* 20, 553–567. doi: 10.1016/0031-9422(81)85134-5

Papanicolaou, A. N., Wacha, K. M., Abban, B. K., Wilson, C. G., Hatfield, J. L., Stanier, C. O., et al. (2015). From soilscapes to landscapes: a landscape-oriented approach to simulate soil organic carbon dynamics in intensively managed landscapes. *J. Geophys. Res. Biogeosci.* 120, 2375–2401. doi: 10.1002/2015jg003078

Papanicolaou, A. N. T., Wilson, C. G., Tsakiris, A. G., Sutarto, T. E., Bertrand, F., Rinaldi, M., et al. (2017). Understanding mass fluvial erosion along a bank profile: using PEEP technology for quantifying retreat lengths and identifying event timing. *Earth Surf. Process. Landf.* 42, 1717–1732. doi: 10.1002/esp.4138

Prior, J. C. (1991). *Landforms of Iowa.* Iowa City, IA: University of Iowa Press.

Raymond, P. A., Saiers, J. E., and Sobczak, W. V. (2016). Hydrological and biogeochemical controls on watershed dissolved organic matter transport: pulse-shunt concept. *Ecology* 97, 5–16. doi: 10.1890/14-1684.1

Richey, J. E., Hedges, J. I., Devol, A. H., Quay, P. D., Victoria, R., Martinelli, L., et al. (1990). Biogeochemistry of carbon in the Amazon river. *Limnol. Oceanogr.* 35, 352–371.

Romans, B. W., Castelltort, S., Covault, J. A., Fildani, A., and Walsh, J. P. (2016). Environmental signal propagation in sedimentary systems across timescales. *Earth Sci. Rev.* 153, 7–29. doi: 10.1016/j.earscirev.2015.07.012

Rose, L. A., Karwan, D. L., and Godsey, S. E. (2018). Concentration-discharge relationships describe solute and sediment mobilization, reaction, and transport at event and longer timescales. *Hydrol. Process.* 32, 2829–2844. doi: 10.1002/hyp.13235

Rowland, R., Inamdar, S., and Parr, T. (2017). Evolution of particulate organic matter (POM) along a headwater drainage: role of sources, particle size class, and storm magnitude. *Biogeochemistry* 133, 181–200. doi: 10.1007/s10533-017-0325-x

Ruark, M. D., Brouder, S. M., and Turco, R. F. (2009). Dissolved organic carbon losses from tile drained agroecosystems. *J. Environ. Qual.* 38, 1205–1215. doi: 10.2134/jeq2008.0121

Ruhe, R. V. (1969). *Quaternary Landscapes in Iowa.* Ames, IA: Iowa State University Press.

Schilling, K. E., and Helmers, M. (2008). Effects of subsurface drainage tiles on streamflow in Iowa agricultural watersheds: exploratory hydrograph analysis. *Hydrol. Process.* 22, 4497–4506. doi: 10.1002/hyp.7052

Schilling, K. E., Jindal, P., Basu, N. B., and Helmers, M. J. (2012). Impact of artificial subsurface drainage on groundwater travel times and baseflow discharge in an agricultural watershed, Iowa (USA). *Hydrol. Process.* 26, 3092–3100. doi: 10.1002/hyp.8337

Schilling, K. E., Wolter, C. F., Isenhart, T. M., and Schultz, R. C. (2015). Tile drainage density reduces groundwater travel times and compromises Riparian buffer effectiveness. *J. Environ. Qual.* 44, 1754–1763. doi: 10.2134/jeq2015.02.0105

Simon, A., Curini, A., Darby, S. E., and Langendoen, E. J. (2000). Bank and near-bank processes in an incised channel. *Geomorphology* 35, 193–217. doi: 10.1016/s0169-555x(00)00036-2

Skaggs, R. W., Breve, M. A., and Gilliam, J. W. (1994). Hydrologic and water-quality impacts of agricultural drainage. *Crit. Rev. Environ. Sci. Technol.* 24, 1–32. doi: 10.1080/10643389409388459

Sutarto, T., Papanicolaou, A. N., Wilson, C. G., and Langendoen, E. J. (2014). Stability analysis of semicohesive streambanks with CONCEPTS: coupling field and laboratory investigations to quantify the onset of fluvial erosion and mass failure. *J. Hydraul. Eng.* 140:04014041. doi: 10.1061/(asce)hy.1943-7900.0000899

Syvitski, J. P. M., Vorosmarty, C. J., Kettner, A. J., and Green, P. (2005). Impact of humans on the flux of terrestrial sediment to the global coastal ocean. *Science* 308, 376–380. doi: 10.1126/science.1109454

Wacha, K. M., Papanicolaou, A. N. T., Giannopoulos, C. P., Abban, B. K., Wilson, C. G., Zhou, S. N., et al. (2018). The role of hydraulic connectivity and management on soil aggregate size and stability in the Clear Creek Watershed, Iowa. *Geosciences* 8:470. doi: 10.3390/geosciences8120470

Wagner, S., Fair, J. H., Matt, S., Hosen, J. D., Raymond, P., Saiers, J., et al. (2019). Molecular hysteresis: hydrologically driven changes in riverine dissolved organic matter chemistry during a storm event. *J. Geophys. Res. Biogeosci.* 124, 759–774. doi: 10.1029/2018jg004817

Wang, Z. G., Hoffmann, T., Six, J., Kaplan, J. O., Govers, G., Doetterl, S., et al. (2017). Human-induced erosion has offset one-third of carbon emissions from land cover change. *Nat. Clim. Change* 7, 345–349. doi: 10.1038/nclimate3263

Wilson, C. G., Abban, B., Keefer, L. L., Wacha, K., Dermisis, D., Giannopoulos, C., et al. (2018). The intensively managed landscape critical zone observatory: a scientific testbed for understanding critical zone processes in agroecosystems. *Vadose Zone J.* 17:180088. doi: 10.2136/vzj2018.04.0088

Wilson, C. G., Papanicolaou, A. N. T., and Denn, K. D. (2012). Partitioning fine sediment loads in a headwater system with intensive agriculture. *J. Soils Sediments* 12, 966–981. doi: 10.1007/s11368-012-0504-2

Wilson, C. G., Wacha, K. M., Thanos Papanicolaou, A. N., Sander, H. A., Freudenberg, V. B., Abban, B. K. B., et al. (2016). Dynamic assessment of current management in an intensively managed agroecosystem. *J. Contemp. Water Res. Educ.* 158, 148–171. doi: 10.1111/j.1936-704X.2016.03225.x

Wohl, E. (2017). Connectivity in rivers. *Prog. Phys. Geogr.* 41, 345–362. doi: 10.1177/0309133317714972

Xu, C., Yang, Z., Qian, W., Chen, S., Liu, X., Lin, W., et al. (2019). Runoff and soil erosion responses to rainfall and vegetation cover under various afforestation management regimes in subtropical montane forest. *Land Degrad. Dev.* 30, 1711–1724. doi: 10.1002/ldr.3377

Yan, Q. N., Iwasaki, T., Stumpf, A., Belmont, P., Parker, G., and Kumar, P. (2018). Hydrogeomorphological differentiation between floodplains and terraces. *Earth Surf. Process. Landf.* 43, 218–228. doi: 10.1002/esp.4234

Yan, Q. N., Le, P. V. V., Woo, D. K., Hou, T. Y., Filley, T., and Kumar, P. (2019). Three-dimensional modeling of the coevolution of landscape and soil organic carbon. *Water Resour. Res.* 55, 1218–1241. doi: 10.1029/2018wr0 523634

Yang, Q. C., Zhang, X. S., Xu, X. Y., Asrar, G. R., Smith, R. A., Shih, J. S., et al. (2016). Spatial patterns and environmental controls of particulate organic carbon in surface waters in the conterminous United States. *Sci. Total Environ.* 554, 266–275. doi: 10.1016/j.scitotenv.2016.02.164

Conflict of Interest: The authors declare that the research was conducted in the absence of any commercial or financial relationships that could be construed as a potential conflict of interest.

frontiers in Water

ORIGINAL RESEARCH
published: 06 July 2021
doi: 10.3389/frwa.2021.578608

Drivers of Dissolved Organic Carbon Mobilization From Forested Headwater Catchments: A Multi Scaled Approach

Thomas Adler[1]*, Kristen L. Underwood[2], Donna M. Rizzo[2], Adrian Harpold[3], Gary Sterle[3], Li Li[4], Hang Wen[4], Lindsey Stinson[1], Caitlin Bristol[1], Bryn Stewart[4], Andrea Lini[1], Nicolas Perdrial[1] and Julia N. Perdrial[1]*

[1] Department of Geology, University of Vermont, Burlington, VT, United States, [2] Department of Civil and Environmental Engineering, University of Vermont, Burlington, VT, United States, [3] Department of Natural Resources and Environmental Science, University of Nevada, Reno, NV, United States, [4] Department of Civil and Environmental Engineering, Penn State University, Centre County, PA, United States

OPEN ACCESS

Edited by:
Carl I. Steefel,
Lawrence Berkeley National
Laboratory, United States

Reviewed by:
Catherine Eimers,
Trent University, Canada
Dipankar Dwivedi,
Lawrence Berkeley National
Laboratory, United States

***Correspondence:**
Thomas Adler
tma1126@comcast.net
Julia N. Perdrial
julia.perdrial@uvm.edu

Specialty section:
This article was submitted to
Water and Critical Zone,
a section of the journal
Frontiers in Water

Received: 30 June 2020
Accepted: 31 May 2021
Published: 06 July 2021

Citation:
Adler T, Underwood KL, Rizzo DM,
Harpold A, Sterle G, Li L, Wen H,
Stinson L, Bristol C, Stewart B, Lini A,
Perdrial N and Perdrial JN (2021)
Drivers of Dissolved Organic Carbon
Mobilization From Forested
Headwater Catchments: A Multi
Scaled Approach.
Front. Water 3:578608.
doi: 10.3389/frwa.2021.578608

Understanding and predicting catchment responses to a regional disturbance is difficult because catchments are spatially heterogeneous systems that exhibit unique moderating characteristics. Changes in precipitation composition in the Northeastern U.S. is one prominent example, where reduction in wet and dry deposition is hypothesized to have caused increased dissolved organic carbon (DOC) export from many northern hemisphere forested catchments; however, findings from different locations contradict each other. Using shifts in acid deposition as a test case, we illustrate an iterative "process and pattern" approach to investigate the role of catchment characteristics in modulating the steam DOC response. We use a novel dataset that integrates regional and catchment-scale atmospheric deposition data, catchment characteristics and co-located stream Q and stream chemistry data. We use these data to investigate opportunities and limitations of a pattern-to-process approach where we explore regional patterns of reduced acid deposition, catchment characteristics and stream DOC response and specific soil processes at select locations. For pattern investigation, we quantify long-term trends of flow-adjusted DOC concentrations in stream water, along with wet deposition trends in sulfate, for USGS headwater catchments using Seasonal Kendall tests and then compare trend results to catchment attributes. Our investigation of climatic, topographic, and hydrologic catchment attributes vs. directionality of DOC trends suggests soil depth and catchment connectivity as possible modulating factors for DOC concentrations. This informed our process-to-pattern investigation, in which we experimentally simulated increased and decreased acid deposition on soil cores from catchments of contrasting long-term DOC response [Sleepers River Research Watershed (SRRW) for long-term increases in DOC and the Susquehanna Shale Hills Critical Zone Observatory (SSHCZO) for long-term decreases in DOC]. SRRW soils generally released more DOC than SSHCZO soils and losses into recovery solutions were higher. Scanning electron microscope imaging indicates a significant DOC contribution from destabilizing soil aggregates mostly from hydrologically disconnected landscape positions. Results from this work illustrate the value of an iterative process and pattern approach to understand catchment-scale response to regional disturbance and suggest opportunities for further investigations.

Keywords: spatial and temporal scales, soil aggregates, acid rain, process and pattern, long-term trends, dissolved organic carbon

INTRODUCTION

Disturbances such as land-cover transformation, amplification of biogeochemical flows, and climate disruption are triggering transitions in the Earth system that are unprecedented on human timescales (Steffen et al., 2018; Abbott et al., 2019). Potential and ongoing ecosystem state changes may impact billions of individuals (Abatzoglou and Williams, 2016; Van Loon et al., 2016; Dupas et al., 2019), highlighting the need to better understand the factors that determine how catchments respond to multiple disturbance types and in different contexts.

However, attributing catchment response to even a specific driver is challenging because the scale of disturbance often transcends the bounds of individual sites that, themselves, have heterogeneous spatial characteristics. While spatial and temporal patterns at larger scales can be extracted from relevant data (e.g., atmospheric deposition data), finding patterns that hold true across individual catchments remains a challenge that was already described decades ago as "uniqueness of place" for hydrological modeling (Beven, 2000). Research shows that a direct scaling of site-specific observations to a larger-scale trend (and vice versa) might not be possible and that scaling mismatches might be the norm rather than the exception (Levin, 1992; NSF, 2018). For example, Preston et al. (2011) used lab mesocosm, field monitoring and long-term stream data to investigate the impact of climate drivers on dissolved organic carbon (DOC) liberation, and found that variations in temperature and moisture impacted DOC concentrations differently for each scale of observation. While direct upscaling and downscaling might lead to loss of information and insight, an approach that does not seek direct links across scales but that investigates larger-scale pattern and site-specific process in an iterative fashion might provide some remedy (Sivapalan, 2005). In such an approach, regional patterns might point to a possible process (i.e., pattern-to-process), while process investigation might provide more insights with each iteration (i.e., process-to-pattern).

Acidification (and ensuing reduction in acid deposition) is a good candidate for iterative pattern and process investigation in the context of disturbances. Large variation in forested catchment signals including increases in stream DOC exports are attributed reductions in acid deposition, but the pattern is not consistent (Driscoll et al., 2003; Burns et al., 2006; De Wit et al., 2007; Monteith et al., 2007; Hruška et al., 2009; Sanclements et al., 2018). For example, some catchments have shown increases in DOC concentration despite continued acid deposition (Oni et al., 2013), while others showed reduced deposition without attendant increases in DOC (Löfgren and Zetterberg, 2011). Concurrent with the reduction in acid deposition, changes to the climate system have led to increasing precipitation, which is amplified by increasing frequency of extreme hydrological events such as heavy precipitation (Jentsch et al., 2007; Campbell et al., 2009; Arnone et al., 2011; Seneviratne et al., 2012). For example, in the case of catchments in the Northeastern US, increased heavy precipitation and reduced acid deposition could lead to increased exports of DOC, as shown in a long-term, paired catchment study (Sanclements et al., 2018) where one catchment received continuous acid treatment while the other was allowed to recover from acidification. The latter catchment exported significantly more DOC, indicating a strong effect of reduced acid deposition; however, the temporal variability in stream DOC concentrations for both catchments was high due to shifts in precipitation patterns. While these overlapping disturbances alone can lead to DOC patterns that are difficult to interpret, variations in catchment-specific characteristics likely drive differences in DOC export patterns in areas that receive similar acid loadings (Clark et al., 2010). The authors of the latter study note that seasonal, short-term inter-annual and longer-term temporal variation interact in complex ways, masking otherwise compatible patterns, and suggest careful process investigation. Lastly, variation in length of record and reporting methods (Eimers et al., 2008a) present a continuous challenge.

At the catchment scale, processes that lead to DOC liberation into streams are coupled and highly complex. Especially in forested headwater catchments, DOC is primarily controlled by soil organic matter (SOM) that supplies DOC when soils are flushed in response to precipitation and, in snow-dominated systems, during snowmelt (Boyer et al., 1996; Raymond and Saiers, 2010; Wilson et al., 2013; Moatar et al., 2017; Perdrial et al., 2018; Zarnetske et al., 2018; Zhi et al., 2020). Thus, DOC is often controlled by discharge (Q) and studies now increasingly use flow-adjusted DOC concentrations (DOC_{FA}) or fluxes in their assessment to test for DOC drivers other than Q (Burns et al., 2006). This hydrological control is also embedded in the broader context of spatial and temporal variability of catchment processes. Recent observations and reactive transport modeling support the shallow and deep hypothesis that high concentration DOC in stream under wet, high discharge conditions comes from shallow soils enriched with SOM, whereas low stream DOC under dry, low discharge conditions originates from deeper groundwater that is often depleted in DOC (Zhi et al., 2019). The concept of ecosystem control points is very useful in exemplifying this complexity and heterogeneity because variable importance of DOC supply vs. transport is acknowledged (Bernhardt et al., 2017). For example, catchment locations such as planar hillslopes accumulate materials until they are hydrologically connected and episodically flushed (export control points) and lead to high temporal variability in DOC exports in streams during events.

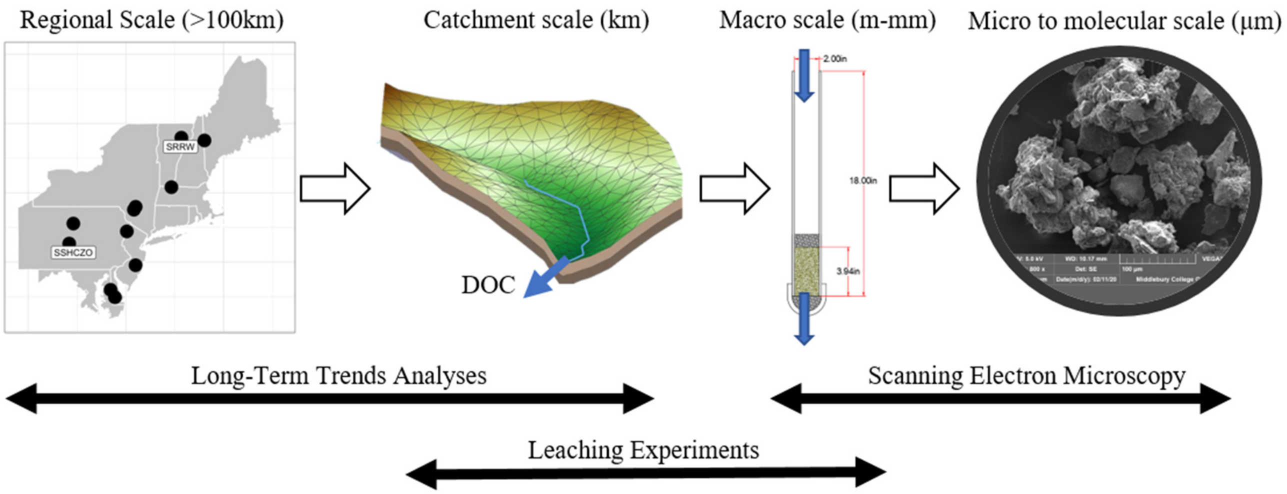

FIGURE 1 | Conceptual depiction of investigated scales.

In contrast, locations such as riparian zones and swales exhibit high degrees of biogeochemical activity and near continuous connectivity to the stream (permanent control points) and the ensuing impact on stream DOC is more continuous. Because microbial processing is regulated by soil temperature and moisture (Wen et al., 2020), landscape positions with favorable soil moisture conditions promote microbial DOC processing and losses to the atmosphere as CO_2, thus reducing DOC concentrations in soil solution (Moyano et al., 2013). In turn, very wet conditions suppress aerobic DOC respiration leading to DOC accumulation available for flushing (Huang and Hall, 2017). Because SOM is an important supplier for DOC, SOM stability also needs to be considered in this context. SOM can be stabilized chemically, through adsorption on clay and silt particles (Six et al., 2002; Perdrial et al., 2010) or physically, through the occlusion within soil micro-aggregates ($<250\,\mu$m) that limit microbial processing (Lin et al., 2006; Mikutta et al., 2006; Kleber and Johnson, 2010; Schmidt et al., 2011; Li et al., 2017). Recent research has indeed begun to link reduced acid deposition and subsequent changes in soil chemistry (ionic strength and pH) to changes in SOM stabilization in aggregates driving DOC loss at the catchment scale (Armfield et al., 2019; Cincotta et al., 2019). Because these conditions vary in scale, both in space (region, catchment, landscape position within a catchment) and time (decadal vs. seasonal), this complexity is difficult to detangle and a good test case for iterative pattern and process investigations.

The overarching goal of this study is to illustrate opportunities and challenges with the process and pattern approach using increased and decreased acid deposition as test case. We apply one iteration as starting point with the intent to critically evaluate the opportunities and limitations of each approach, as well as the integration of observations across these scales. For pattern investigation at the regional scale, we investigate linkages between reduced acid deposition and stream DOC response and the potential role of catchment characteristics as covariates in that response (objective 1). For this we apply regional atmospheric deposition data from the National Atmospheric Deposition Program (NADP), catchment biogeophysical and hydrometeorological attributes (Addor et al., 2017), and a newly curated dataset that includes co-located stream Q and stream chemistry data (Sterle et al., 2019). We use flow-adjusted stream chemistry data to remove the typically dominant Q control from temporal trends and to better isolate potential signals in response to reduced acid deposition in stream DOC concentrations (Helsel et al., 2020). We compute trend analyses for long-term data sets and compare stream water DOC trend directionality against sulfate (SO_4^{2-}) deposition trends as one proxy for shifts in atmospheric deposition, and we compare these trends to catchment attributes (Addor et al., 2017) to determine if common catchment scale characteristics might be associated with these trends. For process investigations, we test the effect of leaching solution composition on soil aggregate stability and DOC release experimentally (objective 2). For this, we use soils cores from several landscape positions and locations in catchments with opposite long-term DOC trends [Susquehanna Shale Hills Critical Zone Observatory (SSHCZO) and the Sleepers River Research Watershed (SRRW)] and critically evaluate opportunities and limitations of integrating these observations with large-scale patterns (**Figure 1**).

METHODS AND MATERIALS

Long-Term Trend Analyses at the Regional Scale

Site Selection and Data Collection

To characterize trends in DOC and Q, we utilized the recently-developed CAMELS-Chem dataset (Sterle et al., 2019). This dataset complements the existing CAMELS dataset with additional atmospheric deposition and water chemistry data for 671 catchments, 499 of which are >50% forest cover. The temporal record of stream chemistry varies depending on the individual catchment, with all records ranging between 1980 and 2019. In this study, we constrained the dataset to forested catchments, that is catchments with >50% forest cover, in the Northeastern United States. This was done to minimize land cover drivers from our analyses (**Figure 2**). Within the Northeast, we further constrained catchments according to their length of available stream DOC and Q records (at least five sequential years) and the density of the records (i.e., no gaps >1/3rd of the total record length) (Meals et al., 2011). Once we identified suitable catchments, we compiled all available DOC concentration and Q records from said catchments for trend and statistical analyses.

To characterize trends in wet deposition of SO_4^{2-}, we utilized the National Atmospheric Deposition Program (NADP) National Trends Data (NADP Program Office, 2021). The daily frequency records in SO_4^{2-} from these sites were then clipped to match the record length of available DOC and Q data from the associated catchments.

Flow-Adjusted Stream Concentration Data

We flow-adjusted the time series of stream DOC concentration data for each selected catchment to remove the typically dominant Q control from temporal trends and to better isolate potential signals of deterministic trends in stream response (such as stream response to reduced acid deposition). This method has been used in a number of studies that sought to describe temporal trends in stream chemistry constituents that are often confounded by varying stream flow conditions (Hirsch and Slack, 1984; Helsel and Hirsch, 2002; Bekele and Mcfarland, 2004). We first regressed log-transformed DOC concentrations on log-Q data, applying a Locally Weighted Scatterplot Smoothing (LOWESS) algorithm and extracted the residuals. For each regression fit, we used a smoothing pattern coefficient of 0.67 ($f = 0.67$). One of the benefits of this technique is that a LOWESS model does not assume linearity or normality in the data, therefore not limiting the concentration (C)-Q relationship in each catchment to one specific model (see **Supplementary Figure 1** for C-Q plots). We then reordered residuals from the LOWESS fit (i.e., DOC_{FA} concentrations), based on the date/time stamp associated with each observation, and performed a monotonic trend analysis on these residuals using a seasonal Mann-Kendall test (section Seasonal Kendall, see **Supplementary Figure 2** and accompanying description for details).

Change Point Detection

We applied a Pettitt test to DOC_{FA} concentrations to identify any threshold effects in trend that would otherwise be missed by simply identifying monotonic trends. The Pettitt test is a non-parametric technique used to identify a single change point in continuous time series data (Pettitt, 1979). This test has been used in a number of studies to detect abrupt changes in hydrologic and climatic variables such as precipitation (Busuioc and Storch, 1996), flood peaks (Liu et al., 2012), and temperature (Wijngaard et al., 2003).

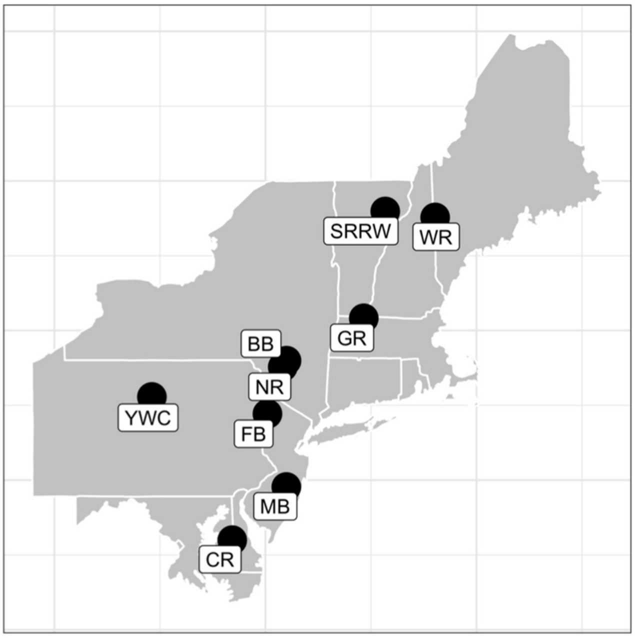

FIGURE 2 | Northeastern headwater catchments in the CAMELS-Chem dataset selected for long-term trend analyses. For full gauge names and gauge numbers see **Table 1**.

Seasonal Kendall

With both DOC_{FA} and SO_4^{2-} deposition data for each catchment, we utilized seasonal Kendall tests to determine the directionality of the aquatic and atmospheric trends. A seasonal Kendall test is widely used as a non-parametric, statistical technique for detecting monotonic trends in time series (Hirsch and Slack, 1984). In this setting, it indicates whether DOC_{FA}, independent of seasonal variability, is increasing or decreasing over time. The product is the normalized test statistic, Kendall's tau, which ranges from −1 to 1. For this analysis, we define "positive trends" as those with a tau value >0.05 and significant beyond an associated alpha threshold of 0.05. "Negative trends" are defined as having a tau value <-0.05 with an alpha threshold of 0.05; and "no trends" are defined as any results that do not meet the requirements of positive or negative trends.

Experiments on Select Catchment Soils

Field Site Descriptions

To test the impact of soil solution and landscape position on DOC dynamics, we sampled soils from two forested headwater catchments with contrasting long-term DOC dynamics for experimentation (**Figure 3**). The SSHCZO is a 0.08-km^2 forested catchment located in central Pennsylvania in close proximity to Young Woman's Creek (YWC, **Figure 3**). The catchment is underlain by thick shale and is a first order basin with steep south- and north-facing slopes (25–35%) and narrow ridges. The SSHCZO has a mean annual temperature of ∼9.8°C and a humid continental climate. Mean annual precipitation averages 1,029-mm and is characterized as acidic (pH ∼4)

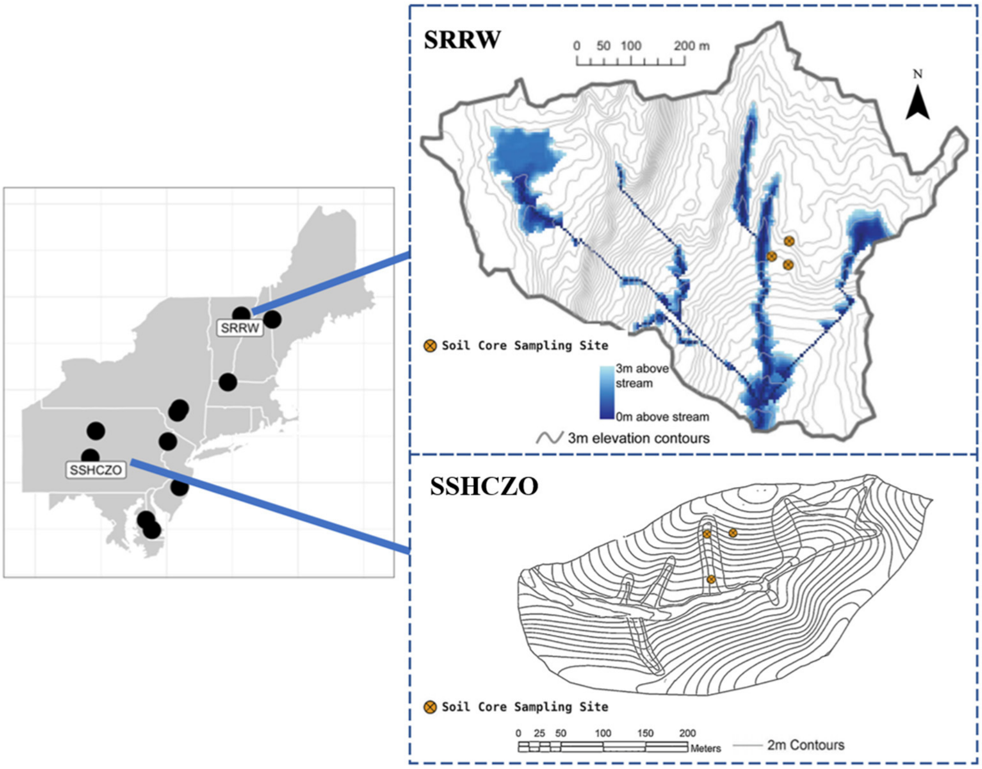

FIGURE 3 | Location of field sites: the Sleeper River Research Watershed (SRRW) map is derived from Shanley et al. (2015) and the Susquehanna Shale Hills Critical Zone Observatory (SSHCZO) map is modified after Lin et al. (2006) with permission. This figure was modified from Hydrological Processes, 29, Shanley, James B., Stephen D. Sebestyen, Jeffrey J. McDonnell, Brian L. McGlynn, and Thomas Dunne. 'Water's Way at Sleepers River watershed – revisiting flow generation in a post-glacial landscape, Vermont USA', 3447–59, Copyright 2014, with permission from John Wiley and Sons and from Geoderma, 131, Soil moisture patterns in a forested catchment: A hydropedological perspective, 345–368, Copyright 2006, with permission from Elsevier.

and stream water is mildly acidic with an average pH of 5.6 (**Supplementary Figure 3**) (Wen et al., 2020). The soils are derived from colluvium and/or residuum from the underlying shale formation and are Inceptisols and Ultisols with primarily silt loam shallow horizons and a 3 to 5-cm organic layer containing decaying leaf litter (Giardino and Houser, 2015). A number of studies that focused on the cycling of DOC have used the SSHCZO including Andrews et al. (2011), who identified hot spots and hot moments of DOC transport, and Bao et al. (2017), who developed a reactive transport model to predict DOC flux (Andrews et al., 2011; Bao et al., 2017; Wen et al., 2020).

The SRRW, as defined in this study, is a 0.41-km^2 completely forested headwater subcatchment located in eastern Vermont (**Figure 3**). It is underlain by calcareous granulite and quartz mica phyllite with a forest cover of primarily northern hardwoods such as beech, maple, birch, and ash (Shanley et al., 2004). The catchment encompasses three tributary streams that begin at headwater swamps and move through steep terrain and mid-elevation benches before meeting in an intersection of slopes at the base of the catchment. The main soil types are Spodosols and Inceptisols in the uplands and Histosols in the lowlands (Kendall et al., 1999). Due to the presence of carbonates in the parent material, ground water and stream water at SRRW are well-buffered with a pH above 7 (Hornbeck et al., 1997; Armfield et al., 2019), also see **Supplementary Figure 3**.

Soil Core Sampling

In both the SSHCZO and SRRW catchments, soil cores, and samples were collected from the top 10-cm of the soil profile (O/A Horizons) in both swales and planar hillslopes to capture important ecosystem control points. We acquired soil cores for the stop-flow experiment by hammering 2-inch inner diameter PVC pipes with beveled bottoms 10-cm into the soil profile after removing any leaf litter. We then gently dug cores out of the soil profile and capped them to not lose any loose material before being put into a cooler with ice for transport. A total of 18 soil cores were collected for each catchment and sampling time (12 from swales and 6 from planar hillslope locations).

Fall soil samples collected for micro-aggregate separation were acquired from the top 10-cm of the soil horizon in plastic bags and also stored in the cooler for transport before being air-dried. For those experiments designated as occurring in the spring, soil cores were collected from SSHCZO on May 28th, 2019 and SRRW on June 10th, 2019. For the fall experiments, soil cores and samples were collected from SSHCZO on November 8th and SRRW on November 17th.

Experimental Approach to Examining Micro-Scale DOC Dynamics

We conducted stop-flow experiments on soil cores sampled during both the spring and fall seasons to account for seasonal variability within 24-h of sample collection (see **Supplementary Figure 4** for a schematic of the core design). Each core was treated with 120-ml of experimental solution that was poured carefully from the top and allowed to saturate the core for 5 min. We used two experimental solutions: the "acidification" solution, simulating acid deposition conditions, had a pH of 3 and an IS of 0.01 M. The "recovery" solution, simulating absence of anthropogenic acids, had a pH of 5.3 and low IS (nanopure water). Note that we refer to this solution as "recovery" solution to indicate near neutral pH and low IS typical for rain in absence of acid deposition and not the ecosystem concept of recovery. After 5 min of interaction time between solution and soils, a valve at the bottom of core was opened, allowing any effluent to drain into a collection vessel. Once the cores drained gravitationally (∼4 min) the valve was closed, and the process repeated three more times yielding 4 separate samples for repeat core treatments. Within 24-h of the experiment, the effluent in each collection vessel was filtered through 0.45-μm polyethersulfone filter before being transferred into combusted amber glass bottles for analysis.

We performed an additional batch experiment with isolated soil micro-aggregates to test specific hypotheses on aggregate break up. To isolate the micro-aggregates, air-dried soil samples were sieved and the fraction smaller than 250-μm and larger than 63-μm was collected. Once isolated, soil aggregates were saturated with one of the two laboratory solutions at a 1:5 aggregate to solution ratio by mass and slowly shaken for 9 min. The aggregates and solution were then gently separated by filtration using a 0.45-μm polyethersulfone filter and a low vacuum pressure.

Laboratory Analyses

To characterize the solid carbon content in SOM for sites without previous data, we analyzed soil subsets of 25 replicated samples collected from SRRW for total organic carbon content (TOC % w/w; note SSHCZO TOC data is available in Andrews et al., 2011). For this, the samples were air-dried, sieved through a 2-mm mesh, homogenized using a ball mill and analyzed using a combustion-based elemental analyzer (CE Instruments NC2500) in the Geology Stable Isotope Laboratory at the University of Vermont. Resulting percent carbon values were compared to standards (B2150 for high organic content sediment standard and B2152 for low organic content soil standard) provided by Elemental Microanalysis Limited.

We characterized aggregates from our batch experiments for changes in size, morphology and composition using a VEGA3 TESCAN Scanning Electron Microscope (SEM) and AZtec Elemental Mapping software. We mounted dried aggregates carefully with double-sided carbon tape on metal stubs and sputter-coated them with carbon before visualizing. Because backscattered electron (BSE) SEM mode captures electron density differences well, we used this mode to identify denser mineral grains vs. less dense organic material. BSE was acquired at 5-keV acceleration voltage; and energy-dispersive spectroscopy (EDS) maps were acquired for 5 min with a probe resolution of 15-mm. To compare aggregate size between samples and treatments, we took images at the same magnification (100x) and used image analysis software (ImageJ) to quantify particle size distribution reported in % covered area. This was achieved by converting 100x magnification images of aggregate clusters to binary, scaling, and using the "analyze particles" function with a minimum area set at 1,500 μm^2 and excluding particles that touch the image edges.

We analyzed effluent samples from full soil core experiments for DOC using a Total Organic Carbon Analyzer (Shimadzu, Columbia, MD, USA) within 24- h after collection. To allow for assessment of total DOC release over the entire experiment, we calculated cumulative DOC release; and to allow for comparison between cores, we normalized to solution and soil amount as shown in Equation (1).

$$DOC\left(\frac{mg}{kg}\right) = \frac{DOC\left(\frac{mg}{L}\right) * \left(L_{Effluent}\right)}{Dry\ Soil\ Mass(kg)} \tag{1}$$

To determine significant differences in the cumulative amount of DOC released by categorical independent variables such as treatment and landscape position, Kruskal-Wallis tests were performed. For categorical variables that showed significant results as defined by an alpha threshold of 0.05, a *post-hoc* Dunn test was used to identify which groups differed from each other group. These statistical tests were also used to determine significant differences in aggregate sizes in the SEM images after the ImageJ particle size distribution analysis was utilized.

RESULTS

Regional Long-Term Trend Analysis

In the Northeastern United States, we identified only nine catchments as having sufficient decadal records of DOC and instantaneous Q to complete our analyses (**Table 1** and **Figure 4**). Of these catchments, six had records that spanned from the 1990s to late 2010s, while three had more limited records between 2003 and 2018 (**Figure 5**). In the time series DOC_{FA} (i.e., residuals from the LOWESS fit of logDOC vs. logQ), we detected change points for six of the nine catchments ranging from the late 1990s and early 2000s [Biscuit Brooks (BB), McDonalds Branch (MB) and Neversink River (NR)] to very recent [2015 for Choptank River (CR), **Table 1**]. Existence of a change point and its position depended strongly on the length of record, and catchments with longer records exhibited more variability. We chose January 1st, 2004 as a defining date to examine before and after trends, in order to treat each of the catchments with a consistent point of reference. This date is close to the arithmetic mean (2006) of the change points detected for six catchments, and was chosen because 2004 was the first full calendar year of available data for three of the catchments.

Of the six catchments with sufficient data prior to 2004, three exhibited increasing DOC_{FA} trends (BB, MDB, and SRRW) while no trend could be confirmed in the other three [Flat Brook (FB), Green River (GR), and NR]. For the nine catchments with data

TABLE 1 | Northeastern catchment attributes, length of DOC$_{FA}$ records and calculated change dates.

USGS Gauge ID	Stream Gauge name	Catchment area (km^2)	Most prominent geology	Length of record	Year of change date	DOC$_{FA}$ sample size (*n*)
1054200	Wild River at Gilead, ME (WR)	181	Metamorphics	2003–2018	N/A*	203
1135100	Sleeper River Research Watershed W-9 Tributary, VT (SRRW)	0.08	Metamorphics	1991–2015	2009	1,326
1170100	Green River Near Colrain, MA (GR)	107	Metamorphics	1993–2018	N/A*	116
1434025	Biscuit Brook Above Pigeon Brook at Frost Valley, NY (BB)	10	Siliciclastic sedimentary	1991–2016	1997	1,871
1435000	Neversink River Near Claryville, NY (NR)	172	Siliciclastic sedimentary	1991–2018	2003	1,138
1440000	Flat Brook Near Flatbrookville, NJ (FB)	168	Siliciclastic sedimentary	1993–2018	N/A*	96
1466500	McDonalds Branch in Lebanon State Forest, NJ (MB)	5	Unconsolidated sediments	1981–2018	2002	477
1491000	Choptank River Near Greensboro, MD (CR)	292	Unconsolidated sediments	2003–2018	2015	287
1545600	Young Woman's Creek near Renovo, PA (YWC)	120	Siliciclastic sedimentary	2003–2018	2010	234

**N/A, No significant ($\alpha \leq 0.01$) change point was identified.*

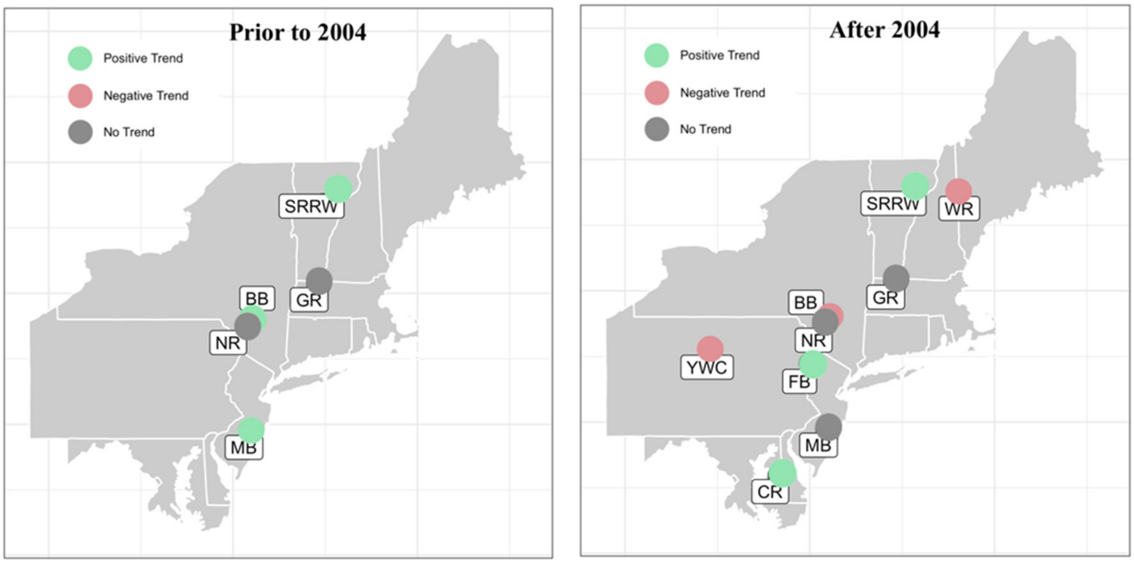

FIGURE 4 | Directionality of catchment flow adjusted dissolved organic carbon concentration (DOC$_{FA}$) trends prior to ($n = 5$) and after ($n = 9$) 2004. Statistically significant ($\alpha \leq 0.05$) positive trends are shaded in green, statistically significant negative trends are shaded in red, and no trend are shaded in gray.

after 2004, three exhibited increasing DOC$_{FA}$ trends (CR, FB, and SRRW), three exhibited no trend (MDB, NR, and GR), and the remaining three exhibited decreasing trends [BB, Wild River (WR), Young Woman's Creek (YWC)]. Spanning the reference point of 2004, the directionality in trend changed for three catchments: from positive to negative (BB); from no trend to positive (FB), and from positive to no trend (MD).

Just as with DOC, wet SO_4^{2-} deposition trends were calculated separately for years prior to and after 2004. Prior to 2004, four catchments (BB, MB, NR, and SRRW) exhibited negative SO_4^{2-} trends and two catchments exhibited no trend (GR and FB). Some catchments with increasing trends in DOC$_{FA}$ also showed decreases in wet SO_4^{2-} deposition while for others a similar relationship was not apparent. For example, NR showed no DOC$_{FA}$ increase despite decreases in wet SO_4^{2-} deposition, while GR showed increases in DOC$_{FA}$ without a change in wet SO_4^{2-} deposition (**Figure 6A**). For the time after 2004, data for three additional catchments were available (YWC, CR and WR) and all exhibited negative SO_4^{2-} trends (**Figure 6B**). Several catchments exhibited increases in DOC$_{FA}$ trends, including catchments experiencing different magnitudes of decrease in wet SO_4^{2-} deposition (**Figure 6B**). To test for connections between catchment attributes and directionality of DOC$_{FA}$ trends, we plotted Kendall tau values after 2004

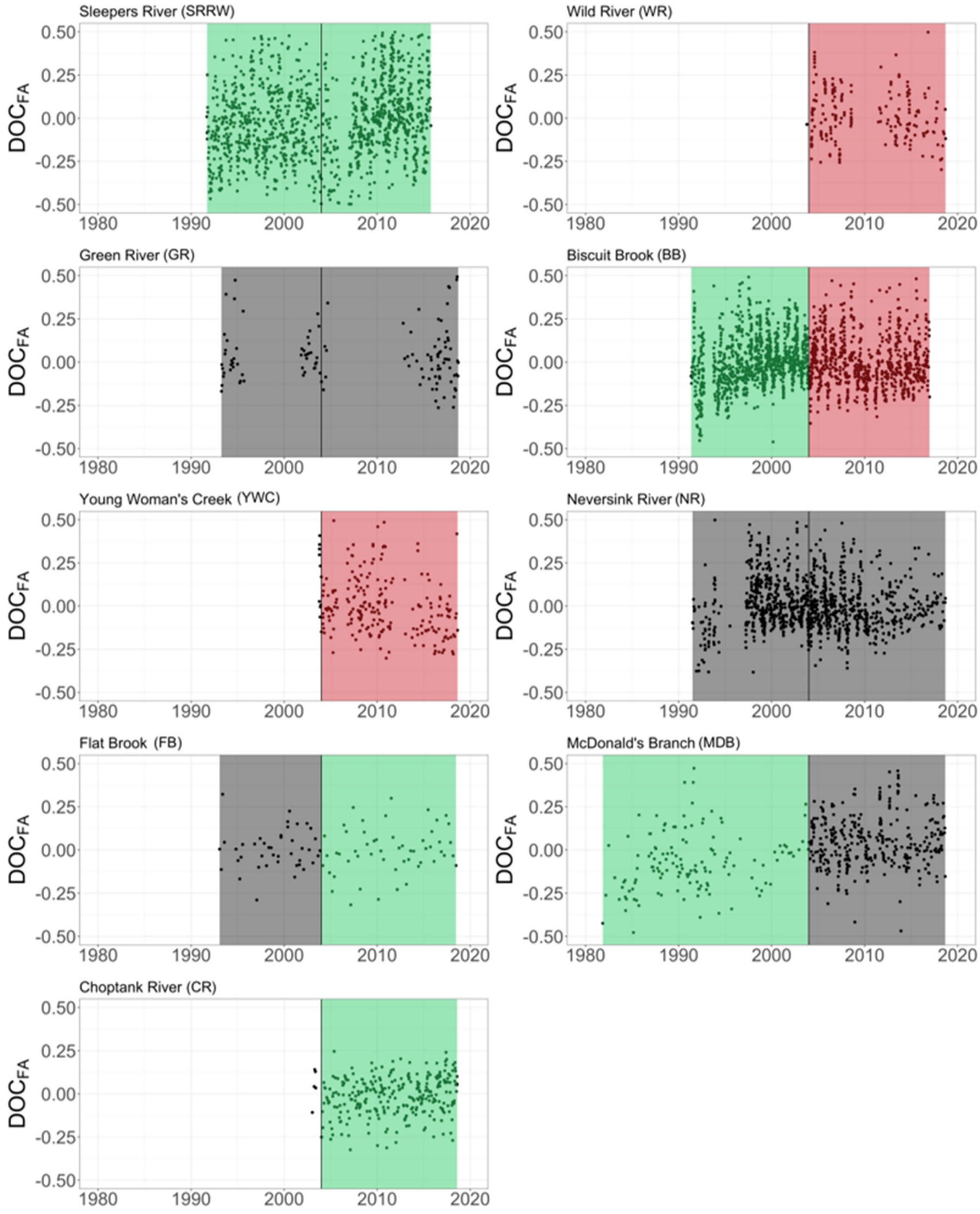

FIGURE 5 | Long-term trends in flow-adjusted DOC concentrat ions (DOC_{FA}). Trends are split between two periods of time: prior to 2004 and after 2004. Statistically significant ($\alpha \leq 0.05$) positive trends are shaded in green, statistically significant negative trends are shaded in red, and no trend are shaded in gray.

against climatic, topographic, and hydrologic attributes from the CAMELS data set (**Figure 7**). Catchments that have a low number of high precipitation days (i.e., events that are five times greater than the mean daily precipitation) and high % of snow cover, tended to show negative DOC_{FA} trends (**Figures 7A,B**). In turn, positive DOC_{FA} trends were associated with more days with high precipitation and lower % snow cover. Soil depth varied greatly between catchments and no direct link between DOC_{FA} trends and soil depth was determined (**Figure 7C**). However, the link between mean slope and DOC_{FA} trends was more

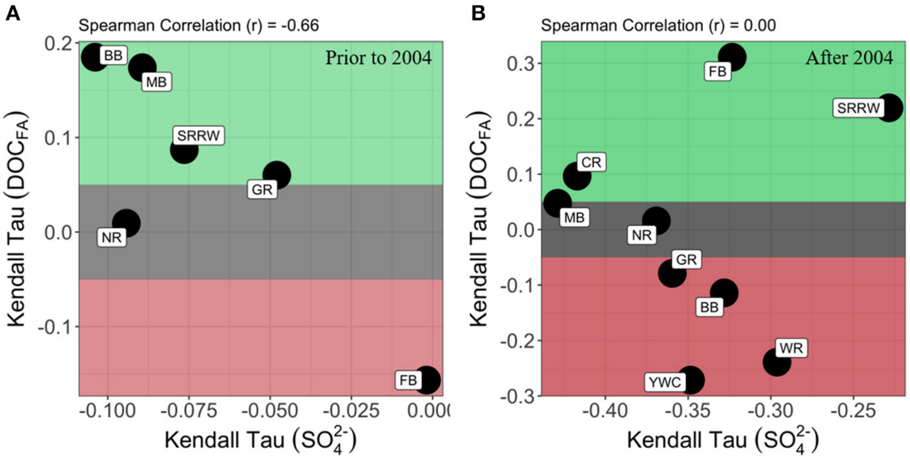

FIGURE 6 | Relationship between trends in flow-adjusted dissolved organic carbon concentration (DOC_{FA}) and trends in sulfate wet deposition (SO_4^{-2}) for Northeast U.S. forested headwater catchments: **(A)** prior to 2004 ($n = 6$) and **(B)** after 2004 ($n = 9$). Shading highlights those regions of the plot where DOC_{FA} exhibits statistically-significant positive trends (tau > 0.05; green), negative trends (tau < −0.05; red), or no significant trend (0.05 > tau > −0.05; gray).

systematic in that catchments with shallow slopes showed no or negative DOC_{FA} trends and catchments with steep slopes showed generally decreasing DOC_{FA} (**Figure 7D**). Catchments with a low number of days where Q is high (high Q frequency) generally showed positive DOC_{FA} trends while catchments with larger high Q frequency showed negative DOC_{FA} trends (**Figure 7E**).

Catchment-Scale Soil Core Experiments at SSHCZO and SRRW

Catchment-scale results of the TOC analysis indicate that carbon content in SRRW soils is variable across landscape positions (**Supplementary Figure 5**). In the top 10 cm of the swale, TOC was ∼20% as opposed to the planar hillslope, which exhibited ∼5% TOC. The DOC effluent per kg of soil released from soil cores cumulated over the four leaching events was variable across catchments, landscape positions, seasons and treatment. Spring soil cores infiltrated with the recovery-simulating solution released more DOC (14.07 ± 14.27 mg/kg) in comparison to those infiltrated with the acidification solutions (6.95 ± 7.53 mg/kg). Planar hillslopes consistently leached significantly more DOC (17.66 ± 8.57 mg/kg) than swales (4.94 ± 8.98 mg/kg, **Figure 8**) during this time. For the fall soils, cores that underwent the recovery treatment released more DOC (18.21 ± 15.45 mg/kg) than the acidification (14.46 ± 18.07 mg/kg) treatments and again planar hillslopes released more DOC (17.96 ± 15.10 mg/kg) than the swales (11.89 ± 14.19 mg/kg).

For SSHCZO, spring soil cores infiltrated with the recovery treatment also released more DOC (6.30 ± 2.43 mg/kg) compared to those infiltrated with the acidification solution (4.79 ± 2.15 mg/kg) and again, planar hillslopes consistently leached significantly more DOC (6.77 ± 1.84 mg/kg) compared to swales (4.95 ± 2.44 mg/kg, **Figure 8**). However, fall soil cores released less DOC during recovery treatment (5.04 ± 3.94 mg/kg) compared to the acidification treatment (9.65 ± 8.63 mg/kg). Consistently, planar hillslopes released more DOC (11.85 ± 7.40 mg/kg) than the swales (4.17 ± 2.72 mg/kg).

Batch Experiment on Separated Aggregates

The results of the SEM analysis showed differences in aggregate size distribution and morphology by location, landscape position and treatment. The SRRW aggregates in both landscape positions showed heterogeneous associations of larger angular fragments (likely primary minerals) and finer grained materials (**Figure 9**). Compared to aggregates after acidification treatment, aggregates after recovery treatment appear smaller (e.g., **Figures 9B,E**). Assessment of particle size distribution from image analyses confirms the qualitative assessment for both swale and hillslope locations. While some larger aggregate/particles are visible after each treatment, the bulk of swale aggregates treated with acidification solution are generally larger (maxima at around 325-μm) than those treated with recovery solution where maximum covered area is at around 175-μm (**Figures 9C,F**). Aggregate constituents from SSHCZO are homogeneously fine-grained and present rounded and tubular particle shapes in both landscape positions (**Figure 10**). Fine-grained materials (<10-μm) are visible for most samples and likely derive from surface coatings and/or disintegrating aggregates. SSHCZO aggregate morphology is similar for both landscape positions and the entire range of particle sizes is represented. Swale aggregates treated with acidification solution show a multimodal particle size distribution with maxima at 225- and 400-μm diameter. After recovery treatment, particles in smaller sizes (below 100-μm) are more abundant (**Figure 10C**). Hillslope particle size distribution is variable and spans the particle size range at similar coverage for both treatments (**Figure 10F**).

DISCUSSION

Understanding and predicting catchment responses to a regional disturbance is difficult because catchments are spatially heterogeneous systems and exhibit unique characteristics that may engender variable degrees of resistance or resilience to

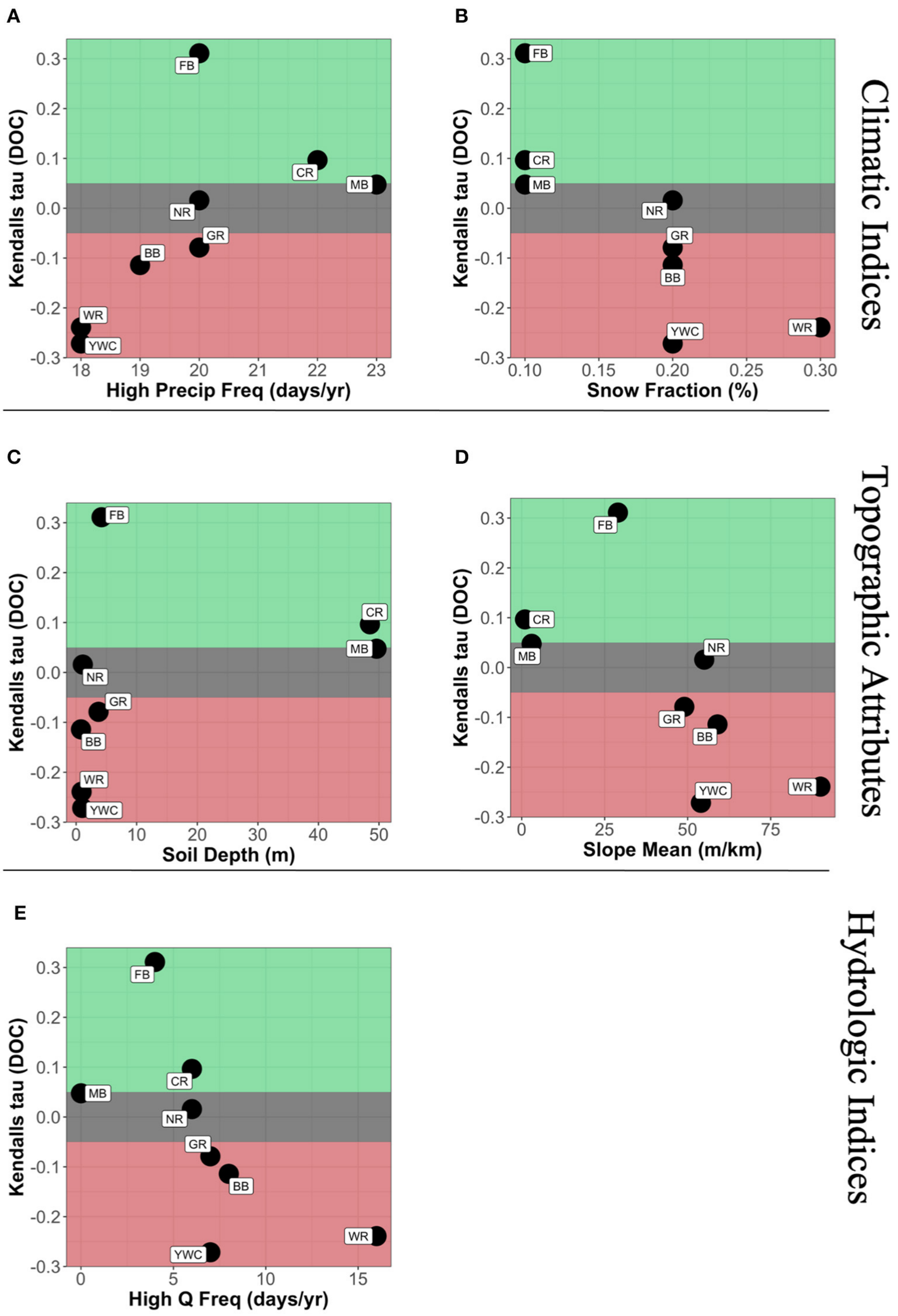

FIGURE 7 | Relationship between trends in flow-adjusted dissolved organic carbon concentration (DOC_{FA}) (2004–2018) and select catchment attributes grouped as climatic indices **(A,B)**, topographic indices **(C,D)**, and hydrologic indices **(E)**. Shading highlights those regions of the plot where DOC_{FA} exhibits statistically-significant positive trends (tau > 0.05; green), negative trends (tau < −0.05; red), or no significant trend (0.05 > tau > −0.05; gray).

disturbance. This "uniqueness of place" has been acknowledged for many decades in hydrological modeling (Beven, 2000) and the conceptual and numerical integration of single site, single plot observations, stream water patterns and a larger scale driver remains a challenge (Levin, 1992; NSF, 2018). To overcome this uniqueness of place challenge, we suggest an investigative

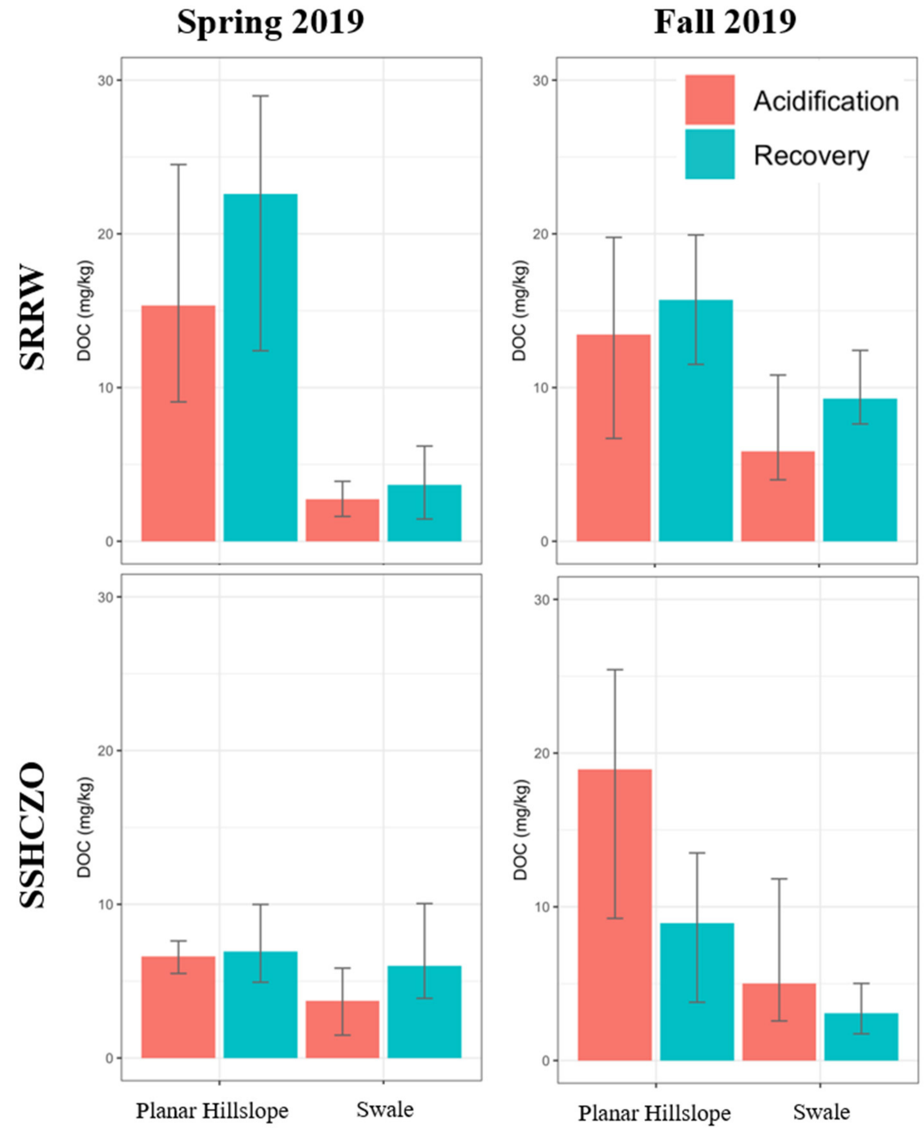

FIGURE 8 | Cumulative DOC effluent released from soil core leaching experiments as a function of treatment, landscape position and catchment.

approach that does not seek direct links across scales but that instead evaluates larger-scale pattern and site-specific process in an iterative fashion, and we use reduced acid deposition as test case of regional disturbance for one such iteration. In this context, reduction in acidification in both wet and dry deposition has been hypothesized to have caused an increase in DOC concentrations from many Northern Hemisphere forested catchments (Driscoll et al., 2003; Burns et al., 2006; De Wit et al., 2007; Monteith et al., 2007; Hruška et al., 2009; Sanclements et al., 2018). However, trends in DOC partially contradict each other, which might be due to other and/or overlapping drivers, differences in record length, variable response of unique catchments and spatiotemporal variability. The overarching goal of this study was thus to investigate opportunities and challenges with the process and pattern approach using changes in acid deposition in the Northeastern U.S. as test case.

Pattern-to-Process Investigation: Exploring Catchment Attributes as Covariates in Stream DOC Response to Changes in Atmospheric Deposition

The integration of regional and catchment-scale atmospheric deposition data and catchment attributes (Addor et al., 2017), with co-located stream Q and stream chemistry time-series data provides novel opportunities to investigate catchment response to a regional driver(s). Thus, our first objective was to use our integrated dataset to explore patterns at the regional scale and investigate linkages between reduced acid deposition and stream

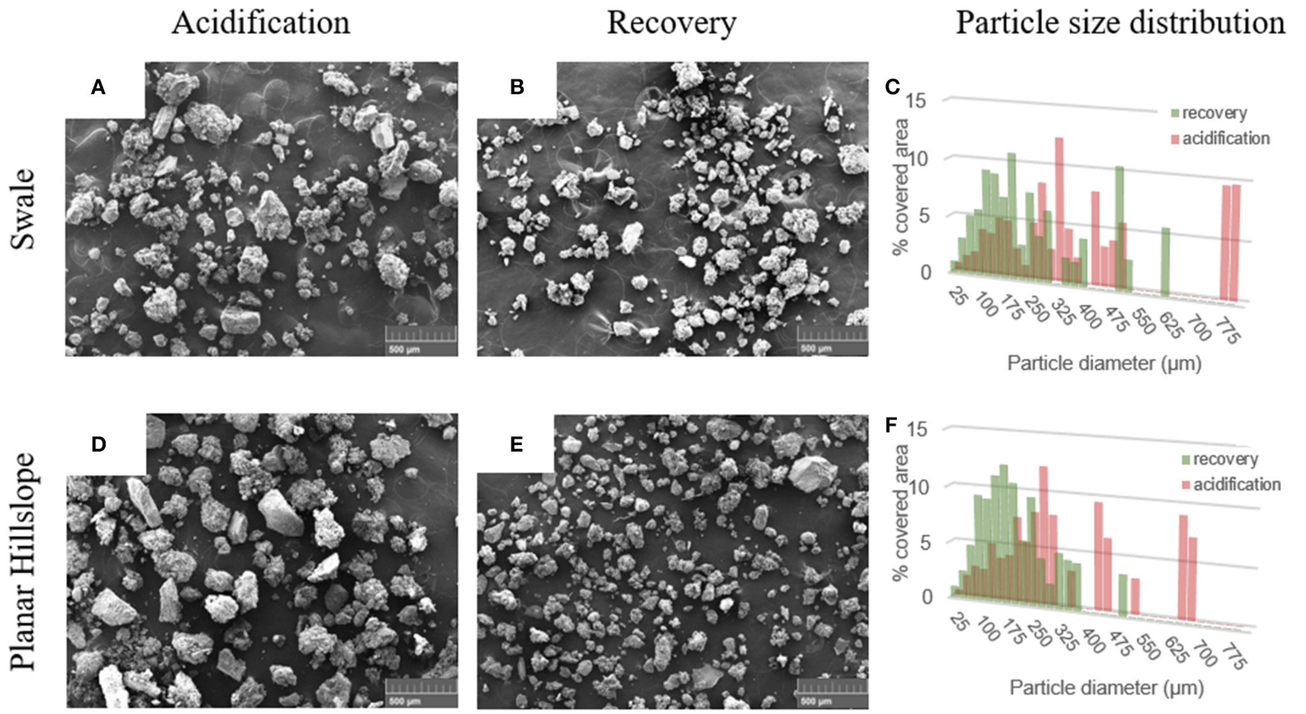

FIGURE 9 | Secondary electron scanning electron microscopy (SE SEM) images of soil aggregates taken from a swale **(A,B)** and planar hillslope **(D,E)** in Sleepers River Research Watershed (SRRW) after treatment with laboratory acidification **(A,D)** and recovery **(B,E)** solutions. Particle size distribution from image analyses for swale **(C)** and planar hillslope **(F)** aggregates are expressed in % covered area (i.e., the area that is covered by particles that belong to a given size bin).

DOC response and the potential role of catchment characteristics as covariates in that response (objective 1).

To test the connection between decreased atmospheric deposition as a potential driver for DOC stream patterns we compared the directionality of stream water DOC trends against that of SO_4^{2-} deposition. The pattern prior to 2004 signals that catchments experiencing the strongest reduction in SO_4^{2-} deposition also show the largest increases in DOC_{FA} (**Figure 4**). However, our results also show that post 2004, the connection between decreases in SO_4^{2-} deposition and increases in DOC_{FA} is not evident for each location. For example, the four catchments that show increases in DOC_{FA} post 2004 (SRRW, FB, CR, MB) show large variability in decadal SO_4^{2-} deposition trends.

These results signal that effects of shifts in atmospheric deposition on DOC are transient or may be confounded by other deterministic trends, and trend analyses thus require explicit temporal contexts. An example are the Catskill catchments (NR and BB), where Burns et al. (2006) found a significant increase in DOC concentrations between 1991 and 2001. Our analysis confirmed this trend for DOC_{FA} until 2004, however, thereafter these catchments exhibit no trends and negative trends (**Figure 5**). In addition to shifts in directionality of trends for many locations, the Pettitt change point analysis also revealed high variability in timing of the change points even for catchments in close proximity to each other. For example, the shift in DOC_{FA} for BB occurred in 1997, whereas for NR, which drains BB and a larger area, the shift occurs in 2003. As noted in **Table 1**, these catchments are dramatically different in size, which may in part contribute to the temporal variability in these responses. Furthermore, all these catchments have unique characteristics that likely modulate their response to this disturbance to varying degrees.

To specifically investigate the possible connection between catchment attributes and variable DOC response we investigated the period where DOC_{FA} trends show high inter catchment variability (2004–2018). Of all catchment attributes included in the CAMELS dataset (Addor et al., 2017), DOC_{FA} trends show systematic variations with some topographic, climatic, and hydrologic indices. For example, catchments with positive DOC_{FA} trends tend to be flat (i.e., average mean slope is low) while catchments with opposite DOC_{FA} trends have opposite characteristics (**Figure 7D**). Catchments with the most negative Kendall tau values for DOC_{FA} each have shallow soils; however, shallow soils also produce some of the highest DOC_{FA} values (**Figure 7C**). Another finding is that catchments with positive DOC_{FA} trends tend to have less frequent high Q days (**Figure 7E**) yet more frequent high precipitation days (**Figure 7A**). The association between increasing DOC_{FA} trends and frequency in high precipitation events is in agreement with previous research that indicates DOC export on an annual basis is predominantly driven by large storm/snow melt events (Raymond and Saiers, 2010; Raymond et al., 2016; Wen et al., 2020).

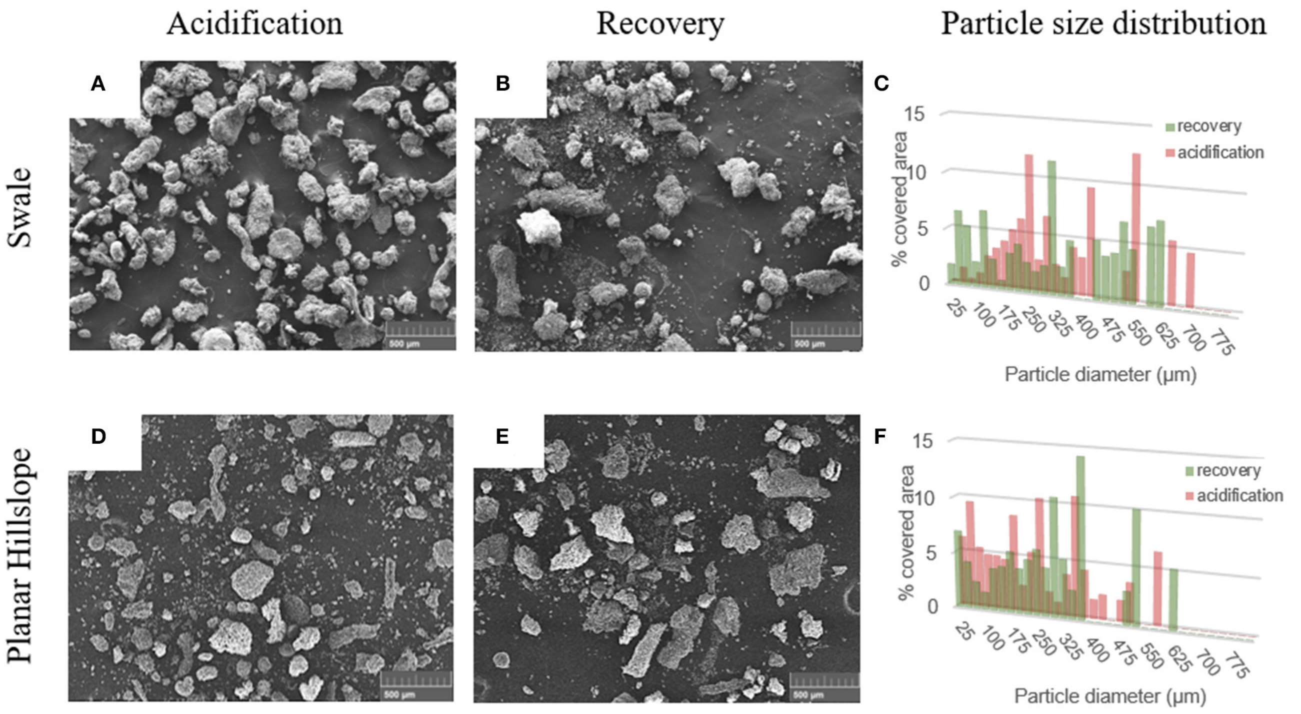

FIGURE 10 | Secondary electron scanning electron microscopy (SE SEM) images of soil aggregates taken from a swale **(A,B)** and planar hillslope **(D,E)** in the Susquehanna Shale Hills Critical Zone Observatory (SSHCZO) after treatment with laboratory acidification **(A,D)** and recovery **(B,E)** solutions. Particle size distribution from image analyses for swale **(C)** and planar hillslope **(F)** aggregates are expressed in % covered area (i.e., the area that is covered by particles that belong to a given size bin).

Our flow adjustment removes the direct influence of Q on trends in DOC concentrations, thus the apparent link between DOC_{FA} trends and frequency in high precipitation events emphasizes that precipitation drives transport of DOC to streams across catchments with very different characteristics, irrespective of which process led to DOC mobilization. Lastly, catchments that exhibit highest Q frequency also show most negative DOC_{FA} trends (**Figure 7E**), which might seem counterintuitive given the fact that the majority of small headwater streams exhibit increasing DOC concentration with increasing Q due to soil flushing (Evans and Davies, 1998; Perdrial et al., 2014; Chorover et al., 2017; Moatar et al., 2017). However, because the flow-adjustment process removes the typically dominant Q control on trends, other controls such as reduced acid deposition are emphasized in the data. In this context, flashy catchments (high Q frequency) might more readily deplete carbon pools (Boyer et al., 1997) and lower water residence time, thus leading to decreased DOC_{FA}. In contrast, catchments with less frequent high Q events might access export-controlled DOC pools, especially as the frequency of high precipitation events increased. Our data set is admittedly small, given the limited availability of sites with sufficiently long data records for DOC (Sterle et al., 2019). While our investigation begins to highlight some potential patterns, more research will be necessary to investigate the multi-variate drivers and catchment specific processes that produce such potential patterns.

Process-to-Pattern Investigation: Soil Processes During Simulated Increased and Decreased Acid Deposition Experiments

Our second objective was to investigate the effect of leaching solution composition on select soil processes, specifically aggregate destabilization, as a mechanism for DOC liberation. For this we selected two locations that are well-studied but exhibit contrasting long-term DOC_{FA} trends: SRRW exhibits increasing DOC_{FA} trends, while SSHCZO, a well-studied catchment in close proximity to YWC, shows decreasing DOC_{FA} trends.

In our simulated soil core flushing experiments on top horizons (O-A), soils from SRRW released more DOC than those from SSHCZO for most locations and seasons (**Figure 8**). These results are in agreement with the higher soil TOC content in SRRW soils (Andrews et al., 2011) and fit the long-term and continued increase in stream DOC over time (**Figures 4**, **5**). Furthermore, SRRW soils show consistently higher DOC releases into recovery solutions, which is again in agreement with the positive DOC_{FA} trend and makes an important connection to reduced acid deposition. The significantly (up to 50%) smaller aggregates after recovery treatment vs. acidification treatment (**Figure 9**) further corroborate these findings and validate the hypothesized role of aggregates in DOC mobilization during reduced acid deposition in this case. Indeed, previous research on SRRW soils has emphasized DOC release due to the breakup of soil aggregates in lower charge density solutions typical for reduced acid deposition (Cincotta et al., 2019). In previous work the authors note that especially the presence of Ca in SRRW soils might aid aggregation through cation bridging, a process that can be reversed when dilute solutions interact with these aggregates (Armfield et al., 2019; Cincotta et al., 2019).

In contrast, for SSHCZO soil cores, solution chemistry had little or the opposite effect on DOC release (**Figure 8**), indicating that recovery conditions did not promote DOC mobilization from these soils. Our SEM analyses furthermore indicated little reduction in aggregate size irrespective of the treatment, indicating generally higher aggregate stability (**Figure 10**). Constituents in SSHCZO aggregates are homogeneously fine-grained, which might promote stability through cohesion. The abundant clay mineral content [45%, mostly illite with small amounts of chlorite, vermiculite, and kaolinite (Macdonald et al., 2010)] promotes aggregation (Six et al., 2002) and aids sorption of organic compounds (Kahle et al., 2003). This high carbon stabilization potential might, however, be counteracted through the high water holding capacity that produces favorable condition for microbial processing, leading to overall lower TOC content (Andrews et al., 2011).

For both SRRW and SSHCZO, DOC release varied by landscape position and seasons, irrespective of treatment, and emphasizes the typical spatiotemporal variability in the catchment. For example, planar hillslopes might act as export control points where labile material accumulates until they are hydrologically connected and episodically flushed (Andrews et al., 2011). Our experiments simulate such flushing or export events and mobilize most DOC from planar hillslopes in most cases (**Figure 8**), despite the fact that TOC content is higher in swales (Andrews et al., 2011). In contrast, swales might represent permanent and/or activated control points where biogeochemical activity is high (but potentially variable) and connectivity to the stream is sustained. Despite ample DOC production, such conditions also lead to losses via microbial processing and/or flushing, thus preventing accumulation (Bernhardt et al., 2017). As a result, cores from swale locations generally release less DOC (**Figure 8**).

The temporal variability of DOC supply due to seasonal shifts in carbon accumulation, processing and transport is superimposed on the spatial control. For example, both catchments experience spring snowmelt, which flushes soils from otherwise unconnected catchment locations (Boyer et al., 1997) and could lead to a temporal depletion of labile carbon. This effect is visible for SSHCZO, however, the fact that spring SRRW soils release some of the highest amounts of DOC is somewhat counterintuitive: SRRW accumulates a significant snowpack and has a high potential for hydrologic flushing of even distal catchment locations (Shanley et al., 2004; Sebestyen et al., 2008; Armfield et al., 2019). However, it is possible that snowmelt flushing was not extensive enough to deplete stores or that enough time had passed to allow for the replenishing of stocks. For SSHCZO in contrast, we observed the highest DOC release for fall soils, which could be due to the recent addition of leaf litter. Even though leaf litter accumulates readily in swales, these locations again also lose carbon readily (Wen et al., 2020) and the high DOC release from planar hillslopes in fall might therefore again reflect the complex balance between accumulation vs. removal in a catchment setting.

Opportunities and Limitations for the Process and Pattern Investigative Approach

Our experiments emphasize the complexity of catchment specific processes that vary across time (e.g., seasonal dynamics), space (e.g., spatial heterogeneity), or both (e.g., temporal variations in spatial catchment connectivity). Indeed, the differences in DOC release for the SRRW vs. SSHCZO experiments agree with the trend directionality from our regional pattern analyses: tested SRRW soils responded strongly to solutions simulating decreased acid deposition by releasing more DOC and, at a larger scale, SRRW is one of the catchments that shows significant increases in DOC_{FA}. For SSHCZO and the larger trend at YWC, the opposite is the case. In this specific case, observations are consistent across scales, which differs from a similarly designed study on DOC release where lab experiments, field observations and historical data analyses yielded conflicting results (Preston et al., 2011). However, given the inherent complexity of catchment processes, it is unlikely that one experimentally investigated process (in our case aggregate destabilization) explains the variation in long-term trends for catchments in general. To the contrary, this process might be relevant only for catchments of specific combination of biogeophysical and hydrometeorological attributes and results from this work thus provides suggestions for the next iteration of pattern analyses.

For example, wetlands have been reported to play a significant role in DOC dynamics by impacting both water and carbon storage and thus the relative importance (and synchronization) of biogeochemical vs. hydrological processes (Eimers et al., 2008b; Bernhardt et al., 2017; Duan et al., 2017; Kang et al., 2018; Casson et al., 2019). However, while the CAMELS-Chem data set includes soil characteristics that often correlate with wetland cover (e.g., soil conductivity, water fraction, and organic fraction), wetland coverage is not included (Addor et al., 2017) but is a likely driver for our observed differences between sites. Indeed, at the SRRW sites, riparian areas act at least seasonally as wetlands, while at SSHCZO, swale locations are better drained (Andrews et al., 2011; Shanley et al., 2015). Therefore, this work offers opportunities for hypothesis generation and further process investigations for catchments with contrasting long-term patterns.

Integrated datasets, such as the CAMELS-Chem dataset used in this study, are fundamental to this type of research, and continued and concerted efforts to generate and compile these types of data in readily-accessible formats will help address current limitations for cross-scale investigations. For example, only ∼7% of CAMELS catchments had DOC records sufficiently long and consistent enough to perform robust long-term trend analyses, with only ∼2% located in the Northeastern US. The CAMELS data set includes a wide variety of catchment attributes; however, it is likely that important attributes are not captured. These spatial and temporal gaps currently limit statistical power and the development of a larger consensus on processes, suggesting a need for more long-term monitoring and data fusion/integration efforts as illustrated here. Overall, consistent, extensive, and multiple-perspective monitoring systems are urgently needed to record long-term alteration of water quantity and quality response to climate change and human perturbation efforts (Lovett et al., 2007; Magner and Brooks, 2008; Li et al., 2021; Zhi et al., 2021). In the meantime, we believe that such integrated datasets, novel data science tools, and process investigations will allow the catchment science community to make progress addressing the problem of scale.

DATA AVAILABILITY STATEMENT

The datasets presented in this study can be found in online repositories. The names of the repository/repositories and accession number(s) can be found at: the dataset [CAMELS-Chem] for this study will be made available in Sterle et al. (2019) upon publication. The stream water dataset analyzed for DOC trends at SRRW can be found at: doi: 10.5066/P9380HQG and doi: 10.5066/P929KMVK.

AUTHOR CONTRIBUTIONS

TA was responsible for sample collection, preparation, analyses, and production of both figures and tables. JP aided in interpretation, authorship, field work, lab work, lab training, and allowed lab use. KU, DR, AH, AL, and LL provided essential expertise to the interpretation of the results. GS compiled and collected data used in analyses. LS, CB, and HW aided in field work, laboratory work, and critical analyses. NP contributed through interpretations, authorship, and lab training. All authors contributed to the article and approved the submitted version.

FUNDING

This work was supported by the National Science Foundation under Grant Nos. NSF-EAR 1724171, 1724440, and 2012123. DR and JP were partially supported by NSF under Vermont EPSCoR Grant Nos. EPS-1101317 and NSF OIA 1556770.

ACKNOWLEDGMENTS

The authors thank James Shanley for assistance with sampling, analyses, and interpretation of results. We thank Sarah Powers, Jody Smith, and Gabriela Mora-Klepeis for assistance and technical support in the labs at the University of Vermont and Middlebury College. USGS participation was supported by the Land Change Science Program. Any use of trade, firm, or product names is for descriptive purposes only and does not imply endorsement by the US Government.

SUPPLEMENTARY MATERIAL

The Supplementary Material for this article can be found online at: https://www.frontiersin.org/articles/10.3389/frwa.2021.578608/full#supplementary-material

REFERENCES

Abatzoglou, J. T., and Williams, A. P. (2016). Impact of anthropogenic climate change on wildfire across western US forests. *Proc. Natl. Acad. Sci. U.S.A.* 113, 11770–11775. doi: 10.1073/pnas.1607171113

Abbott, B. W., Bishop, K., Zarnetske, J. P., Minaudo, C., Chapin, F. S., Krause, S., et al. (2019). Human domination of the global water cycle absent from depictions and perceptions. *Nat. Geosci.*12, 533–540. doi: 10.1038/s41561-019-0374-y

Addor, N., Newman, A. J., Mizukami, N., and Clark, M. P. (2017). The CAMELS data set: catchment attributes and meteorology for large-sample studies. *Hydrol. Earth Syst. Sci.* 21, 5293–5313. doi: 10.5194/hess-21-5293-2017

Andrews, D. M., Lin, H., Zhu, Q., Jin, L., and Brantley, S. L. (2011). Hot spots and hot moments of dissolved organic carbon export and soil organic carbon storage in the shale hills catchment. *Vadose Zone J.* 10, 943–954. doi: 10.2136/vzj2010.0149

Armfield, J. R., Perdrial, J. N., Gagnon, A., Ehrenkranz, J., Perdrial, N., Cincotta, M., et al. (2019). Does stream water composition at sleepers river in vermont reflect dynamic changes in soils during recovery from acidification? *Front. Earth Sci.* 6:246. doi: 10.3389/feart.2018.00246

Arnone, J. A., Jasoni, R. L., Lucchesi, A. J., Larsen, J. D., Leger, E. A., Sherry, R. A., et al. (2011). A climatically extreme year has large impacts on C4 species in tallgrass prairie ecosystems but only minor effects on species richness and other plant functional groups. *J. Ecol* 99, 678–688. doi: 10.1111/j.1365-2745.2011.01813.x

Bao, C., Li, L., Shi, Y., and Duffy, C. (2017). Understanding watershed hydrogeochemistry: 1. Development of RT-Flux-PIHM. *Water Resour. Res.* 53, 2328–2345. doi: 10.1002/2016WR018934

Bekele, A., and Mcfarland, A. (2004). Regression-based flow adjustment procedures for trend analysis of water quality data. *Trans. ASAE* 47, 1093–1104. doi: 10.13031/2013.16582

Bernhardt, E. S., Blaszczak, J. R., Ficken, C. D., Fork, M. L., Kaiser, K. E., and Seybold, E. C. (2017). Control points in ecosystems: moving beyond the hot spot hot moment concept. *Ecosystems* 20, 665–682. doi: 10.1007/s10021-016-0103-y

Beven, K. J. (2000). Uniqueness of place and process representations in hydrological modelling. *Hydrol. Earth Syst. Sci. Discussions* 4, 203–213. doi: 10.5194/hess-4-203-2000

Boyer, E. W., Hornberger, G. M., Bencala, K. E., and Mcknight, D. (1996). Overview of a simple model describing variation of dissolved organic carbon in an upland catchment. *Ecol. Model.* 86, 183–188. doi: 10.1016/0304-3800(95)00049-6

Boyer, E. W., Hornberger, G. M., Bencala, K. E., and Mcknight, D. M. (1997). Response characteristics of DOC flushing in an alpine catchment. *Hydrol. Processes* 11, 1635–1647. doi: 10.1002/(SICI)1099-1085(19971015)11:12<1635::AID-HYP494>3.0.CO;2-H

Burns, D. A., Mchale, M. R., Driscoll, C. T., and Roy, K. M. (2006). Response of surface water chemistry to reduced levels of acid precipitation: comparison of trends in two regions of New York, USA. *Hydrol. Processes Int. J.* 20, 1611–1627. doi: 10.1002/hyp.5961

Busuioc, A., and Storch, H. V. (1996). Changes in the winter precipitation in Romania and its relation to the large-scale circulation. *Tellus A* 48, 538–552. doi: 10.1034/j.1600-0870.1996.t01-3-00004.x

Campbell, J. L., Rustad, L. E., Boyer, E. W., Christopher, S. F., Driscoll, C. T., Fernandez, I. J., et al. (2009). Consequences of climate change for biogeochemical cycling in forests of northeastern North America. *Can. J. Forest Res.* 39, 264–284. doi: 10.1139/X08-104

Casson, N. J., Eimers, M. C., Watmough, S. A., and Richardson, M. C. (2019). The role of wetland coverage within the near-stream zone in predicting of seasonal stream export chemistry from forested headwater catchments. *Hydrol. Processes* 33, 1465–1475. doi: 10.1002/hyp.13413

Chorover, J., Derry, L. A., and Mcdowell, W. H. (2017). Concentration-discharge relations in the critical zone: implications for resolving critical zone structure, function, and evolution. *Water Resources Res.* 53, 8654–8659. doi: 10.1002/2017WR021111

Cincotta, M. M., Perdrial, J. N., Shavitz, A., Libenson, A., Landsman-Gerjoi, M., Perdrial, N., et al. (2019). Soil aggregates as a source of dissolved organic carbon to streams: an experimental study on the effect of solution chemistry on water extractable carbon. *Front. Environ. Sci.* 7:172. doi: 10.3389/fenvs.2019.00172

Clark, J. M., Bottrell, S. H., Evans, C. D., Monteith, D. T., Bartlett, R., Rose, R., et al. (2010). The importance of the relationship between scale and process in understanding long-term DOC dynamics. *Sci. Total Environ.* 408, 2768–2775. doi: 10.1016/j.scitotenv.2010.02.046

De Wit, H. A., Mulder, J., Hindar, A., and Hole, L. (2007). Long-term increase in dissolved organic carbon in streamwaters in norway is response to reduced acid deposition. *Environ. Sci. Technol.* 41, 7706–7713. doi: 10.1021/es070557f

Driscoll, C. T., Driscoll, K. M., Roy, K. M., and Mitchell, M. J. (2003). Chemical response of lakes in the adirondack region of New York to declines in acidic deposition. *Environ. Sci. Technol.* 37, 2036–2042. doi: 10.1021/es020924h

Duan, S., He, Y., Kaushal, S. S., Bianchi, T. S., Ward, N. D., and Guo, L. (2017). Impact of wetland decline on decreasing dissolved organic carbon concentrations along the mississippi river continuum. *Front. Marine Sci.* 3:280. doi: 10.3389/fmars.2016.00280

Dupas, R., Minaudo, C., and Abbott, B. W. (2019). Stability of spatial patterns in water chemistry across temperate ecoregions. *Environ. Res. Lett.* 14:074015. doi: 10.1088/1748-9326/ab24f4

Eimers, M. C., Watmough, S. A., and Buttle, J. M. (2008a). Long-term trends in dissolved organic carbon concentration: a cautionary note. *Biogeochemistry* 87, 71–81. doi: 10.1007/s10533-007-9168-1

Eimers, M. C., Watmough, S. A., Buttle, J. M., and Dillon, P. J. (2008b). Examination of the potential relationship between droughts, sulphate and dissolved organic carbon at a wetland-draining stream. *Global Change Biol.* 14, 938–948. doi: 10.1111/j.1365-2486.2007.01530.x

Evans, C., and Davies, T. D. (1998). Causes of concentration/discharge hysteresis and its potential as a tool for analysis of episode hydrochemistry. *Water Resources Res.* 34, 129–137. doi: 10.1029/97WR01881

Giardino, J. R., and Houser, C. (2015). *Principles and Dynamics of the Critical Zone.* Amsterdam: Elsevier Science.

Helsel, D. R., and Hirsch, R. M. (2002). *Statistical Methods in Water Resources.* Reston, VA: US Geological Survey.

Helsel, D. R., Hirsch, R. M., Ryberg, K. R., Archfield, S. A., and Gilroy, E. J. (2020). "Statistical methods in water resources," in *U.S. Geological Survey Techniques and Methods* (Reston, VA). Retrieved from: http://pubs.er.usgs.gov/publication/tm4A3

Hirsch, R. M., and Slack, J. R. (1984). A nonparametric trend test for seasonal data with serial dependence. *Water Resources Res.* 20, 727–732. doi: 10.1029/WR020i006p00727

Hornbeck, J. W., Bailey, S. W., Buso, D. C., and Shanley, J. B. (1997). Streamwater chemistry and nutrient budgets for forested watersheds in New England: variability and management implications. *Forest Ecol. Manage.* 93, 73–89. doi: 10.1016/S0378-1127(96)03937-0

Hruška, J., Krám, P., Mcdowell, W. H., and Oulehle, F. (2009). Increased dissolved organic carbon (DOC) in central european streams is driven by reductions in ionic strength rather than climate change or decreasing acidity. *Environ. Sci. Technol.* 43, 4320–4326. doi: 10.1021/es803645w

Huang, W., and Hall, S. J. (2017). Optimized high-throughput methods for quantifying iron biogeochemical dynamics in soil. *Geoderma* 306, 67–72. doi: 10.1016/j.geoderma.2017.07.013

Jentsch, A., Kreyling, J., and Beierkuhnlein, C. (2007). A new generation of climate-change experiments: events, not trends. *Front. Ecol. Environ.* 5, 365–374. doi: 10.1890/1540-9295(2007)5[365:ANGOCE]2.0.CO;2

Kahle, M., Kleber, M., and Jahn, R. (2003). Retention of dissolved organic matter by illitic soils and clay fractions: influence of mineral phase properties. *J. Plant Nutr. Soil Sci.* 166, 737–741. doi: 10.1002/jpln.200321125

Kang, H., Kwon, M. J., Kim, S., Lee, S., Jones, T. G., Johncock, A. C., et al. (2018). Biologically driven DOC release from peatlands during recovery from acidification. *Nat. Commun.* 9:3807. doi: 10.1038/s41467-018-06259-1

Kendall, K. A., Shanley, J., and Mcdonnell, J. (1999). A hydrometric and geochemical approach to test the transmissivity feedback hypothesis during snowmelt. *J. Hydrol.* 219, 188–205. doi: 10.1016/S0022-1694(99)00059-1

Kleber, M., and Johnson, M. G. (2010). "Chapter 3 - advances in understanding the molecular structure of soil organic matter: implications for interactions in the environment," in *Advances in Agronomy*, ed L. S. Donald (Amsterdam: Academic Press), 77–142.

Levin, S. A. (1992). The problem of pattern and scale in ecology: the Robert H. MacArthur award lecture. *Ecology* 73, 1943–1967. doi: 10.2307/1941447

Li, L., Maher, K., Navarre-Sitchler, A., Druhan, J., Meile, C., Lawrence, C., et al. (2017). Expanding the role of reactive transport models in critical zone processes. *Earth Sci. Rev.* 165, 280–301. doi: 10.1016/j.earscirev.2016.09.001

Li, L., Sullivan, P. L., Benettin, P., Cirpka, O. A., Bishop, K., Brantley, S. L., et al. (2021). Toward catchment hydro-biogeochemical theories. *WIREs Water* 8:e1495. doi: 10.1002/wat2.1495

Lin, H. S., Kogelmann, W., Walker, C., and Bruns, M. A. (2006). Soil moisture patterns in a forested catchment: a hydropedological perspective. *Geoderma* 131, 345–368. doi: 10.1016/j.geoderma.2005.03.013

Liu, L., Xu, Z.-X., and Huang, J.-X. (2012). Spatio-temporal variation and abrupt changes for major climate variables in the Taihu Basin, China. *Stochastic Environ. Res. Risk Assessment* 26, 777–791. doi: 10.1007/s00477-011-0547-8

Löfgren, S., and Zetterberg, T. J. S. O. T. T. E. (2011). Decreased DOC concentrations in soil water in forested areas in southern Sweden during 1987–2008. *Sci. Total Environ.* 409, 1916–1926. doi: 10.1016/j.scitotenv.2011.02.017

Lovett, G. M., Burns, D. A., Driscoll, C. T., Jenkins, J. C., Mitchell, M. J., Rustad, L., et al. (2007). Who needs environmental monitoring? *Front. Ecol. Environ.* 5, 253–260. doi: 10.1890/1540-9295(2007)5[253:WNEM]2.0.CO;2

Macdonald, S., April, R., and Keller, D. (2010). "Clay mineral weathering in shales and soils in the critical zone," in *Geochimica et Cosmochimica Acta: Pergamon* (Kidlington: Elsevier Science Ltd.), A652.

Magner, J. A., and Brooks, K. N. (2008). Integrating sentinel watershed-systems into the monitoring and assessment of Minnesota's (USA) waters quality. *Environ. Monit. Assess* 138, 149–158. doi: 10.1007/s10661-007-9752-9

Meals, D., Spooner, J., Dressing, S., and Harcum, J. (2011). *Statistical Analysis for Monotonic Trends, Tech Notes 6, November 2011. Developed for US Environmental Protection Agency by Tetra Tech, Inc.* Fairfax, VA.

Mikutta, R., Kleber, M., Torn, M. S., and Jahn, R. (2006). Stabilization of soil organic matter: association with minerals or chemical recalcitrance? *Biogeochemistry* 77, 25–56. doi: 10.1007/s10533-005-0712-6

Moatar, F., Abbott, B. W., Minaudo, C., Curie, F., and Pinay, G. (2017). Elemental properties, hydrology, and biology interact to shape concentration-discharge curves for carbon, nutrients, sediment, and major ions. *Water Resources Res.* 53, 1270–1287. doi: 10.1002/2016WR019635

Monteith, D. T., Stoddard, J. L., Evans, C. D., De Wit, H. A., Forsius, M., Høgåsen, T., et al. (2007). Dissolved organic carbon trends resulting from changes in atmospheric deposition chemistry. *Nature* 450, 537–540. doi: 10.1038/nature06316

Moyano, F. E., Manzoni, S., and Chenu, C. (2013). Responses of soil heterotrophic respiration to moisture availability: an exploration of processes and models. *Soil Biol. Biochem.* 59, 72–85. doi: 10.1016/j.soilbio.2013.01.002

NADP Program Office (2021). *National Atmospheric Deposition Program (NRSP-3).* Madison, WI: NADP Program Office, Wisconsin State Laboratory of Hygiene.

NSF (2018). *Bridging the Atom-to-Global Scale Gap*. Available online at: https://nsf2026imgallery.skild.com/entries/bridging-the-atom-to-global-scale-gap

Oni, S. K., Futter, M. N., Bishop, K., Kohler, S. J., Ottosson-Lofvenius, M., and Laudon, H. (2013). Long-term patterns in dissolved organic carbon, major elements and trace metals in boreal headwater catchments: trends, mechanisms and heterogeneity. *Biogeosciences* 10, 2315–2330. doi: 10.5194/bg-10-2315-2013

Perdrial, J., Brooks, P. D., Swetnam, T., Lohse, K. A., Rasmussen, C., Litvak, M., et al. (2018). A net ecosystem carbon budget for snow dominated forested headwater catchments: linking water and carbon fluxes to critical zone carbon storage. *Biogeochemistry* 138, 225–243. doi: 10.1007/s10533-018-0440-3

Perdrial, J. N., Mcintosh, J., Harpold, A., Brooks, P. D., Zapata-Rios, X., Ray, J., et al. (2014). Stream water carbon controls in seasonally snow-covered mountain catchments: impact of inter-annual variability of water fluxes, catchment aspect and seasonal processes. *Biogeochemistry* 118, 273–290. doi: 10.1007/s10533-013-9929-y

Perdrial, N., Perdrial, J. N., Delphin, J.-E., Elsass, F., and Liewig, N. (2010). Temporal and spatial monitoring of mobile nanoparticles in a vineyard soil: evidence of nanoaggregate formation. *Euro. J. Soil Sci.* 61, 456–468. doi: 10.1111/j.1365-2389.2010.01263.x

Pettitt, A. (1979). A non-parametric approach to the change-point problem. *J. R. Stat. Soc. Ser. C* 28, 126–135. doi: 10.2307/2346729

Preston, M., Eimers, C., and Watmough, S. (2011). Effect of moisture and temperature variation on DOC release from a peatland: conflicting results from laboratory, field and historical data analysis. *Sci. Total Environ.* 409, 1235–1242. doi: 10.1016/j.scitotenv.2010.12.027

Raymond, P. A., and Saiers, J. E. (2010). Event controlled DOC export from forested watersheds. *Biogeochemistry* 100, 197–209. doi: 10.1007/s10533-010-9416-7

Raymond, P. A., Saiers, J. E., and Sobczak, W. V. (2016). Hydrological and biogeochemical controls on watershed dissolved organic matter transport: pulse-shunt concept. *Ecology* 97, 5–16. doi: 10.1890/14-1684.1

Sanclements, M. D., Fernandez, I. J., Lee, R. H., Roberti, J. A., Adams, M. B., Rue, G. A., et al. (2018). Long-term experimental acidification drives watershed scale shift in dissolved organic matter composition and flux. *Environ. Sci. Technol.* 52, 2649–2657. doi: 10.1021/acs.est.7b04499

Schmidt, M. W., Torn, M. S., Abiven, S., Dittmar, T., Guggenberger, G., Janssens, I. A., et al. (2011). Persistence of soil organic matter as an ecosystem property. *Nature* 478, 49–56. doi: 10.1038/nature10386

Sebestyen, S. D., Boyer, E. W., Shanley, J. B., Kendall, C., Doctor, D. H., Aiken, G. R., et al. (2008). Sources, transformations, and hydrological processes that control stream nitrate and dissolved organic matter concentrations during snowmelt in an upland forest. *Water Resour. Res.* 44:W12410. doi: 10.1029/2008WR006983

Seneviratne, S. I., Nicholls, N., Easterling, D., Goodess, C. M., Kanae, S., Kossin, J., et al. (2012). "Changes in climate extremes and their impacts on the natural physical environment," in *Managing the Risks of Extreme Events and Disasters to Advance Climate Change Adaptation,* eds C. B. Field, V. Barros, T. F. Stocker, D. Qin, D. J. Dokken, K. L. Ebi, M. D. Mastrandrea, K. J. Mach, G.-K. Plattner, S. K. Allen, M. Tignor, and P. M. Midgley (Cambridge: Cambridge University Press).

Shanley, J. B., Krám, P., Hruška, J., and Bullen, T. D. (2004). "A biogeochemical comparison of two well-buffered catchments with contrasting histories of acid deposition," in *Biogeochemical Investigations of Terrestrial, Freshwater, and Wetland Ecosystems across the Globe*, eds R. K. Wieder, M. Novák, and M. A. Vile (Dordrecht: Springer), 325–342. doi: 10.1007/978-94-007-0952-2_23

Shanley, J. B., Sebestyen, S. D., Mcdonnell, J. J., Mcglynn, B. L., and Dunne, T. (2015). Water's way at sleepers river watershed – revisiting flow generation in a post-glacial landscape, Vermont USA. *Hydrol. Processes* 29, 3447–3459. doi: 10.1002/hyp.10377

Sivapalan, M. (2005). "Pattern, process and function: elements of a unified theory of hydrology at the catchment scale," in *Encyclopedia of Hydrological Sciences*, eds M. G. Anderson and J. J. McDonnell. doi: 10.1002/0470848944.hsa012

Six, J., Conant, R. T., Paul, E. A., and Paustian, K. (2002). Stabilization mechanisms of soil organic matter: implications for C-saturation of soils. *Plant Soil* 241, 155–176. doi: 10.1023/A:1016125726789

Steffen, W., Rockström, J., Richardson, K., Lenton, T. M., Folke, C., Liverman, D., et al. (2018). Trajectories of the earth system in the anthropocene. *Proc. Natl. Acad. Sci. U.S.A.* 115, 8252–8259. doi: 10.1073/pnas.1810141115

Sterle, G., Harpold, A., Perdrial, J. N., Li, L., Wen, H., Adler, T., et al. (2019). "CAMELS-CHEM: Developing a hydrochemistry dataset for large sample cross-catchment analyses," in *Poster presented at: Gordon Research Conference, Catchment Science: Interactions of Hydrology, Biology, and Geochemistry, Transcending the Uniqueness of Place in the Age of Big Data* (Andover, NH: Proctor Academy).

Van Loon, A. F., Gleeson, T., Clark, J., Van Dijk, A. I. J. M., Stahl, K., Hannaford, J., et al. (2016). Drought in the anthropocene. *Nat. Geosci.* 9, 89–91. doi: 10.1038/ngeo2646

Wen, H., Perdrial, J., Abbott, B. W., Bernal, S., Dupas, R., Godsey, S. E., et al. (2020). Temperature controls production but hydrology regulates export of dissolved organic carbon at the catchment scale. *Hydrol. Earth Syst. Sci.* 24, 945–966. doi: 10.5194/hess-24-945-2020

Wijngaard, J., Klein Tank, A., and Können, G. (2003). Homogeneity of 20th century European daily temperature and precipitation series. *Int. J. Climatol. J. R. Meteorol. Soc.* 23, 679–692. doi: 10.1002/joc.906

Wilson, H. F., Saiers, J. E., Raymond, P. A., and Sobczak, W. V. (2013). Hydrologic drivers and seasonality of dissolved organic carbon concentration, nitrogen content, bioavailability, and export in a forested New England stream. *Ecosystems* 16, 604–616. doi: 10.1007/s10021-013-9635-6

Zarnetske, J. P., Bouda, M., Abbott, B. W., Saiers, J., and Raymond, P. A. (2018). Generality of hydrologic transport limitation of watershed organic carbon flux across ecoregions of the United States. *Geophys. Res. Lett.* 45, 702–711. doi: 10.1029/2018GL080005

Zhi, W., Feng, D., Tsai, W. P., Sterle, G., Harpold, A., Shen, C., et al. (2021). From hydrometeorology to river water quality: can a deep learning model predict dissolved oxygen at the continental scale? *Environ. Sci. Technol.* 55, 2357–2368. doi: 10.1021/acs.est.0c06783

Zhi, W., Li, L., Dong, W., Brown, W., Kaye, J., Steefel, C., et al. (2019). Distinct source water chemistry shapes contrasting concentration-discharge patterns. *Water Resources Res* 55, 4233–4251. doi: 10.1029/2018WR024257

Zhi, W., Williams, K. H., Carroll, R. W. H., Brown, W., Dong, W., Kerins, D., et al. (2020). Significant stream chemistry response to temperature variations in a high-elevation mountain watershed. *Commun. Earth Environ.* 1:43. doi: 10.1038/s43247-020-00039-w

Disclaimer: Any opinions, findings, and conclusions or recommendations expressed in this material are those of the authors and do not necessarily reflect the views of the National Science Foundation or Vermont EPSCoR.

Conflict of Interest: The authors declare that the research was conducted in the absence of any commercial or financial relationships that could be construed as a potential conflict of interest.